Published by Empress Catherine II
Saint Petersburg Mining University

SINCE 1907

E-ISSN 2541-9404
ISSN 2411-3336

JOURNAL OF MINING INSTITUTE

ZAPISKI GORNOGO INSTITUTA

SCIENTIFIC JOURNAL

Volume 272
N 2 • 2025

INDEXING IN
SCOPUS (Q1)
WEB OF SCIENCE (ESCI)

WWW.PMI.SPMI.RU

Journal of Mining Institute

Empress Catherine II Saint Petersburg Mining University

The International Competence Center for Mining Engineering Education under the auspices of UNESCO

The scientific periodical “Journal of Mining Institute” is published since 1907 by Empress Catherine II Saint Petersburg Mining University – the first higher technical educational institution in Russia, founded in 1773 by the decree of Catherine II as the embodiment of the ideas of Peter I and M.V. Lomonosov on the training of engineers for the development of mining business.

The International Competence Center for Mining Engineering Education under the auspices of UNESCO operates on the basis of Empress Catherine II Saint Petersburg Mining University and contributes to active interaction of the Journal with the international scientific community.

The purpose of the Journal is to create an information space in which Russian and foreign scientists can present results of their theoretical and empirical research on the problems of the mining sector.

Published articles cover the issues of geology, geotechnical engineering and engineering geology, mining and petroleum engineering, mineral processing, energy, geoecology and life safety, economics of raw materials industries.

The Journal is indexed by Scopus (Q1), Web of Science Core Collection (ESCI), DOAJ Seal, RSCI, GeoRef, Google Scholar, RSCI. It is included in the White list of the Ministry of Education and Science of the Russian Federation.

The Journal is published six times a year. The average first decision time is one month.

Articles are published free of charge. Translation is provided by the author.

The cover shows an exhibit of the Mining Museum – trilobites in limestone. Leningrad Region. *Asaphus kowalewskii Lawrow* has a solid dorsal carapace and high stalked eyes; the body consists of eight segments with rounded lateral spines. Very long eyestalks look like submarine periscopes. This arrangement of the eyes is associated with the lifestyle of these trilobites – they dug into the sediment to a depth of the eyestalks length and led a discrete living. *Illaenus schmidti Nieszkowski* is characterized by a solid oval-shaped dorsal carapace, genal spines, and narrow sickle-shaped eyes, the body consists of ten segments. These trilobites made it possible to carry out a detailed division of the Lower-Middle Ordovician deposits of the Russian Platform into 18 trilobite zones.

The Mining Museum is the world’s third largest natural-science exposition, it contains more than 230 thousand exhibits, including precious metals and stones, unique collections of minerals, ores, rocks, paleontological remains, meteorites, a collection of models and prototypes of mining equipment, pieces of stone-cutting and jewelry art.

JOURNAL OF MINING INSTITUTE

ZAPISKI GORNOGO INSTITUTA

PEER-REVIEWED SCIENTIFIC JOURNAL

Published since 1907

ISSN 2411-3336
e-ISSN 2541-9404

Volume 272

ST. PETERSBURG • 2025

Journal founder: Empress Catherine II Saint Petersburg Mining University

Sections

• Geology • Geotechnical Engineering and Engineering Geology • Economic Geology • Energy

Registration Certificate PI N FS77-70453 dated 20.07.2017

PH License N 06517 dated 09.01.02

Editorial staff: Head of the Editorial Center V.L.Lebedev, Editors E.S.Dribinskaya, M.G.Khachirova, L.V.Nabieva, A.I.Yakovleva
Computer Design N.N.Sedykh, V.I.Kashirina, E.A.Golovinskaya

Passed for printing 25.04.2025. Format 60 × 84/8. Academic Publishing Division 41.
Circulation: 300 copies. Order 212. Printed by RIC of Empress Catherine II Saint Petersburg Mining University. Free sale price.

Mailing address of the Journal Founder and the Editorial Board
21st Linia, N 2, St. Petersburg, Russia, 199106
Phone: +7 (812) 328-8416; Fax +7 (812) 327-7359;
E-mail: pmi@spmi.ru Journal website: pmi.spmi.ru

CONTENTS

Geology

Geotechnical Engineering and Engineering Geology

Economic Geology

Energy

ISSN 2411-3336; e-ISSN 2541-9404

JOURNAL OF MINING INSTITUTE

Zapiski Gornogo instituta

Journal homepage: pmi.spmi.ru

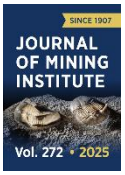

Research article

Geology

Geochemical characteristics of weathering crusts on the Dzhezhimparma Ridge and the Nemskaya Upland (South Timan)

Oksana V. Grakova✉, Nataliya Yu. Nikulova, Yuliya S. Simakova

Institute of Geology FRC Komi SC of the Ural Branch of the RAS, Syktyvkar, Russia

***How to cite this article*:** Grakova O.V., Nikulova N.Yu., Simakova Yu.S. Geochemical characteristics of weathering crusts on the Dzhezhimparma Ridge and the Nemskaya Upland (South Timan). Journal of Mining Institute. 2025. Vol. 272. N 16405, p. 3-15.

Abstract

Numerous local varieties of weathering crusts are known in the South Timan. They differ in their position in the section, type of weathering products, substrates, and occurrence. The aim of the research is to identify patterns in the distribution of rock-forming, rare and rare earth elements and the composition of clay minerals in clay formations of the weathering crusts. The main task is to describe the occurrence and geochemical features that enable determining the genetic type and formation conditions of weathering crusts. The paper presents the results of a study of the distribution of petrogenic, rare earth, rare elements, and clay minerals in weathering crust of different ages, genetic types and occurrence conditions on the Dzhezhimparma Ridge and the Nemskaya Upland in the South Timan. We found that hydromica-kaolinite-type weathering crust is developed after the Late Riphean Dzhezhim Fm. rocks in the basement-cover contact zone on the Dzhezhimparma Upland, and the layer of fine-grained rock at the base of the Devonian section previously considered a weathering crust was formed as a result of mechanical destruction of the Devonian sandstones during movement in the thrust zone. In the Vadyavozh quarry located on the Nemskaya Upland, we studied and described the formations of Mesozoic-Cenozoic areal and linear weathering crusts after the Late Riphean Dzhezhim Fm. rocks. We found that micaceous siltstones in the siltstone-sandstone strata of the Dzhezhim Fm. are associated with the Riphean stage of crust formation and are composed of weathering crust material redeposited in the epicontinental basin.

Keywords

weathering crust; Dzhezhim Formation; suitesandstones; chemical composition; detrital material; sedimentation conditions; South Timan

Funding

The work was carried out under the State assignment for research of the Institute of Geology FRC Komi SC of the Ural Branch of the RAS: “Deep structure, geodynamic evolution, interaction of geospheres, magmatism, metamorphism, and isotope geochronology of the Timan-Northern Urals segment of the lithosphere”, 122040600012-2; “Sedimentary formations: matter, sedimentation, lithogenesis, geochemistry, lithogenesis indicators, sedimentation reconstruction”, 122040600013-9; “Fundamental issues of mineralogy and mineral formation, minerals as indicators of petro- and ore genesis, mineralogy of ore regions and deposits of the Timan-Northern Urals region and Arctic areas”, 122040600009-2.

Received: 11.03.2024 ***Accepted: 07.11.2024*** ***Online: 06.03.2025*** ***Published: 25.04.2025***

Introduction

Commercial deposits of bauxite, titanium ores, gold and diamond occurrences, etc. are associated with weathering crusts in Timan [1-3]. In the Northern Urals, the redistribution and accumulation of ore components, in particular nickel, occurred in weathering crusts of hyperbasites of the Serov-Mauk ophiolite belt [4]. The enrichment of zircon in rare metal and rare earth elements (REE) from the granitoids of the Chukotka plutonic belt [5] and the formation of REE minerals in the Lower Proterozoic metamorphic schists of the Svalbard Archipelago [6] are associated with endogenous processes and hydrothermal alterations. Ancient Early Riphean weathering crusts (secondary quartzites) in the southern part of the Baltic (Fennoscandian) Shield preceded the rapakivi granite formation, 1.65 Ga [7].

In plain South Timan with a developed Quaternary cover, the Paleozoic and Mesozoic-Cenozoic weathering crusts are penetrated by coring boreholes[1,2,3]. They are recorded on the day surface only within the few projections of the Riphean basement (Fig.1, *a*), where their distribution area coincides with the outcrops of arkosic sandstones of the Upper Riphean Dzhezhim Fm. [8, 9]. It should be noted that recent studies report on the discovery of a macrofossil assemblage in the Dzhezhim Fm. rocks, which may attribute the age of the Dzhezhim Fm. to Late Vendian [10-12]. However, since the Interdepartmental Stratigraphic Committee has not made any changes to the current stratigraphic chart, we use the stratigraphic subdivision adopted in the existing geological maps [13, 14].

In the South Timan, numerous local varieties of weathering crusts found by drilling during geological survey differ in their position in the section, type of weathering products, substrates, and occurrences. For example, residual weathering crusts are developed after the substrate of terrigenous Late Riphean and Vendian deposits. They have either areal or linear distribution. Weathering crusts redeposited after carbonate rocks of the Yshkemes and Vapol Fms. are present in the composition of clayey-sandy rocks in karst depressions of the pre-Paleozoic topography and basal horizons of the Asyvvozh and Izyamel Fms. Meso-Cenozoic weathering crusts after the Dzhezhim Fm. substrate are represented by both areal (Vadyavozh and Dzhezhim quarries) and linear ones, associated with the Late Jurassic fault tectonics (Vadyavozh quarry). The discovery in 1998 of diamond crystals in the gritstone-sandstone strata of the Devonian section base in the immediate vicinity of weathering crusts exposed to the day surface in the Asyvvozh[1] quarry area in the basement-cover contact zone predetermined the further studies conducted in South Timan [15-18]. The weathering crusts and the basal part of the Devonian section were considered as promising targets in the search for diamond placers of the so-called Vishera type [19].

Over twenty years that passed since the recent studies, the technical capabilities and instrumentation have advanced, allowing the study of targets promising for placer deposits and clay raw materials at a qualitatively new level. New artificial outcrops are made in the operating quarries, penetrating the weathering crusts. Geochemical study of weathering crusts is necessary for paleogeographical reconstructions, unveiling the development history and sedimentation patterns in a poorly studied potentially diamond-bearing region, as well as clarifying the prospects for clay raw materials.

The main objective of the study is to describe the geochemical features, distribution of rock-forming, rare and rare earth elements, and the mineral composition of clay rocks considered to be weathering crust formations.

Research methods and materials

Samples of weathering crusts (11 pcs.) and substrate rocks (4 pcs.) were collected in artificial outcrops of the Asyvvozh and Dzhezhim quarries on the Dzhezhimparma and Vadyavozh ridges of the Nemskaya Upland (Fig.1, *a*). All analytical work was carried out at the Geoscience Collective Use Centre of the Institute of Geology FRC Komi SC of the Ural Branch of the RAS. The rock-forming oxide contents were determined by the traditional gravimetric analysis in the Laboratory of Chemistry of Mineral Raw Materials, maintaining the metrological standards (Conclusion N 774). The contents of rare and rare earth elements were determined on an Agilent 7700x ICP-MS. To transfer the sample into solution, the multi-acid digestion (a mixture of acids in the ratio HNO_3:HF:HCl = 1:5:2) under microwave heating conditions was used. Digestion was carried out in a Sineo MDS-10 microwave digestion system.

[1] Tereshko V.V., Kirillin S.V., Kazantseva G.Ya. et al. Geological survey at 1:50,000 scale in adjacent sheets R-40-73-C,D; R-40-74-C; R-40-85-B; R-40-86-A. Syktyvkar, 1991.

[2] Kulbakova F.A., Shametko V.G., Torlopova S.M. et al. Prospecting for diamond placers of the Vishera type in the South Timan and southwestern Timan region. Ukhta, 2001.

[3] Kirillin S.V., Zharkov V.A., Shumilov A.V. et al. Report on geological survey at 1:200,000 scale in adjacent sheets P-40-XX, P-40-XXVI (Nemskaya area). Syktyvkar, 2002.

The phase composition of rocks was determined using X-ray diffraction analysis of non-oriented and oriented samples subjected to standard diagnostic treatments, by a Haoyuan DX-2700BH X-ray diffractometer, CuKα radiation, 40 kV at 30 mA, scanning interval at 2θ – 2-70°, scanning step at 2θ – 0.05°, shooting speed – 1 °/min. Semi-quantitative X-ray diffraction analysis of the samples was performed in Profex software.

Brief description of the geological position

The study area is in the southeast of the Timan folded-block structure and is the northeastern part of the Dzhezhim-Ksenofontov megaswell, which formed due to the reverse-thrust displacements and progradation of large block-slices in the Early Jurassic [10]. Such blocks, representing basement projections in which rocks are brought to the surface along a series of thrusts, are the Dzhezhimparma and Vadyavozh anticlinal structures.

The Asyvvozh (I in Fig.1, *a*) and Dzhezhim (II in Fig.1, *a*) quarries are on the Dzhezhimparma ridge, coinciding with the Dzhezhimparma anticlinal structure [13]. In the Asyvvozh quarry (61°47'12" N, 54°06'35" E), weathering crusts are found in the contact zone of the Riphean and

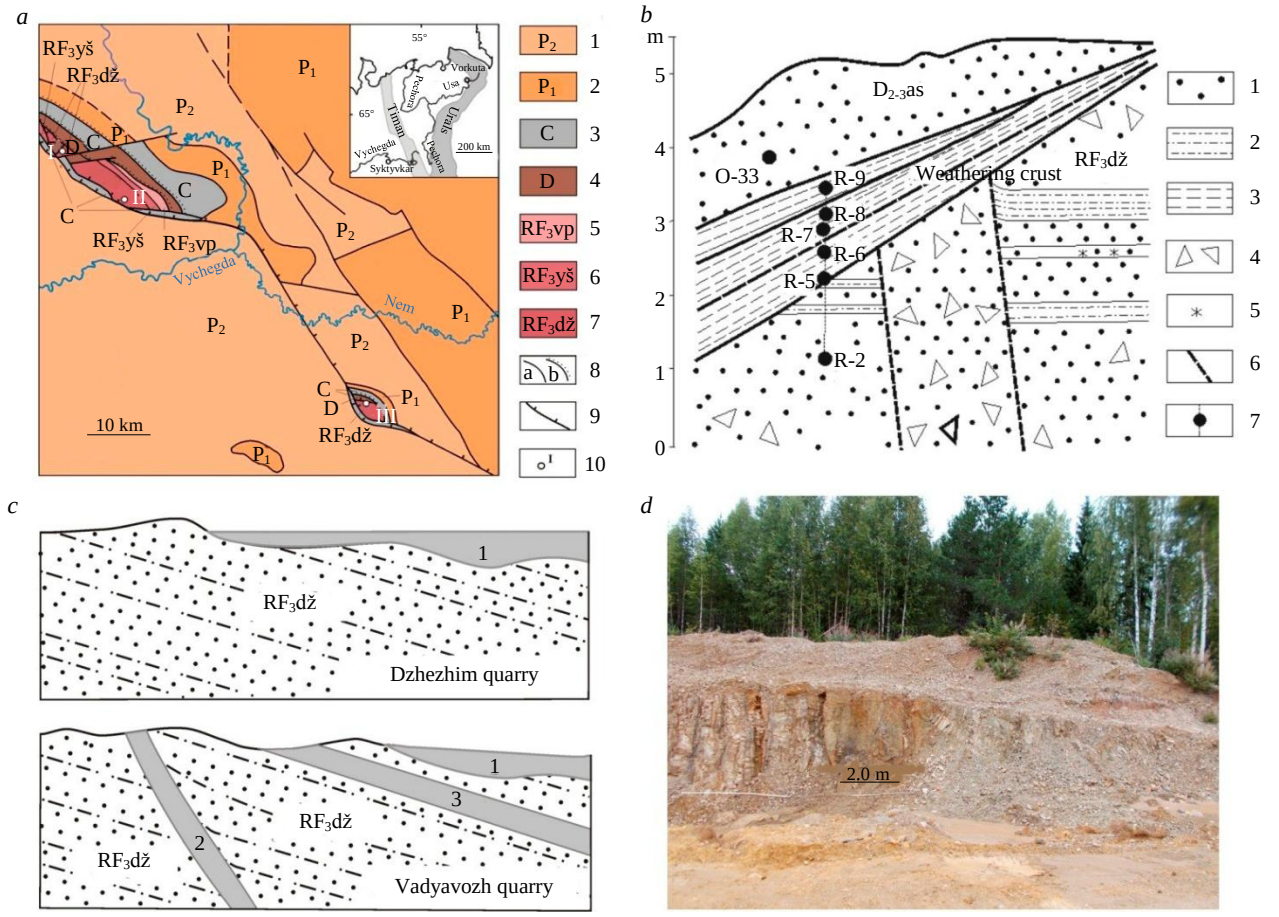

Fig.1. Schematic geological map according to [6]: *a* – 1, 2 – Permian (1 – lower series – limestones, dolomites, siltstones, sandstones, gypsums, 2 – upper series – clays, limestones, sandstones); 3 – Carboniferous – limestones, dolomites, clayey limestones, clays; 4 – Devonian, middle-upper series – gritstones, sandstones, conglomerates, siltstones; 5-7 – Riphean sub-eotheme (5 – Vapol Fm. – dolomites with sandstone, mudstone, and chert interlayers, 6 – Yshkemes Fm. – dolomites, siltstones, mudstones, 7 – Dzhezhim Fm. – sandstones, siltstones, gritstones); 8 – geological boundaries – conformable (a), unconformable (b); 9 – thrust; 10 – studied sections in quarries (I – Asyvvozh, II – Dzhezhim, III – Vadyavozh); *b* – structural diagram of the section of the contact zone of the Riphean and Devonian deposits in the Asyvvozh quarry: 1 – sandstone; 2 – silty sandstone; 3 – clay; 4 – large-block debris; 5 – ferrugination; 6 – faults; 7 – section line and sampling points; *c* – scheme of the relationship between the Dzhezhim Fm. deposits and weathering crust in the Dzhezhim and Vadyavozh quarries: 1 – Mesozoic-Cenozoic areal; 2 – linear; 3 – weathering crust in the Riphean section; *d* – linear weathering crust after the Dzhezhim Fm. rocks in the Vadyavozh quarry

Paleozoic deposits (Fig.1, *a*, *b*). The Late Riphean Dzhezhim Fm. (RF_3dž) represented by feldspar-quartz sandstones with subordinate interlayers of siltstones and gritstones, lie with an azimuth of 190° SSW and a dip angle of 20-25°. In the contact zone, the Dzhezhim Fm. rocks are disintegrated to a thickness of approximately 10-12 cm and consist of small splintered fragments. The Middle-Late Devonian Asyvvozh Fm. is represented by quartz sandstones with conglomerate, gritstone, siltstone, and clay lenses (dipping azimuth 310° NW and angle 15°). The Precambrian and Paleozoic parts of the section are separated by a wedging-out clay layer, which lies on different layers of the Riphean siltstone-sandstone strata and has a three-membered structure (Fig.1, *b*). In the lower part there is a bed of lilac-pink clayey thin horizontally layered rock with a maximum thickness of about 40 cm (Fig.1, *b*, samples R-5, 6). The bulk clay contains sand-sized grains and rare angular fragments of sandstones, shales, and felsic igneous rocks to 3 cm in size. Above lies a layer (0.5-0.6 m) of pinkish-grey clayey rock similar in structure and texture (Fig.1, *b*, samples R-7 and O-33). It contains single fragments of the above-mentioned rocks to 1.5 cm in size. Directly beneath the base of the Devonian sandstones is a wedging-out layer of greyish-beige sandy-clayey rock to 0.5 m thick (Fig.1, *b*, *c*, sample R-8). The bulk of this rock contains unevenly distributed coarse sand-sized grains of quartz, isolated fragments of carbonaceous shales and quartz sandstones to 1.5 cm in size. The rock has an obvious external resemblance to the overlying sandstones, lies unconformably on the underlying clays and, in our opinion, could be formed as a result of mechanical destruction of the Devonian rocks. In the geological survey report[4], clay rocks in this section are classified as linear weathering crusts associated with faults developed after both the Riphean and Devonian rocks. Doubts about this interpretation of the clay rock origin arise from a detailed study of the clay layer structure and its relationship with the underlying rocks (Fig.1, *b*), since hypergene transformations along faults do not cause mechanical redistribution of detrital material and the emergence of thin-layered deposits that lie unconformably on the underlying rocks.

Mesozoic-Cenozoic weathering crusts of the residual areal type, which, according to the geological survey data [14], practically coincide with the Dzhezhim Fm. outcrops of the Upper Riphean, are exposed by the Dzhezhim and Vadyavozh quarries (Fig.1, *a*). In the Dzhezhim quarry (61°42'55" N, 54°21'80" E), the Dzhezhim Fm. is represented by cherry-brown feldspar-quartz sandstones with lenses and interlayers of small-pebble polymictic conglomerates and greyish-brown siltstones. The weathering crust developed after various layers of the Dzhezhim Fm. is expressed by pinkish-grey sandy clay with rare small (to 1.0 cm) fragments of underlying rocks (Fig.1, *d*). The Late Riphean Dzhezhim Fm. exposed by the Vadyavozh quarry (61°27'47" N, 55°49'33" E) is composed of feldspar-quartz sandstones with gritstone, siltstone, and shale interlayers. The Mesozoic-Cenozoic areal residual weathering crust deposits, a few metres thick, in the lower part being the gruss of the original sandstones, siltstones, and shales cemented with clay material, are gradually replaced by a pinkish-yellowish clay mass with an admixture of sand and fragments (to 1.0 cm) of sandstones, siltstones, and shales (Fig.1, *d*). The fact that these crusts were not subject to redeposition is evidenced by the sometimes recognizable relics of the substrate structures[5]. The weathering crusts are covered by a soil and vegetation layer.

Most of the areal weathering crust layer in the Dzhezhim and Vadyavozh quarries was destroyed by previous geological prospecting and modern quarry stone mining. Therefore, the undisturbed weathering crusts are preserved only as individual small outcrops and blocks. The linear weathering crusts that we discovered in the southern wall of the quarry, outside the areal weathering crust zone, where the Riphean rocks are directly overlain by the soil-vegetation layer, are confined to a fault in the Riphean rocks and are represented by a loose olive-brown gruss-sand-clay mixture (Fig.1, *c*). The terrigenous strata of the

[4] Tereshko V.V., Kirillin S.V., Kazantseva G.Ya. et al. Geological survey at 1:50,000 scale in adjacent sheets R-40-73-C,D; R-40-74-C; R-40-85-B; R-40-86-A. Syktyvkar, 1991.

[5] Kirillin S.V., Zharkov V.A., Shumilov A.V. et al. Report on geological survey at 1:200,000 scale in adjacent sheets P-40-XX, P-40-XXVI (Nemskaya area). Syktyvkar, 2002.

Dzhezhim Fm. contains interlayers of grey micaceous siltstones that differ significantly from the surrounding rocks (Fig.1, *d*). Analysis of our previous data on the composition and formation conditions of the terrigenous strata in the Vadyavozh quarry [20] allows us to assume the presence of a significant amount of the Riphean intraformational weathering crust material in the fine-grained rocks.

Geochemical characteristics of rocks

The contents of the main rock-forming oxides, lithochemical modules and indicator ratios used to characterize the deposits and reconstruct their formation conditions are given in Table 1. The studied rocks have low alkali content with a noticeable predominance of potassium over sodium and are arkoses (Table 1, Fig.2, *a*) [21]. In the $\log(Fe_2O_{3tot}/K_2O) - \log(SiO_2/Al_2O_3)$ diagram [22], the figurative points of the rocks from the Asyvvozh and Vadyavozh quarries are in the arkose and subarkose fields, and the Mesozoic-Cenozoic weathering crust points from the Asyvvozh and Dzhezhim quarries fell into the wacke field (Fig.2, *b*).

Table 1

Chemical composition of rocks (wt.%), indicator ratios, coefficients and modules

Quarry	Asyvvozh							Vadyavozh					Dzhezhim		
Age	RF	Pre-Middle Devonian				D		RF	MZ-KZ		RF (?)		RF	MZ-KZ	
Rock	Sandstone	Redeposited weathering crust				Sandstone	Tectonic clay	Sandstone	Areal weathering crust	Linear weathering crust	Areal weathering crust		Sandstone	Areal weathering crust	
Elements, modules	R-2	R-5	R-6	R-7	R-8	O-33	R-9	V 9.4	V 14.4	V 9.10	V 14.3	V 9.3	Dzh 1	Dzh 2	Dzh 3
SiO_2	86.2	84.36	75.60	80.64	81.12	86.79	83.52	93.74	86.48	80.48	62.56	62.22	89.80	62.14	69.40
TiO_2	0.23	0.22	0.50	0.43	0.31	0.34	0.44	0.11	0.26	0.38	0.83	0.71	0.09	0.91	0.62
Al_2O_3	6.57	7.55	11.43	9.50	10.03	7.94	9.04	2.15	6.03	8.90	19.75	17.28	3.59	16.43	13.56
Fe_2O_3	0.42	0.43	2.47	1.14	0.42	0.39	0.47	0.53	1.49	1.78	1.15	3.07	2.22	5.14	3.57
FeO	0.56	0.24	0.24	0.24	0.24	0.14	0.24	1.52	1.34	0.85	0.62	1.68	1.24	0.91	0.88
MnO	0.01	0.01	0.01	0.01	0.01	0.01	0.01	0.02	0.01	0.06	0.01	0.02	0.01	0.03	0.02
MgO	0.26	0.30	0.62	0.46	0.62	0.22	0.46	0.70	0.14	1.02	2.15	3.23	0.15	2.28	1.23
CaO	0.12	0.40	0.40	0.02	0.20	0.26	0.40	0.12	0.23	0.47	0.35	0.47	0.23	0.64	0.70
Na_2O	0.24	0.25	0.34	0.28	0.28	0.07	0.09	0.03	0.16	1.35	0.40	0.32	0.56	1.48	2.67
K_2O	4.19	4.17	5.14	4.87	4.09	1.39	1.06	0.26	1.52	1.52	6.15	5.21	2.12	4.75	3.67
P_2O_5	0.03	0.05	0.05	0.03	0.04	0.02	0.03	0.05	0.04	0.16	0.05	0.17	0.04	0.13	0.12
LOI	2.03	1.91	2.97	2.11	2.59	2.41	2.41	0.87	2.04	3.01	4.94	5.43	0.67	5.22	3.61
Total	100.90	99.89	99.76	99.73	99.90	99.98	98.20	100.00	99.70	100.00	99.00	99.81	100.70	100.06	100.05
$\log(Na_2O/K_2O)$	–1.24	–1.22	–1.18	–1.24	–1.16	–1.30	–1.07	–0.94	–0.98	–0.05	–1.19	–1.21	–0.58	–0.51	–0.14
$\log(SiO_2/Al_2O_3)$	1.12	1.05	0.82	0.93	0.91	1.04	0.97	1.64	1.16	0.96	0.50	0.56	1.40	0.58	0.71
$\log(Fe_2O_{3tot}/K_2O)$	–1.00	–0.99	–0.32	–0.63	–0.99	–0.55	–0.35	0.31	–0.01	0.07	–0.73	–0.23	0.02	0.03	–0.01
F1	–3.44	–3.19	–3.53	–3.60	–3.16	–3.71	–3.47	–3.59	–3.51	–1.72	–2.51	–1.68	–3.41	–2.16	–1.12
F2	–4.26	–3.55	–4.01	–3.93	–2.78	0.65	2.22	2.49	–1.11	2.17	–2.59	–0.63	–2.93	–0.29	–0.78
F3	16.13	13.64	8.66	12.04	8.96	0.60	–1.23	–4.10	–1.53	–0.07	5.85	3.70	5.39	3.03	3.52
F4	4.58	3.98	2.51	4.12	3.43	0.56	0.83	5.01	–3.19	–0.08	4.22	4.46	–5.95	2.24	–0.13
K_2O/Na_2O	17.46	16.68	15.12	17.39	14.61	19.86	11.78	8.67	9.50	1.13	15.38	16.28	3.79	3.21	1.37
SiO_2/Al_2O_3	13.12	11.17	6.61	8.49	8.09	10.93	9.24	43.60	14.34	9.04	3.17	3.60	25.01	3.78	5.12
Al_2O_3/SiO_2	0.08	0.09	0.15	0.12	0.12	0.09	0.11	0.02	0.07	0.11	0.32	0.28	0.04	0.26	0.20
CIA	56.01	57.13	62.47	62.17	65.59	79.11	81.69	79.63	72.12	65.31	71.25	71.06	49.65	65.24	58.42
CIW	91.46	86.88	89.87	95.03	92.40	93.10	91.16	88.92	89.84	74.31	93.84	92.59	72.82	82.02	70.52

Journal of Mining Institute. 2025. Vol. 272. P. 3-15

End of Table 1

Quarry	Asyvvozh							Vadyavozh					Dzhezhim		
Age	RF	Pre-Middle Devonian				D		RF	MZ-KZ		RF (?)		RF	MZ-KZ	
Rock	Sandstone	Redeposited weathering crust				Sandstone	Tectonic clay	Sandstone	Areal weathering crust	Linear weathering crust	Areal weathering crust		Sandstone	Areal weathering crust	
Elements, modules	R-2	R-5	R-6	R-7	R-8	O-33	R-9	V 9.4	V 14.4	V 9.10	V 14.3	V 9.3	Dzh 1	Dzh 2	Dzh 3
ICV	0.97	0.93	0.93	0.87	0.75	0.42	0.45	1.31	0.66	1.01	0.77	1.05	1.55	1.16	1.17
K_2O/Al_2O_3	0.64	0.55	0.45	0.51	0.41	0.18	0.12	0.12	0.25	0.17	0.31	0.30	0.59	0.29	0.27
Na_2O+K_2O	4.43	4.42	5.48	5.15	4.37	1.46	1.15	0.29	1.68	2.87	6.55	5.53	2.68	6.23	6.34
HM	0.09	0.10	0.19	0.14	0.14	0.10	0.12	0.05	0.11	0.15	0.36	0.37	0.08	0.38	0.27
SPM	0.67	0.59	0.48	0.54	0.44	0.18	0.13	0.13	0.28	0.32	0.33	0.32	0.75	0.38	0.47

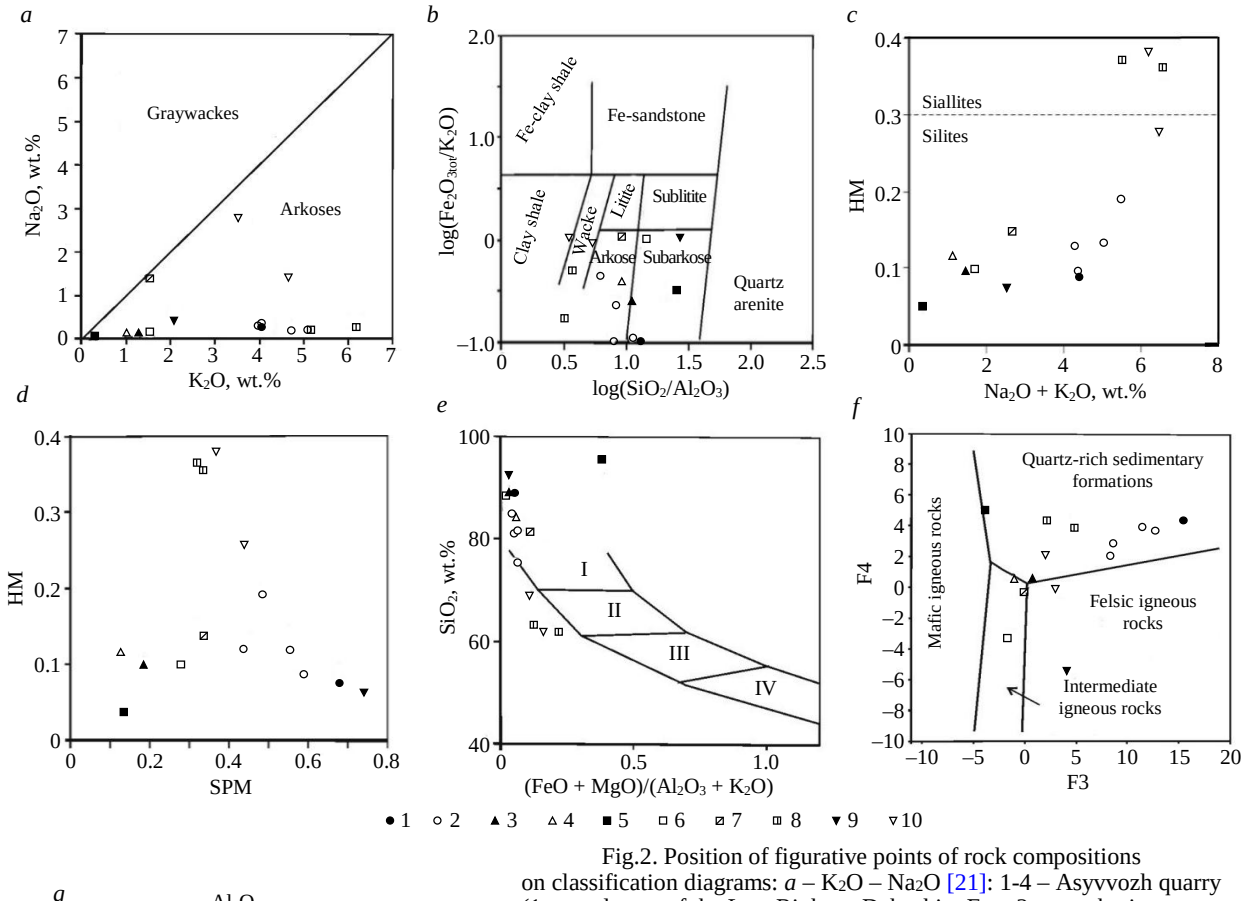

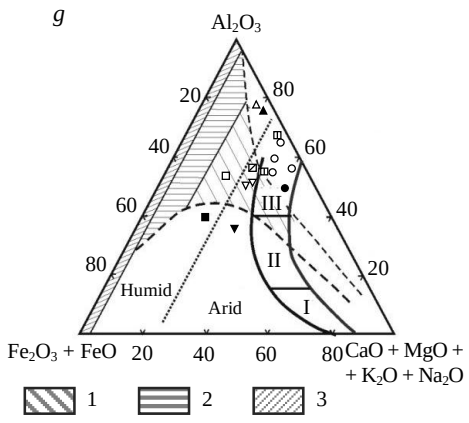

Fig.2. Position of figurative points of rock compositions on classification diagrams: *a* – K_2O – Na_2O [21]: 1-4 – Asyvvozh quarry (1 – sandstone of the Late Riphean Dzhezhim Fm., 2 – weathering crusts after the Dzhezhim Fm. rocks, 3 – sandstone of the Middle-Late Devonian Asyvvozh Fm., 4 – tectonic clay (?); 5-7 –Vadyavozh quarry (5 – sandstone of the Late Riphean Dzhezhim Fm., 6 – areal weathering crusts after the Dzhezhim Fm. rocks, 7 – linear weathering crusts after the Dzhezhim Fm. rocks); 8 – ancient (Riphean) weathering crusts; 9, 10 – Dzhezhim quarry (9 – sandstone of the Late Riphean Dzhezhim Fm., 10 – areal weathering crusts after the Dzhezhim Fm. rocks); *b* – $\log(SiO_2/Al_2O_3)$ – $\log(Fe_2O_{3tot}/K_2O)$ [22]; *c* – Na_2O+K_2O – HM; *d* – SPM – HM [23]; *e* – $(FeO + MgO)/(Al_2O_3 + K_2O)$ – SiO_2: I – rhyolites, granites, II – dacites, granodiorites, III – andesites, diorites, IV – basalts, gabbro [24]; *f* – F3 – F4 [25]; *g* – $Fe_2O_3 + FeO$ – Al_2O_3 – $CaO + MgO + K_2O + Na_2O$ [26]: 1-3 – correlation fields of weathering products (1 – initial, zone of bleaching and mechanical disintegration, 2 – clayey, clay products of hypergene transformation of rocks, 3 – final, kaolin and bauxite clays, bauxites, iron ores); I-III – correlation fields of igneous rocks (I – ultramafic, II – mafic, III – intermediate and felsic)

After the hydrolyzate module (HM) values in accordance with the classification by Ya.E.Yudovich and M.P.Ketris [24], the substrate rocks and most of the clay formations of the weathering crust are silites, and the three points corresponding to the samples distinguished by the maximum contents of hydrolyzate elements are siallites – rocks whose alumina content is due to the presence of kaolinite (Fig.2, *c*). For most of the studied samples, the sodium-potassium module (SPM) value exceeds 0.3 (Fig.2, *d*), which is a criterion [23] for the presence of unaltered potassium feldspar in the rocks. The Riphean sandstones from the Vadyavozh quarry and the linear weathering crust formations, Devonian sandstones and underlying clays, located in the subarkose field on the classification diagram (Fig.2, *a*, *b*) are distinguished by low SPM values (Fig.2, *d*).

In the $(FeO+MgO)/(Al_2O_3+K_2O)$ – SiO_2 diagram [24] showing fragments of various types of igneous rocks in the sediment, most of the figurative points were found to be near the felsic rocks region, and the points of the Mesozoic-Cenozoic areal weathering crusts from the Vadyavozh and Dzhezhim quarries are observed near the field of intermediate rocks (Fig.2, *e*). In the factor diagram F3 – F4 [25], which considers the ratio of rock-forming oxides, the figurative points corresponding to these samples also gravitate toward the field of igneous rocks of intermediate composition (Fig.2, *f*). The Devonian sandstones and underlying clays fell into the field formed by igneous rocks of felsic composition (Fig.2, *f*). The position of most of the figurative points in the diagram of weathering products chemistry [26] allows us to assume that most of the studied rocks contain detrital material inherited from felsic and intermediate igneous rocks that were weakly weathered in arid climate conditions (Fig.2, *g*).

The chemical index of alteration (CIA) values [27] for the Devonian sandstones and underlying clays, the Mesozoic-Cenozoic and Riphean areal weathering crusts in the Vadyavozh quarry slightly exceed 70 and correspond to warm climate conditions in the erosion area (Table 1). A wide range of the index of compositional variability (ICV) values [28] suggests the presence of detrital material of varying maturity in the rock [22]. For most of the studied samples, the chemical index of weathering (CIW) [21] in the range of 82-95 corresponds to rocks containing weathering crust material (Fig.3, *a*). In the K/Al – Mg/Al diagram [29], the points of the Riphean sandstones and weathering crusts are in the area of rocks dominated by illite and potassium feldspar. The points of the Devonian sandstones and underlying clays are near the kaolinite trend (Fig.3, *b*).

According to X-ray diffractometric analysis, the approximate quantitative content of minerals for the studied samples was, %: muscovite (illite) ~ 6-25, chlorite ~ 1-3, smectite ~ 0-15, feldspars ~ 0-10, quartz ~ 20-70. The composition and percentage ratio of finely dispersed component minerals in the samples of different rocks vary. In all the studied samples, the constantly present layered silicate is muscovite of the ordered polytypic structure $2M_1$. A smectite-like mineral (mixed-layer swelling phase) was found in the linear weathering crust samples in the Vadyavozh quarry (Fig.4, *a*, *b*). Disordered swelling mixed-layer phases of the illite/smectite and chlorite/smectite types are observed in

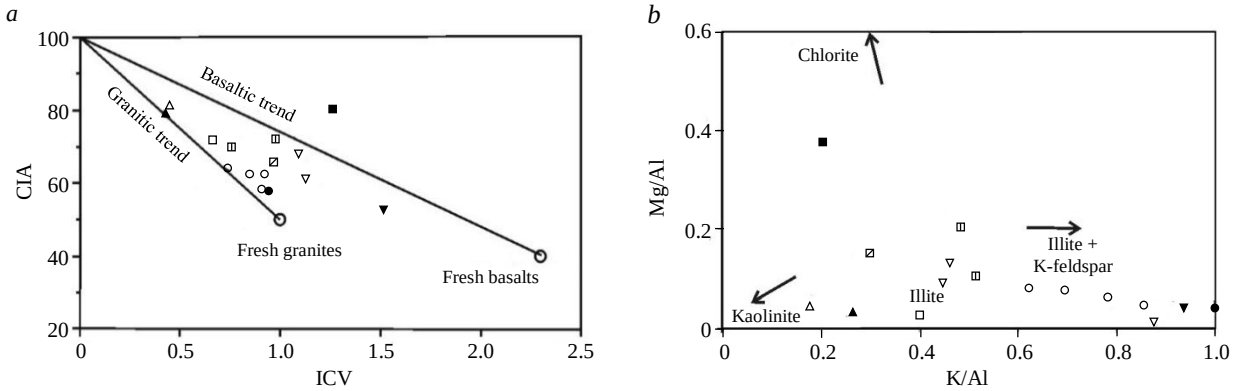

Fig.3. Position of figurative points of rock compositions in diagrams:
a – ICV – CIA [30]; *b* – K/Al – Mg/Al [29]. See Fig.2 for legend

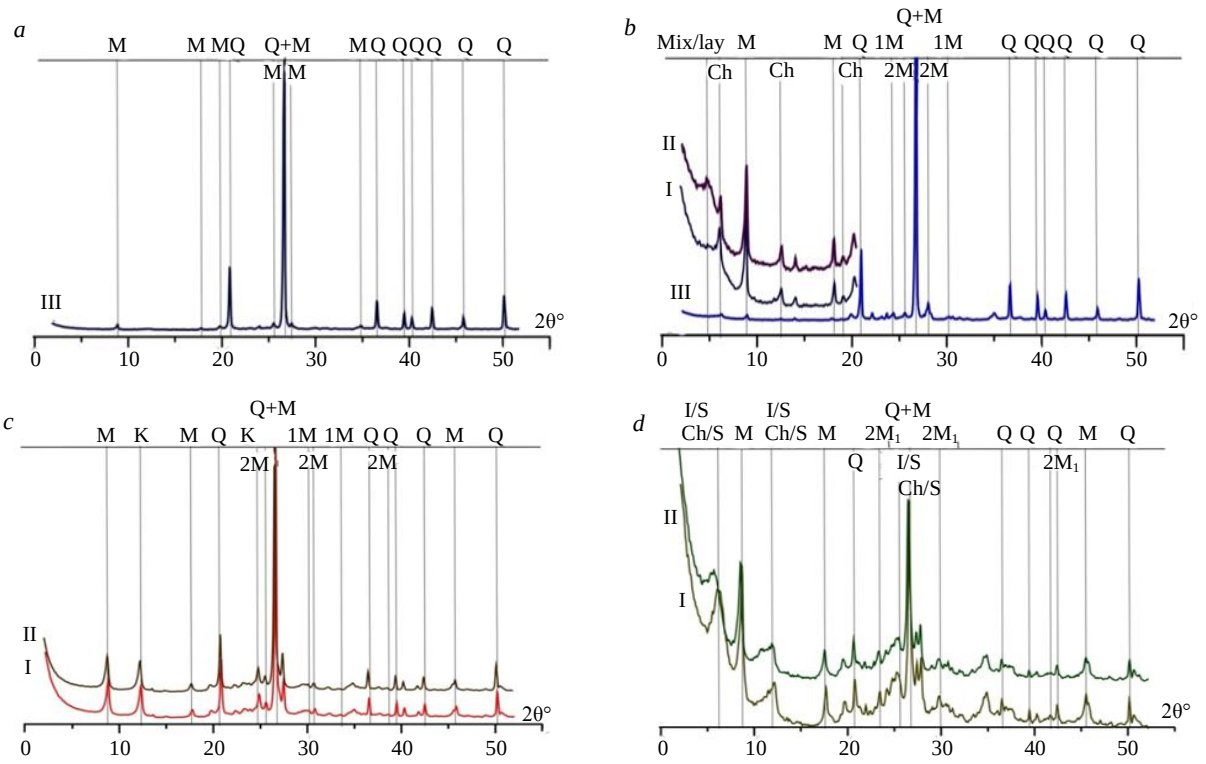

Fig.4. Diffraction patterns of rocks from samples V 14.4 (*a*), V 9.10 (*b*), R-8 (c), Dzh 2 (*d*)

I – oriented, air-dry; II – oriented, saturated with ethylene glycol; III – non-oriented;
M – muscovite ($2M_1$ and 1M – polytypic structures); Ch – chlorite; Mix/lay – swelling smectite-like mixed-layer phase;
I/S and Ch/S – disordered mixed-layer illite/smectite and chlorite/smectite formations; K – kaolinite; Q – quartz
See sample numbers in Table 1

the weathering crusts from the Dzhezhim quarry (Fig.4, *d*). Layered silicates from clays underlying the Devonian sandstones in the Asyvvozh quarry are represented by muscovite and kaolinite (Fig.4, *c*).

The REE and rare element contents and their ratios used to construct the diagrams and compare them with the Riphean and Devonian rocks are given in Table 2. The total contents of REE in the studied rocks differ insignificantly and are close to the post-Archean Australian shale (PAAS). The highest amounts of REE (263 g/t), including Σ LREE (229 g/t), are observed in sample V 9.3 from the linear weathering crust in the Vadyavozh quarry. The graphs of the REE distribution in sandstones and clay formations of the Asyvvozh quarry are similar to PAAS in the slope of the curves and the europium minimum intensity (Fig.5) [31]. Samples of clayey rocks from the base of the Devonian section (R-9) and Devonian sandstones (O-33) differ from the Riphean sandstones and associated clays in a higher LREE content (Table 2, Fig.5, *a*) and the absence of a europium minimum (Eu/Eu* 0.90 and 0.92, respectively). The graphs of REE distribution in clayey formations of the Mesozoic-Cenozoic areal weathering crusts from the Dzhezhim quarry are distinguished by a gentle slope in the LREE region [32] compared to the original Riphean sandstones and PAAS and a weak expressed europium minimum (Fig.5, *c*). The Ce/Ce* ratio of 0.8-1.0 (in sample Dzh 3 – 0.7) in all studied samples corresponds to the values characteristic of epicontinental settings [33, 34]. In the La/Sc, Zr/Sc, and Th/Sc ratios, the studied rocks are close to the Paleozoic sandstones formed as a result of the destruction of igneous rocks of intermediate and felsic composition [35-37]. The slight excess in the LREE content in sample Dzh 2 compared to PAAS and the absence of a europium minimum probably reflect increased amount of plagioclase fragments in the composition of the original rocks.

The graphs of REE distribution in clay formations of the weathering crust in the Vadyavozh quarry differ in the nature of the curves slope and the Eu/Eu* ratio. The REE content in them is higher compared to the original Riphean sandstones. Micaceous siltstones (sample V 9.3), attributed to the Riphean weathering crust in the Dzhezhim Fm. (Table 2, Fig.5, *c*), are distinguished by the maximum

REE content, a steep slope in the LREE region and an intense europium minimum. The studied rocks are close in shape to the upper continental crust (UCC) normalized [38] distribution spectra of trace elements, the content of which in the clay formations of the weathering crust is slightly higher than in the original rocks (Fig.6). The clay formations of the weathering crust are characterized by reduced Co, Ni, Cu, Sr, and Cs contents compared to UCC and increased Zr, Mo, and Pb contents.

Table 2

Content of REE and rare elements, g/t

Quarry	Asyvvozh						Vadyavozh					Dzhezhim		
Age	RF	Pre-Middle Devonian			D		RF	MZ-KZ		RF (?)		RF	MZ-KZ	
Rock	Sandstone	Areal weathering crust			Sandstone	Tectonic clay	Sandstone	Areal weathering crust	Linear weathering crust	Areal weathering crust		Sandstone	Areal weathering crust	
Element	R-2	R-5	R-7	R-8	O-33	R-9	V 9.4	V 14.4	V 9.10	V 14.3	V 9.3	Dzh 1	Dzh 2	Dzh 3
Sc	5.5	3.3	4.8	2.0	3.9	5.4	1.0	7.1	5.6	14.0	15.0	1.0	16.0	4.6
V	21.0	21.0	29.0	9.0	16.0	43.0	6.0	45.0	39.0	170.0	119.0	10	110.0	61.0
Cr	26.0	25.0	29.0	11.0	14.0	35.0	204.0	133.0	45.0	137.0	108.0	345.0	114.0	77.0
Co	1.1	0.5	0.5	0.8	1.0	0.6	4.8	4.6	6.6	2.4	11.0	2.5	12.0	10.0
Ni	3.0	2.0	2.0	4.0	6.0	1.0	29.0	20.0	17.0	30.0	42.0	31.0	74.0	51.0
Cu	5.0	6.0	5.0	6.0	7.0	2.0	15.0	45.0	22.0	25.0	24.0	15.0	5.9	7.4
Zn	8.0	5.0	5.0	4.0	10.0	3.0	12.0	16.0	40.0	16.0	39.0	8.3	89.0	50.0
Ga	6.2	6.4	9.6	3.3	5.8	13.0	1.9	10.0	7.2	35.0	24.0	3.9	22.0	14.0
Rb	61.0	62.0	81.0	23.0	37.0	114.0	7.0	61.0	28.0	66.0	93.0	51.0	158.0	41.0
Sr	21.9	27.8	28.9	6.5	8.9	38.0	3.6	12.0	5.5	19.0	12.0	33.0	70.0	46.0
Y	7.9	7.9	10.1	12.0	15.0	14.0	4.1	7.8	6.2	8.8	15.0	7.3	34.0	15.0
Zr	95.0	107.0	147.0	152.0	173.0	189.0	52.0	153.0	62.0	189.0	119.0	38.0	176.0	142.0
Nb	3.2	3.0	4.6	4.7	7.7	6.0	1.2	5.3	2.7	20.0	11.0	1.8	13.0	8.7
Mo	0.9	0.8	0.2	0.2	0.5	0.2	21.0	2.3	0.9	0.8	0.4	4.8	0.5	0.8
Cs	0.9	1.2	2.0	0.8	3.7	2.8	0.1	0.9	0.4	5.3	1.8	0.5	2.3	0.9
La	17.2	19.8	14.7	11.0	17.0	24.0	4.6	22.0	4.5	12.0	51.0	13.0	45.0	12.0
Ce	33.2	40.6	30.7	23.0	35.0	49.0	9.0	43.0	8.1	22.0	111.0	27.0	78.0	19.0
Pr	4.1	5.0	3.8	2.9	4.2	6.4	1.1	4.9	1.2	3.7	12.0	3.5	12.0	3.6
Nd	14.9	19.0	15.0	11.0	15.0	25.0	4.3	18.0	5.0	14.0	46.0	14.0	49.0	14.0
Sm	2.7	3.6	3.0	2.1	2.9	4.8	0.8	3.1	1.3	3.1	8.0	2.5	9.8	3.0
Eu	0.8	1.0	1.0	0.5	0.7	1.5	0.2	0.8	0.3	0.8	1.4	0.9	2.7	12.0
Gd	3.0	3.9	3.9	2.6	3.5	5.1	1.0	3.6	1.4	3.2	8.4	2.6	10.0	3.3
Tb	0.3	0.4	0.4	0.4	0.5	0.6	0.1	0.4	0.2	0.5	0.9	0.3	1.3	0.5
Dy	1.7	1.9	2.1	2.0	2.5	3.0	0.8	1.7	1.2	3.1	3.7	1.4	6.5	2.7
Ho	0.3	0.3	0.4	0.4	0.5	0.6	0.2	0.3	0.2	0.6	0.6	0.3	1.3	0.6
Er	1.0	1.0	1.3	1.3	1.6	1.8	0.5	0.9	0.7	1.8	2.2	0.1	3.7	1.6
Tm	0.1	0.1	0.2	0.2	0.2	0.3	0.1	0.2	0.1	0.3	0.3	0.1	0.5	0.2
Yb	1.0	0.9	1.3	1.3	1.5	1.1	0.4	1.1	0.6	1.8	1.9	0.7	3.1	1.5
Lu	0.2	0.1	0.2	0.2	0.3	0.3	0.1	0.2	1.0	0.3	0.3	0.1	0.5	0.2
Hf	2.9	3.1	4.4	4.2	5.0	5.8	1.4	4.3	1.6	5.3	3.4	1.0	4.9	3.8
W	0.3	0.3	0.3	0.5	0.7	0.3	0.5	0.8	0.5	2.0	0.8	1.6	1.0	0.6
Pb	31.5	130.3	13.8	12.0	23.0	19.0	26.0	51.0	21.0	239.0	70.0	8.3	8.4	3.7
Th	4.9	6.4	5.5	3.7	5.0	8.1	1.7	8.3	3.6	5.8	9.9	2.5	11.0	3.2
U	0.8	1.0	1.1	1.0	1.4	1.5	0.6	2.5	0.7	3.4	3.7	0.7	3.8	0.8
Eu/Eu*	0.9	0.8	0.9	0.7	0.7	0.9	0.6	0.8	0.8	0.7	0.5	1.1	0.8	1.2
Ce/Ce*	0.9	1.0	1.0	0.9	1.0	0.9	0.9	0.9	1.0	0.8	1.1	0.9	0.8	0.7
Σ LREE	73.0	89.0	68.0	51.0	75.0	111.0	20.0	92.0	33.0	56.0	229.0	61.0	197.0	53.0
Σ REE	89.0	106.0	88.0	71.0	101.0	138.0	27.0	108.0	53.0	76.0	263.0	75.0	257.0	78.0

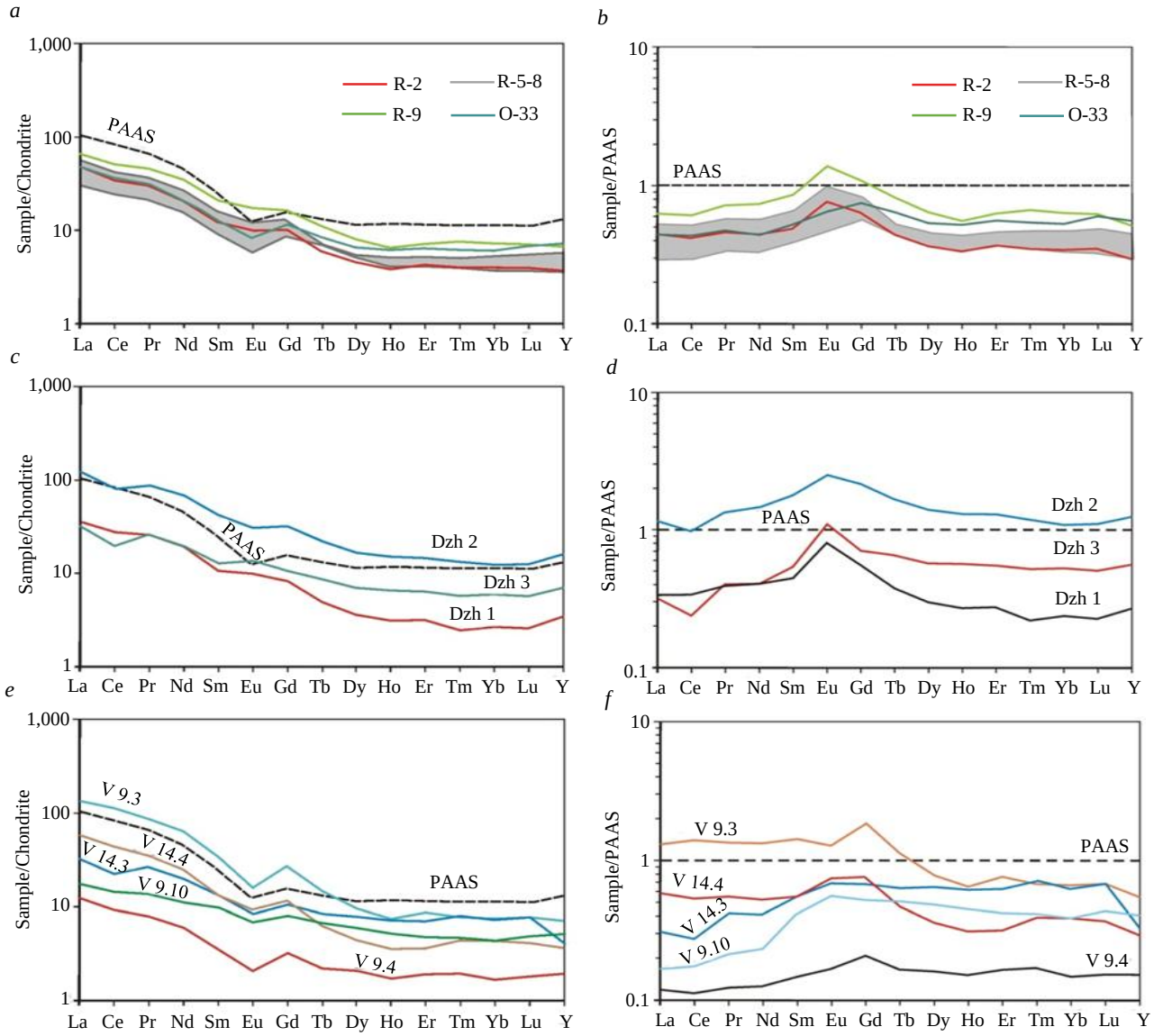

Fig.5. Normalized distribution spectra of REE contents: *a*, *c*, *e* – for chondrite [32]; *b*, *d*, *f* – for PAAS [31]

Discussion of results and conclusions

The studied varieties of weathering crust in the Riphean rocks differ slightly in the ratio of rock-forming elements, the content and composition of micaceous minerals and are diagnosed as rocks of the bleaching and mechanical disintegration zone. The figurative points of sandstones and clay formations in the K_2O – Na_2O ratio [22], which are arkoses in the $\log(Fe_2O_{3tot}/K_2O)$ – $\log(SiO_2/Al_2O_3)$ diagram (see Fig.2, *b*), are in the field of sub-arkoses and wackes, which includes weathering crust samples distinguished by the highest mica content. The (Na_2O+K_2O) – HM and SPM – HM diagrams [23] show an increase in alkalinity (total and normalized) in samples of weathering crust after the Riphean rocks and a decrease in these parameters for clay formations at the base of the Devonian strata. Devonian sandstones and clays are also distinguished by maximum values of the weathering indices CIA and CIW [21, 27]. The CIW values in the Devonian sandstones and underlying clayey rocks (93 and 91, respectively) characterize them as weathering crust formations. All previous geological surveys and investigations noted the presence of crustal material in the rocks of the Middle-Upper Devonian Asyvvozh Fm. [13, 14] this fact served as an argument for searching for placer diamonds[6]. High CIW values (94 and 93) are also noted in the siltstones of the Dzhezhim Fm., which confirms

[6] Tereshko V.V., Kirillin S.V., Kazantseva G.Ya. et al. Geological survey at 1:50,000 scale in adjacent sheets R-40-73-C,D; R-40-74-C; R-40-85-B; R-40-86-A. Syktyvkar, 1991.

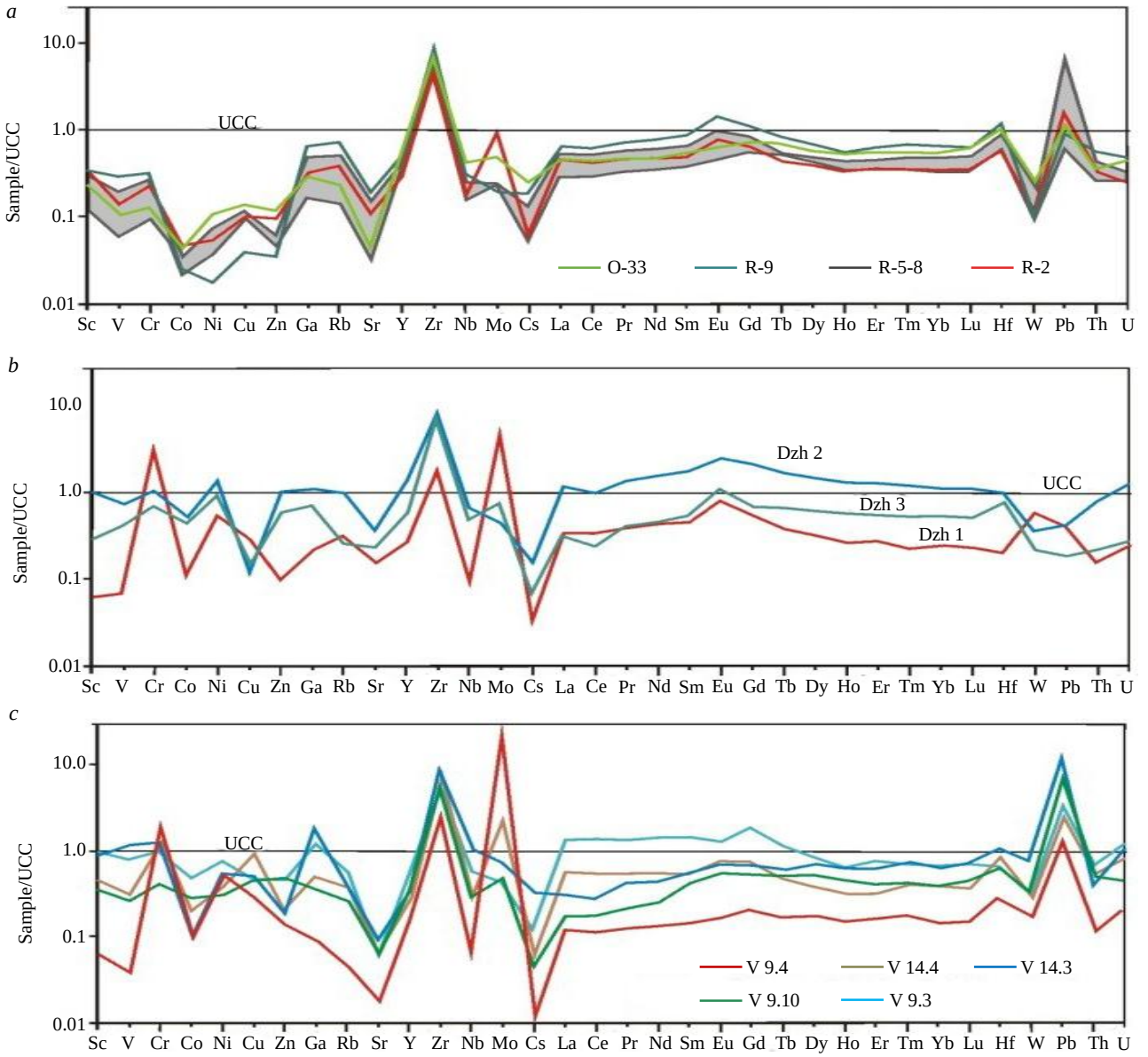

Fig.6. UCC [37] normalized contents of trace elements in the original sandstones and clay rocks

our assumption about their connection with the weathering crust. Riphean sandstones and associated clay formations of the weathering crust from the Asyvvozh quarry contain a significant proportion of feldspars and potassium micas, which, according to the article by Ya.E.Yudovich and co-authors (1991), is characteristic of arid weathering crusts widely developed in the Riphean deposits.

The composition and ratio of clay minerals in multiple-aged weathering crusts differ. The occurrence of disordered swelling mixed-layer formations (illite/smectite, chlorite/smectite) in samples from the Vadyavozh quarry indicates the transformation of the original rocks into weathering crust. A mixed-layer swelling phase was found in the Mesozoic-Cenozoic weathering crust samples. Its content can reach 15 %. In addition to the $2M_1$ structure, they contain a weakly ordered muscovite polytype 1M, the appearance of which is a diagnostic sign of crust formation. The phase composition of layered silicates in the weathering crust of the Asyvvozh quarry is represented only by muscovite and kaolinite.

In the Asyvvozh quarry, the REE content in the Riphean sandstones and clay formations of the weathering crust differs insignificantly and is close to PAAS. The Devonian sandstones and underlying clays lack a europium minimum. In the Vadyavozh quarry, the micaceous siltstones of the ancient weathering crust in the Dzhezhim Fm. are distinguished by the maximum REE content, a steep slope in the LREE region, and an intense europium minimum (see Table 2, Fig.5, *c*). In the clays of the

Mesozoic-Cenozoic weathering crust after the Riphean sandstones, the inherited low contents of Co, Ni, Cu, Sr, and Cs compared to UCC and elevated Zr, Mo, and Pb are preserved.

It should be noted that geologists from industrial organizations, during geological survey and exploration, considered the Dzhezhim Fm. deposits and the weathering crusts developed after them as a potential intermediate collector of placer diamonds. The distribution features of rock-forming oxides and REE in the studied weathering crust varieties after the Riphean rocks and in the Riphean psammites themselves do not reveal any signs of kimberlite destruction products [39, 40]. Our studies confirmed the correct identification of siltstones in the Dzhezhim Fm. in the Vadyavozh quarry as rocks formed as a result of the redeposition of the Riphean terrigenous rocks transformed in the weathering crust.

The petrochemical characteristics of the fine-grained rock from the base of the Devonian section and the overlying sandstones are virtually identical. Since the presence of weathering crust material is characteristic of all rocks of the Asyvvozh Fm., including those lying where no clay layer is at the strata base in the presence of tectonic contact, we believe that the clay layer formed due to mechanical abrasion of the original sandstones.

REFERENCES

1. Pystin A.M., Glukhov Yu.V., Bushenev A.A. A new diamond find and primary diamond potential of the Chetlas uplift (Middle Timan). *Journal of Mining Institute.* 2023. Vol. 264, p. 842-855.

2. Krasotkina A.O., Skublov S.G., Kuznetsov A.B. et al. First Data on the Age (U–Pb, SHRIMP-II) and Composition of Zircon from the Unique Yarega Oil–Titanium Deposit, South Timan. *Doklady Earth Sciences.* 2020. Vol. 495. Part 2, p. 872-879. DOI: 10.1134/S1028334X20120065

3. Skublov S.G., Makeyev A.B., Krasotkina A.O. et al. Isotopic and Geochemical Features of Zircon from the Pizhemskoye Titanium Deposit (Middle Timan) as a Reflection of Hydrothermal Processes. *Geochemistry International.* 2022. Vol. 60. N 9, p. 809-829. DOI: 10.1134/S0016702922090063

4. Ilalova R.K., Duryagina A.M., Ageev A.S. Minerogenesis sequence and processes in weathering mantle of ultrabasitic rocks of the Serov–Mauk ophiolite belt (Northern Urals). *Mining Informational and Analytical Bulletin*. 2020. N 7, p. 13-26 (in Russian). DOI: 10.25018/0236-1493-2020-7-0-13-26

5. Alekseev V.I., Alekseev I.V. Zircon as a Mineral Indicating the Stage of Granitoid Magmatism at Northern Chukotka, Russia. *Geosciences*. 2020. Vol. 10. Iss. 5. N 194. DOI: 10.3390/geosciences10050194

6. Akbarpuran Haiyati S.A., Gulbin Yu.L., Gembitskaya I.M., Sirotkin A.N. Compositional Evolution of REE- and Ti-Bearing Accessory Minerals in Metamorphic Schists of Atomfjella Series, Western Ny Friesland, Svalbard and Its Petrogenetic Significance. *Geology of Ore Deposits.* 2021. Vol. 63. N 7, p. 634-653. DOI: 10.1134/S1075701521070047

7. Terekhov E.N., Makeyev A.B., Skublov S.G. et al. Quartz Porphyries on the Outer Islands in the Gulf of Finland: Volcanic Comagmates of Rapakivi Granites. *Journal of Volcanology and Seismology.* 2023. Vol. 17. N 6, p. 530-549. DOI: 10.1134/S0742046323700318

8. Kuznetsov N.B., Natapov L.M., Belousova E.A. et al. The first results of U/Pb dating and isotope geochemical studies of detrital zircons from the neoproterozoic sandstones of the Southern Timan (Djejim-Parma Hill). *Doklady Earth Sciences.* 2010. Vol. 435. Part 2, p. 1676-1683. DOI: 10.1134/S1028334X10120263

9. Latysheva I.V., Kuznetsov N.B., Shatsillo A.V. et al. U-Pb age of detrital zircon grains from clastic rocks of the Dzhezhim Fm. (Upper Precambrian of South Timan). Geodinamicheskaya evolyutsiya litosfery Tsentralno-Aziatskogo podvizhnogo poyasa (ot okeana k kontinentu): Materialy nauchnoi konferentsii. Irkutsk: Institut zemnoi kory SO RAN, 2022. Iss. 20, p. 166-169.

10. Kolesnikov A.V., Latysheva I.V., Shatsillo A.V. et al. Ediacara-Type Biota in the Upper Precambrian of the Timan Range (Dzhezhim–Parma Hill, Komi Republic). *Doklady Earth Sciences.* 2023. Vol. 510. Part 1, p. 289-292. DOI: 10.1134/S1028334X23600032

11. Kolesnikov A.V., Latysheva I.V., Shatsillo A.V. et al. Discovery of Ediacaran-type biota in South Timan. Geologiya, geoekologiya i resursnyi potentsial Urala i sopredelnykh territorii: Sbornik statei X Vserossiiskoi molodezhnoi konferentsii. Moscow: Pero, 2022, p. 87-88.

12. Kolesnikov A.V. Stratigraphic correlation potential of the Ediacaran palaeopascichnids. *Estudios Geológicos*. 2019. Vol. 75. N 2. N e102. DOI: 10.3989/egeol.43588.557

13. Gosudarstvennaya geologicheskaya karta Rossiiskoi Federatsii. Masshtab 1:1 000 000 (trete pokolenie). Seriya Uralskaya. List R-40 – Severouralsk. Obyasnitelnaya zapiska. St. Petersburg: Kartograficheskaya fabrika VSEGEI, 2005, p. 332.

14. Gosudarstvennaya geologicheskaya karta Rossiiskoi Federatsii. Masshtab 1:200 000. Izdanie vtoroe. Seriya Timanskaya. List R-40-XXVI (Kanava). Obyasnitelnaya zapiska. Moscow: Moskovskii filial FGBU VSEGEI, 2018, p. 105.

15. Grakova O.V. Comparative characteristics and formation conditions of the Devonian diamond-bearing deposits in the South and Middle Timan: Avtoref. dis. … kand. geol.-mineral. nauk. Syktyvkar: Institut geologii Komi NTs UrO RAN, 2014, p. 19.

16. Grakova O.V., Ulyasheva N.S. Petrographic composition and lithochemical characteristic of diamond-bearing deposit of asyvvoj series ($D_{2\text{-}3}$AS) of South Timan. *Vestnik of the Institute of Geology of the Komi Science Center of the Ural Branch of the Russian Academy of Sciences.* 2015. N 12 (252), p. 16-23 (in Russian). DOI: 10.19110/2221-1381-2015-12-16-23

17. Makeev A.B., Rybalchenko A.Ya., Dudar V.A., Shametko V.G. New prospects for diamond potential in Timan. Geologiya i mineralnye resursy evropeiskogo severo-vostoka Rossii. Novye rezultaty i novye perspektivy: Materialy XIII Geologicheskogo sezda Respubliki Komi. Syktyvkar, 1999. Vol. IV, p. 63-66.

18. Tskhadaya N.D., Kobrunov A.I., Shilov L.P. et al. Timan Ridge. In 2 volumes. Vol. 2. Ukhta: Ukhtinskii gosudarstvennyi tekhnicheskii universitet, 2010, p. 437.

19. Rybalchenko A.Ya., Rybalchenko T.M., Silaev V.I. Theoretical basis for forecasting and exploration of primary diamonds deposits of tuffizit type. *Proceedings of the Komi Science Centre of the Ural Division of the Russian Academy of Sciences.* 2011. Iss. 1 (5), p. 54-66 (in Russian).

20. Nikulova N.Yu. Lythological and chemical composition and depositional conditions of metasediment basement rocks of the Vadyavog prominence (Nem upland, South Timan). *Regional Geology and Metallogeny.* 2017. N 69, p. 23-32 (in Russian).

21. Pettijohn F.J., Potter P.E., Siever R. Sand and sandstone. Moscow: Mir, 1976, p. 535 (in Russian).

22. Herron M.M. Geochemical classification of terrigenous sands and shales from core or log data. *Journal of Sedimentary Research*. 1988. Vol. 58. N 5, p. 820-829. DOI: 10.1306/212F8E77-2B24-11D7-8648000102C1865D

23. Yudovich Ya.E., Ketris M.P. Fundamentals of lithochemistry. St. Petersburg: Nauka, 2000, p. 479.

24. Kusunoki T., Musashino M. Comparison of the Middle Jurassic to Earliest Cretaceous sandstones from the Japanese Islands and South Sikhote-Alin. *Earth Science*. 2001. Vol. 55. Iss. 5, p. 293-306. DOI: 10.15080/agcjchikyukagaku.55.5_293

25. Roser B.P., Korsch R.J. Determination of Tectonic Setting of Sandstone-Mudstone Suites Using SiO_2 Content and K_2O/Na_2O Ratio. *The Journal of Geology*. 1986. Vol. 94. N 5, p. 635-650.

26. Erofeev W.S., Tsekhovsky Yu.G. Paragenetic associations of continental deposits (Family of arid parageneses. Evolutionary frequency). Moscow: Nauka, 1983, p. 192 (in Russian).

27. Nesbitt H.W., Young G.M. Early Proterozoic climates and plate motions inferred from major element chemistry of lutites. *Nature*. 1982. Vol. 299. N 5885, p. 715-717. DOI: 10.1038/299715a0

28. Cox R., Lowe D.R. A conceptual review of regional-scale controls on the composition of clastic sediment and the co-evolution of continental blocks and their sedimentary cover. *Journal of Sedimentary Research*. 1995. Vol. 65. N 1a, p. 1-12. DOI: 10.1306/D4268009-2B26-11D7-8648000102C1865D

29. Turgeon S., Brumsack H.-J. Anoxic vs dysoxic events reflected in sediment geochemistry during the Cenomanian–Turonian Boundary Event (Cretaceous) in the Umbria–Marche Basin of central Italy. *Chemical Geology*. 2006. Vol. 234. Iss. 3-4, p. 321-339. DOI: 10.1016/j.chemgeo.2006.05.008

30. Yong Il Lee. Provenance derived from the geochemistry of late Paleozoic–early Mesozoic mudrocks of the Pyeongan Supergroup, Korea. *Sedimentary Geology*. 2002. Vol. 149. Iss. 4, p. 219-235. DOI: 10.1016/S0037-0738(01)00174-9

31. Migdisov A.A., Balashov Yu.A., Sharov I.V. et al. Abundance of rare earth elements in the major lithological rock types in the sedimentary cover of the Russian Platform. *Geokhimiya*. 1994. N 6, p. 789-803.

32. Taylor S.R., McLennan S.M. The Continental Crust: Its Composition and Evolution. Moscow: Mir, 1988, p. 312 (in Russian).

33. Murray R.W., Buchholtz Ten Brink M.R., Gerlach D.C. et al. Rare earth, major, and trace elements in chert from the Franciscan Complex and Monterey Group, California: Assessing REE sources to fine-grained marine sediments. *Geochimica et Cosmochimica Acta*. 1991. Vol. 55. Iss. 7, p. 1875-1895. DOI: 10.1016/0016-7037(91)90030-9

34. Shatrov V.A., Voitsekhovskii G.V. The use of lanthanides for the reconstruction of Phanerozoic and Proterozoic sedimentation environments exemplified by sections in the cover and basement of the East European platform. *Geochemistry International.* 2009. Vol. 47. N 8, p. 758-776. DOI: 10.1134/S0016702909080023

35. Cullers R.L. Implications of elemental concentrations for provenance, redox conditions, and metamorphic studies of shales and limestones near Pueblo, CO, USA. *Chemical Geology*. 2002. Vol. 191. Iss. 4, p. 305-327. DOI: 10.1016/S0009-2541(02)00133-X

36. McLennan S.M., Hemming S., McDaniel D.K., Hanson G.N. Geochemical approaches to sedimentation, provenance, and tectonics. *Processes Controlling the Composition of Clastic Sediments*. Geological Society of America, 1993. Special Paper 284, p. 21-40. DOI: 10.1130/SPE284-p21

37. Maslov A.V., Melnichuk O.Yu., Mizens G.A. et al. Provenance reconstructions. Article 2. Litho- and isotope-geochemical approaches and methods. *Lithosphere.* 2020. Vol. 20. N 1, p. 40-62 (in Russian). DOI: 10.24930/1681-9004-2020-20-1-40-62

38. Taylor S.R., McLennan S.M. The geochemical evolution of the continental crust. *Reviews of Geophysics*. 1995. Vol. 33. Iss. 2, p. 241-265. DOI: 10.1029/95RG00262

39. Gusev N.I., Antonov A.V. Kimberlites of the Serbeyan Prospect (Anabar Shield): melt products enriched with sodium, chlorine, carbonate. *Regional Geology and Metallogeny.* 2020. N 81, p. 105-118 (in Russian).

40. Oparin N.A., Oleinikov O.B. The geology and composition of the Khompu-May field kimberlite pipes (Central Yakutia, Russia). *Arctic and Subarctic Natural Resources.* 2022. Vol. 27. N 4, p. 486-498 (in Russian).

Authors: **Oksana V. Grakova,** *Candidate of Geological and Mineralogical Sciences, Researcher, ovgrakova@geo.komisc.ru, https://orcid.org/0000-0001-5917-9218 (Institute of Geology FRC Komi SC of the Ural Branch of the RAS, Syktyvkar, Russia),* **Nataliya Yu. Nikulova,** *Doctor of Geological and Mineralogical Sciences, Leading Researcher, https://orcid.org/0000-0002-1511-6124 (Institute of Geology FRC Komi SC of the Ural Branch of the RAS, Syktyvkar, Russia),* **Yuliya S. Simakova,** *Candidate of Geological and Mineralogical Sciences, Senior Researcher, https://orcid.org/0000-0003-0409-4019 (Institute of Geology FRC Komi SC of the Ural Branch of the RAS, Syktyvkar, Russia).*

The authors declare no conflict of interests.

ISSN 2411-3336; e-ISSN 2541-9404

JOURNAL OF MINING INSTITUTE

Zapiski Gornogo instituta

Journal homepage: pmi.spmi.ru

Research article *Geology*

Paleoproterozoic Saltakh Pluton, Anabar Shield: mineralogical composition, age and a geodynamic setting

Nikolai I. Gusev[1, 2], **Lyudmila Yu. Romanova**[1, 2]✉

[1] *Karpinsky Russian Geological Research Institute, Saint Petersburg, Russia*

[2] *Institute of Precambrian Geology and Geochronology RAS, Saint Petersburg, Russia*

How to cite this article: Gusev N.I., Romanova L.Yu. Paleoproterozoic Saltakh Pluton, Anabar Shield: mineralogical composition, age and a geodynamic setting. Journal of Mining Institute. 2025. Vol. 272. N 16344, p. 16-39.

Abstract

The Saltakh Massif is located in the northern Anabar Shield, in the Saltakh shear-zone. It consists of two-pyroxene schists and plagiogneisses metamorphosed under granulite-facies conditions. Their chemical composition is consistent with that of a differentiated series of rocks ranging from gabbro to tonalites with abundant alaskitic gneissose granite veins and bodies. The rocks are mainly high-potassium ($K_2O/Na_2O > 0.50$), high-magnesium (mg# 50-70), low-titanium (TiO_2 0.35-1.31 wt.%) with low TiO_2 concentration in clino- and orthopyroxene. Normative olivine makes up 6-9 % of metagabbroic rocks. The rocks display well-defined negative Ti, Nb, Ta, and P anomalies typical of subduction magmatism. The two-pyroxene gneisses show high Sr/Y ratios of 67.6-88 and $(La/Yb)_N$ of 24.8-25.6. Saltakh rocks are part of a shoshonite series, as indicated by Nb/La, La/Yb, Th/Nb and Ce/Yb ratios. All the rocks display positive $\varepsilon_{Nd}(T)$ values of 1.9-4.1 and $\varepsilon_{Sr}(T)$ of 0.77-17.8 indicative of a mantle source of magma and $T_{(Nd)}$DM of 2,20-2,26 Ga. U-Pb zircon dating (SHRIMP II) has shown that the protoliths of Saltakh melanocratic rocks were dated at 2100-2086 Ma, and those of two-pyroxene plagiogneisses of tonalite composition were dated at 2025±7 Ma. Alaskitic gneissose granites were dated at 1969±7 Ma. The study of the trace element composition of zircon has revealed general enrichment in LREE. High LREE concentrations are due to secondary zircon alterations and the shoshonitic pattern of the melt, the high-temperature conditions of crystallization, and an anomalous fluid regime. The geodynamic setting in which the Saltakh Massif was formed was consistent with a pericontinental magmatic arc. The formation of alaskitic gneissose granites was due to anatexis provoked by later collision processes. Saltakh magmatic rocks were formed simultaneously with magmatic rocks from the Khapchan prospect which occur farther south, and were studied earlier (2095±10 Ma tholeiitic metadiorites and 2030±17 Ma calc-alkaline metatonalites). We interpret them as part of a metamorphosed juvenile Paleoproterozoic suprasubduction complex.

Keywords

Anabar Shield; Saltakh Massif; granulites; U-Pb method; geochronology

Funding

Studies were conducted under Russian Science Foundation project N 23-27-00098.

Received: 10.11.2023 ***Accepted: 02.05.2024*** ***Online: 26.08.2024*** ***Published: 25.04.2025***

Introduction

The Siberian Craton is an old platform with an Early Precambrian highly metamorphosed basement located in the northern part of the Eurasian continent. The Anabar Shield, consisting of granulitic terrains, forms a basement scarp in the northeastern Siberian Craton. Extending in the eastern Anabar Shield is the boundary of two Precambrian basement provinces: the Archean Anabar province and the Paleoproterozoic Olenek province formed of the Khapchan foldbelt. The Saltakh complex is located in the Popigai Terrane within the Olenek province. Its massif lies in the northern Saltakh shear-zone.

The Saltakh shear-zone extends in the northeastern Anabar Shield across the upper reaches of the River Staraya, the Popigai terrain and the right-hand bank of the River Nalim-Rassokha (Fig.1) [1]. The visible length of the zone is about 130 km. In the north and south, it is overlain by Riphean sandstones. The zone varies in width from 1-2 km in the south to 17-20 km in the north [2].

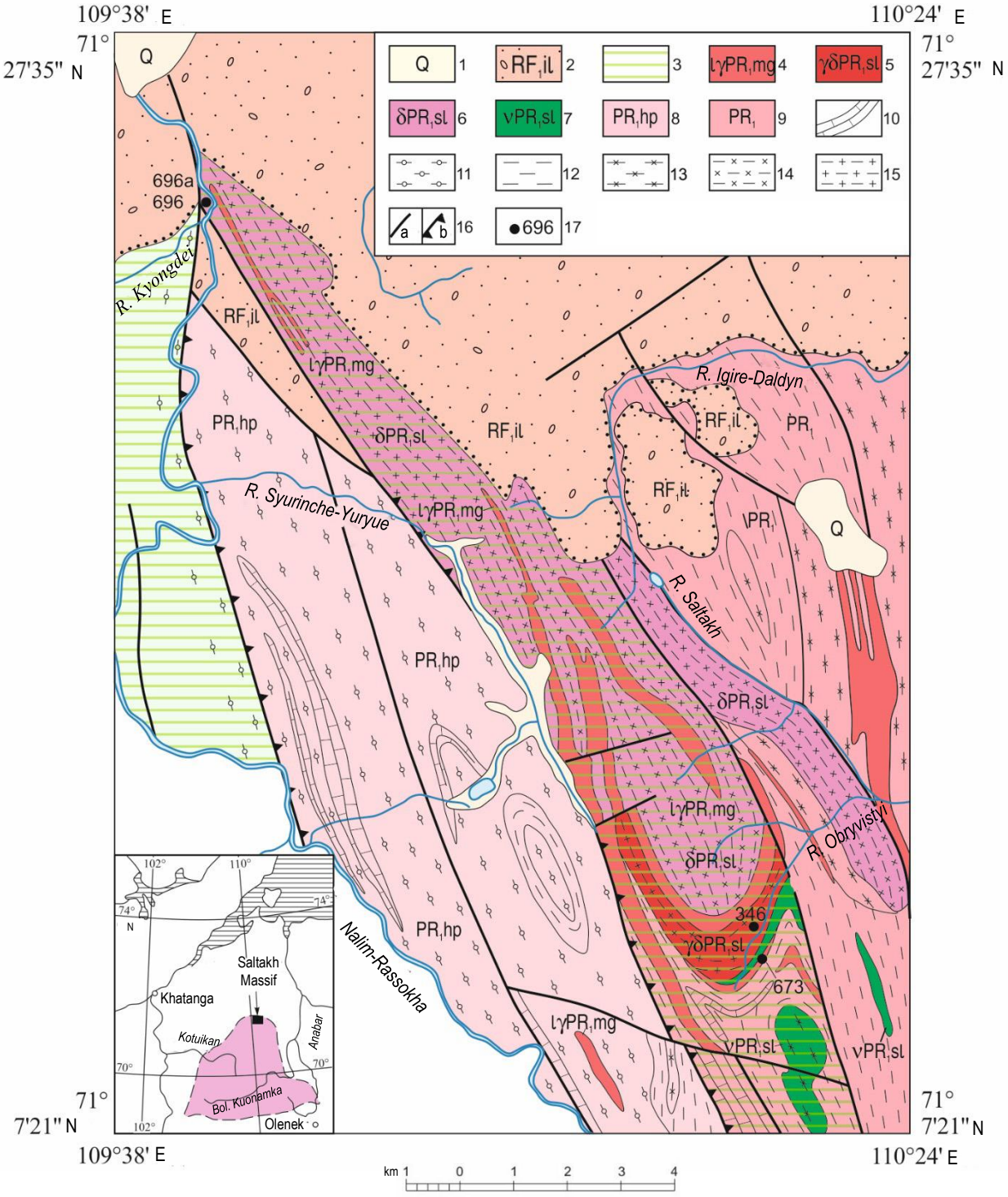

Fig.1. Geologic map of the Saltakh Massif area. Based on Gosgeolmap-200 (A.I.Trukhalev et al., 1972, unpublished data), modified

1 – Quaternary deposits (Q); 2 – red sandstones and gritstones of the Ilyinsk suite (RF_1il); 3 – broken down and retrogressed granulites in shear-zones; 4 – Magan alaskitic-leucogranitic-migmatitic complex ($l\gamma PR_1mg$); 5-7 – Saltakh gabbro-dioritic-tonalitic complex (ν, δ, γδ PR_1sl): 5 – two-pyroxene plagiogneisses (metatonalites), 6 – two-pyroxene gneisses (metadiorites), 7 – two-pyroxene schists (metagabbroic rocks); 8 – Khapchan series (PR_1hp): garnet, biotitic-garnet, garnet-pyroxene and sillimanite-garnet paragneisses, silicate marbles, carbonate-silicate and pyroxene-scapolitic rocks; 9 – undivided Paleoproterozoic (PR_1) rocks: orthopyroxene and two-pyroxene gneisses and plagiogneisses, mesocratic and mafic schists; 10 – silicate marbles, carbonate-silicate and pyroxene-scapolitic rocks; 11 – garnet, hypersthene-garnet gneisses, plagiogneisses and their varieties with biotite and graphite; 12 – hypersthene, two-pyroxene and amphibole-pyroxene plagiogneisses; 13 – clinopyroxene-plagioclase, two-pyroxene-plagioclase and amphibole-pyroxene-plagioclase schists; 14 – mesocratic orthogneisses and plagioschists; 15 – two-pyroxene plagiogneisses; 16 – boundaries: a – steeply dipping faults, b – overthrusts; 17 – sampling sites and the numbers of samples for isotopic analyses

The Saltakh complex consists of two large massifs: the Saltakh Massif (covering an area of 10 × 24 km, including its northeastern satellite) and the Ulkhan Massif (2 × 20 km), as well as 10 smaller lenticular metagabbronorite intrusive units identified during the compilation of the Gosgeol-200 Map in 1971-1972 (A.I.Trukhalev et al., 1972, unpublished). The intrusive units of the Saltakh complex extend northwest for 100 km, varying in width from 10 km in the north to 20 km in the south. Metaintrusive rock exposures are more massive, but the boundaries of the massifs are indistinct, because their rocks have experienced granulite-facies metamorphism. Transitions to the host gneisses and schists are generally gradual. Zones of cataclasis and mylonitization are often formed along the contacts. Banding and stratification in the Saltakh Massif dip at 40-60° from the centre to the periphery of the massif [2].

Salltakh rocks have been metamorphosed along with host rocks under granulite-facies conditions. Most of these rocks contain hypersthene with antiperthitic feldspar. Transitions from the highly granitized host plagiogneisses and crystalline schists to Saltakh rocks are gradual [3]. Stretching along the western pluton boundary is the Saltakh diaphthoresis zone with amphibolite-facies polymetamorphic rocks, migmatites and alaskites [3]. Migmatization in the massif is widespread. It is intersected by numerous lenticular biotitic and alaskitic granite bodies, which vary in thickness (up to 0.5-0.9 km) and length (from several meters to tens of kilometers). The alaskitic granite bodies are affected by cataclasite zones, but they themselves are not cataclastic and are conformable with the western and southern massif boundaries. We have studied two prospects in the Saltakh Massif: one in the north, downstream from the Kyongdei River mouth, and the other in the southern zone of the massif extending along the banks of the Obryvistyi River (Fig.1). In the northern part of the massif, the rocks have been more intensely subjected to cataclasis, while in the southern part, the rocks are better preserved.

Methods

Major elements concentrations in the rocks were calculated by XRF methods, while ferric and ferrous iron concentrations were measured by titration and trace element concentrations by ICP-MS in the Karpinsky Institute laboratory, St.Petersburg.

Zircon samples were subjected to U-Pb dating using a SHRIMP II ion microprobe at the CIS, Karpinsky Institute, St.Petersburg (analyzed by P.A.Lvov) following standard methods [4]. The data obtained were processed with SQUID software (K.Ludwig, 2000). U-Pb ratios were normalized to the value 0.0668 for the TEMORA zircon standard dated at 416.75 Ma [5]. Errors in single analyses (ratios and ages) are given at the 1σ level, and errors in the calculated values of concordant ages and intersections with the Concordia curve are given at the 2σ level. Plots were constructed using ISOPLOT/ET software (K.Ludwig, 1999).

Trace elements in zircon were analyzed using ICP-MS method on a Cameca IMS-4f ion microprobe at the Yaroslavl Branch of the Institute of Physics and Technology, RAS. The study is described in detail in [6]. Data on the trace element composition of the zircon enabled us to reconstruct its conditions of formation [7-9] and to correctly interpret the dating results [10-12].

Rb-Sr and Sm-Nd isotope studies were conducted using the method described in [13]. Isotopic measurements were made on a ThermoFinnigan MAT TRITON mass-spectrometer (CIS, Karpinsky Institute, analyzed by E.S.Bogomolov) in a static regime.

To calculate $\varepsilon_{Nd}(T)$ values, we used the following modern isotopic ratios for a homogeneous chondritic reservoir (CHUR): $^{147}Sm/^{144}Nd = 0.1967$ and $^{143}Nd/^{144}Nd = 0.512638$ [14]. A model age for a one-stage model of $T_{Nd}(DM)$ was calculated relative to relatively depleted mantle (DM) with the parameters $^{147}Sm/^{144}Nd = 0.2136$ and $^{143}Nd/^{144}Nd = 0.51315$ [15]. Mineral symbols are used as per [16].

Results

Geologic-petrographic description. We have identified three rock groups in the Saltakh Massif study areas: two-pyroxene schists (metagabbroic rocks); two-pyroxene and orthopyroxene gneisses (metadiorites and metatonalites); and granitoids.

Two-pyroxene schist – their texture is generally massive and chaotically gneissoid (flaser). Cataclastic varieties display a banded texture. Thin sections are dominated by a granoheteroblastic structure, and a relict gabbroic structure persists locally. We identified two rock varieties:

in one variety, the concentration of plagioclase is either equal to or less than that of dark-colored minerals, while in the other, plagioclase is clearly dominant.

The melanocratic varieties of the schist samples analyzed show the following mineral composition, vol.%: Pl (An_{45-58}) 45-50, Cpx 20-25, Opx 5-10, Bt 10-25, Mag 4, Ilm 1, Ap 1. Leucocratic schist varieties have the following mineral composition, vol.%: Pl (An_{40}) 55-60, Cpx 15, Opx 5, Bt 18-20, Mag 4, Ilm 1, Ap 1.

Plagioclase often forms isometric grains with fractured margins and no twinning. The granulated mass occasionally contains superposed quartz and K-feldspar. Plagioclase occurs mainly as andesine-labradorite. Bitownite is occasionally present (An_{72}) in the Ulkhan Massif, where original rocks are better preserved.

Clinopyroxene of the diopside-hedenbergitic series forms irregular isometric grains and often replaces orthopyroxene. Clinopyroxene crystals generally contain the decay structures and twins of solid solutions with thin orthopyroxene laminae. TiO_2 concentration in the clinopyroxene is as low as 0.06-0.25 wt.% [2].

Orthopyroxene occurs as hypersthene and bronzite, which display pleochroism in pink tones, forming irregular and short-prismatic grains. Orthopyroxene is replaced by clinopyroxene, biotite, and amphibole with magnetite grains. It contains less TiO_2 (0.02 wt.%) than clinopyroxene [2]. Apatite is regularly distributed, forming isomorphic grains often showing hexagonal cross-sections.

A distinctive feature of two-pyroxene gneisses is the presence of antiperthitic plagioclase, quartz and orthopyroxene, which dominates over clinopyroxene. Their mineral composition vol.%: Pl (An_{30-35}) 55-70, Qz 10-15, Opx 6-10, Cpx 4-5, Bt 5-10, Or 0-8, Mag 2, Ilm 1, Ap 0.5.

Red-coloured gneissose granites (sample 347) show the following mineral composition vol.%: Kfs 35, Pl (An_{20-30}) 30, Qz 28-30, Bt 3, Mag 1. Single coarse grains occasionally contain Ap and Ttn, Zrn, and less often Mnz and Rt. Orthopyroxene, replaced by biotite and iddingsite, is occasionally present. Plagioclase is often antiperthitic and is corroded by quartz and orthoclase.

Alaskitic gneissose granites (sample 673) consist, vol.%: Kfs 37, Qz 32, Pl (An_{12}) 27. Microcline aggregates are commonly larger (1-3 mm across) than plagioclase. They often contain relics of myrmekitized plagioclase and orthoclase. Dark-coloured minerals are present as biotite and ore minerals such as magnetite and ilmenite. Articulate twins of rutile are occasionally derived from ilmenite. Grains of Ap, Zr, Mnz, and Aln are scarce.

Petro-geochemical types of rocks. The geochemical features of the rocks were studied based on 13 original analyses (Table 1). In addition, we used earlier evidence to understand better the petrochemical characteristics of the samples, such as 18 silicate analyses of two-pyroxene crystalline schists and gneisses (metadiorites) from the Saltakh Massif [2] and three analyses of crystalline schists (metagabbronorites) from the Ulkhan Massif. The Saltakh Massif [2] contains rocks ranging from monzogabbro to granodiorites, but as rock migmatization is ubiquitous, a TAS diagram can hardly be used. Since intermediate to mafic rocks prevail, our classification was based using all major rock constituents (Fig.2, *a*) and diagrams for the relations of relatively immobile high-charge elements Zr/Ti-Nb/Yb (Fig.2, *e*), equivalent to a TAS diagram (J.A.Pearce, 1996), and a Th-Co diagram (Fig.2, *f*), equivalent to a K_2O-SiO_2 diagram [17]. The correlation of normative feldspars was used for the classification of felsic rocks (Fig.2, *d*) [18].

The chemical composition of *two-pyroxene schist* (Table 1, Fig.2, *a*) is similar to that of gabbro (sample 672c, 672b), gabbronorite (Ulkhan Massif), and monzogabbro (samples 672, 672a, and 696). They are comparable in trace element concentration (Fig.2, *b*) to normal alkaline basaltoids. In the AFM diagram (Fig.2, *c*), the rocks are part of a calc-alkaline series. Earlier analyses indicated higher iron concentrations, which likely resulted from the distinctive analytical identification of elements by the wet chemistry method and a laboratory error.

The samples show a potassium type of alkalinity K_2O/Na_2O = 1.0-1.6, except for cataclastic rocks enriched in plagioclase with superposed quartz (sample 694-696, K_2O/Na_2O = 0.2-0.5). Figure 2, *f* shows that in Th-Co coordinates, all the rocks are part of a calc-alkaline series. However, it should be noted that Th is depleted during granulite-facies metamorphism. In the Ce/Yb-Ta/Yb diagram, the rocks are clearly plotted in the shoshonitic series, which separates calc-alkaline and shoshonitic series using the poorly mobile elements Ce, Yb and Ta (Fig.2, *h*) [19, 20].

Journal of Mining Institute. 2025. Vol. 272. P. 16-39

Table 1

Contents of major (wt.%) and trace (ppm) elements in the rocks of the Saltakh Massif

Groups of rocks	Opx-Cpx shists					Cpx-Opx plagiogneisses						Gneissose granites	
Sample	672c	672b	672	672a	696	696a	695	696b	346	347a	694	347	673
SiO_2	50.9	50.7	51.6	50.8	53.0	62.4	63.4	66.3	62.3	64.6	68.2	70.2	75.2
TiO_2	0.88	0.89	1.29	1.31	1.16	0.92	0.72	0.69	0.49	0.35	0.57	0.23	0.01
Al_2O_3	11.3	11.4	16.3	16.4	18.0	16.1	15.9	15.3	16.4	16.8	14.9	15.5	13.9
Fe_2O_3	3.82	4.18	3.63	5.32	3.01	2.07	2.06	2.23	2.36	1.44	2.15	1.28	0.48
FeO	4.42	4.61	4.87	3.79	4.06	3.25	2.34	1.39	2.44	2.11	1.39	0.97	0.13
MnO	0.18	0.21	0.13	0.14	0.11	0.09	0.06	0.07	0.09	0.08	0.06	0.03	0.02
MgO	10.5	10.2	6.03	5.99	5.43	3.06	3.05	1.80	2.64	1.89	2.11	0.64	0.18
CaO	11.4	11.7	7.36	7.30	6.86	5.06	4.62	5.62	5.32	4.32	4.96	1.46	0.68
Na_2O	2.0	2.21	3.36	3.47	5.14	4.70	4.46	4.95	3.84	3.61	3.83	2.75	2.65
K_2O	2.89	2.29	3.46	3.41	1.67	1.39	2.13	0.79	2.64	3.60	0.70	6.05	6.27
P_2O_5	0.48	0.50	0.69	0.68	0.34	0.27	0.22	0.20	0.22	0.18	0.18	0.14	0.02
LOI	0.52	0.43	0.47	0.52	0.61	0.30	0.68	0.41	0.76	0.78	0.68	0,55	0.34
Total	99.29	99.32	99.19	99.13	99.39	99.61	99.64	99,75	99,50	99.76	99.73	99.80	99.72
Th	1.84	1.67	1.78	2.11	0.69	0.50	0.34	0.97	6.13	2.25	4.55	21.2	0.20
U	0.54	0,46	0.66	0.72	0.20	0.12	0.13	0.18	0.19	0.25	0.71	0.80	0.17
Rb	163	136	133	141	27.4	17.8	55.2	4.46	66.7	74.2	4.14	149	143
Cs	2.03	0.95	1.38	1.71	0.36	0.26	0.37	<0.1	0.27	0.22	0.11	0.27	0.22
Ba	1730	986	2210	2200	292	365	506	255	996	1120	80.9	1960	425
Sr	493	377	997	849	441	494	517	404	646	617	495	498	206
La	20.3	23.9	28.3	30.7	39.6	21.7	23.9	25.6	32.3	25.7	23.7	52.2	5.41
Ce	45.6	53.5	65.3	65	117	48.7	47.4	50.7	64.6	48.9	47.9	94.1	6.27
Pr	5.86	6.72	8.86	8.84	16.6	6.39	5.42	5.88	7.02	5.34	5.54	9.22	0,46
Nd	25	27	38.3	36.1	69.8	25.9	22.4	22.5	25.4	20.2	20.6	32.5	1.37
Sm	5.08	5.29	6.44	6.42	11.5	4.02	3.56	3.52	3.66	3.06	3.63	3.54	0.20
Eu	1.32	1.21	2.12	1.95	2.30	1.30	1.10	1.14	1.08	0.87	0.87	0.91	0.58
Gd	3.84	4.29	5.02	4.89	10	3.25	2.97	3.15	2.94	2.39	2.68	2.17	0.11
Tb	0.62	0.65	0.59	0.66	1.40	0.46	0.42	0.45	0.41	0.29	0.38	0.26	0.02
Dy	3.18	3.17	3.26	3.24	7.26	2.51	2.00	2.40	2.08	1.55	1.94	1.04	0.10
Ho	0.70	0.65	0.55	0.61	1.47	0.47	0.40	0.44	0.33	0.26	0.33	0.14	0.02
Er	1.59	1.74	1.36	1.52	3.99	1.12	1.07	1.12	1.03	0.70	1.06	0.33	0.05
Tm	0.24	0.24	0.21	0.22	0.64	0.20	0.13	0.17	0.14	0.11	0.16	0.06	0.01
Yb	1.67	1.63	1.61	1.43	4.16	1.26	1.01	1.20	0.85	0.70	0.84	0.47	0,09
Lu	0.19	0.26	0.17	0.21	0.57	0.18	0.14	0.15	0.15	0.12	0.15	0.05	0.01
ΣREE	115	130	162	162	286	118	112	118	142	110	110	197	14.7
Zr	117	99.2	132	132	213	165	154	159	110	125	141	241	21.2
Hf	3.61	3.24	3.28	3.30	5.48	3.99	3.42	3.61	2.88	3.09	3.71	5.97	0.88
Ta	0.33	0.41	0.44	0.47	0.92	0.49	0.35	0.90	0.14	0.21	0.91	0.05	0.05
Nb	5.68	6.46	8.32	8.44	16.5	9.19	6.53	9.46	4.13	4.73	8.61	2.05	0.25
Y	16.2	16.5	15.3	15.3	43.4	12.8	10.7	11.6	9.55	7.04	9.69	4.14	0.64
Cr	450	450	59.5	56.1	111	94.8	107	85.8	54.3	40.2	118	42.0	14.4
Ni	125	127	51.7	42.0	107	66.8	45.9	32.2	19.6	18.2	32.2	4.65	2.82
Co	44.5	48.6	35.5	36.7	25.5	17.0	15.9	11.8	15.5	10.1	9.83	4.36	1.00
Sc	38.3	46.0	18.2	17.8	17.1	8.58	9.42	7.76	10.9	7.29	6.24	1.94	0.10
V	217	206	159	177	119	92.7	88.0	71.9	82.5	58.8	76.8	26.0	4.47
Pb	8.38	7.75	17.1	13.7	5.64	5.75	6.78	4.24	16.0	17.5	4.28	32.0	29.2
Ga	13.9	13.4	17.7	18.6	23.0	19.2	19.8	17.5	17.1	15.6	17.8	13.8	13.2
mg#	70	69	57	55	59	52	56	49	51	50	53	35	35
Eu/Eu*	0.91	0.78	1.14	1.06	0.66	1.10	1.03	1.05	1.01	0.98	0.85	1.0	12
$(La/Yb)_N$	8.2	9.9	11.9	14.5	6.4	11.6	16	14.4	25.6	24.8	19	75	40
Sr/Y	30	23	65	55	10	38.6	48	35	67.6	88	51	120	322
Nb/Ta	17	16	19	18	18	19	19	11	30	23	10	41	5

Note. The chemical composition of the rocks corresponds to the samples 672c, 672b – gabbronorites; 672, 672a – gabbro; 696 – gabbrodiorites; 696a, 695, 696b – quartz diorites; 346, 347a, 694 – tonalites; 347, 673 – granits. Rocks in the samples 694-696 cataclazed and quartered.

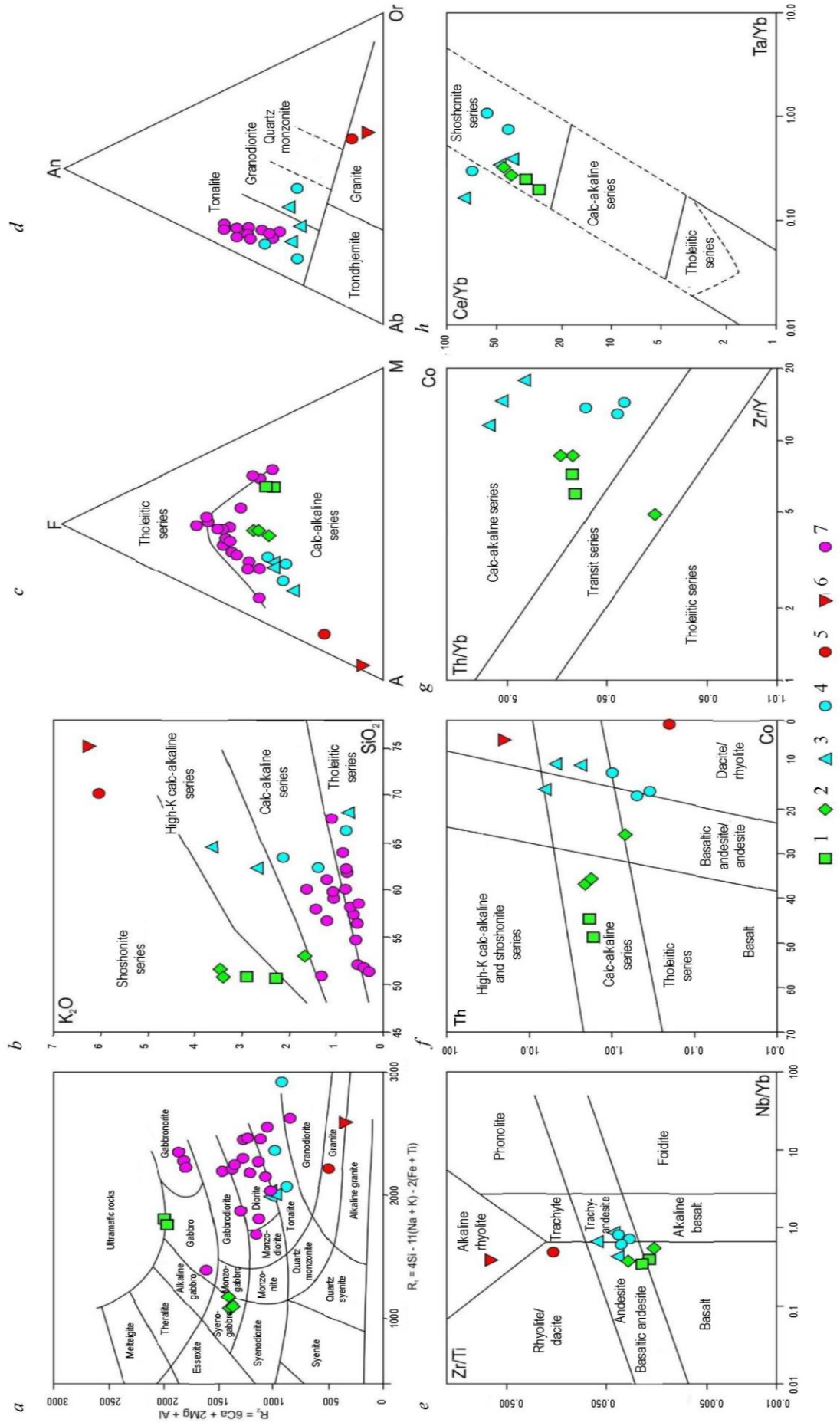

Fig.2. Geochemical diagrams for rocks of the Saltakh Massif after [21] (*a*); [22] (*b*); [23] (*c*); [18] (*d*); [20] (*e*); [17] (*f*); [24] (*g*); [20] (*h*)

1 – melanocratic two-pyroxene shists; 2 – high aluminous two-pyroxene shists; 3, 4 – Cpx-Opx plagiogneisses: 3 – quartz diorite composition, 4 – tonalite and granodiorite composition; 5 – gneissose granites; 6 – alaskitic gneissose granites; 7 – analyses of predecessors from [1] and unpublished data (A.I.Trukhalev et al., 1972)

Melanocratic schists are Mg-richest (mg# = 69-70). They contain high Cr, Ni and V concentrations. The spidergrams (Fig.3, *a*, *b*) show positive anomalies for Ba, Rb, and Pb, and negative anomalies for Ta, Nb, and Zr. The rocks are enriched in REE (ΣREE = 115-130 ppm), with an indistinct Eu-minimum (Eu/Eu* = 0.78-0.91) and fractionated REE distribution $(La/Yb)_N$ = 8.2-25. In schists with more plagioclase than mafic schists, the mg# value decreases to 55-57. The spidergrams are similar, but the Ba concentration is higher (2200 ppm). The presence of a positive Sr anomaly increases Sr/Y ratio to 23-30 for melanocratic crystalline schists and 55-65 for plagiocrystalline schists. REE concentration increases (ΣREE = 162 ppm) mainly due to light lanthanides, resulting in a $(La/Yb)_N$ value of 11.9-14.5 and the formation of a positive Eu anomaly (Eu/Eu* = 1.06-1.14). Cataclased and silicified crystalline schists (sample 696) contain the highest REE concentrations (ΣREE = 286 ppm), show the Eu-minimum (Eu/Eu* = 0.66), and their REE-spectrum in the LREE field is convex.

Two-pyroxene plagiogneisses, which are petrochemically equivalent to diorites and quartz diorites, plot in the tonalite field based on their normative feldspar ratio (see Fig.2, *d*). In two cases, they are present in the granodiorite field (samples 346 and 347a, K_2O/Na_2O = 0.7-1.0). Most rocks of this group display positiveanomalies for Rb, Ba, and Pb, and negative anomalies for Ti, P, Nb, and Ta, with occasional anomalies for Th and U. The REE spidergrams are asymmetric, showing fractionated distribution in the L- and MREE fields and a flat distribution for HREE, beginning with Ho $(Ho/Yb)_N$ = 1.07-1.15. The Eu anomaly is either poorly-defined or absent (Eu/Eu* = 0.85-1.10).

Rocks with high K_2O concentrations (sample 346 and 347a) display positive anomalies for Rb, Ba, Pb, and Sr, the highest depletion in Ta and Nb, and high Sr/Y (68-88), Nb/Ta (23-30), and $(La/Yb)_N$ (248-25.6) ratios. Cataclastic varieties of two-pyroxene gneisses (samples 694 and 695) contain low concentrations of K, Cs, Rb and Ba, and elevated concentrations of U and Th. Zr/Y ratio of 5-17.8 and La/Yb ratio of 9-38 markedly exceed the indicator values for separation of tholeiitic and calc-alkaline series (> 4.5 and > 5.3, respectively) [24], indicating that the rocks discussed are part of a calc-alkaline series (Fig.2, *g*).

Granitoids are described as Mg-rich, calc-alkaline, and peraluminous (ASI = 1.12-1.14). They have potassium levels comparable to shoshonites. The trace-element and rare-earth element spectra of gneissose granites (sample 347) are similar to those of the two-pyroxene gneisses, displaying positive anomalies for Rb, Ba, Th, and Pb, and negative anomalies for Ti, Ta, Nb, and P. A high Sr/Y ratio of 120 and the highest Nb/Ta ratio of 41 were revealed. The REE spectrum is similar to that of two-pyroxene gneisses, and Eu-minimum is absent (Eu/Eu* = 1.0), but REE distribution is more fractionated $(La/Yb)_N$ = 75.

Alaskitic granites (sample 673) display positive Rb, U, Pb, Sr, and Eu anomalies, with the highest Sr/Y ratio of 322 and the lowest Nb/Ta ratio of 5. The rocks are depleted in REE (ΣREE = 14.7 ppm), and show a fractionated REE distribution with $(La/Yb)_N$ = 40. The REE spectrum in the Er-Lu zone is convex, and there is a well-defined positive Eu anomaly (Eu/Eu* = 12).

U-Pb age. Zircon age dating (Table 2) was conducted for five samples: two-pyroxene schists (samples 672 and 696), two-pyroxene plagiogneisses (samples 696a and 346), and alaskitic gneissose granites (sample 673). For sample 672, we obtained only metamorphic zircon with discordant U-Pb age values. The upper intersection of the Discordia curve from six analyses yields an age of 1991±23 Ma.

In *Opx-Cpx schists* (sample 696) of metagabbrodiorite composition, zircon occurs as grey rounded 50-100 μm long short-prismatic grains with the elongation coefficient (EC) of 1-2. The well-defined BSE image (Fig.4, *a*, *b*) shows cores portions with sectoral and oscillatory zoning, and two types of shells: thin white, light-grey, and wider dark-grey to black. The cores have median concentrations of Th at 156 ppm and U at 237 ppm, with a Th/U ratio of 0.65. Two grains with analytical points 1.1 and 6.1 show higher Y 1198-1593 ppm and ΣREE 959-1345 ppm concentrations (Table 3). The REE spectra (Fig.5, *a*) clearly show positive Ce (Ce/Ce* = 8.38-33.4) and negative Eu (Eu/Eu* = 0.38-0.80) anomalies.

Results of U-Pb (SHRIMP II) zircon analyses

Analysis spots	$^{206}Pb_c$,%	U, ppm	Th, ppm	$\frac{^{232}Th}{^{238}U}$	$^{206}Pb^*$, ppm	Age $^{206}Pb/^{238}U$, Ma	Age $^{207}Pb/^{206}Pb$, Ma	*D*, %	(1) $^{238}U/^{206}Pb$	±, %	(1) $^{207}Pb^*/^{206}Pb^*$	±, %	(1) $^{207}Pb^*/^{235}U$	±, %	(1) $^{206}Pb^*/^{238}U$	±, %	Rho
Opx-Cpx shists (sample 696)																	
1.1	0.03	381	292	0.79	124	2071±17	2096±8	1	2.639	0.93	0.12982	0.44	6.783	1.0	0.3790	0.9	0.906
2.1	0.02	412	301	0.75	128	1984±16	2016±8	2	2.774	0.95	0.12410	0.45	6.167	1.0	0.3604	0.9	0.904
3.1	0.04	252	167	0.68	81.9	2066±17	2097±9	1	2.646	0.97	0.12993	0.53	6.769	1.0	0.3779	1.0	0.878
4.1	0.13	129	64	0.52	42.5	2093±19	2074±14	–1	2.606	1.10	0.12830	0.81	6.784	1.3	0.3836	1.1	0.799
5.1	0.01	183	92	0.52	59.0	2050±18	2077±11	1	2.670	1.00	0.12843	0.65	6.631	1.2	0.3745	1.0	0.841
5.2	0.10	367	80	0.22	108	1892±16	1964±9	4	2.930	0.95	0.12050	0.53	5.669	1.1	0.3412	1.0	0.874
6.1	0.03	245	170	0.72	79.3	2060±18	2066±10	0	2.656	1.00	0.12762	0.56	6.625	1.1	0.3765	1.0	0.874
6.2	0.04	584	188	0.33	179	1965±15	1973±7	0	2.806	0.91	0.12116	0.39	5.953	1.0	0.3563	0.9	0.921
7.1	0.12	119	70	0.61	39.4	2103±19	2085±14	–1	2.592	1.10	0.12900	0.81	6.864	1.4	0.3857	1.1	0.801
8.1	0.21	94	96	1.06	28.7	1959±19	1980±19	1	2.815	1.10	0.12160	1.00	5.955	1.6	0.3551	1.1	0.739
8.2	0.05	202	99	0.51	63.2	2000±18	2059±11	3	2.748	1.00	0.12719	0.63	6.380	1.2	0.3638	1.0	0.855
9.1	0.07	211	151	0.74	69.1	2081±18	2090±11	0	2.624	1.00	0.12940	0.61	6.799	1.2	0.3811	1.0	0.858
Cpx-Opx plagiogneisses (sample 696a)																	
1.1	0.05	222	143	0.67	70.8	2035±17	2112±9	4	2.693	0.96	0.13102	0.53	6.707	1.1	0.3713	1.0	0.877
2.1	0.00	163	83	0.53	52.8	2063±18	2092±11	1	2.652	0.99	0.12958	0.60	6.737	1.2	0.3771	1.0	0.856
3.1	0.01	162	100	0.64	51.1	2020±17	2094±11	4	2.718	10.0	0.12974	0.61	6.583	1.2	0.3680	10	0.853
4.1	0.13	206	126	0.63	67.6	2086±18	2095±10	0	2.617	10.0	0.12977	0.57	6.835	1.2	0.3820	10	0.867
5.1	0.09	89	30	0.35	29.7	2118±20	2083±15	–2	2.570	1.10	0.12890	0.83	6.917	1.4	0.3891	1.1	0.795
6.1	0.08	139	64	0.47	45.5	2077±23	2101±12	1	2.630	1.30	0.13019	0.71	6.820	1.5	0.3801	1.3	0.876
7.1	0.01	212	123	0.60	67.6	2032±20	2104±9	4	2.698	1.10	0.13047	0.53	6.668	1.3	0.3706	1.1	0.905
8.1	0.07	364	27	0.08	112	1980±18	1981±8	0	2.780	1.10	0.12166	0.45	6.032	1.2	0.3596	1.1	0.921
8.2	0.08	82	40	0.50	27.0	2097±22	2099±17	0	2.600	1.20	0.13000	0.98	6.890	1.6	0.3845	1.2	0.775
9.1	0.27	17	19	1.13	5.39	1986±26	1979±36	0	2.770	1.50	0.12150	2.00	6.050	2.5	0.3608	1.5	0.601
9.2	0.00	144	63	0.45	46.8	2064±19	2072±12	0	2.649	1.10	0.12809	0.69	6.666	1.3	0.3774	1.1	0.839
10.1	0.03	539	97	0.19	162	1937±16	1988±8	3	2.853	0.93	0.12218	0.46	5.905	1.0	0.3505	0.9	0.897
10.2	0.10	208	102	0.51	67.5	2064±17	2104±10	2	2.649	0.97	0.13045	0.57	6.789	1.1	0.3775	1.0	0.864

Journal of Mining Institute. 2025. Vol. 272. P. 16-39

Analysis spots	$^{206}Pb_c$, %	U, ppm	Th, ppm	$\frac{^{232}Th}{^{238}U}$	$^{206}Pb^*$, ppm	Age $^{206}Pb/^{238}U$, Ma	Age $^{207}Pb/^{206}Pb$, Ma	*D*, %	(1) $^{238}U/^{206}Pb$	±, %	(1) $^{207}Pb^*/^{206}Pb^*$	±, %	(1) $^{207}Pb^*/^{235}U$	±, %	(1) $^{206}Pb^*/^{238}U$	±, %	Rho
Cpx-Opx plagiogneisses (sample 346)																	
1.1	0.13	348	219	0.65	110	2018±16	2040±10	1	2.720	1.0	0.12583	0.59	6.378	1.1	0.3676	1.0	0.849
2.1	0.04	558	288	0.53	170	1958±18	1945±8	–1	2.818	1.1	0.11924	0.43	5.834	1.2	0.3548	1.1	0.929
3.1	0.06	362	151	0.43	114	2014±16	2019±9	0	2.726	0.9	0.12429	0.51	6.286	1.0	0.3668	0.9	0.870
4.1	0.03	326	136	0.43	105	2048±16	2027±9	–1	2.675	0.9	0.12487	0.50	6.437	1.0	0.3739	0.9	0.879
5.1	0.00	942	328	0.36	274	1879±14	2023±6	8	2.955	0.9	0.12461	0.36	5.814	0.9	0.3384	0.9	0.922
6.1	0.38	502	200	0.41	162	2052±16	2033±11	–1	2.668	0.9	0.12529	0.64	6.475	1.1	0.3748	0.9	0.811
7.1	0.06	482	315	0.68	153	2023±15	2025±9	0	2.712	0.9	0.12471	0.48	6.340	1.0	0.3687	0.9	0.877
8.1	0.04	361	160	0.46	115	2029±16	2002±9	–1	2.703	0.9	0.12313	0.50	6.281	1.0	0.3699	0.9	0.875
9.1	0.03	424	247	0.60	133	2006±16	2031±15	1	2.739	0.9	0.12510	0.83	6.298	1.2	0.3650	0.9	0.741
10.1	0.08	247	104	0.44	79.3	2043±17	2025±11	–1	2.682	1.0	0.12470	0.63	6.410	1.1	0.3728	1.0	0.832
Alaskitic gneissose granites (sample 673)																	
1.1	0.52	171	134	0.81	49.5	1861±8	1909±27	3	2.985	0.52	0.11690	1.50	5.393	1.6	0.3347	0.5	0.323
2.1	0.00	401	146	0.38	123	1969±6	1964±10	0	2.799	0.37	0.12054	0.58	5.939	0.7	0.3573	0.4	0.533
3.1	0.00	98	89	0.94	30.2	1970±11	1975±21	0	2.797	0.63	0.12120	1.20	5.976	1.4	0.3575	0.6	0.467
4.1	0.00	72	94	1.35	22.2	1968±12	1984±24	1	2.801	0.72	0.12190	1.40	5.999	1.5	0.3570	0.7	0.470
5.1	0.19	131	119	0.94	39.7	1948±9	1970±22	1	2.834	0.56	0.12090	1.30	5.882	1.4	0.3527	0.6	0.407
6.1	1.17	109	48	0.46	32.1	1884±15	1916±69	2	2.938	0.92	0.11730	3.90	5.490	4.0	0.3395	0.9	0.231
7.1	0.06	583	201	0.36	175	1935±5	1962±10	1	2.856	0.32	0.12037	0.56	5.811	0.7	0.3501	0.3	0.498
8.1	0.00	85	121	1.48	25.9	1964±12	1979±23	1	2.808	0.69	0.12160	1.30	5.970	1.5	0.3561	0.7	0.469
9.1	0.00	77	84	1.12	23.4	1939±12	1948±24	0	2.849	0.72	0.11950	1.40	5.783	1.5	0.3510	0.7	0.467
10.1	0.25	152	155	1.05	46.8	1970±9	1971±24	0	2.796	0.54	0.12100	1.40	5.965	1.5	0.3575	0.5	0.370

Note. Pb_c and Pb* are common and radiogenic Pb respectively. The calibration errors of the standard are 0.35 %. (1) is the correction on ^{204}Pb. *D* is the discordance. Rho is the correlation coefficient. The errors of individual analyses (ratios and ages) are reported on 1σ level, and the errors of the calculated age values are on 2σ level.

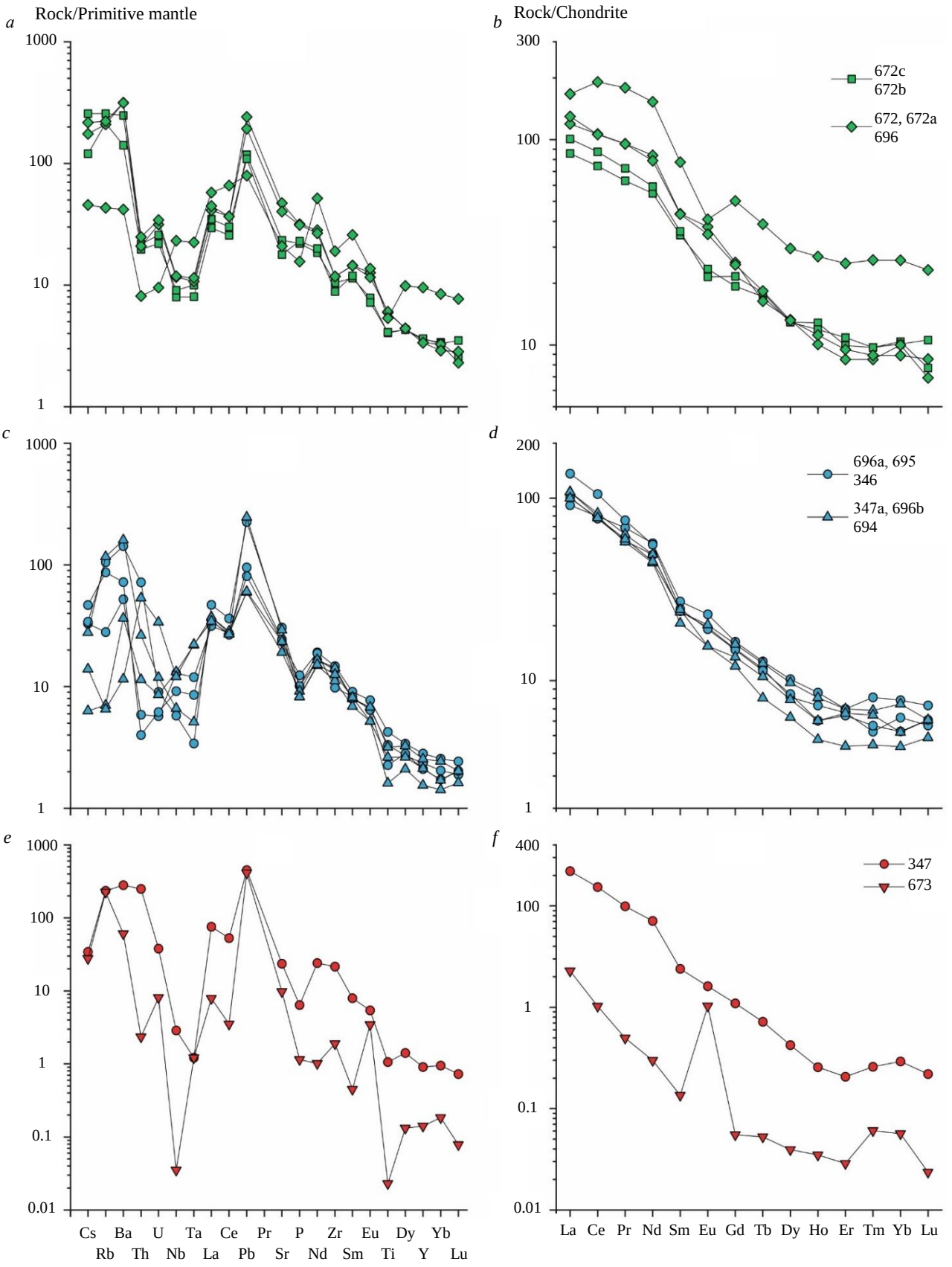

Fig.3. Multi-element diagrams for Saltakh Massif rocks: *a*, *b* – Opx-Cpx schists;
c, *d* – Cpx-Opx plagiogneisses; *e*, *f* – gneissose granites.
Concentrations were normalized for the primitive mantle and CI chondrite compositions after [25]. For sample numbers, see Table 1

The REE distribution pattern is generally consistent with magmatically derived zircon, displaying a steep slope from La to Lu with positive Ce and negative Eu anomalies. In the HREE field, the spectra do not extend outside the magmatic zircon field, while the zircon is richer in LREE than a magmatic type (Fig.5, *a*). The entire zircon deviates in REE (Fig.5, *g*) from a magmatic type, occurring in the porous zircon field. U and Ca concentrations are low (Fig.5, *h*).

The shells show a lower Th/U ratio of 0.16-0.23, Th concentration of 85.2-206 ppm, U concentration of 528-917 ppm, and P concentration is lower – 108-136 ppm. Ce anomalies are weaker than those in the cores (Ce/Ce* = 4.87-7.65), but positive Eu anomalies are present (Eu/Eu* = 1.08-1.18). REE concentration in the shells are lower than in the cores (ΣREE = 164-378 ppm), and the REE distribution spectra are more subdued, showing a low $(Sm/La)_N$ ratio of 1.44-2.67. Metamorphic zircon with low Th concentration and a low Th/U ratio is crystallized near the solidus line simultaneously with monazite and allanite, which are known as major Th concentrators [26]. However, Th/U ratio decreases here due to the growth of U in zircon. P, Y, and ΣREE decrease probably due to the simultaneous zircon and apatite crystallization.

A positive Ce anomaly indicates oxidation conditions during zircon crystallization. The reduced pattern of Ce-anomaly in zircon shells indicates a decline in oxygen activity. A negative Eu anomaly in zircon cores suggests that plagioclase was crystallized together with zircon. A positive Eu anomaly in zircon shells indicates that plagioclase is dissolved, and the zircon crystallization medium is enriched in europium. Maximum age values of $^{207}Pb/^{206}Pb$ in the cores are 2103±19 Ma. The upper intersection of the Discordia line from seven measurements yields an age of 2086±8 Ma (see Fig.4, *b*). Shells that are grey in cathode luminescence (CL) contain more uranium, and show a mean Th concentration of 134 ppm, U concentration of 456 ppm, and a Th/U ratio of 0.28. A cluster of measurements made for the shells yields the value 1971±10 as the upper intersection of the Discordia line from three measurements, indicating multiple partial melting processes. Thin white shells have not been studied due to their thinness.

Cpx-Opx plagiogneisses (sample 696a), petrochemically equivalent to quartz metadiorites, contain zircon similar to sample 696 (Fig.4, *c*, *d*). Shells that are white in CL are wider and can thus be dated. The cores of grains displays the following mean concentrations, ppm: Th 134, U 317, Th/U 0.40, Y 624, Nb 25; ΣREE = 524. The increase in REE concentration is accompanied by a decrease of the Eu-minimum. The Eu/Eu* ratio is generally 0.33-0.66, while at points 1.1 and 4.1, where ΣREE increase to 564-598 ppm, the Eu-anomaly increases and becomes positive (Eu/Eu* = 1.03-2.89). Zircon cores, like those in sample 696, are enriched in LREE (Fig.5, *b*), but some of the cores are enriched in Ca (Fig.5, *h*). The Discordia line, constructed from nine measurements in zircon cores, yields an upper intersection at 2100±7 Ma (Fig.4, *d*), which is accepted as the time of zircon crystallization in the magmatic protolith of two-pyroxene plagiogneisses.

The shell, which is white in CL, with the analytical point 9.1, shows an age of 1986±26 Ma and low Th (24) and U (48) concentrations (ppm), but a Th/U ratio of 0.51 is similar to that of magmatic zircon. Negative Eu anomaly (Eu/Eu* = 0.65) and positive Ce anomaly (Ce/Ce* = 19.8) are well-defined. At this point, REE concentration is lower than in the cores (Fig.5, *c*), and the Eu-minimum decreases (Eu/Eu* = 0.65). Later shells that are dark in CL (points 8.1 and 10.1) show higher concentrations than in white shells, ppm: Th 56-100, U 701-786, and a low Th/U ratio of 0.08-0.13 typical of metamorphic zircon. They generally show low REE (ΣREE = 192-239 ppm), Y of 156-238 ppm, and Ce/Ce* of 3.22-3.58, but they are enriched in Eu (Eu/Eu* = 1.54-2.92), Li 9.72-11.36 ppm, and Hf 15124 ppm. The Discordia line from three measurements in metamorphic shells yields an upper intersection with an age of 1984±11 Ma indicating the time of metamorphism.

Cpx-Opx plagiogneisses (sample 346), petrochemically equivalent to metatonalites, contain grey zircon crystals with yellow and pink shades of colour. These semi-transparent, subidiomorphic crystals exhibit thin, well-defined growth zones under an optical microscope (Fig.4, *e*, *f*). The crystals are 100-220 μm long, with their EC of 2-4. The zircons are dark in CI and their zoning is either oscillatory or is present as relics.

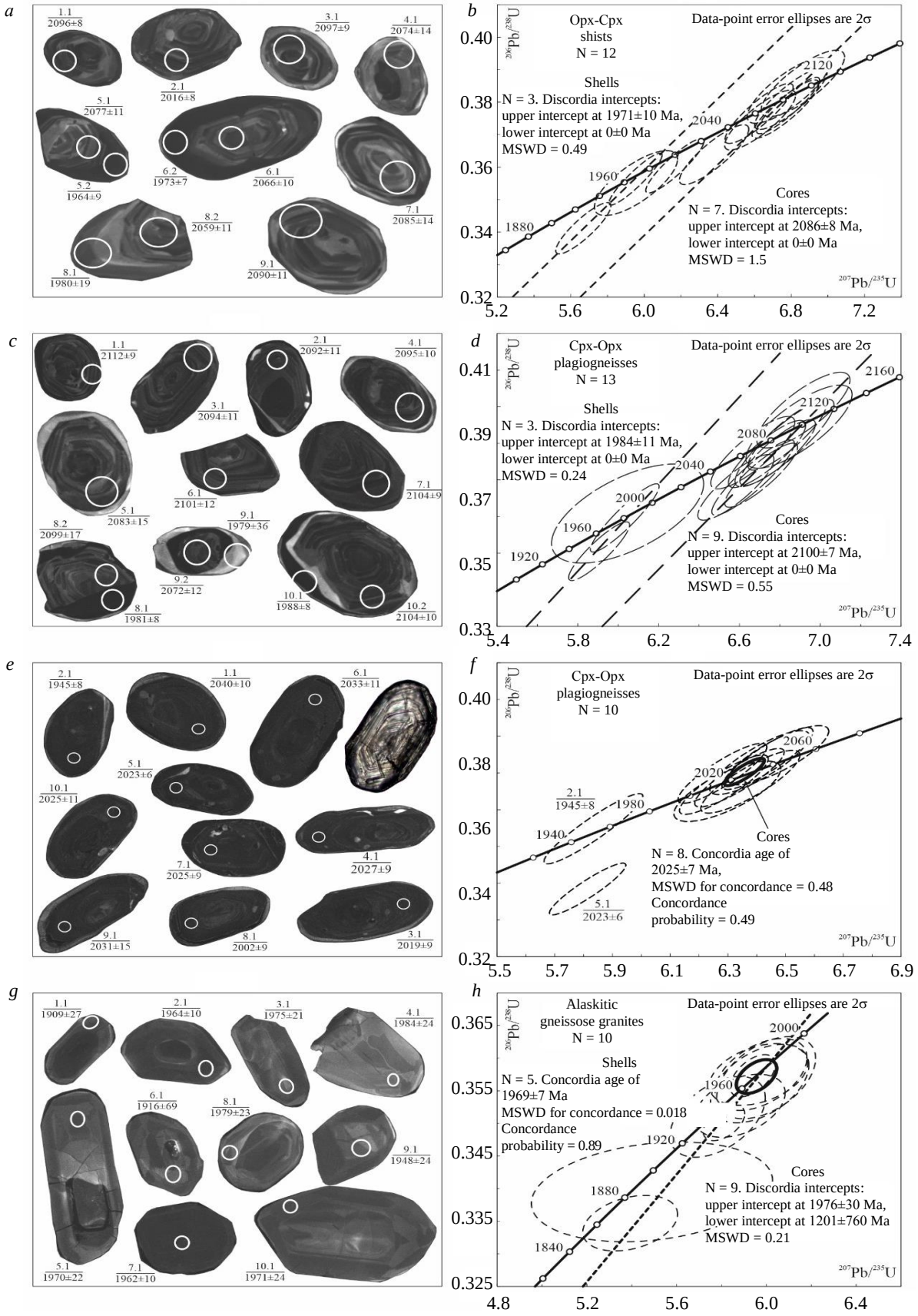

Fig.4. Cathode luminescent images and age of zircon from Opx-Cpx schists (sample 696) (*a*, *b*); Cpx-Opx plagiogneisses (sample 696a) (*c*, *d*); Cpx-Opx plagiogneisses (sample 346) (*e*, *f*); alaskitic gneissose granites (sample 673) (*g*, *h*). From here onwards, white circles indicate analytic craters. Analysis number is in the numerator and $^{207}Pb/^{206}Pb$ age is in the denominator. The crater is about 20 μm in diameter

Table 3

Concentrations (ppm) of trace elements and REE in the zircon

Element	Opx-Cpx shists (sample 696)									Cpx-Opx plagiogneisses (sample 696a)									
	1.1	3.1	4.1	5.1	5.2	6.1	6.2	7.1	9.1	1.1	2.1	3.1	4.1	5.1	6.1	7.1	8.1	8.2	9.1
La	2.06	0.31	0.13	1.28	0.73	1.08	2.75	0.64	0.30	2.04	0.06	0.35	0.62	1.36	0.50	0.35	1.60	1.61	0.30
Ce	67.7	27.1	21.8	27.4	17.8	38.3	36.4	27.8	34.2	39.6	25.4	27.5	31.4	15.8	21.2	31.4	16.4	31.4	25.1
Pr	1.53	0.36	0.19	0.49	0.43	1.11	1.19	0.58	0.31	1.64	0.12	0.43	1.23	0.43	0.58	0.27	0.77	0.89	0.31
Nd	11.3	2.20	1.63	2.32	2.42	8.11	5.95	3.52	2.77	10.3	1.24	3.16	9.94	2.01	4.40	2.97	3.95	6.04	1.42
Sm	10.8	3.16	2.58	1.96	1.23	8.30	2.47	3.03	2.90	4.90	2.07	2.64	5.35	1.03	2.99	3.08	1.22	6.22	1.24
Eu	3.92	0.91	0.63	1.11	0.66	2.40	1.64	0.79	0.86	8.11	0.52	0.56	3.01	0.25	1.36	1.22	1.83	2.47	0.63
Gd	43.3	14.3	9.93	9.05	2.83	32.7	7.28	10.0	14.3	15.0	9.00	9.83	14.7	3.76	12.0	12.4	3.02	23.4	6.98
Dy	140	61.5	46.7	36.0	12.2	102	29.8	35.3	55.5	54.2	38.8	35.6	53.8	14.6	48.8	48.0	12.0	72.4	28.3
Er	299	149	110	86.7	29.4	216	70.6	82.9	125	125	91.6	86.6	120	37.6	123	119	35.0	157	63.8
Yb	651	370	267	205	80.4	467	185	184	284	285	218	199	273	97.6	291	262	97.0	325	138
Lu	115	69.5	47.0	37.2	15.9	81.9	34.7	34.0	51.0	52.8	42.2	36.0	50.4	18.2	57.2	47.2	19.4	57.1	24.9
Li	3.61	5.08	2.94	6.85	12.9	1.19	13.5	2.99	7.58	5.53	3.07	7.10	5.01	2.58	3.98	6.57	9.72	2.46	1.96
P	220	275	158	292	136	175	108	88.4	158	139	118	111	177	208	207	165	66.9	93.8	188
Ca	10.7	31.5	6.74	34.6	123	11.1	6.42	4.36	10.0	173	2.27	27.5	27.3	191	29.8	2.77	4.03	7.13	52.5
Ti	13.6	6.75	8.98	10.9	9.79	7.48	10.8	16.0	7.25	35.5	8.00	13.8	8.88	5.91	9.08	7.16	6.88	7.55	8.51
Sr	0.67	0.46	0.50	0.65	0.83	0.62	0.39	0.45	0.65	2.29	0.34	0.66	0.81	0.77	1.20	0.51	0.57	0.55	0.72
Y	1593	806	576	480	170	1198	402	444	710	711	506	521	679	203	650	621	156	859	315
Nb	83.4	60.9	50.0	61.6	46.9	29.9	34.9	35.7	36.4	29.3	36.4	22.3	20.4	24.1	12.4	20.6	12.4	27.5	30.1
Ba	1.46	1.10	2.15	2.58	3.60	1.98	2.06	2.49	2.21	10.2	1.72	2.73	1.47	1.14	1.83	1.71	1.29	1.03	3.18
Hf	13762	10718	10525	11602	9958	11246	12595	11482	10775	8544	11389	11819	11338	12507	12034	12266	15124	13708	13436
Th	418	171	65.7	153	85.2	217	206	85.0	354	154	104	137	161	34.6	85.3	306	56.2	95.4	24.3
U	708	384	192	392	528	418	917	200	523	300	271	289	345	133	264	488	701	375	48
Th/U	0.59	0.44	0.34	0.39	0.16	0.52	0.23	0.42	0.68	0.51	0.38	0.47	0.47	0.26	0.32	0.63	0.08	0.25	0.51
Eu/Eu*	0.55	0.41	0.38	0.80	1.08	0.44	1.18	0.44	0.40	2.89	0.37	0.33	1.03	0.39	0.69	0.60	2.92	0.62	0.65
Ce/Ce*	9.23	19.7	33.4	8.38	7.65	8.49	4.87	11.0	27.0	5.23	72.7	17.1	8.71	5.02	9.55	24.7	3.58	6.36	19.8
ΣREE	1345	699	507	408	164	959	378	383	571	598	429	401	564	193	563	528	192	684	291
ΣLREE	82.6	30.0	23.7	31.4	21.4	48.6	46.3	32.6	37.6	53.5	26.8	31.5	43.2	19.6	26.7	35.0	22.7	39.9	27.1
ΣHREE	1248	665	480	374	141	900	327	346	530	532	400	367	512	172	532	489	166	635	262
$(Lu/La)_N$	538	2148	3450	281	209	734	122	509	1643	249	6551	989	781	129	1097	1316	116	343	804
$(Lu/Gd)_N$	21.5	39.4	38.3	33.3	45.6	20.3	38.6	27.4	28.9	28.5	37.9	29.6	27.7	39.1	38.7	30.7	51.9	19.8	28.8
$(Sm/La)_N$	8.41	16.2	31.5	2.46	2.67	12.4	1.44	7.55	15.5	3.85	53.5	12.1	13.8	1.21	9.53	14.3	1.21	6.19	6.65
T(Ti),°C	771	710	734	751	741	718	750	786	715	869	724	772	733	699	735	714	711	719	729

End of Table 3

Element	Cpx-Opx plagiogneisses (sample 696a)			Cpx-Opx plagiogneisses (sample 346)								
	9.2	10.1	10.2	1.1	3.1	4.1	5.1	6.1	7.1	8.1	9.1	10.1
La	2.42	2.03	0.64	10.4	5.58	6.64	22.7	7.59	7.07	2.89	28.7	14.0
Ce	35.6	15.5	37.4	88.4	56.9	65.4	106	80.7	49.1	38.9	301	87.1
Pr	2.13	0.67	0.41	10.2	5.83	4.44	14.0	6.28	3.48	2.54	31.4	17.8
Nd	14.6	3.15	3.13	76.1	43.7	30.8	65.8	46.8	23.9	16.5	198	130
Sm	4.87	1.15	3.75	28.0	12.3	12.2	11.6	14.7	9.38	8.67	32.4	24.2
Eu	1.52	1.05	1.14	5.23	2.67	1.82	4.07	3.47	2.62	1.45	16.6	7.00
Gd	11.6	3.73	16.2	48.8	17.9	20.8	29.4	21.9	22.0	16.8	41.8	42.2
Dy	35.6	17.0	75.4	85.9	40.6	39.3	82.2	33.2	54.7	31.3	40.7	55.9
Er	96.1	45.3	205	169	79.8	88.3	200	71.1	128	78.5	115	109
Yb	238	124	472	381	206	224	580	168	304	196	306	267
Lu	43.9	24.6	93.1	69.5	40.9	41.6	126	32.9	55.3	33.8	51.4	54.0
Li	4.14	11.4	2.61	2.55	9.32	6.12	27.5	9.51	2.98	5.28	6.07	9.78
P	913	66.0	268	96	185	135	205	15	61	164	97	124
Ca	1273	20.4	61.2	99	76	82	3558	240	96	122	220	577
Ti	8.38	8.74	10.0	19.5	15.7	12.0	28.6	10.8	12.2	9.97	22.5	24.5
Sr	3.46	0.63	0.65	1.80	1.09	1.33	123	5.01	3.43	2.37	7.17	2.90
Y	476	236	1018	937	500	487	1 198	333	711	421	482	702
Nb	33.8	18.6	25.1	100	63.1	54.9	35.8	56.2	48.8	42.0	81.0	64.9
Ba	2.90	2.05	1.56	3.28	2.59	1.54	11.8	8.23	6.64	6.27	11.7	9.56
Hf	12532	13032	11668	13227	15900	12755	19615	14366	11381	10908	12556	15979
Th	86.4	100	176	284	225	186	494	262	265	149	312	189
U	252	786	453	613	687	567	2 903	709	564	453	713	589
Th/U	0.34	0.13	0.39	0.46	0.33	0.33	0.17	0.37	0.47	0.33	0.44	0.32
Eu/Eu*	0.61	1.54	0.44	0.43	0.55	0.35	0.67	0.59	0.56	0.37	1.37	0.67
Ce/Ce*	3.79	3.22	17.7	2.08	2.41	2.91	1.43	2.83	2.39	3.48	2.42	1.33
ΣREE	487	239	909	972	512	535	1241	486	660	428	1162	809
ΣLREE	54.7	21.4	41.5	185	112	107	208	141	84	61	558	249
ΣHREE	425	215	862	754	385	414	1017	327	564	357	555	529
$(Lu/La)_N$	175	117	1408	64.4	70.6	60.3	53.2	41.8	75.3	113	17.2	37.1
$(Lu/Gd)_N$	30.5	53.3	46.4	11.5	18.5	16.2	34.6	12.2	20.4	16.3	9.90	10.4
$(Sm/La)_N$	3.22	0.91	9.42	4.31	3.52	2.93	0.82	3.09	2.12	4.81	1.81	2.76
T(Ti),°C	728	731	743	805	785	759	845	750	761	743	820	829

Note. Analytical spot numbers correspond to those in Fig.4; *T*(Ti),°C is the zircon crystallization temperature evaluated by the thermometer [27].

Journal of Mining Institute. 2025. Vol. 272. P. 16-39

Journal of Mining Institute. *2025. Vol. 272. P. 16-39*

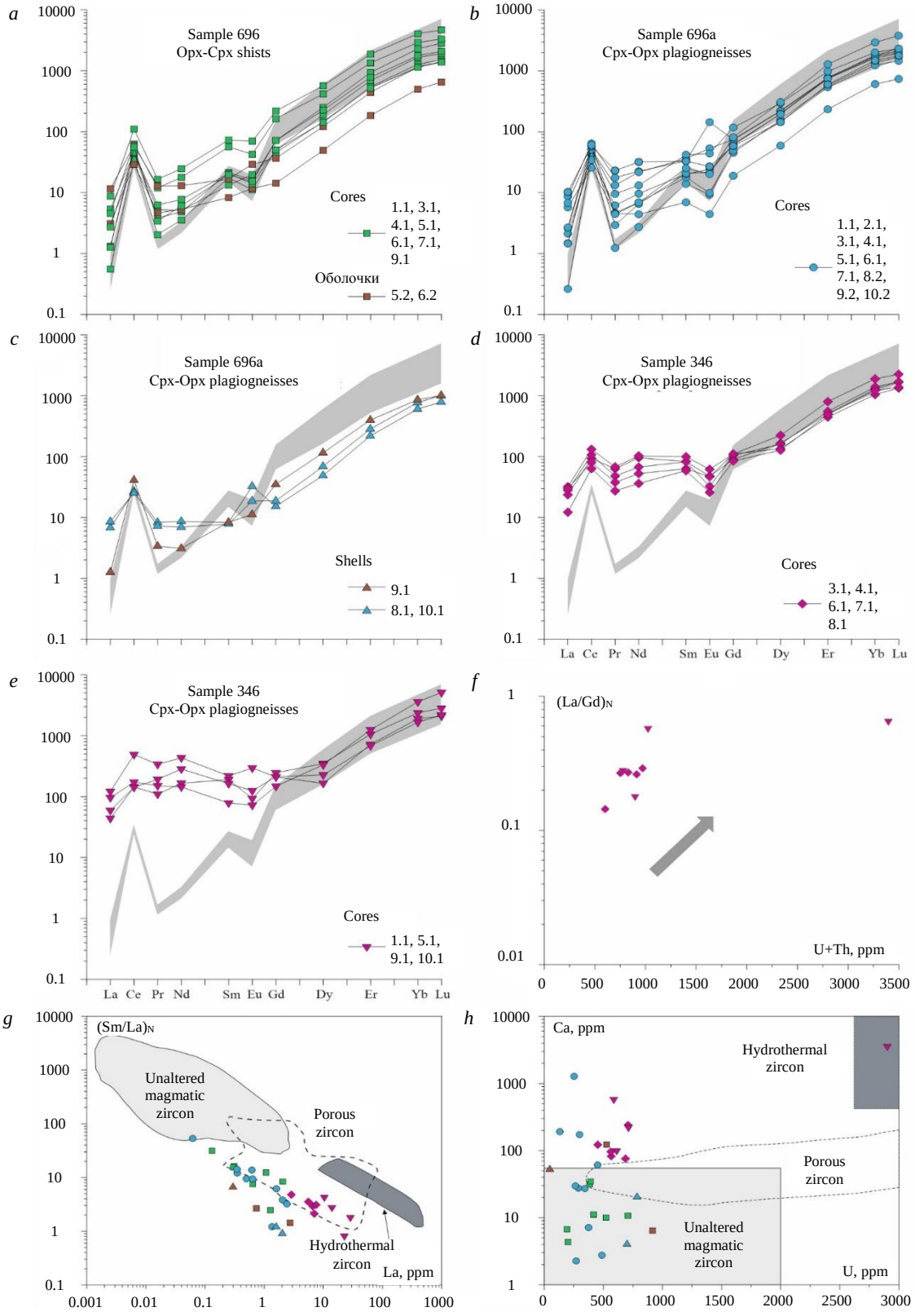

Fig.5. Geochemical diagrams for zircon from Saltakh rocks: *a-e* – diagrams showing REE distribution in zircon from samples 696, 696a and 346. Concentrations normalized for CI chondrite composition after [25]. Grey field – magmatic zircon composition after [28]. Numbers of spectra are consistent with the numbers of analytical points in Fig.4 and in Table 2; *f* – types of zircon in $(La/Gd)_N$-U+Th diagrams (after [29], arrow indicates a LREE concentration trend, provoked by the damage of the crystalline lattice due to radioactive irradiation); *g*, *h* – $(Sm/La)_N$-La and Ca-U diagrams after [30]. Porous zircon is understood as altered magmatic zircon produced by dissolution-redeposition in the presence of water fluid [31]

The zircons contain, ppm: Th 149-494, U 453-713, and Th/U 0.17-0.46. Their distinctive feature is LREE concentration (Fig.5, *d*, *f*). Their REE-richest spectra (ΣLREE = 185-558 ppm) are shown in Fig.5, e. Based on its LREE enrichment, the mineral falls within the porous zircon field, (Fig.5, *g*). Ca concentration is also high (Fig.5, *h*). The zircons exhibit a poorly defined positive Ce anomaly (Ce/Ce* = 1.33-2.91) and and a poorly defined Eu-minimum (Eu/Eu* = 0.35-0.67). The Eu/Eu* ratio shows a positive value (1.37) in zircon with point 9.1. Characteristic Hf concentrations range from 10908 to 19615 ppm.

Most of the figurative points of zircon form a compact field on the Concordia line. A concordant age of 2025±7 Ma was obtained for eight points (see Fig.4, *e*, *f*), except for a grain with an analysis 5.1 showing 8 % discordance and a grain at 2.1, with an age of 1945±8 Ma. The discordant grain with analysis 5.1 contains anomalously high Ca, Sr, P, Y, REE, Th, U, and Hf concentrations.

Zircon from sample 346 has a low $(Lu/Gd)_N$ value of 16.3-34.6. In LREE-richest grains (analytical points 1.1, 6.1, 9.1 and 10.1) a low $(Lu/Gd)_N$ value of 9.9-12.2 suggests the presence of garnet in paragenesis during zircon crystallization.

Zircon from the *alaskitic gneissose granites* (sample 673) appears as grey transparent and semi-transparent, prismatic, and rounded idiomorphic to subidiomorphic crystals. The crystals are 200-400 μm in length with an EC of 1-2. Zircon grains in CL are polygenic, with occasionally identifiable cores and shells. Many grains exhibit coarse concentric and mottled zoning. Zones that are light in CL contain 97 ppm of Th and 83 ppm of U, with a Th/U ratio of 1.22. The grain margins are generally black in CL, containing higher Th (258 ppm) and U (134 ppm) concentrations and have a Th/U ratio of 0.67. The Discordia line from 10 analyses yields an upper intersection age of 1969±7 Ma, which coincides with the age 1971±10 Ma of black shells in sample 696, suggesting the age of rock anatexis in the Saltakh zone and the crystallization age of alaskitic anatectic melt.

The isotopic Sm-Nd and Rb-Sr systems of the analyzed rocks were studied in five samples (Table 4). In most rocks, $^{147}Sm/^{144}Nd$ ratios vary slightly (0.10-0.11), generally lower than a medium crustal value (0.12). All the rocks have positive $\varepsilon_{Nd}(T)$ values ranging from +1.9 to +4.1. Their points are plotted just below the Nd evolution line in a depleted mantle source (Fig.6, *a*), indicating a magma source had a very short crustal prehistory. Only the gabbroic rocks of sample 696 align with the mantle sequence of rock evolution (Fig.6, *b*). The other rocks deviate due to enrichment in radiogenic strontium. Schists in sample 672c exhibit anomalous Nd isotopic characteristics, likely due to multiple processes.

Table 4

Nd and Sr isotope composition on the rocks of the Saltakh Massif

Sample	Age, Ma	Sm, ppm	Nd, ppm	$^{147}Sm/^{144}Nd$	$^{143}Nd/^{144}Nd$	$\varepsilon_{Nd}(T)$	$T_{(Nd)}$DM, Ga	Rb, ppm	Sr, ppm	$^{87}Rb/^{86}Sr$	$^{87}Sr/^{86}Sr$	$\varepsilon_{Sr}(T)$
346	2025	3.94	24.9	0.0957	0.511397	2.1	2.26	65.9	727	0.2621	0.710767	12.0
672	2100	6.79	37.8	0.1085	0.511515	1.9	2.36	133	1116	0.3454	0.713067	8.37
672c	2100	4.49	18.5	0.1469	0.512868	18	–	148	526	0.8136	0.728116	21.0
696	2100	13.9	73.6	0.1144	0.511683	3.6	2.25	29.5	512	0.1667	0.707128	0.77
696a	2100	4.96	27.7	0.1082	0.511621	4.1	2.20	18.6	545	0.0986	0.706265	17.8

Discussion

The Saltakh Massif consists of granulite-facies two-pyroxene schists and plagiogneisses. A differentiated series of rocks, ranging from gabbro to tonalities, was reconstructed, based on their chemical composition. Despite granulite-facies metamorphism, Saltakh rocks have many features indicative of a shoshonitic type. It has been noted in [32] that shoshonitic series have a high K_2O/Na_2O ratio > 0.5, normative hypersthene ± olivine, low iron, high LILE, high but variable Al_2O_3 (9-20 wt.%) and

Journal of Mining Institute. 2025. Vol. 272. P. 16-39

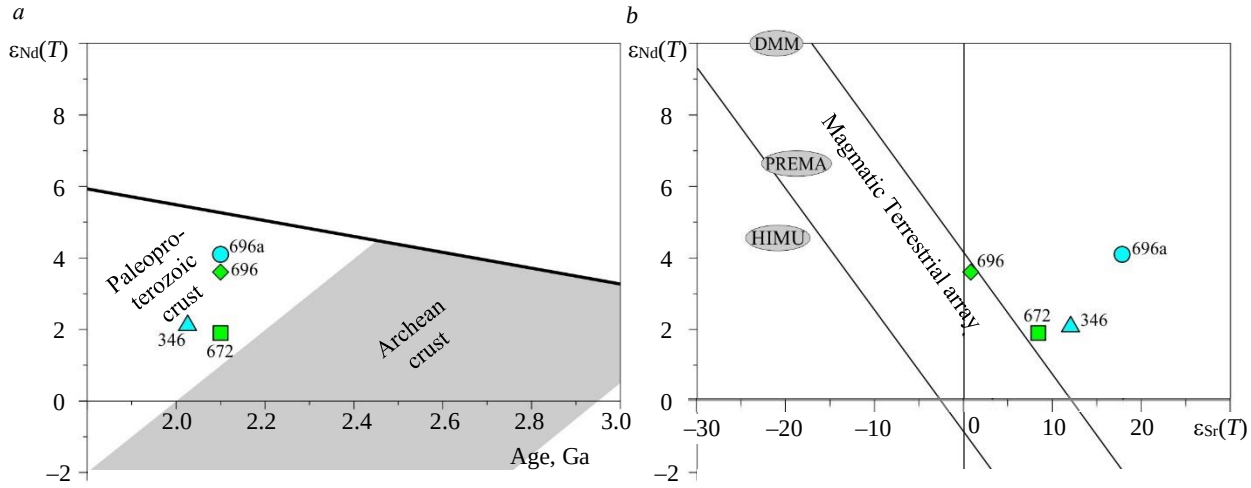

Fig.6. Diagrams of $\varepsilon_{Nd}(T)$ – age (*a*) and $\varepsilon_{Nd}(T)$ – $\varepsilon_{Sr}(T)$ (*b*) for Saltakh Massif rocks. DMM, PREMA, HIMU reservoirs were normalized for their modern isotopic parameters after [33]. Primary isotopic ratios and $\varepsilon_{Nd}(T)$ and $\varepsilon_{Sr}(T)$ values were calculated using values for CHUR $^{143}Nd/^{144}Nd = 0.512638$, $^{147}Sm/^{144}Nd = 0.1967$; UR $^{87}Sr/^{86}Sr = 0.7045$, $^{87}Rb/^{86}Sr = 0.0827$

low TiO_2 concentration. Shoshonites are enriched in both alkaline and alkaline-earth elements, as well as in P, Ce, and Sm, while the concentrations of other incompatible elements, such as Ta, Nb, Zr, Hf, Ti, Y and Yb, remain low [20]. In spite of the slight prevalence of K over Na in some rocks, it is elevated Ce and low Yb concentrations that were responsible for the presence of Saltakh rocks in the shoshonite field (see Fig.2, *h*).

Saltakh rocks are rich in magnesium: mg# is 55-70 in two-pyroxene schists and 50-56 in two-pyroxene plagiogneisses. The protoliths of mafic granulites display the cumulative accumulation of plagioclase. Hence, Al_2O_3, Sr, Ba and REE concentrations increase and positive Eu anomaly appears. Geochemical features ([34] such as MgO/FeOt < 1.39; TiO_2 < 0.41 wt.%; Yb < 1.36 ppm; Sc 38-46 ppm; Eu/Eu* = 0.78-0.91), indicate that the protoliths of melanoschists are non-cumulative rocks, while those of leucoschists (Sc < 33 ppm; Eu/Eu* = 1.06-1.14) are intermediate between cumulative and non-cumulative gabbroic rocks.

Plagiogneisses of diorite composition contain lower Yb (1.02-1.26 ppm), and have more fractionated REE $(La/Yb)_N$ = 11-16. As their silicic acid content increases, Y decreases from 16.5 to 9.55 ppm and the Sr/Y ratio increases to 35-48. The elevated Sr/Y ratio (> 20) is attributed to an abundance of water in the melt, which contributes to the crystallization and fractionation of a phenocryst phase (amphibole and/or biotite), while suppressing plagioclase crystallization [35]. This process is most distinct in two-pyroxene gneisses of tonalite composition (samples 346 and 347a), Sr/Y = 67.6-88. Tonalites are more depleted in HREE $(La/Yb)_N$ = 24.8-25.6, likely due to garnet fractionation. The presence of garnet in the restite is supported by trace element concentrations in zircon, with a low $(Lu/Gd)_N$ value (zircon of sample 346, $(Lu/Gd)_N$ = 9.9-12.2) indicating the presence of garnet in paragenesis upon zircon crystallization. Garnet fractionation is indicated by the increase in $(Dy/Yb)_N$ [36] zircon in mafic rocks $(Dy/Yb)_N$ = 1.23-1.26 to 1.43-1.58 in felsic varieties.

The geochemical characteristics of tonalites suggest that the melt was formed at depth in equilibrium with a garnet-bearing association. Garnetiferous rock varieties are fractionated under similar high-pressure conditions in an aquatic medium, resulting in the formation of TTG-rocks in the lower zone of the island-arc crust [37].

Differences in the geochemistry of potassium granites are noteworthy (see Fig.3, *e*, *f*). Gneissose granites (sample 347) form bands within tonalites. They differ in REE distribution from the 1967±7 Ma anatectic gneissose granites of sample 673 but are similar to tonalites of samples 346 and 347a dated at 2025±7 Ma. Their trace and rare-earth distribution spectra are conformal, showing slightly higher concentrations of Rb, Ba, Th, Pb, Zr, and LREE, but with better-defined depletions in Ti, Ta, Nb, P, and HREE. It appears that the granites of sample 347 were produced by a 2025±7 Ma old impulse of magmatism.

The age of the Saltakh Massif. Zircon monofractions from metadiorites in the northern zone of the massif were dated – the results showed a U-Pb age of 2100-2086 Ma. The structure and geochemistry of the dated zircon cores indicate its magmatic origin. In sample 696, a maximum age value in the cores is 2103±19 Ma, while an age of 2086±8 Ma was obtained from an upper intersection of the Discordia line. For highly metamorphosed rocks, the age decrease along the Concordia line could be due to the loss of radiogenic lead induced by prolonged impact of granulite-facies metamorphism [38]. Thus, an age date of approximately 2100 Ma is the most reliable estimate for the crystallization age of Saltakh gabbrodiorites and diorites.

A smaller concordant age of 2025±7 Ma was obtained for zircon from metatonalites (sample 346) in the southeastern portion of the massif. In CL, these zircons appear magmatic, but their geochemistry differs from that of magmatic zircon due to enrichment in LREE. This type of enrichment has been previously reported for porous zircon described as microporous zircon with hydrothermally indicative geochemistry. Despite this, their morphology does not differ from that of magmatic zircon magmatic zircon [31].

The main characteristic of "typical" REE distribution in magmatic zircon is the increase in REE concentration from La to Lu, as the compatibility of REE with smaller ionic radii increases in this direction in zircon at $La_N > 10$. Th zircon composition (see Fig.5, *g*) closely resembles the porous zircon field, but in Fig.5, *h*, the LRRE-enriched analyses are in the uncertainty field. The anomalous LREE enrichment in zircon could also be due to disequilibrated REE distribution between the rock and the melt, defects imperfections in zircon's crystalline lattice, radioactive U and Th decay damaging zircon's crystalline lattice and multiple hydrothermal processes [39-41].

Elevated LREE concentrations, caused by the presence of monazite or orthite aggregates in zircon fractures, are generally accompanied by an increase in Th [42]. However, in zircon from sample 346, U and Th concentrations are low, and Th does not correlate with LREE (Fig.5, *f*). If inclusions were formed in fractures, then high- and low-LREE zircon analyses could be expected, but all the analyzed zircon from sample 346 is enriched in LREE.

The damage of zircon's crystalline lattice by radioactive U and Th decay is conducive to its LREE enrichment affected by hydrothermal fluids [39] that induce cation exchange in the crystalline lattice. Such enrichment is indicated by a positive correlation between U+Th and the increase of LRRE indicated by a (La/Gd)N ratio [29]. As no correlation of this type has been revealed (Fig.5, *f*), LREE enrichment is not related to radioactive irradiation.

The effect of fluid is felt in zircon with analytical crater 5.1, where the U-Pb isotope system is distorted (discordance $D = 8$ %), and non-formula element concentrations (Ca, Sr, P, Y, REE, Th, U and Hf) in zircon are anomalously high [43]. In Fig.5, *h*, the grain is in the hydrothermal zircon field. In other cases, the U-Pb system discordance is low, and non-formula element concentrations do not differ markedly from those of zircon with a typical magmatic profile on other spidergrams, except for the Ca enrichment of high-LREE zircon that is shown in Fig.5, *h*.

A quantitative assessment of the chemical alterations in zircon (LREE-I index after [44] LREE-I = (Dy/Nd) + (Dy/Sm)) indicates that all of the zircon samples are altered LREE-I = 1.5-8.3 (for altered zircon, this value is expected to be < 10).

LREE enrichment, along with the disturbance of estimated zircon/melt distribution coefficients, has been observed in zircon from sanukitoids. This is due to the originally imperfect structure of the mineral formed upon the crystallization of zircon from melt at high temperature in an anomalous fluid regime [6, 30, 45]. Both Saltakh rocks and sanukitoids [46-48] belong to the shoshonite series or are related to it for tonalities in sample 346. This suggests high temperature crystallization and an anomalous fluid regime leading to the LREE enrichment of zircon. LREE enrichment could have been induced by the simultaneous crystallization of hornblende and clinopyroxene, which remove MREE and HREE from the melt, causing the LREE oversaturation of the melt [29].

We interpret concordant U-Pb age of 2025±7 Ma obtained for porous zircon not as a sign of rejuvenation provoked by hydrothermal alterations, but rather as indicative of the disturbance of the U-Pb isotope system. Most of the age values obtained are concordant. In addition, similar isotopic dating results for metamagmatic rocks have been obtained in the Khapchan belt, located 170 km south of the Saltakh Massif, in the Khapchan prospect, where the concordant U-Pb age of zircon from the dioritic protolith of two-pyroxene plagioschists is 2095±10 Ma, while the tonalitic protolith of two-pyroxene plagiogneisses is 2030±17 Ma. Hence, the Saltakh Massif should be described as polychromous, containing gabbro and diorites dated at ca. 2100 Ma and younger tonalites dated at 2025 Ma.

Geodynamic setting. Calc-alkaline and shoshonitic magmatism is typomorphic for active continental margins. Shoshonitic magmatism in subduction orogens is generally simultaneous with or takes place after calc-alkaline magmatism during postorogenic extension [49, 50]. Experiments have demonstrated that the high-pressure fractional crystallization (10 kbar) of calc-alkaline magma resulting in shoshonite formation, may take place at the base of thick crust in continental or highly mature arcs [51]. The origin of shoshonitic magmatism is related to thermal events in the mantle generally caused by slab detachment or underplating, which can be brought about by the intrusion of basaltic magma into the lower portion of the crust upon extension [49]. Shoshonitic series are known in continental, oceanic, and postcollisional magmatic arc settings, and in intraplate settings [19, 20].

According to the algorithm for assessing the geodynamic setting for rocks of potassium alkalinity ([19], the sequence of diagrams in Fig.7, *a*-*d*), Saltakh rocks do not fit the profile of intraplate magmatic products (Fig.7, *a*, *b*). In Fig.7, *c*, *d*, they are classified as potassium magmatic products (derived from shoshonitic magma) of continental arcs. It should be noted that metagabbroic rocks are consistent with postcollisional arc rocks. A similar geodynamic setting is reconstructed using other poorly mobile elements, e.g., Nb, La, Th and Yb (Fig.7, *e*, *f*).

The compositions of Saltakh rocks are plotted in the alkaline arc field (Fig.7, *e*). The position of gabbroic rocks in the oceanic island field in Fig.7, *f* is likely due to the Th depletion of gabbroic rocks during granulite-facies metamorphism. According to the authors of diagrams 7, *e*, *f* [34], the Aeolian [52] and Apennine-Magrib arcs in the modern Western Mediterranean region [53], related to the postorogenic extension of the Earth's crust, are the tectonotype of modern alkaline arcs.

Available geochemical data indicate that the Saltakh zircon was formed in the continental crust and was concentrated in the continental arc field (Fig.7, *g*). The upward elongation of the point field is interpreted as the formation of magma from an enriched mantle source or the addition of crustal material to the mantle source. In Fig.7, *h*, the zircon composition is positioned in the mantle rock sequence, primarily due to low Yb concentration in zircon, supported by positive $\varepsilon_{Nd}(T)$ values ranging from +1.9 to +4.1 for Saltakh Pluton rocks.

Thus, the geodynamic setting in which the Saltakh Massif was formed appears to be consistent with a near-continental magmatic arc, which experienced postorogenic extension. Shoshonitic series are generally formed in post-collisional, intra-arc, and back-arc rifts, when a compression setting is followed by an extension regime.

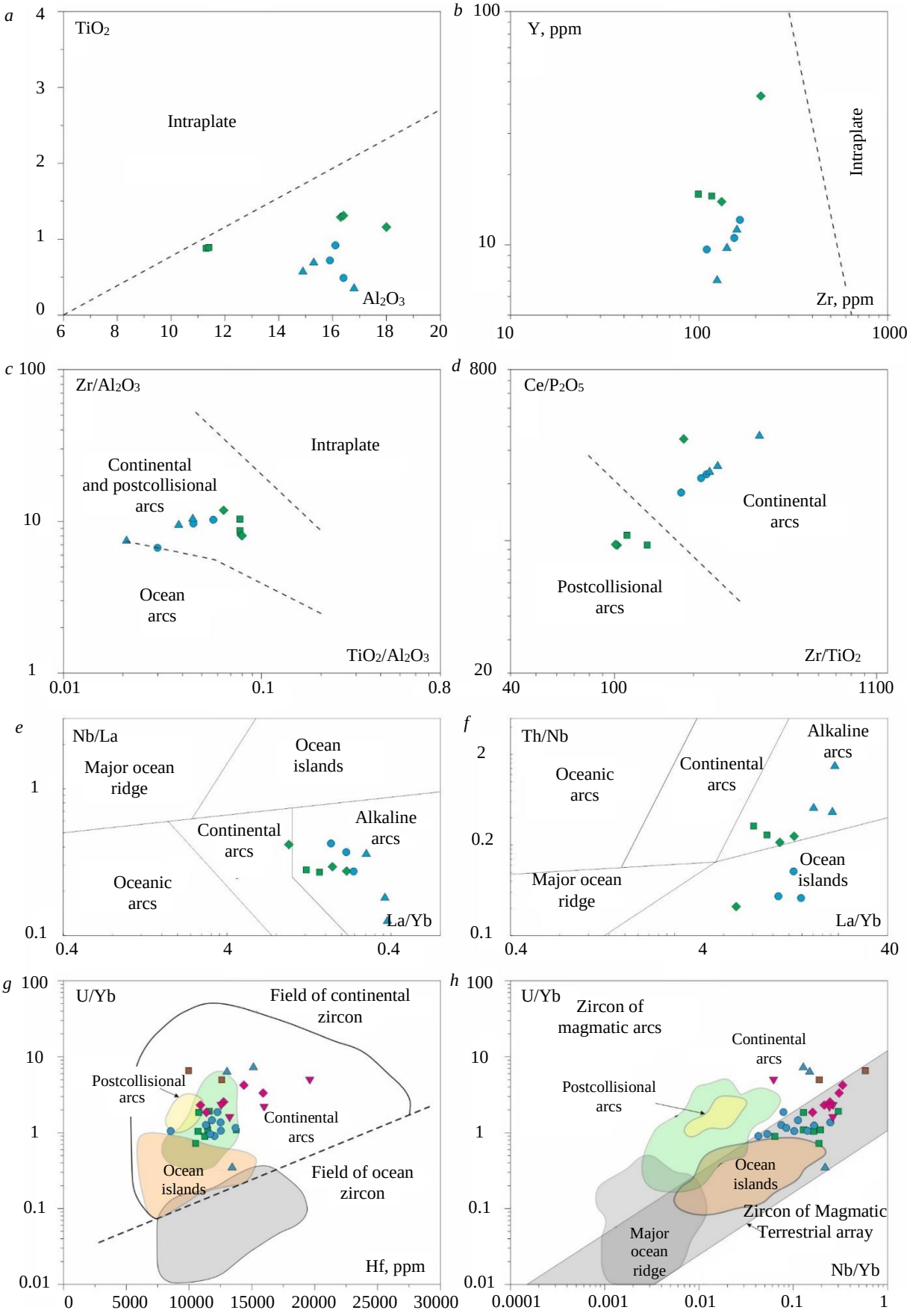

Fig.7. Diagrams of the geodynamic setting of the Saltakh Massif: *a-d* – after [19]; *e*, *f* – after [34]; *g*, *h* – diagrams of the geodynamic setting [54] of Saltakh Massif rocks after zircon composition. For symbols used, see Fig.5

Age of metamorphism and anatexis. Earlier data for the Khapchan belt indicate that sedimentary deposits were fully metamorphosed 1.97 Ga ago and later subjected to areal granulite-facies metamorphism, peaking at 1.91-1.92 Ga ago [55]. Studies in the Billyakh tectonic zone [1] suggest that the Daldyn and Khapchan terrains collided between 1983±3 and 1971±4 Ma. While the current study does not recalculate the time of collisional metamorphism, available age dates indicate distinct pattern and sequence of metamorphic processes at the main stage of metamorphism.

Zircon from the dated samples reveals two types of metamorphic shells. Earlier zircon from the shells (1986±26 Ma), which appears white in CL, is poorly preserved and is usually surrounded by a later zircon rim (1971±10 Ma), which appears almost black in CL. These two types of zircon exhibit the contrasting geochemical characteristics of Th/U, Eu/Eu* and Ce/Ce* ratios. Modelling [26] indicates that the main factors affecting the Th/U value in suprasolidus metamorphic zircon include the Th and U concentrations in the system, as well as the destruction and growth of monazite or allanite, which are in equilibrium with zircon. Monazite and allanite, which are major Th-bearing phases growing alongside subsolidus zircon, decrease Th concentration and thus reduce Th/U [26]. Zircon, that formed during the early stages near the metamorphic peak, would show elevated Th/U values (e.g., white shells with Th/U = 0.51), whereas zircon that formed closer to the solidus line would display relatively low Th/U ratios (dark rims with Th/U = 0.08-0.13).

Zircon, which is white in CL, exhibits a higher Ce/Ce* = 19.8 and a better-defined negative Eu anomaly, (Eu/Eu* = 0.65), indicative of its formation in the plagioclase stability field under high oxygen fugacity conditions [56].

Zircon which is black in CL exhibits a positive Eu anomaly (Eu/Eu* = 1.54-2.92) but a weaker Ce anomaly (Ce/Ce* = 3.22-3.58), characteristic of a highly reducing setting. Besides, the positive Eu anomaly may result from the destruction of plagioclase (replacement of plagioclase by garnet and pyroxene), enriching the zircon crystallization medium in Eu. Similar to dark zircon shells, anatectic alaskitic gneissose granites (sample 673) also display well-defined positive Eu anomaly. However, both types of zircon display relatively high $(Lu/Gd)_N$ ratios: 28.8 in white zircon and 51.9-53.3 in black zircon, indicating the limited involvement of garnet in metamorphic paragenesis. This is likely due to the pattern of their protolith (mafic rocks), where pyroxene, rather than garnet, was formed under granulite-facies conditions.

The formation of alaskitic gneissose granites forming migmatite leucosome appears to be associated to the metamorphic peak. They exhibit high K_2O, La/Yb, and Sr/Y ratios, and positive Eu anomaly (Eu/Eu* = 12). This suggests partial rock melting provoked by potassium fluids resulted in the accumulation of cumulative plagioclase in the migmatite leucosome, which took place in equilibrium with garnet-granulite restite. The formation of leucogranites equilibrated with garnetiferous restite is possible at a temperature of 680 °C and a pressure of 11 kbar, with a high-water content [57]. The geochemical characteristics of alaskitic granites imply that plagioclase was involved in melting, provoking the Al, Sr, and Eu enrichment in the melt. The formation of alaskitic granites is linked to collision processes, with an excessively aquatic type of melting characteristic of collisional overthrusts, where a relatively cold inundated plate releases water into a hotter upper plate [57]. Paleoproterozoic granites of alaskitic type, associated with large lit-par-lit migmatite fields, are part of the Magan alaskitic-leucogranitic-migmatitic complex and are widespread in the Anabar Shield [55]. This suggests that the intensity of alaskitic-granitic magmatism is possibly related to collision processes. U-Pb dating indicates that the Magan complex was formed 1984-1952 Ma ago [55]. The zircon from alaskitic gneissose granites (sample 673) provides a concordant age of 1967±7 Ma.

Conclusion

The Saltakh intrusive massif, composed of gabbro-diorite-tonalit, was metamorphosed under granulite-facies conditions and consists of two-pyroxene schists and plagiogneisses. Geochemical data indicate that it was formed by crystallization of calc-alkaline and shoshonitic magma in the near-continental magmatic arc extension conditions. Its isotopic-geochemical characteristics, including positive $\varepsilon_{Nd}(T)$ values ranging from +1.9 to +4.1 and fractionated HREE, suggest that the melt was formed at depth in equilibrium with a garnetiferous association. U-Pb zircon dating (SHRIMP II) reveals that Saltakh rocks intruded between 2100-2025 Ma ago from a deep source, which had a short crustal prehistory ($T_{(Nd)}DM$ = 2.20-2.26 Ga). The age of the metaintrusive Saltakh rocks is consistent with that of the Khapchan orthogranulites studied earlier [58], which are interpreted as part of a metamorphosed juvenile Paleoproterozoic suprasubduction complex.

REFERENCES

1. Smelov A.P., Kotov A.B., Salnikova E.B. et al. Age and duration of the formation of the Billyakh tectonic melange zone, Anabar shield. *Petrology*. 2012. Vol. 20. N 3, p. 286-300. DOI: 10.1134/S0869591112030058

2. Sukhanov M.K., Rachkov V.S. Saltakh massif of the Anabar shield. *Izvestiya Akademii nauk SSSR. Seriya geologicheskaya*. 1986. N 12, p. 47-58 (in Russian).

3. Lutts B.G., Oksman V.S. Deeply eroded fault zones of the Anabar shield. Moscow: Nauka, 1990, p. 259 (in Russian).

4. Williams I.S. U-Th-Pb Geochronology by Ion Microprobe. *Reviews in Economic Geology*. 1998. Vol. 7, p. 1-35. DOI: 10.5382/Rev.07

5. Black L.P., Kamo S.L., Allen C.M. et al. TEMORA 1: a new zircon standard for Phanerozoic U–Pb geochronology. *Chemical Geology*. 2003. Vol. 200. Iss. 1-2, p. 155-170. DOI: 10.1016/S0009-2541(03)00165-7

6. Fedotova A.A., Bibikova E.V., Simakin S.G. Ion-microprobe zircon geochemistry as an indicator of mineral genesis during geochronological studies. *Geochemistry International*. 2008. Vol. 46. N 9, p. 912-927. DOI: 10.1134/S001670290809005X

7. Skublov S.G., Levashova E.V., Mamykina M.E. et al. The polyphase Belokurikhinsky granite massif, Gorny Altai: isotope-geochemical study of zircon. *Journal of Mining Institute*. 2024. Vol. 268, p. 552-575.

8. Levashova E.V., Mamykina M.E., Skublov S.G. et al. Geochemistry (TE, REE, Oxygen) of Zircon from Leucogranites of the Belokurikhinsky Massif, Gorny Altai, as Indicator of Formation Conditions. *Geochemistry International*. 2023. Vol. 61. N 13, p. 1323-1339. DOI: 10.1134/S001670292311006X

9. Skublov S.G., Petrov D.A., Galankina O.L. et al. Th-Rich Zircon from a Pegmatite Vein Hosted in the Wiborg Rapakivi Granite Massif. *Geosciences*. 2023. Vol. 13. Iss. 12, p. 1-13. DOI: 10.3390/geosciences13120362

10. Levashova E.V., Skublov S.G., Oitseva T.A. et al. First Age and Geochemical Data on Zircon from Riebeckite Granites of the Verkhnee Espe Rare Earth–Rare Metal Deposit, East Kazakhstan. *Geochemistry International*. 2022. Vol. 60. N 1, p. 1-15. DOI: 10.1134/S0016702922010086

11. Rumyantseva N.A., Skublov S.G., Vanshtein B.G. et al. Zircon from Gabbroids of the Shaka Ridge (South Atlantic): U-Pb Age, Oxygen Isotope Ratios and Trace Element Composition. *Proceedings of the Russian Mineralogical Society*. 2022. Vol. 151. N 1, p. 44-73 (in Russian). DOI: 10.31857/S0869605522010099

12. Skublov S.G., Rumyantseva N.A., Li Qiuli et al. Zircon Xenocrysts from the Shaka Ridge Record Ancient Continental Crust: New U-Pb Geochronological and Oxygen Isotopic Data. *Journal of Earth Science*. 2022. Vol. 33. N 1, p. 5-16. DOI: 10.1007/s12583-021-1422-2

13. Adamskaya E.V., Badinova V.P., Belyatskii B.V. et al. Isotope geology of Norilsk deposits. St. Petersburg: VSEGEI, 2017, p. 348 (in Russian).

14. Jacobsen S.B., Wasserburg G.J. Sm-Nd isotopic evolution of chondrites and achondrites, II. *Earth and Planetary Science Letters*. 1984. Vol. 67. Iss. 2, p. 137-150.

15. Goldstein S.J., Jacobsen S.B. Nd and Sr isotopic systematics of river water suspended material: implications for crustal evolution. *Earth and Planetary Science Letters*. 1988. Vol. 87. Iss. 3, p. 249-265. DOI: 10.1016/0012-821X(88)90013-1

16. Whitney D.L., Evans B.W. Abbreviations for names of rock-forming minerals. *American Mineralogist*. 2010. Vol. 95. N 1, p. 185-187. DOI: 10.2138/AM.2010.3371

17. Hastie A.R., Kerr A.C., Pearce J.A., Mitchell S.F. Classification of Altered Volcanic Island Arc Rocks using Immobile Trace Elements: Development of the Th–Co Discrimination Diagram. *Journal of Petrology*. 2007. Vol. 48. Iss. 12, p. 2341-2357. DOI: 10.1093/petrology/egm062

18. O'Connor J.T. A classification for quartz-rich igneous rocks based on feldspar ratios. U.S. Geological Survey. Professional Paper 525-B. 1965, p. 79-84.

19. Müller D., Rock N.M.S., Groves D.I. Geochemical discrimination between shoshonitic and potassic volcanic rocks in different tectonic settings: A pilot study. *Mineralogy and Petrology*. 1992. Vol. 46. Iss. 4, p. 259-289. DOI: 10.1007/BF01173568

20. Pearce J.A. Trace element characteristics of lavas from destructive plate boundaries. Andesites. Orogenic Andesites and Related Rocks. John Wiley & Sons, 1982, p. 525-548.

21. de la Roche H., Leterrier J., Grandclaude P., Marchal M. A classification of volcanic and plutonic rocks using R_1R_2-diagram and major-element analyses – Its relationships with current nomenclature. *Chemical Geology*. 1980. Vol. 29. Iss. 1-4, p. 183-210. DOI: 10.1016/0009-2541(80)90020-0

22. Peccerillo A., Taylor S.R. Geochemistry of eocene calc-alkaline volcanic rocks from the Kastamonu area, Northern Turkey. *Contributions to Mineralogy and Petrology*. 1976. Vol. 58. Iss. 1, p. 63-81. DOI: 10.1007/BF00384745

23. Irvine T.N., Baragar W.R.A. A Guide to the Chemical Classification of the Common Volcanic Rocks. *Canadian Journal of Earth Sciences*. 1971. Vol. 8. N 5, p. 523-548. DOI: 10.1139/e71-055

24. Ross P.-S., Bédard J.H. Magmatic affinity of modern and ancient subalkaline volcanic rocks determined from trace-element discriminant diagrams. *Canadian Journal of Earth Sciences*. 2009. Vol. 46. N 11, p. 823-839. DOI: 10.1139/E09-054

25. Sun S.-s., McDonough W.F. Chemical and isotopic systematics of oceanic basalts: implications for mantle composition and processes. *Geological Society, London, Special Publications*. 1989. Vol. 42, p. 313-345. DOI: 10.1144/GSL.SP.1989.042.01.19

26. Yakymchuk C., Kirkland C.L., Clark C. Th/U ratios in metamorphic zircon. *Journal of Metamorpic Geology*. 2018. Vol. 36. Iss. 6, p. 715-737. DOI: 10.1111/jmg.12307

27. Watson E.B., Harrison T.M. Zircon Thermometer Reveals Minimum Melting Conditions on Earliest Earth. *Science*. 2005. Vol. 308. Iss. 5723, p. 841-844. DOI: 10.1126/science.1110873

28. Hoskin P.W.O. Trace-element composition of hydrothermal zircon and the alteration of Hadean zircon from the Jack Hills, Australia. *Geochimica et Cosmochimica Acta*. 2005. Vol. 69. Iss. 3, p. 637-648. DOI: 10.1016/J.GCA.2004.07.006

29. Whitehouse M.J., Kamber B.S. On the overabundance of light rare earth elements in terrestrial zircons and its implication for Earth's earliest magmatic differentiation. *Earth and Planetary Science Letters*. 2002. Vol. 204. Iss. 3-4, p. 333-346. DOI: 10.1016/S0012-821X(02)01000-2

30. Bouvier A.-S., Ushikubo T., Kita N.T. et al. Li isotopes and trace elements as a petrogenetic tracer in zircon: insights from Archean TTGs and sanukitoids. *Contributions to Mineralogy and Petrology*. 2012. Vol. 163. Iss. 5, p. 745-768. DOI: 10.1007/s00410-011-0697-1

31. Grimes C.B., John B.E., Cheadle M.J. et al. On the occurrence, trace element geochemistry, and crystallization history of zircon from in situ ocean lithosphere. *Contributions to Mineralogy and Petrology*. 2009. Vol. 158. Iss. 6, p. 757-783. DOI: 10.1007/s00410-009-0409-2

32. Morrison G.W. Characteristics and tectonic setting of the shoshonite rock association. *Lithos*. 1980. Vol. 13. Iss. 1, p. 97-108. DOI: 10.1016/0024-4937(80)90067-5

33. Zindler A., Hart S. Chemical Geodynamics. *Annual Review of Earth and Planetary Sciences*. 1986. Vol. 14, p. 493-571. DOI: 10.1146/annurev.ea.14.050186.002425

34. Hollocher K., Robinson P., Walsh E., Roberts D. Geochemistry of Amphibolite-Facies Volcanics and Gabbros of the Støren Nappe in Extensions West and Southwest of Trondheim, Western Gneiss Region, Norway: A Key to Correlations and Paleotectonic Settings. *American Journal of Science*. 2012. Vol. 312. Iss. 4, p. 357-416. DOI: 10.2475/04.2012.01

35. Richards J.P., Spell T., Rameh E. et al. High Sr/Y Magmas Reflect Arc Maturity, High Magmatic Water Content, and Porphyry Cu ± Mo ± Au Potential: Examples from the Tethyan Arcs of Central and Eastern Iran and Western Pakistan. *Economic Geology*. 2012. Vol. 107. N 2, p. 295-332. DOI: 10.2113/econgeo.107.2.295

36. Ze Liu, Di-Cheng Zhu, Jagoutz O. et al. Magmatic Evolution following Damp Tholeiitic and Wet Calc-alkaline Liquid Lines of Descent: an Eastern Pontides (NE Turkey) Example. *Journal of Petrology*. 2021. Vol. 62. Iss. 5. N egaa088. DOI: 10.1093/petrology/egaa088

37. Jagoutz O., Schmidt M.W., Enggist A. et al. TTG-type plutonic rocks formed in a modern arc batholith by hydrous fractionation in the lower arc crust. *Contributions to Mineralogy and Petrology*. 2013. Vol. 166. Iss. 4, p. 1099-1118. DOI: 10.1007/s00410-013-0911-4

38. O'Brien T.M., Miller E.L. Continuous zircon growth during long-lived granulite facies metamorphism: a microtextural, U–Pb, Lu–Hf and trace element study of Caledonian rocks from the Arctic. *Contributions to Mineralogy and Petrology*. 2014. Vol. 168. Iss. 4. N 1071. DOI: 10.1007/s00410-014-1071-x

39. Rayner N., Stern R.A., Carr S.D. Grain-scale variations in trace element composition of fluid-altered zircon, Acasta Gneiss Complex, northwestern Canada. *Contributions to Mineralogy and Petrology*. 2005. Vol. 148. Iss. 6, p. 721-734. DOI: 10.1007/s00410-004-0633-8

40. Cavosie A.J., Valley J.W., Wilde S.A., E.I.M.F. Correlated microanalysis of zircon: Trace element, $\delta^{18}O$, and U–Th–Pb isotopic constraints on the igneous origin of complex > 3900 Ma detrital grains. *Geochimica et Cosmochimica Acta*. 2006. Vol. 70. Iss. 22, p. 5601-5616. DOI: 10.1016/j.gca.2006.08.011

41. Shao-Bing Zhang, Yong-Fei Zheng, Zi-Fu Zhao. Temperature effect over garnet effect on uptake of trace elements in zircon of TTG-like rocks. *Chemical Geology*. 2010. Vol. 274. Iss. 1-2, p. 108-125. DOI: 10.1016/j.chemgeo.2010.04.002

42. Whitehouse M.J., Kamber B.S. Assigning Dates to Thin Gneissic Veins in High-Grade Metamorphic Terranes: A Cautionary Tale from Akilia, Southwest Greenland. *Journal of Petrology*. 2005. Vol. 46. Iss. 2, p. 291-318. DOI: 10.1093/petrology/egh075

43. Pidgeon R.T., Nemchin A.A., Roberts M.P. et al. The accumulation of non-formula elements in zircons during weathering: Ancient zircons from the Jack Hills, Western Australia. *Chemical Geology*. 2019. Vol. 530. N 119310. DOI: 10.1016/j.chemgeo.2019.119310

44. Bell E.A., Boehnke P., Harrison T.M. Recovering the primary geochemistry of Jack Hills zircons through quantitative estimates of chemical alteration. *Geochimica et Cosmochimica Acta*. 2016. Vol. 191, p. 187-202. DOI: 10.1016/j.gca.2016.07.016

45. Skublov S.G., Lobach-Zhuchenko S.B., Guseva N.S. et al. Rare earth and trace element distribution in zircons from miaskite lamproites of the Panozero complex, Central Karelia. *Geochemistry International*. 2009. Vol. 47. N 9, p. 901-913. DOI: 10.1134/S0016702909090043

46. Stevenson R., Henry P., Gariépy C. Assimilation–fractional crystallization origin of Archean Sanukitoid Suites: Western Superior Province, Canada. *Precambrian Research*. 1999. Vol. 96. Iss. 1-2, p. 83-99. DOI: 10.1016/S0301-9268(99)00009-1

47. Lobach-Zhuchenko S.B., Rollinson H.R., Chekulaev V.P. et al. The Archaean sanukitoid series of the Baltic Shield: geological setting, geochemical characteristics and implications for their origin. *Lithos*. 2005. Vol. 79. Iss. 1-2, p. 107-128. DOI: 10.1016/j.lithos.2004.04.052

48. Lobach-Zhuchenko S.B., Rollinson H., Chekulaev V.P. et al. Petrology of a Late Archaean, Highly Potassic, Sanukitoid Pluton from the Baltic Shield: Insights into Late Archaean Mantle Metasomatism. *Journal of Petrology*. 2008. Vol. 49. Iss. 3, p. 393-420. DOI: 10.1093/petrology/egm084

49. Pe-Piper G., Piper D.J.W., Koukouvelas I. et al. Postorogenic shoshonitic rocks and their origin by melting underplated basalts: The Miocene of Limnos, Greece. *GSA Bulletin*. 2009. Vol. 121. N 1-2, p. 39-54. DOI: 10.1130/B26317.1

50. Solovev S.G. Metallogeny of Shoshonitic magmatism. In 2 volumes. Vol. 1. Moscow: Nauchnyi mir, 2014, p. 528 (in Russian).

51. Meen J.K. Formation of shoshonites from calcalkaline basalt magmas: geochemical and experimental constraints from the type locality. *Contributions to Mineralogy and Petrology*. 1987. Vol. 97. Iss. 3, p. 333-351. DOI: 10.1007/BF00371997

52. de Astis G., Ventura G., Vilardo G. Geodynamic significance of the Aeolian volcanism (Southern Tyrrhenian Sea, Italy) in light of structural, seismological, and geochemical data. *Tectonics*. 2003. Vol. 22. Iss. 4. N 1040. DOI: 10.1029/2003TC001506

53. Carminati E., Lustrino M., Doglioni C. Geodynamic evolution of the central and western Mediterranean: Tectonics vs. igneous petrology constraints. *Tectonophysics*. 2012. Vol. 579, p. 173-192. DOI: 10.1016/j.tecto.2012.01.026

54. Grimes C.B., Wooden J.L., Cheadle M.J., John B.E. «Fingerprinting» tectono-magmatic provenance using trace elements in igneous zircon. *Contributions to Mineralogy and Petrology*. 2015. Vol. 170. Iss. 5-6. N 46. DOI: 10.1007/s00410-015-1199-3

55. Gusev N.I. Anabar shield of the Siberian Craton: composition, geochemistry, geochronology. Saarbrucken: LAP LAMBERT Academic Publishing, 2013, p. 188.

56. Trail D., Watson E.B., Tailby N.D. Ce and Eu anomalies in zircon as proxies for the oxidation state of magmas. *Geochimaca et Cosmochimica Acta*. 2012. Vol. 97, p. 70-87. DOI: 10.1016/j.gca.2012.08.032

57. Frost C.D., Swapp S.M., Frost B.R. et al. Leucogranites of the Teton Range, Wyoming: A record of Archean collisional orogeny. *Geochimica et Cosmochimica Acta*. 2016. Vol. 185, p. 528-549. DOI: 10.1016/j.gca.2015.12.015

58. Gusev N.I., Sergeeva L.Y., Skublov S.G. Evidence of Subduction of the Paleoproterozoic Oceanic Crust in the Khapchan Belt of the Anabar Shield, Siberian Craton. *Petrology*. 2021. Vol. 29. N 2, p. 95-113. DOI: 10.1134/S0869591121020041

***Authors*: Nikolai I. Gusev,** *Head of Department, https://orcid.org/0000-0002-3461-0961* (*Karpinsky Russian Geological Research Institute, Saint Petersburg, Russia*; *Institute of Precambrian Geology and Geochronology RAS, Saint Petersburg, Russia*), **Lyudmila Yu. Romanova,** *Candidate of Geological and Mineralogical Sciences, Leading Engineer, sergeeva.luda02@yandex.ru, https://orcid.org/0009-0005-2766-0097* (*Karpinsky Russian Geological Research Institute, Saint Petersburg, Russia*; *Institute of Precambrian Geology and Geochronology RAS, Saint Petersburg, Russia*).

The authors declare no conflict of interests.

ISSN 2411-3336; e-ISSN 2541-9404

JOURNAL OF MINING INSTITUTE

Zapiski Gornogo instituta

Journal homepage: pmi.spmi.ru

Research article *Geology*

Comparative analysis of nitrogen and carbon isotopic fractionation during diamond formation based on β-factor determination

Dmitrii P. Krylov
Institute of Precambrian Geology and Geochronology RAS, Saint Petersburg, Russia

***How to cite this article*:** Krylov D.P. Comparative analysis of nitrogen and carbon isotopic fractionation during diamond formation based on β-factor determination. Journal of Mining Institute. 2025. Vol. 272. N 16406, p. 40-50.

Abstract
First quantitative estimates are presented for nitrogen isotopic fractionation during diamond crystallization with respect to nitrogen-bearing fluid components using quantum-mechanical (DFT) calculations on the defect (with the substitutional nitrogen) diamond lattice. Provided equilibrium isotopic fractionation, $^{15}N/^{14}N$ ratio decreases within the sequence of compounds $NH_4^+ > N_2 >$ (diamond, NH_3) > $CH_3N > CN^- > NH_2$. At temperatures of 1,100 to 1,200 °C fractionation among diamond and fluid N-compounds are estimated at –2.23, –0.77, 0.01, 0.44, 1.31 and 2.85 ‰ and substantially (over 1 ‰) exceed the already available estimates based on the modeling diamond C-N bonds by analogy with HCN or CN^- molecules. Depending on the dominant nitrogen and carbon substance in the mineral-forming fluid, diamond formation can be accompanied by different isotope compositional trends, as expressed either by zoned patterns within individual diamond grains or by isotopic $\delta^{15}N$ *vs* $\delta^{13}C$ covariations during successive crystallization. Provided the dominance of NH_3 component (the reduced conditions, high pressures and the cold geotherm) nitrogen isotope fractionation between diamond and fluid does not exceed 0.1-0.2 ‰ and the isotope shifts at temperature ca. 1100 °C $\Delta^{15}N << \Delta^{13}C$. In nitrogen depleted reduced mantle fluids possible existence of compounds with low heavy isotope affinity at temperature of diamond formation (especially NH_2) implies high isotope fractionation between diamond and the fluid and hence, evolved $\Delta^{15}N/\Delta^{13}C$ ratios. Oxidized fluids dominated by CO_2 or CO_3 coupled with N_2 component are characterized by close to zero $\Delta^{15}N/\Delta^{13}C$ ratios as inferred by prevailing carbon isotope fractionation with respect to nitrogen isotopes, the latter change considerably with nitrogen distribution coefficient among diamond and the growth media.

Keywords
diamond; isotope fractionation factors; $^{15}N/^{14}N$; $^{13}C/^{12}C$

Funding
The work was carried out within the framework of the State assignment FMVW-2021-0003.

Received: 11.03.2024 ***Accepted: 24.09.2024*** ***Online: 06.12.2024*** ***Published: 25.04.2025***

Introduction

The conditions of diamond growth and transformation are reflected by the morphological properties, spectroscopic features, impurity compositions [1-3], and inclusions [4, 5]. One of the most important indicators of the formation conditions – isotopic composition of carbon in diamond – characterize both the initial substrate (eclogites, peridotites, websterites, with different proportions of sedimentary and mantle components) as well as a mineral-forming fluid (oxidized, reduced, mantle, surface) [6]. Diamond can represent the most ancient isolated parts of the mantle [7] and thus retains carbon isotopic labels from the early stages of the Earth formation. In addition to carbon, diamond is characterized by significant amounts of nitrogen (up to thousands and even tens of thousands ppm in subduction-related microdiamonds), the occurrence of which is driven by mineral-forming fluids [8]. The combination of isotopic systems ^{12}C-^{13}C and ^{14}N-^{15}N is widely used not only to reveal the conditions of formation, but also to characterize the cycles of carbon and nitrogen in deep conditions. Very high retention of carbon and nitrogen in diamonds [9] encourages preservation of isotopic systems both in conditions of formation at great depths (>110 km) and during rise to the surface.

Hence, the two elements in diamond taken together provide a unique opportunity to study the Earth's mantle down to depths of about 800 km and ages up to 3.5 billion years [10]. Considering generally low nitrogen content in the upper mantle, diamond $^{15}N/^{14}N$ isotopic ratio could be a sensitive indicator of mantle and sedimentary reservoirs mixing [11].

The observed large variations of diamond isotopic composition can be explained by both isotopic heterogeneity (including mixing) of the initial substrate and by fractionation of isotopes during crystallization. Quantitative characterization for processes related to diamond genesis primarily requires estimated isotope fractionation factors between diamond and the crystallization medium. Carbon isotopic fractionation factors depending on temperature have been determined for many systems related to diamond formation, including diamond-CO_2, diamond-$CaCO_3$, diamond-CH_4, and a number of others [12-14]. Unlike carbon isotopes, fractionation of nitrogen isotopes with diamond are barely studied. There are still no experimental data on the distribution of nitrogen isotopes between diamond and possible nitrogen-containing substances in diamond growth media. The available calculated (theoretical) nitrogen isotopic fractionation factors are restricted to individual molecules (NH_4^+, NH_3, N_2) in equilibrium with arbitrary molecular analogues of the C-N bond of diamond, such as HCN or CN^- [9]. In the absence of more or less reliable determinations of nitrogen fractionation factors between diamond and mantle fluids, it is impossible for example, to distinguish the processes of mixing nitrogen of fluid from different sources, to assess the evolution of the isotopic composition under various mechanisms of interaction between fluids and the nascent diamond, etc.

The present work aims to provide first quantitative estimates of equilibrium isotope fractionation of nitrogen during diamond crystallization relative to nitrogen-containing fluid compounds using quantum-mechanical calculations (within the framework of the density functional theory DFT) for the defective (N-containing) lattice of diamond and N-containing molecules of the mineral-forming fluid. For comparison, calculations were also carried out for diamond without nitrogen (fractionation of carbon isotopes) and the carbon-containing fluid molecules.

Calculation methodology

Isotope fractionation factor between phases *A* and *B*, α_{AB} (R_A/R_B, *R* being the ratio of the atomic concentrations of the heavier and lighter isotopes in a given compound) at isotopic equilibrium is expressed by

$$1,000 \ln \alpha_{AB} = 1,000 \ln \beta_A - 1,000 \ln \beta_B, \quad (1)$$

in which β – values (the reduced partition function ratios of the isotopologues under consideration, or so-called β-factors) without accounting for anharmonicity are calculated from the frequencies of oscillations (phonon spectra) of isotopologues depending on temperature [15],

$$\beta = \prod_i \left(\frac{u_i^*}{u_i} \right) \left(\frac{e^{-u_i^*/2}}{e^{-u_i/2}} \right) \left(\frac{1-e^{-u_i}}{1-e^{-u_i^*}} \right),$$

or, in logarithmic form:

$$\ln \beta = \sum_i \ln \frac{\sinh\left(0,5u_i\right)}{\sinh\left(0,5u_i^*\right)} - \sum_i \ln \frac{u_i}{u_i^*}; \quad (2)$$

u – the dimensionless frequency, $u = h\nu/kT$; ν – the frequency of the harmonic oscillator; *T* – temperature, K; *h* and *k* – are the Planck and Boltzmann constants; superscript * refers to the heavier isotope; the subscript *i* numbers independent harmonic vibrational frequencies for a compound. Summation is carried out for all vibrational states (3*N*-6 for nonlinear molecules, 3*N*-5 for linear molecules, 3*N*-3 for crystals); *N* – number of atoms of a compound. Hyperbolic sinus $\sinh(x) \equiv (\exp(x) - \exp(-x))/2$.

Experimental vibrational frequencies are mostly known only for the prevalent isotopologues (or for their natural mixtures) of individual substances. Therefore, to determine the values of ν for the expression above, calculations "from the first principles" (ab initio) are currently used based on the

position of nuclei and the electronic properties of elements. In the present work, the vibrational frequencies of isotopologous are determined by the "frozen phonons" approach of the density functional theory as implemented in the CRYSTAL code (current version CRYSTAL23 [16]) with a set of Gaussian all-electron bases 6-311G(d). The basis sets for carbon and nitrogen are presented at the program site (https://www.crystal.unito.it/Basis_Sets/). Before calculating the phonon spectra, the parameters of the outer orbitals of the basic functions were optimized and the values of the vibration frequencies for the crystal lattice of pure diamond and diamond with different nitrogen impurity contents were compared, as well as structural optimization. Among the tested functionals of interaction between atoms (including LDA, GGA, hybrid), the minimum discrepancy with the experimental values of the calculated vibrational frequencies of pure diamond was obtained for the WC1LYP functional. The energy convergence threshold for self-matched field (SCF) calculations was chosen at the level of 10^{-11} amu. (Hartree) both during the optimization of the structure and calculation of vibrational frequencies, and the truncation of the summation series was controlled by the parameters of the CRYSTAL (TOLINTEG) program at values of (9; 9; 9; 9; 25).

Nitrogen in diamond occurs at various positions, including in place of carbon (substitutional nitrogen) and is present in various forms of aggregation [17]. Aggregated forms of nitrogen (*A* and *B* centers) usually are not associated with the initial defect formation, but are considered as secondary products during a long-term, of the order of billions of years residence (natural annealing) at high temperatures. The aggregation is restricted to the displacement of atoms within separate grains and does not affect the bulk isotope balance of diamond crystals. The present work deals with isotope effects associated with the primary (during diamond growth) entry of nitrogen into carbon sites with the appearance of substitutional nitrogen (*C*-centers). The possibility of nitrogen atoms being outside the *C*-center (dislocations, between lattice nodes, etc.) is not considered, as well as the entry of nitrogen in the form of *A*-center during crystallization [18]. Thus, carbon atoms were replaced by nitrogen atoms during calculations and the most energetically advantageous configurations of atoms in the diamond structure with *C*-centers have been determined, followed by the phonon spectra determination for nitrogen isotopologues and calculation of β-factors for substituted nitrogen. To adequately display real nitrogen concentrations, the method of expanded cells (super cells) with the number of carbon atoms n = 16; 32; 54; 128 (replacing one carbon atom with nitrogen atom in the cubic lattice) was used. The convergence of the results is achieved at n = 32-54 (corresponding to 20,000-30,000 ppm and exceeds maximum nitrogen concentrations in natural diamonds). Further volume increase of expanded cells leads to large costs of computing resources without any significant improvement of the results (including values of β-factors).

Calculations of β-factors for molecules representing possible fluid components during diamond formation (the set of molecules such as NH_3, NH_4^+, and N_2 has been accomplished by NH_2, CH_3N, C_2H_6 in the work) included a sequence of nuclei coordinate optimization followed by vibrational level determination and calculation of β values. The B3LYP hybrid functional and basis vector sets of the TVZP quality in conjunction with the D3 dispersion correction [19], which minimized the discrepancy between calculated and experimentally determined frequencies, were used for molecular calculations. A more accurate presentation of the experimental spectra was achieved using the scaling factor, SF [20], with the reduction of the calculated frequencies of the main isotopologues to the experimental data together with the corresponding change of the frequencies of the heavier isotopologues.

Values of the β-factors were estimated from the expression (2) for temperatures from 0 to 2,500 °C with a step of 10 °C, the corresponding dependencies were approximated by polynomials $x = 10^6/T^2$ (K^{-2}): $1{,}000 \ln \beta = \sum a_i x^i$. The results (Table 1) for diamond and molecular species are presented in the form of the 5th degree polynomials (i = 6 for CO_2 and NH_2). The approximation error in all cases does not exceed 0.02 % at temperatures above 100 °C and 0.04 % at temperatures above 0 °C (coefficient of determination $r^2 > 0.999$).

Results

Table 1 shows the obtained temperature dependencies for determinations of diamond $^{15}N/^{14}N$ β-factors. Estimates are based on calculations for an expanded cell of 54 atoms. As noted above, further increase of the cell volume (with a corresponding decrease in the concentration of nitrogen in diamond)

with the substitution of one atom C => N does not yield any noticeable change in isotopic fractionation factors. The Table 1 also lists newly calculated (NH_2, CH_3N) as well as previously known (N_2, NH_3, NH_4^+) results for probable nitrogen-containing components of mantle fluids, together with the results for carbon β-factors of diamond without nitrogen impurities as well as β-factors of fluid-carbon compounds. The presented data can be used to deduce (see expression (1) isotopic fractionation factors for nitrogen ($\alpha^{15/14}$) and carbon ($\alpha^{13/12}$) between diamond and fluid components possible during crystallization. Hereafter, isotopic fractionation factors are presented in the form of the conventional values $\Delta = 1{,}000 \ln(\alpha)$.

Table 1

Temperature dependences of 1000 lnβ to calculate nitrogen and carbon fractionation between diamond and fluid

Compound	a_1	a_2	a_3	a_4	a_5	a_6	Source
			$^{15}N/^{14}N$				
Diamond	13.13525 +0.05589*P*	–0.454961 –0.00471*P*	0.023558 +0.00038*P*	–0.000965 –1.9619E^{-5}*P*	1.92024E^{-5} +4.3816E^{-7}*P*	–	This work
N_2	15.27791	–2.088265	0.248047	–0.015932	0.0004036	–	[21]
NH_3	13.91689	–2.437494	0.339134	–0.023827	0.0006369	–	[21]
NH_4^+	18.40726	–3.003117	0.397865	–0.027115	0.0007104	–	[21]
Diamond (CN^-)	10.97264	–1.275805	0.138451	–0.008467	0.0002086	–	[21]
NH_2	8.293659	–1.827601	0.351646	–0.038804	0.0021684	–4.751E^{-5}	This work
CH_3N	12.69071	–1.384621	0.155546	–0.009723	0.0002388	–	This work
			$^{13}C/^{12}C$				
Diamond	20.931829 +0.10803*P*	–0.859144 –0.010389*P*	0.048253 +9.129E^{-4}*P*	–0.0020401 –4.8886E^{-5}*P*	4.09635E^{-5} +1.115E^{-6}*P*	–	This work
Diamond	21.649 0.10768*P*	–0.9790 –0.0097*P*	0.052834 0.00079*P*	–0.001879 –3.7385E^{-5}*P*	0.30747E^{-4} 7.6468E^{-7}*P*	–	[22]
Diamond	19.856	–0.4086	–	–	–	–	[23]
Diamond	20.398968	–0.858690	0.050281	–0.002209	4.56732E^{-5}		[24]
Diamond	19.949068 +0.08177*P*	–0.622300 –0.00609*P*	0.014645 +0.00024*P*	–	–	–	[6]
CO_3^{2-}	24.74146	–1.08996	0.03178	–	–	–	This work
CO_2	31.32194	–3.969173	0.485570	–0.032037	0.0008268	–	This work
CO_2	30.48662	–4.092939	0.620806	–0.061011	0.0032451	–7.027E^{-5}	[13]
CH_4	20.23303	–2.915760	0.371371	–0.024974	0.0006513	–	[9]
CH_4	18.81124	–1.818667	0.136254	–0.005159	0.0000743	–	[25]
CO	17.00663	–1.647067	0.122574	–0.004226	3.76328E^{-5}	–	[26]
C_2H_6	20.71712	–2.397034	0.275367	–0.017105	0.0004143	–	This work
C_2H_6	19.84650	–1.631380	0.115636	–0.004252	0.0000601	–	[25]
CH_3N	22.33125	–2.555513	0.291656	–0.018280	0.0004487	–	This work

Notes. The results recalculated in the form of of *x* polynomials [9, 21]; *P*, GPa dependence is estimated according to [22, (9)]; determinations based on the density of states (DOS) obtained from inelastic neutron scattering [24]; DFT calculations at $0 < P < 80$ GPa [6]; experimental data [26]; temperature range: $0 < T < 1{,}000$ °C [23]; $300 < T < 1{,}200$ °C [26]; $0 < T < 800$ °C [25]. Hyphen – not calculated.

In the temperature range within 1,000 and 1,400 °C (probable conditions of the lithospheric diamond formation) isotopic fractionation factors estimated from the calculated values of β are shown in Fig.1 in comparison with previously obtained results of the theoretical calculations. Such calculations of diamond nitrogen isotopic fractionation have been based so far on β-factors of molecules, which are assumed to represent C-N bonds in diamond. The molecules of HCN and CN^- are considered as the analogues [9]. At 1,127 °C, $\Delta^{15}N$ between HCN molecule (diamond) and fluid is –2.3 (for NH_3) and –1.1 ‰ (for N_2). According to the results of the DFT calculations, isotopic fractionation between diamond and NH_3

Journal of Mining Institute. 2025. Vol. 272. P. 40-50

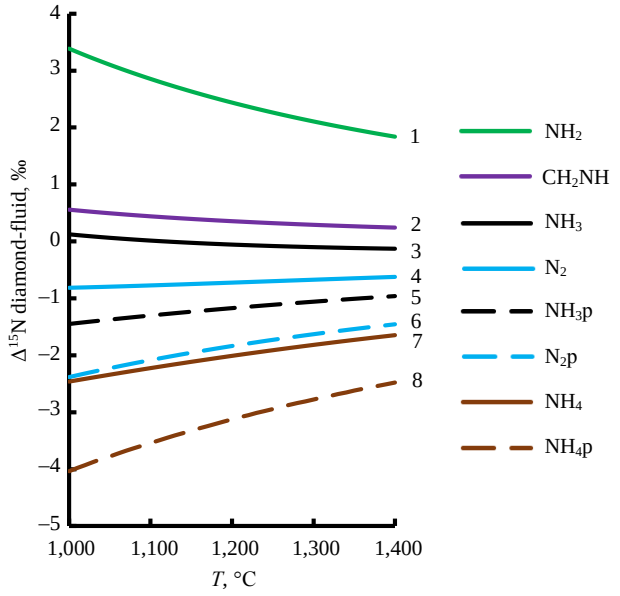

Fig.1. Isotopic fractionation of nitrogen between diamond and fluid

1-4, 7 – isotope fractionation factors, determined by DFT; 5, 6, 8 – isotope fractionation when modelling CN diamond bonds by CN^- molecule

molecule is nearly absent (–0.01 ‰ at 1127 °C), and between diamond and N_2 equals, given the same temperature –0.76 ‰. The results differ by –2.3 and –0.3 ‰. A decrease of $^{15}N/^{14}N$ occurs in the series of compounds $NH_4^+ > N_2 >$ (diamond, NH_3) > $CH_3N > CN^- > NH_2$. At temperature of 1,100 °C, fractionation between diamond and the above N-containing fluid compounds is estimated at –2.23, –0.77, 0.01, 0.44, 1.31 and 2.85 ‰, respectively, and significantly (over 1 ‰) exceeds estimates based on C-N bond in diamond by analogy with CN^- molecule.

Significant discrepancies in the substitution of nitrogen bonds in diamond with the molecular bonds are due to substantially different strength and nature of the bonds (which is manifested, for example, in the parameters of vibrational spectra). Isotopic fractionation with condensed phases is different from that of gases with the same composition [27], so that nitrogen in diamond can concentrate the heavy isotope more than gas molecules HCN or CN^-. Consi-dering CN^- molecule as a model of nitrogen isotopic fractionation, the positive value of $\Delta^{15}N$ between diamond and fluid corresponds to N-containing fluid compounds which are common for upper mantle, but have not yet been identified by either experimental or theoretical studies. Thus, calculated β-factors of HCN and CN^- molecules can be considered at best only as very rough approximations for estimating diamond isotopic fractionation [9]. For a number of nitrogen and carbon compounds that may be specific to the sublithospheric mantle, the values of β-factors are already known (Table 1). Our calculations show that nitrogen β-factors of NH_2 are significantly smaller than those of other molecules under consi-deration, so that even at temperatures exceeding the lithospheric values, there is a noticeable enrichment of diamond by ^{15}N isotope relative to the equilibrium fluid (about 2 ‰ at equilibrium fractionation diamond-NH_2, T = 1,400 °C). Isotopic fractionation of carbon between diamond and C_2H_6 molecule roughly corresponds to the fractionation with CH_4 (differ by ≈ 0.2 ‰, T = 1,400 °C). These compounds can be considered as possible fluid components provided sublithospheric diamond origin.

Isotopic fractionation of nitrogen between diamond and fluid under mantle conditions is considered to exceed significantly carbon isotopic fractionation with most of the known carbon-containing diamond forming fluids [21]. Our results demonstrate that at a temperature of 1,200 °C, diamond nitrogen β-factors are reduced relative to the molecules of N_2 and NH_4^+ by 0.8 and 1.0 ‰, respectively, but exceed β-factors of CH_3N and especially, NH_2 by 0.3 and 2.4 ‰. Fractionation of carbon isotopes between diamond and fluid species at the same temperature increases from negative values of –3.5 (CO_2), –1.8 (CO_3^{2-}) and –0.4 ‰ (CH_3N) to positive 1.1 ‰ (CH_4).

Pressure effect

Available calculations of β-factor on pressure dependencies [28, 23] demonstrate significant (about 0, *n* ‰) increase in diamond $\beta^{13}C$ at $T \approx$ 1,000-1,200 °C and $P >$ 10 GPa. Within the framework of the DFT method, pressure effect can be determined by β-factor variations with the lattice volume (within the quasi-harmonic approximation – QHA), including dependence of the volume V on polynomial coefficients 1,000 lnβ with variable $x = 10^6/T^2$. All polynomial coefficients linearly ($r^2 > 0.99$) depend on diamond volume with a decrease of V/V_0 to 0.88 (which approximately corresponds to a pressure up to 110 GPa):

$$\Delta a_1 V / \Delta V \approx -24.701; \quad \Delta a_2 V / \Delta V \approx 2.08287; \quad \Delta a_3 V / \Delta V \approx -0.16878;$$
$$\Delta a_4 V / \Delta V \approx 0.00867; \quad \Delta a_5 V / \Delta V \approx -0.00019 \ (^{15}\mathrm{N} / {}^{14}\mathrm{N}); \tag{3}$$

$$\Delta a_1 V / \Delta V \approx -47.795; \quad \Delta a_2 V / \Delta V \approx 4.5919; \quad \Delta a_3 V / \Delta V \approx -0.40351;$$
$$\Delta a_4 V / \Delta V \approx 0.021607; \quad \Delta a_5 V / \Delta V \approx -0.0004926 \ (^{13}\mathrm{C} / {}^{12}\mathrm{C}). \tag{4}$$

Thus, the following decomposition is valid

$$\Delta(a_i) \cong \frac{\Delta(a_i)}{\Delta V}\left\{\left[\left(\frac{\partial V}{\partial P}\right)\Delta P\right] + \frac{1}{2}\left[\left(\frac{\partial^2 V}{\partial P^2}\right)\Delta P^2\right]\right\} + \ldots. \tag{5}$$

Using the definition of the isothermal bulk modulus of elasticity $\mathrm{K}_T = -V\partial P/\partial V$ and confining to the second-order members, the relation (5) can be represented as

$$\Delta(a_i) \cong \frac{\Delta(a_i)V}{\Delta V}\left\{-\frac{1}{\mathrm{K}}\Delta P + \frac{1}{2}\frac{1}{\mathrm{K}^2}\left(\left(\frac{\partial \mathrm{K}}{\partial P}\right)+1\right)\Delta P^2\right\} + \ldots.$$

For diamond, V_0 = 3.416 cm^3, K = 442 GPa, $\partial \mathrm{K}/\partial P$ = 3.61 (our QHA calculation results, which are almost identical to the experimental data [29]: K = 445 GPa, with $\partial \mathrm{K}/\partial P$ = 4). In general, change in the coefficients a_i as a function of pressure (Table 1) is determined by the expression

$$\Delta a_i(P) \approx V(\Delta a_i)/\Delta V\left\{-0.00226\Delta P + 1.1799 \cdot 10^{-5}\Delta P^2\right\}.$$

At T = 1,000 °C, carbon β-factor increases by 0.6 (given P = 10 GPa), and the nitrogen factor increases by 0.33 ‰. At T = 1,700 °C, the change in carbon β-factor is 0.25 (10 GPa), and that of nitrogen 0.14 ‰. Thus, the dependence of β-factors on pressure for nitrogen isotopes is approximately 2 times lower than that for carbon. For control, the data on the change in the lattice constant of diamond during the substitution of carbon isotopes can be used. In particular, at T = 25 °C $(\partial\beta/\partial P)_T$ = 0.619 (GPa^{-1}), and the calculated value of the change in the coefficient of thermal expansion, α at isotopic substitution $(\Delta\alpha)/\alpha = \Delta V/3V = -(\partial\beta/\partial P)_T RT/(3V)$ is 1.50E^{-4}, which is equal to the experimental value [23]. The obtained diamond β^{13}C or β^{15}N dependencies on pressure are insufficient however, to determine the isotope fractionation between diamond and fluid, since for high-density fluids the assessment of the effect of P on β-factors of mineral-forming solutions is still a challenge.

β-factors considered determine the values of isotope fractionation during diamond formation for the volume (bulk) properties of the crystal lattice under conditions of equilibrium with the growth medium. The values of β can decrease significantly (up to several permille) in natural nanocrystalline diamonds (the size effect). For example, based on phonon density of states (PDOS) from the results of inelastic neutron scattering on diamonds with different size, isotopic shifts of carbon β-factors $10^3\ln\beta_{\mathrm{bulk}}$-$10^3\ln\beta_{\mathrm{nano}}$ relative to the bulk values were estimated [24, Fig.6]. For nanodiamonds, the change of the coefficient Δa_1 was estimated from the approximate digitization of the lines [24, Fig.6], corrected for the deviation of the phonon DOS from the parabolic ratio due to surface inclusions. Interpolation of Δa_1 value for nanodiamonds by linear dependence on size: $\Delta a_1 \approx 1.7768 - 0.0092 \times$size, nm with the coefficient of determination $r^2 \approx 0.99$. Shifts of 1,000 lnβ^{13}C for nanodiamonds at 5 nm Δa_1 – 1.799; at 40 nm Δa_1 – 1.321; at 170 nm Δa_1 – 0.227 ‰. Given the diamond size of 5 nm, isotopic ratio shifts due to surface effects can reach –1 ‰.

It is possible to assess the surface effects due to the preferential development of certain facets during diamond growth and the formation of sectorial (including isotopic) zoning [30]. The composition of the growing crystal is a consequence of the competition of growth and diffusion at the surface (for example, GEM is a model of growth capture [31]). The crystal inherits the composition of the growth surface at low diffusion at the surface, which can be characterized by the Peclet number:

$$\mathrm{Pe} = r \cdot 0.5L/D,$$

where r – is the growth rate, mm/s; L – is the thickness of the surface layer, nm; D is the diffusion coefficient of the element (or isotope) under consideration. The growth face is represented by a periodic plate with the number of layers *LS*. The inner layer is determined by the structure of the gross diamond, the outer *LS*-1 layers are reconstructed [32]. The parameters of the CRYSTAL calculation and sets of basis vectors are the same as during calculations on the bulk (gross) structure. Change of 1,000 lnβ relative to the gross values of $\sum_i \left(a_i^0 - a_i\right) x^i$; a_i^0 – are given in Table 1.

Table 2

1000 lnβ for diamond growth facets

Edge Index*	*LS*	a_1	a_2	a_3	a_4	a_5
			$^{15}N/^{14}N$			
{111}	2	12.14579	–0.59010	0.03920	–0.00176	4.190E^{-5}
	4	12.93791	–0.60624	0.04139	–0.00204	4.621E^{-5}
{110}	2	10.99022	–0.52717	0.02365	–0.00097	1.948E^{-5}
	4	12.70019	–0.69832	0.04544	–0.00304	3.966E^{-5}
{100}	2	8.66005	–0.20426	0.01380	–0.00129	9.954E^{-7}
	4	11.30632	–0.41044	0.02322	–0.00102	2.129E^{-5}
	6	12.67306	–0.44731	0.02390	–0.00100	2.015E^{-5}
			$^{13}C/^{12}C$			
{111}	2	19.98622	–1.11557	0.08240	–0.00415	9.234E^{-5}
	4	20.50007	–1.17320	0.08803	–0.00447	9.997E^{-5}
	6	20.82774	–1.18265	0.08748	–0.00432	9.623E^{-5}
{110}	2	18.23049	–0.93891	0.05031	–0.00205	4.197E^{-5}
	4	20.55262	–1.14874	0.08495	–0.00428	9.542E^{-5}
{100}	2	14.19463	–0.44483	0.02006	–0.00074	1.364E^{-5}
	4	18.91818	–0.81383	0.04992	–0.00227	4.770E^{-5}
	6	20.02506	–0.85221	0.04975	–0.00216	4.402E^{-5}

* Miller's index.

The key parameters of the model can be controlled by experimental observations but in most cases, they are not determined under natural conditions [32]. Since the volume β-factors characterize growth at equilibrium (Pe << 1), the values of β-factors for individual faces (Table 2) provide possibilities to estimate deviations from ideal conditions.

Comparison with natural $^{15}N/^{14}N$ fractionation

In the conditions of isotopic equilibrium between growth medium (homogeneous fluid) and the surface of the produced diamond (according to the Rayleigh mechanism), linear relationships can arise between ratios $^{13}C/^{12}C$, $^{15}N/^{14}N$ and the logarithm of nitrogen concentration ln(N) which are noted in numerous works [21, 33, 34]. The observed covariances both within individual diamond grains and among genetically related diamonds enable estimates "natural" isotopic nitrogen fractionation. The regression slope between genetically related diamonds in coordinates is determined by the equality

$$\delta^{13}C \textit{ vs } \delta^{15}N = \Delta^{13}C/(\Delta^{15}N K_N),$$

where K_N – is the nitrogen partition coefficient between diamond and fluid; Δ = 1,000 lnα, α – being factors of equilibrium isotope fractionation of carbon $^{13}C/^{12}C$ or nitrogen $^{15}N/^{14}N$ between diamond surface and growth medium [21]:

$$\delta^{15}N - \delta^{15}N_0 = \Delta^{15} \ln f_N = \Delta^{15} K_N \ln f,$$

f – fraction of fluid consumed; f_N – fraction of fluid nitrogen species consumed.

Provided $f = f_C$ (the fraction of fluid consumed equals the fraction of carbon species in the fluid), the following expression is valid

$$\delta^{13}C = \left(\delta^{15}N - \delta^{15}N_0\right)\Delta^{13} \Big/ \left(\Delta^{15}K_N\right)^* + \delta^{13}C_0,$$

where $\delta^{13}C_0$ or $\delta^{15}N$ – diamond isotope composition at the initial growth stage. The value of K_N is defined by the dependence of $\delta^{13}C$ on nitrogen content in diamond ln(N),

$$\delta^{13}C = \left[\left(\ln(N) - \ln(N_0)\right)\right]\Delta^{13} \Big/ \left(K_N - 1\right) + \delta^{13}C_0.$$

The above expressions are restricted to fluids dominated by carbon species although can be generalized for fluids of mixed composition. For example, $^{15}N/^{14}N$ fractionation between diamond and growth media was estimated at −4.0 ‰ (given T = 1,100 °C for a fluid dominated by CO_3^{2-} carbonate ion, $\Delta^{13}C \approx -1.7$ ‰, K_N = 4.4, Jericho kimberlite [33]). Data on the bulk isotopic composition of carbon and nitrogen in diamonds from a lherzolite xenolith (representing the lithospheric mantle) were used to estimate $\Delta^{15}N$ value at +1.2 ‰ (T = 1,200 °C, provided the methane-rich fluid [35]). Data on ultra-deep diamonds from Guinea, with a crystallization temperature of about 1,725 °C, were applied to determine $\Delta^{15}N$ between diamond and fluid (–4.5 ‰) in the conditions of crystallization from a fluid dominated by CO_3^{2-}, $\Delta^{13}C$ = –0.9 ‰ [36].

Isotopic fractionation factors of nitrogen in diamonds, $\Delta^{15}N$ estimated from natural covariances $\delta^{13}C$-$\delta^{15}N$-ln(N) depend, in addition to the choice of $\Delta^{13}C$ values, on the balance of fluid components as well as other parameters, including the fractionation model and the accepted crystallization temperature. Despite numerous assumptions and speculations especially regarding the values of K_N, in the absence of other calibrations, this method has so far been practically the only way to estimate $\Delta^{15}N$ between diamond and fluid.

The results of $\Delta^{15}N/\Delta^{13}C$ estimates by covariances from the natural genetically related samples can be compared with empirical dependencies and fractionation factors determined within the work. 64 series of conventionally cogenetic diamonds have been identified among the available dataset [9, 37] with the significant correlation $\Delta^{15}N$ *vs* $\Delta^{13}C$ (at a confidence level of 1σ), with the derived distribution of $\Delta^{15}N/\Delta^{13}C$ ratio (Fig.2, solid red line). At 2σ confidence level, the number of the series decreases (57 series), with no significant change in the distribution (the main maximum of Δ^{15}/Δ^{13} of about 0 and local peaks around 1 and 2). The representativeness of each series was assessed using the Student's *t*-distribution. The lines represent theoretical (see Table 1) $\Delta^{15}N/\Delta^{13}C$ values among diamond and fluid of different composition calculated at temperatures of 800 to 1,800 °C. Composition

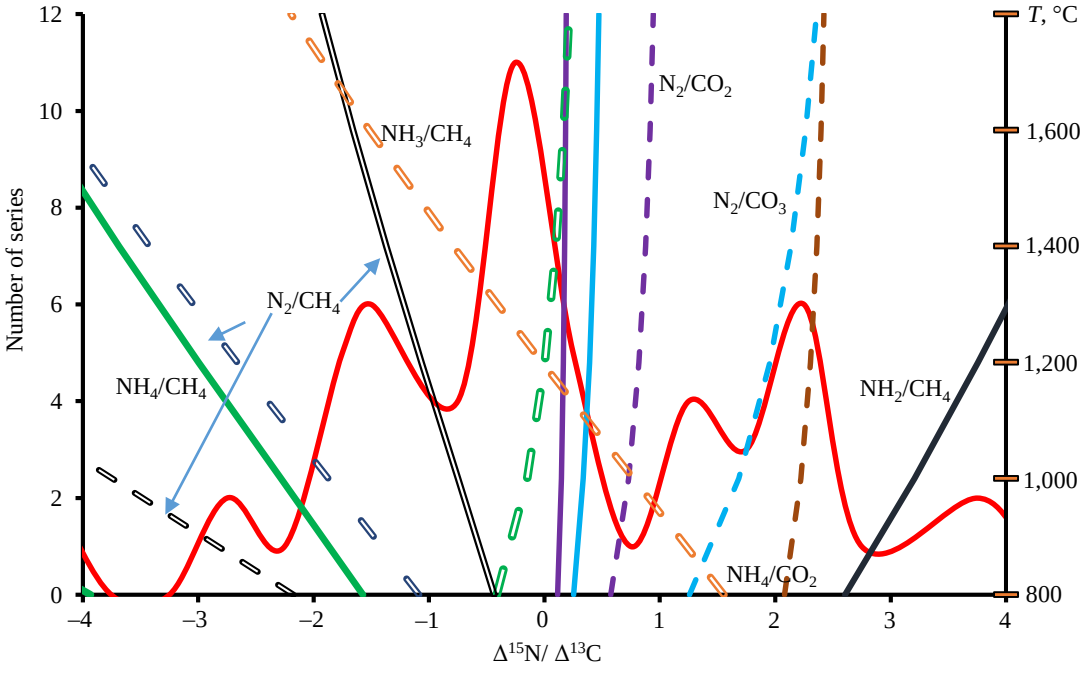

Fig.2. Frequency distribution of $\Delta^{15}N/\Delta^{13}C$ ratio in a series analysis of natural diamonds

of nitrogen species shown as the numerator, carbon species – as the denominator. Solid lines – assuming independent fractionation from $K_N = 1$, dashed $K_N = 5$, double dashed line $K_N = 2.5$. Double dashed green line – NH_3/CO_2, purple – N_2/CO_2, blue – N_2/CO_3. The figure was constructed with no use of the "empirical" fractionation factors estimated from natural nitrogen and carbon isotopic distributions. Most of the $\Delta^{15}N/\Delta^{13}C$ ratios fall within the values of –1.5 to 0.5 (with a maximum of about –0.3). Close to zero $\Delta^{15}N/\Delta^{13}C$ ratios may reflect the predominance of NH_3 as nitrogen-containing fluid compound during diamond genesis ($\Delta^{15}N$ close to zero) and/or the dominance of carbon-containing component with relatively high fractionation of $^{13}C/^{12}C$ during diamond growth (CO_2, CO_3). CO_2+N_2 or CO_3+N_2 dominated fluids have positive $\Delta^{15}N/\Delta^{13}C$ ratios. Provided two-component carbon source, the maximum distribution of $\Delta^{15}N/\Delta^{13}C$ may represent isotopic exchange of diamond with CO_2 or carbonate ion mixed with CH_4, with N_2 dominating as the nitrogen source. Evolved $\Delta^{15}N/\Delta^{13}C$ ratios (local maxima of the $\Delta^{15}N/\Delta^{13}C \approx$ ratio at 1.5 and 2.3) may correspond to diamond crystallization from a fluid dominated by NH_4/CO_2, N_2/CO_3 or NH_2/CH_4. C_2H_6 or CH_3N species are possible as a source. Negative $\Delta^{15}N/\Delta^{13}C$ correspond to a combination of such components as NH_4/CH_4, N_2/CH_4 or NH_3/CH_4 (the latter, at temperatures above 1,250-1,300 °C). It should be noted that temperature increase shifts the equilibrium isotopic ratios of $^{15}N/^{13}C$. Empirically estimated values of the $\Delta^{15}N/\Delta^{13}C$ ratio beyond the range of –4 to +4 may indicate extreme nitrogen partitions between diamond and the growth medium, or the presence of some unconsidered fluid components enriched in either ^{15}N or ^{13}C relative to diamond. Depending on the $\Delta^{15}N/\Delta^{13}C$ ratio, the Rayleigh crystallization within the cogenetic series of diamond may be accompanied by the increase of $\delta^{15}N$, by the decrease of this value or by the lack of any trend.

Conclusion

Isotopic fractionation factors have been relatively well established for carbon in many systems related to diamond genesis. The distribution of nitrogen isotopes between diamond and the mineral-forming fluid is, however much less studied and is mainly based on empirically observed trends from natural diamonds, yielding significant uncertainties in estimates and the need for more rigorous constrains [11]. The reliable values of nitrogen isotope fractionation factors should be a prerequisite for revealing the causes of the observed isotopic heterogeneity of diamond, the nature of covariances in $\delta^{13}C$-$\delta^{15}N$-N values, the composition of fluids and, possibly, other conditions during diamond formation. In this paper, an attempt is made to quantify the fractionation of nitrogen isotopes "from first principles" based on crystallo-chemical properties of diamond with nitrogen substitution and nitrogen-containing fluid species.

In particular, the "frozen phonon" method within the density functional theory using the full-electron bases was adopted to determine the sets of β-factors ($^{15}N/^{14}N$, $^{13}C/^{12}C$) of diamond in harmonic and quasi-harmonic approximations at temperatures from 0 to 2,500 °C. To achieve representativeness of the calculations, the method of expanded cells (with an increase in volume by 8, 16, 27 times) was utilized. In addition, some β-factors of fluid components (including carbon C_2H_6, CH_2NH and nitrogen CH_2NH) have been deduced to estimate isotopic fractionations during diamond formation. The results of the *ab initio* calculations differ significantly from the previously obtained theoretical results based on the representation of the CN bonds of diamond by the molecular compounds HCN or CN^-. In the conditions of diamond formation, with a volume decrease under pressure, factors of isotopic fractionation of nitrogen and carbon can increase by tenths of permille for carbon. Pressure effects diamond nitrogen isotope fractionation more than carbon isotope fractionation, which in extreme conditions (super cold subduction) can lead to an increase in fractionation factors up to significant values. The volume increase in diamond lattice due to thermal expansion however, partially reduces the effect of pressure, so that the shifts in isotopic ratios are generally determined by the value of the $\Delta P/\Delta T$ gradient. In the "standard" lithospheric conditions of diamond genesis (about 6 GPa and 1,100 °C), factors of carbon and nitrogen isotopic fractionation do not change significantly.

Depending on the dominant nitrogen and carbon substances, fractionation of isotopes during diamond formation can result either in various zonation of isotopic composition within individual grains and different variations within cogenetic series. In most cases (maximum in the $\Delta^{15}N/\Delta^{13}C$ distribution, Fig.2), nitrogen isotope fractionation is negligible ($\Delta^{15}N << \Delta^{13}C$), which is consistent with calculations of the fractionation factors between diamond and NH_3-CO_2 or N_2-CO_2 fluids. Shifts in the $\Delta^{15}N/\Delta^{13}C$ ratio to the negative values may indicate reduced conditions at high pressures and the "cold" geotherm [38]. In nitrogen-poor reduced mantle fluids [39], amines (NH_2) or methanimine (CH_3N) may play an important role and their dominance may also correspond to the occurrence of local maxima within the $\Delta^{15}N/\Delta^{13}C$ distribution. Oxidized fluids dominated by CO_2 or CO_3 in combination with the N_2 component yield positive $\Delta^{15}N/\Delta^{13}C$ between diamond and fluid and significantly depend on the nitrogen partition coefficient ratio.

REFERENCES

1. Vasilev E., Zedgenizov D., Zamyatin D. et al. Cathodoluminescence of Diamond: Features of Visualization. *Crystals*. 2021. Vol. 11. Iss. 12. N 1522. DOI: 10.3390/cryst11121522
2. Klepikov I.V., Vasilev E.A., Antonov A.V. Regeneration Growth as One of the Principal Stages of Diamond Crystallogenesis. *Minerals*. 2022. Vol. 12. Iss. 3. N 327. DOI: 10.3390/min12030327
3. Gubanov N.V., Zedgenizov D.A., Vasilev E.A., Naumov V.A. New data on the composition of growth medium of fibrous diamonds from the placers of the Western Urals. *Journal of Mining Institute.* 2023. Vol. 263, p. 645-656.
4. Zedgenizov D., Kagi H., Ohtani E. et al. Retrograde phases of former bridgmanite inclusions in superdeep diamonds. *Lithos*. 2020. Vol. 370-371. N 105659. DOI: 10.1016/j.lithos.2020.105659
5. Puchkov V.N., Zedgenizov D.A. Mantle convection and diamonds. *Lithosphere.* 2023. Vol. 23. N 4, p. 476-490 (in Russian). DOI: 10.24930/1681-9004-2023-23-4-476-490
6. Liu J., Wang W., Yang H. et al. Carbon isotopic signatures of super-deep diamonds mediated by iron redox chemistry. *Geochemical Perspectives Letters*. 2019. Vol. 10, p. 51-55. DOI: 10.7185/geochemlet.1915
7. Cartigny P., Palot M., Thomassot E., Harris J.W. Diamond Formation: A Stable Isotope Perspective. *Annual Review of Earth and Planetary Sciences*. 2014. Vol. 42, p. 699-732. DOI: 10.1146/annurev-earth-042711-105259
8. Cartigny P., Harris J.W., Javoy M. Diamond genesis, mantle fractionations and mantle nitrogen content: a study of $\delta^{13}C$–N concentrations in diamonds. *Earth and Planetary Science Letters*. 2001. Vol. 185. Iss. 1-2, p. 85-98. DOI: 10.1016/S0012-821X(00)00357-5
9. Stachel T., Cartigny P., Chacko T., Pearson D.G. Carbon and Nitrogen in Mantle-Derived Diamonds. *Reviews in Mineralogy and Geochemistry*. 2022. Vol. 88. N 1, p. 809-875. DOI: 10.2138/rmg.2022.88.15
10. Smit K.V., Timmerman S., Aulbach S. et al. Geochronology of Diamonds. *Reviews in Mineralogy and Geochemistry*. 2022. Vol. 88. N 1, p. 567-636. DOI: 10.2138/rmg.2022.88.11
11. Cartigny P., Marty B. Nitrogen Isotopes and Mantle Geodynamics: The Emergence of Life and the Atmosphere–Crust–Mantle Connection. *Elements*. 2013. Vol. 9. N 5, p. 359-366. DOI: 10.2113/gselements.9.5.359
12. Richet P., Bottinga Y., Javoy M. A Review of Hydrogen, Carbon, Nitrogen, Oxygen, Sulphur, and Chlorine Stable Isotope Fractionation Among Gaseous Molecules. *Annual Review of Earth and Planetary Sciences*. 1977. Vol. 5, p. 65-110. DOI: 10.1146/annurev.ea.05.050177.000433
13. Polyakov V.B., Kharlashina N.N. The use of heat capacity data to calculate carbon isotope fractionation between graphite, diamond, and carbon dioxide: a new approach. *Geochimica et Cosmochimica Acta*. 1995. Vol. 59. Iss. 12, p. 2561-2572. DOI: 10.1016/0016-7037(95)00150-6
14. Horita J. Carbon isotope exchange in the system CO_2-CH_4 at elevated temperatures. *Geochimica et Cosmochimica Acta*. 2001. Vol. 65. Iss. 12, p. 1907-1919. DOI: 10.1016/S0016-7037(01)00570-1
15. Bigeleisen J., Mayer M.G. Calculation of Equilibrium Constants for Isotopic Exchange Reactions. *The Journal of Chemical Physics*. 1947. Vol. 15. N 5, p. 261-267. DOI: 10.1063/1.1746492
16. Erba A., Desmarais J.K., Casassa S. et al. CRYSTAL23: A Program for Computational Solid State Physics and Chemistry. *Journal of Chemical Theory and Computation*. 2023. Vol. 19. Iss. 20, p. 6891-6932. DOI: 10.1021/acs.jctc.2c00958
17. Yuting Zheng, Chengming Li, Jinlong Liu et al. Diamond with nitrogen: states, control, and applications. *Functional Diamond*. 2021. Vol. 1. N 1, p. 63-82. DOI: 10.1080/26941112.2021.1877021
18. Palyanov Y.N., Borzdov Y.M., Khokhryakov A.F. et al. Effect of Nitrogen Impurity on Diamond Crystal Growth Processes. *Crystal Growth & Design*. 2010. Vol. 10. Iss. 7, p. 3169-3175. DOI: 10.1021/cg100322p
19. Grimme S., Hansen A., Brandenburg J.G., Bannwarth C. Dispersion-Corrected Mean-Field Electronic Structure Methods. *Chemical Reviews*. 2016. Vol. 116. Iss. 9, p. 5105-5154. DOI: 10.1021/acs.chemrev.5b00533
20. Schauble E.A., Young E.D. Mass Dependence of Equilibrium Oxygen Isotope Fractionation in Carbonate, Nitrate, Oxide, Perchlorate, Phosphate, Silicate, and Sulfate Minerals. *Reviews in Mineralogy and Geochemistry*. 2021. Vol. 86. N 1, p. 137-178. DOI: 10.2138/rmg.2021.86.04
21. Petts D.C., Chacko T., Stachel T. et al. A nitrogen isotope fractionation factor between diamond and its parental fluid derived from detailed SIMS analysis of a gem diamond and theoretical calculations. *Chemical Geology*. 2015. Vol. 410, p. 188-200. DOI: 10.1016/j.chemgeo.2015.06.020
22. Polyakov V.B., Kharlashina N.N., Shiryaev A.A. Thermodynamic properties of ^{13}C-diamond. *Diamond and Related Materials*. 1997. Vol. 6. Iss. 1, p. 172-177. DOI: 10.1016/S0925-9635(96)00587-0

23. Bottinga Y. Carbon isotope fractionation between graphite, diamond and carbon dioxide. *Earth and Planetary Science Letters*. 1968. Vol. 5, p. 301-307. DOI: 10.1016/S0012-821X(68)80056-1

24. Shiryaev A.A., Polyakov V.B., Rols S. et al. Inelastic neutron scattering: a novel approach towards determination of equilibrium isotopic fractionation factors. Size effects on heat capacity and beta-factor of diamond. *Physical Chemistry Chemical Physics*. 2020. Vol. 22. Iss. 23, p. 13261-13270. DOI: 10.1039/d0cp02032j

25. Polyakov V.B., Horita J. Equilibrium carbon isotope fractionation factors of hydrocarbons: Semi-empirical force-field method. *Chemical Geology*. 2021. Vol. 559. N 119948. DOI: 10.1016/j.chemgeo.2020.119948

26. Kueter N., Schmidt M.W., Lilley M.D., Bernasconi S.M. Experimental determination of equilibrium CH_4–CO_2–CO carbon isotope fractionation factors (300-1200 °C). *Earth and Planetary Science Letters*. 2019. Vol. 506, p. 64-75. DOI: 10.1016/j.epsl.2018.10.021

27. Horita J., Wesolowski D.J. Liquid-vapor fractionation of oxygen and hydrogen isotopes of water from the freezing to the critical temperature. *Geochimica et Cosmochimica Acta*. 1994. Vol. 58. Iss. 16, p. 3425-3437. DOI: 10.1016/0016-7037(94)90096-5

28. Polyakov V.B., Kharlashina N.N. Pressure effect on isotope fractionation *Doklady Akademii nauk SSSR*. 1989. Vol. 306. N 2, p. 390-395.

29. Kunc K., Loa I., Syassen K. Equation of state and phonon frequency calculations of diamond at high pressures. *Physical Review B*. 2003. Vol. 68. Iss. 9. N 094107. DOI: 10.1103/PhysRevB.68.094107

30. Reutsky V.N., Kowalski P.M., Palyanov Y.N. et al. Experimental and Theoretical Evidence for Surface-Induced Carbon and Nitrogen Fractionation during Diamond Crystallization at High Temperatures and High Pressures. *Crystals*. 2017. Vol. 7. Iss. 7. N 190. DOI: 10.3390/cryst7070190

31. Watson E.B. A conceptual model for near-surface kinetic controls on the trace-element and stable isotope composition of abiogenic calcite crystals. *Geochimica et Cosmochimica Acta*. 2004. Vol. 68. Iss. 7, p. 1473-1488. DOI: 10.1016/j.gca.2003.10.003

32. de la Pierre M., Bruno M., Manfredotti C. et al. The (100), (111) and (110) surfaces of diamond: an ab initio B3LYP study. *Molecular Physics*. 2014. Vol. 112. Iss. 7, p. 1030-1039. DOI: 10.1080/00268976.2013.829250

33. Smart K.A., Chacko T., Stachel T. et al. Diamond growth from oxidized carbon sources beneath the Northern Slave Craton, Canada: A $\delta^{13}C$–N study of eclogite-hosted diamonds from the Jericho kimberlite. *Geochimica et Cosmochimica Acta*. 2011. Vol. 75. Iss. 20, p. 6027-6047. DOI: 10.1016/j.gca.2011.07.028

34. Smit K.V., Stachel T., Luth R.W., Stern R.A. Evaluating mechanisms for eclogitic diamond growth: An example from Zimmi Neoproterozoic diamonds (West African craton). *Chemical Geology*. 2019. Vol. 520, p. 21-32. DOI: 10.1016/j.chemgeo.2019.04.014

35. Thomassot E., Cartigny P., Harris J.W., Viljoen K.S. Methane-related diamond crystallization in the Earth's mantle: Stable isotope evidences from a single diamond-bearing xenolith. *Earth and Planetary Science Letters*. 2007. Vol. 257. Iss. 3-4, p. 362-371. DOI: 10.1016/j.epsl.2007.02.020

36. Palot M., Pearson D.G., Stern R.A. et al. Isotopic constraints on the nature and circulation of deep mantle C–H–O–N fluids: Carbon and nitrogen systematics within ultra-deep diamonds from Kankan (Guinea). *Geochimica et Cosmochimica Acta*. 2014. Vol. 139, p. 26-46. DOI: 10.1016/j.gca.2014.04.027

37. Curtolo A., Novella D., Logvinova A. et al. Petrology and geochemistry of Canadian diamonds: An up-to-date review. *Earth-Science Reviews*. 2023. Vol. 246. N 104588. DOI: 10.1016/j.earscirev.2023.104588

38. Yuan Li, Keppler H. Nitrogen speciation in mantle and crustal fluids. *Geochimica et Cosmochimica Acta*. 2014. Vol. 129, p. 13-32. DOI: 10.1016/j.gca.2013.12.031

39. Sokol A.G., Tomilenko A.A., Bulbak T.A. et al. Composition of Reduced Mantle Fluids: Evidence from Modeling Experiments and Fluid Inclusions in Natural Diamond. *Russian Geology and Geophysics*. 2020. Vol. 61. N 5-6, p. 663-674. DOI: 10.15372/RGG2020103

***Author* Dmitrii P. Krylov,** *Doctor of Geological and Mineralogical Sciences, Leading Researcher, d.p.krylov@ipgg.ru, https://orcid.org/0000-0001-6654-8659* (*Institute of Precambrian Geology and Geochronology RAS, Saint Petersburg, Russia*).

The author declares no conflict of interests.

ISSN 2411-3336; e-ISSN 2541-9404

JOURNAL OF MINING INSTITUTE

Zapiski Gornogo instituta

Journal homepage: pmi.spmi.ru

Research article *Geotechnical Engineering and Engineering Geology*

Combined method for processing spent acid etching solution obtained during manufacturing of titanium products

Nikolai A. Bykovskii[1]✉, **Evgenii A. Kantor**[2], **Nikolai S. Shulaev**[1], **Vadim S. Fanakov**[2]

[1] *Institute of Chemical Technologies and Engineering – Branch of the Ufa State Petroleum Technological University, Republic of Bashkortostan, Sterlitamak, Russia*

[2] *Ufa State Petroleum Technological University, Ufa, Republic of Bashkortostan, Russia*

***How to cite this article*:** Bykovskii N.A., Kantor E.A., Shulaev N.S., Fanakov V.S. Combined method for processing spent acid etching solution obtained during manufacturing of titanium products. Journal of Mining Institute. 2025. Vol. 272. N 16446, p. 51-58.

Abstract

Possessing high strength, low density and significant chemical resistance, titanium has found wide application in various fields of the national economy – the chemical industry, aviation and rocket technology, mechanical engineering, medicine, etc. The production of titanium products is hampered by a fairly strong oxide film covering its surface. Removal of the oxide film from the surface of titanium workpieces is carried out by etching in solutions of mineral acids of various compositions. A spent acid etching solution (SAES) is formed, containing titanium salt and the remainder of unreacted acids. Almost all etching solutions contain HF and one of the strong acids. This is H_2SO_4, HCl or HNO_3. Thus, the SAES includes ions of titanium, fluorine or chlorine, orsulfate, or nitrate. SAES is quite toxic and must be diluted or cleaned several times before being discharged into a reservoir. Most of the methods used to extract impurities contained in SAES lead to a decrease in their content. As a result of such purification, there is a loss of substances contained in SAES in significant quantities and of interest for further use. The work presents experimental results obtained from the combined processing of SAES containing titanium fluoride, hydrofluoric and hydrochloric acids. At the first stage, SAES is treated with sodium hydroxide. The resulting titanium hydroxide precipitate is filtered off. At the second stage, the filtrate containing sodium fluoride and chloride is processed in a membrane electrolyzer. In this case, not only the extraction of sodium salts from the filtrate occurs, but also the production of sodium hydroxide and a mixture of hydrofluoric and hydrochloric acids. Sodium hydroxide can be used for processing SAES, and a mixture of acids for etching titanium workpieces.

Keywords

titanium etching; spent etching solution; electrochemical processing; membrane electrolyzer; titanium hydroxide; sodium hydroxide; hydrochloric acid; hydrofluoric acid

Received: 10.04.2024 ***Accepted: 03.06.2024*** ***Online: 19.07.2024*** ***Published: 25.04.2025***

Introduction

Titanium and its alloys are widely used in the manufacture of a wide variety of equipment, which is in high demand due to its anti-corrosion resistance, a good combination of strength properties, temperature resistance, low density and relatively high metal consumption. The main consumers of titanium and its compounds are aircraft and rocket manufacturing [1], chemical industry [2-4], metallurgy [5], medicine [6, 7], catalyst production [8], paint and varnish industry [9]. As a rule, the manufacture of titanium products is accompanied by heating, as a result of which its surface is covered with a fairly strong oxide film. To ensure the manufacturability of titanium workpieces, especially when applying modifying coatings to its surface, it is necessary to remove the oxide film from the surface. To perform this operation, various methods are used [10-12].

In addition to mechanical, thermal and other methods, thermochemical methods are also widely used [13-15]. Such methods consist in treating the surface of products with mineral acids at certain

temperatures [16, 17]. Hydrochloric, sulfuric, nitric, phosphoric and other acids are used as acids to dissolve oxide films on the surface of titanium and its alloys in various concentrations and at different temperatures [16, 17]. In contrast to these acids, hydrofluoric acid dissolves titanium at room temperature. In order to regulate the rate of dissolution of titanium, acids such as HCl, H_2SO_4, and HNO_3 are introduced into the solution of hydrofluoric acid [18]. If the presence of sulfuric acid slightly increases the rate of the titanium dissolution process, then with the introduction of hydrochloric acid into the solution, it almost doubles, and the use of nitric acid leads to a decrease in the rate of dissolution*.

In AO Bashkir Soda Company for etching the surface of titanium in the production of oxide-ruthenium-titanium anodes (ORTA), hydrochloric acid is used. The etching process is carried out in 25-27 % HCl at a temperature of about 85 °C. The resulting spent acid etching solution (SAES) in this case contains up to 180 g/l of titanium chloride and up to 110 g/l of hydrochloric acid.

VSMPO-AVISMA Corporation uses a mixture of aqueous solutions of HF and HCl at room temperature to etch the surface of titanium. The resulting SAES contains about 22 g/l of titanium fluoride, about 1.7 g/l of hydrofluoric acid and about 6.2 g/l of hydrochloric acid. This solution is even more toxic than a solution containing only titanium chloride and hydrochloric acid, due to the presence of anion fluoride. The maximum permissible concentrations of SAES components in water bodies of domestic and domestic water use are for ions, mg/l: fluorine 1.5, chlorine 350, sulfate 500, titanium 0.1 (GN 2.1.5.1315-03. Hygienic standards. Maximum permissible concentrations (MPC) of chemicals in the water of water bodies for domestic and domestic water use). Thus, when SAES is discharged into a water body, significant water costs are required to dilute it. In addition, in this case, there is a loss of valuable components that can serve as raw materials for obtaining marketable products. There are known methods for the utilization and neutralization of SAES using ion exchange [19-21], coagulation and sedimentation [22-24], and neutralization [25, 26].The process of neutralization of SAES leads to the consumption of alkaline reagents, the formation of toxic solid wastes such as CaF_2 and Na_2TiF_6 of the 2nd hazard class, as well as to the loss of mineral acids [27-30].

In the authors' previous works, the possibility of processing wastewater containing various substances to obtain products that can be used in the production process was considered [31-33]. This article presents the results of research on the processing of SAES containing titanium fluoride, hydrofluoric and hydrochloric acids. The SAES was processed in two stages. At the first stage, the SAES was treated with sodium hydroxide titanium. The resulting titanium hydroxide precipitate was filtered off and dried. At the second stage, the filtrate containing fluorine, chlorine and sodium ions was processed in a membrane electrolyzer. As a result of electrochemical treatment of the filtrate in the electrolyzer, sodium hydroxide and a mixture of hydrofluoric and hydrochloric acids were generated.

Methodology

Experimental studies were carried out in two stages. At the first stage, SAES was treated with crystalline sodium hydroxide. For this purpose, crystalline NaOH was added to 100 ml of SAES. The resulting precipitate of titanium hydroxide was filtered and dried at a temperature of 200 °C to a constant weight. The sediment mass was used to determine the degree of titanium recovery from the SAES. The second stage consisted of electrochemical treatment of the filtrate obtained after the separation of titanium hydroxide in electrolyzers with ion-exchange membranes. Two types of electrolyzers were used for the research – without a flow and with the flow of solutions through the chambers.

The study of the distribution of components in the electrolyzer chambers, the determination of the current yield and the specific energy consumption for the leachate processing process was carried out in a four-chamber membrane electrolyzer without the flow of solutions through the chambers (Fig.1).

* Acid solutions used in the chemical method of cleaning the surface of semi-finished products made of titanium alloys. URL: https://sv-barrisol.ru/polufabrikaty/102-kislotnye-rastvory-primenyaemye-pri-himicheskom-sposobe-ochistkipoverh-nosti-polufabrikatov-iz-titanovyh-splavov.html (accessed 09.04.2024).

The electrolyzer chambers with a diameter of 6 cm were made of plexiglass plates with a thickness of 2.5 cm. Membranes manufactured by OOO Shchekinoazot were used to separate the chambers: cation exchange membranes of the MK-40 brand, anion exchange membranes of the MA-40 brand. The working surface of each membrane separating the chambers was 14.1 cm^2. The cathode material is a stainless steel plate, the anode material is a titanium plate coated with ruthenium oxide (ORTA). A 0.1 n sodium hydroxide solution was loaded into the cathode chamber of the 1st electrolyzer. The filtrate obtained after the extraction of titanium from the SAES was loaded into chamber 2. In chamber 3 – 0.1 n solution of hydrochloric acid. A 0.1 n solution of sulfuric acid was placed in the anode chamber 4. The volume of solutions loaded into all chambers of the electrolyzer was 60 ml.

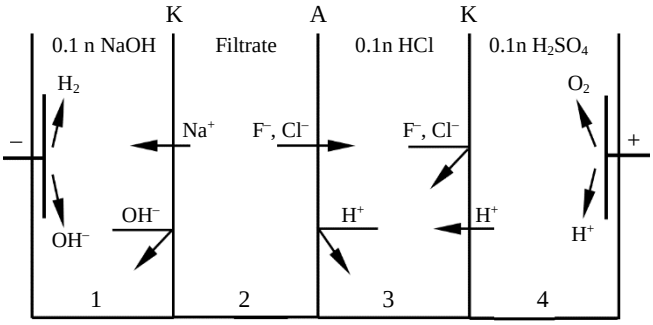

Fig.1. Diagram of a non-flowing electrolyzer for processing leachate obtained after removing titanium from the SAES

A – anion exchange; K – cation exchange membrane

In the process of treating the filtrate in an electrolysis cell (Fig.1), water decomposes on the cathode to form hydrogen gas and generate hydroxyl ions. At the anode, water decomposes with the release of gaseous oxygen and the generation of hydrogen ions. Sodium and hydrogen ions migrate to the cathode, and hydroxyl, fluorine, and chlorine ions migrate to the anode. The migration of hydrogen ions is hindered by the anion exchange membrane, and the migration of hydroxyl, fluorine, and chlorine ions is hindered by the cation exchange membrane. As a result, sodium hydroxide accumulates in the cathodic chamber 1 of the electrolyzer, and a mixture of hydrofluoric and hydrochloric acids accumulates in chamber 3 of the electrolyzer.

To determine the maximum concentrations of alkali and acid mixtures generated in the cathode and chamber 3 of the electrolyzer, a membrane electrolyzer with a flow of solutions in the chambers of the apparatus was used, schematically shown in Fig.2. The electrolyzer consisted of four cells separated by electrode plates. Each cell is divided into four chambers, which are separated from each other by cation exchange and anion exchange membranes. The working surface of each membrane was 30 cm^2. Framed chambers were made of a polyvinyl chloride plate 2 mm thick. To prevent the membranes from sticking together, a mesh stretched from calendered vinyl was placed in each chamber. The entire structure was pulled into a single package by plexiglass plates.

The concentrations of solutions used in an electrolyzer with flow chambers (Fig.2) are similar to the concentrations of solutions used in an electrolyzer without their flow through the chambers of the apparatus (see Fig.1).

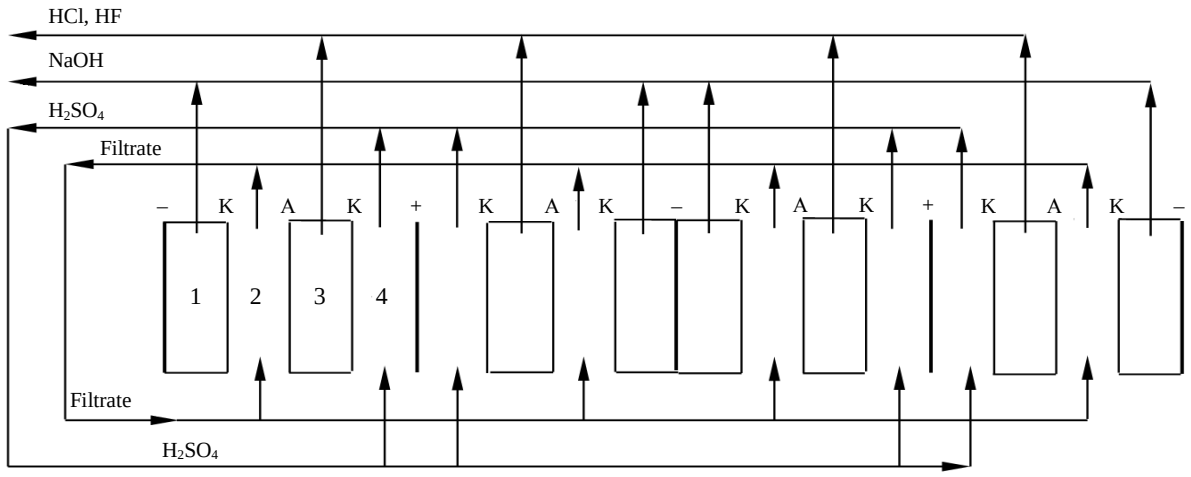

Fig.2. Diagram of a flow-through electrolyzer for processing leachate obtained after removing titanium from the SAES

In chamber 2 of the electrolyzer, filtrate circulated, in the anode chamber – a solution of sulfuric acid. The cathode chamber and chamber 3 are made without the flow of solutions and were pre-filled with 0.1 n solutions of sodium hydroxide and hydrochloric acid, respectively. Solutions of sodium hydroxide and mixtures of hydrofluoric and hydrochloric acids left their respective chambers as they accumulated.

The studies were carried out with a model solution containing titanium fluoride, hydrofluoric acid and hydrochloric acid. The studied solution was obtained by dissolving metallic titanium in a mixture of hydrofluoric and hydrochloric acids. For this purpose, 10 g of VT1-0 titanium was dissolved in 1 l of a mixture of hydrofluoric and hydrochloric acids containing 14.7 g/l of HF and 6.2 g/l of HCl. The composition of the resulting model SAES designed for titanium fluoride is 22 g/l, 0.21 mol/l; hydrofluoric acid – 1.7 g/l, 0.085 mol/l; hydrochloric acid – 6.2 g/l, 0.17 mol/l.

Results and discussion

The results of experiments on the extraction of titanium from the SAES by its treatment with sodium hydroxide are presented in Table 1.Treatment of SAES with sodium hydroxide leads to complete recovery of titanium when the pH of the filtrate reaches 7.6. The filtrate obtained after sedimentation and washing contained 0.92 mol/l of sodium fluoride and 0.17 mol/l of sodium chloride.

Table 1

Dependence of the degree of titanium recovery from the SAES on the mass of NaOH and pH of the filtrate

NaOH mass added to 100 ml of SAES, g	2.4	2.6	2.8	3.0	3.2	3.4	3.6	3.8	4.0	4.2
pH	3.75	5.5	6.45	7.2	7.6	7.8	9.4	9.85	10.6	12.8
Recovery rate, %	85.4	89.8	96.5	98.1	99.6	100	99.8	100	100	100

To study the distribution of sodium, fluorine and chlorine ions in the electrolyzer chambers, to determine the current yield and specific energy consumption for the process, an apparatus without the flow of solutions through the chambers was used (see Fig.1). The weight of the components in the electrolyzer before the experiments, determined by a calculation based on the volume of solutions used and their concentration, was: sodium ions 0.138 g in chamber 1 and 1.504 g in chamber 2; fluorine ions 1.048 g in chamber 2; chlorine ions 0.362 g in chamber 2 and 0.213 g in chamber 3. The current density in the process of filtrate processing varied from 20 to 80 mA/cm^2. The amount of electricity passed in all experiments remained constant and amounted to 1.2 A·h. The distribution of sodium, fluorine and chlorine ions is shown in Table 2.

Table 2

Distribution of sodium, fluorine and chlorine ions in the electrolyzer chambers

Current density, mA/cm^2	Weight, g						Violation of the material balance calculated for chlorine, %
	Sodium		Fluorine		Chlorine		
	Chamber 1	Chamber 2	Chamber 2	Chamber 3	Chamber 2	Chamber 3	
20	0.955	0.687	0.606	0.422	0.233	0.312	5.2
40	0.929	0.713	0.593	0.455	0.228	0.311	6.3
60	0.987	0.655	0.590	0.458	0.237	0.324	3.8
80	0.967	0.675	0.602	0.446	0.235	0.329	5.7
	Averages						
	0.964	0.683	0.598	0.450	0.233	0.319	

In the process of electrolysis, sodium ions migrate to chamber 1 of the electrolyzer. In this chamber, sodium ions are concentrated to form hydroxide. In chambers 3 and 4, the presence of sodium ions was not detected. There is no dependence of the degree of extraction of sodium, fluorine and chlorine ions from chamber 2 on the membrane density of the current. This made it possible to determine

the average values of the mass of ions in the electrolyzer chambers and calculate the error in the results obtained. The calculation of the relative error according to the Student's distribution for a 95 % confidence level for all components varies from 2 % for fluorine ions in electrolyzer chamber 2 to 5.6 % for sodium ions in the same chamber. The average recovery rate of sodium ions from chamber 2 was 79.8 %. Fluorine and chlorine ions migrate to the electrolyzer chamber 3 and accumulate in it, forming hydrofluoric and hydrochloric acids. The presence of fluorine and chlorine ions in chambers 1 and 4 was not detected. The average recovery rate was 36.4 % fluorine ions and 35.6 % chlorine ions. Since the extraction of sodium ions from the filtrate was calculated by increasing the concentration of sodium hydroxide in chamber 1 of the electrolyzer, and the extraction of fluorine was calculated by increasing the concentration of hydrofluoric acid in chamber 3, it is not possible to calculate the violation of the material balance for these elements. In contrast, the content of chloride ions was determined in all chambers of the apparatus, which made it possible to calculate a violation of the material balance, which amounted to 3.8 to 6.3 %.

Table 3 shows the specific consumption of electrical energy for the leachate processing process and current yield. The data presented are calculated from the results obtained for the extraction of sodium from the filtrate.

Table 3

Current yield and specific energy consumption of the leachate processing process

Voltage, V	Current density, mA/cm^2	Current yield, %	Electricity consumption	
			W·h/g	W·h/mol
1.97	20	79.3	2.36	65.67
4.12	40	76.8	4.94	145.41
7.06	60	82.4	8.47	228.97
12.14	80	80.5	14.89	413.67

The current yield (average value 79.8 %) is independent of current density. The consumption of electrical energy for the extraction of sodium fluoride and sodium chloride ions from the filtrate is determined by a membrane current density. An increase in the membrane current density is accompanied by a quite sharp increase in the electricity specific consumption for the process. For example, a change in the current density by 20 mA/cm^2 in the range of 20-40 mA/cm^2 is accompanied by an increase in energy consumption by 79 W·h/mol, and in the range of 60-80 mA/cm^2 – by an increase in energy consumption of 185 W·h/mol, i.e. 2.3 times.

Studies on the processing of filtrate in a non-flowing four-chamber electrolyzer with cation exchange and anion exchange membranes indicate the possibility of obtaining solutions containing sodium hydroxide and a mixture of hydrofluoric and hydrochloric acids. To determine the maximum concentration of sodium hydroxide solutions and a mixture of hydrofluoric and hydrochloric acids, a series of experiments was carried out in an electrolyzer with flow-through chambers 2 and 4 (Fig.2). The filtrate treatment process was carried out until the concentration values of sodium hydroxide and a mixture of hydrofluoric and hydrochloric acids generated in the electrolyzer ceased to change. The volume of solutions circulating in chambers 2 and 4 of the electrolyzer was 2 l each.

Figure 3 shows changes in the concentration of sodium hydroxide, hydrofluoric acid and hydrochloric acid over time at different current densities. The intensity of concentration of alkali and acids is determined by the current density and is maximum at the initial moment of time. Over the course of leachate processing time, the concentration rate decreases and then stops changing. The maximum concentration of substances generated in chambers 1 and 3 of the electrolyzer, achieved in the experiments, is determined by the amount of water transported with the corresponding ions through the ion-exchange membranes, and increases with an increase in current density. The values of the maximum concentrations of sodium hydroxide, hydrofluoric and hydrochloric acids are given in Table 4.

Journal of Mining Institute. 2025. Vol. 272. P. 51-58

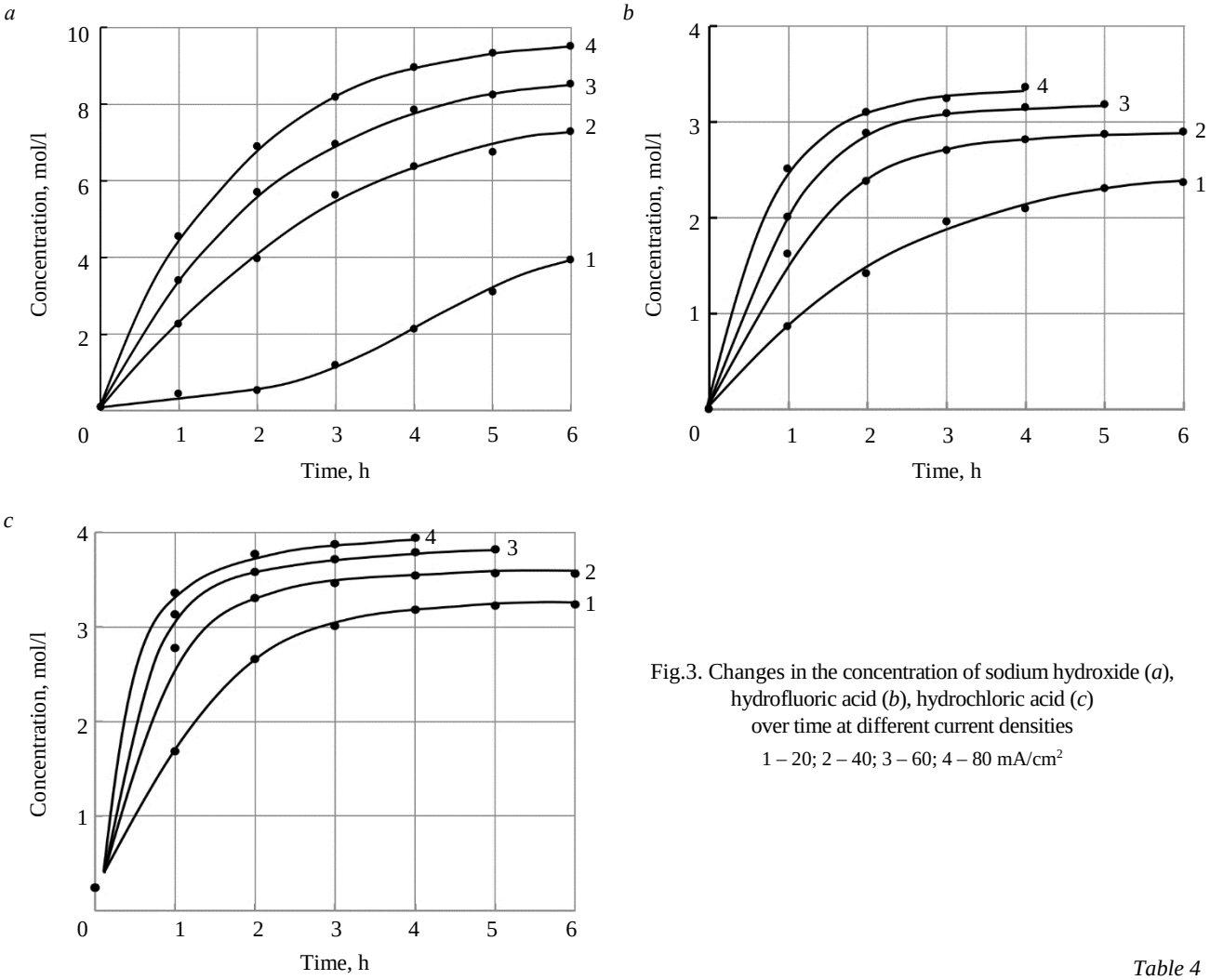

Fig.3. Changes in the concentration of sodium hydroxide (*a*), hydrofluoric acid (*b*), hydrochloric acid (*c*) over time at different current densities
1 – 20; 2 – 40; 3 – 60; 4 – 80 mA/cm^2

Table 4

Maximum NaOH, HF and HCl concentrations achieved

Current density, mA/cm^2	Sodium hydroxide		Hydrofluoric acid		Hydrochloric acid	
	g/l	mol/l	g/l	mol/l	g/l	mol/l
20	15.7	3.94	47.3	2.36	47.4	1.31
40	291.4	7.29	57.7	2.89	52.0	1.42
60	341.1	8.53	63.6	3.18	55.8	1.53
80	380.4	9.51	67.0	3.35	57.6	1.58

The change in the concentration of sodium hydroxide, hydrofluoric acid and hydrochloric acid in the concentration chambers of the electrolyzer is determined by the mobility of sodium, fluorine and chlorine ions that create an electric current, the design parameters of the unit and is described by the equation

$$\frac{dc}{dt} = \left(C_{\text{nas}} - C\right)\frac{jSt}{q}, \tag{1}$$

where C_{nas} is the limit concentration of these compounds; j – current density; S is the area of the ion-exchange membrane; q is a parameter depending on the mobility of ions and technological modes, determined experimentally for each of these compounds.

The solution of equation (1) has the form:

$$C\left(t\right) = C_{\text{nas}}\left(1 - e^{\frac{-jSt}{q}}\right). \tag{2}$$

It follows from the ratio (2) that the change in the concentration of sodium hydroxide, hydrofluoric acid and hydrochloric acid in the concentration chambers of the electrolysis cell occurs according to an exponential law, depending on the parameter q, which coincides with the experimental curves (Fig.3). As follows from the above experimental studies, for sodium hydroxide C_{nas} = 380.4 g/l, $q \approx 4.06 \cdot 10^3$ C; hydrochloric acid C_{nas} = 57.6 g/l, $q \approx 2.84 \cdot 10^3$ C; hydrofluoric acid C_{nas} = 67.0 g/l, $q \approx 2.44 \cdot 10^3$ C.

The above ratios can be used in process design. The results obtained during the study of the process of processing of spent acid etching solution of titanium production, containing titanium, fluorine and chlorine ions, made it possible to propose an approximate technological scheme of processing (Fig.4).

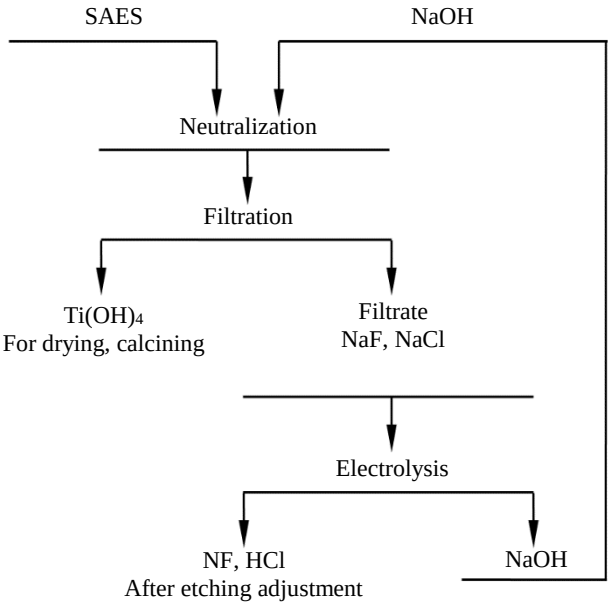

Fig.4. Technological scheme for processing spent acid etching solution

Conclusion

The presented results obtained during the study of the process of SAES processing containing 22 g/l of titanium fluoride, 1.7 g/l of hydrofluoric acid and 6.2 g/l of hydrochloric acid without taking into account impurities in metallic titanium of the VT1-0 grade, allow us to draw the following conclusions.

SAES contains significant amounts of titanium fluoride, hydrofluoric acid and hydrochloric acid. Such a solution has increased toxicity and must be cleaned of impurities before being discharged into a water body. It is possible to process SAES to obtain substances used in production.

Treatment of SAES with sodium hydroxide to the pH of a solution of 7.6 makes it possible to completely recover titanium. After drying and calcining the sludge, titanium oxide can be used in the paint and varnish industry (titanium white). The filtrate after the separation of titanium hydroxide consists of a solution of fluoride and sodium chloride. Processing of this filtrate in a four-chamber electrolyzer with cation exchange and anion exchange membranes makes it possible to obtain solutions of sodium hydroxide and mixtures of hydrofluoric and hydrochloric acids. Sodium hydroxide can be used to treat SAES to extract titanium. A mixture of hydrofluoric and hydrochloric acids, after adjustment, can be used for etching the surface of titanium billets.

REFERENCES

1. Lysenko M.P., Tlekhusezh M.A. Titanium and its application in various industries. *Scientific Review. Pedagogical science.* 2019. N 4. Part 4, p. 64-67 (in Russian).

2. Dyachenko A.N., Dyachenko E.N., Kraidenko R.I. Titanium dioxide: market, production, new technologies. *Russian Coatings Journal.* 2021. N 7-8, p. 41-50 (in Russian).

3. Petrova T.A., Epishina A.D. Anti-corrosion protection of pipelines at mining and processing enterprises. *Obogashchenie rud.* 2023. N 6, p. 52-58 (in Russian). DOI: 10.17580/or.2023.06.09

4. Soldatov V.G., Vavilin Ya.A. The use of titanium for the deoxidation of steel. *Uralskii nauchnyi vestnik.* 2019. Vol. 9. N 2, p. 17-21 (in Russian).

5. Zeynalov E.B., Huseynov E.R., Salmanova N.I., Abdurahmanova N.A. Nano-grade titanium dioxide on the nanocarbon carrier as catalyst in aerobic oxidation of alkyl aromatic hydrocarbons. *Chemical Problems*. 2020. N 3 (18), p. 351-360. DOI: 10.32737/2221-8688-2020-3-351-360

6. Trushin P.V. Application of finely granulated titanium nickelide in surgical practice. *Medical News of North Caucasus.* 2019. Vol. 14. N 3, p. 472-475. DOI: 10.14300/mnnc.2019.14114

7. Marin E., Lanzutti A. Biomedical Applications of Titanium Alloys: A Comprehensive Review. *Materials*. 2024. Vol. 17. Iss. 1. N 114. DOI: 10.3390/ma17010114

8. Lakshmanan V.I., Roy R., Halim M.A. Innovative Process for the Production of Titanium Dioxide. Innovative Process Development in Metallurgical Industry. Cham: Springer, 2016, p. 359-383. DOI: 10.1007/978-3-319-21599-0_18
9. Sadeghi M.H., Esfahany M.N. Development of a Safe and Environmentally Friendly Sulfate Process for the Production of Titanium Oxide. *Industrial and Engineering Chemistry Research*. 2022. Vol. 61. N 4, p. 1786-1796. DOI: 10.1021/acs.iecr.1c03364
10. de Formanoir C., Suard M., Dendievel R. et al. Improving the mechanical efficiency of electron beam melted titanium lattice structures by chemical etching. *Additive Manufacturing*. 2016. Vol. 11, p. 71-76. DOI: 10.1016/j.addma.2016.05.001
11. Liu Z., Tsai I.-L., Thompson G.E. et al. Chemical etching behaviour of titanium in bromine-methanol electrolyte. *Materials Chemistry and Physics*. 2015. Vol. 160, p. 329-336. DOI: 10.1016/j.matchemphys.2015.04.045
12. Marin E., Diamanti M.V., Boffelli M. et al. Effect of etching on the composition and structure of anodic spark deposition films on titanium. *Materials & Design*. 2016. Vol. 108, p. 77-85. DOI: 10.1016/j.matdes.2016.06.088
13. Cheremisina O.V., Sergeev V.V., Fedorov A.T., Alferova D.A. Separation of rare-earth metals and titanium in complex apatite concentrate processing. *Obogashchenie rud.* 2020. N 5, p. 30-34 (in Russian). DOI: 10.17580/or.2020.05.05
14. Denisova O.V., Karapetyan K.G. Carbon materials surface modified with transition metal ions. *Tsvetnye metally*. 2023. N 8, p. 56-61 (in Russian). DOI: 10.17580/tsm.2023.08.10
15. Kovalskaya K.V., Gorlanov E.S. Ligatures Al – Ti – B: Structure Formation in Modified Alloys. *Tsvetnye metally*. 2022. N 7, p. 57-64. DOI: 10.17580/tsm.2022.07.06
16. Tyulagin P.E., Murashova N.M., Morozova Ya.A., Nasakina E.O. Etching of titanium with reverse microemulsions of sodium dodecylsulfate containing inorganic acids. *Uspekhi v khimii i khimicheskoi tekhnologii*. 2021. Vol. 35. N 9 (244), p. 53-55 (in Russian).
17. Spitaels L., Rivière-Lorphèvre É., Díaz M.C. et al. Surface finishing of EBM parts by (electro-) chemical etching. *Procedia CIRP*. 2022. Vol. 108, p. 112-117. DOI: 10.1016/j.procir.2022.03.023
18. Motasim M., Aydoğan S., Agacayak T. et al. The influence of sodium fluoride on the dissolution kinetics of metallic titanium in citric acid solution using the rotating disc method. *Hydrometallurgy*. 2024. Vol. 226. N 106297. DOI: 10.1016/j.hydromet.2024.106297
19. Cheremisina O.V., Ponomareva M.A., Molotilova A.Yu. et al. Sorption purification of acid storage facility water from iron and titanium on organic polymeric materials. *Journal of Mining Institute.* 2023. Vol. 264, p. 971-980. DOI: 10.31897/PMI.2023.28
20. Kolomensky A.B., Shakhov S.V., Kolomensky B.A. Influence of gas-saturated layers and oxide films on the impact toughness of titanium alloys of different strength. *Bulletin of Voronezh State Technical University.* 2017. Vol. 13. N 2, p. 132-139 (in Russian).
21. Shtefan V.V., Smirnova A.Yu. Oxidation of titanium in Zr- and Mo-containing solutions. *Protection of Metals and Physical Chemistry of Surfaces.* 2017. Vol. 53. N 2, p. 322-328. DOI: 10.1134/S2070205117020241
22. Lyubushkin T.G., Nosova T.I., Kuzin E.N. Influence of titanium-containing reagent addition on the coagulation process of galvanic wastewater. *Uspekhi v khimii i khimicheskoi tekhnologii.* 2021. Vol. 35. N 12 (247), p. 108-110 (in Russian).
23. Bhattacharya S., Saha I., Mukhopadhyay A. et al. Role of nanotechnology in water treatment and purification: Potential applications and implications. *International Journal of Chemical Science and Technology*. 2013. Vol. 3. Iss. 3, p. 59-64.
24. Kuzin E.N., Averina Yu.M., Kurbatov A.Yu., Cherednichenko A.G. Increasing the efficiency of wastewater treatment from galvanic production using titanium-containing coagulants and membrane treatment. *Ecology and Industry of Russia.* Vol. 28. N 3, p. 27-31 (in Russian). DOI: 10.18412/1816-0395-2024-3-27-31
25. El Khalloufi M., Drevelle O., Soucy G. Titanium: An Overview of Resources and Production Methods. *Minerals*. 2021. Vol. 11. Iss. 12. N 1425. DOI: 10.3390/min11121425
26. Karshyga Z., Ultarakova A., Lokhova N. et al. Processing of Titanium-Magnesium Production Waste. *Journal of Ecological Engineering*. 2022. Vol. 23. Iss. 7, p 215-225. DOI: 10.12911/22998993/150004
27. Osipenko N.G., Kirjanov S.V., Rzjankin S.A., Teterin V.V. Patent N 2538900 RU. Treatment of effluents of titanium-magnesium production. Publ. 10.01.2015. Bul. N 1 (in Russian).
28. Ismailov T.A., Shangereeva B.A., Shakhmaeva A.R., Kazalieva E. Patent N 2786369 RU. Method for treatment before spraying of titanium-germanium (Ti-Ge). Publ. 20.12.2022. Bul. N 35 (in Russian).
29. Orlov A.P. Patent N 2758704 RU. Method for treatment of thin titanium sheets. Publ. 01.11.2021. Bul. N 31 (in Russian).
30. Ivanova L.S., Makshakov V.V., Zadorozhnyj S.V. Patent N 2522061 RU. Method of producing anodes. Publ. 10.07.2014. Bul. N 19 (in Russian).
31. Bykovskii N.A., Vinokurov E.G., Shulaev N.S. Experimental analysis of efficiency of electrochemical process of processing waste water for production of sodium bicarbonate with production of sodium hydroxide. *ChemChemTech.* 2021. V. 64. N 8, p. 139-145 (in Russian). DOI: 10.6060/ivkkt.20216408.6445
32. Meshalkin V.P., Aristov V.M., Shulaev N.S., Bykovskii N.A. Physicochemical Foundations of an Energy and Resource Efficient Combined Technology for Processing of Soda Ash Production Wastewater. *Doklady Chemistry*. 2020. Vol. 494. Part 1, p. 145-148. DOI: 10.1134/S0012500820090025
33. Bykovskii N.A., Puchkova L.N., Fanakova N.N. et al. Recycling the Wastewater in the Production of Ethylenediamine. *Chemical and Petroleum Engineering*. 2019. Vol. 54. Iss. 11-12, p. 787-794. DOI: 10.1007/s10556-019-00551-7

Authors: **Nikolai A. Bykovskii,** *Candidate of Engineering Sciences, Associate Professor, nbikovsky@list.ru, https://orcid.org/0000-0001-9692-7203* (*Institute of Chemical Technologies and Engineering – Branch of the Ufa State Petroleum Technological University, Sterlitamak, Republic of Bashkortostan, Russia*), **Evgenii A. Kantor,** *Doctor of Chemical Sciences, Professor, https://orcid.org/0000-0002-9629-3324* (*Ufa State Petroleum Technological University, Ufa, Republic of Bashkortostan, Russia*), **Nikolai S. Shulaev,** *Doctor of Engineering Sciences, Professor, https://orcid.org/0000-0002-3595-6948* (*Institute of Chemical Technologies and Engineering – Branch of the Ufa State Petroleum Technological University, Sterlitamak, Republic of Bashkortostan, Russia*), **Vadim S. Fanakov,** *Assistant, https://orcid.org/0009-0007-4583-4593* (*Ufa State Petroleum Technological University, Ufa, Republic of Bashkortostan, Russia*).

The authors declare no conflict of interests.

ISSN 2411-3336; e-ISSN 2541-9404

JOURNAL OF MINING INSTITUTE

Zapiski Gornogo instituta

Journal homepage: pmi.spmi.ru

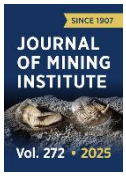

Research article *Geotechnical Engineering and Engineering Geology*

Mercury contamination of sediments at Indonesia Ciujung watershed: contribution of artisanal small-scale gold mining

Willy C. Nugraha[1,2], Huiho Jeong[2], Phan Dinh Quang[2,3], Randy Novirsa[2,4], Tomohiro Komorita[2], Yasuhiro Ishibashi[2], Jun Kobayashi[2], Koji Arizono[2], Asep Bayu Dani Nandiyanto[5]✉

[1] *Research Center for Environmental and Clean Production, National Research and Innovation Agency, South Tangerang, Indonesia*
[2] *Prefectural University of Kumamoto, Kumamoto, Japan*
[3] *Vietnam National Institute of Occupational Safety and Health, Hanoi, Vietnam*
[4] *University of Andalas, West Sumatra, Indonesia*
[5] *Universitas Pendidikan Indonesia, Bandung, Indonesia*

***How to cite this article*:** Willy C. Nugraha, Huiho Jeong, Phan Dinh Quang, Randy Novirsa, Tomohiro Komorita, Yasuhiro Ishibashi, Jun Kobayashi, Koji Arizono, Asep Bayu Dani Nandiyanto. Mercury contamination of sediments at Indonesia Ciujung watershed: contribution of artisanal small-scale gold mining. Journal of Mining Institute. 2025. Vol. 272. N 16339, p. 59-71.

Abstract

Artisanal small-scale gold mining is the largest artificial source of mercury pollution and has been a very common problem recently. This study examined the contribution of Hg release due to artisanal small-scale gold mining in contaminating the sediment of the watershed in Indonesia. Different from other methods, we measured Hg pollution using the stable isotopes of carbon and nitrogen. This report is the first time analytical reports in Indonesia since most papers focus primarily on only detecting heavy metals in river water and sediments, neglecting deep research on Hg pollution and resources. The findings of this study indicate that artisanal and small-scale gold mining activities, located in the upstream areas of the tributaries that act as point sources, are the primary source of mercury in the sediment of the Ciujung watershed. The isotopes $\delta^{13}C$ and $\delta^{15}N$ successfully trace the Hg-contaminated sediment in the Ciujung watershed derived from the Cisimeut and Ciberang Rivers based on soil organic matter. The biological effect showed the Hg concentration in most of the sampling sites exceeded the effects-range medium and probable effect limit values. The risk quotient values of Hg indicated the Hg pollution had a possibility effect on the benthic organism. Several limitations have also been added in this study and needs for further investigation.

Keywords

artisanal small-scale gold mining; mercury; sediment; Ciujung

Funding

This study was funded by an international postgraduate scholarship for research on mercury from the Kumamoto Prefectural Government, Japan.

Received: 02.11.2023 ***Accepted: 24.09.2024*** ***Online: 11.02.2025*** ***Published: 25.04.2025***

Introduction

Metal contamination in the Ciujung watershed has recently received increasing attention due to urbanization and industrialization [1, 2]. The Ciujung watershed, the longest river in Banten Province, Indonesia, is used for sanitation and irrigation activities. It has a catchment area of 1,858 km^2 and flows from the south to the north with a total length of 179 km (based on Environmental and forestry agency of Banten Province in the Final Report of Environmental Protection and Management Plan. Banten, Indonesia, 2019).

In recent decades, the rapid development of industrialization has caused the Ciujung watershed to receive different pollutant sources discharged through two tributaries: Cisimeut and Ciberang River [3]. A published report by the Indonesian Center for Environmental Law in 2013 (Final Report: Strengthening the Right to Information for People and Environment. 2013, p. 1-57) estimated that the overall input

of industrial wastewater discharged into the Ciujung watershed reached 43,044.35 m^3/day from a significant number of industries disposing of, for instance, pulp and paper, fertilizer, coal combustion, electroplating, chemical industry as well as domestic waste. The untreated wastewater discharge flown directly into the river causes the degradation quality of the Ciujung watershed leading heavy metal concentrations in surface water and sediment to exceed the acceptable limit as prescribed in environmental standards or regulations. Therefore, the demurrage and instability among residents to local governments keep rising every year.

Most studies done in the Ciujung watershed have dwelt on heavy metals contamination, however, there is still no available information regarding Hg contamination in the Ciujung watershed sediment. One of the biggest artisanal small-scale gold mining (ASGM) hotspots in Indonesia is found in Cisitu village, Lebak District, Banten Province and these activities are unregistered and have informal operations located upstream of the Ciujung tributaries [4]. Blacksmith Institute in 2013 reported* that 1,000 t of mercury was still used in ASGM where 95 % of all Hg used illegally in the amalgamation process is released into the environment, and it was estimated to affect 300,000-500,000 people. This attracted many researchers to investigate the effect of ASGM activities in this area. Several studies have been conducted in Cisitu village, reporting that Hg concentration from the collected soil, sediment, human hair, blood also fish nearby ASGM activities exceeded the acceptable limit value [3, 5-7]. Worst of all, some studies reported that the fish collected in Cisitu pond were found to be high in Hg concentration. Other reports [8] reported that 70-90 % of the organic Hg that exists in fish and shellfish is methylmercury (CH_3Hg^+) which is the most toxic form of Hg [9]. It was revealed that ASGM activities were the point source of Hg contamination in these matrices.

Hg contamination from ASGM is likely to be highly heterogeneous [10]. Mercury can be deposited in specific hotspots where mining activities are concentrated, and its distribution can vary significantly over short distances due to differences in mining intensity, local hydrology, and sediment transport [11]. Understanding how Hg is transported within the river systems and the mainstream (e.g., through sediments, water column, biota) necessitates a denser network of sampling points to map out these pathways accurately. We can infer that Hg released into the river flows through settling, dissolving in the water, and getting deposited in sediments can pose long-term environmental and health risks in downstream areas. Therefore, monitoring of the Ciujung watershed is essential to be conducted.

Sediments can vary widely in their geochemical properties, such as organic content, particle size distribution, pH, and mineralogy, all of which affect Hg mobility and bioavailability [12]. In this study, sedimentary organic matter and isotope ($\delta^{13}C$ and $\delta^{15}N$) are used as an environmental pollutant tracer to identify the Hg source in downstream sediment. The Hg has a strong correlation with organic matter (OM) which affects the partitioning of mercury to suspended solids in the water column and the sequestration of mercury to sediments [12]. Therefore, the mercury source can be represented based on sedimentary organic matter. Stable isotopes ($\delta^{13}C$ and $\delta^{15}N$) in OM in lake sediments are frequently used to trace organic matter sources due to the isotopic composition of sedimentary organic matter being relatively unaffected by post-photosynthetic, or diagenetic processes [13]. By using the isotope mixing model, we can determine the source of Hg in a certain mixture.

We conducted a field survey in the wet season to trace and quantify the sedimentary OM composition and total mercury (THg) contamination due to ASGM in the Ciujung watershed in Indonesia. The investigation of this issue was conducted in the wet season because, during the wet season, heavy rainfall causes an increase in the water level of rivers (flood), soil run-off, and also flash out sediment, which can lead to increased sediment transport from upstream to downstream area of the Ciujung watershed. Moreover, biological effects and ecological risk assessment of Hg to the benthic organism in the sediment of the Ciujung watershed were evaluated based on sediment quality guideline values

* Mitigating Mercury Emission from Artisanal and Small Scale Gold Mining in Indonesia. Program Report. 2013, p. 39. URL: https://wedocs.unep.org/bitstream/handle/20.500.11822/31242/MercE.pdf?sequence=1 (accessed 02.11.2023).

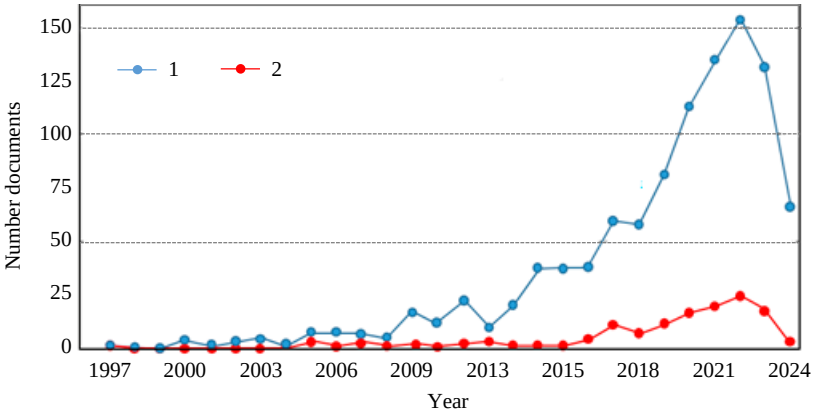

Fig.1. Bibliometric analysis for research trend using keyword "artisanal small-scale gold mining" (1) and "artisanal small-scale gold mining Indonesia" (2) [14]. Data was taken on 25 June 2024

(SQGV). This study was the first to examine the sediment associated with Hg pollution in the Ciujung watershed. This is the first time analytical reports in Indonesia since most papers focus primarily on only detecting heavy metals in river water and sediments, neglecting deep research on Hg. It is also confirmed by the bibliometric analysis based on Scopus database that only 136 documents until now for articles relating to ASGM in Indonesia (Fig.1), which is less number compared to general ASGM publication (reaching 1,024 documents). This makes the scientific publication relating ASGM in Indonesia needed to be reported.

This insists our novelties in this paper, including:

• evaluating Hg in two rivers in West Java Indonesia, namely Cisimeut and Ciberang Rivers and their tributaries, which are one of the important rivers in Indonesia;

• understanding the detection of Hg in sediment level that is possible from ASGM activities;

• evaluating sedimentary organic matter in the level of sediment, which were examined based on OM in soil organic matter (SOM);

• using stable isotopes of $\delta^{13}C$ and $\delta^{15}N$ to trace the source of Hg;

• evaluating Hg-contaminated sediment by the risk quotient;

• analyzing and understanding potential effects of Hg in rivers on benthic organisms (biological effects).

Methods

Study Area. The research was conducted in the Ciujung watershed, Banten Province, Indonesia. The sampling area was distributed in latitude 6°1'28.423"E to 6°34' 3.031"E and longitude 106°10' 9.354"S to 106° 9'53.67"S. We also showed the magnification from the map in Fig.2, *a*, which is

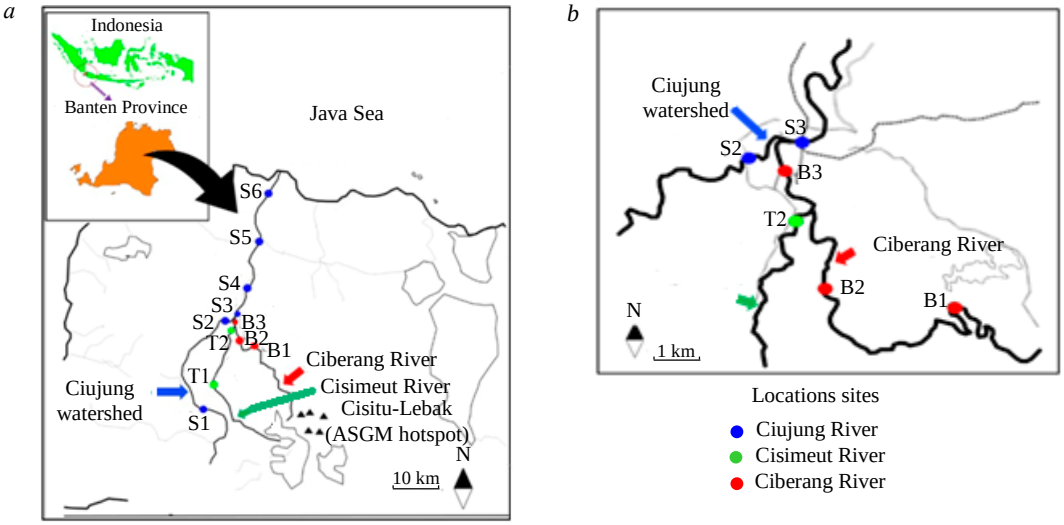

Fig.2. The location of surface sediment sampling (*a*) and detailed sediment sites (*b*) according to [15]

presented in Fig.2, *b*. In 2019, the Agency of Environment and Forestry, Banten Province, reported that the Ciujung watershed has two large tributaries: the Cisimeut River (458 km^2) and the Ciberang River (305 km^2). The water from these two rivers is used, specifically by the population for sanitation, daily activities, and agriculture. Thus, the research direction can have a wider impact on the importance of this study.

In the south of Rangkasbitung City, which is the capital city of Banten Province, these tributaries unite and flow to the North into the Java Sea. Interestingly, the upstream tributaries also come from the Karang and Halimun mountains [3] where the inhabitants of the upstream areas of the Ciujung watershed are mainly employed as farmers and gold miners, particularly in the Lebak District [3, 16]. Residents used the amalgamation processes in the forest, water river, and also their yard.

Sampling. In January 2021 (wet season) the sediment samples (0-10 cm) were collected from 11 sampling stations in the Ciujung watershed including two large tributaries: the Cisimeut and the Ciberang River (Fig.2, *a*). Six sites were distributed in the mainstream from the upstream (S1), middle stream (S2 and S3), and downstream (S4, S5, and S6). Two locations along the Cisimeut River: T1 and T2 and from three locations in the Ciberang River: B1, B2, and B3 (Fig.2, *b*). The sediment was collected one day after the big flood occurred in the Ciujung watershed which might lead to variations in the Hg content in the sediment [17].

The sediments were collected using a grab sampler and three times, were homogenized, and then stored in a cool box. They were then transported immediately to the laboratory before the analyses. Subsequently, the material was sieved through a 150 μm-sized sieve [18] and dried at 20 °C at room temperature. The dried samples were measured using a direct mercury analyzer.

Surface water was collected in each site using a point sampler horizontal based on Indonesian National Standard (SNI 6995:2021) method for water and wastewater, then surface waters were filtered with 0.45 μm of pore size and collected in polypropylene bottle, then acidified by using nitric acid until pH < 2. All bottles were transported to the laboratory in an ice-cooled container and stored in the refrigerator (4 °C) until analysis. THg concentration in the surface water sample was measured using Cold Vapour – Direct Mercury Analyzer.

Chemical and Sample Digestion. A high-purity Hg standard solution (1000 mg/l) was used for the calibration (Merck, Germany and Wako, Japan). The mercury concentration in the sediment was determined through the EPA method 7473, using thermal combustion with amalgamation atomic absorption spectrometry (Direct Mercury Analyzer 3,000 NIC, Japan). For determining the characteristics of the sediment, the total organic carbon (TOC) and total nitrogen (TN) were analyzed using an elemental analyzer (Thermo Fisher Scientific, ConFloIV).

The particulate organic phosphorous (POP) was determined by subtracting the sum of the inorganic phosphorus fractions from the total amount of phosphorus in the sediment after performing the ignition method [19]. Bulk surface sediment samples were collected for isotopic analysis (δ^{13}C and δ^{15}N). The sediment sample was acidified for 24 h in a bath containing 1N HCl solution to remove carbonates from the sediment matrix. The samples were washed with ultrapure water and oven-dried overnight at < 80 °C. The dry sediment sample was then ground to a fine powder using a mortar and pestle.

Isotopic analysis was performed using an elemental analyzer coupled online with an isotope ratio mass spectrometer using air nitrogen and Pee Dee Belemnite standards for N and C, respectively (Thermo Fisher Scientific: Flash 1112 Series, ConFloIV, DELTA Plus). The δ^{13}C and δ^{15}N values were compared with the Vienna Pee Dee Belemnite and air nitrogen standards, respectively [20]. The C:N, N:P, and C:P ratios were calculated by their respective molecular weights (‰),

$$\delta^{15}\mathrm{N} = \left\{\left(\frac{R_{\text{sample}}}{R_{\text{standard}}}\right) - 1\right\} \cdot 1000;$$

$$\delta^{13}\mathrm{C} = \left\{\left(\frac{R_{\text{sample}}}{R_{\text{standard}}}\right) - 1\right\} \cdot 1000,$$

where R corresponded to the ^{13}C/^{12}C or ^{15}N/^{14}N ratios.

Quality control and quality assurance. Certified reference material (CRM) marine sediment NMIJ 7302-a (Japan) was used for internal quality control to assess the validity of the data, and the number of replicates of CRM and samples were examined in duplo and triplicates. According to the analytical parameters, the accuracy of the method was 101.28 %, repeatability was 3.68 % of RSD, and the limit of detection (3SD of blank) was 20 ng/kg. This shows that the method was efficacious in determining the Hg content in the sediment.

Mixing model of isotope. All analyses were performed using freeware R version 4.0.2. The proportional contribution of each end-member (i.e., SOM of each tributary) to the surface sediment of each station was estimated using Bayesian mixing models according to the Markov chain Monte Carlo method [21]. The analyses were performed using the R package "simmr", which is the upgraded version of the "siar" and a prior distribution for this analysis is the Dirichlet, a generalization of the Beta distribution [22]. The trophic enrichment factor was set to zero concerning the non-trophic relationship among them. Four Markov chains with lengths of 10,000,000 were run, and the first 100,000 samples were discarded during burn-in. The thinning was adjusted to 100 depending on the convergence of the chains. The obtained Gelman – Rubin diagnostic statistics were close to 1 for all the estimated parameters, which satisfied the rules of thumb for the convergence assessment (less than 1.1) [23].

Biological Effects. According to Australian and New Zealand Environment and Conservation Council (ANZECC) guidelines, there are two recommended SQGV points, namely effective range low/median (ERL/ERM) trigger values representing the threshold value to trigger an adverse effect and threshold/probable effect level (TEL/PEL) value representing the high probability effect to evaluate the biological effect.

To evaluate the risk level of Hg in sediment, we used index RQ which is the most feasible method for risk assessment of pollutants in the environment [24, 25]:

$$\mathrm{RQ} = \frac{\mathrm{MEC}}{\mathrm{SQC}},$$

where MEC is the measured concentration for a single chemical measured at a sample, μg/kg; SQC is the sediment quality criterion, ng/g.

The sediment quality criterion of mercury

$$\mathrm{SQC} = \mathrm{K_p} \cdot \mathrm{WQC}, \quad (1)$$

where K_p is the partition coefficient of Hg between solid phase and interstitial water, l/kg.

The partition coefficient of Hg was calculated using equation

$$\mathrm{K_p} = \mathrm{S_s(Hg)}/\mathrm{S_w(Hg)},$$

where S_s (Hg) – Hg in sediment sample of each site, μg/kg; S_w (Hg) – Hg in water sample of each site, μg/kg.

In this study, the dissolved Hg concentrations ranged from n.d. (not detection) to 46 ng/l with an average of 14.2 ng/l. The partitioning coefficients (log K_p) of Hg between particulate matter and water in the Ciujung watershed were obtained at 0-5.21 with an average of 4.28. The average K_p derived in this study was calculated at 19,054 l/kg, and WQC is the water quality criterion (ng/l). The WQC was derived from tissue-based criterion (TBC) and bioaccumulation factor (BAF) using equation

$$\mathrm{WQC} = \frac{\mathrm{TBC}}{\mathrm{BAF}}. \quad (2)$$

The TBC is the tissue-based criterion derived by the species-sensitive distribution method. In this study, the TBC (HC5) value was 0.062 mg/kg based on data reported by [25]. BAF value was 3,023.00 l/kg based on data reported by previous reports [4]. Then using equation (2). The WQC of

Hg in the Ciujung watershed is 20.5 ng/l. Based on the average value of K_p (19,054 l/kg), the SQC of Hg was calculated to be 390.80 ng/g using equation (1). To evaluate the ecological risk of mercury: if RQ > 1, the risk posed by Hg is high; if 0.1 < RQ < 1.0, the ecological risk is moderate, and if RQ ≤ 0.1, the ecological risk is low [25].

Results and discussion

Hg distribution in the sampling sites. Table 1 lists the THg concentration in the mainstream of the Ciujung watershed ranging from 0.02 to 0.91 mg/kg of dry weight with average values of 0.59±0.32 mg/kg. Detailed analysis in Table 1 is shown in Fig.3. In the middle stream areas (S2 and S3), the THg concentration was relatively high, particularly in S3, it can be caused by confluence between tributaries (the Cisimeut (T1 and T2), the Ciberang River (B1-B3)) and mainstream (S1-S6) of the Ciujung watershed where the concentrations of Hg transported by these tributaries were extremely high ranging between (0.42-0.83 mg/kg). It showed that these high levels of Hg-contaminated sediments might have been caused by illegal small-scale gold mining activities that operated in the upstream areas of these tributaries as shown in Fig.2, *a*. To prove this, we examined the soil paddy field located within 500 m near the ASGM hotspot in Cisitu, Lebak District which acts as an Hg source in upstream of these tributaries. Based on research reported by other reports [6], the water used for the irrigation system is derived from Hg-contaminated water from the amalgamation process. The Hg concentration in the soil paddy field (n = 3) was obtained at 45.86±2.37 mg/kg of dry weight. The Hg concentration in soil paddy field was above than permissible level by the World Health Organization (Hg in soil for agriculture is 0.05 mg/kg) [26].

Table 1

Sediment characteristics and THg (dry weight) concentration in mainstream and its tributaries of the Ciujung River

Location sites	TOC*, μmol/g	TN*, μmol/g	POP*, μmol/g	C/N	N/POP	C/POP	$\delta^{13}C^*$, ‰	$\delta^{15}N^*$, ‰	THg**, mg/kg
Mainstream									
S1	174±30	20±2	1.0±0.9	8.8	18.2	138	–25.1	1.4	0.02±0.01
S2	800±33	81±3	3±1	9.9	27.3	232	–26.0	2.9	0.62±0.04
S3	1,174±110	110±2	6±2	10.7	18.5	170	–25.9	3.1	0.65±0.05
S4	958±370	94±37	6.0±0.8	10.2	15.3	134	–25.8	2.5	0.91±0.04
S5	707±190	74±8	5.0±7	9.7	13.8	114	–25.7	2.6	0.86±0.06
S6	357±150	38±12	4.0±0,1	9.3	9.8	78.8	–25.5	2.7	0.46±0.04
Min	174	20.0	1.0	8.8	9.8	78.8	–26.0	1.4	0.02
Max	1,174	110.0	6.0	10.7	27.3	232.0	–25.1	3.1	0.91
Mean	695.0	69.5	4.2	9.8	17.1	144.5	–25.7	2.6	0.59
SD	372.9	34.2	1.9	0.7	5.9	52.4	0.3	0.6	0.32
Cisimeut River									
T1	192±10	16±1	3±0.1	11.6	5.9	58	–26.2	2.0	0.62±0.04
T2	405±30	45±5	3±0.2	9.1	14.6	113	–25.3	3.2	0.52±0.04
Min	192	16	3	9.1	5.9	58	–26.2	2.0	0.52
Max	405	45	3	11.6	14.6	113	–25.3	3.2	0.62
Mean	298.5	30.5	3.0	10.4	10.2	85.5	–25.7	2.6	0.57
Ciberang River									
B1	320±30	33±4	4±0.1	9.8	7.8	65.4	–25.7	3.5	0.77±0.04
B2	397±63	44±3	4±0.8	9.1	12.0	94.3	–25.2	3.1	0.83±0.09
B3	281±21	28±1	3±0.8	10.0	10.4	89.3	–26.1	2.4	0.42±0.05
Min	281	28	3.0	9.1	7.8	65.4	–26.1	2.4	0.42
Max	397	44	4.0	10.0	12.0	94.3	–25.2	3.5	0.83
Mean	332.7	35.0	3.7	9.6	10.1	83.0	–25.7	2.0	0.67
SD	59.0	8.2	0.6	0.5	2.1	15.5	0.5	0.5	0.22

* Number of samples (n = 3); ** (n = 2).

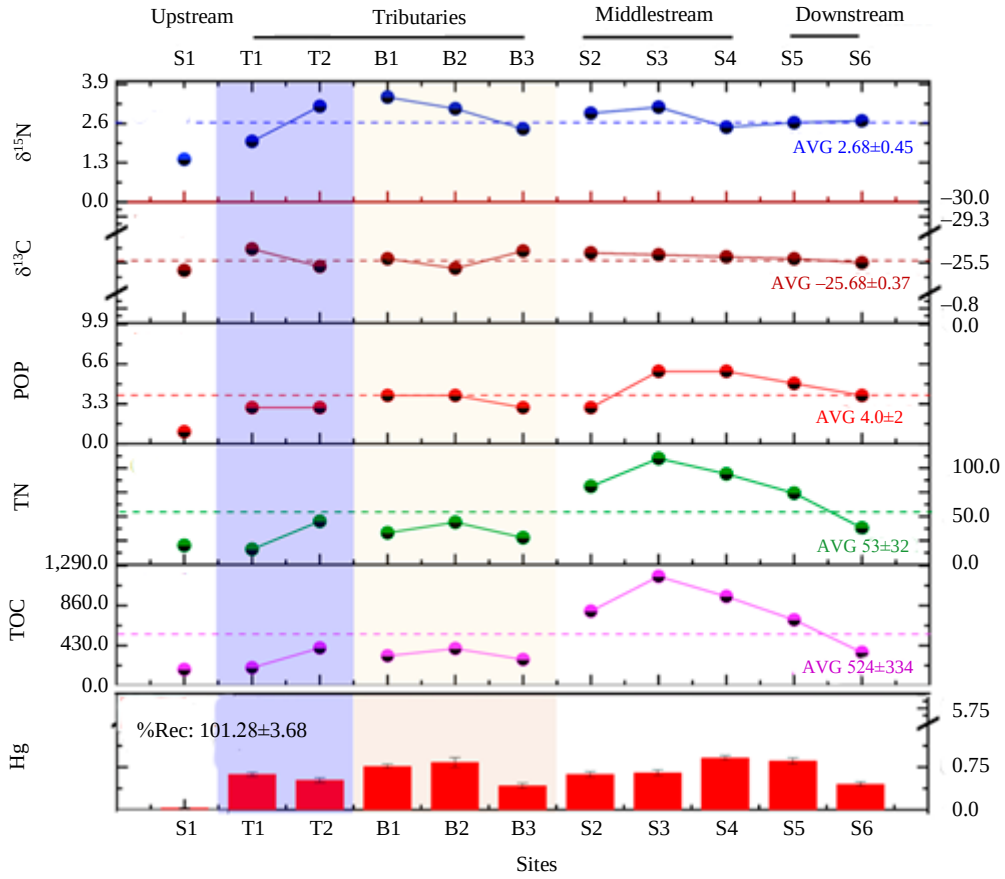

Fig.3. The distribution pattern of the $\delta^{13}C$ and $\delta^{15}N$ values (‰), organic matter, and THg concentration (μmol·g^{-1}) from each stream of rivers

When the Hg is discharged into the soil paddy field, it can be strongly bonded with the SOM. The soil will be transported into the river and accumulated in the sediment due to soil run-off during the wet season. Moreover, the highest Hg concentration occurred at S4 (0.91 mg/kg) followed by S5 (0.84 mg/kg) which is located downstream of the Ciujung watershed. The high Hg concentration at S4 and S5 might be due to these sites being the deepest sites in the Ciujung watershed with total depths of 6.72 and 4.22 m, respectively causing deposition of more suspended particles at these sites when the low flow rate occurs.

The accumulation of Hg in mainstream and tributaries was a serious problem where the THg concentrations in the mainstream and tributaries sediment of the Ciujung watershed were above the permissible limit set (0.15 mg/kg) by the Australian and New Zealand Environment and Conservation Council Interim Sediment Quality Guidelines (ANZECC ISQG) and Hongkong Interim Sediment Quality Guidelines (Hongkong ISQG) except in the S1 (upstream) [27]. Values of sediment quality indicators: the threshold values to trigger and adverse effect (ERL – 0.15; ERM – 0.7 mg/kg), evaluation the biological effect (TEL – 0.13; PEL – 0.7 mg/kg). The information of sediment quality from Indonesia government is still not available. Therefore, the sediment in the mainstream and tributaries had a high potential ecological risk due to Hg contamination, particularly for aquatic organisms.

Worldwide comparison of mean Hg. Among the Indonesia River, data from the Ciujung watershed are very limited. Results of other rivers from previous published are presented for comparison. Table 2 presents a comparison of the THg concentrations obtained in the study with the results of studies from other countries [28-31]. The THg concentrations in the Ciujung watershed were higher than those in the unpolluted areas, such as the Yangsuri lacustrine wetland, Korea; they were roughly comparable to the concentrations in Jiaozhou Bay, China, but were lower than those in other polluted areas, including Minamata Bay, Japan, and the Hunza River, Pakistan. The THg in the sediment of the Ciujung watershed and its tributaries indicated that they were moderately polluted by Hg.

Table 2

Comparison of THg in surface sediment in different basins/countries

Basin	Source of Hg	THg in surface sediment, mg/kg	Reference
Yangsuri Lacustrine wetland, Korea	Wetland	0.001-0.086	[28, 30]
Minamata Bay, Japan	Industrial activities	0.1-3.34	[29, 31]
Jiazhou Bay, China	Industrial activities	0.12-0.58	[30, 32]
Hunza River, Pakistan	ASGM	0.22-6.40	[31, 33]
Ciujung watershed, Indonesia	ASGM	0.02-0.91	This study

Characteristics of OM (TOC, TN, and POP) in sediment. TOC, TN, and POP concentrations are essential parameters for describing and determining the abundance of OM in sediments [32]. The distribution of TOC, TN, and POP in the Ciujung watershed sediments (S1-S6) was found to be similar. They were found to increase from upstream to the middle stream areas but decrease in the downstream areas (see Fig.3). The TOC, TN and POP concentrations in the mainstream were found in S3 (TOC – 1,174; TN – 110; POP – 6 μmol/g) followed by S4 (TOC – 958; TN – 94; POP – 6 μmol/g), and S5 (TOC – 707; TN – 74; POP – 5 μmol/g) and the mean concentration of TOC, TN and POP was 695, 69.5 and 4.17 μmol/g, respectively.

The TOC, TN, and POP were found to be highly concentrated in S3, it might be caused by high terrestrial input of OM, and, it might also impact the composition of OM in the sediment during heavy rain [33]. Meanwhile, the mean concentration of TOC, TN, and POP generated was 298.5, 30.50, and 3.00 μmol/g, respectively, in the Cisimeut River and 332.67, 35.00, and 3.67 μmol/g, respectively, in the Ciberang River. The varying concentrations of TOC, TN, and POP in these tributaries indicate the variation in the origin of these compound accumulations in the rivers. Other reports [34] reported similar research to our study that the concentrations of TOC, TN, and POP in the sediment of the Mianjiang River sub-watershed were significantly different.

Correlation between Hg, TOC, TN, and POP and their molar ratio. Pearson's correlation analysis was performed on the concentration data about the following: Hg, carbon, nitrogen, and phosphorus as well as for their molar ratios and isotopes, and the results have been presented in Table 3. The amount of TOC concentration was positively correlated with TN, POP, C/N, N/POP, C/POP, $\delta^{15}N$, and Hg content. A strong correlation existed between the amount of TOC and TN in the sediments of the Ciujung watershed and its tributaries ($r = 1.00$; $P < 0.01$), which suggests that a major part of TN was associated with TOC that can be considered as organic nitrogen [35]. Moreover, a strong correlation existed between the TOC and POP ($r = 0.78$; $P < 0.05$).

Table 3

Pearson's correlation matrix of Hg, $\delta^{15}N$, $\delta^{13}C$, TOC, TN, and POP and their molar ratio from the Ciujung watershed and its tributaries

Items	TOC	TN	POP	C/N	N/POP	C/POP	$\delta^{13}C$	$\delta^{15}N$
TOC								
TN	1.0**							
POP	0.78**	0.77**						
C/N	0.27	0.20	0.35					
N/POP	0.57	0.60	–0.04	–0.21				
C/POP	0.66*	0.68*	0.07	–0.06	0.99**			
$\delta^{13}C$	–0.28	–0.22	–0.29	–0.87	0.06	–0.08		
$\delta^{15}N$	0.37	0.40	0.51	–0.05	0.03	0.06	–0.03	
Hg	0.51	0.52	0.79**	0.33	–0.14	–0.06	–0.30	0.61

*$p < 0.05$; **$p < 0.01$.

The results suggested that the type of OM should be similar at all sites. Therefore, we can assume that the Hg accumulation in the sediment can be represented by OM. The findings of this study are consistent with the findings reported in the previous research conducted by other reports [36] that found that the Hg concentrations correlated significantly with the TOC contents in Bohay Bay, Northern China, and Tianjin's Haihe River caused by the thermally labile fraction of OM released during pyrolysis at 300 °C. It revealed that the strong correlations between the TOC, TN, POP, and Hg concentrations indicate the strong correlation between OM and Hg adsorption onto the sediment. The meaning of this result is Hg released from amalgamation processes is strongly bonded in the organic matter of sediment.

Identification of the type of OM. OM in the sediments in the mainstream and tributaries was analyzed to investigate the source of Hg in the mainstream of the Ciujung watershed (see Table 1). The molar ratio and stable isotope ratio of both organic C and N were used to determine the origin and transformation of OM affected by the anthropogenic impacts on local and regional ecosystems [32]. An analysis of the C/N ratio together with $\delta^{13}C$ and $\delta^{15}N$ can provide information on the OM sources and identify the type of OM). The narrow range (from −26.2 to −25.1 ‰) of δ13C in the sediment collected from the Ciujung watershed and its tributaries was attributed to the prevalence of higher hydrodynamic energy conditions in this watershed [36].

This study was conducted during the rainy season; therefore, the flow rate of the river was high, and the spatial distribution of sedimentary OM was expected to be strongly affected by river flow. Therefore, we assumed that during the wet season, the SOM in upstream of these tributaries can be transported in the mainstream of the Ciujung watershed. To identify the type of OM, we evaluated it according to $\delta^{13}C$ and $\delta^{15}N$ (Fig.4, *a*).

The results failed to distinguish between the types of OM based on some values derived from phytoplankton and OM in the soil. However, as predicted by the C/N ratio and $\delta^{13}C$ values, the mean $\delta^{13}C$ values indicated that the OM derived from the soil was abundant, which agrees with the soil organic properties of OM (Fig.4, *b*) [37]. This revealed that OM in the sediment of the Ciujung watershed and its tributaries was not generated by the phytoplankton and this result is consistent with that reported by other reports [38].

Mixing model of stable isotopes. A Bayesian mixing model was used to estimate the proportional contribution of each OM to the sediment at each site using the stable isotope and the three sources: S1 as uncontaminated upstream of the mainstream, T1 as a contaminated tributary (the Cisimeut River), and B1 + B2 as a contaminated tributary (the Ciberang River). In this case of B1 + B2 as points of sources, it can be caused because these areas have similar isotopic and geological characteristics. Therefore, we assume that these sites are treated as one group.

In this study, the proportion of the contribution of n + 1 different sources could be determined by different isotopic tracers. Based on the conservation of mass of the stable isotope. Based on the biplot of $\delta^{15}N$ and $\delta^{13}C$ (Fig.5), OM, which accumulates sediment downstream of the Ciujung watershed (mixtures S4, S5, and S6), had similar characteristics to the OM obtained from the mixtures T2 and B3; these sites were relatively close to the source (T1 and B1 + B2). In the case of S3 and B2 which are out of the triangle, we used the "siar" package based on a Monte Carlo simulation of mixing polygons to apply the point-in-polygon assumption to these models [22].

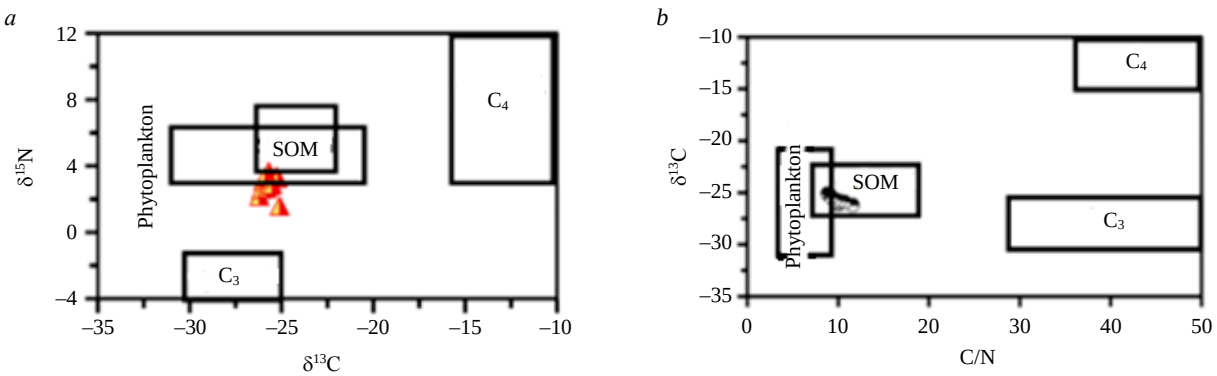

Fig.4. Plot of $\delta^{13}C$ vs $\delta^{15}N$ (*a*) and plot of C/N radio vs $\delta^{13}C$ (*b*)

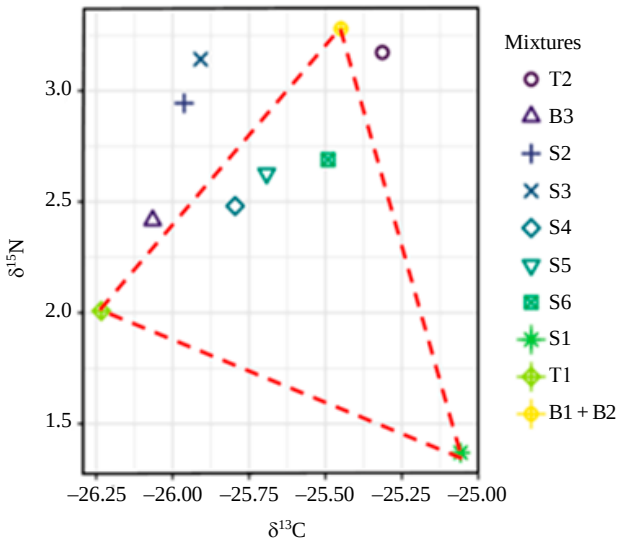

Fig.5. Mixing model of isotope using Bayesian mixing model

The mixing polygons (i.e., mixing model) were iterated using the distributions of the proposed OM sources, and the proportion of sources that have a solution was calculated. This proportion could be interpreted as the frequentist probability that the proposed mixing model could calculate source contributions to explain isotopic signatures. Since this analysis does not calculate a linear solution, we could obtain the contribution of the outside of the polygon.

The contribution of soil OM represented by (mean±SD) from the Cisimeut River (T1) was found in most of the downstream sediment in S3-S6, in which the highest was S4 (60.79±0.05 %), followed by S5 (49.32±0.07 %), S3 (39.00±0.0 %), and S6 (23.83±0.09 %). The OM from the Ciberang River contributed to the downstream sediment in S3-S6, with the highest contribution in S6 (47.51±0.01 %), S5 (36.29±0.01 %), and S4 (26.00±0.01 %). It was revealed that the soil OM from the Ciujung and Ciberang Rivers, which contained Hg, contributed to the accumulation of Hg in the sediment in the downstream area of the Ciujung watershed caused by a strong formation and complexation ionic bonds between mercury and SOM affected the sequestration of mercury to sediment [39]. Therefore, it can be assumed that the sediment organic matter in the downstream is predominantly derived from these tributaries.

Biological effect. Hg-contaminated sediment affects benthic organisms. Therefore, assessment of ecotoxicology of the Hg concentration in sediment was used effect range low (ERL)/effect range median (ERM) and threshold effect level (TEL)/threshold probable effect level (PEL). Due to the ERL and TEL values being less than expected to have adverse effects on sediment-dwelling organisms, we evaluated the biological effect using the ERM and PEL values indicating the chemical concentration above which adverse effects are likely to occur in the aquatic ecosystem [40]. These values provide a reliable tool to evaluate the quality of sediment and adverse biological effects on estuarine sediment [41].

As shown in Table 1, except for in S1, Hg concentrations in all sampling sites exceeded the TEL and ERL values. Based on PEL and ERM values, several sampling sites showed that extremely high concentrations of Hg exceeding the PEL and ERM values were found in downstream S4 and S5, and also in tributaries B1 and B2. Therefore, these sites can be categorized as potential toxicity to the benthic organisms. The impact of contaminated sediment on aquatic ecosystems is likely to be due to remobilization and re-suspension processes [40].

The data of Hg toxicity including abnormal and deformed aquatic organism-based tissue according to NOEC (no observed effects concentration) and LOEC (lowest observed effect concentration) values was reported by previous reports [25] for several benthic organisms, for instance, mollusks, crustaceans, aquatic insects, and fish. The deformed of growth in aquatic organism was found in mollusks (*Pyganodon grandis*, Hg = 0.686 mg/kg) and fish (*Perca flavescens*, Hg = 0.125 mg/kg; *Sandae vitreus*, Hg = 0.25 mg/kg); the abnormality of the cellular system was found in fish (*Liza aurata*, Hg = 0.1 mg/kg; *Bileophtalmus dussumieri*, Hg = 0.59 mg/kg); the biochemistry disorder was found in fish (*Ameiurus males*, Hg = 0.59 mg/kg; *Brycon amazonicus*, Hg = 0.63 mg/kg); crustaceans (*Dapnia magna*, Hg = 0.859 mg/kg); aquatic insects (*Hexagenia sp.*, Hg = 0.166 mg/kg), and the effect of mortality was found in molluscs (*Mytillus edulis*, Hg = 1.12 mg/kg); fish (*Poecilia reticulate*, Hg = 0.2 mg/kg; *Onchorhynchus keta*, Hg = 0.8 mg/kg). The previous study reported by other reports [3] showed the bioaccumulation factor of the selected fish namely *Barbonymus gonionotus* and *Channa striata* in the Ciujung watershed is found to be higher than 1,000 which includes dangerous categories if consumed and also consistent with the research reported by other reports [7] that the Hg concentrations found in Cisitu ponds ranging from 0.1-1.3 mg/kg which exceeding the maximum quantity for human consumption.

In this study, the ecological risk of Hg toxicity based on RQ at the 11 sampling sites show that the RQ values of 10 sediment sampling sites in the Ciujung watershed including mainstream and tributaries are more than 1, while the RQ of S1 is less than 0.1. RQ values of Hg at the 11 sampling sites of Ciujung watershed: mainstream – S1 – 0.05; S2 – 1.59; S3 – 1.66; S4 – 2.33; S5 – 2.20; S6 – 1.18; tributaries (Cisimeut River) – T1 – 1.59; T2 – 1.33; tributaries (Ciberang River) – B1 – 1.97; B2 – 2.12; B3 – 1.07.

A similar result was reported by a previous report [25] in Taihu Lake where almost the range of RQ values in the 31 sites was between 0.10-1.00, and two sites showed higher than 1 were S12 (RQ = 2.04) and S13 (RQ = 2.18). Based on that, the ecological risk of Taihu Lake is in the middle level.

The results of this study showed that the RQ values in the Ciujung Watershed were quite higher compared to the Taihu Lake, indicating that overall, the ecological risk level of Hg in Ciujung sediment was high. Regarding this, we can infer that Hg contamination in the Ciujung watershed has the potential effect on benthic organisms as a food chain in most of the sampling sites except S1. Future research is highly required to examine different species of fish and benthic organisms from those sampling sites in the Ciujung watershed.

Limitations of this study as follows:

• Indonesia's rivers are managed by local government authorities. To collect samples from these rivers, individuals or organizations must obtain specific permissions from local government.

• Local governments are responsible for the monitoring and supervision of rivers and have designated specific sampling points, individuals or organizations must adhere to the procedures established by local authorities.

• The challenging access to the rivers, which are surrounded by dense forests. Therefore, we have to follow the procedure established by local government. This process could limit the temporal and spatial representation of the collected data.

• Reliable identification of spatial patterns and correlations with other geochemical characteristics typically requires a larger dataset (30 samples at least) to ensure statistical significance and to reduce the impact of outliers.

• A small number of samples (11 samples) inadequately represents geochemical diversity and does not account for the influence of environmental factors such as vegetation cover, land use, and human activities, nor does it capture the temporal fluctuations in mercury levels due to seasonal changes such as varying water flow rates, sediment deposition, and erosion patterns; thus, it provides insufficient geographic coverage and risks missing significant variations in mercury contamination within the river system. Therefore, further investigation should be conducted to ensure sufficient geographic coverage for a comprehensive result.

• Besides ASGM, other potential sources of Hg contamination, such as industrial discharges, atmospheric deposition, and historical contamination, need to be considered. Understanding the relative contributions of these sources requires a more comprehensive sampling strategy.

Conclusion

The average concentration of total Hg on the surface sediment of the Ciujung watershed ranges from 0.02-0.91 mg/kg d.w., and based on the sediment quality guideline, the concentration of Hg on the surface sediment exceeded the normal limit value in all the sampling sites except S1. This study is important since it is the first to investigate Hg contamination in the mainstream of the Ciujung watershed, Banten Province as a result of illegal ASGM activities.

This study confirmed the presence of mercury contamination in the Ciujung watershed, where the average total concentration of Hg in the surface sediment of the Ciujung watershed ranges from 0.02-0.91 mg/kg d.w., and based on sediment quality guidelines, the concentration of Hg in surface sediment exceeds the normal limit value in all sampling locations except S1. The Bayesian mixing model using isotopes shows that the percentage of SOM distribution in the main stream of the Ciujung watershed consists of 23.8-60.8 % from the Cisimeut River and 26.0-47.51 % from the Ciberang River. The results utilizing C/N and $\delta^{13}C$ revealed that the OM sedimentary is composed of SOM

where THg concentration and C, N, and P was strongly correlated based on Pearson's correlation analysis. This revealed that these rivers have contributed to the Hg contamination of the mainstream of the Ciujung watershed due to illegal ASGM activities carried out in the upstream areas of the tributaries that act as point sources.

The biological effects evaluated by ERM and PEL showed that the concentration of Hg exceeded the normal limit value with a moderate index risk quotient level. It can be concluded that sediment in the Ciujung watershed confirms the high probability of its effect on residents with Hg. This study is significant because it addresses Hg pollution and provides suggestions for further environmental management of Hg and sediment remediation.

REFERENCES

1. Mulyaningsih Th.R., Alfian, Sutisna. Distribution of heavy metals in sediments of the Ciujung watersheds Banten. *Journal of Nuclear Reactor Technology*. 2012. Vol. 14. N 3, p. 157-169 (in Indonesian).
2. Akbari T., Pangesti F.S.P. Water Quality Index of Cisadane River and Ciujung River. Advances in Social Science, Education and Humanities Research: Proceedings of the 1st International Multidisciplinary Conference on Education, Technology, and Engineering, 5-6 November 2019, Serang Banten, Indonesia. Atlantis Press, 2019. Vol. 410, p. 131-134. DOI: 10.2991/assehr.k.200303.032
3. Prilia D., Qginawati K., Ariesyady H.D. Analysis of Mercury in Water and Sediment Distribution and Its Bioaccumulation Potential in Fish in the Small Scale Gold Mining Area (Case Study: Ciberang River, Lebak, Banten). *Journal of Water Sustainability*. 2013. Vol. 3. Iss. 2, p. 107-116. DOI: 10.11912/jws.3.2.107-116
4. Libassi M. Indonesia: Adaptation and Differentiation in Informal Gold Mining. Global Gold Production Touching Ground. Cham, 2020, p. 321-338. DOI: 10.1007/978-3-030-38486-9_17
5. Getriana A., Achmadi U.F., Leometa C.H. Behavioral Mercury Exposure of People in Artisanal and Small-Scale Gold Mining Site Area at Lebaksitu Village, 2017. *Indian Journal of Public Health Research & Development*. 2018. Vol. 9. N 6, p. 432-438. DOI: 10.5958/0976-5506.2018.00593.4
6. Novirsa R., Dinh Q.P., Jeong H. et al. The dietary intake of mercury from rice and human health risk in artisanal small-scale gold mining area, Indonesia. *Fundamental Toxicological Sciences*. 2020. Vol. 7. Iss. 5, p. 215-225. DOI: 10.2131/fts.7.215
7. Bose-O'Reilly S., Schierl R., Nowak D. et al. A preliminary study on health effects in villagers exposed to mercury in a small-scale artisanal gold mining area in Indonesia. *Environmental research*. 2016. Vol. 149, p. 274-281. DOI: 10.1016/j.envres.2016.04.007
8. Hong Y.-S., Kim Y.-M., Lee K.-E. Methylmercury Exposure and Health Effects. *Journal of Preventive Medicine and Public Health*. 2012. Vol. 45. Iss. 6, p. 353-363. DOI: 10.3961/jpmph.2012.45.6.353
9. Kim T.-H., Cho M.-J., Lee Y. et al. Methylmercury Determination in Fish by Direct Mercury Analyzer. *Journal of AOAC INTERNATIONAL*. 2020. Vol. 103. Iss. 1, p. 244-249. DOI: 10.5740/jaoacint.18-0254
10. Gutiérrez-Mosquera H., Marrugo-Negrete J., Díez S. et al. Distribution of chemical forms of mercury in sediments from abandoned ponds created during former gold mining operations in Colombia. *Chemosphere*. 2020. Vol. 258. N 127319. DOI: 10.1016/j.chemosphere.2020.127319
11. Palacios-Torres Y., Caballero-Gallardo K., Olivero-Verbel J. Mercury pollution by gold mining in a global biodiversity hotspot, the Choco biogeographic region, Colombia. *Chemosphere*. 2018. Vol. 193, p. 421-430. DOI: 10.1016/j.chemosphere.2017.10.160
12. Chakraborty P., Sarkar A., Vudamala K. et al. Organic matter – A key factor in controlling mercury distribution in estuarine sediment. *Marine Chemistry*. 2015. Vol. 173, p. 302-309. DOI: 10.1016/j.marchem.2014.10.005
13. Ankit Y., Muneer W., Gaye B. et al. Apportioning sedimentary organic matter sources and its degradation state: Inferences based on aliphatic hydrocarbons, amino acids and $\delta^{15}N$. *Environmental Research*. 2022. Vol. 205. N 112409. DOI: 10.1016/j.envres.2021.112409
14. Al Husaeni D.F., Nandiyanto A.B.D. Bibliometric Using Vosviewer with Publish or Perish (using Google Scholar data): From Step-by-step Processing for Users to the Practical Examples in the Analysis of Digital Learning Articles in Pre and Post Covid-19 Pandemic. *ASEAN Journal of Science and Engineering*. 2022. Vol. 2. N 1, p. 19-46. DOI: 10.17509/ajse.v2i1.37368
15. Willy Cahya Nugraha, Yasuhiro Ishibashi, Koji Arizono. Assessment of heavy metal distribution and contamination in the sediment of the Ciujung Watershed, Banten Province, Indonesia. *Journal of Material Cycles and Waste Management*. 2023. Vol. 25, p. 2619-2631. DOI: 10.1007/s10163-023-01661-4
16. Haq A., Achmadi U.F., Mallongi A. Environmental Health Risk Assessment Due to Exposure to Mercury in Artisanal and Small-Scale Gold Mining Area of Lebak District. *Global Journal of Health Science*. 2018. Vol. 10. N 3, p. 125-131. DOI: 10.5539/gjhs.v10n3p125
17. Ali M.M., Ali M.L., Islam Md. S., Rahman Md. Z. Preliminary assessment of heavy metals in water and sediment of Karnaphuli River, Bangladesh. *Environmental Nanotechnology, Monitoring & Management*. 2016. Vol. 5, p. 27-35. DOI: 10.1016/j.enmm.2016.01.002
18. Haiyan Li, Anbang Shi, Xiaoran Zhang. Particle size distribution and characteristics of heavy metals in road-deposited sediments from Beijing Olympic Park. *Journal of Environmental Sciences*. 2015. Vol. 32, p. 228-237. DOI: 10.1016/j.jes.2014.11.014
19. Rippey B., Campbell J., McElarney Y. et al. Timescale of reduction of long-term phosphorus release from sediment in lakes. *Water Research*. Vol. 200. N 117283. DOI: 10.1016/j.watres.2021.117283
20. Berke M.A. Reconstructing Terrestrial Paleoenvironments Using Sedimentary Organic Biomarkers. *Methods in Paleoecology*. Springer, 2018, p. 121-149. DOI: 10.1007/978-3-319-94265-0_8
21. Mihailescu M.-D. Bayesian analysis on mixture models, for understanding the process of myosin binding to the thin filament: A thesis presented for the degree of Doctor of Philosophy. Essex: University of Essex, 2021, p. 180.
22. Torres-Martínez J.A., Mora A., Knappett P.S.K. et al. Tracking nitrate and sulfate sources in groundwater of an urbanized valley using a multi-tracer approach combined with a Bayesian isotope mixing model. *Water Research*. 2020. Vol. 182. N 115962. DOI: 10.1016/j.watres.2020.115962
23. Stock B.C., Jackson A.L., Ward E.J. et al. Analyzing mixing systems using a new generation of Bayesian tracer mixing models. *PeerJ*. 2018. Vol. 6. N e5096. DOI: 10.7717/peerj.5096

24. Meng Du, Dongbin Wei, Zhuowei Tan et al. Predicted no-effect concentrations for mercury species and ecological risk assessment for mercury pollution in aquatic environment. *Journal of Environmental Sciences*. 2015. Vol. 28, p. 74-80. DOI: 10.1016/j.jes.2014.06.042

25. Hailei Su, Di Shi, Jiwei Yang et al. Distribution Characteristics and Risk Assessment of Mercury in Sediments From Taihu Lake. *Frontiers in Environmental Science*. 2021. Vol. 9. N 695470. DOI: 10.3389/fenvs.2021.695470

26. Novirsa R., Quang P.D., Jeong H. et al. The evaluation of mercury contamination in upland rice paddy field around artisanal small-scale gold mining area, Lebaksitu, Indonesia. *Journal of Environment and Safety*. 2019. Vol. 10. N 2, p. 119-125. DOI: 10.11162/daikankyo.E19RP0103

27. Karaouzas I., Kapetanaki N., Mentzafou A. et al. Heavy metal contamination status in Greek surface waters: A review with application and evaluation of pollution indices. *Chemosphere*. 2021. Vol. 263. N 128192. DOI: 10.1016/j.chemosphere.2020.128192

28. Chun Liu, Dong Wang, FeiFei Dong et al. Modeling organic matter sources of sediment fluxes in eroding landscapes: Review, key challenges, and new perspectives. *Geoderma*. 2021. Vol. 383. N 11470. DOI: 10.1016/j.geoderma.2020.114704

29. Balogh S.J., Tsui M.T.-K., Blum J.D. et al. Tracking the Fate of Mercury in the Fish and Bottom Sediments of Minamata Bay, Japan, Using Stable Mercury Isotopes. *Environmental Science & Technology*. 2015. Vol. 49. Iss. 9, p. 5399-5406. DOI: 10.1021/acs.est.5b00631

30. Yichen Lin, Fanping Meng, Yongxiang Du, Yuhan Tan. Distribution, speciation, and ecological risk assessment of heavy metals in surface sediments of Jiaozhou Bay, China. *Human and Ecological Risk Assessment: An International Journal*. 2016. Vol. 22. Iss. 5, p. 1253-1267. DOI: 10.1080/10807039.2016.1159503

31. Riaz A., Khan S., Muhammad S., Shah M.T. Mercury Contamination in Water and Sediments and the Associated Health Risk: A Case Study of Artisanal Gold-mining. *Mine Water and the Environment*. 2019. Vol. 38. Iss. 4, p. 847-854. DOI: 10.1007/s10230-019-00613-5

32. de la Lanza Espino G., Soto L.A. C:N:P Molar Ratios, Sources and ^{14}C Dating of Surficial Sediments from the NW Slope of Cuba. *PLoS One*. 2015. Vol. 10. N 6. N e0125562. DOI: 10.1371/journal.pone.0125562

33. Kobayashi S., Fujiwara T. Influences of Terrestrial Inputs of Organic Matter on Coastal Water and Bottom Sediments in the Seto Inland Sea, Japan. *Journal of Water and Environment Technology*. 2018. Vol. 16. N 3, p. 138-148. DOI: 10.2965/jwet.17-035

34. Hongmeng Ye, Hao Yang, Nian Han et al. Risk Assessment Based on Nitrogen and Phosphorus Forms in Watershed Sediments: A Case Study of the Upper Reaches of the Minjiang Watershed. *Sustainability*. 2019. Vol. 11. Iss. 20. N 5565. DOI: 10.3390/su11205565

35. Chakraborty P., Sarkar A., Vudamala K. et al. Organic matter – A key factor in controlling mercury distribution in estuarine sediment. *Marine Chemistry*. 2015. Vol. 173, p. 302-309. DOI: 10.1016/j.marchem.2014.10.005

36. Conghui Sun, Qi Wei, Lixia Ma et al. Trace metal pollution and carbon and nitrogen isotope tracing through the Yongdingxin River estuary in Bohai Bay, Northern China. *Marine Pollution Bulletin*. 2017. Vol. 115. Iss. 1-2, p. 451-458. DOI: 10.1016/j.marpolbul.2016.10.066

37. Bakshi M., Ghosh S., Chakraborty D. et al. Assessment of potentially toxic metal (PTM) pollution in mangrove habitats using biochemical markers: A case study on Avicennia officinalis L. in and around Sundarban, India. *Marine Pollution Bulletin*. 2018. Vol. 133, p. 157-172. DOI: 10.1016/j.marpolbul.2018.05.030

38. van Hardenbroek M., Chakraborty A., Davies K.L. et al. The stable isotope composition of organic and inorganic fossils in lake sediment records: Current understanding, challenges, and future directions. *Quaternary Science Reviews*. 2018. Vol. 196, p. 154-176. DOI: 10.1016/j.quascirev.2018.08.003

39. Beckers F., Rinklebe J. Cycling of mercury in the environment: Sources, fate, and human health implications: A review. *Critical Reviews in Environmental Science and Technology*. 2017. Vol. 47. Iss. 9, p. 693-794. DOI: 10.1080/10643389.2017.1326277

40. Meng Chuan Ong, Hui-Juan Pan, Shazili N.A.M. et al. Heavy Metals Concentration in Sediments of South Brittany Waters, France: An Ecological Risk Assessment Approach Assessment Approach. *Open Journal of Marine Science*. 2021. Vol. 11. N 1, p. 55-68. DOI: 10.4236/ojms.2021.111004

41. Hyeryeong Jeong, Jin Young Choi, Jihyun Lee et al. Heavy metal pollution by road-deposited sediments and its contribution to total suspended solids in rainfall runoff from intensive industrial areas. *Environmental Pollution*. 2020. Vol. 265. Part A. N 115028. DOI: 10.1016/j.envpol.2020.115028

***Authors*: Willy C. Nugraha,** *Doctor of Philosophy, Researcher, Doctoral student, https://orcid.org/0000-0003-1542-6701 (Research Center for Environmental and Clean Production, National Research and Innovation Agency, South Tangerang, Indonesia; Prefectural University of Kumamoto, Kumamoto, Japan)*, **Huiho Jeong,** *Doctor of Philosophy, Doctoral student, https://orcid.org/0000-0003-1987-1386 (Prefectural University of Kumamoto, Kumamoto, Japan)*, **Phan Dinh Quang,** *Doctor of Philosophy, Doctoral student, Researcher, https://orcid.org/0000-0002-4553-5581 (Prefectural University of Kumamoto, Kumamoto, Japan; Vietnam National Institute of Occupational Safety and Health, Hanoi, Vietnam)*, **Randy Novirsa,** *Doctor of Philosophy, Doctoral student, Lecture, https://orcid.org/0000-0003-0477-1067 (Prefectural University of Kumamoto, Kumamoto, Japan; University of Andalas, West Sumatra, Indonesia)*, **Tomohiro Komorita,** *Associate Professor, Lecture, https://orcid.org/0000-0002-9469-5602 (Prefectural University of Kumamoto, Kumamoto, Japan)*, **Yasuhiro Ishibashi,** *Professor, Head of Department Environmental and Symbiotic System, https://orcid.org/0000-0002-2610-0849 (Prefectural University of Kumamoto, Kumamoto, Japan)*, **Jun Kobayashi,** *Professor, https://orcid.org/0000-0003-0493-6386 (Prefectural University of Kumamoto, Kumamoto, Japan)*, **Koji Arizono,** *Professor, https://orcid.org/0000-0002-9148-9176 (Prefectural University of Kumamoto, Kumamoto, Japan)*, **Asep Bayu Dani Nandiyanto,** *Professor, Lecture, nandiyanto@upi.edu, https://orcid.org/0000-0002-9753-1267 (Universitas Pendidikan Indonesia, Bandung, Indonesia)*.

The authors declare no conflict of interests.

ISSN 2411-3336; e-ISSN 2541-9404

JOURNAL OF MINING INSTITUTE

Zapiski Gornogo instituta

Journal homepage: pmi.spmi.ru

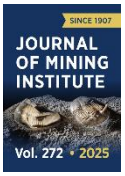

Research article *Geotechnical Engineering and Engineering Geology*

Justification on the safe exploitation of closed coal warehouse by gas factor

Semen G. Gendler, Anastasiya Yu. Stepantsova✉, Mikhail M. Popov
Empress Catherine II Saint Petersburg Mining University, Saint Petersburg, Russia

***How to cite this article*:** Gendler S.G., Stepantsova A.Yu., Popov M.M. Justification on the safe exploitation of closed coal warehouse by gas factor. Journal of Mining Institute. 2025. Vol. 272. N 16519, p. 72-82.

Abstract
The annual increase of coal production and its demand lead to the necessity in temporary storage places (warehouses) organization to accommodate raw coal materials before the shipment. It is noted that at the open method of coal storing the dust emission from loading/unloading operations and from the pile surface effects negatively the health of the warehouse workers and adjacent territories. An alternative solution is closed-type warehouses**.** One of the main hazards of such coal storage can be the release of residual methane from coal segregates into the air after degassing processes during mining and extraction to the surface, as well as transportation to the place of temporary storage. The study carries the analysis of methane content change in coal during the processes of extraction, transportation and storage. Physical and chemical bases of mass transfer during the interaction between gas-saturated coal mass and air are studied. It is determined that the intensity of methane emission depends on: the coal seam natural gas content, parameters of mass transfer between coal, and air and the ambient temperature. The dynamics of coal mass gas exchange with atmospheric air is evaluated by approximate approach, which is based on two interrelated iterations. The first one considers the formation of methane concentration fields in the air space of the bulk volume and the second accounts the methane emission from the pile surface to the outside air. It is determined that safety of closed coal warehouses exploitation by gas factor can be ensured by means of artificial ventilation providing volumetric methane concentration in the air less than 1 %. The flow rate sufficient to achieve this methane concentration was obtained as a result of computer modeling of methane concentration fields formation in the air medium at theoretically calculated methane emission from the pile surface.

Keywords
hard coal; coal dust; coal warehouse; methane; residual methane content; hard coal transportation; methane desorption; effective diffusion coefficient

Received: 17.06.2024 ***Accepted: 17.07.2024*** ***Online: 03.10.2024*** ***Published: 25.04.2025***

Introduction

The coal industry is one of the key sectors of Russian industry, including mining, production, transportation and marketing of coal. The Russian Federation ranks 2nd place in the world in terms of coal reserves, most of which are located in Siberia and the Far East [1-3]. Coal production in 2023 amounted to 438 million t, including 213 million t of coal exported to China, BRICS countries and others [4, 5].

The growth of coal production and increased commercial interest in its acquisition lead to the need for coal's temporary storages in port terminals and storage areas to be shipped to the consumer in future [6-8].

Nowadays, the most common method of temporary coal storage is its placement in open area [9-11]. However, data analysis shows, this method, firstly, reduces the raw materials quality, and secondly, there is an aerotechnogenic load on the environment and workforce due to the dust emissions [12-14]. The cause of coal's piles high dusting is wind flow, the value of which reaches 20 m/s in some regions. Calculation of coal dust emissions into the atmosphere from the open warehouses operations was carried out

according to the Industry methodology*. Dependence of atmospheric air dustiness (points at different distances from the piles) on the wind speed is presented in Fig.1.

The obtained analysis indicate that at low wind speed (1-5 m/s) removal of coal dust from the pile surface and its dispersion occurs mainly in the storage area and the adjacent territory of the enterprise, exposing the negative impact of the workforce. Due to wind flow increasing, dusting from the pile intensifies, but at the same time, dispersion and settling of coal dust will occur mainly outside the industrial territory, inducing aerotechnogenic impact on the environment.

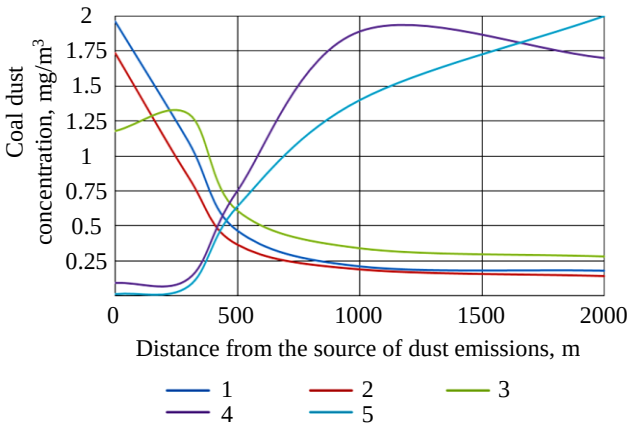

Fig.1. Dependence of coal dust dispersion on the distance to the dust source at different air velocities

1 – 1 m/s; 2 – 3 m/s; 3 – 5 m/s; 4 – 10 m/s; 5 – 20 m/s

An alternative solution for the environmental problem and prevention of coal quality reduction is the exploitation of temporary closed warehouses [15-17]. Following this method, the air velocity is determined only by the parameters of natural or forced ventilation. In comparison with the wind flow velocity, the air inside closed warehouse moves less faster which contributes to minimal dust disruption from the surface of coal pile. Meanwhile, the high residual methane content in coal segregates can lead to the formation of explosive concentrations in the warehouse air environment [18]. In order to avoid such cases, the maximum methane content in the closed warehouse air is limited by the current regulations (1 % of the volume) [19].

The obtained analysis indicate that many Russian coal deposits are characterized by high natural gas content. This information is presented in the Table, which contains the values of minimum and maximum natural methane content of some Kuzbass coal seams [20-22].

Methane content of some Kuzbass coal seams

Coal deposit	Minimum natural methane content, m^3/t	Maximum natural methane content, m^3/t
Alardinskoye	0.10	44.7
Baidayevskoye	0	30.3
Berezovo-Biryulinskoye	2.0	36.7
Egozovo-Krasnoyarskoye	0.3	13.5
Kedrovsko-Krokhalevskoye	0.01	17.6
Kiselevskoye	0	35
Leninskoye	0	25
Olzherasskoye	1	31
Raspadskoye	1	22
Sokolovskoye	2	17.1
Shelkanskoye	1	23.5
Chertinskoye	0	35

Reduction of gas content (methane content) relative to its initial value takes place in several stages: coal extraction to the surface, loading into railcars, transportation by rail, unloading

* Industry methodology for calculating the amount of harmful waste captured and emitted into the atmosphere by coal mining enterprises. Perm: MNIIECO TEK, 2003, p. 115.

to the warehouse. The coal mass degassing processes at each stage depend on such parameters as petrographic coal composition, ash content, average size of a coal piece, ambient temperature, etc. [23-25].

Hence, the purpose of the work is to study the influence of residual gas content of coal on closed coal warehouse's safe operating conditions and to choose the ventilation mode for gas regime normalization when required.

Methods

Methane in coal seams is in a bound sorbed state. During the coal massif distructure, a part of methane, located in seam pores and cracks, escapes into the mine space instantly, and the other part of gas – continue to desorb, but at a slower rate. The intensity of gas emissions from coal depends on several factors: ambient temperature, mass transfer parameters, initial gas coal content, etc. [26-28].

After mining and extraction to the surface and during transportation to the customer, coal is stored in various shapes of piles, which are bulk volumes containing coal pieces surrounded by air space. Piles may include coal mounds before loading into railcars, coal volumes filling in railway, and coal mounds formed in temporary storage places (port terminals, storage facilities at thermal power plants, chemical and metallurgical plants, etc.) [19, 29, 30].

If during the coal transportation from the extraction place to the final destination, degassing of initially contained in the coal methane occur only partially, the coal mass have some residual gas content.

The degassing process of coal stored in piles is carried out as follows. In the initial period, immediately after the pile formation, the methane concentration in the air, that filing intergranular voids is 0. Over time, the air voids begin to be filled with methane coming from the surface of each coal unit, and the methane concentration in the air voids continuously increases, reaching a certain asymptotic value. If the a coal pile surface is washed by air, then simultaneously with the increasing of methane concentration in the depths of the pile, an outflow of methane from the surface occurs, and in the adjacent to the pile surface zones, zones are formed with a reduced concentration of methane relative to the areas to which the influence of gas exchange from the surface has not yet spread.

It may appear that firstly the methane flow from the pile surface increases to a certain value, but then it decreases monotonously.

To estimate the dynamics of coal mass gas exchange with atmospheric air at all stages of its storage in piles or railcars, an approximate approach based on the use of two interrelated iterations determining both the formation of methane concentration fields in the air space of the bulk volume and the values of methane emission from the pile surface to the outside air is proposed.

The first iteration is performed under the assumption that methane emission per unit volume of the coal mass, where the coal particles surface area is F_{vol}, occurs under the condition of isolation of this volume, in which the coal particles and voids filled with air occupy volumes $1 - m$ and m, respectively, from the outside air surrounding its surface. The methane flow j from the each coal particle surface is calculated under the assumption that it can be represented in the form of a ball with radius r_0, and the methane flow from its surface is determined by the effective diffusion coefficient D_{eff}, the value of which was established on the basis of experimental studies (Fig.2) for Kuzbass coals ranks gas and fat (bituminous) coal [31].

The graph in the Fig.2 shows the increasing of effective diffusion coefficient with ambient temperature raising.

The differential equation of methane diffusion in each coal particle can be represented in the form:

$$\frac{\partial C}{\partial \mathrm{Fo}^{\mathrm{coal}}} = D_{eff}\ \frac{\partial^2 C}{\partial R^2} + \frac{2}{r}\frac{\partial C}{\partial R}; \qquad (1)$$

$$C(R,0) = C_0;$$

$$\partial C = C\left(R; \mathrm{Fo}^{\mathrm{coal}}\right);$$

$$C(1,\tau) = C_\tau;$$

$$\frac{\partial C\left(0, \mathrm{Fo}^{\mathrm{coal}}\right)}{\partial R} = 0,$$

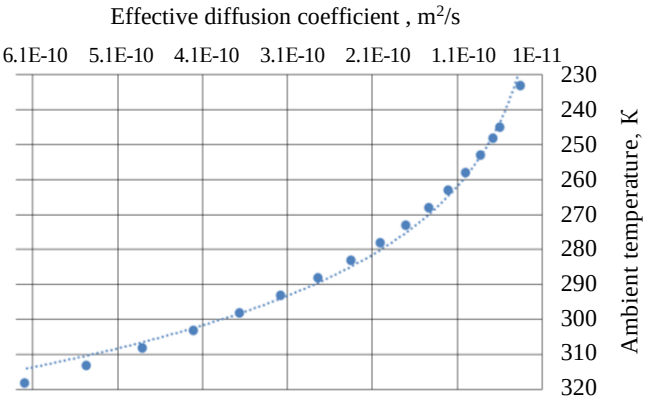

Fig.2. Graph of the change in effective diffusion coefficient from ambient temperature.
Correlation ratio $\sqrt{0.993}$

where C – methane concentration in coal particles, kg/m^3; $\mathrm{Fo}^{\mathrm{coal}}$ – Fourier diffusion number for coal, m^2/s, $\mathrm{Fo}^{\mathrm{coal}} = D_{eff}\tau / r_0^2$; τ – time, s; C_0 – initial methane concentration in coal mass, kg/m^3; R – dimensionless radius, $R = r/r_0$; r_0 – average radius of coal particles of bulk coal volume, m; C_τ – methane concentration in the air, kg/m^3.

The solution of equation (1), presented in a general form, at C_τ = const, has a complex form, which complicates its further use for calculating the methane concentration dynamics in air voids. Therefore, the asymptotic representation of the general solution at actual values of the Fourier diffusion number for the considered conditions was used to determine $C(R, \mathrm{Fo}^{\mathrm{coal}})$:

$$\mathrm{Fo}^{\mathrm{coal}} = \frac{(10^{-10}\text{-}10^{-11})(1.5\text{-}4)\cdot 10^6}{0.05^2} = 0.1\text{-}0.2. \qquad (2)$$

Then the diffusion flow for these Fourier number with high accuracy can be represented as:

$$j\left(\mathrm{Fo}^{\mathrm{coal}}\right) = D_{eff} / r_0 \left(-1 + \frac{1}{\sqrt{\pi \mathrm{Fo}^{\mathrm{coal}}}}\right)(C_0 - C_\tau). \qquad (3)$$

In case C_τ varies according to an arbitrary law, the methane flow is established on the Duhamel's theorem:

$$j\left(\mathrm{Fo}^{\mathrm{coal}}\right) = -\frac{D_{eff}}{r_0}\frac{\partial}{\partial \mathrm{Fo}^{\mathrm{coal}}}\int_0^{\mathrm{Fo}^{\mathrm{coal}}}\left(-1 + \frac{1}{\sqrt{\pi\xi}}\right)\left[C_0 - C_\tau\left(\mathrm{Fo}^{\mathrm{coal}} - \xi\right)\right]d\xi. \qquad (4)$$

Methane concentration changes in per unit volume of bulk airspace:

$$m\frac{dC\left(\mathrm{Fo}^{\mathrm{coal}}\right)}{d\mathrm{Fo}^{\mathrm{coal}}} = (1-m)F_{\mathrm{vol}}\, j\left(\mathrm{Fo}^{\mathrm{coal}}\right). \qquad (5)$$

Initial conditions $C\left(\mathrm{Fo}^{\mathrm{coal}}\right)|_{\mathrm{Fo}^{\mathrm{coal}}=0} = 0$.

The solution of equation (5), using the Laplace transform, with respect to the methane concentration in the air space can be represented in the form:

$$C_\tau\left(\mathrm{Fo}^{\mathrm{coal}}\right) = C_0 f(Z), \qquad (6)$$

where $f(Z)$ – tabulated function,

$$f(Z) = 1 - \exp\left(k^2 \mathrm{Fo}^{\mathrm{coal}}\right)\mathrm{erfc}\left(k\sqrt{\mathrm{Fo}^{\mathrm{coal}}}\right);$$

$$\mathrm{erfc}\left(k\sqrt{\mathrm{Fo}^{\mathrm{coal}}}\right) = 1 - \frac{2}{\sqrt{\pi}}\int_0^{k\sqrt{\mathrm{Fo}^{\mathrm{coal}}}} \exp(-\xi^2)d\xi;$$

$\frac{2}{\sqrt{\pi}}\int_0^{k\sqrt{\mathrm{Fo}^{\mathrm{coal}}}} \exp(-\xi^2)d\xi$ – probability integral at $k = \frac{r_0}{m}F_{\mathrm{vol}}(1-m)$; F_{vol} – total surface of coal particles in unit of coal mass bulk volume, m^2/m^3; m – the relative volume occupied by air per unit bulk volume of coal mass, unit fraction.

Initial methane concentration in coal mass is related to gas content (methane content) by the following:

$$C_0 = \rho_{\mathrm{met}}\rho_{\mathrm{coal}}X_{\mathrm{met}}, \quad (7)$$

where ρ_{met} – methane density, kg/m^3; ρ_{coal} – coal density, m^3/t; X_{met} – initial methane concentration, m^3/t.

One way to calculate the average methane concentration in the bulk volume airspace $\overline{C_\tau\left(\mathrm{Fo}^{\mathrm{coal}}\right)}$ over the storage or transportation time $\mathrm{Fo}^{\mathrm{coal}}$ is to integrate expression (6) with subsequent averaging over time $\mathrm{Fo}^{\mathrm{coal}}$. However, in this case, the expression $\overline{C_\tau\left(\mathrm{Fo}^{\mathrm{coal}}\right)}$ turns out to be rather cumbersome, that is not effective for further estimates.

Another way to calculate $\overline{C_\tau\left(\mathrm{Fo}^{\mathrm{coal}}\right)}$ is to use the balance equation, based on total methane flow calculation, that enters to the bulk volume airspace from the coal particles during the time $\mathrm{Fo}^{\mathrm{coal}}$. This is possible under the condition of the average methane concentration constancy for this time and with the subsequent calculation of the increment of the average methane concentration in the air space relative to the initial value equal to zero. The dependence can be presented as:

$$\overline{C_\tau\left(\mathrm{Fo}^{\mathrm{coal}}\right)} = \frac{C_0 k\left[2\left(\frac{\mathrm{Fo}^{\mathrm{coal}}}{\pi}\right)^{0.5} - \mathrm{Fo}^{\mathrm{coal}}\right]}{1 + 0{,}5k\left[2\left(\frac{\mathrm{Fo}^{\mathrm{coal}}}{\pi}\right)^{0.5} - \mathrm{Fo}^{\mathrm{coal}}\right]}. \quad (8)$$

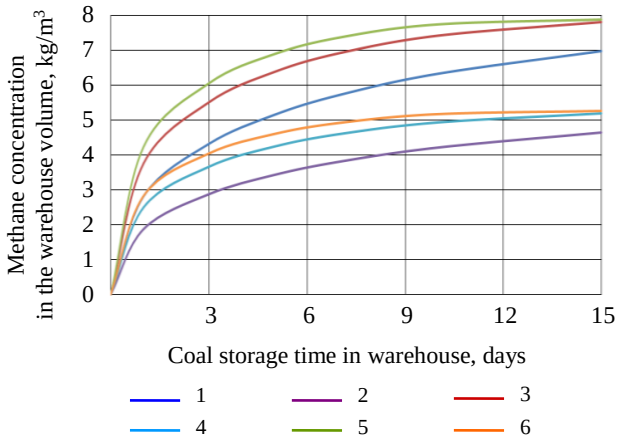

Fig.3. Graph of methane concentration changes in the airspace of the bulk volume over time

1 – residual methane content after transportation 15 m^3/t (–20 °C); 2 – 15 m^3/t (0 °C); 3 – 15 m^3/t (+10 °C); 4 – 10 m^3/t (–20 °C); 5 – 10 m^3/t (0 °C); 6 – 10 m^3/t (+10 °C)

Calculations of $\overline{C_\tau\left(\mathrm{Fo}^{\mathrm{coal}}\right)}$ for various diffusion coefficients are shown in Fig.3.

According to calculations, the average methane concentration sharply increases after 1 day of storage. This raising of concentration is especially noticeable for high ambient temperatures, as the value of the effective diffusion coefficient increases with increasing temperature [32, 33]. For example, at residual methane content after transportation of 10 m^3/t and duration of coal storage in the warehouse for 15 days, the methane concentration in the warehouse volume will tentatively be 8 kg/m^3 in summer and 7 kg/m^3 in winter period.

The second iteration allows to establish the methane emissions from the surface of the bulk

volume into the air surrounded this surface at each time instant τ. To determine methane emissions from the bulk volume surface, it is necessary to choose its geometric shape. For the bulk volume of the railcars, it is proposed to use the semi-constrained space model, and for the bulk volume in the form of a pile, placed in a closed warehouse, the geometric model of an unconstrained cylinder with an equivalent radius R_{surf}.

In this case, it is assumed that the methane flow from the surface of the bulk volume for the time τ is determined by the resulting effective diffusion coefficient D_{eff}^{res} calculated according to the methodology similar to this work [34]. This methodology is based on the assumption that the coal mass can be considered as two binary mixtures, one of which consists of coal particles surrounded by voids containing air $D_{eff\,1}$, and the other, on the contrary, of voids with air, which are surrounded by coal particles $D_{eff\,2}$ The effective diffusion coefficient is calculated using the formulas:

$$D_{eff\,1} = D_{eff}^{\text{air}}\left[1+v_{\text{coal}}\frac{\left(1-\dfrac{D_{eff}^{\text{air}}}{D_{eff}^{\text{coal}}}\right)}{1-\sqrt[3]{v_{\text{coal}}}\left(1-\dfrac{D_{eff}^{\text{air}}}{D_{eff}^{\text{coal}}}\right)}\right]; \tag{9}$$

$$D_{eff\,2} = D_{eff}^{\text{coal}}\left[1+v_{\text{air}}\frac{\left(1-\dfrac{D_{eff}^{\text{coal}}}{D_{eff}^{\text{air}}}\right)}{1-\sqrt[3]{v_{\text{air}}}\left(1-\dfrac{D_{eff}^{\text{coal}}}{D_{eff}^{\text{air}}}\right)}\right], \tag{10}$$

where D_{eff}^{coal} – effective diffusion coefficient of methane in coal according to the graph in Fig.2, m^2/s; D_{eff}^{air} – effective diffusion coefficient of methane in the air, $D_{eff}^{\text{air}} = 2\cdot10^{-5}$ m^2/s [35-37]; v_{coal} – relative volume of coal particles, $v_{\text{coal}} = 1 - m$; v_{air} – relative air space volume corresponding to the porosity of the bulk volume, $v_{\text{air}} = m$.

Based on formulas (9) and (10) the resulting effective diffusion coefficient of methane is:

$$D_{eff}^{\text{res}} = 0.2D_{eff\,1} + 0.8D_{eff\,2}. \tag{11}$$

The methane emissions (methane flow) from the railcar's surface and from the pile surface are:

$$J_{\text{train}} = \sqrt{\frac{D_{eff}^{\text{res}}}{\pi\tau}}\left[\overline{C\left(\text{Fo}^{\text{coal}}\right)} - C_{\text{air}}\right]; \tag{12}$$

$$J_{\text{pile}} = \frac{D_{eff}^{\text{res}}}{R_{\text{surf}}}\left(-0.5+\frac{1}{\left(\pi\text{Fo}^{\text{pile}}\right)^{0.5}}\right)\left[\overline{C_{\tau}\left(\text{Fo}^{\text{coal}}\right)} - C_{\text{air}}\right], \tag{13}$$

where Fo^{pile} – Fourier diffusion number for coal pile; C_{air} – methane concentration in the air, kg/m^3.

The total methane amount entering the air from the railcar bulk volume of coal is based on dependence (12). Furthermore, the total methane amount entering the air surrounding the open coal

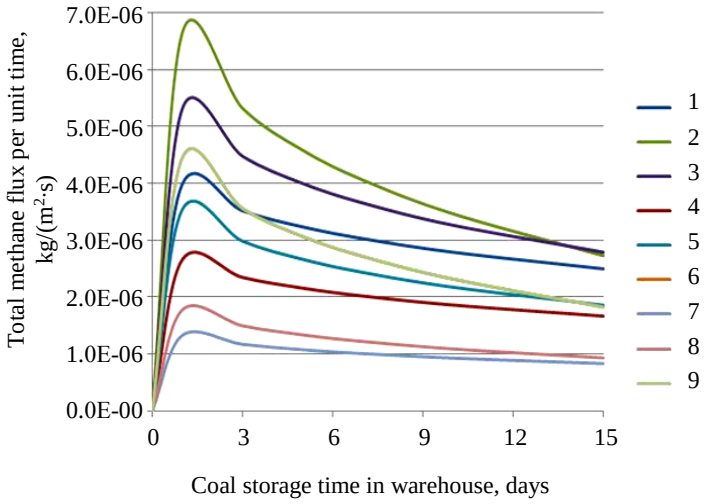

Fig.4. Dependence of methane flow from the open coal pile surface on its storage time

1 – 15 m³/t (–20 °C); 2 – 15 m³/t (+10 °C); 3 – 15 m³/t (0 °C); 4 – 10 m³/t (–20 °C); 5 – 10 m³/t (0 °C); 6 – 10 m³/t (+10 °C); 7 – 5 m³/t (–20 °C); 8 – 5 m³/t (+10 °C); 9 – 5 m³/t (0 °C)

surface is determined firstly, and then – the residual gas content (methane content) of coal mass for the transportation time τ_{transp} by next formula:

$$X_{transp} = X_0 - \frac{J_{train} F_{surf}^{rail}}{\rho_{met} P_{rail}}, \qquad (14)$$

where F_{surf}^{rail} – railcar open surface area, m²; P_{rail} – railcar load capacity, t.

Based on the results, the residual methane content of coal mass, loaded into the stockpile, can be from 14 to 7 m³/t depending on the ambient temperature and transportation time.

According to the formula (9), a dependence graph of methane flow from the open coal pile surface during its storage time was plotted (Fig.4). The initial methane concentration in the coal pile C_0 was calculated with the residual methane content calculated by formula (14).

The methane concentration's change in the closed warehouse, assuming a plane-parallel character of air movement along the pile surface, is determined by the following expression:

$$C_{tl} = C_{pile}\left(1 - e^{-J_{pile} PL}\right), \qquad (15)$$

where C_{tl} – threshold level value, C_{tl} = 1 %; P – pile lateral side perimeter, m²; L – pile length, m;

Based on formulas (13) and (15) the air flow rate vary from 5 to 27 m³/s in winter (average ambient temperature –20 °C) and from 11 to 45 m³/s in summer (average ambient temperature +20 °C) for different residual coal methane content before loading into the stockpile. The maximum air flow rate corresponds to the maximum value of methane flow.

Mathematical modelling of methane flow aerodynamics in the volume of a closed warehouse. The mathematical modelling of the gas transfer was carried out, taking into account the air flow aerodynamics where methane enters from the pile surface. It was accomplished to verify the validity of using a plane-parallel scheme of air movement in the coal warehouse and to establish the distribution of methane concentrations along the length of the warehouse, The Flow Vision software package was used for this purpose. The real geometry of the warehouse and the coal pile (height 23 m, width on the base 65 m and length 600 m) were taken as initial data. In addition, the mathematical model considered the influence of the loading and unloading equipment inside the warehouse (portal reclaimer) on the airflow aerodynamics.

Calculations is carried out for the residual methane content before loading to the stockpile, equal to 15 m³/t and at ambient temperature +20 °C. For these conditions, the average methane flow from the coal pile surface is $6\text{-}10^{-6}$ kg/(m²·s).

The warehouse ventilation is carried out according to the fresh air supply scheme through openings located on the lateral side at the end of warehouse, and exhaust of polluted air through a centre pipe (Fig.5).

Due to the symmetry of the closed warehouse with respect to vertical planes passing perpendicular (in the central section of the warehouse) and parallel (along the length of the warehouse perpendicular to its base) to the horizontal axis, the calculation area was divided into 4 equal parts (Fig.5). All calculations were performed for one of these parts.

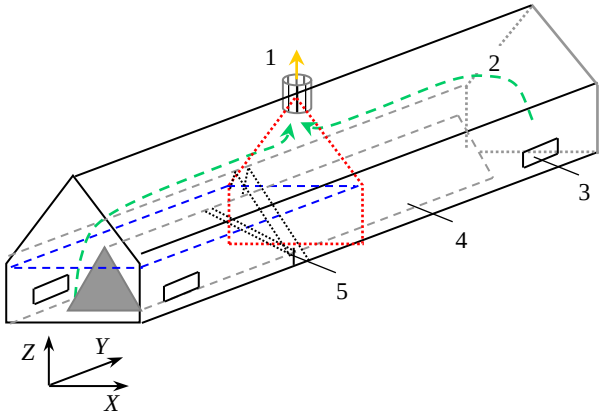

Fig.5. Scheme of a closed coal warehouse

1 – air exhaust pipe; 2 – airflow; 3 – open for air supply; 4 – coal pile; 5 – portal reclaimer

Gas admixture transfer process modelling was carried out for 16 h until the methane concentration stabilized. To establish the regularities of methane concentration distribution over the warehouse volume, the points 0-10 were chosen, located every 30 m from the air exhaust pipe towards the air supply openings (Fig.6).

Resulting from the turbulent nature of air mass flow and the influence of loading and unloading equipment on the trajectory of their movement, the methane concentrations distribution over the volume of the closed warehouse will look as follows. The methane concentration takes the maximum value of 0.00547-0.99 % by volume (red colour) near the air exhaust pipe (Fig.6). This is explained by the post-penetration accumulation of methane during the rotational movement of air mass over the coal surface, emitting methane.

The methane concentration changes with time at different space points of a closed warehouse is presented in Fig.7. According to this figure, the growth of methane concentration up to 0.99 % occurs before it reaches quasi-stationary values within ~45000 s, which corresponds to 12.5 h of coal storage in the warehouse.

Thus, according the influence of complex flow aerodynamics, the air flow rate providing dilution of methane concentration up to threshold values by calculations is 48 m^3/s. Satisfactory coincidence

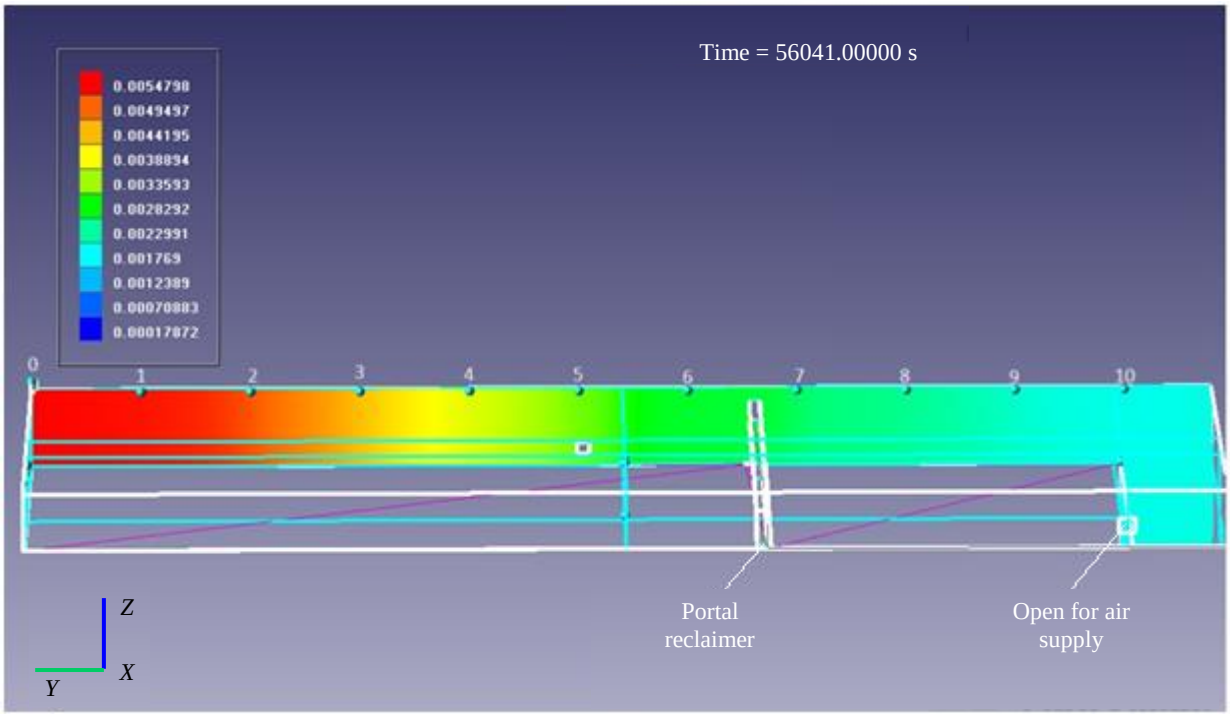

Fig.6. Methane mass fractions and location of measurement points

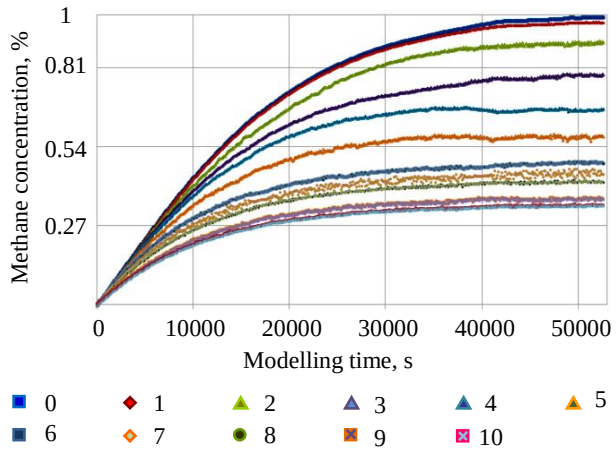

Fig.7. The graph of methane concentration changes with time at different space points (0-10) of a closed warehouse

of the analytical calculations with the results of mathematical modelling (the discrepancy does not exceed 6 %), confirms the validity of the assumptions used in the mathematical model development.

Conclusion

Coal placement in closed warehouses is an actual method of mineral temporary storage with the possibility to limit the climatic conditions impact on it, as well as to reduce the aerotechnogenic impact on the environment.

The high natural gas content of some coal seams can lead to explosive situations during mining, transport and temporary storage of raw materials due to the limited gas volume (mine, railcars, warehouse). In this regard, the ensuring safe operation problems of closed warehouses will be related to the released methane gas.

The information about the residual methane content of coal is important to prevent explosive situations at each stage:

• after coal mining, its extraction to the surface and temporary storage before loading into railcars;

• during transportation before coal placement in closed warehouses;

• during direct coal storage.

Despite reduction of residual gas coal content after each stage of handling and transportation, it can reaches values at which the operation of closed coal storage becomes unsafe, due to the possibility of exceeding the maximum permissible value of methane concentration in the air, taken as 1 % by volume.

The safety of closed coal warehouse operation in terms of methane factor will depend not only on residual methane content, but also on the ambient temperature, which directly affects the rate of methane release from coal particles: then higher the temperature, the more intense the methane release process is.

The reduction of methane content in summer (average ambient temperature +20 °C) is higher than in winter (average ambient temperature –20 °C) by almost 2 times. Thus, the accumulation of methane concentration in the closed warehouse volume in summer period will be faster, which requires more intensive ventilation for this period.

The analytical calculations results of the required air flow rate do not take into account the complex aero-dynamics of the air flow in contrast to mathematical modelling. Satisfactory coincidence of the obtained data confirms the validity of the assumptions used in the development of the mathematical model.

REFERENCES

1. Kornev A.V., Spitsyn A.A., Zaimentseva L.A., Zubko M.V. Research of the physico-chemical properties of hydrogel as a means of dust-explosion protection and dust reduction in coal mines. *Mining Informational and Analytical Bulletin.* 2023. N 9-1, p. 180-198 (in Russian). DOI: 10.25018/0236_1493_2023_91_0_180

2. Overland I., Loginova J. The Russian coal industry in an uncertain world: Finally pivoting to Asia? *Energy Research & Social Science*. 2023. Vol. 102. N 103150. DOI: 10.1016/j.erss.2023.103150

3. Korshunov G.I., Safina A.M., Karimov A.M. Research and Analysis of the Sources of Emission of Respirable Fraction of Dust at the Coal Mines. *Occupational Safety in Industry.* 2021. N 10, p. 65-70 (in Russian). DOI: 10.24000/0409-2961-2021-10-65-70

4. Novak A. Fuel and energy Complex of Russia today and tomorrow: results and objectives. *Energeticheskaya politika*. 2024. N 1 (192), p. 6-13 (in Russian). DOI: 10.46920/2409 5516_2024_1192_6

5. Magomet R.D., Rodionov V.A., Soloviov V.B. Methodological Approach to Issue of Researching Dust-Explosion Protection of Mine Workings of Coal Mines. *International Journal of Civil Engineering and Technology*. 2019. Vol. 10. Iss. 2, p. 1154-1161.

6. Rush E.A., Vlasova N.V. Promising measures aimed at environmental protection when working with coal at the production sites of the terminal and storage complex. *Modern Technologies. System Analysis. Modeling.* 2023. N 2 (78), p. 20-32 (in Russian). DOI: 10.26731/1813-9108.2023.2(78).20-32

7. Golovina E.I., Grebneva A.V. Management of groundwater resources in transboundary territories (on the example of the Russian Federation and the Republic of Estonia). *Journal of Mining Institute.* 2021. Vol. 252, p. 788-800. DOI: 10.31897/PMI.2021.6.2

8. May Chan Myae Zaw, Alpatova P.N. Ambiguity in the Russian terminology of the energy industry. *XLinguae*. 2023. Vol. 16. Iss. 1, p. 60-69. DOI: 10.18355/XL.2023.16.01.05

9. Mazurenko O., Rusinov I. Analysis of the current state and development of Russian marine coal terminals. *Transport business in Russia*. 2020. N 4, p. 154-159 (in Russian).

10. Korshunov G.I., Karimov A.M., Magamedov G.S., Tyulkin S.A. Reduction of respirable dust-induced impact on open pit mine personnel in large-scale blasting. *Mining Informational and Analytical Bulletin.* 2023. N 7, p. 132-144 (in Russian). DOI: 10.25018/0236_1493_2023_7_0_132

11. Smirnyakov V.V., Rodionov V.A., Smirnyakova V.V., Orlov F.A. The influence of the shape and size of dust fractions on their distribution and accumulation in mine workings when changing the structure of air flow. *Journal of Mining Institute*. 2022. Vol. 253, p. 71-81. DOI: 10.31897/PMI.2022.12

12. Vasina D., Rapoport I., Teslenko I. Solving environmental problems of open coal terminals in Vladivostok. *International Journal of Professional Science.* 2021. N 6, p. 27-36 (in Russian).

13. Khokhlov S., Abiev Z., Makkoev V. The Choice of Optical Flame Detectors for Automatic Explosion Containment Systems Based on the Results of Explosion Radiation Analysis of Methane- and Dust-Air Mixtures. *Applied Science*. 2022. Vol. 12. Iss. 3. N 1515. DOI: 10.3390/app12031515

14. Krivopishina M.E., Kostenko N.I. Rational equipment of the seaport terminal for export coal. *Nauchno-tekhnicheskoe i ehkonomicheskoe sotrudnichestvo stran ATR v XXI veke*. 2021. Vol. 1, p. 86-90 (in Russian).

15. Qing-Wei Li, Yang Xiao, Cai-Ping Wang et al. Thermokinetic characteristics of coal spontaneous combustion based on thermogravimetric analysis. *Fuel*. 2019. Vol. 250, p. 235-244. DOI: 10.1016/j.fuel.2019.04.003

16. Afanasev P.I., Makhmudov K.F. Assessment of the Parameters of a Shock Wave on the Wall of an Explosion Cavity with the Refraction of a Detonation Wave of Emulsion Explosives. *Applied Sciences*. 2021. Vol. 11. Iss. 9. N 3976. DOI: 10.3390/app11093976

17. Jinling Guo, Junlian Gao, Kejia Yan, Bo Zhang. Unintended mitigation benefits of China's coal de-capacity policies on methane emissions. *Energy Policy*. 2023. Vol. 181. N 113718. DOI: 10.1016/j.enpol.2023.113718

18. Gridina E.B., Kovshov S.V., Antonenko T.I., Miroshnichenco A.K. Development of fire safety measures aimed at preventing and responding to spontaneous combustion in brown coal mines. *Naukovyi Visnyk Natsionalnoho Hirnychoho Universytetu*. 2021. N 6, p. 96-101. DOI: 10.33271/NVNGU/2020-6/096

19. Gendler S.G., Stepantsova A.Yu., Mozzhanov D.B. Change of coal's gas content during transportation to the temporary storage. *Journal of Civil Protection.* 2024. Vol. 8. N 2, p. 188-198. DOI: 10.33408/2519-237X.2024.8-2.188

20. Vasilenko T., Kirillov A., Islamov A. et al. Permeability of a coal seam with respect to fractal features of pore space of fossil coals. *Fuel*. 2022. Vol. 329. N 125113. DOI: 10.1016/j.fuel.2022.125113

21. Li Kh.U., Mashchenko I.D., Belaventsev L.P., Shlapakov P.A. On petrographic method of coal sorption properties definition. *Industrial Safety.* 2012. N 1, p. 31-44 (in Russian).

22. Smirnyakov V.V., Smirnyakova V.V., Pekarchuk D.S., Orlov F.A. Analysis of methane and dust explosions in modern coal mines in Russia. *International Journal of Civil Engineering and Technology*. 2019. Vol. 10. Iss. 2, p. 1917-1929.

23. Kongar-Syuryun C., Klyuev R., Golik V. et al. Principles of Sustainable Development of Georesources as a Way to Reduce Urban Vulnerability. *Urban Science*. 2024. Vol. 8. Iss. 2. N 44. DOI: 10.3390/urbansci8020044

24. Dwivedi K.K., Chatterjee P.K., Karmakar M.K., Pramanick A.K. Pyrolysis characteristics and kinetics of Indian low rank coal using thermogravimetric analysis. *International Journal of Coal Science & Technology*. 2019. Vol. 6. Iss. 1, p. 102-112. DOI: 10.1007/s40789-019-0236-7

25. Litvinova T.E., Tsareva A.A., Poltoratskaya M.E., Rudko V.A. The mechanism and thermodynamics of ethyl alcohol sorption process on activated petroleum coke. *Journal of Mining Institute.* 2024. Vol. 268, p. 615-636.

26. Alpatova P.N., May Chan Myae Zaw The componential semantic reflection of Russian energy industry terms in scientific articles. *Research Journal in Advanced Humanities*. 2024. Vol. 5. Iss. 2, p. 29-40. DOI: 10.58256/d498dh32

27. Mustafin M.G. Modeling of rock massif geomechanical state at gas extraction from coal seams. *Journal of Mining Institute.* 2015. Vol. 216, p. 57-61 (in Russian).

28. Sikarev S.N., Adamov E.I., Smirnov S.G. Development of a mathematical model of behavior of air flows in the territory of open port coal warehouses. *Russian Journal of Water Transport.* 2020. N 62, p. 20-26 (in Russian). DOI: 10.37890/jwt.vi62.37

29. Goncharov E.V., Tsyrel S.V. Geodynamic methods for assessing methane distribution in bituminous coal deposits and measures to intensify methane fluxes during mine gas drainage. *Journal of Mining Institute.* 2016. Vol. 222, p. 803-808. DOI: 10.18454/PMI.2016.6.803

30. Safiullin R., Arias Z.P. Comprehensive Assessment of the Effectiveness of Passenger Transportation Processes using Intelligent Technologies. *Open Transportation Journal.* 2024. Vol. 18. N E26671212320514. DOI: 10.2174/0126671212320514240611100437

31. Gendler S.G., Vasilenko T.A., Stepantsova A.Yu. Investigation of mass transfer of hard coal during its transportation to the place of temporary storage. *Mining Informational and Analytical Bulletin.* 2023. N 9-1, p. 135-148 (in Russian). DOI: 10.25018/0236_1493_2023_91_0_135

32. Smirnov V.G., Manakov A.Y., Dirdin V.V. Activation energy for decomposition and formation of methane hydrates in pores of natural coal. *Bulletin of the Kuzbass State Technical University.* 2014. N 3 (103), p. 24-28 (in Russian).

33. Gaidarov B.A. Review of the key characteristics of experimental methods for coalbed methane diffusion coefficient measurement. *Trudy Instituta geologii Dagestanskogo nauchnogo tsentra RAN.* 2022. N 4 (91), p. 24-31 (in Russian). DOI: 10.33580/2541-9684-2022-91-4-24-31

34. Misnar A. Thermal conductivity of solids, liquids, gases and their compositions. Moscow: Mir, 1968, p. 459 (in Russian).

35. Starikov G.P., Yurchenko V.M., Melnik T.N. Activation of methane diffusion in coal under varied mechanical and thermodynamical parameters of a coal seam. *Physics and High Pressure Technology.* 2019. N 3, p. 122-130 (in Russian).

36. Haoran Song, Baiquan Lin, Zheng Zhong, Ting Liu. Experimental study on methane diffusion kinetics in three typical metamorphic coals. *Fuel*. 2022. Vol. 311. N 122601. DOI: 10.1016/j.fuel.2021.122601

37. Shaposhnik V.A. Activation energies of ion exchange processes. *Sorption and Chromatography Processes.* 2022. Vol. 22. N 5, p. 622-629 (in Russian). DOI: 10.17308/sorpchrom.2022.22/10683

Authors: **Semen G. Gendler,** *Doctor of Technical Sciences, Head of Department, https://orcid.org/0000-0002-7721-7246* (*Empress Catherine II Saint Petersburg Mining University, Saint Petersburg, Russia*), **Anastasiya Yu. Stepantsova,** *Postgraduate Student, s215060@stud.spmi.ru, https://orcid.org/0000-0002-5027-4742* (*Empress Catherine II Saint Petersburg Mining University, Saint Petersburg, Russia*), **Mikhail M. Popov,** *Candidate of Technical Sciences, Associate Professor, https://orcid.org/0000-0002-6857-7215* (*Empress Catherine II Saint Petersburg Mining University, Saint Petersburg, Russia*).

The authors declare no conflict of interests.

ISSN 2411-3336; e-ISSN 2541-9404

JOURNAL OF MINING INSTITUTE

Zapiski Gornogo instituta

Journal homepage: pmi.spmi.ru

Research article

Geotechnical Engineering and Engineering Geology

Determination of impact hazard potential of rocks in the Norilsk Industrial Region

Aleksandr P. Gospodarikov[1], **Mikhail A. Zatsepin**[1]✉, **Aleksandr P.Kirkin**[2]

[1] *Empress Catherine II Saint Petersburg Mining University, Saint Petersburg, Russia*

[2] *Gipronikel Institute LLC, Saint Petersburg, Russia*

***How to cite this article*:** Gospodarikov A.P., Zatsepin M.A., Kirkin A.P. Determination of impact hazard potential of rocks in the Norilsk Industrial Region. Journal of Mining Institute. 2025. Vol. 272. N 16498, p. 83-90.

Abstract

The deeper the mineral deposits developments are, the worse the mining and geological conditions become. Significant growth of stress level in the rock mass contributes to possible manifestation of rock pressure in dynamic form. The resulting task of assessment of rock impact hazard is closely related to the task of obtaining more accurate results of compression tests of samples in rigid or servohydraulic test presses using graphs of their full deformation. This approach requires special expensive equipment, considerable time resources, and sufficient core material. Therefore, it is important to have an approach that allows to assess the propensity of rocks to brittle fracture with research methods simple enough not to result in the loss of quality and reliability of the obtained results. This paper presents the results of laboratory tests of rocks from the Norilsk Industrial Region to determine their tensile and compressive strengths. Test methods involved both domestic and foreign standards for determining the value of the brittleness coefficient. The impact hazard potential of rocks was determined using the Kaiser criterion. It is found that the tested lithological types (rich sulfide ores, hornblende, disseminated ores, and gabbro-dolerite rocks), with the exception of anhydrite, have a low impact hazard potential.

Keywords

impact hazard potential; rock impact, rocks; Kaiser criterion; brittleness coefficient; uniaxial compression and tension; servohydraulic test press

Received: 17.05.2024 ***Accepted: 28.01.2025*** ***Online: 27.03.2025*** ***Published: 25.04.2025***

Introduction

Development of mineral deposits at great depths generally leads to more complicated geomechanical conditions [1-3] such as increased rock pressure, as well as increased risk of its dynamic manifestation [4-6]. For example, the depth of the Talnakh mine development in some areas today reaches more than 1000 m at the known critical depth of the impact hazard of 700 m [7-9]. At such great depths and consequently high stress values, the rock mass is characterized by the fracturing of its edge part, potentially manifested in brittle form with the release of elastic energy, i.e. in the form of a rock impact [10-12].

According to the recommended practices, it is necessary to identify areas in a rock mass where the possibility of rock impact is the highest, i.e. it is necessary to assess the propensity of rocks to brittle fracture [13-15]. One of the most accurate ways to assess the propensity of rocks to brittle fracture is the ratio of the elasticity modulus E to the decrease of material modulus M. Given the ratio $(E/M) > 1$, the test specimen is assumed as not vulnerable to impact, and in the case of $(E/M) \leq 1$, the test specimen is assumed as vulnerable to impact. Such an assessment requires compression tests on

specimens to obtain full deformation diagrams. This approach can be carried out on either rigid or servohydraulic test presses, taking into account the increase in the transverse strain rate [16-18]. Such tests require specialized equipment, a large time frame both for the tests and for logistics, and quality core material in sufficient quantity.

A rather simplified method for assessing the brittle fracture susceptibility of rocks is the method of Ya.A.Bich [19, 20], which consists in comparing the values of elastic and total deformations. In this case, the impact hazard coefficient is determined by the formula

$$k_{\text{imp}} = \frac{\varepsilon_{\text{el}}}{\varepsilon_{\text{tot}}},$$

where ε_{el} is deformations in the elastic zone; ε_{tot} is total deformations (before fracture).

A rock is considered impact hazardous at $k_{\text{imp}} > 0.7$. According to the recommended practices*, when determining the correlation between the value *E/M* and the impact hazard coefficient k_{imp}, it is allowed to carry out the number of tests for the sixth and subsequent specimens at pre-limit loads [21, 22].

Due to the large number of tests, the possibility of applying the well-known Kaiser criterion [23], which consists in determining the value of the impact hazard potential of rocks [24], seems quite promising. Application of this criterion requires only the results of the determination of the compressive and tensile strength of rocks. Thus, in this case, the propensity of rocks to brittle fracture is determined in a rather simple way, which allows us to obtain a quick assessment of the impact hazard potential of the studied rocks [25-27].

Research method

Studies of the rock impacts in Canadian mines have shown that the rock impact hazard can be estimated quite accurately using the indicator of rock impact hazard potential [23]. This indicator takes into account such parameters as UCS (uniaxial compressive strength) and the ratio of the compressive strength of rocks to their tensile strength UCS/UTS, defined as their brittleness coefficient [28].

It is known that the compressive strength of rocks is characterized by the energy accumulated in the rock mass up to the moment of its fracture: the higher limit of rock strength corresponds to large values of potential energy of elastic deformations and kinetic energy, which leads to dynamic destruction of the mass in the form of ejection of rock mass and distribution of individual rock pieces. Another important indicator of the propensity of rock to fracture as a result of thin plate detachment is the brittleness coefficient defined as the ratio of the compressive strength to the tensile strength of the examined rock samples (core material) [29].

While studying impact hazard of deposits located in the territory of the Russian Federation, this approach was successfully applied to ores and rocks of deposits of the Khibiny massif the and Novoshirokinskoe polymetallic ore deposit located in the Zabaikalsky Krai [30-32].

When carrying out underground mining operations at great depths in rocks with the potential for impact hazard, rock impacts are possible, and if there is no such potential, the probability of dynamic manifestation of rock pressure is close to zero [27, 28].

It should be noted that after obtaining the test results for determining the compressive and tensile strength of rocks, it is possible, by increasing the scale of the work performed, to obtain more reliable and statistically significant results. For this purpose, the results of laboratory tests for determining the physical and mechanical properties of ores and rock mass of two deposits of the Norilsk Industrial Region in 2018-2023 were used.

* Recommended practices for assessment of the propensity of ore and nonmetallic mineral deposits to rock impact. Approved by the Order 216 of the Federal Service for Environmental, Technological and Nuclear Supervision dated 23.05.2013.

Several types of ores and rocks of the Norilsk Industrial Region were considered for the assessment of the impact hazard potential (Table 1). These ores and rocks have been chosen because the first four lithological types for the Talnakh mines were classified as brittle fracture-prone rocks, according to the Federal Industrial Safety Standards and Regulations. It should be noted that anhydrite is not classified as an impact-prone rock in the Talnakh mines [33, 34].

Data obtained from uniaxial compression and tensile tests was used for assessment of the impact hazard potential of rocks and ores. The results according to GOST and ASTM (ISRM) were compared. Sample preparation and testing were performed according to GOST 21153.2-84 "Rocks. Methods of Determining Uniaxial Compressive Strength" and GOST 21153.3-85 "Rocks. Methods of Determining Uniaxial Tensile Strength". Determination of tensile strength is regulated by standards "ASTM D7012-14. Standard Test Methods for Compressive Strength and Elastic Moduli of Intact Rock Core Specimens under Varying States of Stress and Temperatures" and "ISRM Suggested Methods for Determining Tensile Strength of Rock Materials" [35, 36].

In the tests carried out according to the GOST regulated methods, the specimens had a ratio of height to diameter of 2:1 for compression and 1:1 for tension. For tests carried out according to foreign standards, the ratio of height to diameter for compression specimens was 2:1 and 2.5:1, for tensile specimens – 0.5:1. For the first sample, a series of tests was performed, including six specimens for compression, six specimens for tension, according to GOST, and four specimens for tension (as per ASTM). The obtained test results were averaged.

Laboratory test results

The experimental studies resulted in determining of the strength properties of five lithological types of ores and rocks of the Norilsk Industrial Region. The obtained results concerning the determination of the impact hazard potential of rocks and ores are summarized in Table 1.

Table 1

Distribution of the impact hazard potential of rocks and ores of the Norilsk Industrial Region

Indicator	Rich ores		Hornblende		Disseminated ores		Rock gabbro-dolerites		Anhydrites	
	I	II	I	II	I	II	I	II	I	II
Total samples	51		96		140		144		47	29
No potential, %	80.4	68.6	54.2	76.0	60.0	70.0	57.6	61.8	0.0	0.0
Low potential, %	15.7	27.5	40.6	23.0	33.6	27.1	36.1	34.0	0.0	0.0
Medium potential, %	3.9	3.9	5.2	1.0	6.4	2.9	5.6	4.2	0.0	0.0
High potential, %	0.0	0.0	0.0	0.0	0.0	0.0	0.7	0.0	0.0	0.0
Very high potential, %	0.0	0.0	0.0	0.0	0.0	0.0	0.0	0.7	0.0	0.0

Note. Method I – GOST, method II – ASTM.

Graphic distribution of samples is shown on Fig.1.

According to the obtained results, samples of all lithological types with the exception of anhydrite have a low level of impact hazard potential [37, 38]. At the same time, the ratio of non-impact-prone samples ranged from 54 to 80 %, depending on the lithology type and test methodology. These percentages are quite sufficient to classify these lithological types as impact-prone, since, according to the recommended practices, the minimum percentage of impact-prone rocks should be at least 10 %. The best matching of results from different methods is observed in the testing of rock gabbro-dolerites. Thus, in the case of rich ores, the number of samples with impact hazard potential was 12 % higher when tested by foreign methods compared with domestic ones. For disseminated ores and hornblende, the highest percentage of impact-prone samples was obtained when tested as per domestic methods. However, despite some discrepancies in the obtained proportions, no significant differences were observed [39, 40].

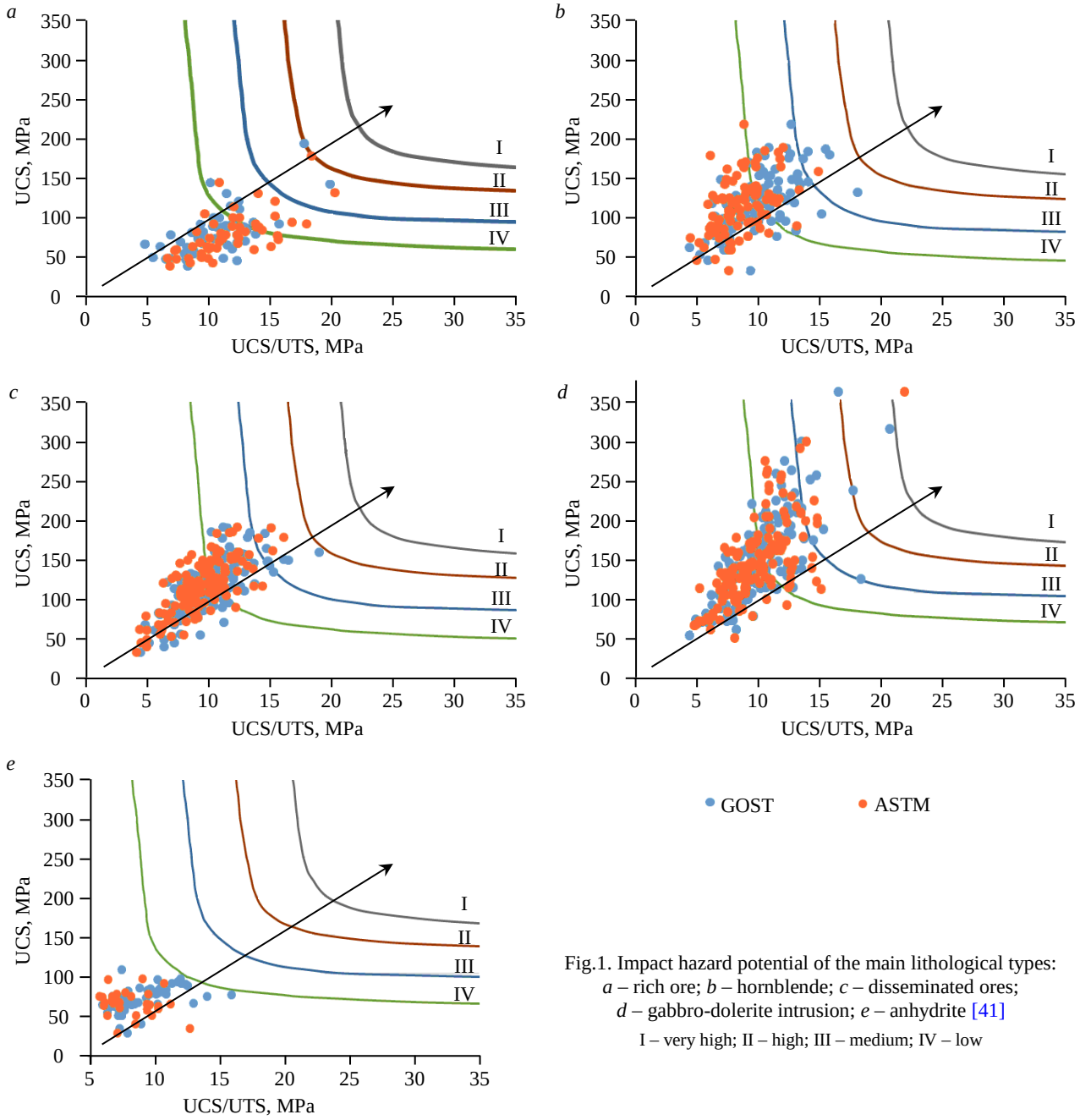

Fig.1. Impact hazard potential of the main lithological types: *a* – rich ore; *b* – hornblende; *c* – disseminated ores; *d* – gabbro-dolerite intrusion; *e* – anhydrite [41]

I – very high; II – high; III – medium; IV – low

As expected, anhydrites are non-impact-hazardous and, according to the results obtained, do not possess the potential of impact hazard.

The impact hazard of hornblende and gabbro-dolerites is conditioned mainly by their high compressive strength which can reach up to 300 MPa in a sample, while rich ores are characterized by a higher value of the brittleness coefficient (Table 2) compared to other rocks, which indicates the propensity of such rocks to spalling in thin plates as a result of their detachment (pressing off).

Table 2

Average value of brittleness coefficient of the studied lithological types

Method	Rich ore	Hornblende	Disseminated ores	Rock gabbro-dolerites
GOST	10.57/13.73*	9.85/11.98	9.63/11.93	9.29/11.59
ASTM	11.73/14.81	8.49/10.93	8.95/11.53	9.10/11.63

* All samples/impact hazardous samples.

Fig.2. Examples of ore delamination in the border zone under the action of high level stresses

Such a characteristic feature (high value of brittleness coefficient) is manifested in rich ores and in rock mass. Thus, during the development of mineral deposits at deep horizons, the border zone of the ore massif is pressed off, forming characteristic delaminations (Fig.2), while in other geological varieties such effect usually does not occur [42].

The average brittleness coefficient of anhydrites is not shown in Table 2, it amounted to 8.75; compressive strength did not exceed 105 MPa.

The same conclusion about the lower brittleness coefficient in the strongest rocks was also made in [30] when investigating the impact hazard potential of rocks at apatite-nepheline deposits.This is clearly presented in Fig.3, which shows the distribution of lithological types in the diagram according to the average values of brittleness coefficients and compressive strength (samples without impact hazard potential were not considered in this sample).

Thus, taking into the account the rock test results it can be determined that, despite the different nature of possible impact hazard, all the rocks considered with the exception of anhydrite are assigned a low level of impact hazard.

Laboratory studies carried out to assess the impact hazard of rich ores of the Norilsk Industrial Region by means of compression tests of samples in the mode of controlling the growth rate of transverse deformation [19], showed that they are impact hazardous. This confirms the possibility of using the Kaiser criterion to assess the impact hazard potential in the considered conditions.

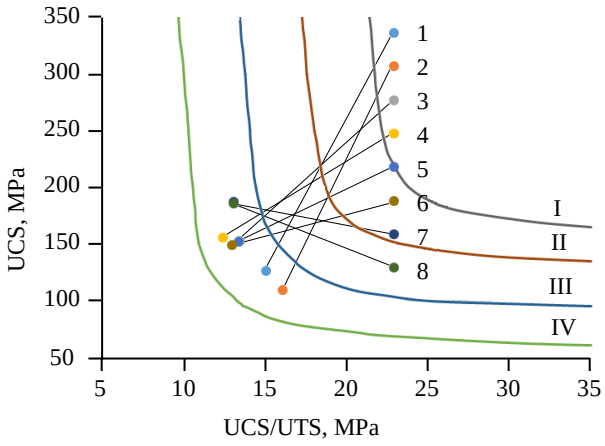

Fig.3. Average values of impact hazard potential of the studied lithological types: rich ore (1 – GOST, 2 – ASTM); hornblende (3 – GOST, 4 – ASTM); disseminated ores (5 – GOST, 6 – ASTM); rock gabbro-dolerites (7 – GOST, 8 – ASTM)

I-IV – see Fig.1

Conclusion

• As a result of tests using domestic and foreign methods, the strength properties of various rocks and ores of the Norilsk Industrial Region have been determined and the values of their brittleness coefficients have been calculated.

• Using the Kaiser criterion, it was found that the percentage of non-impact-prone samples varied from 54 to 80 % depending on the type of lithology and testing methodology, which

confirms the propensity to dynamic fracture of rocks of the Norilsk Industrial Region. The highest percentage of impact-prone samples obtained during hornblende testing according to Russian methods amounted to almost half of the tested samples. The best matching between the methods used was observed when testing rock gabbro-dolerites. The obtained research results reflected a sufficient qualitative convergence between domestic and foreign methods.

• It is noted that rich ores have the lowest compressive strength than other impact-prone rock types, but at the same time have the highest brittleness coefficient, which indicates their tendency to spalling in the form of thin plates. The latter fact is confirmed by the results of field studies in mines, where ore plates were pressed off under high stress levels from the border zone of the rock mass.

• It is determined that the studied lithological types with the exception of anhydrite have a low impact hazard potential. There is no impact hazard potential of anhydrites, i.e. they are non-impact-prone.

To assess the impact hazard of rich ores of the Norilsk Industrial Region using the Kaiser criterion, a broad comparison with the results of compression tests of samples in the mode of controlling the growth rate of transverse deformation was carried out. The comparison confirmed that the rich ore is impact hazardous.

REFERENCES

1. Rybak J., Khayrutdinov M.M., Kuziev D.A. et al. Prediction of the geomechanical state of the rock mass when mining salt deposits with stowing. *Journal of Mining Institute.* 2022. Vol. 253. p. 61-70. DOI: 10.31897/PMI.2022.2

2. Hongpu Kang, Pengfei Jiang, Yongzheng Wu, Fuqiang Gao. A combined "ground support-rock modification-destressing" strategy for 1000-m deep roadways in extreme squeezing ground condition. *International Journal of Rock Mechanics and Mining Sciences*. 2021. Vol. 142. N 104746. DOI: 10.1016/j.ijrmms.2021.104746

3. Jian Zhou, Chao Chen, Kun Du et al. A new hybrid model of information entropy and unascertained measurement with different membership functions for evaluating destressability in burst-prone underground mines. *Engineering with Computers*. 2022. Vol. 38. Iss. 1 Suppl, p. 381-399. DOI: 10.1007/s00366-020-01151-3

4. Konicek P., Schreiber. Rockburst prevention *via* distress blasting of competent roof rocks in hard coal longwall mining. *Journal of the Southern African Institute of Mining and Metallurgy*. 2018. Vol. 118. N 3, p. 235-242. DOI: 10.17159/2411-9717/2018/v118n3a6

5. Tyupin V.N. Estimation of Critical Depth of Deposits by Rock Bump Hazard Condition. *Journal of Mining Institute.* 2019. Vol. 236, p. 167-171. DOI: 10.31897/PMI.2019.2.167

6. Sidorov D.V., Potapchuk M.I., Sidlyar A.V., Kursakin G.A. Assessment of Rock-Burst Hazard in Deep Layer Mining at Nikolayevskoye Field. *Journal of Mining Institute.* 2019. Vol. 238, p. 392-398. DOI: 10.31897/PMI.2019.4.392

7. Pleshko M.S., Davydov A.A., Silchenko Yu.A., Kaledin O.S. Effective lining solutions for super-deep shaft SKS-1 in Skalisty mine in difficult geomechanical conditions. *Gornyi zhurnal.* 2020. N 6, p. 57-62 (in Russian). DOI: 10.17580/gzh.2020.06.08

8. Sergunin M.P., Alborov A.E., Andreev A.A., Buslova M.A. Stress assessment ahead of stoping front with widening stress relief zone – A case study of the Oktyabrsky and Talnakh deposits. *Gornyi zhurnal.* 2020. N 6, p. 38-41 (in Russian). DOI: 10.17580/gzh.2020.06.06

9. Balandin V.V., Leonov V.L., Kuranov A.D., Bagautdinov I.I. Application of generalized Hoek – Brown criterion to selection and design of mine support systems for the Oktyabrsky copper-nickel deposit: Case study. *Gornyi zhurnal.* 2019. N 11, p. 14-18 (in Russian). DOI: 10.17580/gzh.2019.11.01

10. Zakalinsky V.M., Mingazov R.Y., Shipovskii I.E. The influence of mining and technological factors on drilling and blasting operations during the development of deposits at great depth. *Problems of Subsoil Use.* 2022. N 2 (33), p. 46-54 (in Russian). DOI: 10.25635/2313-1586.2022.02.046

11. Aleksandrova T.N., Afanasova A.V., Kuznetsov V.V., Babenko T.A. Process analysis of selective disintegration of Zapolyarny copper–nickel ore. *Mining Informational and Analytical Bulletin.* 2021. N 12, p. 73-87 (in Russian). DOI: 10.25018/0236_1493_2021_12_0_73

12. Aleksandrova T.N., Chanturiya A.V., Kuznetsov V.V. Mineralogical and technological features and patterns of selective disintegration of ferruginous quartzites of the Mikhailovskoye deposit. *Journal of Mining Institute.* 2022. Vol. 256, p. 517-526. DOI: 10.31897/PMI.2022.58

13. Pershin G.D., Pshenichnaya E.G., Mazhitov A.M. Energy criteria for quasi-brittle fracture of rocks in technological processes of mining and primary processing. *Russian Mining Industry.* 2022. N 2, p. 84-89 (in Russian). DOI: 10.30686/1609-9192-2022-2-84-89

14. Korchak P.A., Karasev M.A. Geomechanical prediction of the brittle fracture zones in rocks in the vicinity of the excavation junction of Ltd "Apatit" mines. *Sustainable Development of Mountain Territories.* 2023. Vol. 15. N 1 (55), p. 67-80 (in Russian). DOI: 10.21177/1998-4502-2023-15-1-67-80

15. Sonnov M.A., Trofimov A.V., Rumyantsev A.E., Shpilev S.V. Application of Numerical and Block Geomechanical Modelling to Determine Parameters of Large-Section Chambers. *Russian Mining Industry.* 2021. N 2, p. 127-131 (in Russian). DOI: 10.30686/1609-9192-2021-2-127-131

16. Ulusay R., Hudson J.A.The Complete ISRM Suggested Methods for Rock Characterization, Testing and Monitoring: 1974-2006. International Society for Rock Mechanics, Commission on Testing Methods, 2007, p. 628.

17. Protosenya A.G., Belyakov N.A., Bouslova M.A. Modelling of the stress-strain state of block rock mass of ore deposits during development by caving mining systems. *Journal of Mining Institute.* 2023. Vol. 262, p. 619-627.

18. Morozov K.V., Demekhin D.N., Bakhtin E.V. Multicomponent strain gauges for assessing the stress-strain state of a rock mass. *Mining Informational and Analytical Bulletin.* 2022. N 6-2, p. 80-97 (in Russian). DOI: 10.25018/0236_1493_2022_62_0_80

19. Gospodarikov A.P., Trofimov A.V., Kirkin A.P. Evaluation of deformation characteristics of brittle rocks beyond the limit of strength in the mode of uniaxial servohydraulic loading. *Journal of Mining Institute.* 2022. Vol. 256, p. 539-548. DOI: 10.31897/PMI.2022.87

20. Bich Ya.A., Melkov A.D., Dyakonov Yu.Ya. Prevention of rock impacts in development of anthracite seams. Moscow: Nedra, 1993, p. 159 (in Russian).

21. Subrahmanyam D.S. Evaluation of Hydraulic Fracturing and Overcoring Methods to Determine and Compare the In Situ Stress Parameters in Porous Rock Mass. *Geotechnical and Geological Engineering*. 2019. Vol. 37. Iss. 6, p. 4777-4787. DOI: 10.1007/s10706-019-00937-7

22. Krietsch H., Gischig V., Evans K. et al.Stress Measurements for an In Situ Stimulation Experiment in Crystalline Rock: Integration of Induced Seismicity, Stress Relief and Hydraulic Methods. *Rock Mechanics and Rock Engineering*. 2019. Vol. 52. Iss. 2, p. 517-542. DOI: 10.1007/s00603-018-1597-8

23. Ming Cai, Kaiser P.K. Rockburst Support. Reference Book. In 2 volumes. Vol. 1: Rockburst Phenomenon and Support Characteristics. Sudbury: Laurentian University, 2018, p. 284.

24. Aynbinder I.I., Ovcharenko O.V. Potential rockburst hazard research at the project mining depth at the Valunistoe deposit. *Mining Informational and Analytical Bulletin.* 2022. N 6, p. 35-45 (in Russian). DOI: 10.25018/0236_1493_2022_6_0_35

25. Aleksandrova T., Nikolaeva N., Afanasova A. et al. Selective Disintegration Justification Based on the Mineralogical and Technological Features of the Polymetallic Ores. *Minerals*. 2021. Vol. 11. Iss. 8. N 851. DOI: 10.3390/min11080851

26. Winn K. Multi-approach Geological Strength Index (GSI) Determination for Stratified Sedimentary Rock Masses in Singapore. *Geotechnical and Geological Engineering*. 2020. Vol. 38. Iss. 2, p. 2351-2358. DOI: 10.1007/s10706-019-01149-9

27. Samsonov A.A. Assessment of rock mass state of Oleniy Ruchey rock burst deposit based on the results of stress measurements. *Herald of the Kola Science Centre of RAS.* 2019. N 1 (11), p. 62-67 (in Russian). DOI: 10.25702/KSC.2307-5228.2019.11.1.62-67

28. Závacký M., Štefaňák J. Strains of rock during uniaxial compression test. *The Civil Engineering Journal*. 2019. Vol. 28. N 3, p. 398-403. DOI: 10.14311/CEJ.2019.03.0032

29. Biryuchev I.V., Makarov A.B., Usov A.A. Geomechanical model of underground mine. Part II. Application. *Gornyi zhurnal.* 2020. N 2, p. 35-44 (in Russian). DOI: 10.17580/gzh.2020.02.04

30. Kuznetcov N.N., Kondrashov L.Yu. Rockburst hazard potential assessment of rocks of the Khibiny massif deposits according to the Kaiser criterion. *Vestnik of MSTU.* 2023. Vol. 26. N 2, p. 170-179 (in Russian). DOI: 10.21443/1560-9278-2023-26-2-170-179

31. Eremenko A.A., Shaposhnik Yu.N., Filippov V.N., Konurin A.I. Development of scientific framework for safe and efficient geotechnology for rockburst-hazardous mineral deposits in Western Siberia and the Far North. *Gornyi zhurnal.* 2019. N 10, p. 33-39 (in Russian). DOI: 10.17580/gzh.2019.10.03

32. Bertuzzi R. Revisiting rock classification to estimate rock mass properties. *Journal of Rock Mechanics and Geotechnical Engineering*. 2019. Vol. 11. Iss. 3, p. 494-510. DOI: 10.1016/j.jrmge.2018.08.011

33. Marysyuk V.P., Shilenko S.Yu., Trofimov A.V., Kuzmin S.V. Risk assessment in main ore chute construction in difficult geological conditions based on integrated geotechnical research. *Gornyi zhurnal.* 2020. N 1, p. 62-66 (in Russian). DOI: 10.17580/gzh.2020.01.12

34. Marysyuk V.P., Shilenko S.Yu., Andreev A.A., Shabarov A.N. Interwell area design procedure to generate safe zones in rockburst-hazardous conditions of Talnakh deposits. *Gornyi zhurnal.* 2023. N 1, p. 106-112 (in Russian). DOI: 10.17580/gzh.2023.01.18

35. Saadatmand Hashemi A., Katsabanis P. Tunnel face preconditioning using destress blasting in deep underground excavations. *Tunnelling and Underground Space Technology*. 2021. Vol. 117. N 104126. DOI: 10.1016/j.tust.2021.104126

36. Kozyrev A.A., Kuznetsov N.N., Fedotova Iu.V., Shokov A.N. The determination of rockburst hazard degree of hard rocks by the test results under uniaxial compression. *News of the Higher Institutions. Mining Journal.* 2019. N 6, p. 41-50 (in Russian). DOI: 10.21440/0536-1028-2019-6-41-50

37. Kovalevsky V.N., Mysin A.V. Performance of tubular elastic charges in natural stone production. *Mining Informational and Analytical Bulletin.* 2023. N 1, p. 20-34 (in Russian). DOI: 10.25018/0236_1493_2023_1_0_20

38. Zubov V.P., Than Van Duy, Fedorov A.S. Technology of underground mining of thick coal seams with low strength properties. *Ugol.* 2023. N (5), p. 41-49 (in Russian). DOI: 10.18796/0041-5790-2023-5-41-49

39. Verbilo P., Karasev M., Belyakov N., Iovlev G. Experimental and numerical research of jointed rock mass anisotropy in a three-dimensional stress field. *Rudarsko-geološko-naftni zbornik.* 2022. Vol. 37. N 2, p. 109-122. DOI: 10.17794/rgn.2022.2.10

40. Vennes I., Mitri H., Chinnasane D.R., Yao M. Effect of Stress Anisotropy on the Efficiency of Large-Scale Destress Blasting. *Rock Mechanics and Rock Engineering*. 2021. Vol. 54. Iss. 1, p. 31-46. DOI: 10.1007/s00603-020-02252-7

41. Kirkin A.P. Impact hazard management of solid sulfide ore mass by drilling and blasting in conditions of complex stress state: Avtoref. dis. … kand. tekhn. nauk. St. Petersburg: Saint Petersburg Mining University, 2023, p. 22 (in Russian).

42. Marinin M.A., Karasev M.A., Pospekhov G.B. et al. Engineering and geological parameters for heap leaching of gold from low-grade sandy clay ores: a feasibility study. *Mining Informational and Analytical Bulletin.* 2023. N 9, p. 22-37 (in Russian). DOI: 10.25018/0236_1493_2023_9_0_22

***Authors*: Aleksandr P. Gospodarikov,** *Doctor of Engineering Sciences, Head of Department,* *https://orcid.org/0000-0003-1018-6841* (*Empress Catherine II Saint Petersburg Mining University, Saint Petersburg, Russia*), **Mikhail A. Zatsepin,** *Candidate of Physics and Mathematics, Associate Professor, zatsepin_ma@pers.spmi.ru,* *https://orcid.org/0000-0002-6304-8349* (*Empress Catherine II Saint Petersburg Mining University, Saint Petersburg, Russia*), **Aleksandr P. Kirkin,** *Candidate of Engineering Sciences, Senior Researcher,* *https://orcid.org/0000-0002-4830-8042* (*Gipronikel Institute LLC, Saint Petersburg, Russia*).

The authors declare no conflict of interests.

ISSN 2411-3336; e-ISSN 2541-9404

JOURNAL OF MINING INSTITUTE

Zapiski Gornogo instituta

Journal homepage: pmi.spmi.ru

Research article

Geotechnical Engineering and Engineering Geology

The effect of mechanical and thermal treatment on the characteristics of saponite-containing material

Tatyana N. Orekhova[1], **Mariana N. Sivalneva**[1]✉, **Mariya A. Frolova**[2], **Valeriya V. Strokova**[1], **Diana O. Bondarenko**[1]

[1] *Belgorod State Technological University named after V.G.Shukhov, Belgorod, Russia*

[2] *Northern (Arctic) Federal University named after M.V.Lomonosov, Arkhangelsk, Russia*

***How to cite this article*:** Orekhova T.N., Sivalneva M.N., Frolova M.A., Strokova V.V., Bondarenko D.O. The effect of mechanical and thermal treatment on the characteristics of saponite-containing material. Journal of Mining Institute. 2025. Vol. 272. N 16487, p. 91-99.

Abstract

Solving the problems of modern building materials science is reduced to obtaining high-quality materials, expanding and searching for a rational raw material base, which can be carried out through the use of various industrial wastes. In this paper, the possibility of using waste from the mining industry – saponite-containing material (SCM) obtained during the enrichment of kimberlite ores from the Lomonosov diamond deposit, as an active mineral additive for cement binders and concretes is considered. The influence of mechanical and thermal treatment on a number of properties of the material selected from the tailings dump and in its initial state was studied. The study of the surface activity of SCM samples consisted in determining the sorption capacity, acid-base centers and their distribution. An increase in the activity of the surface of the material particles as a result of mechanical activation and its decrease during temperature treatment were determined. These effects are associated with phase rearrangements and structural changes in the sandy-clay rock, which was confirmed during thermal analysis. The temperature effect has no pronounced effect on the microstructure, the "smoothness" of the particles and the formation of a consolidated surface of the structural elements of the saponite-containing material are noted.

Keywords

saponite-containing material; ore dressing waste; surface activity; mechanical activation; firing

Funding

The work was carried out within the framework of the implementation of the State task of the Ministry of Education and Science of the Russian Federation N FZWN-2023-0006 using the equipment of the High Technology Center of BSTU named after V.G.Shukhov.

Received: 08.05.2024 ***Accepted: 07.11.2024*** ***Online: 12.12.2024*** ***Published: 25.04.2025***

Introduction

Construction materials science in modern conditions is focused on the production of high-quality materials while achieving effective technical and economic indicators. The search for rational solutions makes it possible to expand the raw material base, which can be carried out by using secondary products of various industries and industrial waste.

Waste of man-made origin, in particular from the mining industry, is an important source of raw materials for the construction materials industry (CMI). About 40 billion t of such waste, of which at least 30 % of overburden and tailings of enrichment, almost all metallurgical and fuel slags, are potential raw materials for the CMI industry [1]. The volume of waste increases annually, is stored and occupies huge areas. Mining waste can reasonably be considered a backup reserve of the raw material base of the Russian Federation, equivalent to the opening of new deposits. Despite the huge resource potential as a source of raw materials and the possibility of reducing pressure on the environment, they have not found the proper degree of application in our country, they are used irrationally and in small quantities.

In foreign countries, the level of waste involvement in economic turnover is much higher and has some application experience. Many developed countries are focusing their policies on energy and resource conservation, actively implementing the practice of recycling man-made waste and developing new technological solutions through reuse in various industries. For example, the leaders in waste recycling are the USA and Japan, the share of waste in the total raw material balance of these Countries is about 26 %, in most economically developed countries this indicator ranges from 16-20 %, in the USSR it was 15 %, in modern Russia – about 10 % [1, 2]. Secondary use resources are gaining momentum in other countries [3-6] (Canada, Great Britain, South Africa, Spain, India, etc.)*.

Representatives of the M.V.Lomonosov NARFU Scientific School, together with AO Severalmaz and scientists of BSTU named after V.G.Shukhov, are actively conducting research on one of the types of waste from the mining industry – saponite-containing material (SCM), which is a secondary product of the enrichment of kimberlite ores from the Lomonosov diamond deposit of the AO Severalmaz processing plant (Arkhangelsk region), for its use in the production of building materials [7]. Technologies for the use of SCM in the manufacture of ceramic tiles, mineral wool materials, magnesia and composite binders have already been developed [8-11]. The paper proposes to expand the range of SCM applications in the building materials industry, as the largest in terms of consumed raw materials and manufactured products, through the development of an active mineral additive for cement binders and concretes.

The specificity of the composition and properties of SCM has predetermined a fairly wide range of areas of its use, in addition to CMI. Thus, this secondary product is used as a base for drilling mud [12], as a sorbent for cleaning industrial wastewater [13], for waterproofing in the construction of landfills for storing solid household waste, radioactive burial grounds and for wastewater filtration, as well as in medicine and resort business [14]. Saponite occupies a special place in agriculture as a mineral additive to feed and fertilizers, filler and granulant, is used for soil detoxification, sorption of herbicides and pesticides introduced into the soil, heavy metals, etc. [14].

Saponite-containing material is a sandy-clay rock in a watered state (with a humidity of at least 60 %) and has:

• mineralogical composition – the main component is saponite (60-70 %), the remaining mass of the rock is quartz, montmorillonite, palygorskite, phlogopite, clinochlorite, talc, dolomite;

• the chemical composition – the main oxides are SiO_2 (53 %), MgO (17 %), Fe_2O_3 (10 %), Al_2O_3 (9 %), CaO (4 %) [8].

The process of enrichment of clay rock requires a large amount of water consumption. The presence of raw materials in a suspended state makes it difficult for its further use in the construction industry, difficulties in separating the solid fraction do not allow the use of water as a circulating water due to the low degree of purification [12, 13, 15-17]. In this regard, it is necessary to select the method and parameters of processing the raw materials that allow the rational and effective use of SCM in the building materials industry.

It is known that mechanical activation affects not only the dispersion characteristics of the raw material, but also the properties of its surface [18-21], increasing the activity for subsequent interaction of the material components [22, 23].

Due to the affiliation of SCM to clay minerals, the effect of temperature treatment should be considered. The use of burnt clays as mineral additives in cement systems has a fairly long history [24-27]. This component is characterized by increased activity, which is due to the processes caused by temperature exposure and associated with the formation of primary dehydration products and the destruction of clay minerals, which leads to a restructuring of the crystal lattice. It is noted that the main clay minerals (kaolinite, montmorillonite, illite, bentonite, etc.) pass into the active form

* Cement Statistics and Information. URL: https://www.usgs.gov/centers/national-minerals-information-center/cement-statistics-and-information (accessed 08.05.2024).

precisely at a temperature of 200±600 °C [25, 26, 28, 29]. When referring to saponite-containing material isolated from a recycled water suspension, it was found that modification transformations stop at a temperature of 900 °C, the effect of which leads to a change in a number of properties – an increase in true density, a decrease in specific surface area, porosity, and water absorption [8, 30].

The structure of saponite, which acts as the main mineral of the waste from the enrichment of kimberlite ores, is represented by a three-layer structure with an expanding crystal lattice, which allows moisture to be sorbed. Saponite has rather weak bonds between the layers, which are formed by Van der Waals forces. As a result, the process of grinding raw materials can be accompanied by modification of the resulting powder. Mechanical action contributes to the transformation of the crystal lattice of the material [22], followed by a transition to a two-layer serpentine structure [25]. Serpentine itself can also be an effective component of building materials [31, 32]. Further high-temperature treatment leads to the modification of serpentine into forsterite [30]. Thus, a chain of mineral transformations is built as a result of mechanical and thermal treatment (Fig.1). Initially, mechanical grinding of saponite-containing raw materials intensifies the stages of the chemical transformation process, and increasing the duration of the grinding unit allows increasing the quantitative yield of serpentine and, as a result, forsterite.

To determine the nature of the effect of SCM emission technology on its properties, it is necessary to investigate the effect of mechanical and thermal effects on the initial suspension selected from the tailings before the insertion of various flocculants and other substances.

Methods

The paper considers the potential possibility of using saponite-containing material as a mineral additive for concrete. The suspension was studied in the initial (i.e., watered rock of sandy-clay composition), as well as mechanically activated dried and burnt states.

The SCM was dried to a constant mass in a drying cabinet with a thermostat at a temperature of 70 °C. Next, dry grinding was carried out to a highly dispersed state in a laboratory ball mill with uralite grinding media to eliminate the possibility of milling (usually happens in metal mills). The specific surface area was measured by the PSKh-11M(SP) device, which uses the generally accepted in world practice method of Kozeni – Karman gas permeability.

The temperature treatment was carried out in a muffle furnace at 700 °C, the choice of temperature regime was consistent with the known data.

The reactivity of [33-35] saponite-containing raw materials based on:

• sorption capacity determined by the Zaporozhets method by changing the concentration of $Ca(OH)_2$ in a saturated solution due to the absorption of lime by SCM particles. The amount of $Ca(OH)_2$ in the solution was determined by titration with a solution of hydrochloric acid with a concentration of 0.05 N. The amount of absorbed calcium hydroxide (1 mg per 1 g of the test substance) from the lime solution was estimated by the difference between the initial and final concentrations. In this case, the measurements were carried out at specified time intervals (1; 3; 6; 24 and 30 h from the moment of introduction of the test material into the lime solution), selected according to the required measurement accuracy and the specifics of the samples;

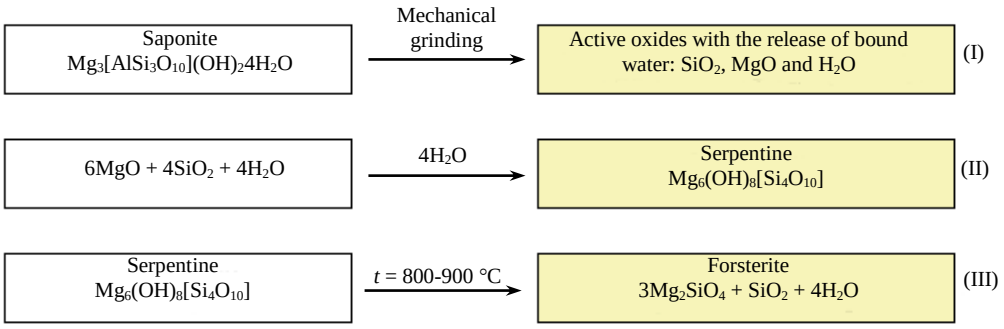

Fig.1. Schemes of mineral transformations [30]

• acid-base properties that allow to evaluate changes in surface characteristics by using the indicator method of distribution of adsorption centers (DAC) and the theory of Bronsted – Lowry and Lewis. The point of the method is that various acidic and basic centers on the surface of a solid selectively adsorb indicator molecules. The study of the surface properties of a solid substance implies the determination of the concentration of active centers of *q*pKa, equivalent to the amount of adsorbed indicator of the acidic strength of pKa. The results obtained make it possible to regulate and predict the mechanism of physical and chemical processes on the surface of a solid.

When determining the activity, three parallel measurements of the selected samples were performed, the error between the obtained values was 2-3 %.

Using the NETZSCH synchronous thermal analysis device STA 449 F1 Jupiter, which allows combining the methods of differential scanning calorimetry (DSC) and thermogravimetry (TG), a sample of the initial SCM, dried to a constant mass, was studied in the temperature range of 25-1200 °C. The method is based on recording the difference in heat fluxes coming from the test and reference samples. The heat flow is measured as the temperature difference at two points of the measuring system at a certain point in time. Measurements of heat and mass fluxes were carried out under completely identical conditions.

The microstructure of the SCM was studied using the Mira 3 FesSem scanning electron microscope (Tescan). The shooting took place in high vacuum discharge mode.

Discussion of the results

A specific surface area of 165 m^2/kg, optimal for this type of equipment (ball mill), was determined for the dried initial SCM containing clay and sand components. The grinding time was 40 min. Longer grinding is not effective, since there is no significant increase in the specific surface area, but energy consumption increases significantly.

To determine the sorption capacity of the samples after mechanical activation, the activity and dynamics of absorption of lime $Ca(OH)_2$ from a solution of a sub-sample material were studied. In order to detail the result, SCM samples were studied at all stages of grinding – after 10, 20, 30 and 40 min.

Based on the results obtained, it can be concluded that with an increase in the specific surface area, the volume of lime absorbed from the solution ($Ca(OH)_2$) increases. The activity for samples crushed for 40 min is 69.2 mg/g, which is 6 % higher than for crushed at 10 min, and 39 % higher than for dried SCM (without grinding – 0 min). The positive dynamics is caused by mechanical activation, which is an affordable and effective way to increase the activity of mineral dispersed materials [23, 34].

Due to the obvious positive effect of mechanical activation on the value of the sorption capacity, samples of the control composition (initial sample, without grinding) and crushed within 40 min after firing were fired.

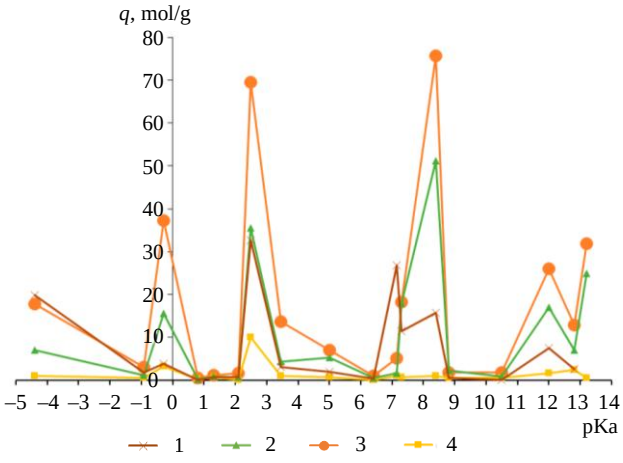

Fig.2. Distribution of adsorption centers on the surface of the SCM after mechanical and thermal exposure

1 – without grinding; 2 – grinding for 10 min; 3 – grinding for 40 min; 4 – grinding for 40 min + firing

Temperature treatment helps to reduce the activity of the material by 5.7 %, compared with the material after 40 min of grinding, which is caused by the interaction of the components during firing, the processes of destruction of the crystalline lattice of the clay fraction.

To analyze the acid-base properties of the surface, SCM samples were studied, dried and selected at different stages of grinding: control – without grinding, at the initial point of grinding – grinding for 10 min, at the final point – grinding for 40 min, as well as a sample after mechanical activation for 40 min and firing at 700 °C (Fig.2).

Over the entire range of the pKa scale, the surface of the SCM sample has the highest concentration of active centers after 40 min of grinding. Their

predominance in the area of Bronsted centers is noted: for Bronsted acids (pKa = 2.5) – 70 mmol/g, for bases (pKa = 8.4) – 75 mmol/g. The sample after 10 min of grinding is characterized by a decrease in activity by 32 % (pKa = 8.4). This fact has a logical explanation. Mechanical activation for 10 min is not sufficient to achieve high dispersion and a highly developed surface, as at 40 min, when an optimal specific surface is reached and longer grinding is not required. The mechanically activated and fired SCM sample has a minimum number of active centers in all areas. This correlation of values is maintained when calculating the total number of adsorption centers (Table 1).

Table 1

The number of adsorption centers of different nature on the surface of the SCM particles

SCM sample	Number of adsorption centers, mmol/g, ±2			
	Lewis bases	Bronsted acids	Bronsted bases	Total number
Without grinding	25.5	39.7	64.9	130.1
Grinding for 40 min	58.3	94.6	141.9	294.8
Grinding 40 min + firing	4.9	13.0	7.8	25.6
Grinding for 10 min	23.7	47.5	98.2	169.5

Thus, an increase in the activity of the surface of SCM particles as a result of mechanical activation and its decrease during temperature treatment associated with phase rearrangements and structural changes of sandy-clay rock were noted.

A study of the reactivity of saponite-containing raw materials in the initial and pretreated state (grinding, firing) was carried out. For a detailed assessment of the results, a comparison of these indicators with traditional components of natural and man-made origin currently used as mineral pozzolan additives is presented (Table 2): natural silica-containing raw materials – quartz sand, granite, silica clay, perlite; man-made raw materials – ash of Nazarovskaya TPP (Krasnoyarsk region) and Troitskaya SDPP (Chelyabinsk region).

It should be noted that acid-base properties are presented selectively, only in the area of Bronsted acid centers, which mainly determine the growth of activity.

According to the Table 2 the studied samples of SCM have sufficiently high activity indicators comparable to the activity results for natural and man-made materials used as pozzolan additives.

Table 2

Comparison of the reactivity indicators of traditional and investigated components of mineral pozzolan additives

Raw materials components	Method of treatment	Concentration of Bronsted acid centers, mmol/g	Sorption capacity, mg/g	Source
Sand	Dry grinding	33.5	33.5	[36]
Granite		36.3	27.9	
Silica clay		22.3	53.1	
Perlite		35.3	30.2	
Ash of the Nazarovskaya TPP	–	4.4	1.0	[37]
Ash of Troitskaya SDPP		45.4	3.0	
SCM	–	39.7	49.5	Author's data
	Dry grinding (40 min)	94.6	69.2	
	Dry grinding (40 min) + firing	13.0	65.1	
	Dry grinding (10 min)	47.5	65.2	

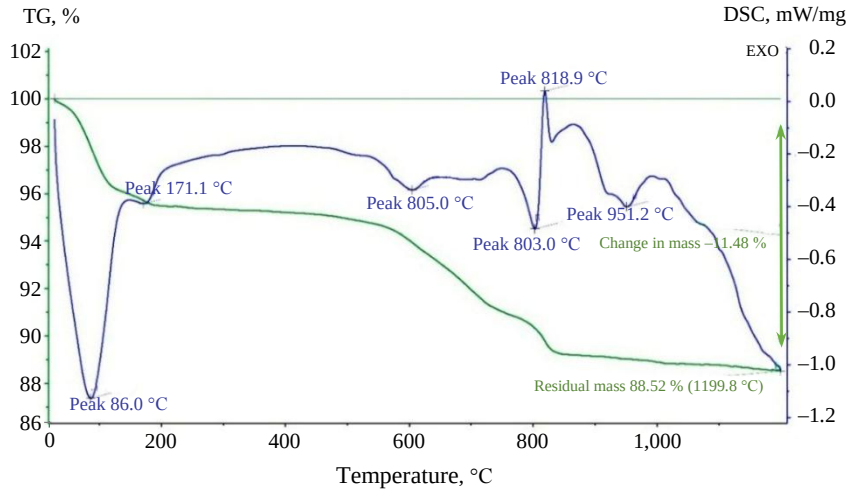

Fig.3. Thermogram of the SCM sample

Thermal analysis methods are based on the course of various chemical transformations in materials when they are heated, which are usually accompanied by a change in mass. During this type of research, the sample of the initial SCM was dried to a constant mass and tested in the temperature range of 25-1,200 °C.

The thermogram obtained (Fig.3) shows the presence of thermal effects. The course of endothermic processes occurs at peaks, the minima of which correspond to temperatures of 86; 171; 605; 803; 819 and 951 °C.

The presence of the first peak (86 °C), representing an endothermic thermal effect, is associated with the removal of adsorption-bound water. It is with this fact that the choice of the temperature value for drying saponite suspension samples is 70 °C, due to the possibility of minimizing structural changes and preserving the initial parameters and characteristics of the material. The second peak (171 °C) is also characterized by an endoeffect and corresponds to the removal of interplane/interpack water.

A small endothermic peak was noted at 575 °C (it is not indicated on the thermogram), which is associated with the transition of low-temperature α-quartz SiO_2 to high-temperature β-quartz.

Peaks of 605 and 803 °C, as well as peaks of insignificant size at a temperature of about 700 °C (not indicated in Fig.3) are endothermic effects corresponding to the dehydroxylation of serpentine, which in the form of various modifications is part of the saponite-containing material [30]. Its formation can be caused by the formation of the active form of magnesium and silicon oxides in an aqueous dispersion medium. The most pronounced peak of the exothermic thermal effect corresponds to 819 °C, associated with the formation of high-temperature forsterite from serpentine (this peak also means that the dehydration of serpentine has ended). The results obtained are confirmed by previously performed studies [8, 30]. At the end of heating, the particles of the saponite-containing material gradually sinter.

Thermogravimetric analysis records a mass loss curve depending on temperature changes. The total mass loss of the sample is 11.48 %. At a temperature range of 200-600 °C, a section of the plateau is marked, which demonstrates sufficient stability and the absence of chemical transformations. A sharp drop in the gravimetric curve indicates the chemical decomposition of the material.

The study of the microstructure of a material is one of the informative research methods that allows identifying the structural features of an object, determining the dimensional parameters of individual elements, the shape and morphology of the particle surface, observe the interaction of system components, the formation of new structures, defects, etc. With regard to raw materials for the production of building materials, these studies in combination with physical and chemical methods of substance analysis allow to make a predictive assessment of the effectiveness of using certain components in the composition of polymineral polydisperse raw materials mixtures, as well as to explain the results obtained analytically.

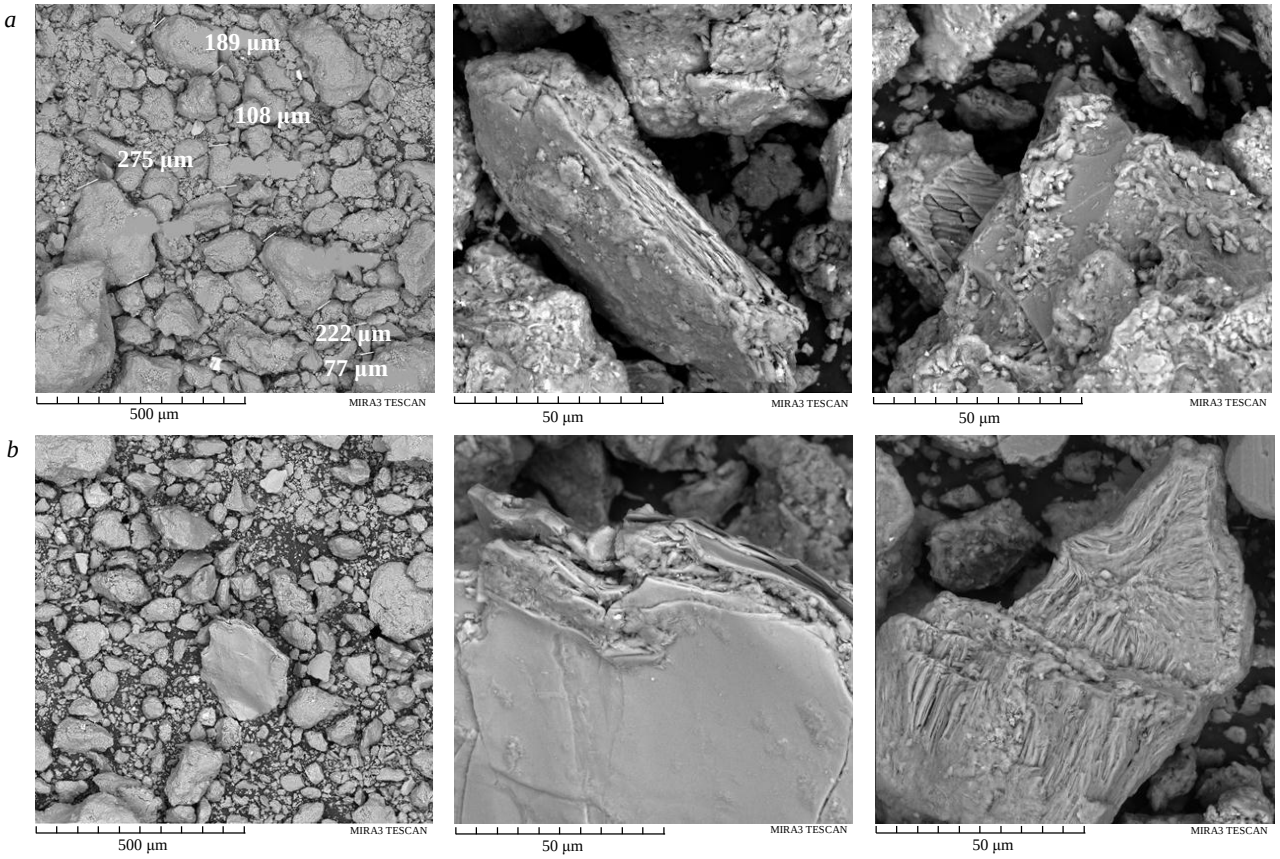

Fig.4. The microstructure of the SCM:
a – mechanically activated; *b* – mechanically activated and thermally treated

The microstructure was studied on similar samples of dried SCM after mechanical and thermal treatment. It follows from the analysis of the images that the bulk of the sample of mechanically activated SCM is composed of polydisperse particles of sandy and clay components (Fig.4, *a*). Quartz particles with a size of up to 300 μm are the largest. The morphology of the particles is angular, with a shell-like fracture typical of quartz. Quartz mineral grains have varying degrees of roughness. There is a "pouring" of clay aggregates onto quartz particles. Clay particles are well identified by their characteristic plate-like shape and layered structure. The layers of clay minerals are formed mainly by thin leaf-like structures tightly adjacent to each other.

The general character of the microstructure of the SCM samples after temperature exposure is preserved and ensured by the presence of a polydisperse system of granular quartz particles and clay aggregates of plate-like shape (Fig.4, *b*). The difference from the samples before heat treatment consists in the purchase by the material of some consolidated surface of the particles of the SCM.

Based on the microscopic analysis of the SCM samples in the form of mechanically activated and burnt dispersed powder, it was determined that the bulk of the material is composed of quartz grains with an angular fracture and plate-like particles of clay minerals with different layering.

Conclusion

The article considers the possibility of using saponite-containing material, which is a waste product of the enrichment of kimberlite ores during diamond mining at the Lomonosov deposit, as an active mineral additive for cement binders and concretes. For this purpose, the influence of mechanical and thermal treatment on a number of properties of the material selected from the tailings dump and in its initial state was evaluated.

The study of the surface activity of SCM samples was reduced to determining the sorption capacity, acid-base centers, and their distribution and allowed to determine the increase in the surface

activity of material particles as a result of mechanical activation and its decrease during temperature treatment, which is associated with phase rearrangements and structural changes of sandy-clay rock.

As a result of the thermal analysis method, endothermic thermal effects associated with the removal of adsorption-bound and interplane water, the transition of low-temperature α-quartz SiO_2 to high-temperature β-quartz, the dehydroxylation of serpentine and the subsequent formation of high-temperature forsterite were revealed.

Microscopic analysis indicates the predominance of the bulk of the material from quartz grains and plate-like particles of clay minerals with different layering. The temperature effect has no pronounced effect, there is some "smoothing" and consolidation (sintering) of the surface of the structural elements of the saponite-containing material.

REFERENCES

1. Larichkina F.D., Knysha V.A. Rational use of secondary mineral resources in the context of Ecologization and the introduction of the best available technologies.Apatity: Izd-vo FITs KNTs RAS, 2019, p. 252.
2. Vinslav Yu.V., Lisov S.V., Lunjkin A.N. For efficient management of mineral-raw material complex in Russia: problems of subsurface use. *Russian Economic Journal.* 2017. N 3, p. 37-60 (in Russian).
3. Marrocchino E., Zanelli C., Guarini G., Dondi M. Recycling mining and construction wastes as temper in clay bricks. *Applied Clay Science*. 2021. Vol. 209. N 106152. DOI: 10.1016/j.clay.2021.106152
4. Vo T.L., Nash W., Del Galdo M. et al. Coal mining wastes valorization as raw geomaterials in construction: A review with new perspectives. *Journal of Cleaner Production*. 2022. Vol. 336. N 130213. DOI: 10.1016/j.jclepro.2021.130213
5. Benahsina A., El Haloui Y., Taha Y. et al. Substitution of natural clay by Moroccan solid mining wastes to manufacture fired bricks. *Materials Today: Proceedings*. 2022. Vol. 58. Part 4, p. 1324-1330. DOI: 10.1016/j.matpr.2022.02.211
6. Dod R.D., Dhodare S.S., Bhandari J. et al. Extraction of sand from the complex matrix of coal mining dump waste: A sustainable approach in Indian context. *Cleaner Materials*. 2024. Vol. 12. N 100243. DOI: 10.1016/j.clema.2024.100243
7. Pashkevich M.A., Alekseenko A.V. Reutilization Prospects of Diamond Clay Tailings at the Lomonosov Mine, Northwestern Russia. *Minerals*. 2020. Vol. 10. Iss. 6. N 517. DOI: 10.3390/min10060517
8. Malygina M.A., Ayzenshtadt A.M., Drozdyuk T.A. et al. Structural modification of saponite-containing material during its mechanical dispersion. *Construction Materials.* 2022. N 9, p. 32-38 (in Russian). DOI: 10.31659/0585-430X-2022-806-9-32-38
9. Buravchuk N.I., Guryanova O.V., Parinov I.A. Use of technogenic raw materials in ceramic technology. *Open Ceramics*. 2024. Vol. 18. N 100578. DOI: 10.1016/j.oceram.2024.100578
10. Migunthanna J., Rajeev P., Sanjayan J. Waste Clay Bricks as a Geopolymer Binder for Pavement Construction. *Sustainability*. 2022. Vol. 14. Iss. 11. N 6456. DOI: 10.3390/su14116456
11. Juenger M.C.G., Winnefeld F., Provis J.L., Ideker J.H. Advances in alternative cementitious binders. *Cement and Concrete Research*. 2011. Vol. 41. Iss. 12, p. 1232-1243. DOI: 10.1016/j.cemconres.2010.11.012
12. Zubkova O.S., Pankratieva K.A. Complex processing of saponite ore of the Lomonosovsky diamond deposit. *Achievements in chemistry and chemical technology*. 2021. Vol. 35. N 8 (243), p. 129-130 (in Russian).
13. Zubkova O.S., Pyagay I.N., Pankratieva K.A., Toropchina M.A. Development of composition and study of sorbent properties based on saponite. *Journal of Mining Institute.* 2023. Vol. 259, p. 21-29. DOI: 10.31897/PMI.2023.1
14. Kosareva E.N., Kabachkova N.V., Romanov E.M., Shabanova E.N. The use of saponite-containing materials as fertilizers in the cultivation of potatoes. *Bulletin of the Russian State Agrarian Correspondence University*. 2018. N 28 (33), p. 11-20 (in Russian).
15. Oblicov A.Yu. Some aspects of utilization of high-clay enrichment waste. *Mining Informational and Analytical Bulletin.* 2013. N 7, p. 390-392 (in Russian).
16. Alexeev A.I., Zubkova O.S., Polyanskiy A.S. Improving the technology of enrichment of saponite ore in the process of diamond mining. *Bulletin of Higher Educational Institutions. North Caucasus region. Technical Sciences.* 2020. N 1 (205), p. 74-80 (in Russian). DOI: 10.17213/1560-3644-2020-1-74-80
17. Jones T.R., Poitras J., Paterson D., Southam G. Historical diamond mine waste reveals carbon sequestration resource in kimberlite residue. *Chemical Geology*. 2023. Vol. 617. N 121270. DOI: 10.1016/j.chemgeo.2022.121270
18. Stroganov V., Sagadeev E., Ibragimov R., Potapova L. Mechanical activation effect on the biostability of modified cement compositions. *Construction and Building Materials*. 2020. Vol. 246. N 118506. DOI: 10.1016/j.conbuildmat.2020.118506
19. Sanchez F., Sobolev K. Nanotechnology in concrete – A review. *Construction and Building Materials*. 2010. Vol. 24. Iss. 11, p. 2060-2071. DOI: 10.1016/j.conbuildmat.2010.03.014
20. Sadique M., Al-Nageim H., Atherton W. et al. Mechano-chemical activation of high-Ca fly ash by cement free blending and gypsum aided grinding. *Construction and Building Materials*. 2013. Vol. 43, p. 480-489. DOI: 10.1016/j.conbuildmat.2013.02.050
21. Sharmin S., Sarker P.K., Biswas W. et al. Characterization of waste clay brick powder and its effect on the mechanical properties and microstructure of geopolymer mortar. *Construction and Building Materials*. 2024. Vol. 412. N 134848. DOI: 10.1016/j.conbuildmat.2023.134848
22. Ayzenshtadt A., Strokova V., Nelyubova V. Physical and chemical characteristics of the surface of powders of saponite-containing material after its mechanical dispersion. *Physics and Chemistry of Materials Treatment.* 2024. N 1, p. 53-64 (in Russian). DOI: 10.30791/0015-3214-2024-1-53-64
23. Alfimova N.I., Kalatozi V.V., Karacupa S.V. et al. Mechanical activation as a way of improving the efficiency use of raw materials of different genesis in building materials science. *Bulletin of Belgorod State Technological University named after V.G.Shukhov.* 2016. N 6, p. 85-89 (in Russian).

24. Fernandez R., Martirena F., Scrivener K.L. The origin of the pozzolanic activity of calcined clay minerals: A comparison between kaolinite, illite and montmorillonite. *Cement and Concrete Research*. 2011. Vol. 41. Iss. 1, p. 113-122. DOI: 10.1016/j.cemconres.2010.09.013

25. Sabir B.B., Wild S., Bai J. Metakaolin and calcined clays as pozzolans for concrete: a review. *Cement and Concrete Composites*. 2001. Vol. 23. Iss. 6, p. 441-454. DOI: 10.1016/S0958-9465(00)00092-5

26. Balykov A.S., Nizina T.A., Volodin V.V., Korovkin D.I. Strength of cement stone with mineral additives based on calcined clay and carbonate rocks. *Expert: Theory and Practice*. 2020. N 4 (7), p. 26-30 (in Russian). DOI: 10.24411/2686-7818-2020-10031

27. Volodin V.V., Balykov A.S., Nizina T.A et al. The activity of a mixed cement binder with additives of thermally activated clays. Young scientists – development of the National Technology Initiative (POISK): sbornik materialov Natsionalnoi molodezhnoi nauchno-tekhnicheskoi konferentsii, 22-24 aprelya 2020, Ivanovo, Russia. 2020. N 1, p. 779-782.

28. van Jaarsveld J.G.S., van Deventer J.S.J., Lukey G.C. The effect of composition and temperature on the properties of fly ash- and kaolinite-based geopolymers. *Chemical Engineering Journal*. 2002. Vol. 89. Iss. 1-3, p. 63-73. DOI: 10.1016/S1385-8947(02)00025-6

29. Gerasimov A.M., Eremina O.V. Application microwave radiation for directional changes of layered silicates properties. *Eurasian Mining*. 2021. N 1, p. 55-60. DOI: 10.17580/em.2021.01.11

30. Drozdyuk T., Frolova M., Ayzenshtadt A. et al. Preliminary Study on the Mechanical Activation and High-Temperature Treatment of Saponite-Containing Tailings Generated during Kimberlite Ore Dressing. *Applied Sciences*. 2022. Vol. 12. Iss. 10. N 4957. DOI: 10.3390/app12104957

31. Jain A., Agrawal V., Gupta R. Using serpentine in concrete: A literature review. *Materials Today: Proceedings*. 2023, p. 5. DOI: 10.1016/j.matpr.2023.03.138

32. Zinchuk N.N. Specific features of kimberlites serpentinization. *Proceedings of Voronezh State University. Series: Geology*. 2017. N 3, p. 66-74 (in Russian).

33. Shekhovtsova J., Zhernovsky I., Kovtun M. et al. Estimation of fly ash reactivity for use in alkali-activated cements – A step towards sustainable building material and waste utilization. *Journal of Cleaner Production*. 2018. Vol. 178, p. 22-33. DOI: 10.1016/j.jclepro.2017.12.270

34. Yadykina V.V., Trautvain A.I. The influence of the active filler based on the technogenic siliceous raw materials on the strength cement systems. *Fundamental Research*. 2015. N 5, p. 174-179 (in Russian).

35. Skvortsova L.N., Chukhlomina L.N., Minakova T.S., Sherstoboeva M.V. Investigation of acid-base and sorption properties of surface of metal–ceramic composites. *Russian Journal of Applied Chemistry*. 2017. Vol. 90. N 8, p. 1246-1251. DOI: 10.1134/S1070427217080092

36. Nelyubova V.V., Strokova V.V., Danilov V.E., Aizenshtadt A.M. Comprehensive activity analysis of silicacontaining raw materials for use in mechanical activation efficiency evaluations. *Obogashchenie rud*. 2022. N 2, p. 17-25 (in Russian). DOI: 10.17580/or.2022.02.03

37. Markov A.Yu., Strokova V.V., Markova I.Yu. Evaluation of properties of fuel ashes as components of composite materials. *Construction Materials*. 2019. N 4, p. 77-83 (in Russian). DOI: 10.31659/0585-430X-2019-769-4-77-83

Authors: **Tatyana N. Orekhova,** *Candidate of Engineering Sciences, Associate Professor, https://orcid.org/0000-0002-8284-9811 (Belgorod State Technological University named after V.G.Shukhov, Belgorod, Russia)*, **Mariana N. Sivalneva,** *Candidate of Engineering Sciences, Associate Professor, 549041@mail.ru, https://orcid.org/0000-0002-4957-9207 (Belgorod State Technological University named after V.G.Shukhov, Belgorod, Russia)*, **Mariya A. Frolova,** *Candidate of Chemical Sciences, Associate Professor, https://orcid.org/0000-0003-4079-5066 (Northern (Arctic) Federal University named after M.V.Lomonosov, Arkhangelsk, Russia)*, **Valeriya V. Strokova,** *Doctor of Engineering Sciences, Head of Department, https://orcid.org/0000-0001-6895-4511 (Belgorod State Technological University named after V.G.Shukhov, Belgorod, Russia)*, **Diana O. Bondarenko,** *Candidate of Engineering Sciences, Associate Professor, https://orcid.org/0000-0001-9708-2791 (Belgorod State Technological University named after V.G.Shukhov, Belgorod, Russia)*.

The authors declare no conflict of interests.

ISSN 2411-3336; e-ISSN 2541-9404

JOURNAL OF MINING INSTITUTE
Zapiski Gornogo instituta
Journal homepage: pmi.spmi.ru

Research article *Geotechnical Engineering and Engineering Geology*

Laboratory studies of hydraulic fracturing of intersecting boreholes in a non-uniform stress field

Andrey V. Patutin ✉, Aleksandr A. Skulkin, Leonid A. Rybalkin, Andrey N. Drobchik
Chinakal Institute of Mining, Siberian Branch of the RAS, Novosibirsk, Russia

How to cite this article: Patutin A.V., Skulkin A.A., Rybalkin L.A., Drobchik A.N. Laboratory studies of hydraulic fracturing of intersecting boreholes in a non-uniform stress field. Journal of Mining Institute. 2025. Vol. 272. N 16319, p. 100-109.

Abstract
This study focuses on the features of hydraulic fracture propagation in intersecting boreholes in polymethyl methacrylate blocks in a non-uniform stress field. Glycerol aqueous solution and plasticine were used as the working fluids. According to linear fracture mechanics, a stress concentrator at the borehole intersection contributes to the beginning of crack formation, with further crack propagation occurring in the plane containing their axes. The relevance of this study is due to the search for innovative approaches and the development of technological solutions to address the issue of effective longitudinal crack formation and its further propagation in a rock mass under unfavourable stress field conditions. This paper provides a scheme of laboratory stand operation and a general view of the sealing packers used to isolate a specified interval when performing tests. The graphs of glycerol pressure versus injection time are presented, and the breakdown pressure in the blocks is specified. The shape of fractures formed during the indentation of plasticine into the borehole system was investigated. The findings of physical modelling indicate that longitudinal cracks are predominantly formed in the boreholes. The deviation of the crack trajectory from the vertical plane containing the borehole axes is primarily affected by the magnitude of the horizontal compressive stress field rather than the increase in the angle between them. In addition, the angles of inclination of the longitudinal crack plane measured at its intersection with the side face of the block are specified.

Keywords
hydraulic fracture; artificial block; stress state; laboratory experiment

Funding
The study was supported by the Russian Science Foundation and the Government of the Novosibirsk region, project N 22-27-20061.

Received: 02.10.2023 ***Accepted: 07.11.2024*** ***Online: 20.03.2025*** ***Published: 25.04.2025***

Introduction

The emergence and development of hydraulic fracturing (HF) is closely associated with enhanced oil recovery from producing wells [1-4]. This approach is commonly used due to the relatively straightforward underlying principle. The final shape of a crack in rocks largely depends on the direction and magnitude of compressive stresses [5, 6]. During hydraulic fracturing operations conducted at significant depths commonly observed in numerous oil and gas fields, the possible orientation of the resulting cracks is limited by the maximum vertical stress. In such conditions, the initiation of a longitudinal crack in a vertical well or a radial transverse crack in a horizontal well is most often observed.

The implementation of the HF method in mines is complicated by some features. The challenge in accurately predicting the path of cracks to be formed is due to high horizontal stresses [7, 8] as well as the impact of nearby underground workings and inseam boreholes on the stress state of the rocks. Additionally, there are various tasks to be tackled, such as intensifying the methane drainage from coal seams

[9-12], controlling hard roof collapse [13-16], protecting underground workings from pressure filtration [17], and conducting in situ stress measurements [18-21]. Of interest are methodological and technical solutions aimed at increasing heavy oil production by hydraulic fracturing in the Yaregskoye field, which is developed using the thermal mining method [22].

Increasing the efficiency of the mine modification of the HF method requires establishing the features of crack propagation in a non-uniform stress field in laboratory conditions. Most testing systems used for these purposes are specifically engineered to analyze the initiation of cracks in a core subjected to axial loading and uniform compression along its side surface [23-25]. Such experimental setups do not accurately replicate the reservoir conditions and do not allow addressing the problems characteristic of underground mining.

The increasing popularity of laboratory units that can subject cubic samples to true triaxial loading is driven by the need for reliable results in hydraulic fracturing physical modelling [26, 27]. Such cubic samples should be sufficiently large, with an edge length of 150-200 mm or more, to exclude the influence of edge effects on crack propagation and to incorporate models of underground working or several boreholes.

The results of previous studies demonstrate that the crack path can be controlled in several ways. For example, it is possible to use various technical means for cutting initiating slots on borehole walls [28], performing directional loading or unloading in the target interval [29, 30], creating additional cracks in advance to alter the local stress field [31], or changing the properties of the working agent [32] and parameters of its injection into the rock mass [33, 34]. In addition, crack growth direction is influenced by various factors, such as the complex geometry perforation of the casing, the specific arrangement of several boreholes of different directions, and the presence of additional sidetracks.

One promising way to create longitudinal cracks is to perform HF in intersecting boreholes. Cracks are assumed to grow in the plane containing their axes. A similar approach was used in the development of directional hydraulic fracturing technology, which involves the creation of several radial boreholes of small diameter from a vertical one and further injection of working fluid into the formed system [35]. It has been shown that a crack is highly likely to initiate in the plane formed by radial boreholes, regardless of the stress field within the massif. Additionally, the influence of the relative position of radial boreholes on fracture propagation was studied [36]. The experimental results demonstrate that increasing the angle between the borehole axis and the direction of maximum stress results in a higher breakdown pressure.

A similar solution for the in-mine hydraulic fracturing of a coal seam yielded a high convergence of the results of mathematical modelling and experimental measurements [37]. The application of the developed technology was found to reduce the breakdown pressure and allow the direction of the initial growth of cracks to be controlled.

This study investigates the possibility of longitudinal crack formation between intersecting boreholes in a stress field unfavourable for its propagation. During the experiments, such a field was created by applying the maximum stress perpendicular to the plane containing the borehole axes.

Methods

A laboratory system was developed and implemented to study the HF process in cubic blocks. This system was installed on the basis of a hydraulic press PG-100. Presented below are the specifics regarding the operation of the system. The sample compression in a horizontal plane in two orthogonal directions is performed using four flat jacks DN10P10 with a load capacity of 10 tf installed in a load-bearing frame. A similar jack is fixed on the upper part of the frame to provide loading along the vertical axis. The sample can be independently loaded in a triaxial fashion by connecting the jacks separately to the high-pressure manual pump. A more comprehensive description of the laboratory system design can be found in [38, 39]. A schematic diagram of the system is illustrated in Fig.1, *a*.

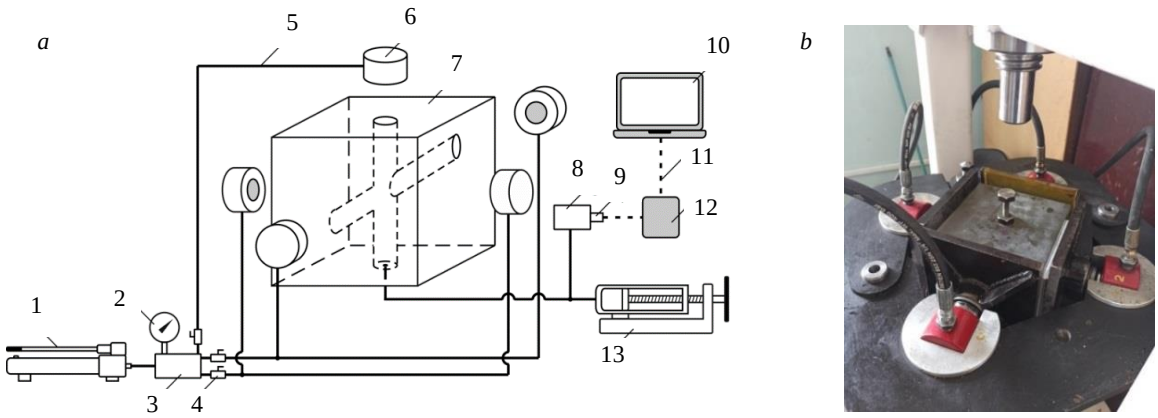

Fig.1. A schematic diagram of the laboratory system (*a*) and a plexiglass block in a testing cell prepared for indentation of plasticine (*b*)

1 – manual pump; 2 – pressure gauge; 3, 8 – collectors; 4 – shut-off valve; 5 – high-pressure pipelines; 6 – hydraulic flat jack; 7 – sample with intersecting boreholes; 9 – pressure sensor; 10 – laptop computer; 11 – data communication channel; 12 – pressure data logger; 13 – mechanical syringe pump

The collection and recording of data during the experiments were conducted using a pressure sensor, specifically the MIDA-PI-51P, which was connected to a data logger through a cable. The logger is equipped with a 24-bit analogue-to-digital converter (ADC), which allows the signal to be transmitted to a laptop via Bluetooth for further processing and visualization [40].

Physical modelling of hydraulic fracturing was performed in artificial blocks made of polymethyl methacrylate (plexiglass) with an edge length of 180 mm. Two factors influenced the choice of materials for this study. The first is optical transparency, which facilitates accurate control of crack growth without the need for additional technical means. The second is the brittle fracture that occurs when a crack propagates in the plexiglass. This fracture is characterized by the absence of any significant plastic component, making it possible to exclude its effect on the final crack path. The analysis can then focus only on the impact of compressive stresses and the angle between intersecting boreholes. The combination of these features and the similarity of the mechanical properties of plexiglass (compressive strength of about 70 MPa) and rock massif, led to its widespread use in HF modeling in laboratory conditions [41-43].

Two intersecting boreholes with a diameter of 14 mm were created in each block. One of the boreholes was vertical, with the other forming an angle γ of 30 or 60 deg. The bottom of the inclined borehole was inside the block, with its head sealed by a device equipped with two rubber rings (Fig.2, *a*) [44].

Fig.2. Sealing device for isolating an inclined borehole (*a*) and a double packer tool (*b*)

Two different working fluids were used in the laboratory experiment: a coloured aqueous solution of distilled glycerol (GOST 6824-96) and plasticine. In the first case, a vertical borehole was drilled through the sample, and the fracturing interval was isolated by a special double packer tool (Fig.2, *b*). Glycerol was injected using a mechanical syringe pump. In the second case, the distance from the bottom of the vertical borehole to the lower face of the block was approximately 20 mm. The plasticine was pressed by tightening the bolt, with a thread created in the upper part of the borehole (see Fig.1, *b*). Figure 3 displays the location and type of boreholes in the block, depending on the working fluid used and the direction of compressive stresses [44].

In accordance with the main purpose of laboratory tests, S_{xx} was specified as the maximum compressive stress in the experiment. The excess of this particular stress over the others affects the rate of rotation and the deviation of the formed longitudinal fracture from the plane defined by the intersecting boreholes. The features of hydraulic fracture propagation in a similar problem statement were investigated using numerical analysis [45] and physical modelling on sand concrete samples [46]. Table 1 provides the angles γ for all manufactured blocks, the loading conditions during the physical modelling process, and the working fluid used for HF [44].

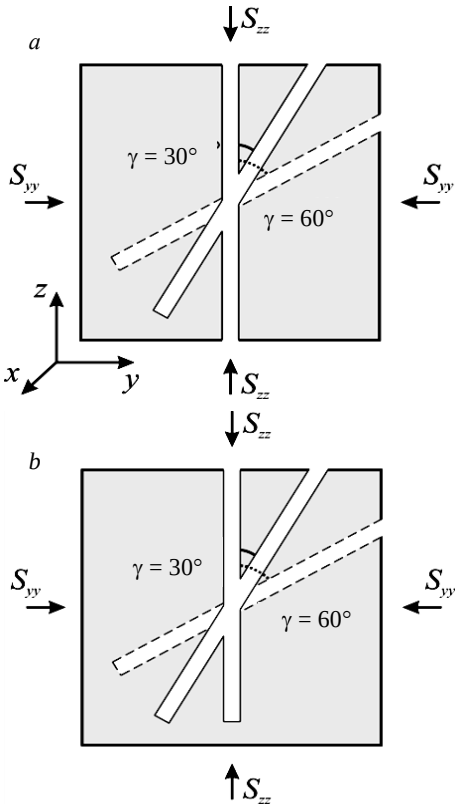

Fig.3. The location and type of boreholes in the block during fracturing with glycerol (*a*) and plasticine (*b*) in a compressive stress field

Table 1

The main characteristics of the blocks and experimental parameters

Block number	Angle γ, deg	Loading conditions, MPa			Working fluid
		S_{xx}	S_{zz}	S_{yy}	
1	30	1.3	1.0	1.0	Glycerol
2	60	1.3	1.0	1.0	Glycerol
3	30	1.3	0	1.0	Plasticine
4	60	1.3	0	1.0	Plasticine
5	30	1.5	0	1.0	Plasticine
6	60	1.5	0	1.0	Plasticine

Results and discussion

During the hydraulic fracturing of block 1, two independent cracks were formed within the boreholes and partially merged near the stress concentrator (Fig.4, *a*, *b*). The resulting fracture exhibited a distinct deviation from the plane encompassing the axes of the boreholes, with glycerol leakage observed on the lower face of the block. The breakdown pressure, P_b, observed during the experiment was 11.9 MPa, with the residual pressure measuring 0.6 MPa at the end of the test.

In block 2, the crack was formed at a fairly high pressure of 33.5-37.2 MPa (residual pressure of 0.81 MPa), which is almost three times higher than that recorded for block 1. This significant discrepancy can be attributed to variations in the borehole wall conditions and the structural features of specific blocks. At the same time, a rather clear longitudinal fracture connecting both boreholes was formed in block 2 due to virtually no differences between the horizontal stresses S_{xx} and S_{yy} for such a high value of P_b pressure (Fig.4, *c*, *d*). With the deviation of the crack plane from the vertical of 10 deg, the crack was visually observed to extend to the side and bottom faces of the block [44].

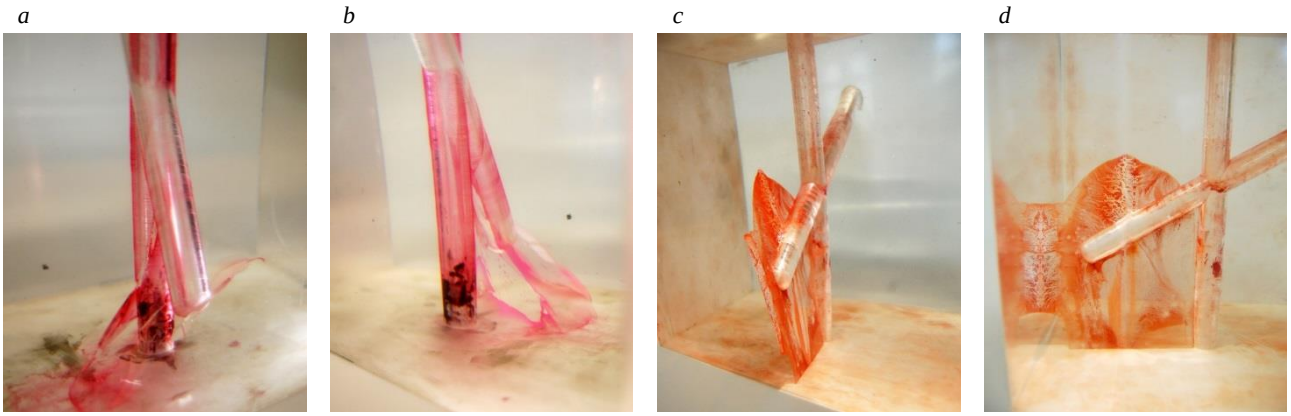

Fig.4. The photographs of the cracks formed during the injection of glycerol in block 1 (*a*, *b*) and block 2 (*c*, *d*)

Glycerol injection pressure graphs for the cases described are shown in Fig.5. The injection rate was kept constant at approximately 10 ml/min.

The observed pressure change in block 1 implies that the packers were deformed and compressed from the load chamber before the crack formation, resulting in a minor depressurization of the interval isolated by the packers (Fig.5, *a*). When a maximum pressure of 37.2 MPa was reached in block 2, the leakage of working fluid from the fracturing interval through the packers was also observed. Following the cessation of the leakage, a subsequent rise in glycerol pressure due to its injection by a mechanical syringe pump produced a crack at 33.5 MPa (see Fig.5, *b*). A lower pressure value may be associated with irreversible microdestruction of the material around the borehole [47].

In a series of tests, plasticine as the working fluid was indented through the vertical borehole at $S_{zz} = 0$. The procedure involved placing and tightly packing the plasticine into intersecting boreholes, followed by installing the sealing device into the inclined borehole and tightening the metal bolt along the thread previously cut on the vertical borehole wall. The gradual introduction of plasticine into the cracks caused enough pressure to break the plexiglass. The breakdown pressure was not recorded.

During the experiments conducted on blocks 3 and 4, the compressive stress ratio was found to be $S_{xx} = 1.3S_{yy}$. During the injection of plasticine, crack formation began in both boreholes, and then the growing cracks merged into a single longitudinal fracture (Fig.6). Special attention should be given to the intricate geometry of the resulting cracks, their curvature, and twisting around the borehole, with these effects being more pronounced when $\gamma = 60°$. The results of other laboratory studies provided evidence for the creation of branched fracture systems from a single borehole with increasing viscosity of the working fluid [48].

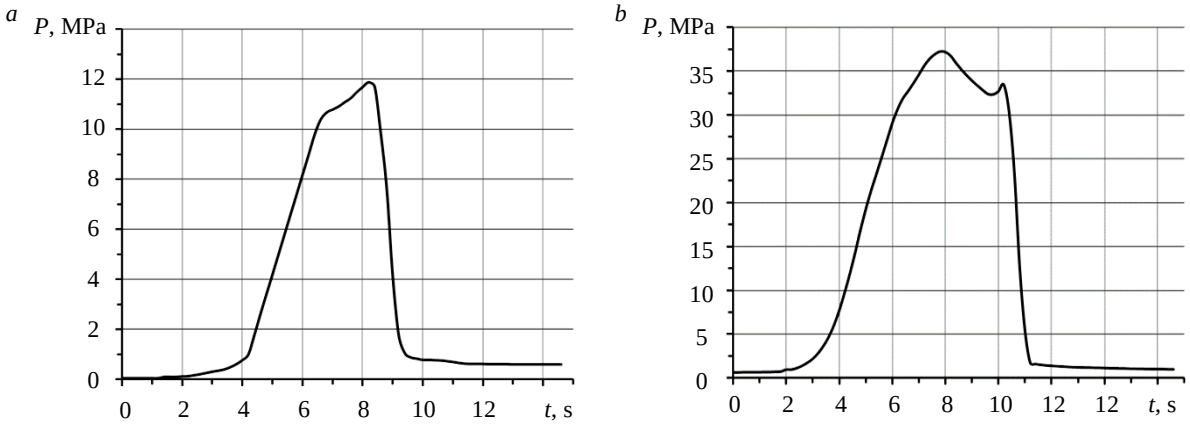

Fig.5. Glycerol injection pressure graphs as a function of injection time *t* for block 1 (*a*) and block 2 (*b*)

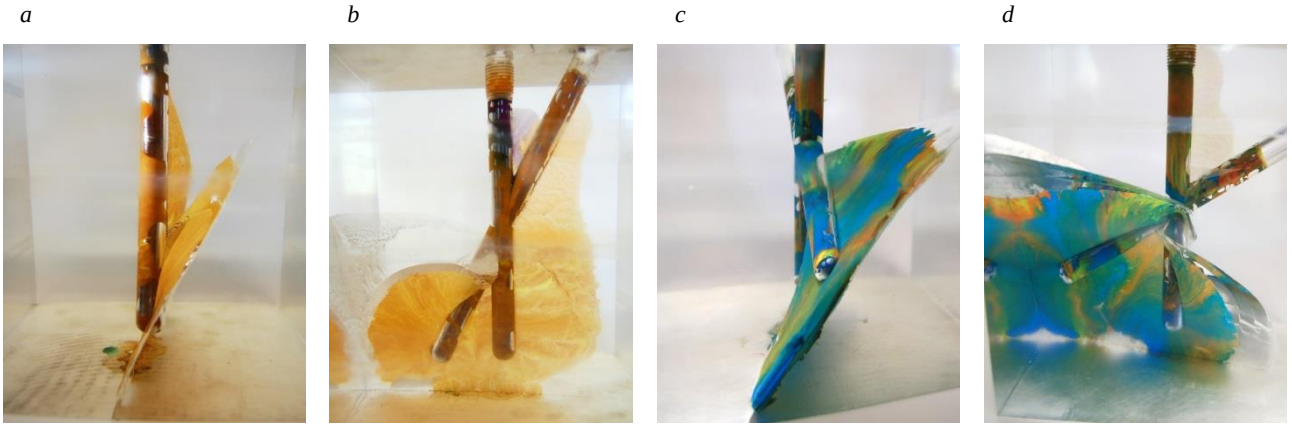

Fig.6. The photographs of the cracks formed during the indentation of plasticine in block 3 (*a*, *b*) and block 4 (*c*, *d*)

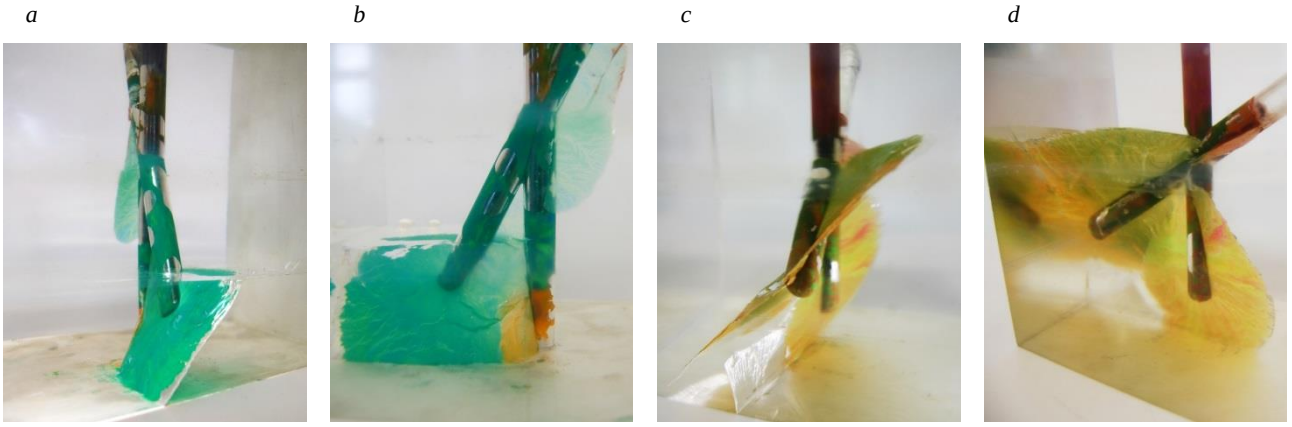

Fig.7. The photographs of the cracks formed during the indentation of plasticine in block 5 (*a*, *b*) and block 6 (*c*, *d*)

According to the test conditions in blocks 5 and 6, the maximum compressive stress S_{xx} was one and a half times higher than S_{yy}. At the same time, a similar development of cracks was observed as in the previous experiment (Fig.7). In block 5, the heterogeneity and delamination in the horizontal plane owing to the plasticine indentation, the vertical growth of the crack stopped. Previous laboratory experiments have shown similar findings regarding the interplay between created and pre-existing cracks under compressive stresses [49-51]. In block 6, the most challenging conditions were created for the formation of a single longitudinal fracture, with $\gamma = 60°$. In this case, an incomplete connection of the boreholes by HF was observed, including due to the rotation of the crack plane growing in the inclined borehole (Fig.7, *c*).

In order to assess the influence of experimental conditions on the final shape of the cracks formed in blocks 3-6, we measured the inclination angle of the longitudinal fracture plane at its exit to the side face of the block. For convenience, the angle measured from the vertical will be referred to as α, with its values given in Table 2.

Table 2

The value of angle α for blocks 3-6

Block number	Loading conditions, MPa		Angle γ, deg	Angle α, deg
	S_{xx}	S_{yy}		
3	1.3	1.0	30	29
4	1.3	1.0	60	36
5	1.5	1.0	30	44
6	1.5	1.0	60	48

The findings demonstrate that the crack plane in a non-uniform stress field is more effectively stabilized when boreholes are closely spaced (γ = 30°). The deviation from the vertical plane containing the borehole axes was estimated to be 29° and 44° at S_{xx} = 1.3 and 1.5 MPa, respectively. The analysis of the angles α obtained during the HF of blocks 4 and 5 revealed the following features. Despite the significantly large distance between the walls of the boreholes far from the concentrator area in block 4 (γ = 60°) and the limited potential of this scheme to keep the crack in a given plane, the angle α was found to be smaller than in block 5 (γ = 30°). These results indicate that the compressive stress field parameters have a stronger influence on the deviation of the longitudinal fracture from the vertical plane containing the borehole axes compared to the increase in the angle γ. The earlier findings demonstrate that, given a uniform stress field, the crack propagation caused by the indentation of plastic substances tends to occur in the plane of the boreholes or along the initially specified direction [52].

The features of crack growth established in the paper can be used in practice when designing HF operations carried out in mine workings. The stresses applied to the cubic sample during tests were limited by the technical capabilities of the laboratory system and were equivalent to the lithostatic pressure of rocks at a depth of about 200 m. This corresponds to many mineral deposits extracted by the underground mining method, including the Yaregskoye field of high-viscosity oil, uranium deposits of the Streltsovskoye ore field, the Handiza* polymetallic deposit (Uzbekistan), Mezhegeyskoye, Karagaylinskoye coal deposits and others [53-56].

The ratios between maximum and minimum compressive stresses (1.3-1.5) used in the experiments are observed in many mined seams and fields. The results of studies of natural stress state in the upper part of the cross section of domestic and foreign deposits are summarized in [57]. It is noted that horizontal stresses are widely exceeded over vertical ones in both igneous and sedimentary metamorphosed rocks, in some cases by a factor of 10. Similar results are also given in publications [56, 58], describing the distribution of active stresses in coal mines in China.

The success of the in-mine implementation of the approach studied in this article depends on the possibility of forming a stress concentrator in the rock mass due to the intersection of boreholes. In underground workings, this can be achieved by installing an oriented wedge-deflector in a given place of a horizontal in-seam borehole and then cutting a sidetrack from it [59]. The Y-shaped system of the borehole and sidetrack created in this way will have the necessary geometry for solving the existing problem. Then the borehole section with the sidetrack is sealed using a packer and the working fluid is pumped in. The viscosity of the fluid can be increased by special chemical additives or two-component resins with a pre-selected polymerization time [60].

Conclusion

The HF method can be used to significantly improve the development of mineral deposits by creating cracks in a specific direction. In mine environments, the formation of longitudinal cracks can be a viable solution to address specific mining issues. This study aimed to explore the potential for developing longitudinal fractures within a system of intersecting boreholes, especially when the direction of maximum stress was perpendicular to the plane containing their axes.

The experiments revealed the tendency for the cracks to initiate independently in vertical and inclined boreholes. However, with further growth, they combined and were stabilized by the boreholes to form a single fracture, also due to the area close to the concentrator. Under the most unfavourable conditions ($S_{xx} = 1.5S_{yy}$, γ = 60°), the incomplete connection of the boreholes by HF was

* About the activities of the Handiza mine. URL: https://agmk.uz/ru/news/xondiza-koni-polimetallar-ombori (accessed 21.07.2024).

observed upon plasticine indentation, partially due to the rotation of the plane of the crack growing in the inclined borehole. Particular emphasis should be placed on the complex geometry of the resulting cracks, their curvature, and twisting around the boreholes, with these effects more pronounced when $\gamma = 60°$.

The physical modelling findings indicate that the parameters of the horizontal compressive stress field have a greater effect on the deviation of the longitudinal crack from the vertical plane containing the borehole axes compared to the increase in the angle between them. Measuring the angle of inclination of the longitudinal crack at its intersection with the side face of the block revealed that closely spaced boreholes ($\gamma = 30°$) better stabilize the fracturing plane in a given non-uniform stress field.

REFERENCES

1. Koplos J., Tuccillo M.E., Ranalli B. Hydraulic fracturing overview: How, where, and its role in oil and gas. *Journal AWWA*. 2014. Vol. 106. Iss. 11, p. 38-46. DOI: 10.5942/jawwa.2014.106.0153

2. Bin Chen, Barboza B.R., Yanan Sun et al. A Review of Hydraulic Fracturing Simulation. *Archives of Computational Methods in Engineering*. 2022. Vol. 29. Iss. 4, p. 2113-2170. DOI: 10.1007/s11831-021-09653-z

3. Filippov E.V., Zakharov L.A., Martyushev D.A., Ponomareva I.N. Reproduction of reservoir pressure by machine learning methods and study of its influence on the cracks formation process in hydraulic fracturing. *Journal of Mining Institute.* 2022. Vol. 258, p. 924-932. DOI: 10.31897/PMI.2022.103

4. Bosikov I.I., Klyuev R.V., Mayer A.V. Comprehensive assessment of hydraulic fracturing technology efficiency for well construction during hydrocarbon production. *Journal of Mining Institute.* 2022. Vol. 258, p. 1018-1025. DOI: 10.31897/PMI.2022.98

5. Bakhshi E., Golsanami N., Lianjun Chen. Numerical Modeling and Lattice Method for Characterizing Hydraulic Fracture Propagation: A Review of the Numerical, Experimental, and Field Studies. *Archives of Computational Methods in Engineering*. 2021. Vol. 28. Iss. 5, p. 3329-3360. DOI: 10.1007/s11831-020-09501-6

6. Dutler N., Valley B., Gischig V. et al. Hydraulic fracture propagation in a heterogeneous stress field in a crystalline rock mass. *Solid Earth*. 2019. Vol. 10. Iss. 6, p. 1877-1904. DOI: 10.5194/se-10-1877-2019

7. Kang H., Zhang X., Si L. et al. In-situ stress measurements and stress distribution characteristics in underground coal mines in China. *Engineering Geology*. 2010. Vol. 116. Iss. 3-4, p. 333-345. DOI: 10.1016/j.enggeo.2010.09.015

8. Lovchikov A.V. Difference in rockburst hazard in ore and coal mines. *IOP Conference Series: Earth and Environmental Science*. 2018. Vol. 134. N 012039. DOI: 10.1088/1755-1315/134/1/012039

9. Qian Li, Yiyu Lu, Zhaolong Ge et al. A New Tree-Type Fracturing Method for Stimulating Coal Seam Gas Reservoirs. *Energies*. 2017. Vol. 10. Iss. 9. N 1388. DOI: 10.3390/en10091388

10. Yubing Liu, Zuxun Zhang, Bozhi Deng, Minghui Li. Liquid carbon dioxide fracturing application and its effect on gas drainage in low permeability coal seams of underground coal mine. *Energy Sources, Part A: Recovery, Utilization, and Environmental Effects*. 2023. Vol. 45. Iss. 3, p. 6534-6546. DOI: 10.1080/15567036.2019.1675809

11. Slastunov S., Kolikov K., Batugin A. et al. Improvement of Intensive In-Seam Gas Drainage Technology at Kirova Mine in Kuznetsk Coal Basin. *Energies*. 2022. Vol. 15. Iss. 3. N 1047. DOI: 10.3390/en15031047

12. Klishin V.I., Opruk G.Y., Tatsienko A.L. Technology and means of a coal seam interval hydraulic fracturing for the seam degassing intensification. *IOP Conference Series: Earth and Environmental Science*. 2017. Vol. 53. N 012019. DOI: 10.1088/1755-1315/53/1/012019

13. Lekontsev Yu.M., Sazhin P.V. Directional hydraulic fracturing in difficult caving roof control and coal degassing. *Journal of Mining Science.* 2014. Vol. 50. N 5, p. 914-917. DOI: 10.1134/S106273911405010X

14. Jiangwei Liu, Changyou Liu, Qiangling Yao, Guangyao Si. The position of hydraulic fracturing to initiate vertical fractures in hard hanging roof for stress relief. *International Journal of Rock Mechanics and Mining Sciences*. 2020. Vol. 132. N 104328. DOI: 10.1016/j.ijrmms.2020.104328

15. Wenli Zhai, Fulian He, Liang Li et al. Roof cutting mechanism and surrounding rock control of small pillar along-gob roadway driving in super high coal seam. *Bulletin of Engineering Geology and the Environment*. 2023. Vol. 82. Iss. 4. N 151. DOI: 10.1007/s10064-023-03189-1

16. Yongxin Sun, Yukai Fu, Tao Wang. Field application of directional hydraulic fracturing technology for controlling thick hard roof: a case study. *Arabian Journal of Geosciences*. 2021. Vol. 14. Iss. 6. N 438. DOI: 10.1007/s12517-021-06790-4

17. Shilova T.V., Rybalkin L.A. Study of polymer compositions for formation of impermeable inclusions in rock mass. *IOP Conference Series: Earth and Environmental Science*. 2022. Vol. 991. N 012008. DOI: 10.1088/1755-1315/991/1/012008

18. Serdyukov S.V., Kurlenya M.V., Patutin A.V. Hydraulic fracturing for in situ stress measurement. *Journal of Mining Science*. 2016. Vol. 52. N 6, p. 1031-1038. DOI: 10.1134/S1062739116061563

19. Oldenburg C.M., Dobson P.F., Yuxin Wu et al. Hydraulic fracturing experiments at 1500 m depth in a deep mine: Highlights from the kISMET project. 42nd Workshop on Geothermal Reservoir Engineering, 13-15 February 2017, Stanford, CA, USA. Stanford Geothermal Program, 2017. N SGP-TR-212.

20. Rubtsova E.V., Skulkin A.A. Hydraulic fracturing stress measurement in underground salt rock mines at Upper Kama Deposit. *IOP Conference Series: Earth and Environmental Science*. 2018. Vol. 134. N 012049. DOI: 10.1088/1755-1315/134/1/012049

21. Qiang Xu, Qiangling Yao, Changhao Shan, Chuangkai Zheng. A New Hydraulic Fracturing Instrument to Measure In Situ Stress and Its Application in Chahasu Coal Mine. *Geotechnical Testing Journal*. 2022. Vol. 45. Iss. 5, p. 901-914. DOI: 10.1520/GTJ20210207

22. Serdyukov S.V., Kurlenya M.V. Application of local hydrofrac for the intensification of steam assisted gravity reservoir drainage. XII Mezhdunarodnye nauchnyi kongress i vystavka "Interehkspo GEO-Sibir-2016": Materialy Mezhdunarodnoi nauchnoi konferentsii "Ehkonomicheskoe razvitie Sibiri i Dalnego Vostoka. Ehkonomika prirodopolzovaniya, zemleustroistvo, lesoustroistvo, upravlenie nedvizhimostyu", 18-22 April 2016, Novosibirsk, Russia. Novosibirsk: Sibirskii gosudarstvennyi universitet geosistem i tekhnologii, 2016. Vol. 2, p. 8-13 (in Russian).

23. Yunzhong Jia, Zhaohui Lu, Qiquan Xiong et al. Laboratory characterization of cyclic hydraulic fracturing for deep shale application in Southwest China. *International Journal of Rock Mechanics and Mining Sciences*. 2021. Vol. 148. N 104945. DOI: 10.1016/j.ijrmms.2021.104945

24. Li Zhuang, Kwang Yeom Kim, Melvin Diaz, Sun Yeom. Evaluation of water saturation effect on mechanical properties and hydraulic fracturing behavior of granite. *International Journal of Rock Mechanics and Mining Sciences*. 2020. Vol. 130. N 104321. DOI: 10.1016/j.ijrmms.2020.104321

25. Bobrova M., Stanchits S., Shevtsova A. et al. Laboratory Investigation of Hydraulic Fracture Behavior of Unconventional Reservoir Rocks. *Geosciences*. 2021. Vol. 11. Iss. 7. N 292. DOI: 10.3390/geosciences11070292

26. Deb P., Düber S., Guarnieri Calò Carducci C., Clauser C. Laboratory-scale hydraulic fracturing dataset for benchmarking of enhanced geothermal system simulation tools. *Scientific Data*. 2020. Vol. 7. N 220. DOI: 10.1038/s41597-020-0564-x

27. Patutin A.V., Serdyukov S.V. Laboratory stands for hydraulic fracturing simulation in a nonuniform stress field. *IOP Conference Series: Earth and Environmental Science*. 2022. Vol. 991. N 012035. DOI: 10.1088/1755-1315/991/1/012035

28. Feiteng Zhang, Xiangyu Wang, Jianbiao Bai et al. Fixed-length roof cutting with vertical hydraulic fracture based on the stress shadow effect: A case study. *International Journal of Mining Science and Technology*. 2022. Vol. 32. Iss. 2, p. 295-308. DOI: 10.1016/j.ijmst.2021.09.007

29. Pavlov V.A., Serdyukov S.V., Martynyuk P.A., Patutin A.V. Optimisation of borehole-jack fracturing technique for *in situ* stress measurement. *International Journal of Geotechnical Engineering*. 2019. Vol. 13. Iss. 5, p. 451-457. DOI: 10.1080/19386362.2017.1363347

30. Karev V.I., Kovalenko Yu.F., Ustinov K.B. Modeling of geomechanical processes in the vicinity of oil and gas wells. Moscow: Institut problem mekhaniki im. A.Yu.Ishlinskogo RAN, 2018, p. 528 (in Russian).

31. Shaohua Gai, Zhihong Nie, Xinbin Yi et al. Study on the Interference Law of Staged Fracturing Crack Propagation in Horizontal Wells of Tight Reservoirs. *ACS Omega*. 2020. Vol. 5. Iss. 18, p. 10327-10338. DOI: 10.1021/acsomega.9b04423

32. Kalam S., Afagwu C., Al Jaberi J. et al. A review on non-aqueous fracturing techniques in unconventional reservoirs. *Journal of Natural Gas Science and Engineering*. 2021. Vol. 95. N 104223. DOI: 10.1016/j.jngse.2021.104223

33. Jiangzhan Chen, Xibing Li, Han Cao, Linqi Huang. Experimental investigation of the influence of pulsating hydraulic fracturing on pre-existing fractures propagation in coal. *Journal of Petroleum Science and Engineering*. 2020. Vol. 189. N 107040. DOI: 10.1016/j.petrol.2020.107040

34. Wenfeng Li, Frash L.P., Carey J.W. et al. Injection Parameters That Promote Branching of Hydraulic Cracks. *Geophysical Research Letters*. 2021. Vol. 48. Iss. 12. N e2021GL093321. DOI: 10.1029/2021GL093321

35. Tiankui Guo, Zhenhua Rui, Zhanqing Qu, Ning Qi. Experimental study of directional propagation of hydraulic fracture guided by multi-radial slim holes. *Journal of Petroleum Science and Engineering*. 2018. Vol. 166, p. 592-601. DOI: 10.1016/j.petrol.2018.03.102

36. *Zhaoquan Guo, Shouceng Tian, Qingling Liu et al.* Experimental investigation on the breakdown pressure and fracture propagation of radial borehole fracturing. *Journal of Petroleum Science and Engineering*. 2022. Vol. 208. Part A. N 109169. DOI: 10.1016/j.petrol.2021.109169

37. Shaojie Zuo, Zhaolong Ge, Kai Deng et al. Fracture initiation pressure and failure modes of tree-type hydraulic fracturing in gas-bearing coal seams. *Journal of Natural Gas Science and Engineering*. 2020. Vol. 77. N 103260. DOI: 10.1016/j.jngse.2020.103260

38. Rubtsova E.V. Three-axial independent loading bench for physical modeling of hydraulic fracturing for stress measurement. XI Mezhdunarodnye nauchnyi kongress i vystavka "Interehkspo GEO-Sibir-2015": Materialy Mezhdunarodnoi nauchnoi konferentsii "Nedropolzovanie. Gornoe delo. Napravleniya i tekhnologii poiska, razvedki i razrabotki mestorozhdenii poleznykh iskopaemykh. Geoehkologiya", 13-25 April 2015, Novosibirsk, Russia. Novosibirsk: Sibirskii gosudarstvennyi universitet geosistem i tekhnologii, 2015. Vol. 3, p. 211-215 (in Russian).

39. Rubtsova E., Skulkin A. Physical simulation the process of measurement hydrofracturing in specimen under their non-equicomponent loading. *Problems of Subsoil Use.* 2017. N 2 (13), p. 42-46 (in Russian). DOI: 10.18454/2313-1586.2017.02.042

40. Kachalsky V.G., Leontev A.V., Rubtsova E.V. Portable pressure recorder at complex "hydrofracturing" for experimental stress determination in the solid. XV Mezhdunarodnyi nauchnyi kongress "Interehkspo GEO-Sibir": Materialy Mezhdunarodnoi nauchnoi konferentsii "Nedropolzovanie. Gornoe delo. Napravleniya i tekhnologii poiska, razvedki i razrabotki mestorozhdenii poleznykh iskopaemykh. Ehkonomika. Geoehkologiya", 24-26 April 2019, Novosibirsk, Russia. Novosibirsk: Sibirskii gosudarstvennyi universitet geosistem i tekhnologii, 2019. Vol. 2. N 4, p. 38-44 (in Russian). DOI: 10.33764/2618-981X-2019-2-4-38-44

41. Quan Gan, Elsworth D., Alpern J.S. et al. Breakdown pressures due to infiltration and exclusion in finite length boreholes. *Journal of Petroleum Science and Engineering*. 2015. Vol. 127, p. 329-337. DOI: 10.1016/j.petrol.2015.01.011

42. Khadraoui S., Hachemi M., Allal A. et al. Numerical and experimental investigation of hydraulic fracture using the synthesized PMMA. *Polymer Bulletin*. 2021. Vol. 78. Iss. 7, p. 3803-3820. DOI: 10.1007/s00289-020-03300-6

43. Mouli-Castillo J., Kendrick J.E., Lightbody A. et al. Cyclical hydraulic pressure pulses reduce breakdown pressure and initiate staged fracture growth in PMMA. *Geomechanics and Geophysics for Geo-Energy and Geo-Resources*. 2024. Vol. 10. Iss. 1. N 65. DOI: 10.1007/s40948-024-00739-z

44. Patutin A.V., Skulkin A.A. Hydraulic fracturing of intersecting boreholes in a non-uniform stress field: laboratory studies. Fizicheskaya mezomekhanika. Materialy s mnogourovnevoi ierarkhicheski organizovannoi strukturoi i intellektualnye proizvodstvennye tekhnologii: Tezisy dokladov Mezhdunarodnoi konferentsii, 11-14 September, 2023, Tomsk, Russia. Tomsk: Institut fiziki prochnosti i materialovedeniya SO RAN, 2023, p. 176-177 (in Russian).

45. Azarov A.V., Patutin A.V., Serdyukov S.V. Shapes of Hydraulic Fractures in the Vicinity of Borehole-and-Branch Hole Junction. *Journal of Mining Science.* 2022. Vol. 58. N 5, p. 741-753. DOI: 10.1134/S1062739122050052

46. Patutin A.V., Skulkin A.A., Prasolova V.S. Physical Modeling of Hydraulic Fracturing in Branched Borehole in Manmade Block. *Journal of Mining Science.* 2023. Vol. 59. N 2, p. 191-198. DOI: 10.1134/S1062739123020023

47. Jing-Nan Dong, Guang-Jie Yuan, Xiang-Yang Wang et al. Experimental study of multi-timescale crack blunting in hydraulic fracture. *Petroleum Science*. 2021. Vol. 18. Iss. 1, p. 234-244. DOI: 10.1007/s12182-020-00479-1

48. Panov A.V., Kolykhalov I.V. Numerical and experimental modeling of propagation of longitudinal fractures in multi-stage hydraulic fracturing with viscous fluid. XVII Mezhdunarodnyi nauchnyi kongress "Interehkspo GEO-Sibir": Materialy Mezhdunarodnoi nauchnoi konferentsii "Nedropolzovanie. Gornoe delo. Napravleniya i tekhnologii poiska, razvedki i razrabotki mestorozhdenii poleznykh iskopaemykh. Ehkonomika. Geoehkologiya", 19-21 May 2021, Novosibirsk, Russia. Novosibirsk: Sibirskii gosudarstvennyi universitet geosistem i tekhnologii, 2021. Vol. 2. N 4, p. 41-51 (in Russian). DOI: 10.33764/2618-981X-2021-2-4-41-51

49. Zi-Xiao Xie, Xiao-Guang Wu, Teng-Da Long et al. Visualization of hydraulic fracture interacting with pre-existing fracture. *Petroleum Science*. 2023. Vol. 20. Iss. 6, p. 3723-3735. DOI: 10.1016/j.petsci.2023.07.014

50. Leontiev A., Rubtsova E. Analysis of Crack Formation in Model Specimens During Hydraulic Fracturing in Holes. Trigger Effects in Geosystems. Springer, 2019, p. 247-256. DOI: 10.1007/978-3-030-31970-0_27

51. Qiao Lu, EI-Fayoumi A., Adachi J. et al. Laboratory demonstration of the impact of weak interfaces and layered rock properties on hydraulic fracture containment and height growth. *Geomechanics and Geophysics for Geo-Energy and Geo-Resources*. 2023. Vol. 9. Iss. 1. N 113. DOI: 10.1007/s40948-023-00649-6

52. Kyu N.G. Directional Conjugate Fracturing in Rock Mass Using Holes as Plastic Fluid Front Guides. *Journal of Mining Science*. 2020. Vol. 56. N 5, p. 784-792. DOI: 10.1134/S1062739120057117

53. Konoplev Yu.P., Demchenko A.G., Demchenko A.A. Oil mine – a technology that is capable of providing half of oil production in the 21st century in the open and developed fields of Russia. *Nedropolzovanie XXI vek.* 2020. N 1 (83), p. 46-55 (in Russian).

54. Lizunkin M.V., Beidin A.V. Assessment of the stress-strain state of the rock massif of the Streltsovsky ore field. Geomekhanika v gornom dele: Doklady Vserossiiskoi nauchno-tekhnicheskoi konferentsii s mezhdunarodnym uchastiem, 4-5 June 2014, Ekaterinburg, Russia. Ekaterinburg: Uralskoe otdelenie RAN, 2014, p. 30-38 (in Russian).

55. Belov S.V. Geological and engineering mining conditions of coal development at the "Karagaylinskaya mine field". Mezhdistsiplinarnye podkhody v biologii, meditsine i naukakh o Zemle: teoreticheskie i prikladnye aspekty: Materialy simpoziuma XVIII (L) Mezhdunarodnoi nauchnoi konferentsii studentov, aspirantov i molodykh uchenykh "Obrazovanie, nauka, innovatsii: vklad molodykh issledovatelei", priurochennoi k 50-letiyu KeMGU, 24-29 April 2023, Kemerovo, Russia. Kemerovo: Kemerovskii gosudarstvennyi universitet, 2023. Iss. 24, p. 118-120 (in Russian).

56. Kang H., Zhang X., Si L. et al. In-situ stress measurements and stress distribution characteristics in underground coal mines in China. *Engineering Geology*. 2010. Vol. 116. Iss. 3-4, p. 333-345. DOI: 10.1016/j.enggeo.2010.09.015

57. Kozyrev A.A. Modern results of experimental study of natural stresses in the upper part of the Earth's crust and the problem of overburden pressure. Geomekhanika v gornom dele: Doklady Vserossiiskoi nauchno-tekhnicheskoi konferentsii s mezhdunarodnym uchastiem, 4-5 June 2014, Ekaterinburg, Russia. Ekaterinburg: Uralskoe otdelenie RAN, 2014, p. 39-53 (in Russian)

58. Peng Li, Meifeng Cai, Qifeng Guo et al. Current stress field and its relationship to tectonism in a coal mining district, central China, for underground coal energy exploration. *Energy Reports*. 2022. Vol. 8, p. 5313-5328. DOI: 10.1016/j.egyr.2022.04.008

59. Serdyukov S.V., Patutin A.V., Azarov A.V., Rybalkin L.A., Shilova T.V. Patent N 2730688 RF. Method of directed hydraulic fracturing of coal bed. Publ. 25.08.2020. Bul. N 24 (in Russian).

60. Langbauer C., Tehrani F.F., Mastobaev B. A holistic review on hydraulic fracturing stimulation laboratory experiments and their transition to enhanced geothermal system field research and operations. *Liquid and Gaseous Energy Resources*. 2021. Vol. 1. Iss. 1, p. 30-63. DOI: 10.21595/lger.2021.22043

***Authors*: Andrey V. Patutin,** *Candidate of Technical Sciences, Senior Researcher, andrey.patutin@gmail.com, https://orcid.org/0000-0002-3240-7134* (*Chinakal Institute of Mining, Siberian Branch of the RAS, Novosibirsk, Russia*), **Aleksandr A. Skulkin,** *Junior Researcher, https://orcid.org/0009-0005-7733-7482* (*Chinakal Institute of Mining, Siberian Branch of the RAS, Novosibirsk, Russia*), **Leonid A. Rybalkin,** *Candidate of Technical Sciences, Researcher, https://orcid.org/0000-0003-2648-1909* (*Chinakal Institute of Mining, Siberian Branch of the RAS, Novosibirsk, Russia*), **Andrey N. Drobchik,** *Research Engineer, https://orcid.org/0009-0002-7567-6497* (*Chinakal Institute of Mining, Siberian Branch of the RAS, Novosibirsk, Russia*).

The authors declare no conflict of interests.

ISSN 2411-3336; e-ISSN 2541-9404

JOURNAL OF MINING INSTITUTE
Zapiski Gornogo instituta
Journal homepage: pmi.spmi.ru

Research article *Geotechnical Engineering and Engineering Geology*

Analysis of the stress state of rocks transformation near a horizontal well during acid treatment based on numerical simulation

Sergei N. Popov[1], **Sergei E. Chernyshov**[2]✉, **Wang Xiaopu**[3]
[1] *Oil and Gas Research Institute, RAS, Moscow, Russia*
[2] *Perm National Research Polytechnic University, Perm, Russia*
[3] *China University of Petroleum, Qingdao, China*

***How to cite this article*:** Popov S.N., Chernyshov S.E., Wang Xiaopu. Analysis of the stress state of rocks transformation near a horizontal well during acid treatment based on numerical simulation. Journal of Mining Institute. 2025. Vol. 272. N 16413, p. 110-118.

Abstract
The article presents an overview of the assessment and modelling of the stress state of rocks in the near-wellbore zone of horizontal wells during acid stimulation of the formation for improving the efficiency of oil and gas field development. A numerical finite element model of near-wellbore zone of the reservoir drilled by a horizontal section was compiled using one of oil fields in the Perm Territory as an example. The distribution of physical and mechanical properties of the terrigenous reservoir near the well was determined considering transformation under the action of mud acid for different time periods of its injection. Multivariate numerical simulation was performed and the distribution of horizontal and vertical stresses in near-wellbore zone was determined with regard for different values of pressure drawdown and changes in stress-strain properties depending on the area of mud acid infiltration. It was found that a change in elastic modulus and Poisson's ratio under the influence of acid led to a decrease in stresses in near-wellbore zone. Analysis of the stress distribution field based on the Coulomb – Mohr criterion showed that the minimum safety factor of rock even after the effect of mud acid was 1.5; thus, under the considered conditions of horizontal well modelling, the reservoir rock remained stable, and no zones of rock destruction appeared.

Keywords
horizontal well; stress-strain properties; near-wellbore zone; numerical model; finite element method; stress state; strength safety factor; acid treatment; wellbore wall stability

Funding
The work was accomplished under the State assignment “Investigation of properties of oil and gas reservoir systems under physical, geomechanical and physicochemical impact on hard-to-recover hydrocarbon reserves for improving the efficiency of their development” (FMME 2025-0010).

Received 20.03.2024 ***Accepted: 07.11.2024*** ***Online: 27.02.2025*** ***Published: 25.04.2025***

Introduction

Acid treatment of formation is one of the most frequently used enhancement methods for intensifying the inflow of hydrocarbons into the well as well as cleaning the near-wellbore zone from the components of technological fluids used in drilling [1-3]. Despite a high efficiency of this method, it also has disadvantages – under the action of acid reagents, not only the substances clogging the near-wellbore zone, but also the rock matrix minerals dissolve. On the one hand, this effect is manifested in increasing permeability; on the other hand, the chemical interaction of rock and acid should lead to a deterioration in stress-strain properties of reservoir. During acid

treatment of a carbonate reservoir the effect of acid usually leads to the appearance of "wormholes" [4-6] and should not significantly affect the wellbore stability, whereas for a terrigenous formation, due to dissolution of intergranular rock cement, a major decrease in Young's modulus and ultimate strength of reservoir rock will occur [7, 8].

When studying acid effect on core samples, the impact of this reagent on permeability is often investigated, and the amount of pore volumes for acid breakthrough and the Damkohler number are determined [4, 6, 9]. At the same time, the effect of acid compositions on physical and mechanical properties of reservoir rocks was not sufficiently investigated. In some articles by foreign experts [9-11] the effect of acid treatment on the dynamic Young's modulus and Poisson's ratio was investigated; however, only carbonate reservoirs and filtration of a small amount of pore volume of acid composition were investigated – prior to its "breakthrough" from the opposite end of samples. At the same time, as shown in publications [12-14] based on the studies of core samples, the porosity and permeability properties of reservoir rock can change not only under the influence of physicochemically active liquids, but also of the changing effective stresses. In this case, the shows of conjugated mechanical and chemical effects will even more intensely transform the natural properties of reservoir rocks (porosity, permeability, physical and mechanical properties, etc.) and affect the stress-strain state of formation, stability of wells and their productivity (injectivity).

When modelling acid action on the formation, the geometry of the forming wormholes and their impact on permeability are usually investigated [15-17] as well as possible chemical reactions of the interaction of reagent with rock minerals [18]. However, the influence of such effects on the stress-strain state of the near-wellbore zone and the destruction of rocks was not sufficiently investigated.

One of the most efficient methods of developing oil and gas fields is the use of horizontal wells [19-21], since in this case the filtration area increases. The use of wells with a horizontal shaft is most efficient in low-permeability reservoirs. This type of wells is most efficiently used in development of low-permeability formations [21-24]; multi-stage hydraulic fracturing cracks are created including the use of acid reagents as fracking fluid [23-25]. Despite the fact that the efficiency of fracking is directly related to a reliable determination of stress-strain properties and the stress state of formation, this problem was virtually not investigated from the viewpoint of joint geomechanical and chemical effects.

Well stability is very important, since wellbore walls can collapse in the process of drilling and operation, which can lead to an emergency when developing oil and gas fields, particularly, for horizontal [26], deep and superdeep wells [27]. To solve this class of problems, 1D geomechanical modelling methods are currently widely used [28-30]. However, this approach has certain disadvantages: stresses are commonly calculated only on wellbore wall, so their distribution at a distance from the wall cannot be determined; well design (column, cement stone) is not taken into account; stress state cannot be calculated near the perforation channels, or perforation holes are considered ideally as cylindrical surfaces [31].

This article based on the numerical finite element method considers how a change in stress-strain properties during acid treatment affects the transformation of stresses in the near-wellbore zone and stability of the open horizontal hole in the terrigenous reservoir. Numerical simulation was performed using the example of a well drilled in one of oil fields in the southern Perm Territory. Mud acid was considered as a reagent, which is quite often used for this type of reservoir, primarily due to its ability to dissolve clay particles [32, 33].

Methodology

Papers [7, 8] present the results of laboratory experiments in which the effect of different numbers of pore volumes of acid reagent on stress-strain properties of core samples taken from a terrigenous reservoir was investigated. Core samples were 6 cm long and 3 cm in diameter. Mud acid,

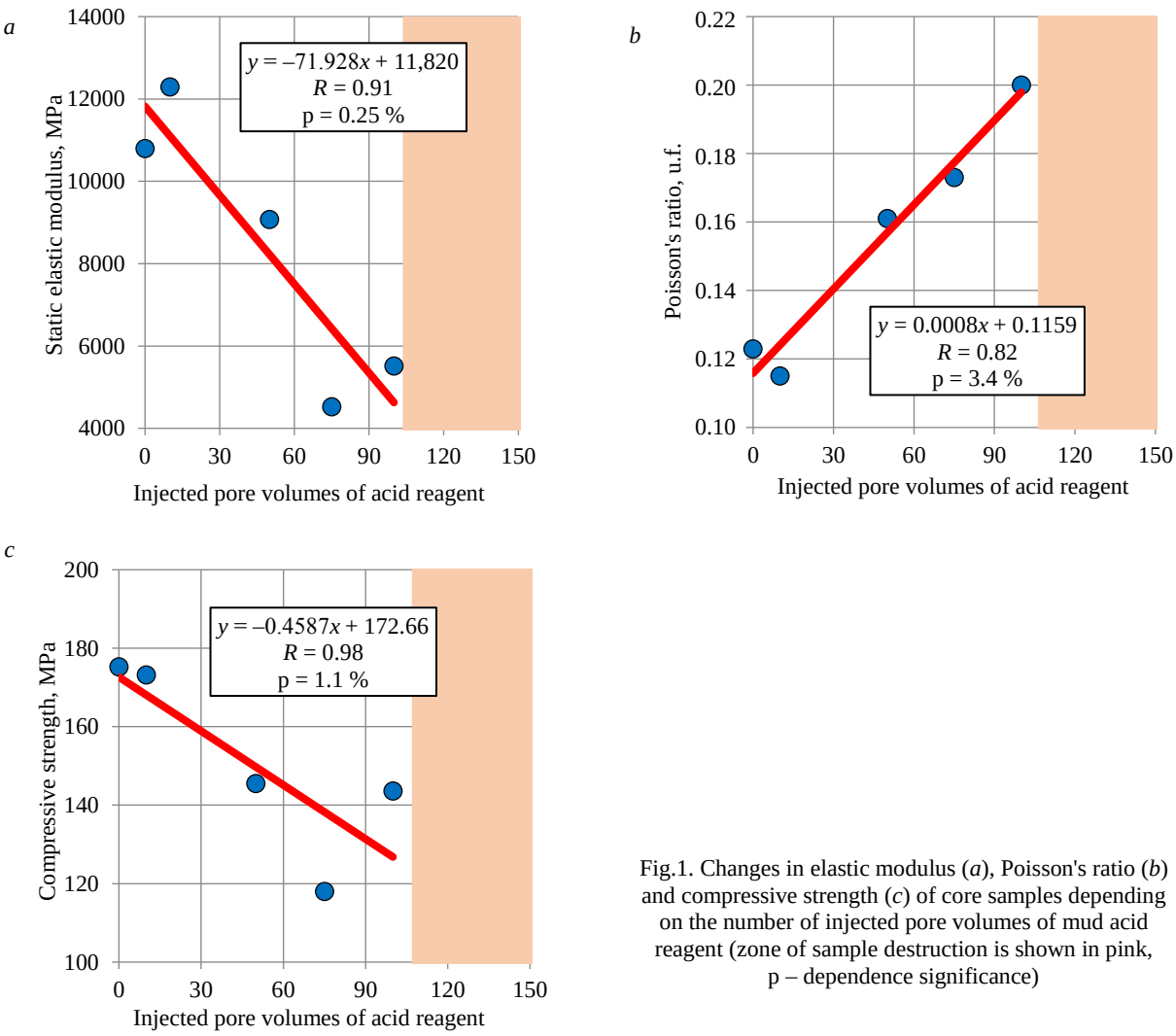

Fig.1. Changes in elastic modulus (*a*), Poisson's ratio (*b*) and compressive strength (*c*) of core samples depending on the number of injected pore volumes of mud acid reagent (zone of sample destruction is shown in pink, p – dependence significance)

which comprised 12 % hydrochloric acid (HCl) and 3 % hydrofluoric acid (HF), was used as a reagent. During experiments residual water saturation was created in samples, and oil saturation was modelled using kerosene. At the start of the experiment, kerosene was injected into samples, then different pore volumes of acid reagent were filtered, and samples were kept under its influence for 4 h, and at the end of the experiment, kerosene was injected again. As a result of research, it was ascertained that acid treatment of formation led to a decrease in Young's modulus and compressive strength and to an increase in Poisson's ratio (Fig.1).

As can be seen from Fig.1, acid treatment resulted in an almost threefold decrease of elastic modulus, 18 % decrease of compressive strength and an approximately twofold increase of the Poisson's ratio. With increasing number of pore volumes over 100, samples were destroyed after acid filtration; in Fig.1, the area on the graph over 100 pore volumes is highlighted in pink. The significance of dependence is given; its value is less than 5 %, which points to applicability of the ratios used; this is also evidenced by sufficiently high coefficients of their correlations. The dependences in Fig.1 are used for the numerical computation of the stress state of a horizontal well under conditions of acid treatment of the formation.

Numerical simulation was performed in the ANSYS finite element modelling software package [34-36]. This software implements the numerical computation of differential equations describing the poroelastic behaviour of a solid body:

$$\begin{cases} \nabla \bullet \sigma + f = 0 \text{ or } \nabla \bullet \left(\sigma' - \alpha p I\right) + f = 0, \\ \alpha \dot{\varepsilon}_V + \dfrac{1}{K_m} \dot{p} + \nabla \bullet q = S, \end{cases}$$

where σ is stress tensor; $\bullet$ – derivative operator; $\nabla \bullet$ – divergence operator; σ' – effective stress tensor; α – Biot coefficient; p – pore pressure; I – second-order unit tensor; f – force vector; ε_V – volumetric strain of rock matrix; K_m – Biot modulus; q – fluid flow vector; S – flow source.

The following ratios are also applied for stress and strain relationship:

$$\sigma' = D\varepsilon^e,$$

where ε^e is strain tensor; D – matrix of elastic constants.

Darcy's law was applied to describe fluid flow in a porous medium:

$$q = -k\nabla p / \mu,$$

where k is the second-order permeability tensor; ∇ – gradient operator; μ – fluid viscosity.

To calculate the stress field in ANSYS, a finite element model was created using the poroelastic finite element cpt212, including a 20 m thick formation section and an open hole well with a 0.108 m radius (Fig.2). The well was in the centre of reservoir at a depth of 10 m from its roof. Due to the symmetry, only half of the selected section of the near-wellbore zone was considered.

The main physical characteristics of the model for the conditions of the considered terrigenous reservoir in one of oil fields in the southern Perm Territory: elastic modulus of rock without acid treatment is 11.8 GPa; Poisson's ratio of rock without acid treatment 0.116 u.f.; Biot coefficient 0.85 u.f.; angle of internal friction of rock 30 deg; reservoir depth 1,500 m; vertical stress 33 MPa; horizontal stress 15.8 MPa; reservoir pressure 15.5 MPa; pressure drawdown 1; 5; 10 MPa. Vertical and horizontal stresses were calculated for an average formation occurrence depth of 1,500 m. Since the value of Biot coefficient was not determined in experiments, it was taken as a constant equal to 0.85.

The following boundary conditions were adopted in the numerical model:

• at the lower boundary, displacements in direction of the normal to the surface were fixed (zero displacements along the vertical axis);

• vertical stress was applied to the upper boundary calculated from the formation depth and average density of rocks in the overlying strata equalling 2,200 kg/m^3;

• horizontal stress determined from vertical stress and Poisson's ratio of rock was applied to the right lateral surface;

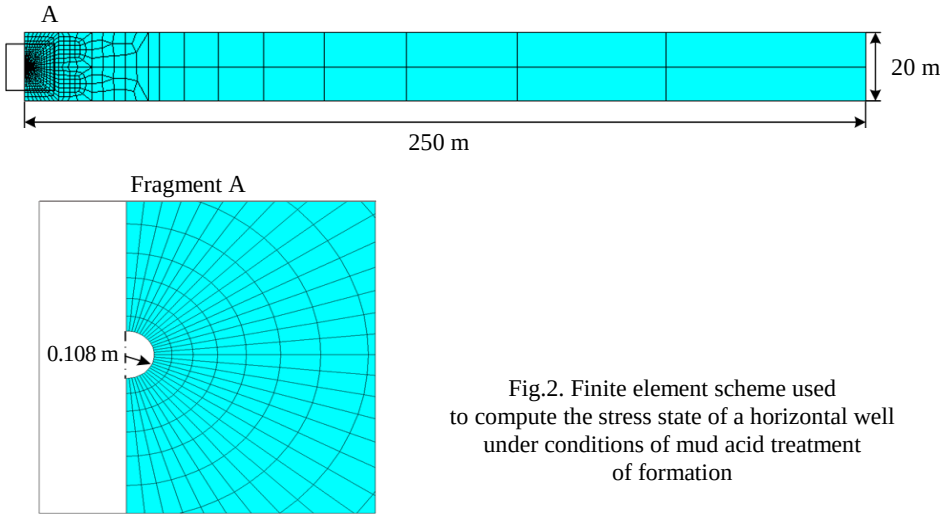

Fig.2. Finite element scheme used to compute the stress state of a horizontal well under conditions of mud acid treatment of formation

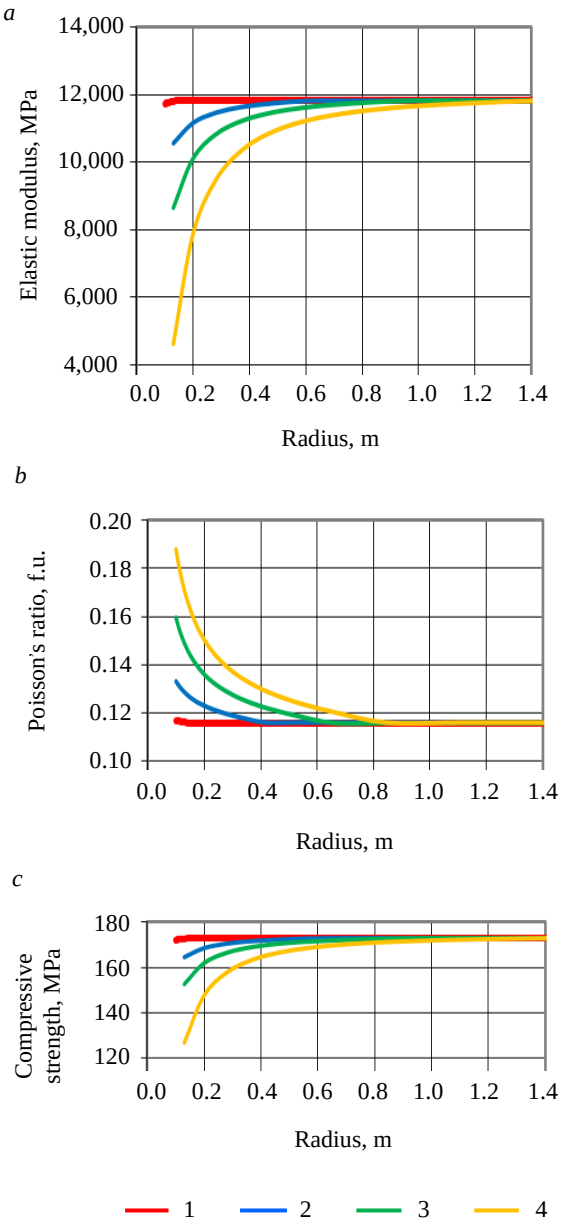

Fig.3. Change in elastic modulus (*a*), Poisson's ratio (*b*) and compressive strength (*c*) depending on radius of distance from well and injection time of mud acid reagent
1 – 14 min; 2 – 4 h, 3 – 9 h; 4 – 32 h

• at the left boundary, due to the symmetry of the model, displacements were fixed in direction of the normal to the surface (zero displacements in horizontal direction).

Using the compiled finite element model, multivariate numerical computations of the stress state of the near-wellbore zone were accomplished taking into account gradual infiltration of acid into the reservoir. It should be noted that non-stationary filtration of liquid was not calculated, and the distribution area of acid reagent was taken based on data from article [7]. Figure 3 shows how the stress-strain properties of rocks change at different time of filtration and exposure to mud acid. The change in these characteristics takes into account, in addition to filtration time of reagent, its effect when holding samples without filtration for 4 h. In the process of computation, in addition to transformation of physical and mechanical properties, pressure drawdown also varied simulating well operation after acid treatment. Pressure drawdown is 1; 5, and 10 MPa.

Discussion of results

Figures 4, 5 show the distribution of horizontal and vertical stresses in case of limiting pressure drawdown values (1 and 10 MPa) and mud acid reagent injection time (14 min and 4 h). As can be seen from Fig.4, 5, an increase in pressure drawdown in most computation versions led to the growing values of effective stresses, both horizontal and vertical. At the maximum acid injection time, the maximum values of effective stresses decrease at the same pressure drawdown. The minimum values of effective stresses behave as follows: for the horizontal stress component and pressure drawdown 1 MPa, they increase, at pressure drawdown 10 MPa, decrease; for the vertical component at pressure drawdown 1 and 10 MPa, they decrease.

Analysing Fig. 4, 5, it can be concluded that there is a tendency to stress reduction in near-wellbore zone at acid treatment, which is associated with a change in elastic characteristics of rocks. It should be also noted that at pressure drawdown 1 MPa, the distribution of tensile stresses (negative values) is recorded in the upper and lower parts of the well. Despite the fact that their value is small – a maximum of 1.78 MPa (Fig.4, *a*), tensile strength of rock can decrease under the influence of acid, which can lead to rock inrushes in these areas.

The next stage involved the assessment of the strength of reservoir rocks near the well based on the Coulomb – Mohr criterion. Fluid pressure in the formation was taken into account in computations, so this criterion was written as follows:

$$\sigma_1 - \alpha p = USC + (\sigma_3 - \alpha p)\frac{1+\sin\varphi}{1-\sin\varphi},$$

where σ_1, σ_3 are the principal maximum and minimum stresses; *USC* – ultimate strength of rock under uniaxial compression; φ – angle of internal friction; *p* – formation pressure.

Fig.6 shows the results of determining the safety factor of reservoir rocks based on the Coulomb – Mohr criterion at pressure drawdown 1; 5, and 10 MPa for different time of reagent injection. If this factor is higher than 1, this points to rock stability; if it is less than 1, then its destruction is likely.

Computation results showed that for the simulated conditions, the destruction of reservoir rocks should not occur, although the minimum safety factor is 1.5, i.e. rocks are close to destruction. As can be seen from Fig.6, the area with the lowest safety factor lies near the lateral surface of the well, which is caused by the effect of vertical stresses, which are much higher than the horizontal ones. A decrease in elastic properties due to the action of mud acid reagent led to a decrease in stresses

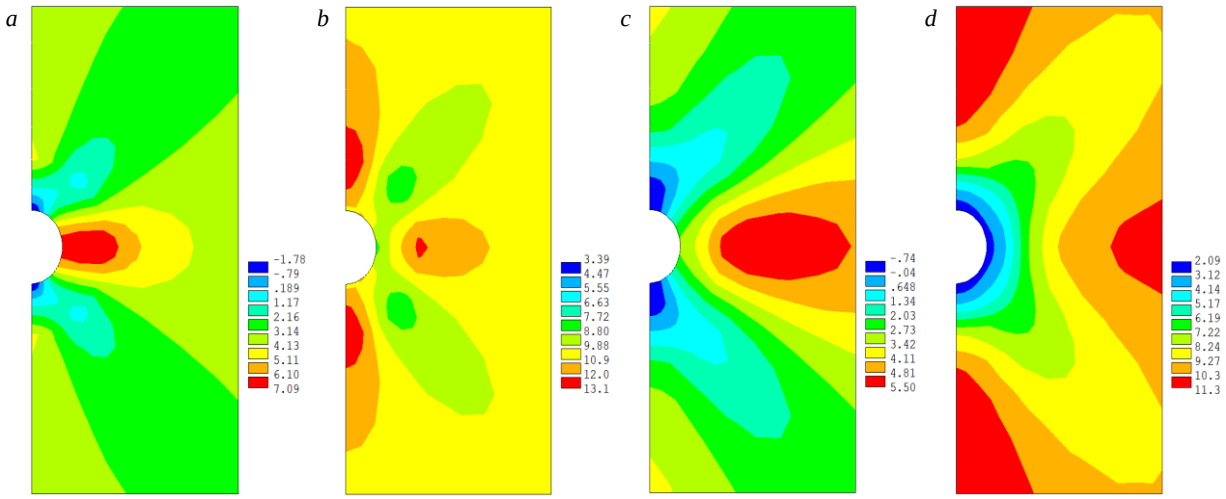

Fig.4. Distribution of horizontal effective stresses at pressure drawdown 1 (*a*, *c*) and 10 (*b*, *d*) MPa after injection of mud acid reagent for 14 min (*a*, *b*) and 4 h (*c*, *d*)

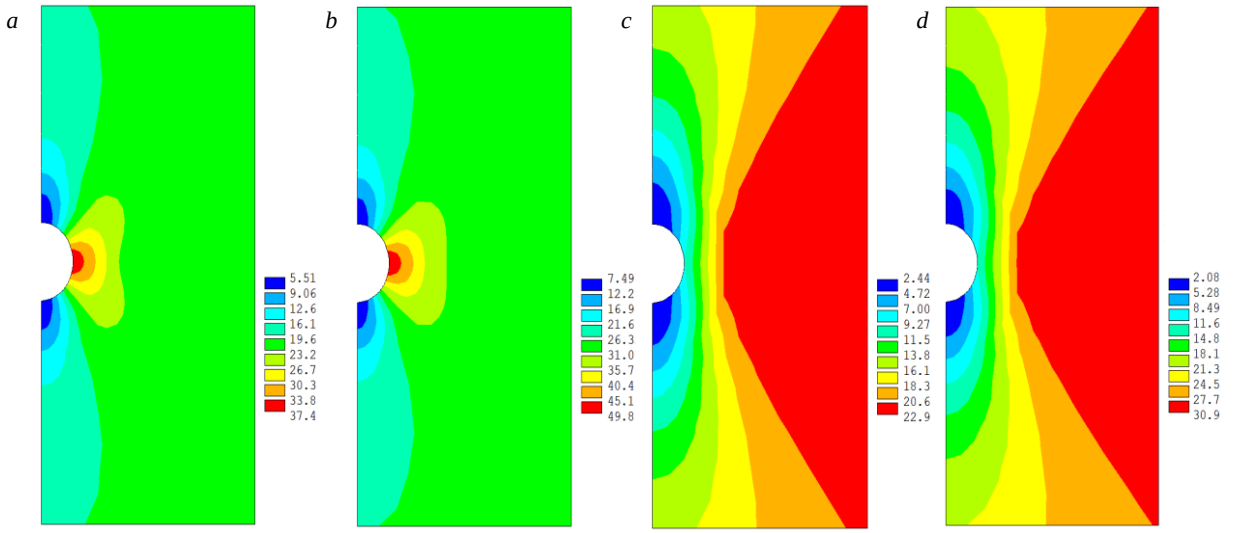

Fig.5. Distribution of vertical effective stresses at pressure drawdown 1 (*a*, *c*) and 10 (*b*, *d*) MPa after injection of mud acid reagent for 14 min (*a*, *b*) and 4 h (*c*, *d*)

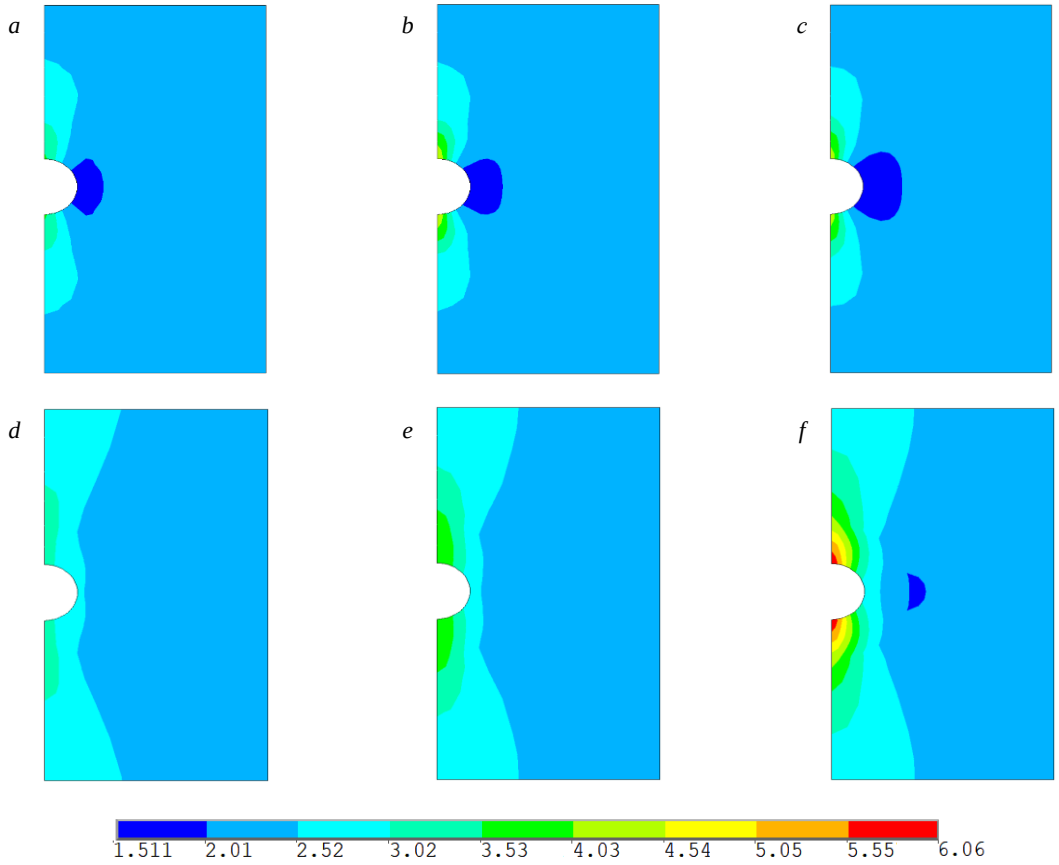

Fig.6. Distribution of rock safety factor near the well for pressure drawdown 1 (*a*, *d*), 5 (*b*, *e*) and 10 (*c*, *f*) MPa after injection of mud acid reagent for 14 min (*a*, *b*, *c*) and 4 h (*d*, *e*, *f*)

and an increase in safety factor, especially in the upper and lower parts of the well (Fig.6, *f*), while an increase in pressure drawdown value led to an increase in this parameter in the areas under consideration and a decrease in the lateral area of the well.

In the course of further investigation of this problem it is planned to compare field data on horizontal wells in which mud acid treatment will be conducted to assess the probability of sand ingress depending on exposure time and volumes of reagent injection, as well as changes in permeability in the near-wellbore zone.

The investigation results can be applied to terrigenous reservoir rocks of the Tulskii and Bobrikovskii producing formations in the southern group of fields in the Perm Territory with similar porosity and permeability, physical and mechanical properties. Difference in permeability values leads to a change in acid filtration area depending on time, and the difference in initial mechanical properties will lead to other ratios describing the relationship of their change depending on the injected pore volumes of reagent, which can require additional laboratory and numerical experiments.

Conclusion

Using the example of a terrigenous reservoir in one of oil fields in the southern Perm Territory, the analysis of the stress state of reservoir near the open hole of a horizontal well was conducted taking into account the transformation of the stress-strain properties of rocks under the action of mud acid reagent. Based on results of analysis, the following main conclusions can be drawn:

• As part of this work, the numerical finite element model of a region of terrigenous formation was compiled including an open hole of a horizontal well and allowing for changes in stress-strain properties of reservoir rocks during mud acid treatment.

• Using the compiled model, a multivariate numerical simulation of the stress state of reservoir was accomplished for different values of pressure drawdown and filtration time of mud acid reagent.

• Analysis of stress distribution field showed that an increase in pressure drawdown led to increasing values of effective stresses in reservoir, while the consequence of a change in elastic properties of rocks under the influence of acid was, on the contrary, their decrease.

• Based on application of the Coulomb – Mohr criterion, the distribution of rock safety factor was determined, which showed that the reservoir was in a stable state both without the effect of mud acid, and with treatment of the near-wellbore zone with this reagent. At the same time, an increase in pressure drawdown led to a decreasing rock safety factor, and the effect of acid led to its increase.

• The numerical model compiled as part of the work can be used to calculate the stress distribution field near horizontal wells for other types of reservoirs, both considering and without considering the change in stress-strain properties under the action of not only mud acid reagent, but also different other physicochemically active liquids.

REFERENCES

1. Peifeng Jia, Chuanzhi Cui, Yingfei Sui et al. Uniform Acid Cleaning Technology and Its Application in Horizontal Wells with Open Hole Screen Tube. *Journal of Physics: Conference Series*. 2023. Vol. 2594. N 012052. DOI: 10.1088/1742-6596/2594/1/012052

2. Ganiev Sh.R., Lysenkov A.V., Gafarov Sh.A. Development of an algorithm for wells and technologies selection for hydrochloric acid treatment of carbonate oil-saturated reservoirs in the Republic of Bashkortostan. *Oil Industry Journal.* 2021. N 2, p. 77-81 (in Russian). DOI: 10.24887/0028-2448-2021-2-77-81

3. Krivoshchekov S.N., Kochnev A.A., Ravelev K.A. Development of an algorithm for determining the technological parameters of acid composition injection during treatment of the near-bottomhole zone, taking into account economic efficiency. *Journal of Mining Institute.* 2021. Vol. 250, p. 587-595. DOI: 10.31897/PMI.2021.4.12

4. Al-Arji H., Al-Azman A., Le-Hussain F., Regenauer-Lieb K. Acid stimulation in carbonates: A laboratory test of a wormhole model based on Damköhler and Péclet numbers. *Journal of Petroleum Science and Engineering*. 2021. Vol. 203. N 108593. DOI: 10.1016/j.petrol.2021.108593

5. Yifan Dong, Yu Lei, Ting Jin et al. Optimized Acidizing Stimulation Technology Achieves Production Increase in Ultra-High Temperature Carbonate Reservoirs. SPE International Hydraulic Fracturing Technology Conference and Exhibition, 12-14 September 2023, Muscat, Sultanate of Oman. OnePetro, 2023. N SPE-215682-MS. DOI: 10.2118/215682-MS

6. Alameedy U., Fatah A., Abbas A.K., Al-Yaseri A. Matrix acidizing in carbonate rocks and the impact on geomechanical properties: A review. *Fuel*. 2023. Vol. 349. N 128586. DOI: 10.1016/j.fuel.2023.128586

7. Popov S.N., Smetannikov O.Yu. Numerical simulation of permeability and stress-strain state change of the near-well zone of a productive reservoir under the combined action of acid composition and varying effective stresses. *Geology, geophysics and development of oil and gas fields.* 2017. N 12, p. 45-53 (in Russian).

8. Plotnikov V.V., Rehachev P.N., Barkovsky N.N. et al. The Effect of Acid Treatments on the Bottom Zone of Clastic Reservoir Rocks of Perm Region. SPE Russian Petroleum Technology Conference and Exhibition, 24-26 October 2016, Moscow, Russia. OnePetro, 2016. N SPE-182063-MS. DOI: 10.2118/182063-MS

9. Mustafa A., Alzaki T., Aljawad M.S. et al. Impact of acid wormhole on the mechanical properties of chalk, limestone, and dolomite: Experimental and modeling studies. *Energy Reports*. 2022. Vol. 8, p. 605-616. DOI: 10.1016/j.egyr.2021.11.249

10. Alameedy U., Alhaleem A.A., Isah A. et al. Effect of acid treatment on the geomechanical properties of rocks: an experimental investigation in Ahdeb oil field. *Journal of Petroleum Exploration and Production Technology*. 2022. Vol. 12. Iss. 12, p. 3425-3441. DOI: 10.1007/s13202-022-01533-x

11. Jahani N., Berge G., Haugen B. Prediction of Rock Strength with Matrix Acidizing Stimulation and Induced Wormhole by Computational Simulation Methods. ISRM Regional Symposium – EUROCK 2014, 27-29 May 2014, Vigo, Spain. OnePetro, 2014. N ISRM-EUROCK-2014-213.

12. Zhukov V.S., Kuzmin Yu.O. Comparison of the approaches to assessing the compressibility of the pore space. *Journal of Mining Institute.* 2022. Vol. 258, p. 1008-1017. DOI: 10.31897/PMI.2022.97

13. Petrakov D.G., Penkov G.M., Zolotukhin A.B. Experimental study on the effect of rock pressure on sandstone permeability. *Journal of Mining Institute.* 2022. Vol. 254, p. 244-251. DOI: 10.31897/PMI.2022.24

14. Karev V.I., Kovalenko Yu.F., KhimuliaV.V., Shevtsov N.I. Parameter determination of the method of directional unloading of the reservoirbased on physical modelling on a true triaxial loading setup. *Journal of Mining Institute.* 2022. Vol. 258, p. 906-914. DOI: 10.31897/PMI.2022.95

15. Turegeldieva K.A., Zhapbasbayev U.K., Assilbekov B.K., Zolotukhin A.B. Matrix acidizing modeling of near-wellbore with reduced reservoir properties (part 2). *Oil Industry Journal.* 2016. N 4, p. 108-110 (in Russian).

16. Deng J., Mou J., Hill A.D., Zhu D. A New Correlation of Acid-Fracture Conductivity Subject to Closure Stress. S*PE Production & Operation*. 2012. Vol. 27. Iss. 2, p. 158-169. DOI: 10.2118/140402-PA

17. Mingwei Wang, Wen Zhou, Song Li, Wen Wu. Simulated Investigation in Wormhole Expansion Law of Gelling Acid Etching and Its Influencing Factors in Deep Carbonate Reservoirs. *Gels*. 2022. Vol. 8. Iss. 8. N 470. DOI: 10.3390/gels8080470

18. Khasanov M.M., Maltcev A.A. Modeling the acid treatment of a polymictic reservoir. *Journal of Mining Institute.* 2021. Vol. 251, p. 678-687. DOI: 10.31897/PMI.2021.5.7

19. Suleymanova M.V., Trofimchuk A.S., Khabibullin G.I. Experience of horizontal injection wells application in the development of terrigenous reservoir of RN-Yuganskneftegas LLC fields. *Oil Industry Journal.* 2023. N 1, p. 23-27 (in Russian). DOI: 10.24887/0028-2448-2023-1-23-27

20. Deryaev A.R. Well trajectory management and monitoring station position borehole. *SOCAR Proceedings.* 2023. Special Issue N 2, p. 1-6 (in Russian). DOI: 10.5510/OGP2023SI200870

21. Murtazin R.R., Aksakov A.V., Yamilev I.M. et al. The study of multiple hydraulic fractures propagation along the horizontal wellbore. *Oil Industry Journal.* 2023. N 2, p. 90-94. DOI: 10.24887/0028-2448-2023-2-90-94

22. Osorgin P.A., Kashapov A.A., Egorov E.L. et al. Development of low-permeable terrigenous reservoirs using horizontal wells with multiple hydraulic fractures at Priobskoye license area of RN-Yuganskneftegas LLC. *Oil Industry Journal.* 2023. N 6, p. 38-43 (in Russian). DOI: 10.24887/0028-2448-2023-6-38-43

23. Li W., Chen L., Wang X. et al. Acid Fracturing Technology and Effect Evaluation of Carbonate Horizontal Well in Fuman Oilfield. *Journal of Physics: Conference Series*. 2024. Vol. 2679. N 012010. DOI: 10.1088/1742-6596/2679/1/012010

24. Fei Liu, Yu Fan, Li Li et al. Case Study of Successfully Staged Acid Fracturing on the Ultra-Deep Horizontal Well for the Qixia Fm HTHP Tight Carbonate Gas Reservoir in China. *Frontiers in Energy Research*. 2022. Vol. 10. N 917740. DOI: 10.3389/fenrg.2022.917740

25. Safari R., Smith C., Fragachan F. Improved Recovery of Carbonate Reservoir by Optimizing Acidizing Strategy; Coupled Wellbore, Reservoir, and Geomechanical Analysis. Abu Dhabi International Petroleum Exhibition & Conference, 13-16 November 2017, Abu Dhabi, United Arab Emirates. OnePetro, 2017. N SPE-188683-MS. DOI: 10.2118/188683-MS

26. Kozyrev A.S., Ermolaev N.I., Mishin A.V. et al. Engineering solutions for horizontal wellbore stabilization in the presence of coal deposits. *Oil Industry Journal.* 2023. N 4, p. 28-33 (in Russian). DOI: 10.24887/0028-2448-2023-4-28-33

27. Dvoynikov M.V., Sidorkin D.I., Yurtaev S.L. et al. Drilling of deep and ultra-deep wells for prospecting and exploration of new raw mineral fields. *Journal of Mining Institute.* 2022. Vol. 258, p. 945-955. DOI: 10.31897/PMI.2022.55

28. Lutfullin A.A., Girfanov I.I., Usmanov I.T., Sotnikov O.S. Software for geomechanical simulation. *Oil Industry Journal.* 2021. N 7, p. 49-52 (in Russian). DOI: 10.24887/0028-2448-2021-7-49-52

29. Tappi N., Cherdasa J.R. 1D Geomechanical Model For Wellbore Stability in Z Field, Y Well Sanga Sanga Working Area, Kutai Basin. *Journal of Geoscience, Engineering, Environment, and Technology*. 2023. Vol. 8. N 02-2, p. 72-84. DOI: 10.25299/jgeet.2023.8.02-2.13871

30. Linsheng Wang, Xinpu Shen, Baocheng Wu et al. Integrated Analysis of the 3D Geostress and 1D Geomechanics of an Exploration Well in a New Gas Field. *Energies*. 2023. Vol. 16. Iss. 2. N 806. DOI: 10.3390/en16020806

31. Fallahzadeh S.H., Shadizadeh S.R., Pourafshary P., Zare M.R. Modeling the Perforation Stress Profile for Analyzing Hydraulic Fracture Initiation in a Cased Hole. Nigeria Annual International Conference and Exhibition, 31 July – 7 August, 2010, Tinapa – Calabar, Nigeria. OnePetro, 2010. N SPE-136990-MS. DOI: 10.2118/136990-MS

32. Magadova L.A., Sirotin A.N., Pakhomov M.D., Davletov Z.R. The Analysis of the Dissolving Ability of Fluorine-Containing Acid Compositions against Silicate Components of Terrigenous Formation. *Oil and Gas Territory*. 2020. N 7-8, p. 72-80 (in Russian).

33. Magadova L.A., Davletshina L.F., Pakhomov M.D., Davletov Z.R. Generation of sedimentation in the interaction with acid compositions of a terrigene reservoir. *Oilfield engineering.* 2015. N 9, p. 31-36 (in Russian).

34. Chernyshov S.E., Popov S.N., Varushkin S.V. et al. Scientific justification of the perforation methods for Famennian deposits in the southeast of the Perm Region based on geomechanical modelling. *Journal of Mining Institute.* 2022. Vol. 257, p. 732-743. DOI: 10.2118/206161-PA

35. Jiecheng Zhang, Moridis G., Blasingame T. Message Passing Interface (MPI) Parallelization of Iteratively Coupled Fluid Flow and Geomechanics Codes for the Simulation of System Behavior in Hydrate-Bearing Geologic Media. Part 1: Methodology and Validation. *SPE Reservoir Evaluation & Engineering*. 2022. Vol. 25. Iss. 03. p. 600-620. DOI: 10.2118/206161-PA

36. Kharlamov S.N., Janghorbani M., Zaykovskiy V.V. Transportation of cuttings by drilling mud in horizontal wells. Part 1. Modeling the structure of dispersed currents. *Bulletin of the Tomsk Polytechnic University. Geo Assets Engineering.* 2023. Vol. 334. N 10, p. 34-48 (in Russian). DOI: 10.18799/24131830/2023/10/4433

Authors: **Sergei N. Popov,** *Doctor of Engineering Sciences, Head of Laboratory, https://orcid.org/0000-0002-1110-7802* (*Oil and Gas Research Institute, RAS, Moscow, Russia*), **Sergei E. Chernyshov,** *Doctor of Engineering Sciences, Head of Department, nirgnf@bk.ru, https://orcid.org/0000-0002-2034-3014 (Perm National Research Polytechnic University, Perm, Russia*), **Wang Xiaopu,** *Doctor of Sciences, Professor, https://orcid.org/0000-0003-1013-2691* (*China University of Petroleum, Qingdao, China*).

The authors declare no conflict of interests.

ISSN 2411-3336; e-ISSN 2541-9404

JOURNAL OF MINING INSTITUTE

Zapiski Gornogo instituta

Journal homepage: pmi.spmi.ru

Review article

Geotechnical Engineering and Engineering Geology

Well killing with absorption control

Danabek S. Saduakasov[1], Akshyryn T. Zholbasarova[1], Ryskol U. Bayamirova[1], Aliya R. Togasheva[1], Maksat T. Tabylganov[1], Manshuk D. Sarbopeeva[1], Aktoty G. Kasanova[1], Viktor N. Gusakov[2], Aleksei G. Telin[3]✉

[1] *S.Yessenov Caspian University of Technologies and Engineering, Aktau, Republic of Kazakhstan*

[2] *Institute of Petrochemistry and Catalysis, UFRC RAS, Ufa, Republic of Bashkortostan, Russia*

[3] *Ufa Scientific and Technical Center LLC, Ufa, Republic of Bashkortostan, Russia*

How to cite this article: Saduakasov D.S., Zholbasarova A.T., Bayamirova R.U., Togasheva A.R., Tabylganov M.T., Sarbopeeva M.D., Kasanova A.G., Gusakov V.N., Telin A.G. Well killing with absorption control. Journal of Mining Institute. 2025. Vol. 272. N 16420, p. 119-135.

Abstract

The development of new fields with low-permeability reservoirs required the introduction of new production technologies, of which the most significant for well killing and underground repair were multi-ton hydraulic fracturing, the simultaneous operation of two or three development sites by one well grid, and an increase in the rate of fluid extraction. These global decisions in field development have led to the need to search for new effective materials and technologies for well killing. The article is devoted to the analysis of problems associated with the process of killing production wells in fields characterized by increased fracturing, both natural and artificial (due to hydraulic fracturing), with reduced reservoir pressure and a high gas factor. The relevance of the analysis is due to the increase in the number of development sites where complications arise when wells are killed. Particular attention is paid to technical solutions aimed at preserving the filtration and capacity properties of the bottomhole formation zone, preventing the absorption of process fluid, and blocking the manifestation of gas. The classification of block-packs used in killing is given, based on the nature of the process fluid. Suspension thickened water-salt solutions are considered, forming a waterproof crust on the surface of the rock, which prevents the penetration of water and aqueous solutions into the formation. This approach ensures the safety and efficiency of killing operations, especially when working with formations in which maintaining water saturation and preventing the ingress of the water phase are of critical importance. Modern trends in the development of technology are revealed, and promising areas for further improvement of well killing with absorption control are outlined.

Keywords

well killing; well repair; blocking compound; filtration; absorption control; rheological properties

Funding

The work was carried out with the support of the Science Committee of the Ministry of Science and Higher Education of the Republic of Kazakhstan (grant N AP19679430).

Received: 29.03.2024 ***Accepted: 07.11.2024*** ***Online: 26.02.2025*** ***Published: 25.04.2025***

Introduction

The article is a review of scientific and technical literature devoted to the problem of well killing with absorption control for the period from the mid-1970's to the present. The relevance of the work is the generalization of published materials and the determination of the possibility of using blocking compositions of different nature as process fluids for well killing in complicated mining and geological conditions. Particular attention is paid to polymer-based blocking fluids containing suspended particles with a solid phase, as the most universal and effective.

The global trend in oil field exploitation is a gradual deterioration in the structure of reserves [1-4]. Well operation is also accompanied by deterioration of the filtration and capacity characteristics of the bottomhole formation zone [5, 6], gas or water breakthroughs through highly permeable channels, mechanical wear of underground equipment. In order to effectively overcome these complications and maintain the target level of oil production, it is necessary to carry out routine and major repairs. One of the important stages of preparation for such work – well killing – includes the introduction of process fluid into the wellbore to create back pressure in order to prevent oil and gas shows. Analysis of the killing results showed that process fluids have a significant negative impact on the production potential of wells in formations with low permeability and low formation pressure due to the absorption of salt solutions into the productive formation [7, 8].

Killing of wells is the most common operation that accompanies a well throughout its entire period of operation. All underground and major repairs, as well as the treatment of the bottomhole zone of wells, begin with killing. The main causes of complications during well killing are well known. The first in importance is associated with a decrease in phase permeability for oil, which occurs due to an increase in water saturation in the bottomhole zone of the formation. When the water-based repair and technological fluid is absorbed at low reservoir pressures, an increase in water saturation occurs in the bottomhole zone, which is uncharacteristic for the formation as a whole at the current stage of development. This problem is especially acute in low-permeability hydrophilic reservoirs, and to eliminate it, hydrophobizers from among cationic surfactants are added to the killing fluid or mutual solvent treatments are carried out [9]. Such measures make it possible to return wells to their pre-repair operational parameters, but are accompanied by significant additional costs.

The second important reason for the complication is also associated with the penetration of salt solutions into the bottomhole zone – swelling of clay minerals and the formation of poorly soluble salts due to a violation of the salt balance [10]. In this case, permeability for liquid decreases and oil inflow decreases. To prevent these negative phenomena, clay swelling reducers and salt deposit inhibitors are added to the killing fluids, which help to remove the complication, but significantly increase the cost of the process.

There is another type of complications during killing, typical for wells with a high gas factor or development objects in the section of which there are gas interlayers [11]. Gas egress during repair is unacceptable, and to prevent it, surfactant solutions are injected into the bottomhole zone so that the escaping gas forms foam, which again means additional costs. The use of fluids with absorption control essentially eliminates all of the above problems. Absorption control is carried out when repair and technological fluids have properties that prevent them from escaping into the formation.

The objective of the review is to analyze technological solutions related to well killing with absorption control in the conditions of development of fields with low-permeability reservoirs, including natural and artificial fracturing, with a high gas factor and low reservoir pressure. The materials presented in the review work will be useful to field workers when performing well killing in complex mining and geological conditions.

Materials and methods of research

To obtain emulsion blocking compounds for killing, degassed oil, diesel fuel, condensate, mineralized water, emulsifiers, and microcalcites are used [12, 13]. To obtain thickened compositions, water-soluble polymers of synthetic nature (polyacrylamide, polyacrylic acid, polyvinylpyrrolidone, polyethylene oxide) and plant origin (carboxymethyl cellulose, hydroxyethyl cellulose, hydroxypropyl guar), biopolymers (xanthan, succinoglucan, scleroglycan), as well as viscoelastic surfactants (zwitterionic compounds) are used [13, 14]. Chalk, microcalcites, boiled halite, dolomite, and siderite are used as colmatants to obtain thickened dispersions [13, 14]. For fractured collectors, fibrous materials are used: asbestos, peat, water-swelling and degradable synthetic fibers [15-17].

The following acids are used as breakers after killing during well development: hydrochloric, formic, acetic, sulfamic; enzymes specific for the decomposition of bio- and plant polymers; peroxides (persulfates, peroxocarbonates, urea hydroperoxide); complexones (oxyethylidenediphosphonic, nitrilotrimethylphosphonic, oxalic acids) [14]. To determine the rheological parameters of blocking fluids (ultimate shear stress, elastic modulus and viscosity modulus), modern rotational viscometers are used, including those with an oscillatory rheometry option [18]. Filtration-blocking characteristics are studied on low- and high-pressure filter presses, as well as using filtration units: imported, for example FDES-645 (Coretest Systems Corporation), and domestic, for example SMP-PS/FES-2R (Kortekh LLC) [19, 20].

Industrial implementation of the preparation of blocking liquids is carried out in accordance with the provisions described in the article [21]. Blocking compounds are prepared at specialized mortar units [12, 22] or using a mobile mixing and averaging unit. The containers used must be equipped with paddle mixers that ensure uniform distribution of chemical reagents throughout the volume, eliminating the occurrence of "dead zones". The reagent preparation unit or container of the required volume must be equipped with an external electric centrifugal pump, a paddle mixer, an ejector for feeding bulk products, piping to the pump, as well as a line for filling and unloading. It is possible to disperse the powder of the water-soluble reagent-thickener through a dry hydrofunnel of the ejector into a stream of water-salt base created by an electric centrifugal pump. It is allowed to disperse the polymer by pouring it into the water-salt solution in the mixing zone of the paddle mixer in the preparation container.

The piping of the tanks for preparing blocking fluids must have a design that provides for the possibility of flushing it in the event of the occurrence of "gel defects". Blocking compositions of increased viscosity are prepared by dissolving a water-soluble polymer thickener in a water-salt base and are intended for temporary and reversible reduction of permeability at the boundary of the well wall – the entrance to the formation, control of the absorption of the killing fluid during underground repair of production and injection wells without hydraulic fracturing, including those with abnormally high reservoir pressure (AHRP).

The preparation of a blocking composition with a solid phase includes dissolving a water-soluble polymer thickener on a water-salt basis with subsequent dispersion of particles with a solid phase, which is used as microcalcite of different grades, boiled halite, dolomite. Suspension of solid particles in a polymer solution is intended for temporary and reversible reduction of permeability at the boundary of the well wall – the entrance to the formation, control of absorption of killing fluids during underground repair of production and injection wells, including those with hydraulic fracturing, wells with super-collector interlayers in the section, wells with slotted and gravel filters in conditions with abnormally low reservoir pressure (ALRP) and AHRP.

The preparation of an emulsion blocking composition for killing requires effective dispersion of degassed oil in a water-salt base and a chemical reagent-emulsifier. Emulsion blocking compositions are intended for temporary and reversible reduction of permeability at the boundary of the well wall – the entrance to the formation of producing wells, control of absorption of killing fluids during repair of wells without hydraulic fracturing, wells with a high gas factor (more than 400 m^3/t), wells operating water-sensitive reservoirs. The technology for preparing emulsion blocking compositions includes a set of the calculated amount of degassed oil or hydrocarbon solvent in the reagent preparation unit. Then the emulsifier is dosed and mixed for at least 30 min with the electric centrifugal pump of the mixer and stirrer turned on. Then the required amount of water-salt base is added and mixed again for at least 2 h. The emulsion blocking composition can be stored in the preparation container before shipment for no more than 2 h. Before shipment after the specified period, this composition is mixed in the container using a centrifugal pump.

Discussion

Absorption control during well killing is ensured by two main mechanisms: an increase in the viscosity of the process fluid, as well as crust formation on the surface of the rock, when a suspension of solid particles clogs the pores and filtration channels. In particular, thickened polymer solutions, hydrogels, and reverse emulsions operate according to the first mechanism, while suspension systems operate according to the second. There are several essentially similar classifications of blocking compositions [23, 24]. The scheme proposed in the article [24], based on the nature of blocking fluids seems to us more illustrative (Fig.1). Let us dwell in more detail on the main types of blocking compositions used in killing with absorption control. Historically, the mass introduction of reverse emulsions in well killing was first carried out at Tatneft PJSC in the 1970's [12]. Special stationary solution units were built, where the reverse emulsion of the required density was prepared. This technology is successfully used at present [25], being a popular tool in capital and underground repair work. Service contractors use emulsifiers that allow creating reverse emulsions for different temperature ranges. Reverse emulsions have proven their effectiveness in killing wells in granular reservoirs. In the case of well killing in fractured reservoirs, as well as in wells with hydraulic fracturing, reverse emulsions do not always cope with their task, because natural and artificially created cracks are capable of absorbing viscous liquids.

An illustrative example of the change in the efficiency of the invert dispersion "Disin", which is a reverse emulsion stabilized by calcium carbonate and calcium oxide hydrate, was demonstrated at Yuganskneftegaz PJSC. This reagent was proposed by G.S.Pop for killing wells at facilities in Western Siberia [26, 27]. At the beginning of its use, when wells with low-volume hydraulic fracturing were killed, the inverted dispersion "Disin", which belongs to the class of Pickering emulsion stabilized by solid particles, coped with its task perfectly [28-30]. As the hydraulic fracturing method developed, when the mass of pumped proppant increased to 200-300 t, "Disin" as a block pack ceased to exhibit blocking properties. The fact is that during the operation of the multi-layer object of the Priobskoye field with a single filter, the highly permeable layer is produced more intensively and the formation pressure in it decreases more significantly. And, although "Disin" contained solid stabilizers, it was not possible to create a strong crust on the surface of the proppant packing, because the dispersed particles were submicron in size and were absorbed by the formation. During repair work, a significant amount of repair and technological fluid had to be added to the wells, and subsequently these wells took a long time to develop and did not reach the pre-repair production level. This problem was solved by specialists of RN-UfaNIPIneft LLC by using suspension blocking fluids based on xanthan polymer solutions with a suspended dispersion of microcalcite. Under the leadership of V.N.Gusakov, together with field engineers (O.V.Akimov and others), suspension killing fluids were developed, where xanthan polymer solutions were used as a dispersion medium, and microcalcites of different grades were used as a dispersed phase [31, 32].

More effective invert dispersions with a solid phase were proposed to be used by D.V.Mardashov and Sh.R.Islamov [33, 34]. These are reverse emulsions in which dispersions of microcalcite of dif-

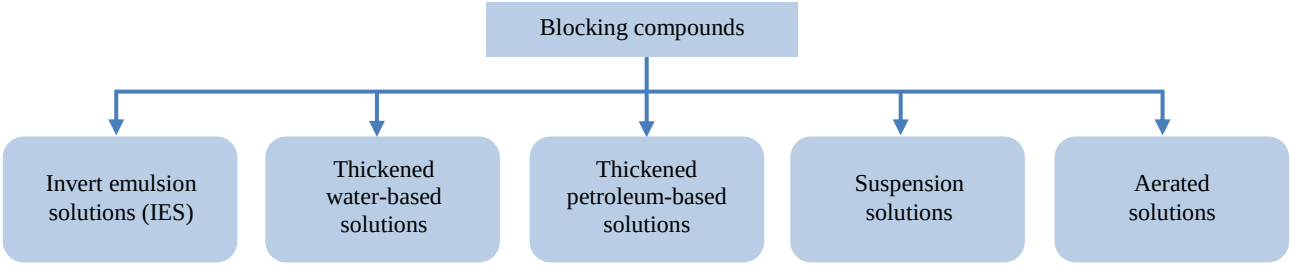

Fig.1. Main types of well killing blocking compounds

ferent sizes are suspended depending on the degree of crack opening (for which an effective emulsifier was selected) for the purpose of killing wells in fractured-porous reservoirs with reduced formation pressure. The fractional composition of microcalcites was calculated purely geometrically according to the criteria of M.Kaeuffer or S.Vickers.

A significant advantage of the block composition based on inverse emulsions is the fact that their external phase is hydrocarbon and does not cause additional filtration resistance when inducing oil inflow after repair. Invert dispersions with granular and fibrous fillers have been successfully used in killing absorbing wells in carbonate reservoirs [35, 36]. This combined solution allows combining two important effects from the use of blocking fluids – not increasing the water saturation of the reservoir and forming a filter cake of solid colmatants. If we compare the effectiveness of invert dispersions with granular fillers and thickened water-based fluids with the same colmatants, then preference should be given to invert dispersions, since they do not introduce an additional water phase into the bottomhole formation zone [37]. The use of invert dispersion is especially relevant in water-sensitive low-permeability granular reservoirs, where the ingress of the aqueous phase into the bottomhole formation zone is unacceptable.

An interesting approach to the use of Pickering emulsion is shown in the work [38], in which emulsions were stabilized by hydrophobic and hydrophilic nanosilicas, which ensured their stability at high temperatures. In the article [39] the emulsion composition was obtained on the basis of "green chemistry". In particular, biodiesel was used as the hydrocarbon phase – methyl esters of fatty acids obtained by transesterification of rapeseed oil.

The use of thickened water-based solutions for killing wells has also been known for a long time. B.A.Andreson (1976) proposed using salt solutions thickened with polyacrylamide with the addition of surfactants for killing wells at Bashneft PJSC. The surfactant-containing polymer solution "Chance" was successfully used at the fields of YUKOS Oil Company [40] with the introduction of refining additives.

Unlike polymer solutions, hydrogels used as block packs for well killing are more effective because, due to their cross-linked structure, they are practically not filtered into the formation. In particular, in order for a polysaccharide killing fluid based on xanthan or hydroxypropyl guar solutions cross-linked with a borate cross-linker to begin to filter into the formation, a pressure differential of more than 6.0 MPa is required [41, 42]. For killing wells in fractured-porous reservoirs with a high gas factor by D.V.Mardashov and A.V.Bondarenko [20, 43] proposed a hydrogel based on xanthan gum cross-linked with chromium acetate as a block pack. The advantage of such a hydrogel is that it successfully blocks cracks, while possessing high gas-retaining capacity.

The use of hydrogels as blocking fluids has been rapidly developing in recent years due to the possibility of flexible regulation of their properties depending on the conditions of use. Thus, when killing wells in fractured reservoirs, a viscoelastic gel based on oxyethylated cellulose cross-linked with copper sulfate was used. A peroxyhydrate-citric acid system was used as a breaker [44]. For the same purpose in the work [45] a hydrogel based on guar and xanthan gum crosslinked with a borate crosslinker is proposed. This technology is distinguished by a controlled gel decomposition time, which is achieved through the use of an encapsulated breaker – the same peroxyhydrate system with citric acid.

For killing wells in fractured reservoirs with high formation pressure, a sodium bromide-weighted nanocomposite hydrogel system cross-linked with covalent bonds with a density of 1.2-1.5 g/cm^3 has been developed [46]. The heat resistance of the blocking composition is determined up to 160 °C, and the gelation time is regulated from 8 to 12 h.

Foam gel based on a double-crosslinked hydrogel (polyacrylamide + Cr^{3+} + polyethyleneimine), foamed due to the release of CO_2 during the reaction of acid with carbonates, and was used in the overhaul of wells in reservoirs with low formation pressure and low temperature [47, 48].

For killing wells containing toxic acid gases in associated gas, such as H_2S, CO_2, SO_2, a gel based on plant resin with a crosslinker and pH regulator is proposed. At pH 8, the gel does not break down for 72 h at 150 °C with a concentration in water of H_2S – 300 mg/l and CO_2 – 100 mg/l. After gelation, the viscosity is 30 Pa·s, and after the introduction of a breaker for 6 hours it decreases to 3 mPa·s [49].

A block composition based on salt-resistant partially hydrolyzed polyacrylamide when killing highly watered wells in fractured reservoirs allows not only to carry out repair work without problems, but also to reduce water cut and increase oil production due to the effect of water insulation when gel leaks into cracks [50]. In the article [51] the use of a high-viscosity gel plug in well repair is described, which is convenient in that the viscosity of the gelled composition reaches 30,000 mPa·s, and after exposure to an acid breaker after 4 h it decreases to 5 mPa·s. Viscous gelled blocking compositions with adjustable gel decomposition time are used for routine and major repairs of wells in order to reduce the risk of gas manifestations [52].

It should be noted that hydrogels based on partially hydrolyzed polyacrylamide have been increasingly modified with nanoparticles in recent years. The fact is that under severe conditions of temperature and salt aggression, decomposition of block packs based on cross-linked polymer systems occurs. The destruction of hydrogels consists of rupture of the main polymer chains, rupture of cross-links, hydrolysis of the polymer and syneresis [53]. Nanosilica particles interact with their silanol groups with the carboxyl group of partially hydrolyzed polyacrylamide to form a hydrogen bond (proven by IR spectra) [54], thereby enhancing the interaction with water molecules and preventing dehydration and syneresis of the gel [55]; in this case, the nanoparticles are evenly distributed throughout the entire volume of the hydrogel. In the work [56] it has been shown that the introduction of 9 % nanosilica increases the strength of the hydrogel by 5000 %. From the images obtained using an electron microscope, it is evident that the nanoparticles reinforce the hydrogel during gelation *in situ*, which allows the temporarily blocking material to significantly better withstand temperature, salt and shear effects compared to the hydrogel without the addition of nanosilica. In fractured carbonate formations with low reservoir pressure, it is sufficient to introduce 5 % nanoparticles into the hydrogel, and at the same time, the increase in the structural and mechanical properties of such a nanocomposite allows for trouble-free repair work [57]. Data are provided that the addition of 8 % nanosilica to a gel based on partially hydrolyzed polyacrylamide and an environmentally friendly crosslinker – polyethyleneimine provides a 14-fold increase in the elastic modulus with a viscosity modulus of only 71 Pa, which is extremely favorable from the point of view of low damage to the granular collector [58]. For wells in high-temperature development objects, the nanocomposite gel is obtained from heat-resistant sulfonated polyacrylamide with the addition of secondary-modified laponite, thiourea, and a crosslinker – polyethyleneimine [59]. Authors of the article [60] noted that the linear dimensions of nanosilica significantly affect the properties of nanocomposites. Thus, a hydrogel based on partially hydrolyzed sulfonated polyacrylamide cross-linked with chromium acetate has maximum strength characteristics with nanoparticles of 20-30 nm in size compared to similar gels with the addition of nanosilica of 7-10 nm and 60-70 nm in size.

Specialists from different countries around the world pay much attention to self-destructing hydrogels. Thus, in the works [61, 62] self-destructing gels under the influence of temperature based on pre-formed gel particles are proposed. In the articles [63, 64] gels with an internal breaker with adjustable decomposition time are described. Safe repair time is determined based on laboratory experiments at reservoir temperature. In order to predict the time of thermal self-destruction of hydrogel block compositions in the work [65] kinetic experiments were conducted and a mathematical model was developed that coincided with the results of the study of temperature aging with a correlation coefficient of 0.988. This approach allows us to predict the time that block compositions will be in working condition and to estimate the safe period for carrying out repair work on wells.

Variants of using gel-fiber systems for temporary blocking of the formation are considered. Cellulose nanofibrils were added to the hydrogel based on heat-resistant sulfonated polyacrylamide cross-linked with polyethyleneimine [66]. At the same time, such a nanofibrous composite was superior in its structural-mechanical and heat-resistant properties to a nanocomposite with the addition of an equal amount of nanosilica. The fibrous synthetic filler was fed into a high-temperature well in a polymer solution, where, over a pre-calculated time, the synthetic fibers were hydrolyzed with the release of organic acids, which in turn destroyed the polymer [67]. Summarizing the analysis of the use of block compositions, we can note the review in the article [68], where the properties of gels obtained *in situ*, methods for increasing their thermal stability and structural-mechanical properties, regulating the rate of gelation, methods of destruction and self-destruction are summarized.

Viscoelastic surfactant compositions based on zwitterionic compounds are increasingly used as hydrogel block packs [69, 70], which have a significant advantage over hydrogels based on water-soluble polymers – they are destroyed upon contact with oil and water, causing an influx after repairs.

Thickened petroleum-based solutions (commercial thickened petroleum) [71] are used to kill wells with low reservoir pressure. Recently, their use has been very limited in accordance with fire safety regulations. Although in some production enterprises, for example in Slavneft-Megionneftegaz PJSC, hydrocarbon-based blocking fluids were once quite widely used [72].

The use of water-based suspension blocking compositions has also been known for a long time. At first, clay solutions were used in this capacity, which, although they had a slight advantage over mineral salt solutions, were not effective enough due to the colmatation of the bottomhole formation zone. In particular, S.Z.Zaripov (1981) showed that killing wells with clay solutions (Bashneft PJSC) in the 1970s led to a significant decrease in well productivity. Research by the service company M-I Swako convincingly showed that it is most expedient to suspend the colmatant particles in thickened solutions of biopolymers. Since biopolymers of microbial origin have a branched structure and fairly high values of the viscoelastic component of complex viscosity, suspended particles do not settle. In addition, in the works [73, 74] the calculation of the optimal fractional composition of colmatating particles depending on the diameter of the pores of the rock is given. Implementation of technologies using absorption control materials (Liquid Control Materials – LCM), or LCM technologies, involves the use of such components as a water-salt base, a water-soluble polymer thickener, a breaker for breaking down the polymer and restoring permeability (Fig.2) [75]. Industrial water is used as a water-salt base, as well as solutions of mineral salts (water-soluble polymers used as thickeners).

The main technological disadvantages of polymer thickeners are the risk of obtaining "gel defects" [76] and a significant loss of viscosity with increasing temperature. Only systems thickened with succinoglycan and erucylamidopropyl betaine (belongs to the class of high-viscosity surfactants) retain their viscosity up to 70 °C [75].

To maintain the production potential of wells and quickly bring them into operation after killing when using polymer blocking fluids, it is necessary to use breakers individually selected for each class of thickeners. Breakers affect the carbon chains of polymers, chemically modify

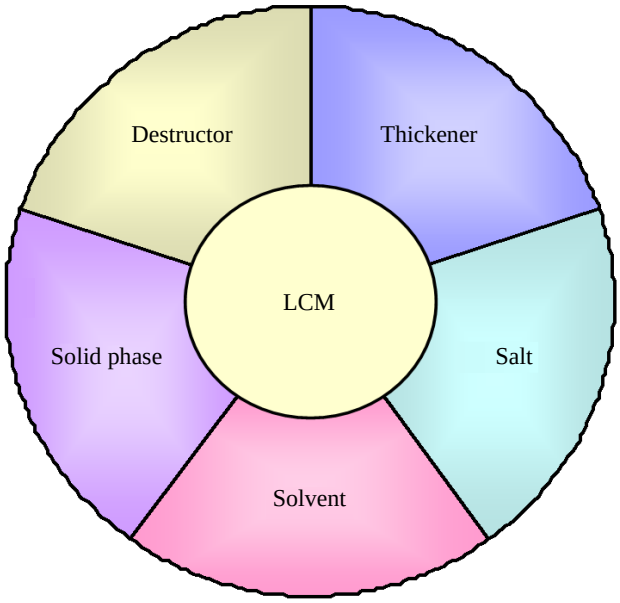

Fig.2. System of components for the implementation of LCM technologies

the functional groups of macromolecules and destroy the network structure of hydrogels. Peroxides, enzymes, acids and complexones are used for these purposes. Breakers are used in two variants. In the first case, the breaker is a component of the process fluid. This variant is possible when the breaker action begins with a long induction period. By this time, the main operations of the current well repair should be completed, and after the destruction of polymer molecules when well is stimulated, the permeability coefficient is restored. According to the second variant, the breaker is pumped in after the main stages of well repair and also ensures permeability restoration. Polymer-free thickened fluids do not require the use of a breaker, since the viscosity of such a system is reduced upon contact with water or oil, causing an influx after repair [77, 78]. Due to the fact that the zwitterionic surfactants used for these purposes have good surface-active properties, after the destruction of cylindrical micelles with viscoelastic properties, an easier influx triggering is achieved. When using suspension blocking killing fluids, it is possible to use modifying additives from the glycol class, which reduce the adhesion of the colmatant crust to the surface of the rock [74].

Another method of forming a filter cake with a small depth of penetration of colmatants into the formation is carried out by selecting the fractional composition of the colmatant corresponding to the distribution of pores by size. If the particle size is much smaller than the average diameter of the pores, then undesirable penetration of these particles into the filtration channels will occur; particles with a diameter much larger than the pore sizes are not capable of forming a low-permeability cake, which leads to fluid absorption during repair.

Optimization of the colmatant size comes down to selecting the composition of dispersions of different sizes [79]. According to the Ideal Packing Theory (IPT, M.Kaeuffer), the selection is carried out by the method of approximating the dependence "integral fractional composition – square root of the particle diameter" to an ideal straight line. Another option for optimizing the particle size distribution (according to S.Vickers) is specified by a curve with parameters [79] at diameters: D_{max} – particle fraction 90 %; $2/3D_{max}$ – 75 %; $1/3D_{max}$ – 50 %; $1/7D_{max}$ – 25 %; D_{min} – 10 %. To create the densest filter cake according to the A.Abrams criterion, a colmatant with a particle diameter of 1/7 to 1/3 of the pore diameter is required. The densest low-permeability and thin filter cake can be obtained by selecting particles by size according to the S.Vickers criterion (Table 1 [79]).

Table 1

Results of tests of filter cakes formed by well killing fluids

Disc pore size, μm	Parameter	Calculation of the fractional composition of the colmatant according to the criteria		
		S.Vickers	M.Kaeuffer	A.Abrams
5	Filtration efficiency, cm^3/30 min	21.0	22.0	30.0
	Recovery coefficient, %	93.8	49.5	61.5
20	Filtration efficiency, cm^3/30 min	20.0	42.0	23.0
	Recovery coefficient, %	85.7	69.5	80.9
60	Filtration efficiency, cm^3/30 min	20.8	31.0	19.0
	Recovery coefficient, %	86.2	78.1	93.5

It should be noted that the justified composition of the colmatant can be determined with knowledge of the distribution of pore sizes in the porous medium. For the use of a blocking fluid with a solid phase in wells after hydraulic fracturing, finding the optimal size of dispersed particles is simplified, since the proppant size for each well is known (Fig.3). The algorithm of actions intended for the practical use of the technology of killing with absorption control is indicated in Table 2 [14]. The field experience of RN-Yuganskneftegaz LLC in killing wells with absorption control, carried out according to the algorithm given in Table 2, confirmed the correctness of the chosen solution [14, 31]. The use of microcalcite as a solid phase for suspension blocking fluids is safe, since this colmatant is easily soluble in acid when needed [80]. The use of polymer thickeners is characterized by the risk of the formation of so-called gel defects, which arise due to incomplete polymer dissolution in a

water-salt base. To prevent this phenomenon, dispersion of the polymer in non-aqueous polar solvents is used. Modern technologies of well killing with absorption control are developing rapidly, since they reduce the consumption of aqueous brines and, accordingly, reduce the number of complications caused by the intensive development of terrigenous and carbonate reservoirs. Thus, in 2008, RN-UfaNIPIneft LLC, together with employees of RN-Yuganskneftegaz LLC, developed and patented an effective solution for killing multi-layer wells of the Priobskoye field with multi-tonnage hydraulic fracturing [32, 81]. In comparative tests with the technology of M-I Swaco (Seal-N-Peel), the Russian version using a block-composition of muffling with microcalcite (BSG-MK) showed comparable efficiency.

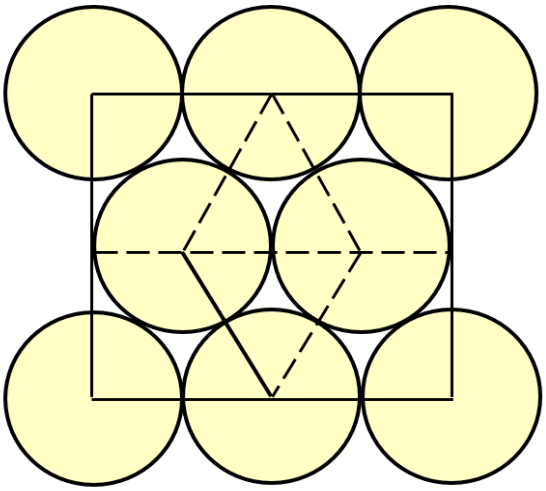

Fig.3. Graphical construction of calculation of proppant packing transparency

Table 2

Algorithm for selecting a well killing design with absorption control

Required calculation parameter	Source of information	The characteristic being determined	Algorithm of action
Volume of blocking killing fluid V, m^3	Oil and gas production workshop data	Specific volume of the well in the zone from the current bottomhole to the upper perforation holes	$V = 0.001V_{sp}\,[h_{crnt.btm} - h_{up} + 150] + V_{exc}$
Excess volume of blocking killing fluid V_{exc}, m^3	Oil and gas production workshop data	Position of the upper perforations and the perforated interval	$V_{exc} = 0.0007h_{up} + Kh_{perf}$ K = 0.05 и 0.01 m^3/m for directional and horizontal wells
Reservoir pressure P_0 at the start of repairs, Pa	Oil and gas production workshop data	Excessive wellhead pressure P_{exc} by water at the beginning of repairs	$P_0 = \rho gh + P_{exc}$
Reservoir pressure P_r for the duration of the repair, Pa	Data from hydrodynamic studies of wells	Pressure recovery curve for a well	$P_r = P_0 + K(T)½$
Density of the killing fluid at 20 °C taking into account thermal expansion at positive temperature $\rho(t)$, kg/m^3	Reference literature	Thermal expansion coefficient of the kill solution $\alpha \approx 0.5838$ kg/(m^3·°C)	$\rho(t) = \rho(20) - \alpha(t - 20)$
Daily forecast of change in density of kill fluid taking into account the pressure recovery curve	Estimated data	Reservoir temperature and pressure $p(T,t) = \frac{P_0 + K\sqrt{T}}{gh_{vert}} + \alpha(t - 20)$	Calculation of the density of the killing fluid with correction for the pressure recovery curve
Proppant grain pore mouth diameter $D_{max} - D_{min}$, μm	Well passport	Fractional composition of proppant	Proppant brand
Fractional composition of a mixture of microcalcites for the formation of a filter cake	Filling theory (according to S.Vickers criterion)	Criterion according to S.Vickers: D_{max} – 90 % 2/3D_{max} – 75 % 1/3D_{max} – 50 % 1/7D_{max} – 25 % D_{min} – 10 %	Minimization of deviation of the model curve of microcalcites from the curve according to S.Vickers (software product)
Thickener concentration in the blocking killing fluid	Experimental data	Dependence of sedimentation stability of suspension on thickener concentration	Visual observation of suspension stability
Effective viscosity of blocking killing fluid	Experimental data	Flow time of 500 cm^3 of blocking liquid on the VBR-2 viscometer in laboratory and field conditions	Determination of the flow time of 500 cm^3 of blocking liquid on the VBR-2 viscometer

Notes: K – permeability, μm^2; $h_{crnt.btm}$ – distance from wellhead to current bottomhole, m; h_{up} – distance from wellhead to upper perforation holes, m; h_{perf} – perforation interval, m; h_{vert} – vertical depth of upper perforation holes, m; g – acceleration of gravity, m/s^2; T, t – formation temperature, °C.

In 2009, a number of production companies of Rosneft Oil Company introduced the technology of a suspension blocking fluid with a self-destructing colmatating solid phase – halite (BSG-halite) [82]. The main technological advantage of such a composition is the ability of solid shunting particles to completely dissolve when causing an influx of watered products after completion of underground well repair (UWR). This feature allows eliminating the risk of colmatation of the bottomhole formation zone, installing a block pack with squeezing onto the formation, carrying out flushing and normalization of the bottomhole in conditions of absorption. Due to the growth of the initial shear gradient when a free gas phase appears, this material can be successfully used for killing oil wells with a high gas factor and gas condensate wells [83]. A similar approach to the use of water-soluble salt dispersions is described in a later publication [84]. The use of a dispersion of polyethylene wax and oil-soluble phenolic resin with rosin is known as oil-soluble colmatants. The advantage of such materials is that when well is stimulated they completely dissolve in oil. According to core studies, they provide a permeability recovery coefficient from 0.90 to 0.95 [85].

Another typical example of the use of block packs is demonstrated during the killing of wells at Jurassic sites developed by Kharampurneftegaz LLC, where the work is complicated by a number of negative factors, such as low permeability of the hydrophilic reservoir, high gas factor, and low reservoir pressure. In order to eliminate the impact of these complications on the success of UWR, an approach to the killing technology was developed, which consists in combining several types of process fluid, which, when used together, allow to minimize the risks of reducing the production potential of wells [19]. Thus, to prevent gas leaks, a blocking liquid based on the polymer "Biopol" and surfactants (gas blocking composition – GazoBS) has been developed, which acts due to its viscoelastic properties (polymer) and foaming ability upon contact with gas (surfactant).

A spacer fluid designed to prevent swelling of clay cement, reduce interfacial tension and restore phase permeability to oil was developed on the basis of a 6 % HCl solution with the addition of a surfactant-hydrophobizing agent (spacer hydrochloric acid fluid – BufSK). The blocking killing compositions BSG-MK and BSG-halite were used to prevent absorption of the killing fluid at reduced formation pressure in wells with hydraulic fracturing. Pilot-field work was carried out on 23 wells, where the GazoBS block-packs were used 21 times, BufSK – 9 times, BSG-halite and BSG-MK – 14 and 9 times, respectively (Table 3). All wells underwent UWR to replace the electric centrifugal pump without changing its size, as well as to replace/review the tubing. Borehole normalization was performed on two wells. The observed slight increase in fluid flow rate after UWR is due to cleaning of perforation holes from calcite deposits due to the action of BufSK and abrasive cleaning of paraffin deposits – with BSG-halite and BSG-MK compositions.

Table 3

Results of pilot-field work tests of process fluids

Blocking liquid	Number of tests		Total relative flow rate, before UWR / after UWR (bringing to stable production), %	
	Total	With a decrease in oil flow rate during the well's commissioning	Liquid	Oil
BSG-MK	9	2	100/100.6	100/100.5
BSG-halite	14	2	100/102.4	100/104.3
BufSK	9	0	100/100.7	100/105.4
GazoBS	21	3	100/102.7	100/101.6
Total wells	23	3	100/102.5	100/102.8

The use of aerated fluids for well killing is necessary in fields with ALRP to avoid the absorption of the killing fluid into the formation. Back in the 1970s, A.V.Amiyan proposed using two- and three-phase foams for this purpose [86]. Subsequently, this technology was successfully extended to gas and gas condensate fields, which are very sensitive to the water phase in the bottomhole formation zone [87]. At the same time, the use of foam systems for well killing is complicated by their instability

over time, as well as destruction upon contact with oil. Rapid restoration of the properties of foam systems in the wellbore is possible by their repeated circulation.

For the suppression of gas condensate objects with low reservoir pressure and high temperature, a foam-polymer composition with increased foam stability based on sodium dodecyl sulfonate and dodecyl methyl betaine, stabilized with xanthan gum [88] and polyurethane thickener [89] is proposed. The composition remains functional at mineralization up to 10,000 mg/l and temperature up to 150 °C for 24 h. If the well repair lasts longer, it is necessary to restore the foam system in the wellbore by pumping in new portions [88]. This article provides an example of a well repair to remove sand from the bottomhole, which lasted 58 h and went without complications. The work described [88] the technical solution involves the use of complex additional equipment – a tanker-pumper of liquid nitrogen or a mobile truck-generator of nitrogen, a foam generator. The use of self-generating foam gel systems as blocking liquids [90] allows for repair work at high temperatures without the risk of reducing the volume of nitrogen foam. This foam gel system consists of a gel-forming composition, a gas-generating mineral composition, and a surfactant. Due to its low density, the foam gel is easily removed from the wellbore when well is stimulated. The high stability of foam gels over time and at elevated temperatures is due to the fact that the foam lamellas are a cross-linked polymer composition with high structural and mechanical properties [91].

Another promising direction for objects with ALRP is the use of aphrons – microbubble systems stabilized from polymer and surfactant solutions, first proposed by M-I Drilling Fluids. Initially, these aerated fluids were used in drilling [92, 93].

Based on the materials presented in this review article, recommendations have been made for the use of various blocking compositions of killing fluids (Table 4). For killing in conditions of multiple complications, a combination of several types of blocking killing fluids is required, as well as the development of a selection matrix and application technology in the conditions of a specific research object, fixing the injection order, risks, and limitations of applicability.

Table 4

Selection of well killing fluids

Blocking fluid for well killing	Basis for selection of blocking killing fluid
IES	Wells in granular and fractured reservoirs without hydraulic fracturing with normal reservoir pressure
IES with dispersed or fibrous fillers	Wells in granular reservoirs with hydraulic fracturing. Wells in fractured reservoirs with normal reservoir pressure and ALRP. Fact of gas shows for the previous UWR
BSG-halite	Wells in granular and fractured reservoirs with normal reservoir pressure and ALRP. The fact of excess of the kill solution consumption is 30 m^3 higher than according to the technological plan of kill for the previous DPW (or excess of the kill solution filling rate by more than 1 m^3/h)
BSG-MK	Wells in granular and fractured reservoirs with hydraulic fracturing with normal reservoir pressure, ALRP and AHRP. The fact of excess of the consumption of the killing solution is 30 m^3 higher than according to the technological plan of killing for the previous UWR (or excess of the rate of adding the killing solution over 1 m^3/h)
BSG-MK	Wells in multi-layer objects operated by a single filter, granular and fractured reservoirs with hydraulic fracturing with normal reservoir pressure, ALRP and AHRP. The fact of excess of the consumption of the killing solution is higher by 30 m^3 than according to the technological plan of killing for the previous UWR (or excess of the rate of adding the killing solution over 1 m^3/h)
IES with dispersed or fibrous fillers	Wells in multi-layer objects operated by a single filter, granular and fractured reservoirs with hydraulic fracturing with normal reservoir pressure, ALRP and AHRP. The fact of excess of the consumption of the killing solution is higher by 30 m^3 than according to the technological plan of killing for the previous UWR (or excess of the rate of adding the killing solution over 1 m^3/h)
GazoBS	Wells in granular and fractured reservoirs with normal reservoir pressure, ALRP and AHRP. Fact of gas shows for the previous UWR with a gas flow rate of at least 1000 m^3/day
BufSK	Wells in granular low-permeability water-sensitive reservoirs. Water cut of produced fluid is less than 50 %. Requires combination with a second block-pack (IES, BSG-halite, BSG-MK)

Conclusion

Let us note several main trends in the development of the technology of well killing with absorption control. In the perimeter of the post-soviet countries, the first trend is the implementation of scientific development of these technologies in oil universities and institutes. Thus, at the St. Petersburg Mining University, under the leadership of M.K.Rogachev and D.V.Mardashov, a range of modern well killing technologies has been developed that respond to almost all production challenges [94-97]. At the Russian Gubkin State University of Oil and Gas, under the supervision of L.A.Magadova and M.A.Silin, a method of killing using a polysaccharide liquid as a block pack was developed and implemented [98]. At the Ufa State Petroleum Technological University, under the leadership of Yu.V.Zeigman and V.Sh.Mukhametshin, this direction is also successfully developing [99].

The second trend is the development, adaptation and optimization of the technology of killing with absorption control in industry research institutes. Here, the undisputed leader is RN-BashNIPIneft LLC. This institute supports this direction in the perimeter of Rosneft Oil Company, where development objects, radically different from each other in their geological and physical characteristics, are geographically located in almost all regions of Russia. In this regard, universal technical solutions are impossible, and for each characteristic group of fields it is necessary to optimize the best technologies. It should be noted that the systematic approach of RN-BashNIPIneft LLC employees allowed them to first systematize technical solutions for well killing in different mining and geological conditions, clearly substantiate the criteria for the applicability of block packs of different nature [100], and then adapt and optimize the technologies of well killing for specific development objects. Thus, for the carbonate object of the Kuyumbinskoye oil and gas condensate field, suspension and foam gel block-packs were adapted [101]. For deposits in Eastern Siberia with low-temperature, highly permeable terrigenous reservoirs, suspension block packs with instant filtration are recommended, capable of quickly forming a strong crust and preventing the absorption of process fluid [102]. For killing gas wells exploiting Achimov deposits, RN-BashNIPIneft LLC recommended the use of suspension block packs, in which a heat-resistant polymer is used as a thickener, as well as a modified salt composition based on viscoelastic surfactants [103].

The third trend is the wide variety of technical solutions offered by service companies on the service market. Each service company has its own range of technical solutions, with which they present them to tender commissions of oil companies. In this type of business, it is necessary to note such service companies as Mirrico Group of Companies [104], Zirax Group of Companies [105].

The use of nanocomposite hydrogels is clearly visible in the development trend of absorption-controlled wellbore killing technologies abroad; moreover, the application options for hydrogel-based block compositions are quite diverse depending on reservoir conditions and the technical task of repair [68]. Comparing the technical level of Russian and foreign approaches, it can be noted that the development of the level of technology and engineering in this direction is proceeding in parallel courses without any obvious advancement or lag of either side. Publications by Russian specialists are regularly published in prestigious international journals of the Q1 level, which testifies to the worldwide recognition of the relevance and novelty of the published materials.

Thus, it is safe to state that today well killing technologies with absorption control in the oil industry are successfully used all over the world. In Russia, the production needs for adapting technical solutions to specific geological and physical conditions are met by industry institutes and service firms. A stable services market has formed, which undoubtedly contributes to progress in this area. Let us pay attention to aerated fluids for absorption control, in particular aphrons, the discussion of the structure and properties of which continues to this day [106]. However, they are already being used stably in drilling, and this direction is developing [107-110]. There is a mention of the use of aphron-like compounds for waterproofing [111], and there are only a few publications on their use for well killing, from which the potential of this approach is evident; for example, in the use of aphron-like foam plastic blocking fluids formed by the interaction of surfactants and polymers with a gas-liquid system, which are called fuzzy-balls [112, 113].

REFERENCES

1. Shmal G.I. The Problem of Developing Oil Difficult to Recover in Russia and Solution Approaches. *Georesources.* 2016. Vol. 18. N 4. Part 1, p. 256-260 (in Russian). DOI: 10.18599/grs.18.4.2

2. Iskritskaya N.I., Makarevich V.N., Schepochkina A.A. Changes in the structure of the hard-to-recover oil reserves caused by transition to the new classification. *Neftegazovaya Geologiya. Teoriya i praktika.* 2016. Vol. 11. N 4, p. 12 (in Russian). DOI: 10.17353/2070-5379/44_2016

3. Khafizov F.Z. Problems of development of hard-to-recover reserves. *Nedropolzovanie XXI vek.* 2014. N 3 (47), p. 68-73 (in Russian).

4. Korotkevich A.I. The role of hard to recover reserves in conditions of deterioration of the structure of reserves. *Neftegaz.RU.* 2018. N 6 (78), p. 52-57 (in Russian).

5. Fung Van Khay, Shamaev G.A., Nguen Khyu Nyan et al. Basic problems reducing permeability near wellbore of the lower oligocene ("White tiger" oilfield). *Bashkir chemistry journal.* 2008. Vol. 15. N 2, p. 135-139 (in Russian).

6. Erofeev A.A., Mordvinov V.A. Changing the properties bottom-hole within the development of Bobrikovsky Unvinskogo deposit. *Perm Journal of Petroleum and Mining Engineering.* 2012. Vol. 11. N 5, p. 57-62 (in Russian).

7. Dmitruk V.V., Rakhimov S.N., Boyarkin A.A., Shtakhov E.N. Improving the effectiveness of killing wells of Urengoyskoye field. *Oil Industry Journal.* 2010. N 5, p. 130-135 (in Russian).

8. Vakhrushev S.A., Mikhailov A.G., Kostin D.S. et al. Production wells killing on R.Trebs high-temperature cavernous-fractured carbonate deposits. *Oil Industry Journal.* 2017. N 10, p. 41-45 (in Russian). DOI: 10.24887/0028-2448-2017-10-41-45

9. Khakimov A.M., Makatrov A.K., Karavaev A.D. et al. Filtration testing of a new generation of domestic and foreign surfactants as additives to repair and technological fluids during underground repairs and wellbore maintenance in hydrophilic reservoirs. *Neftepromyslovoe delo.* 2005. N 12, p. 48-53 (in Russian).

10. Atvinovskaya T.V. The role of killing fluid in the well repair process. Vestnik Gomel'skogo gosudarstvennogo tekhnicheskogo universiteta imeni P.O.Sukhogo. 2018. N 2, p. 34-41 (in Russian).

11. Kravtsov A.A., Mukhutdinov A.A., Gryadunov D.A. Killing wells in conditions of low production rates and high gas factor at the fields of JSC Orenburgneft. *Inzhenernaya praktika*. 2018. N 11 (in Russian).

12. Orlov G.A., Kendis M.Sh., Glushchenko V.N. Применение обратных эмульсий в нефтедобыче. Moscow: Nedra, 1991, p. 224 (in Russian).

13. Mardashov D.V. Justification of technologies for regulating the filtration characteristics of the bottomhole zone of wells during underground repairs: Avtoref. dis. ... kand. tekhn. nauk. St. Petersburg: Sankt-Peterburgskii gosudarstvennyi gornyi institut imeni G.V.Plekhanova, 2008, p. 20 (in Russian).

14. Akimov O.V. Improving well killing technologies during intensification of development of low-permeability terrigenous reservoirs: Avtoref. dis ... kand. tekhn. nauk. Ufa: Ufimskii gosudarstvennyi neftyanoi tekhnicheskii universitet, 2011, p. 23 (in Russian).

15. Bustos O., Ali S., Ngujen C. Patent N 2499131 RF. Application of degradable fibers in solutions of inverted emulsions for well killing. Publ. 20.11.2013. Bul. N 32 (in Russian).

16. Perejma A.A., Cherkasova V.E., Gasumov R.R. Patent N 2330055 RF. Method of making polydisperse peat reagent for boring solutions and kill fluids. Publ. 27.07.2008. Bul. N 21 (in Russian).

17. Gasumov R.A., Kostyukov S.V., Gasumov R.R. et al. Maintenance of filtration and capacitive reservoir properties during temporary isolation. *Oil and Gas Studies.* 2017. N 4, p. 58-66 (in Russian). DOI: 10.31660/0445-0108-2017-4-58-66

18. Schramm G. A practical approach to rheology and rheometry. Moscow: KolosS, 2003, p. 312 (in Russian).

19. Gusakov V.N., Korolev A.Yu., Yagudin R.A. et al. Well silencing technologies in conditions of multiple complications. *Petroleum Engineering.* 2023. Vol. 21. N 2, p. 17-24 (in Russian). DOI: 10.17122/ngdelo-2023-2-17-24

20. Bondarenko A.V., Mardashov D.V., Islamov Sh.R. Assessing the Effective Implementation of Blocking Polymer Compositions for Well Control Operation in the Conditions of Carbonate Reservoir and High Gas-Oil Ratio. *Petroleum Engineering.* 2022. Vol. 20. N 1, p. 53-64 (in Russian). DOI: 10.17122/ngdelo-2022-1-53-64

21. Silin M.A., Magadova L.A., Akimov O.V. et al. Advanced technologies for wells killing. *Oil Industry Journal.* 2015. N 1, p. 66-70 (in Russian).

22. Mannapov G.M., Khazimuratov R.Kh., Smykov Yu.V., Safuanova R.M. Experience in organizing the work of the process fluid preparation unit. *Neftepromyslovoe delo*. 2006. N 4, p. 36-39 (in Russian).

23. Mardashov D.V. Development of blocking compositions with a bridging agent for oil well killing in conditions of abnormally low formation pressure and carbonate reservoir rocks. *Journal of Mining Institute*. 2021. Vol. 251, p. 667-677. DOI: 10.31897/PMI.2021.5.6

24. Kraevskiy N.N., Islamov R.A., Lind Yu.B. Selection of well killing technology for complex geological and technological conditions. *Petroleum Engineering.* 2020. Vol. 18. N 4, p. 16-26 (in Russian). DOI: 10.17122/ngdelo-2020-4-16-26

25. Glushchenko V.N., Khizhnyak G.P. Directions for Improving the Compositions of Reverse Emulsions for Well Plugging. *Perm Journal of Petroleum and Mining Engineering.* 2023. Vol. 23. N 1, p. 44-50 (in Russian). DOI: 10.15593/2712-8008/2023.1.6

26. Pop G.S. Causes of occurrence and methods of elimination of gas manifestations in wells. Moscow: VNIIEgazprom, 1991, p. 19 (in Russian).

27. Pop G.S., Kucherovskii V.M., Zotov A.S., Bodachevskaya L.Yu. Killing wells in conditions of decreasing reservoir pressure at fields in Western Siberia. *Neftepromyslovoe delo*. 2002. N 11, p. 26-29 (in Russian).

28. Kulikov A.N., Ismagilov T.A., Shadymukhametov S.A., Telin A.G. Development and application of new compositions for well killing at YUKOS oil fields. *Vestnik Inzhiniringovogo tsentra YuKOS*. 2002. N 4, p. 52-55 (in Russian).

29. Kulikov A.N., Ismagilov T.A., Telin A.G., Khakimov A.M. Application of invert dispersion "Disin" for killing of absorption wells after hydraulic fracturing. *Bashkir chemistry journal*. 2001. N 3, p. 73-75 (in Russian).

30. Lezov G.O., Yashin V.I., Ismagilov T.A. et al. Technology of combined killing and secondary opening of oil wells using inverted dispersion "Disin". *Oil Industry Journal*. 1994. N 2, p. 48-51 (in Russian).

31. Zdolnik S.E., Zgoba I.M., Telin A.G., Gusakov V.N. Problems of well killing at Priobskoye field and ways to solve them. *Nauchno-tekhnicheskii vestnik OAO "NK "Rosneft*". 2006. N 1, p. 36-39 (in Russian).

32. Akimov O.V., Zdolnik S.E., Khudyakov D.L. et al. Well kill technologies with fluid loss control for hydro-fractured wells under AHFP and ALFP Conditions. *Oil Industry Journal.* 2010. N 2, p. 92-95 (in Russian).

33. Islamov Sh.R., Bondarenko A.V., Mardashov D.V. Substantiation of a well killing technology for fractured carbonate reservoirs. Youth Technical Sessions Proceedings. CRC Press, 2019, p. 256-264. DOI: 10.1201/9780429327070-35

34. Mardashov D., Islamov S., Nefedov Yu. Specifics of well killing technology during well service operation in complicated conditions. *Periódico Tchê Química*. 2020. Vol. 17. N 34. p. 782-792. DOI: 10.52571/PTQ.v17.n34.2020.806_P34_pgs_782_792.pdf

35. Islamov Sh.R. Justification of the technology of killing oil wells before underground repair in conditions of fractured-porous carbonate reservoirs: Avtoref. dis. ... kand. tekhn. nauk. St. Peterburg: Sankt-Peterburgskii gornyi universitet, 2021, p. 20 (in Russian).

36. Shamsutdinov R.D. Application of fibrous fillers in invert emulsion solutions to improve the quality of well workovers: Avtoref. dis. ... kand. tekhn. nauk. Ufa: Ufimskii gosudarstvennyi neftyanoi tekhnicheskii universitet, 2002, p. 24 (in Russian).

37. Islamov S., Islamov R., Shelukhov G. et al. Fluid-Loss Control Technology: From Laboratory to Well Field. *Processes*. 2024. Vol. 12. Iss. 1. N 114. DOI: 10.3390/pr12010114

38. Sergeev V., Tanimoto K., Abe M. Innovative Emulsion-Suspension Systems Based on Nanoparticles for Drilling and Well Workover Operation. Abu Dhabi International Petroleum Exhibition & Conference, 11-14 November 2019, Abu Dhabi, United Arab Emirates. OnePetro, 2019. N SPE-197510-MS. DOI: 10.2118/197510-MS

39. Uliasz M. Workover fluid for the reconstruction of wells with reduced reservoir pressure. *Nafta-Gaz*. 2020. Vol. 76. N 7, p. 457-465 (in Polish). DOI: 10.18668/NG.2020.07.04

40. Shadymukhamedov S., Kulikov A. Development of work to improve the quality of well killing at YUKOS Oil Company. *Nauchno-tekhnicheskii vestnik YuKOS*. 2003. N 7, p. 30-32 (in Russian).

41. Magadova L.A., Silin M.A., Gaevoy E.G. et al. Killing and washing fluids preserving reservoir characteristics of the formation. *Coiled Tubing Times.* 2009. N 3 (028), p. 72-80 (in Russian).

42. Silin M.A., Magadova L.A., Ponomareva V.V. et al. Development of a non-filterable, high-density, water-based polysaccharide kill fluid. *Territoriya "Neftegaz*". 2010. N 8, p. 56-61 (in Russian).

43. Bondarenko A.V., Islamov S.R., Ignatyev K.V., Mardashov D.V. Laboratory investigation of polymer compositions for well killing in fractured reservoirs. *Perm Journal of Petroleum and Mining Engineering*. 2020. Vol. 20. N 1, p. 37-48 (in Russian). DOI: 10.15593/2224-9923/2020.1.4

44. Okromelidze G.V., Nekrasova I.L., Garshina O.V. et al. Well killing operation using viscoelastic gels – from theory to practice. *Oil Industry Journal.* 2016. N 10, p. 56-61 (in Russian).

45. Martyushev D.A., Govindarajan S.K. Development and study of a Visco-Elastic Gel with controlled destruction times for killing oil wells. *Journal of King Saud University – Engineering Sciences*. 2022. Vol. 34. Iss. 7, p. 408-415. DOI: 10.1016/j.jksues.2021.06.007

46. Hu Jia, Zheng Kang, Jinzhi Zhu et al. High density bromide-based nanocomposite gel for temporary plugging in fractured reservoirs with multi-pressure systems. *Journal of Petroleum Science and Engineering*. 2021. Vol. 205. N 108778. DOI: 10.1016/j.petrol.2021.108778

47. Hu Jia, Xin-Yu Yang, Jin-Zhou Zhao. Development of a Novel In-Situ-Generated Foamed Gel as Temporary Plugging Agent Used for Well Workover: Affecting Factors and Working Performance. *SPE Journal*. 2019. Vol. 24. Iss. 4, p. 1757-1776. DOI: 10.2118/194215-PA

48. Hu Jia, Hao Chen, Jin-Zhou Zhao. Development of a Highly Elastic Composite Gel through Novel Intercalated Crosslinking Method for Wellbore Temporary Plugging in High-Temperature Reservoirs. *SPE Journal*. 2020. Vol. 25. Iss. 6, p. 2853-2866. DOI: 10.2118/201090-PA

49. Xu Yuan, Tang Yongfan. Development and Application of Temporary Plugging and Killing System Suitable for Sour Gas Field. *Oilfield Chemistry*. 2022. Vol. 39. N 3, p. 381-386. DOI: 10.19346/j.cnki.1000-4092.2022.03.001

50. Hu Jia, Hao Chen. The Potential of Using Cr^{3+}/Salt-Tolerant Polymer Gel for Well Workover in Low-Temperature Reservoir: Laboratory Investigation and Pilot Test. *SPE Productions & Operations.* 2018. Vol. 33. Iss. 3, p. 569-582. DOI: 10.2118/189460-PA

51. Xiong Ying, Xi Yuan, Zhang Yadong, Fu Ziyi. Study of Gel Plug for Temporary Blocking and Well-Killing Technology in Low-Pressure, Leakage-Prone Gas Well. *SPE Production & Operations*. 2021. Vol. 36. Iss. 1, p. 234-244. DOI: 10.2118/204213-PA

52. Shaydullin V.A., Vakhrushev S.A., Magzumov N.R. et al. Features of Killing Wells Operating Fractured Formations with Abnormally Low Formation Pressures and High Gas Factor. SPE Russian Petroleum Technology Conference, 26-29 October 2020. OnePetro, 2020. N SPE-202071-MS. DOI: 10.2118/202071-MS

53. Chunming Xiong, Falin Wei, Weitao Li et al. Mechanism of Polyacrylamide Hydrogel Instability on High-Temperature Conditions. *ACS Omega*. 2018. Vol. 3. Iss. 9, p. 10716-10724. DOI: 10.1021/acsomega.8b01205

54. Zhongliang Hu, Maje Haruna, Hui Gao et al. Rheological Properties of Partially Hydrolyzed Polyacrylamide Seeded by Nanoparticles. *Industrial & Engineering Chemistry Research*. 2017. Vol. 56. Iss. 12, p. 3456-3463. DOI: 10.1021/acs.iecr.6b05036

55. Pan Xu, Zhijie Shang, Meiling Yao, Xinxue Li. Mechanistic insight into improving strength and stability of hydrogels via nano-silica. *Journal of Molecular Liquids*. 2022. Vol. 357. N 119094. DOI: 10.1016/j.molliq.2022.119094

56. Zareie C., Bahramian A.R., Sefti M.V., Salehi M.B. Network-gel strength relationship and performance improvement of polyacrylamide hydrogel using nano-silica; with regards to application in oil wells conditions. *Journal of Molecular Liquids*. 2019. Vol. 278, p. 512-520. DOI: 10.1016/j.molliq.2019.01.089

57. Hu Jia, Cheng-Cheng Niu, Xin-Yu Yang. Improved understanding nanocomposite gel working mechanisms: From laboratory investigation to wellbore plugging application. *Journal of Petroleum Science and Engineering*. 2020. Vol. 191. N 107214. DOI: 10.1016/j.petrol.2020.107214

58. Hu Jia, Xin-Yu Yang. Environmental and strength-enhanced nanosilica-based composite gel for well temporary plugging in high-temperature reservoirs. *Asia-Pacific Journal of Chemical Engineering*. 2019. Vol. 14. Iss. 1. N e2270. DOI: 10.1002/apj.2270

59. Hu Jia, Dong-Shan Xie, Zheng Kang. Secondary surface modified laponite-based nanocomposite hydrogel for gas shutoff in wellbore. *Journal of Petroleum Science and Engineering*. 2020. Vol. 191. N 107116. DOI: 10.1016/j.petrol.2020.107116

60. Dijvejin Z.A., Ghaffarkhah A., Sadeghnejad S., Sefti M.V. Effect of silica nanoparticle size on the mechanical strength and wellbore plugging performance of SPAM/chromium (III) acetate nanocomposite gels. *Polymer Journal*. 2019. Vol. 51. N 7, p. 693-707. DOI: 10.1038/s41428-019-0178-3

61. Dao-Yi Zhu, Xing-Yu Fang, Ren-Xian Sun et al. Development of degradable pre-formed particle gel (DPPG) as temporary plugging agent for petroleum drilling and production. *Petroleum Science*. 2021. Vol. 18. Iss. 2, p. 479-494. DOI: 10.1007/s12182-020-00535-w

62. Hong-Jun Zhang, Dao-Yi Zhu, Yong-Long Gong et al. Degradable preformed particle gel as temporary plugging agent for low-temperature unconventional petroleum reservoirs: Effect of molecular weight of the cross-linking agent. *Petroleum Science*. 2022. Vol. 19. Iss. 6, p. 3182-3193. DOI: 10.1016/j.petsci.2022.07.013

63. Bougha A., Ndukauba G., Okeke C., Abudu R. Restoring Integrity and Production on a Well with Compromised Barriers: Use of Crosslinked Polymer Gel to Prevent Fluid Loss Post Well Kill to Enable the Safe Repair of Compromised Christmas Tree Valves. Gas & Oil Technology Showcase and Conference, 13-15 March 2023, Dubai, United Arab Emirates. OnePetro, 2023. N SPE-214228-MS. DOI: 10.2118/214228-MS

64. Zeeshan Ahmad, Abdullah Alhaj Al Hosini, Mohammed Ibrahim Al Janahi et al. Challenges of Gas Wells Killing Operation with Emphasis on Reservoir & Completion Integrity Issues. Abu Dhabi International Petroleum Exhibition & Conference, 15-18 November 2021, Dubai, United Arab Emirates. N SPE-208063-MS. DOI: 10.2118/208063-MS

65. Hu Jia, Zheng Kang, Sanxi Li et al. Thermal degradation behavior of seawater based temporary plugging gel crosslinked by polyethyleneimine for fluid loss control in gas well: Kinetics study and degradation prediction. *Journal of Dispersion Science and Technology*. 2021. Vol. 42. Iss. 9, p. 1299-1310. DOI: 10.1080/01932691.2020.1740727

66. Yang Yang, Xiaoxuan He, Dalong Sun et al. Pseudointerpenetrating network nanocomposite hydrogel for temporary plugging in fractured reservoirs. *Colloids and Surfaces A: Physicochemical and Engineering Aspects*. 2023. Vol. 656. Part A. N 130369. DOI: 10.1016/j.colsurfa.2022.130369

67. Uguna G., Rachid R., Milne A., Ali S. Controlling Losses When Recompleting Low-Pressure Reservoirs. SPE European Formation Damage Conference and Exhibition. 2015. N SPE-174169-MS. DOI: 10.2118/174169-MS

68. Zheng Kang, Yin-Tao Liu, Hu Jia et al. Progress and Prospects of In Situ Polymer Gels for Sealing Operation in Wellbore and Near-Well Zone. *Energy & Fuels*. 2024. Vol. 38. Iss. 5, p. 3539-3563. DOI: 10.1021/acs.energyfuels.3c04382

69. Telin A., Lenchenkova L., Yakubov R. et al. Application of Hydrogels and Hydrocarbon-Based Gels in Oil Production Processes and Well Drilling. *Gels*. 2023. Vol. 9. Iss. 8. N 609. DOI: 10.3390/gels9080609

70. Magadova L.A., Silin M.A., Malkin D.N., Krisanova P.K. Patent N 2746499 RF. Viscoelastic composition for use in oil and gas production techniques. Publ. 14.04.2021. Bul. N 11 (in Russian).

71. Tokunov V.I., Saushin A.Z. Process fluids and mixtures for oil and gas well production increase. Moscow: Nedra-Biznestsentr, 2004, p. 711.

72. Rjabokon S., Martinov B., Doctor S. Technological decisions at completion and workover of the wells, directed on preservation collected properties of productive layers. *Burenie & neft.* 2008. N 9, p. 4-7 (in Russian).

73. Ross C.M., Williford J., Sanders M.W. Current Materials and Devices for Control of Fluid Loss. SPE Asia Pacific Oil and Gas Conference and Exhibition, 20-22 April 1999, Jakarta, Indonesia. OnePetro, 1999. N SPE-54323-MS. DOI: 10.2118/54323-MS

74. Dick M.A., Heinz T.J., Svoboda C.F., Aston M. Optimizing the Selection of Bridging Particles for Reservoir Drilling Fluids. SPE International Symposium on Formation Damage Control, 23-24 February 2000, Lafayette, LA, USA. OnePetro, 2000. N SPE-58793-MS. DOI: 10.2118/58793-MS

75. Svoboda C. Optimizing High-Temperature Kill Pills: The Åsgard Experience. *SPE Drilling & Completion*. 1999. Vol. 17. Iss. 1. N SPE-76639-PA. DOI: 10.2118/76639-PA

76. Foks K.B. Patent N 2287549 RF. Stable liquid suspension compositions and the method of their production and application. Publ. 20.11.2006. Bul. N 32 (in Russian).

77. Semyuel M., Marsinev R., Dzhun K.Zh. Patent N 2004120281 RF. Non-damaging fluid for reducing drilling mud losses and its method of application. Publ. 27.03.2005. Bul. N 9 (in Russian).

78. Samuel M., Marcinew R., Al-Harbi M. et al. A New Solids-Free Non-Damaging High Temperature Lost-Circulation Pill: Development and First Field Applications. SPE Middle East Oil and Gas Show and Conference, 9-12 June 2003, Bahrain. OnePetro, 2003. N SPE-81494-MS. DOI: 10.2118/81494-MS

79. Vickers S., Cowie M., Jones T. et al. A new methodology that surpasses current bridging theories to efficiently seal a varied pore throat distribution as found in natural reservoir formations. AADE Drilling Fluids Technical Conference, 11-12 April 2006, Houston, TX, USA. American Association of Drilling Engineers, 2006. N AADE-06-DF-HO-16.

80. Araujo A., Calderon A. Field Use of Temporary Fluid-Loss Control Pill During Deepwater Completions in HighPermeability Formations. SPE Latin America and Caribbean Petroleum Engineering Conference, 21-23 April 1999, Caracas, Venezuela. OnePetro, 1999. N SPE-53924-MS. DOI: 10.2118/53924-MS

81. Akimov O.V., Zdolnik S.E., Gusakov V.N., Khudjakov D.L., Kraevskij N.N. Patent N 2380391 RF. Well process fluid with controlled absorption in thermo baric-reservoir conditions. Publ. 27.01.2010. Bul. N 3 (in Russian).

82. Gusakov V.N., Kraevskiy N.N., Khakimov A.F. et al. Technology of absorption prevention during workover in conditions of low reservoir pressure. *Oil Industry Journal*. 2013. N 10, p. 50-51 (in Russian).

83. Zdolnik S.E., Akimov O.V., Khudjakov D.L., Malyshev A.S., Gusakov V.N., Kraevskij N.N. Patent N 2482152 RF. Borehole process fluid with low damaging properties and controlled absorption in thermobaric formation conditions. Publ. 20.05.2013. Bul. N 14 (in Russian).

84. Youssry Abd El-Aziz Mohamed, El-Gindy A.T., El-Agamy H.A. et al. Field Application of Newly Designed Non-Damaging Sealing Killing Fluid to Control Losses in Completion and Workover Operations in Western Desert, Egypt. SPE Trinidad and Tobago Section Energy Resources Conference, 28-30 June 2021. OnePetro, 2021. N SPE-200936-MS. DOI: 10.2118/200936-MS

85. Cuixia Li, Xiaoping Qin, Liangchuan Li et al. Preparation and Performance of an Oil-Soluble Polyethylene Wax Particles Temporary Plugging Agent. *Journal of Chemistry*. 2018. Vol. 2018. Iss. 1. N 7086059. DOI: 10.1155/2018/7086059

86. Amiyan V.A., Amiyan A.V. Increasing well productivity. Moscow: Nedra, 1986, p. 159 (in Russian).

87. Tagirov K.M., Gasumov R.A., Pereima A.A., Minlikaev V.Z. Foam systems with filler for well killing. *Gazovaya promyshlennost*. 1999. N 8, p. 50-51 (in Russian).

88. Lijuan Pan, Huifeng Liu, Wu Long et al. A Novel Foamy Well Killing Fluid for Low-Pressure Gas Reservoirs in Tarim Basin, China. International Petroleum Technology Conference, 23 March – 1 April 2021. OnePetro, 2021. N IPTC-21434-MS. DOI: 10.2523/IPTC-21434-MS

89. Dongdong Liu, Renyuan Sun, Yunfei Zhang et al. A Low Density Micro-Foam Workover Fluid for Deep and Ultra-Deep Wells with Low-Pressure Coefficient and High Inorganic Salt. *Colloids and Surfaces A: Physicochemical and Engineering Aspects*. 2024. Vol. 682. N 132870. DOI: 10.1016/j.colsurfa.2023.132870

90. Gurbanov A.G., Baspayev E.T. New kill method for gas producing wells. *SOCAR Proceedings*. 2022. N 2, p. 28-34 (in Russian). DOI: 10.5510/OGP20220200671

91. Telin A., Karazeev D., Vezhnin S. et al. Use of Self-Generating Foam Gel Composition with Subsequent Injection of Hydrogel to Limit Gas Inflow in Horizontal Wells of Vostochno-Messoyakhskoye Field. *Gels*. 2024. Vol. 10. Iss. 4. N 215. DOI: 10.3390/gels10040215

92. Vasilchenko C.V., Medentsev S.V. Solving the problems of opening up depleted formations: Aphron technology. *Burenie & neft*. 2003. N 6, p. 36-37 (in Russian).

93. Usanov N.G., Andreson R.K., Gil'vanova E.A., Gusakov V.N., Telin A.G., Kalimullina G.Z. Patent N 2322472 RF. Technological liquid for damping oil and gas hole and method for its preparing. Publ. 20.04.2008. Bul. N 11 (in Russian).

94. Bondarenko A.V., Islamov Sh.R., Mardashov D.V. Complex Algorithm for Developing Effective Well-Killing Fluids for Production Wells. *Oil and Gas Territory*. 2018. N 10, p. 42-49 (in Russian).

95. Mardashov D.V., Rogachev M.K., Zeigman Y.V., Mukhametshin V.V. Well Killing Technology before Workover Operation in Complicated Conditions. *Energies*. 2021. Vol. 14. Iss. 3. N 654. DOI: 10.3390/en14030654

96. Duryagin V.N., Limanov M.N., Onegov N.A., Shamsutdinova G.T. Offshore well killing. *Burenie & neft*. 2023. Special Issue 1, p. 44-47 (in Russian).

97. Mardashov D., Duryagin V., Islamov S. Technology for Improving the Efficiency of Fractured Reservoir Development Using Gel-Forming Compositions. *Energies*. 2021. Vol. 14. Iss. 24. N 8254. DOI: 10.3390/en14248254

98. Silin M.A., Magadova L.A., Gaevoy E.G. et al. Application of killing fluids on the polysaccharide base in wells with low pressure and after fracturing. *Oil Industry Journal*. 2010. N 4, p. 104-107 (in Russian).

99. Zejgman J.V., Mukhametshin V.Sh., Khafizov A.R., Kharina S.B. Prospects of Application of Multi-Functional Well Killing Fluids in Carbonate Reservoirs. *Socar Proceedings*. 2016. N 3, p. 33-39 (in Russian). DOI: 10.5510/OGP20160300286

100. Nikulin V.Yu., Mukminov R.R., Mukhametov F.Kh. et al. Overview of promising killing technologies in conditions of abnormally low formation pressures and risks of gas breakthrough. Part 1. Technology classification and experience with water-based and hydrocarbon-based thickened liquids. *Petroleum Engineering*. 2022. Vol. 20. N 3, p. 87-96 (in Russian). DOI: 10.17122/ngdelo-2022-3-87-96

101. Grebenyuk A.N., Kurshev A.V., Korytko I.A. et al. Justification of effective well killing technologies in fractured carbonate reservoirs of Eastern Siberia. *Inzhenernaya praktika*. 2023. N 3 (in Russian).

102. Nikulin V.Yu., Britov E.V., Mukminov R.R. et al. The utilization of composition with spurt loss for control absorptions during killing wells in low-temperature terrigenous reservoirs in Eastern Siberia. *Exposition Oil Gas*. 2023. Iss. 1, p. 76-80 (in Russian). DOI: 10.24412/2076-6785-2023-1-76-80

103. Nikulin V.Yu., Mukminov R.R., Nigmatullin T.E. Reducing the negative impact of high density killing solutions on the productivity of gas wells operating Achimov reservoirs. Part 2. Rationale for the use of blocking compositions. *Exposition Oil Gas*. 2023. Iss. 4, p. 16-21 (in Russian). DOI: 10.24412/2076-6785-2023-4-16-21

104. Demakhin S.A., Merkulov A.P., Kasyanov D.N. et al. Killing wells with block packs is an effective means of preserving the filtration properties of the productive formation. *Neft. Gaz. Novatsii*. 2015. N 1, p. 66-69 (in Russian).

105. Merkulov A.P., Mershiev M.P. Well killing process in conditions of abnormal low formation pressure (ALFP) by the reagent of Zirax group of companies. *Neft. Gas. Novacii*. 2019. N 7, p. 13-15 (in Russian).

106. Yong-li Yan, Yang Zhang, Christian-chibuike Una. On the nature of colloidal aphrons. *Colloid and Interface Science Communications*. 2020. Vol. 34. N 100232. DOI: 10.1016/j.colcom.2019.100232

107. Usanov N.G., Andreson R.K., Gilvanova E.A., Zobov P.M., Andreev V.E., Kotenev Y.A., Khajredinov N.Sh., Poljakov V.N., Kuznetsov Y.S., Khuzin R.R. Patent N 2301822 RF. Drilling fluid. Publ. 27.06.2007. Bul. N 18 (in Russian).

108. Natsepinskaja A.M., Grebneva F.N., Iljasov S.E., Okromelidze G.V., Garshina O.V., Khvoshchin P.A., Popov S.G., Klykov P.I. Patent N 2563856 RF. Method of drilling of wells complicated by absorbing horizons. Publ. 20.09.2015. Bul. N 26 (in Russian).

109. Rabaev R.U. On the Question of Afron-containing Borehole Mud Application for Drilling Wells under Complicated Conditions on Black Sea Shelf Fields. *Problems of Gathering, Treatment and Transportation of Oil and Oil Products.* 2021. Iss. 5 (133), p. 9-23 (in Russian). DOI: 10.17122/ntj-oil-2021-5-9-23

110. Jinliang Han, Jinsheng Sun, Kaihe Lv et al. Polymer Gels Used in Oil–Gas Drilling and Production Engineering. *Gels.* 2022. Vol. 8. Iss. 10. № 637. DOI: 10.3390/gels8100637

111. Volkov V.A., Belikova V.G. Patent N 2332439 RF. Gas-filled composition for insulation of water-supply to hole. Publ. 27.08.2008. Bul. N 24 (in Russian).

112. Xiaoyong Li., Lihui Zheng, Yuanbo Chen et al. Fuzzy-Ball Fluids Enhance the Production of Oil and Gas Wells: A Historical Review. *Energies.* 2023. Vol. 16. Iss. 18. N 6647. DOI: 10.3390/en16186647

113. Fanghui Zhu, Lihui Zheng, Yang Zhao et al. Plugging Efficiency in Fractured Carbonate Gas Reservoirs Using Fuzzy-Ball Fluids Combined with Solid Plugging Agents. *Energies*. 2023. Vol. 16. Iss. 18. N 6688. DOI: 10.3390/en16186688

***Authors*: Danabek S. Saduakasov,** *Candidate of Engineering Sciences, Acting Associate Professor, https://orcid.org/0000-0003-1248-8747* (*S.Yessenov Caspian University of Technologies and Engineering, Aktau, Republic of Kazakhstan*), **Akshyryn T. Zholbasarova,** *Candidate of Engineering Sciences, Acting Associate Professor, https://orcid.org/0000-0002-4258-7933* (*S.Yessenov Caspian University of Technologies and Engineering, Aktau, Republic of Kazakhstan*), **Ryskol U. Bayamirova,** *Candidate of Engineering Sciences, Acting Associate Professor, https://orcid.org/0000-0003-1588-3144* (*S.Yessenov Caspian University of Technologies and Engineering, Aktau, Republic of Kazakhstan*), **Aliya R. Togasheva,** *Candidate of Engineering Sciences, Acting Associate Professor, https://orcid.org/0000-0002-5615-2711* (*S.Yessenov Caspian University of Technologies and Engineering, Aktau, Republic of Kazakhstan*), **Maksat T. Tabylganov,** *Candidate of Engineering Sciences, Acting Associate Professor, https://orcid.org/0000-0003-3807-2774* (*S.Yessenov Caspian University of Technologies and Engineering, Aktau, Republic of Kazakhstan*), **Manshuk D. Sarbopeeva,** *PhD, Acting Associate Professor, https://orcid.org/0000-0003-1721-119X* (*S.Yessenov Caspian University of Technologies and Engineering, Aktau, Republic of Kazakhstan*), **Aktoty G. Kasanova,** *PhD Student, https://orcid.org/0000-0002-6604-2575* (*S.Yessenov Caspian University of Technologies and Engineering, Aktau, Republic of Kazakhstan*), **Viktor N. Gusakov,** *Candidate of Chemical Sciences, Deputy Director for Research, https://orcid.org/0009-0005-3831-7251* (*Institute of Petrochemistry and Catalysis, UFRC RAS, Ufa, Republic of Bashkortostan, Russia*), **Aleksei G. Telin,** *Candidate of Chemical Sciences, Deputy Director for Research, telinag@ufntc.ru, https://orcid.org/0000-0002-0822-8515* (*Ufa Scientific and Technical Center LLC, Ufa, Republic of Bashkortostan, Russia*).

The authors declare no conflict of interests.

ISSN 2411-3336; e-ISSN 2541-9404

JOURNAL OF MINING INSTITUTE
Zapiski Gornogo instituta
Journal homepage: pmi.spmi.ru

Research article *Geotechnical Engineering and Engineering Geology*

Determination of the tangential component of cutting resistance during frozen sedimentary rock cutting using blocked, deeply blocked and cell cutting methods

Stanislav A. Shemyakin, Evgenii A. Shishkin✉
Pacific National University, Khabarovsk, Russia

***How to cite this article*:** Shemyakin S.A., Shishkin E.A. Determination of the tangential component of cutting resistance during frozen sedimentary rock cutting using blocked, deeply blocked and cell cutting methods. Journal of Mining Institute. 2025. Vol. 272. N 16356, p. 136-144.

Abstract
Due to the insufficient accuracy of existing studies of frozen sedimentary rock cutting process for practical calculations, the article solves the problem of determining the tangential component cutting resistance for blocked, deep blocked and cell cutting, which are currently the most commonly used methods in earthmoving equipment. The cutting tool and rock mass force interaction is considered from the point of view of the emerging stresses, which act on the separated chip element. The analytical dependences for determining the tangential component of cutting resistance were obtained. The numerical explanation of the choice of cell cutting in relation to blocked and deeply blocked cutting is given. For all three methods of cutting, under equal geometrical parameters of the cutting tool and the physical and mechanical properties of the frozen rock, the numerical value of the tangential component of cutting resistance is obtained. The comparison of the cutting resistance estimated values has shown that cell cutting requires relatively less energy and is preferred during the process of frozen sedimentary rock excavation. During field and laboratory investigations with the use of a multi-purpose cutting stand, a sufficient convergence of the analytical statements with the physics of frozen sedimentary rock cutting process was established. The results of the research allow a more reasonable approach to the adjustment of existing methods for determining the required tractive force and power for the drive of an excavation machine, and, therefore, to the actual efficiency and profitability of work.

Keywords
frozen sedimentary rocks; blocked cutting; deeply blocked cutting; cell cutting; cutting tool; stresses; cutting resistance; cutting stand

Received: 07.12.2023 ***Accepted: 07.11.2024*** ***Online: 07.04.2025*** ***Published: 25.04.2025***

Introduction

Most of the surface layer of the Russian Federation territory is covered with sedimentary rocks (clays, loams, sandy loams, sands), which are in a frost or permafrost state for 6-8 months a year due to the mountain climatic conditions [1]. Mining companies use a localized or major blast in order to destruct the frozen rock in quarry during winter [2]. Taking into consideration all costs of drilling and blasting operations, including the cost of explosives, storage buildings and their security, the transportation, the cost of the blasting and drilling equipment, the maintenance of explosives technicians and drillers, the downtime of the mining equipment while anticipating the blast and waiting for the explosion cloud dissipation, the estimated cost of a frozen rock layer destruction is rather high [3]. The increase in the cost of explosives and, in a number of instances, difficulties in their acquisition has led to the attempts to reject the drilling and blasting method. The other way is to use special machines, which work on the principle of mechanical destruction, specifically of loosening (cutting) [4, 5]. This category includes attached rippers on industrial tractors, excavators with milling equipment, ditch excavators (rotary or chain), surface miners, drilling machines, etc. [6, 7]. The mechanical method is not associated with conducting significant preparation works and makes it possible to use a number of mining

machines designed primarily for the excavation of thawed rock along with the special earthmoving machines. The mechanical method of frozen rock excavation, which works on the cutting principle, predominates in the construction and mining industries [8, 9].

For more than seventy years, a pleiad of Russian scientists has been conducting research in the field of frozen rock cutting and excavating resistance [10, 11]. The studies by N.G.Dombrovsky, A.N.Zelenin, V.V.Abeshaus, M.I.Galperin, V.I.Balovnev, Yu.A.Vetrov, etc. have given a certain material for understanding the regular patterns of frozen rock cutting. However, the knowledge of the frozen rock cutting process still does not meet the current requirements of the industry when creating new equipment. The dependences for determining the rock cutting resistance are of an empirical nature and do not take the physics and the essence of cutting method into consideration [12-14]. There are discrepancies in determining the influence of rock hardness upon the cutting resistance [15]. The results of calculation using known empirical dependences of the cutting force tangential component represent a considerable divergence of values, while the maximum value exceeds the minimum value by 4.8 times [16-18].

The fundamental difference of the proposed method for determining the frozen sedimentary rock cutting resistance lies in its analytical nature with the further experimental verification of the results for the major cutting methods applied in practice: blocked, deeply blocked and cell cutting.

Methodology

The purpose of the study is to develop the analytical dependences for determining the tangential component of resistance to blocked, deeply blocked and cell cutting. The comparison of the numerical values of the cutting resistance tangential component for the given cutting methods, under equal geometrical parameters of the cutting tool and the frozen rock type, will allow determining the most effective rock excavation method from the point of view of energy intensity.

The scheme of blocked cutting is shown in Fig.1 [19]. During blocked cutting the separated chip elements have a complex shape (Fig.2) [19].

With small assumptions, the chip element has a shape of a truncated cone half [20-22] with the depth ($h - h_2$), bound by the surface ODC. The cutting tangential component P_{01} can be determined while studying the chip element limit state before separation from the main rock mass [23]. The parameters of the cutting tool are: cutting angle α_c, cutting edge angle 180°. Fracture stresses σ_f act normally on the separation surface, and shearing stresses τ act tangentially to the surface [24]. The stiff core is formed in the lower part (area h_2S), therefore, the rock is crushed by the stresses σ_{cr} [25, 26].

This method considers cutting with teeth, in which the slot dimensions h, S, α_c, h_2 can vary in a wide range. The cutting was performed on coherent and incoherent frozen sedimentary rocks (loams and sand respectfully), which is taken into consideration in the dependences σ_f, τ, and σ_{cr}. During the experiments the slot parameters were measured, particularly the zone h_2, which is characterized by the absence of camber at the θ angle and the formation of the crushed rock stiff core. The established empirical pattern for defining the value of h_2 is as follows [11, 19]:

- for incoherent frozen sedimentary rocks (sand) $h_2 = 1.021h^{-0.46}e^{0.029h}$;
- for coherent frozen sedimentary rocks (loams) $h_2 = 0.728h^{-0.024}e^{0.067h}$.

Depending on the h_2 value, the slot section is divided into two zones.

In the scheme of forces effect (Fig.2) force N and its components P_{01} and P_{02} are the external forces, which act on the rock mass from the working body. The force P and its components P_1 and P_2 are the internal forces, which act on the separated chip element from the stiff core. The forces P'_{01} and P'_{02} are the components of the internal resistance to crushing, which act on the stiff core from the rock mass. The forces P_x^{bp} and P_y^{bp} are the components of the rock mass internal resistance, which act on the working

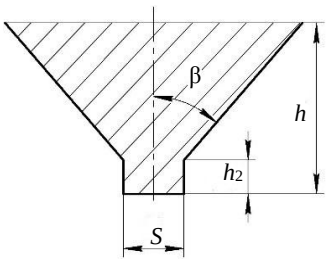

Fig.1. The scheme of slot section during the process of blocked cutting

β – camber angle; S – cutting tool width; h – slot depth; h_2 – slot bottom depth

Journal of Mining Institute. 2025. Vol. 272. P. 136-144

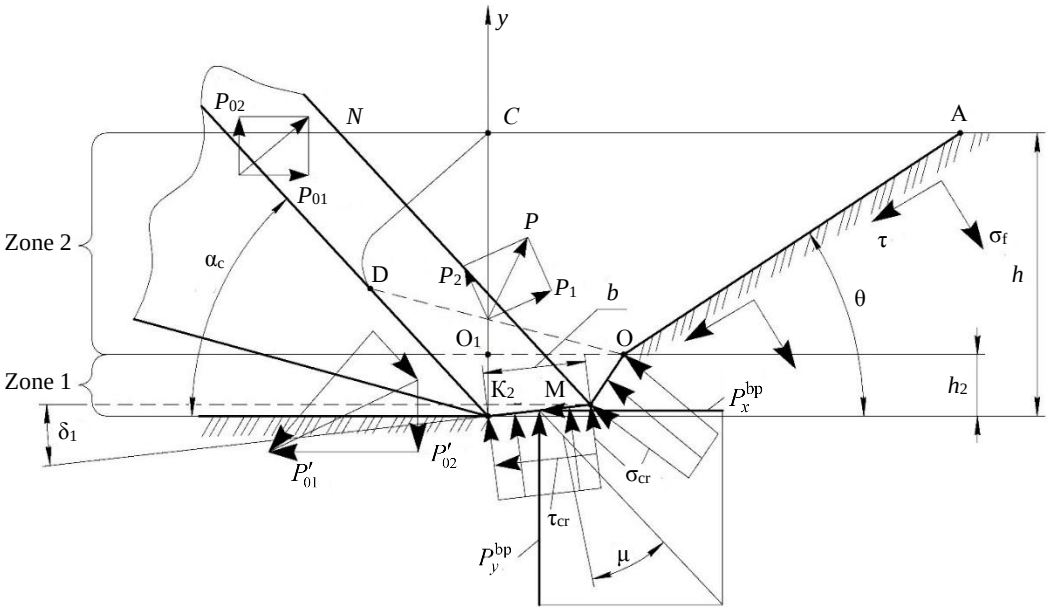

Fig.2. The calculation scheme of blocked cutting

body blunting place. The force P_{01} is equal the sum of three summands, specifically of the tangential component of the rock mass force effect on the stiff core, the tangential component of the rock mass force effect on the separated chip element, and the tangential component of the rock mass force effect on the working body blunting place. All tangential components of the internal forces effect on the working body are summarized in the formula with definite inclination angles to the *x*-axis. Thus, the force application in the scheme (Fig.2) is performed for a general idea of the internal resistances during the working body movement in the frozen rock mass, but not for the correspondence to each other.

Omitting the trigonometric ratios of sizes and stresses and summing the resistances in the zones 1 and 2, as well as the resistances associated with the cutting tool blunting, the analytical dependency for determining the tangential component of the frozen sedimentary rock resistance to blocked cutting is obtained:

$$P_{01} = \sigma_{cr}\left[Sh_2 + \frac{\xi_1 h_2^2 \operatorname{tg}\varphi_2 \sin(2\alpha_c + \psi)}{\sin(\alpha_c + \psi)} + \frac{\xi_1 S^2 \operatorname{tg}\varphi_2}{8} + \frac{\pi S h_2 \operatorname{tg}\varphi_2 \operatorname{ctg}(\alpha_c + \psi)}{2}\right] + \\ + (\tau - \sigma_f \operatorname{tg}\theta)\left[\frac{h - h_2}{\operatorname{tg}^2\theta}(S\operatorname{tg}\theta + h - h_2)\right] + \frac{\sigma_{cr} bS \sin(\delta_1 + \mu)}{\cos\mu}, \quad (1)$$

where b stands for the width of the worn place; δ_1 stands for the angle of inclination between the worn place surface and the tangential to the cutting tool movement trajectory; μ stands for the friction angle of the rock on the cutting tool; ξ_1 stands for the lateral earth pressure index; φ_2 stands for the friction angle of the rock against the rock; α_c stands for the cutting angle; θ stands for the front separation angle; ψ stands for the angle between the front surface of the stiff core and the front surface of the cutting tool.

In matters of frozen rock cutting, the stress differentiation in various cross-sectional zones of the chip was not carried out. Therefore, the main difference of the conducted research is the division of the slot section into zones with different stresses. Summing the tangential components of the resistances, which occur in zones of chip elements separation, in the stiff core and in the blunting place, was carried out on the basis of the fundamental laws of solid-state physics, theoretical mechanics and strength of materials.

The degree of rock hardness is taken into account depending (1) on the stresses σ_f, τ, σ_{cr}, the values of which, based on the temperature, are given in technical literature concerning the frozen rock (soil) mechanics. In this case the studies by A.N.Zelenin, G.M.Veselov, A.N.Stepanov, N.K.Pekarskaya, S.S.Vialov, M.I.Rovinsky, G.A.Shloydo, L.I.Sverdlova and many other researchers should be noted.

Journal of Mining Institute. 2025. Vol. 272. P. 136-144

Deeply blocked cutting (Fig.3) is used for frozen rock destruction less often compared to blocked method [27-29]. During the work of rotary ditch excavators on frozen rocks in the lower part of the face, the rock is cut in thin chips and does not collapse in slots after the cutting tool passage [30, 31]. In this case deeply blocked cutting is observed. A similar process occurs during the work of milling machines on any type of rock of a low or medium hardness [32]. If the ripper tooth of a ripper bulldozer is inserted in the slot again after the passage through the rock using blocked cutting method in order to deepen the slot, deeply blocked cutting occurs [33]. Deeply blocked cutting was investigated using only experimental methods [34, 35], thus, the theoretical interpretation of the issue is of a considerable interest.

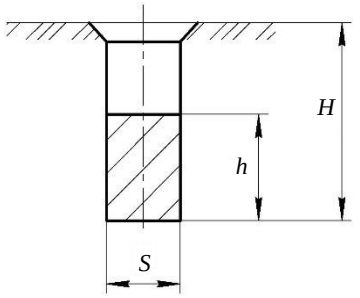

Fig.3. The scheme of slot section during the process of deeply blocked cutting

H – distance between the rock mass surface and the slot bottom

The tangential component of the frozen rock resistance to deeply blocked cutting is defined by summing the values of cutting resistance in zones 1 and 2 (Fig.4), taking into account the tangential component of the cut chip shearing resistance along two lateral planes ABCD, as well as along the plane AD and the front surface of the blunted cutting tool from the slot.

As a result, the analytical dependency for determining the tangential component of the resistance to deeply blocked cutting is as follows:

$$P_{01} = \sigma_{cr}\left[Sh_2 + \frac{\xi_1 h_2^2 \operatorname{tg}\varphi_2 \sin(2\alpha_c + \psi)}{\sin(\alpha_c + \psi)} + \frac{\xi_1 S^2 \operatorname{tg}\varphi_2}{8} + \frac{\pi S h_2 \operatorname{tg}\varphi_2 \operatorname{ctg}(\alpha_c + \psi)}{2}\right] +$$
$$+ 2\tau\cos\theta\left\{\frac{(h-h_2)^2}{2\operatorname{tg}\alpha_c} + \frac{h_2^2}{\operatorname{tg}\alpha_c} + h_2^2 \operatorname{tg}\left[\psi - (90 - \alpha_c)\right] + \frac{h_2 S}{2} + \frac{(h-h_2)^2}{2\operatorname{tg}\theta}\right\} + \quad (2)$$
$$+ S(h-h_2)(\tau\cos\theta - \sigma_f \sin\theta) + h(H-h)S\gamma_r \operatorname{ctg}\alpha_c(\mu_1 \cos\alpha_c + \sin\alpha_c),$$

where μ_1 stands for the rock against steel friction index; γ_r stands for the gravity body force of the cut rock.

The calculation according to the formula (2) with the parameter values equal to the above stated values shows that the tangential component of cutting resistance is P_{01} = 85,600 N, which is 1.6 times more than during blocked cutting.

Cell cutting (Fig.5) is a widely used method for frozen rock excavating machines [36]. They include rotary and chain ditch excavators, ditch-digging attachments on tractors, quarry milling combines, etc. [37, 38].

In order to analytically determine the tangential component of resistance to cutting P_{01}, it is advisable to divide the surfaces into four zones (Fig.6) [19], integrate the emerging stresses in each zone and sum the resulting forces, taking trigonometric functions into account.

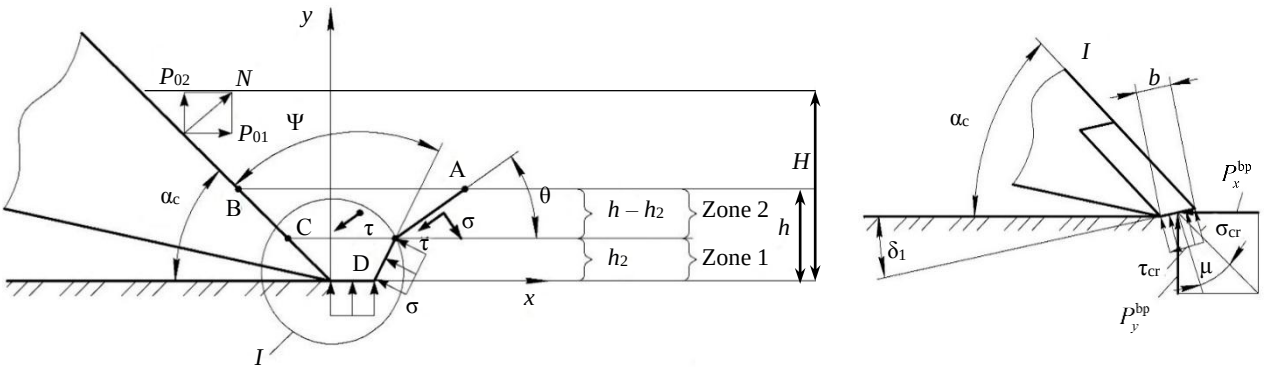

Fig.4. The scheme of emergence of the resistance stresses acting on the separated chip element in limit state during deeply blocked cutting

Journal of Mining Institute. 2025. Vol. 272. P. 136-144

As a result, the analytical dependency for determining tangential component of resistance to cell cutting is as follows:

$$P_{01} = \sigma_{cr}\left[Sh_2 + \frac{bS\sin(\delta_1+\mu)}{\cos\mu}\right] + \frac{(\tau-\sigma_f \operatorname{tg}\theta)}{\operatorname{tg}^2\theta}\left\{\left[\frac{h}{2}\left(S\operatorname{tg}\theta+\frac{h}{2}\right)+\frac{2h_2^2(S\operatorname{tg}\theta+h-h_2)}{3(S\operatorname{tg}\theta+h)}\right]+\right.$$
$$\left.+\left[\frac{(S\operatorname{tg}\theta+2h-2h_2)^2-(S\operatorname{tg}\theta+h)^2}{4}\right]\left[\frac{S\operatorname{tg}\theta+h-2h_2}{3.5(S\operatorname{tg}\theta+h)}+\frac{2.5S\operatorname{tg}\theta}{3.5(S\operatorname{tg}\theta+2h-2h_2)}\right]\right\}. \quad (3)$$

With the before stated quantity values, which are included in the formula (3), the tangential component of cutting resistance to cell cutting is P_{01} = 33,400 N, which is 1.63 times less than to blocked cutting and 2.5 times less than to deeply blocked cutting.

The procedure of field and laboratory investigations

In order to confirm the convergence of resulting interrelations (1)-(3) with the physics of frozen sedimentary rock cutting process, a series of experiments on cutting frozen loams and sands with the hardness index 2 in natural environment with the surrounding air temperature from –10 to –15 °C was conducted [39-41]. The cutting process was carried out with the use of multi-purpose cutting stand (Fig.7), geared with a DT-75 tractor. Since finding sand in natural occurrence presents certain difficulties, as it is not to be found anywhere except flood plains, the process of sand cutting was performed in laboratory setting, specifically in a freezing chamber with the temperature from –15 to –20 °C, on frozen blocks with the dimensions of 1.2×1.2×0.4 m. The frozen block was then installed under the cutting tool of the stand.

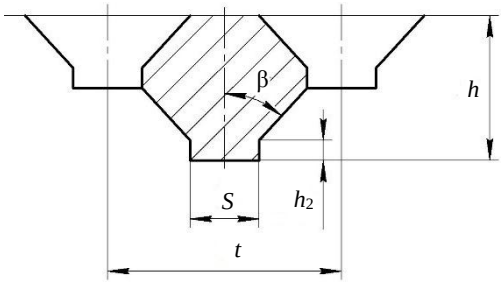

Fig.5. The scheme of slot section during the process of frozen rock cell cutting

t – cutting pitch

Steel teeth, which acted as a cutting tool, had the cutting edge width of 40 mm with WC-8 brazed elements and the blunting place of 3 mm. The possibility of teeth penetration into rock was 300 mm.

Cutting stand characteristics are: maximum cutting speed – 0.8 m/s, maximum cutting force – 180 kN, maximum cutting depth – 0.4 m. The stand includes the measuring trolley 6, which is installed on the frame 4 (Fig.7). During the measurement process the horizontal position of the frame is achieved by skids 3, and the tractive force is transmitted from the tractor to the frame through the ball joint 1. The

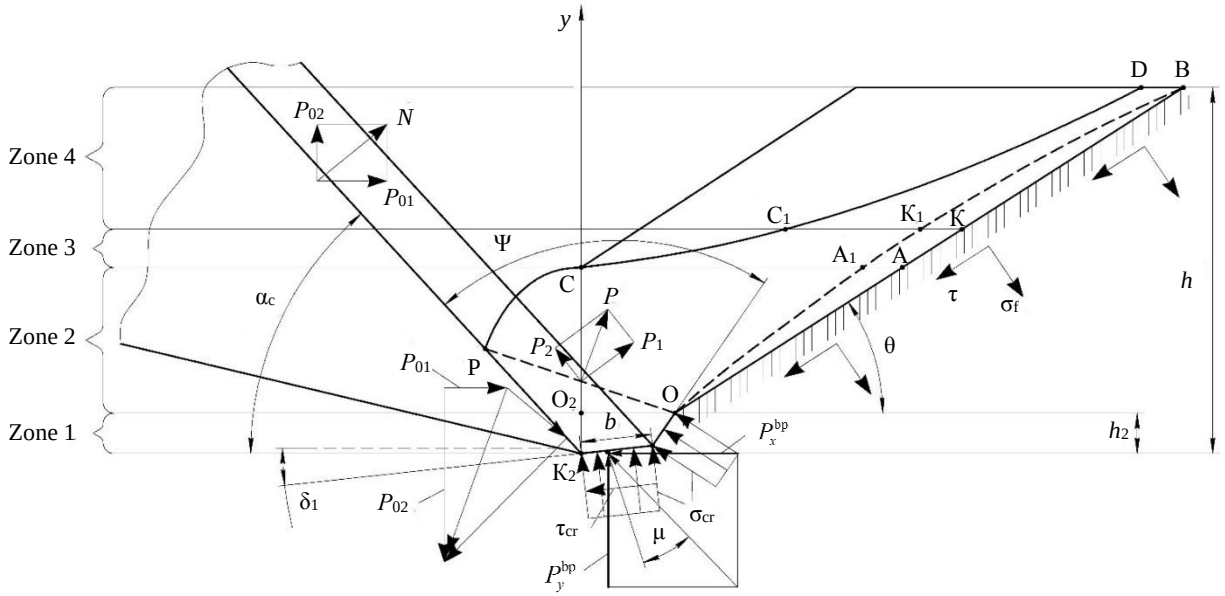

Fig.6. The calculation scheme of cell cutting

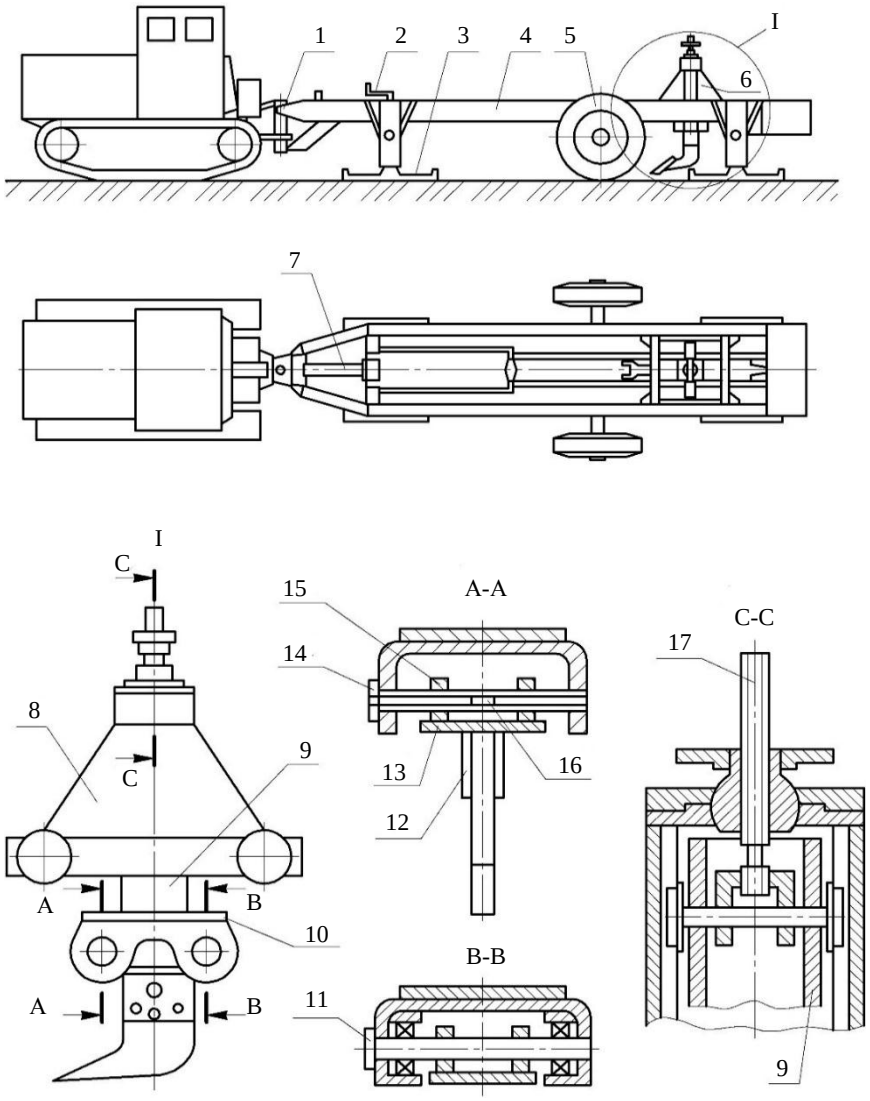

Fig.7. The scheme of the cutting stand for layer-by-layer rock cutting

transportation of the stand to the measurement point is performed by means of the pneumatic wheels 5. The distance between the frame and a rock layer is changed with the jackscrews 2, which are built in the skids 3. The measuring trolley 6 movement along the frame 4 guides is performed using the hydraulic cylinder 7, which is connected to the hydraulic system of the tractor. The rack 9, which is installed in the measurement trolley frame 8, is moved using the screw 17. The measuring axis 14 and the rear axis 11 are installed in the holes of flange 10. The working body is suspended on the axes 11, 14 by means of the flanges 13 with the lugs 15 and the guides 12. The tangential component of cutting resistance is measured with the sensors 16, which are installed on the axis 14 vertically. The normal component of cutting resistance is measured with the sensors installed on the axis 14 horizontally.

The rock samples with the height of 100 mm and the diameter of 71.4 mm were used during the compression and tensile shear test by the indirect diametral compression method. The bearing stress was measured by pressing a steel punch with a universal testing machine UMM-50 (GOST 7855-61) in the rock.

During the experimental investigations the following parameters of the slot made by the cutting tool were determined: camber angle β, depth h_2 and h, front separation angle θ, the angle between the front surface of the stiff core and the front surface of the cutting tool ψ.

Discussion

As a result of experimental and estimated data comparison using the dependences (1)-(3), a sufficient convergence of the analytical statements with the physics of blocked, deeply blocked and cell methods of frozen sedimentary rock cutting was established (the discrepancy does not exceed 11 %). In this case, several experiments were selected from a large number (Table 1-3).

Journal of Mining Institute. 2025. Vol. 272. P. 136-144

Table 1

The estimated maximum values of the tangential component of resistance to blocked cutting with one tooth according to equation (1)

Experiment number	Rock type	h, m	α_c, deg	S, mm	b, mm	δ_1, deg	μ, deg	h_2, mm	ξ_1	φ_2, deg	θ, deg	ψ, deg	σ_{cr}, N/cm^2	τ, N/cm^2	σ_f, N/cm^2	T, °C	P_{01}, N (estimated)	P_{01}, N (experimental)	Calculation mistake, %
1	Frozen sand	0.1	35	40	5	5	12	20	0.4	40	38	80	2,000	300	195	–10	5,350	5,280	11
2	Frozen sand	0.2	35	40	5	5	12	25	0.4	40	38	80	2,000	300	195	–15	1,070	1,050	10.8
3	Frozen loam	0.1	35	40	5	5	12	23	0.4	35	36	75	1,800	250	180	–10	19,000	20,000	–8.15
4	Frozen loam	0.2	35	40	5	5	12	25	0.4	35	36	75	1,800	250	180	–10	38,000	37,000	10.5

Table 2

The estimated maximum values of the tangential component of resistance to deeply blocked cutting with one tooth according to equation (2)

Experiment number	Rock type	h, m	α_c, deg	S, mm	b, mm	δ_1, deg	μ, deg	h_2, mm	φ_2, deg	ψ, deg	σ_{cr}, N/cm^2	τ, N/cm^2	σ_f, N/cm^2	T, °C	P_{01}, N (estimated)	P_{01}, N (experimental)	Calculation mistake, %
1	Frozen sand	0.1	35	40	5	5	12	20	40	38	2,000	300	195	–10	8,480	8,300	9.6
2	Frozen sand	0.2	35	40	5	5	12	23	40	38	2,000	300	195	–15	16,000	15,900	9.7
3	Frozen loam	0.1	35	40	5	5	12	23	35	36	1,800	250	180	–10	30,400	30,800	–9.7
4	Frozen loam	0.2	35	40	5	5	12	25	35	36	1,800	250	180	–10	60,800	60,100	9.1

Table 3

The estimated maximum values of the tangential component of resistance to cell cutting with one tooth according to equation (3)

Experiment number	Rock type	T, °C	σ_f, N/cm	μ, deg	t, mm	h, m	S, mm	α_c, deg	δ_1, deg	θ, deg	h_2, mm	τ, N/cm^2	σ_{cr}, N/cm^2	P_{01}, N (estimated)	P_{01}, N (experimental)	Calculation mistake, %
1	Frozen sand	–10	120	12	132	0.1	35	45	15	25	11	300	2,000	19,300	18,000	–7.2
2	Frozen sand	–10	120	12	300	0.2	35	45	15	25	12	300	2,000	20,300	19,000	–6.9
3	Frozen sand	–10	120	12	140	0.1	35	45	15	25	9	300	2,000	18,000	17,500	–2.86
4	Frozen loam	–10	120	12	350	0.2	58	45	15	25	13	300	2,000	34,500	32,000	–7.8
5	Frozen loam	–8	87	24	230	0.2	35	45	15	27	16	250	1,800	6,500	7,000	7.1
6	Frozen loam	–8	87	24	140	0.11	22	45	15	27	20	250	1,800	5,550	6,100	9

Conclusion

The developed analytical dependences for determining the tangential component of the process of frozen sedimentary rock cutting with a single cutting tool provide a reasonable opportunity to determine the required tractive forces for the excavating machine cutting tools the and power for the drive under given shearing, tensile and bearing limit stresses. Therefore, the actual efficiency and profitability of work is determined. The presented analytical dependences allow obtaining the calculation results with a permissible error compared to data, which results from the experimental investigations. The numerical calculations conducted using the three analytical dependences for determining the tangential component of cutting resistance under equal parameters of the cutting tool, cut chip thickness and width, strength properties of the rock show that the value of resistance to deeply blocked cutting is 1.6 times more than to blocked cutting and 2.5 times more than to cell cutting. Thus, it is preferred to use cell cutting in machines designed for frozen sedimentary rock excavation.

REFERENCES

1. Subbotin Yu.V., Oveshnikov Yu.M., Avdeev P.B. Preparation of frozen rocks for excavation in placer mining in Transbaikal region. *Mining Informational and Analytical Bulletin.* 2019. N 3, p. 125-133 (in Russian). DOI: 10.25018/0236-1493-2019-03-0-125-133

2. Tikhonov V.A., Dudnik G.A., Panfilov S.Yu., Zhulikov V.V. Specific Features of Blasting Operations in Mining Minerals in Northern and Arctic Regions of Russia. *Russian Mining Industry.* 2021. N 2, p. 102-106 (in Russian). DOI: 10.30686/1609-9192-2021-2-102-106

3. Egorov V.V., Volokitin A.N., Ugolnikov N.V., Sokolovsky A.V. Justification of parameters and technology of drilling and blasting operations to ensure the required lumpiness. *Russian Mining Industry*. 2021. N 3, p. 110-115 (in Russian). DOI: 10.30686/1609-9192-2021-3-110-115

4. Kamenev A.V. Analysis of frozen soil loosening. *Nauchno-prakticheskie issledovaniya*. 2020. N 5-2 (28), p. 114-118.

5. Iliukhin A.V., Marsov V.I., Dzhabrailov Kh.A., Chantieva M.E. Features of soil development processes by digging and transporting machines. *The Eurasian Scientific Journal.* 2018. Vol. 10. N 2. N 65SAVN218 (in Russian).

6. Perepelking M.A., Mokritskaya N.I. Revisiting: the development of earthmoving, excavating and transportation machinery implements. *Russian Mining Industry.* 2019. N 2 (144), p. 81-82 (in Russian). DOI: 10.30686/1609-9192-2019-2-144-81-82

7. Tretyak A.Ya., Popov V.V., Grossu A.N., Borisov K.A. Innovative approaches to designing highly efficient rock-breaking tool. *Mining Informational and Analytical Bulletin*. 2017. N 8, p. 225-230 (in Russian). DOI: 10.25018/0236-1493-2017-8-0-225-230

8. Yi Liu, Feng Dai. A review of experimental and theoretical research on the deformation and failure behavior of rocks subjected to cyclic loading. *Journal of Rock Mechanics and Geotechnical Engineering*. 2021. Vol. 13. Iss. 5, p. 1203-1230. DOI: 10.1016/j.jrmge.2021.03.012

9. Pebrianto R., Asof M., Susilo B.K., Gofar N. Evaluation of Factors Affecting Ripping Productivity in Open Pit Mining Excavation. *Electronic Journal of Geotechnical Engineering*. 2014. Vol. 19. Bund. Z_3, p. 10447-10456.

10. Ivkin V.S., Volynshchikov P.Yu. Frozen ground excavation under reduced building conditions. *Vestnik of Ulyanovsk State Technical University.* 2013. N 2 (62), p. 62-66 (in Russian).

11. Shemyakin S.A., Gamolya Yu.A., Cheban A.Yu. Technical and technological solutions of the development of frozen and hard rocks in mining and construction. Khabarovsk: Izd-vo DVGUPS, 2017, p. 188.

12. Buryy G.G., Poteryaev I.K., Skobelew S.B., Kovalevskiy V.F. Improving the productivity of a single-buckle hydraulic excavator with a bucket of new construction. *News of the Tula State University. Technical sciences.* 2019. Iss. 9, p. 12-19 (in Russian).

13. Zhabin A.B., Polyakov A.V., Averin E.A. et al. Ways of development for the theory of rock and coal destruction by picks. *Ugol*. 2019. N 9 (1122), p. 24-28 (in Russia). DOI: 10.18796/0041-5790-2019-9-24-28

14. Xinzhong Wang, Weiquan Fang, Dianlei Han, Xuegeng Chen. Review of the Research on Soil Disturbance by Tools. *Applied Sciences*. 2023. Vol. 13. Iss. 1. N 338. DOI: 10.3390/app13010338

15. Feng Hou, Yuanming Lai, Enlong Liu et al. A creep constitutive model for frozen soils with different contents of coarse grains. *Cold Regions Science and Technology*. 2018. Vol. 145, p. 119-126. DOI: 10.1016/j.coldregions.2017.10.013

16. Shemyakin S.A., Shishkin E.A. Analytical theories for determining the resistances to frozen rock cutting (loosening) and their application in the practice of earthmoving machines calculation. Khabarovsk: Izd-vo Tikhookeanskogo gosudarstvennogo universiteta, 2014, p. 144.

17. Kyznetsova V.N., Savinkin V.V., Ratushnaya T.Y. et al. Study of the Spatial Distribution of Forces and Stresses on Wear Surfaces at Optimization of the Excavating Part of an Earthmoving Machine Transverse Profile. *Coatings*. 2021. Vol. 11. Iss. 2. N 182. DOI: 10.3390/coatings11020182

18. Shemyakin S.A., Cheban A.Yu. Determination of resistance to cutting of frozen rocks deeply blocked (slot). *Journal of Mining equipment and electromechanics.* 2015. N 6, p. 39-44 (in Russian).

19. Shemyakin S.A. Justification of surface mining effective technologies based on the improvement of rock excavation process: Avtoref. dis. ... d-ra tekhn. nauk. Khabarovsk: Institut gornogo dela DVO RAN, 2004, p. 34.

20. Aresh B., Khan F.N., Haider J. Experimental investigation and numerical simulation of chip formation mechanisms in cutting rock-like materials. *Journal of Petroleum Science and Engineering*. 2022. Vol. 209. N 109869. DOI: 10.1016/j.petrol.2021.109869

21. Kuznetsova V.N. Physical modeling of the contact process interactions of the working body of the digging machine with frozen soil. *Tomsk State University Journal of Mathematics and Mechanics.* 2019. N 61, p. 70-81 (in Russian). DOI: 10.17223/19988621/61/7

22. Xuezhen Wang, Sen Zhang, Hongbo Pan et al. Effect of soil particle size on soil-subsoiler interactions using the discrete element method simulations. *Biosystems Engineering*. 2019. Vol. 182, p. 138-150. DOI: 10.1016/j.biosystemseng.2019.04.005

23. Zhelykevich R.B., Selivanov N.I., Kaiser Yu.F., Lysyannikov A.V. Determination of stresses caused in the disc cutter, blocked cutting of frozen soils. *News of the Tula State University. Technical sciences.* 2015. Iss. 8. Part 2, p. 66-78 (in Russian).

24. Kuznetsova V.N., Kuznetsov I.S. Simulation of the contact process interactions of land-moving and earth-transport machines' working bodies with frozen soil. *The Russian Automobile and Highway Industry Journal*. 2018. Vol. 15. N 2 (60), p. 189-198 (in Russian). DOI: 10.26518/2071-7296-2018-2-189-198

25. Hu M., Gao T., Dong X et al. Simulation of soil-tool interaction using smoothed particle hydrodynamics (SPH). *Soil and Tillage Research*. 2023. Vol. 229. N 105671. DOI: 10.1016/j.still.2023.105671

26. Tekeste M.Z., Way T.R., Syed Z., Schafer R.L. Modeling soil-bulldozer blade interaction using the discrete element method (DEM). *Journal of Terramechanics*. 2020. Vol. 88, p. 41-52. DOI: 10.1016/j.jterra.2019.12.003

27. Troyanovskaya I.P., Raznoshinskaya A.V., Kozminykh V.A., Leshchenko E.A. Experimental tests of industrial-scale ripping of soil. *Gornyi zhurnal.* 2021. N 5, p. 87-90 (in Russian). DOI: 10.17580/gzh.2021.05.11

28. Rashidov T., Djuraeva N., Atamirzayev M., Normuminov B. Strain state agrogenic soil under its interaction with a deep ripper. *IOP Conference Series: Materials Science and Engineering*. 2020. Vol. 896. N 012109. DOI: 10.1088/1757-899X/896/1/012109

29. Ucgul M., Saunders C., Fielke J.M. Comparison of the discrete element and finite element methods to model the interaction of soil and tool cutting edge. *Biosystems Engineering*. 2018. Vol. 169, p. 199-208. DOI: 10.1016/j.biosystemseng.2018.03.003

30. Shemyakin S.A., Shishkin E.A. Physical and mathematical model of rock destruction by a milling machine cutter. *Journal of Mining Institute.* 2021. Vol. 251, p. 639-647. DOI: 10.31897/PMI.2021.5.3

31. Yadav S., Saldana C., Murthy T.G. Experimental investigations on deformation of soft rock during cutting. *International Journal of Rock Mechanics and Mining Sciences*. 2018. Vol. 105, p. 123-132. DOI: 10.1016/j.ijrmms.2018.03.003

32. Nikolayev V.A. Calculation of energy consumption for soil cutting horizontal blade by the analysis process. *Scientific and Technical Journal of Bryansk State University.* 2019. N 2, p. 243-250 (in Russian). DOI: 10.22281/2413-9920-2019-05-02-243-250

33. Katinas E., Chotěborský R., Linda M., Jankauskas V. Wear modelling of soil ripper tine in sand and sandy clay by discrete element method. *Biosystems Engineering*. 2019. Vol. 188, p. 305-319. DOI: 10.1016/j.biosystemseng.2019.10.022

34. Makange N.R., Changying Ji, Nyalala I. et al. Prediction of precise subsoiling based on analytical method, discrete element simulation and experimental data from soil bin. *Scientific Reports*. 2021. Vol. 11. N 11082. DOI: 10.1038/s41598-021-90682-w

35. Cviklovič V., Mojžiš M., Majdan R. et al. Data Acquisition System for On-the-Go Soil Resistance Force Sensor Using Soil Cutting Blades. *Sensors.* 2022. Vol. 22. Iss. 14. N 5301. DOI: 10.3390/s22145301

36. Boyarkina I.V. The specific energy consumption for processes of soil digging by digging machine bucket. *Omsk Scientific Bulletin.* 2017. N 2 (152), p. 5-7 (in Russian).

37. Hegde A., Murthy T.G. Experimental studies on deformation of granular materials during orthogonal cutting. *Granular Matter*. 2022. Vol. 24. Iss. 3. N 70. DOI: 10.1007/s10035-022-01227-5

38. Hegde A., Murthy T. An experimental study on shear bands in sand using the orthogonal cutting setup. *EPJ Web of Conferences*. 2021. Vol. 249. N 10007. DOI: 10.1051/epjconf/202124910007

39. Aresh B., Khan F.N., Haider J. Experimental investigation and numerical simulation of chip formation mechanisms in cutting rock-like materials. *Journal of Petroleum Science and Engineering*. 2022. Vol. 209. N 109869. DOI: 10.1016/j.petrol.2021.109869

40. Zaied M.B., El Naim A.M., Abdalla O.A., Sulieman A.M. Effect of Tine Depth and Width on Soil Failure Angle, Cutting Coefficients and Power in Three-Dimensional Case: Computer Modeling. *World Journal of Agricultural Research*. 2016. Vol. 4. N 1, p. 24-30. DOI: 10.12691/wjar-4-1-4

41. Masch F.R., Hecker R.L., Flores G.M. et al. On-the-go sensor with embedded load cells for measuring soil mechanical resistance. *Ciencia del Suelo*. 2020. Vol. 38. N 1, p. 21-28.

Authors: **Stanislav A. Shemyakin,** *Doctor of Engineering Sciences, Professor, https://orcid.org/0000-0002-3238-0840 (Pacific National University, Khabarovsk, Russia),* **Evgenii A. Shishkin,** *Candidate of Engineering Sciences, Associate Professor, 004655@pnu.edu.ru, https://orcid.org/0000-0003-4387-0228 (Pacific National University, Khabarovsk, Russia).*

The authors declare no conflict of interests.

ISSN 2411-3336; e-ISSN 2541-9404

JOURNAL OF MINING INSTITUTE
Zapiski Gornogo instituta
Journal homepage: pmi.spmi.ru

Research article *Economic Geology*

Public-private partnership in the mineral resources sector of Russia: how to implement the classical model?

Sergei M. Lavlinskii✉, Artem A. Panin, Aleksandr V. Plyasunov
Sobolev Institute of Mathematics, Siberian Branch of the RAS, Novosibirsk, Russia

How to cite this article: Lavlinskii S.M., Panin A.A., Plyasunov A.V. Public-private partnership in the mineral resources sector of Russia: how to implement the classical model? Journal of Mining Institute. 2025. Vol. 272. N 16412, p. 145-158.

Abstract
A comparative financial and economic analysis is conducted of different public-private partnership (PPP) models for industrial infrastructure construction projects in an underdeveloped resource-rich region. The Stackelberg game theory-based model is used to build a parametrized family of bilevel mathematical programming models that describe an entire spectrum of partnership schemes. This approach enables a comparison of different strategies for the distribution of infrastructure investments between the government and the subsoil user and hence a scenario of transformation of Russia's current PPP scheme into the classical partnership model, which is practiced in developed economies. To this end, a database is created on fifty polymetallic deposits in Transbaikalia, and a comparative analysis is conducted of Stackelberg equilibrium development programs that implement different PPP models. The numerical experiment results show the classical PPP model to be most effective in the case of a budget deficit. The analysis helps assess the economic consequences of a gradual transformation of the partnership institution in industrial infrastructure construction from investor support in the Russian model to government support in the classical scheme. Intermediate partnership models, which act as a transitional institution, help reduce the budget burden. These models can be implemented by clustering the deposits, developing subsoil user consortia, and practicing shared construction of necessary transport and energy infrastructure. The intensification of horizontal connections between subsoil users creates favorable conditions for additional effects from the consolidation of resources and can serve as a foundation for a practical partnership scheme within the framework of the classical model.

Keywords
mineral resource base development program; industrial infrastructure projects; public-private partnership; subsoil user consortium; Stackelberg model; bilevel mathematical programming problems

Funding
This work was supported by the Russian Science Foundation, project N 23-28-00849, https://rscf.ru/project/23-28-00849.

Received: 18.03.2024 ***Accepted: 07.11.2024*** ***Online: 14.01.2025*** ***Published: 25.04.2025***

Introduction

The public-private partnership (PPP) scheme is widely used in many sectors of economy to coordinate the interests of the government and those of the private investor [1-3]. World experience demonstrates the efficiency of PPP, primarily, in the provision of new and maintenance of existing public sector infrastructure. In the mineral resources sector, PPP is practiced mostly in the construction of new industrial infrastructure; it allows one to considerably expand project funding sources and encourages subsoil users to develop new deposits in hard-to-reach areas. The partnership institution in developed economies has been evolving for two hundred years, starting in the 19th century with the concession, a model traditionally referred to as BOT (Built, Own, Transfer). This model involves the transfer of certain projects from the government to the private sector and was used to provide transport infrastructure [4].

The Australian BOOT (Built, Own, Operate, Transfer) model [5] largely expanded the functionality of partnerships. The private investor constructs, finances, manages, and operates the facility but owns it only until the end of the contract, after which the ownership passes to the government [6]. This model prevailed in infrastructure projects at the end of the 20th century.

The next stage in the evolution of PPP is associated with the DBFO (Design, Built, Finance, Operate) model [7] and the adoption of a new strategy – Private Finance Initiative – for government projects in the United Kingdom [8]. A private investor sets up for a long term (30 to 60 years) a special management company that constructs, finances, and manages the facility and provides services specified by the government in the contract.

This evolution of the partnership institution in developed economies [9-11] explains why a PPP model [12-14] that can be called classical gained here a foothold. Its idea lies with the construction of a publicly owned facility by a private company with the subsequent transfer of the facility to the government when the terms of the contract and the scenario of mutual settlements are fulfilled [15, 16]. In the mineral resources sector, this PPP scheme allows one to diversify project funding sources, reduce risks [17-19], and encourage subsoil users to reach out into undeveloped areas with promising deposits [20-22].

The development of the PPP institution in the Russian raw materials sector is now in an early stage, and the government has so far no clear understanding on how the starting model should transform [23-25]. Unlike, for example, road construction projects in a developed industrial region, where a concession may be profitable for the investor because of the paid use of the public road, with the profitability guaranteed by the budget [26], industrial infrastructure construction projects in an underdeveloped resource-rich area do not attract private investors for several reasons, even in oil and gas regions [27, 28]. The government, which is interested in the development of the mineral resource base (MRB), seeks to attract private investors to these regions by providing large-scale support to subsoil users in creating infrastructure and implementing some of the necessary environmental protection activities [29-31]. The Russian government used this strategy of cooperation with private investors in the Comprehensive Development Program for the Lower Angara Region [32, 33], Transport Infrastructure Project for the Development of Mineral Resources in the Southeast of the Chita Region [34, 35], and South Yakutia Comprehensive Development Project [36]. In the above cases the government used funds from the Russian Direct Investment Fund for the design and construction of transport and power grid infrastructure for the Kankunskaya Hydroelectric Power Station in Yakutia and the construction of the Naryn – Lugokan Railway in Transbaikalia; in the Krasnoyarsk Region, the government financed not only large infrastructure projects but also the costs associated with preparing the reservoir bed for the Boguchanskaya Hydroelectric Power Station and the resettlement of the population.

The current results of these projects do not meet budget expectations and raise fair criticism on the part of expert community. Experience has shown that the current PPP scheme requires not only excessive budget expenditures but also an evidence-based evaluation whether a balance is indeed achieved between the interests of society and entrepreneurs. This is confirmed by the current experience of implementing the Yenisei Siberia Megaproject. There is not enough evidence to confirm public efficiency of the strategy to construct the Elegest – Kyzyl – Kuragino Railway and the Beya transport infrastructure using budget funds. The feasibility studies of these projects focus on efficiency assessments from the standpoint of the private investor; thus, the key question of achieving a compromise between the interests of the partnership participants remains unanswered [37-39]. Under what conditions will the classical PPP model be efficient in today's mineral resources sector of Russia? How to transform the Russian version of partnership and make a transition from investor support to government support? How to build a PPP scheme that will be efficient in a particular resource-rich region?

The aim of this work is to conduct a comparative financial and economic analysis of different partnership schemes within the Stackelberg game theory-based model. By leaving aside the issues of legal regulation of PPP and focusing on the economic efficiency assessment of specific partnership models, we can answer the key questions in terms of achieving a compromise between the interests of the government and business and suggesting transitional forms of the partnership institution, which could open, in the long run, the possibility of transformation into the classical model. The corresponding economic and mathematical models complement the strategic planning toolkit and can be incorporated into digital technologies of subsoil use management.

Methods

The process of forming a particular partnership scheme can be described by a variety of mathematical models, whose solutions enable us to a priori assess the efficiency of a given managerial decision [40-43]. However, we are faced with a much broader problem, i.e., how to link the nomenclature and launch times of mineral deposit development projects with plans for providing the necessary yet currently nonexistent industrial infrastructure; the latter is to be built within a partnership scheme that remains to be determined [44]. This problem is relevant for most resource-rich territories in Russia; i.e., an investor cannot launch deposit development projects due to the lack of roads and power lines, and the government is not ready to build infrastructure facilities unless it is sure that their capacity is utilized. In most regions of Siberia and the Far East, this factor hinders the development of regional economies and encourages the search for ways to achieve a compromise between the interests of the participating parties.

The process of forming a subsoil use program in a resource-rich region with underdeveloped transport and energy infrastructure is defined by a hierarchy of interactions between the government and the private investor. This is why we find it appropriate to propose the Stackelberg game as a partnership model [45-47]. Two players with individual objective functions – the leader and the follower – take turns in making decisions. The effectiveness of each player's decisions depends on the decision made by the other player. The leader makes the decision first; the follower does so second, constructing its decision in an optimal way with respect to the leader's actions. The aim is to find equilibrium solutions that provide the leader with the maximum value of the objective function on the entire set of alternatives. In our case, the role of the leader belongs to the government, which makes the first move by selling a license and determining the scope of infrastructure construction on the territory. Without this step, the investor cannot make a decision on implementing a deposit development project; therefore, it acts as a follower.

We consider three basic partnership models. The first one is the classical PPP model. Since there is no industrial infrastructure available for the implementation of deposit development projects, the investor coordinates with the authorities a nomenclature of infrastructure objects that "open up" resource base objects it is interested in and builds these roads, power lines, etc. at its own expense. The government pays the investor at a later point in time, e.g., from the moment of receiving the first rent payments. Two reimbursement mechanisms are used to compensate for the infrastructure costs borne by the investor. The first alternative is that the investor receives compensation payments with the investor discount according to a government-defined schedule, which does not depend on the overall results of the partnership (model C1). The second algorithm of mutual settlements builds upon an integral assessment of the investor's *NPV* in the implemented subsoil development program, taking into account the investor's incidental infrastructure costs, compensation payments, and the share of the rent it received while developing the deposits (model C2).

Unlike the classical models C1 and C2, the second model, R, captures the Russian practices of recent years and assumes that the government itself builds infrastructure in an underdeveloped territory.

The third – transitional – model assumes that both the government and the investor build the infrastructure using two types of reimbursement mechanisms to compensate for the investor's infrastructure costs (models T1 and T2).

The investor's objective function in all the models is its net present value. The government's target is to maximize budget revenues, taking into account the compensations paid and its own construction costs. We introduce the binary parameters α and β, which define the participation of the government and private investor in infrastructure construction. This way we are able to parameterize the entire family of the above-described PPP models. Thus, in the first, classical PPP model, $\alpha = 0$ and $\beta = 1$. In the Russian model R, $\alpha = 1$ and $\beta = 0$. The transition model uses unity values of α and β.

We introduce the following notation: *NP* – the number of deposit development projects; *NI* – the number of industrial infrastructure construction projects; *T* – the time horizon.

Deposit development (mining) project *i*: CFP_{it} – the operating cash flow; DBP_{it} – the budget tax revenues from the project in year *t*.

Infrastructure construction project *j*: ZI_{jt} – the required investment volume in year *t*; VDI_{jt} – additional budget revenues associated with the multiplicative impact of the infrastructure on the local economy.

The connection between infrastructure and mining projects is represented by the indicator μ_{ij}. If mining project *i* cannot be launched without infrastructure facility *j*, then $\mu_{ij} = 1$; otherwise $\mu_{ij} = 0$.

The budget constraints: $BudI_t$ for the investor and $BudG_t$ for the government.

The partner discounts: *DI* for the investor and *DG* for the government.

The Boolean variables of the model: if the government offers in the leader – follower dialogue to undertake infrastructure project *j*, then $\bar{x}_j = 1$; otherwise $\bar{x}_j = 0$. If the government itself implements infrastructure project *j*, then $x_j = 1$; otherwise $x_j = 0$. If the investor implements mining project *i*, then $z_i = 1$; otherwise $z_i = 0$. If the investor implement infrastructure project *j*, then $v_j = 1$; otherwise $v_j = 0$.

The real variables: $\overline{W_t}$ is the schedule of compensation payments to the investor, which is offered by the government; W_t is the actual schedule of payments from the government to the investor for the infrastructure.

The Stackelberg model. The upper-level problem (the government)

$$\sum_{t=1}^{T}\left(\sum_{i=1}^{NP} DBP_{it} z_i + \sum_{j=1}^{NI} VDI_{jt}(\alpha x_j + \beta v_j) - \alpha\sum_{j=1}^{NI} ZI_{jt} x_j - \beta W_t\right)/(1+DG)^t \to \max \quad (1)$$

subject to

$$\beta\overline{W}_t + \alpha\sum_{j=1}^{NI} ZI_{jt}\bar{x}_j \le BudG_t, \quad t = 1, \ldots, T; \quad (2)$$

$$\overline{W_t}\beta \ge 0, \quad t = 1, \ldots, T; \quad (3)$$

$$\overline{W_t}\beta = 0, \quad t = 1, \ldots, T_0; \quad (4)$$

$$(v, z, x) \in Q^*(\alpha\bar{x}, \beta\overline{W}); \quad (5)$$

$$\bar{x}_j \in \{0,1\}, \quad j = 1, \ldots, NI, \quad (6)$$

where $Q^*(\alpha\bar{x}, \beta\overline{W})$ – the set of optimal solutions for the investor's problem.

The lower-level problem (the investor)

$$\sum_{t=1}^{T}\left(\sum_{i=1}^{NI} CFP_{it} z_i - \beta\sum_{j=1}^{NI} ZI_{jt} v_j + \beta W_t\right)/(DI+1)^t \to \max \quad (7)$$

subject to

$$\sum_{t=1}^{T}\left(-\beta\sum_{j=1}^{NI} ZI_{jt} v_j + \beta W_t\right)/(1+DI)^t \ge 0; \quad (8)$$

$$\sum_{t=1}^{T}\left[\sum_{i=1}^{NP} DBP_{it} z_i - \beta W_t\right] / (1+DG)^t \geq 0; \quad (9)$$

$$-\sum_{i=1}^{NP} CFP_{it} z_i + \beta \sum_{j=1}^{NI} ZI_{jt} v_j - \beta W_t \leq BudI_t, \quad t = 1, \ldots, T; \quad (10)$$

$$\alpha x_j + \beta v_j \geq z_i \mu_{ij}, \quad i = 1, \ldots, NP, \quad j = 1, \ldots, NI; \quad (11)$$

$$\alpha x_j + \beta v_j \leq 1, \quad j = 1, \ldots, NI; \quad (12)$$

$$\alpha x_j \leq \alpha \bar{x}_j, \quad j = 1, \ldots, NI; \quad (13)$$

$$\beta W_t \leq \beta \overline{W_t}, \quad t = 1, \ldots, T; \quad (14)$$

$$x_j, z_i, v_j \in \{0;1\}, \quad i = 1, \ldots, NP, \quad j = 1, \ldots, NI. \quad (15)$$

The government's objective function is the part of the natural resource rent it receives in the form of taxes, taking into account the government's own infrastructure costs and its compensation payments to the investor. Budget constraints (10) and (2) limit the number of projects implemented by the partners. The connection between the mining and infrastructure projects is defined by constraints (11). Constraint (9) blocks those mining programs that do not guarantee a positive balance between the budget revenues and compensation payments, taking into account the government discount, which formalizes the degree of liberality of the investment policy pursued by the government. Condition (8) plays an important role in choosing the mechanism for generating compensation payments to the investor. Problem (1)-(15) realizes the investor's requirement to compensate for its incidental costs without taking into account that it receives a share of the resource rent directly in the process of developing the deposit.

An alternative principle of mutual settlements is realized in the models C2 and T2. It is based on assessing the investor's overall effect obtained in the process of developing the deposits, building the necessary infrastructure facilities, and receiving compensations from the government, which ensures a positive *NPV* of program (7) implemented by the investor. Such a scheme assumes a higher level of trust in the partnership and the presence of institutions for monitoring the investor's effect. Formally, such a partnership scheme is described by the same bilevel problem but without constraint (8): {(1)-(7), (9)-(15)}.

The solution to problem (1)-(15) ({(1)-(7), (9)-(15)}) defines the MRB development program: an infrastructure construction front opened by the government; a list of infrastructure and mining projects to be implemented by the private investor; a schedule of budgetary compensations for the investor's infrastructure costs. Filling the bilevel mathematical programming problem (1)-(15) with practical data requires a fairly extensive information base. The initial data for the government's problem include schedules of investment costs for infrastructure projects and expert assessments of their multipliers. As far as mining projects are concerned, one assumes there are forecasts of the corresponding tax revenues of the budget. In practice, the government obtains these data on infrastructure from design organizations and on deposits from the subsoil user's feasibility studies in the section on expected payments to employees and budget revenues. The database of the investor's problem also includes *CFP*, which is derived from estimates for the necessary investments and from details of the production technology applied at the deposit. What is required here is a forecast of changes in market prices for raw materials and a detailed analysis of the development project.

To solve the bilevel mathematical programming problems (1)-(15), ({(1)-(7), (9)-(15)}), which belong to the class of $\sum_2^p$ – hard problems, we used stochastic algorithms of local search and coordinate descent [48-50]. For a comparative analysis of the effectiveness of the classical and Russian partnership model, we used a model database on fifty polymetallic deposits and ten transport and

energy infrastructure construction projects in Transbaikalia. Some of the model infrastructure projects describe the construction (currently underway) of the Naryn – Lugokan Railway and four power transmission lines. Other model infrastructure projects generate an additional road network, currently nonexistent yet necessary for some deposits. The database is arranged in such a way that the implementation of all infrastructure projects opens up the possibility of developing the entire set of deposits.

The initial information for the database of model (1)-(15) in the calculations was sourced from the feasibility studies of the mining and infrastructure projects. We possessed information on nine deposits; two road construction projects; one power line; and design documentation for the Naryn – Lugokan Railway, which included mostly the cost sections. The feasibility studies themselves were conducted in different years of the period 2006-2017, so we had to convert the data to the baseline year of 2010 using regional deflators. For the remaining deposits, we used resource estimates and constructed the cost characteristics of the development technologies on the expert basis by choosing a prototype with the closest parameters from among nine options. The planning period in the calculations was 20 years, from 2010 to 2030. The inflation and national currency exchange rate scenarios for the period 2020-2030 followed the existing trends.

For the mining projects, we used a special modeling toolkit [51] that allowed us to make long-term forecasts for metal prices and generate a cash flow in the forecast prices on the basis of a simulation model of the ore deposit development process. The processes of building transport and energy infrastructure were described by the graphs of the partners' infrastructure costs with respect to the PPP model and inflation. For each deposit, we made a forecast of tax payments and cash flow, after which we applied the deflation procedure to generate a total database of the bilevel planning model (1)-(15) in comparable prices. The solution of this model determined the MRB development program in the region.

The resulting information base is largely consistent with the management technologies in the subsoil use sector and is configured for investment processes with a long time horizon and nonstationary market prices. This approach takes into account the features of the object being modeled, i.e., the process of forming a MRB development program in a territory rich in raw materials yet lacking production infrastructure. Since such a program rests upon the Stackelberg equilibrium, our primary interest lies with understanding how the solution of problems (1)-(15) ({(1)-(7), (9)-(15)}) changes with variations in the main parameters of the model. This is especially important for the partner discounts, whose working ranges can only be estimated approximately by experts.

This circumstance determines the focus of attention in the numerical experiment, i.e., on analyzing the dependence of the efficiency of the Stackelberg equilibrium program on the parameters *DG* and *DI*. The former parameter reflects the quality of investment climate from the point of view of the investor. In the calculations, a favorable investment climate corresponds to $DI = 0.11$ (the expert assessment for today's Transbaikalia is $DI = 0.15$-0.17). The government discount reflects the level of liberality of the government's investment policy. Operating with a discount of 0.01, a liberal government understands that on the long-term horizon, the most important role belongs to multiplier effects, which exceed the direct return from budget investments into the infrastructure projects (including compensation payments) in the form of subsoil users' tax payments. A conservative government runs its investment policy with a tangibly larger discount, which reflects its aspirations to materialize the expectations of the subsoil owner [52].

Results and discussion

Numerical experiments reveal a substantial dependence of the effectiveness of the development programs generated by the different partnership models on the investment climate and on the degree of liberality of the government.

We present some of the calculated results, which help quantify and compare the key characteristics of the deposit development programs generated under the assumption of unlimited budgets of the partners with the different algorithms of compensating the investor's infrastructure costs, α and β.

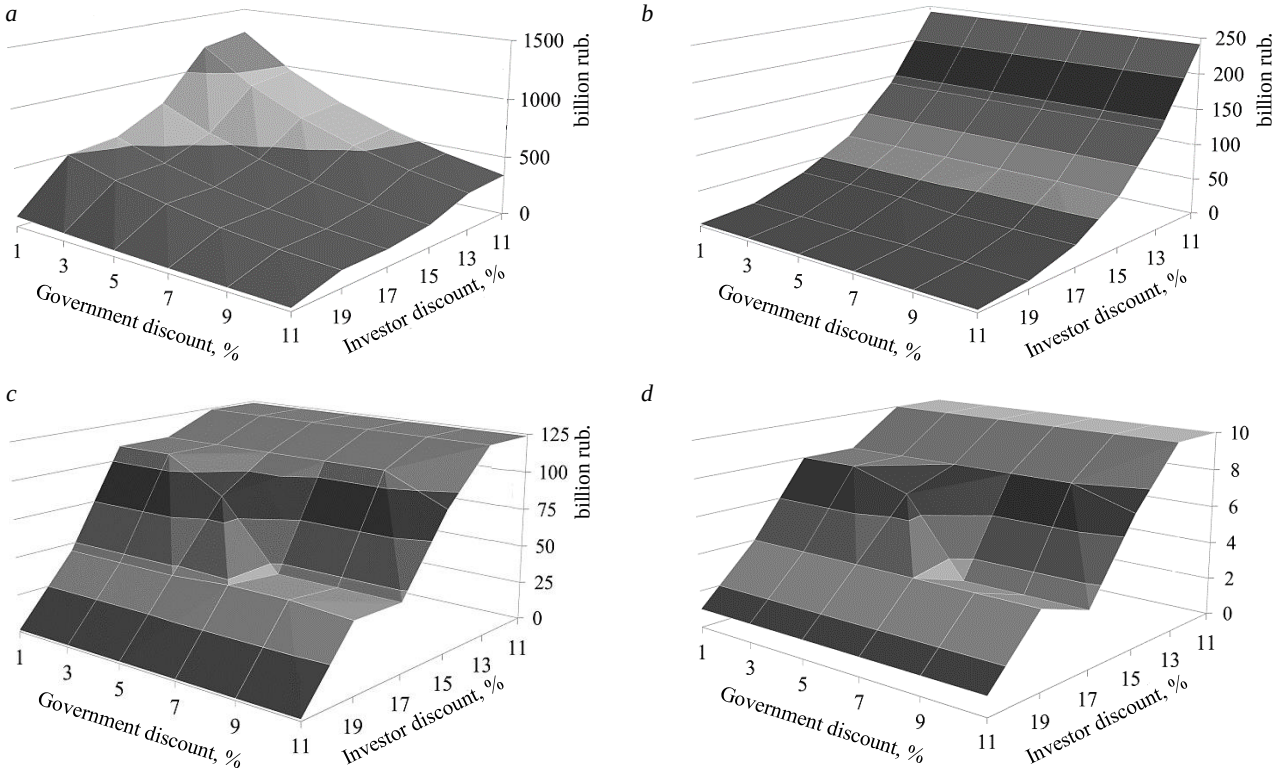

Fig.1. PPP model based on the Investment Fund of Russia (the R model: $\alpha = 1$ and $\beta = 0$): values of the objective functions of the government (*a*) and the investor (*b*); government costs (*c*); and number of implemented infrastructure projects (*d*)

Within the Russian model (Fig.1), the government spends, given a favorable investment climate, 125 billion rub. and implements the entire program of infrastructure construction. This outcome does not depend on the government discount and enables the investor to launch the maximum number of mining projects. If the investment climate worsens (*DI* grows), the government is forced to reduce the amounts of infrastructure construction, which naturally compels the investor to curtail the mining program and leads to a decrease in the values of the partners' objective functions. Outside the favorable investment climate, the government discount, too, tangibly affects the results; i.e., the transition to a conservative investment policy narrows the range of infrastructure projects that are effective for the government.

The transition to the classical partnership model markedly changes the territorial development program. In the case of a low investor discount, the C1 model generates a program in which five or six infrastructure projects are implemented out of the ten possible ones, depending on the level of the government discount (Fig.2). Starting with $DI = 0.19$, the amounts of infrastructure construction and compensation payments to the investor drop sharply. The C2 model starts with eight projects, and this number falls quickly with the deterioration of the investment climate. It is important that the level of compensation payments is much lower here than in the option with the investor demanding immediate compensation for its infrastructure costs. The reason is that in the process of mutual settlements, the government takes into account the rent obtained from the mining projects and adjusts the payments accordingly.

In the transition model, the total number of infrastructure projects is less depends on the investor costs compensation algorithm (Fig.3) and the government discount. The government ceases to participate in infrastructure construction depending on the level of liberality as early as at $DI = 0.13$ within a conservative investment policy, shifting the boundary with the decrease in *DG*.

The government's costs on paying the compensations (Fig.4) behave in a rather complex manner. In a favorable investment climate, the T2 model requires noticeably smaller payments to the investor than T1, with the payments growing as the investment climate worsens. In the T1 model,

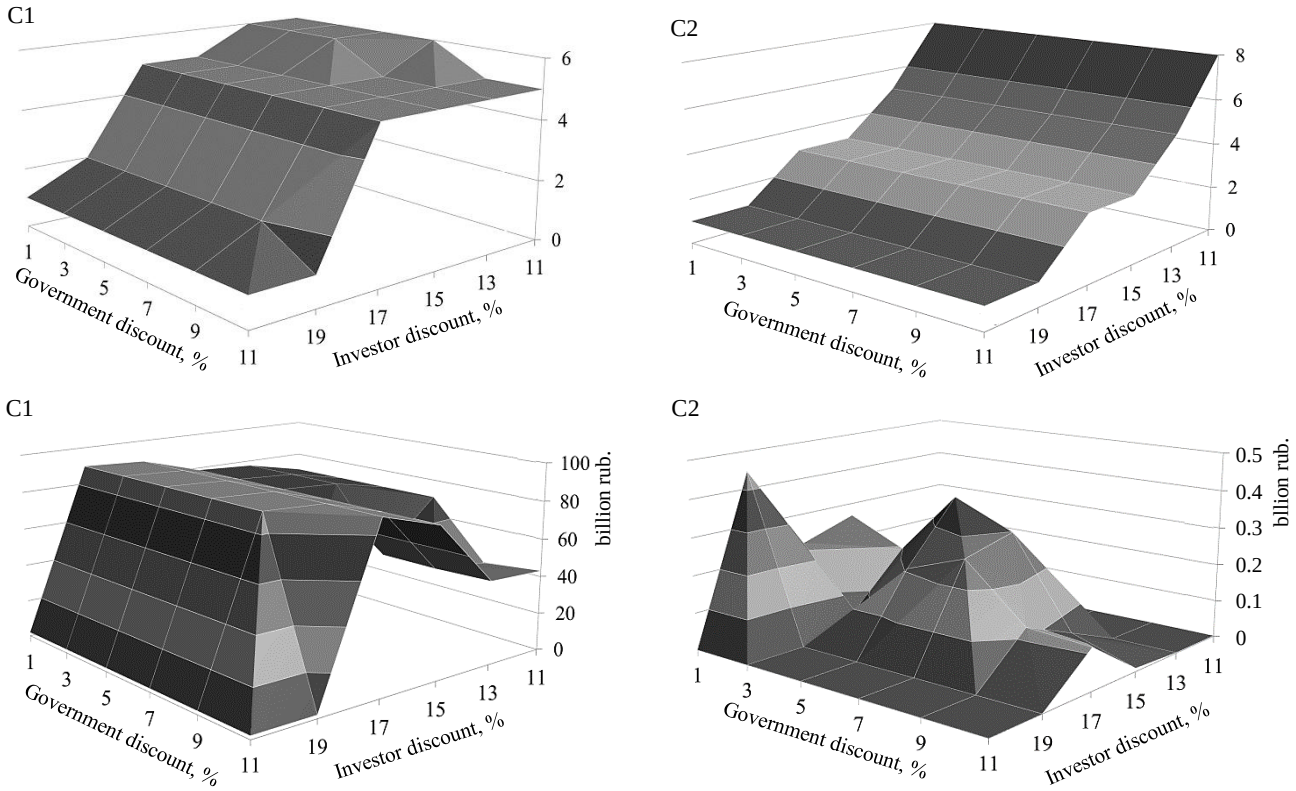

Fig.2. Classical PPP model: number of infrastructure projects implemented by the investor (above); amount of compensations payments received (below)

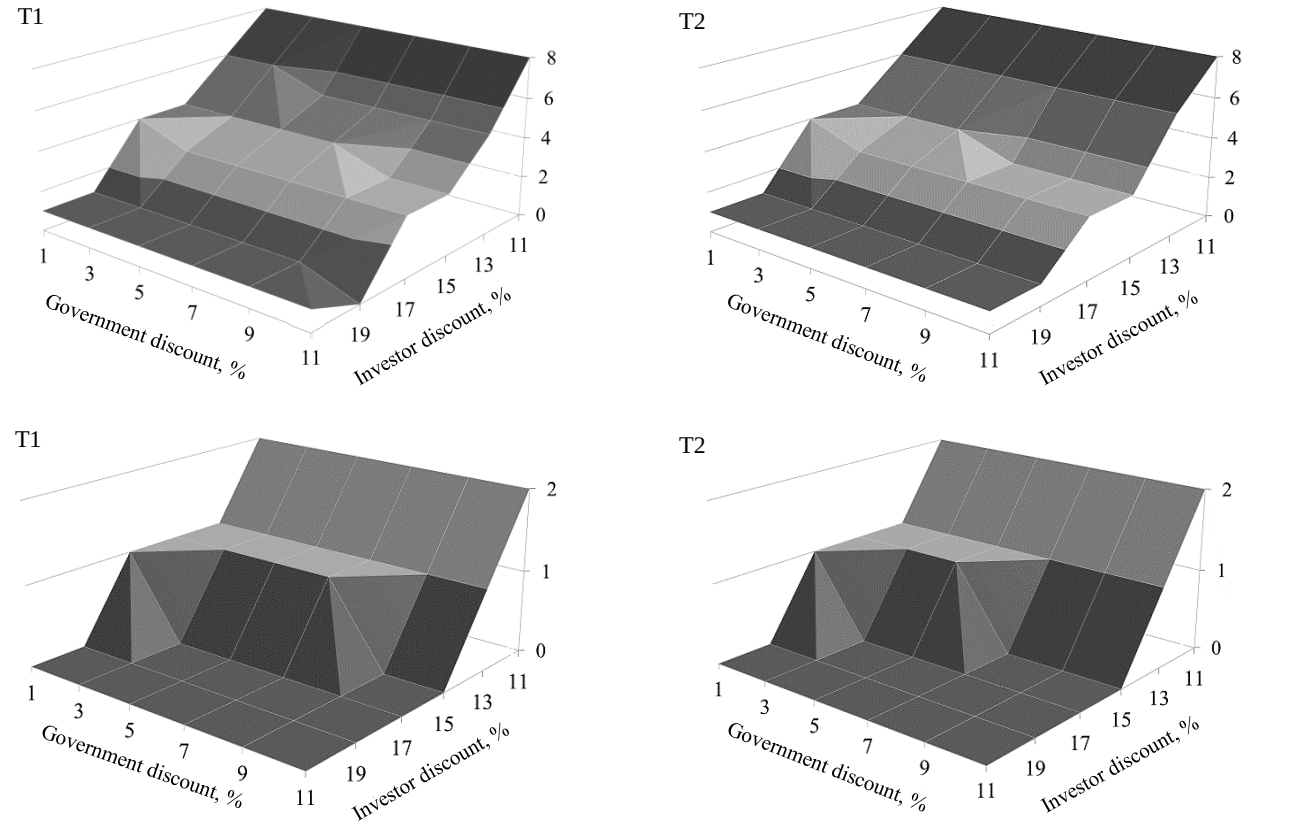

Fig.3. Transitional PPP model: number of infrastructure projects implemented by the partners together (above); including by the government (below)

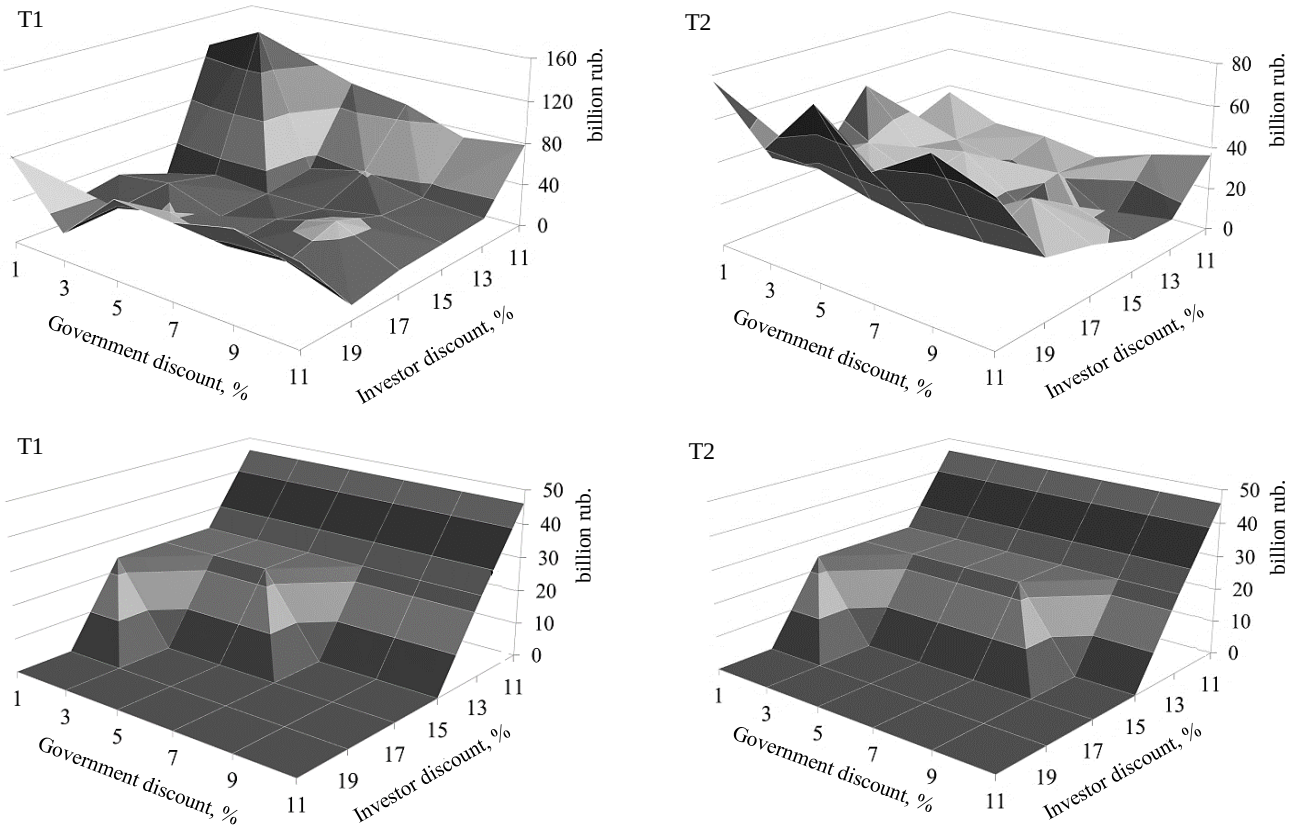

Fig.4. Transitional PPP model: the government's costs: compensation payments (above); costs of implementing infrastructure projects (below)

on the contrary, the compensation payments reach a peak at small *DI* values and largely depend on the degree of conservatism of the government's investment policy. As in the classical model, a government faced with a budget deficit prefers an investor who fully trusts it and consents to the second-type procedure of mutual settlements.

Figures 5 and 6 show the resulting dependences of the values of the government and investor's objective functions under all possible combinations of the partner discounts in the different models. Based on these data, we can rank the entire spectrum of the partnership models in accordance with the government's interests. If we attempt, while analyzing Fig.1 and 5, to rank all the five models according to the value of the government's objective function, we see that at any degree of favorableness of the investment climate, the Russian model, under the assumption of an unlimited budget, formally provides the best result. However, today it seems unlikely that the government would decide to finance on a large scale the construction of industrial infrastructure for the needs of the mineral resources sector.

Under budget deficit, the priority shifts to the classical PPP model. Direct budget investments start from the time of launching the construction of the necessary infrastructure, while the compensation payments are deferred until the time of receiving the first taxes from subsoil users. This approach allows for a considerable decrease in the budget funds needed to fulfill the partnership obligations on the part of the government.

That is why, when choosing a PPP model, we should consider only the models C1, C2, T1, and T2. By analyzing the calculation results presented in Fig.5, we can rank them according to the value of the government's objective function (1) for each value of *DI*. For a favorable investment climate (*DI* = 0.11), the desired sequence has the form (C2, T2, T1, C1); for *DI* = 0.13 – (T2, C2, T1, C1); and for *DI* > 0.13 – (C1, C2, T2, T1).

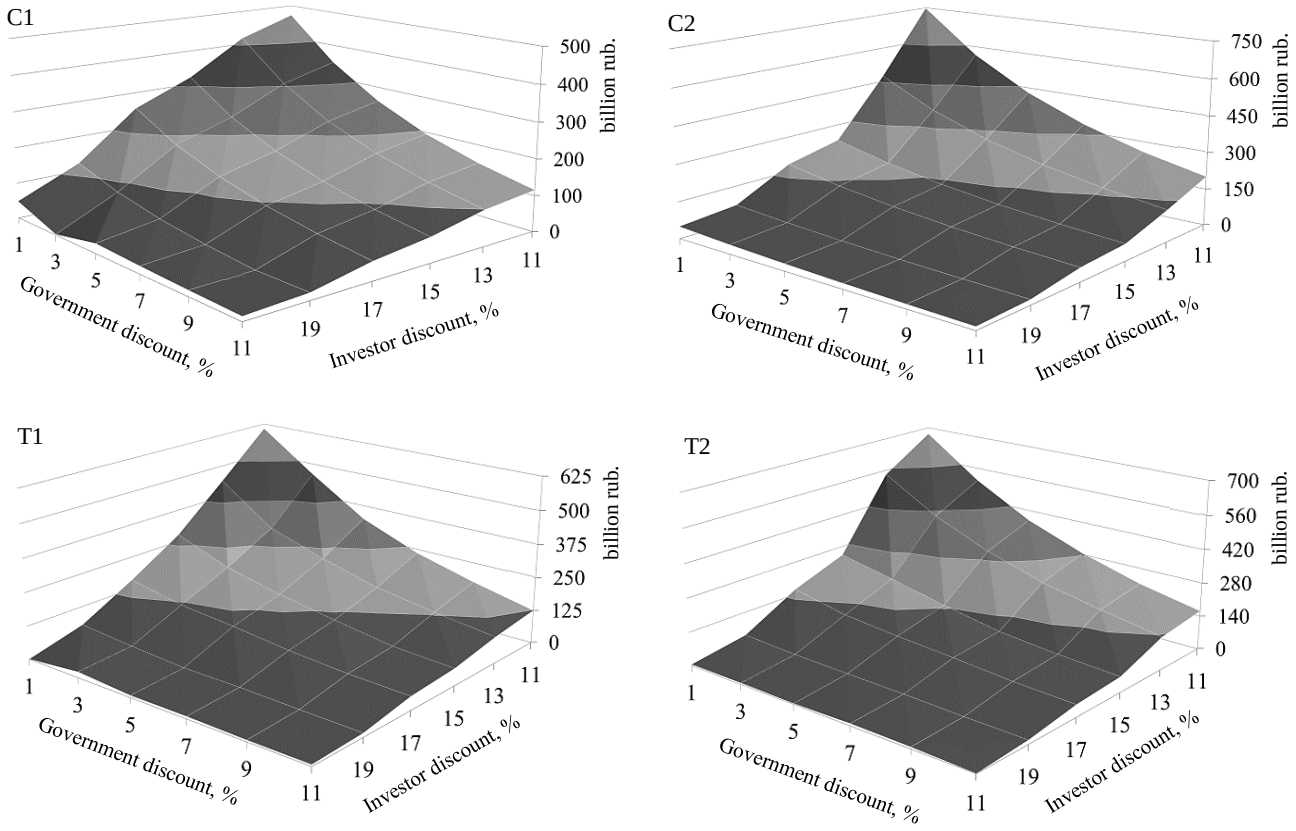

Fig.5. Values of the government's objective function in different models

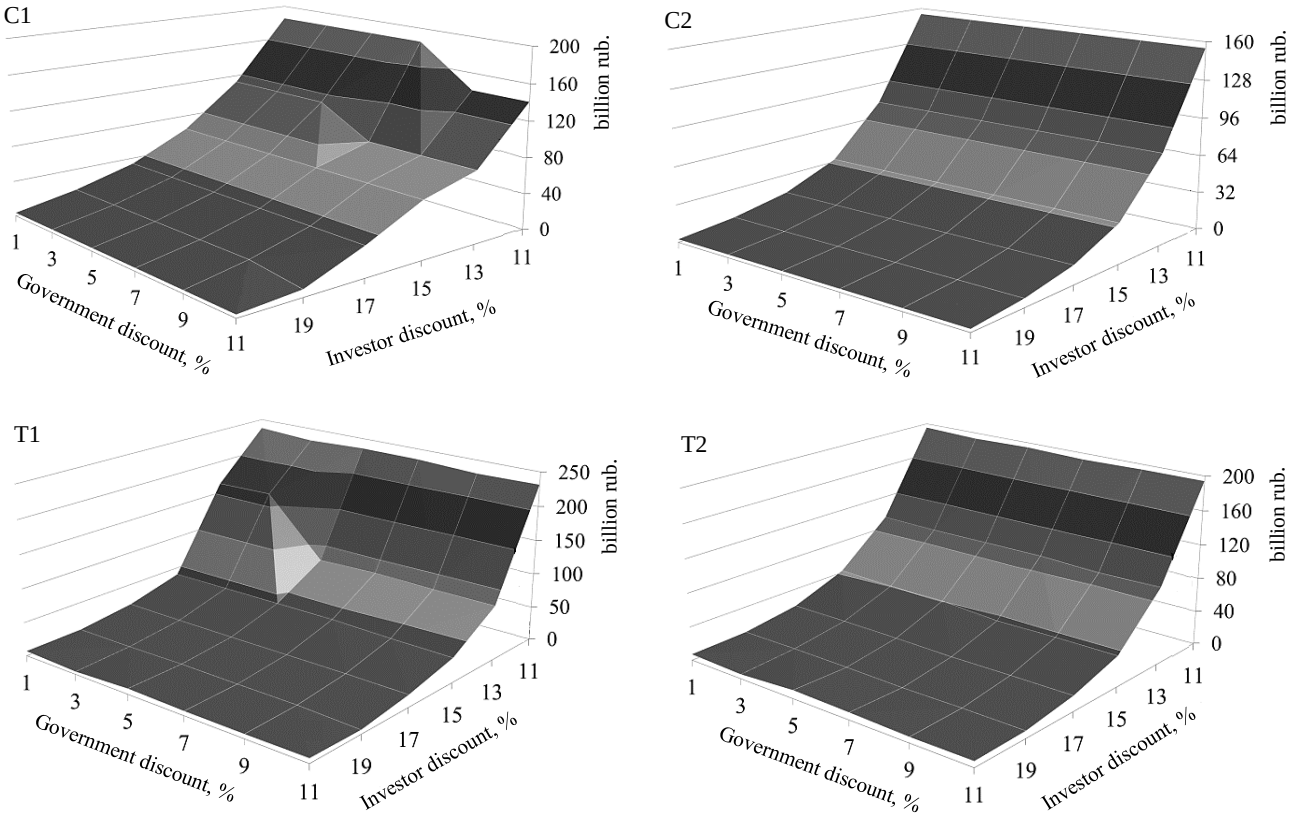

Fig.6. Values of the investor's objective function in different models

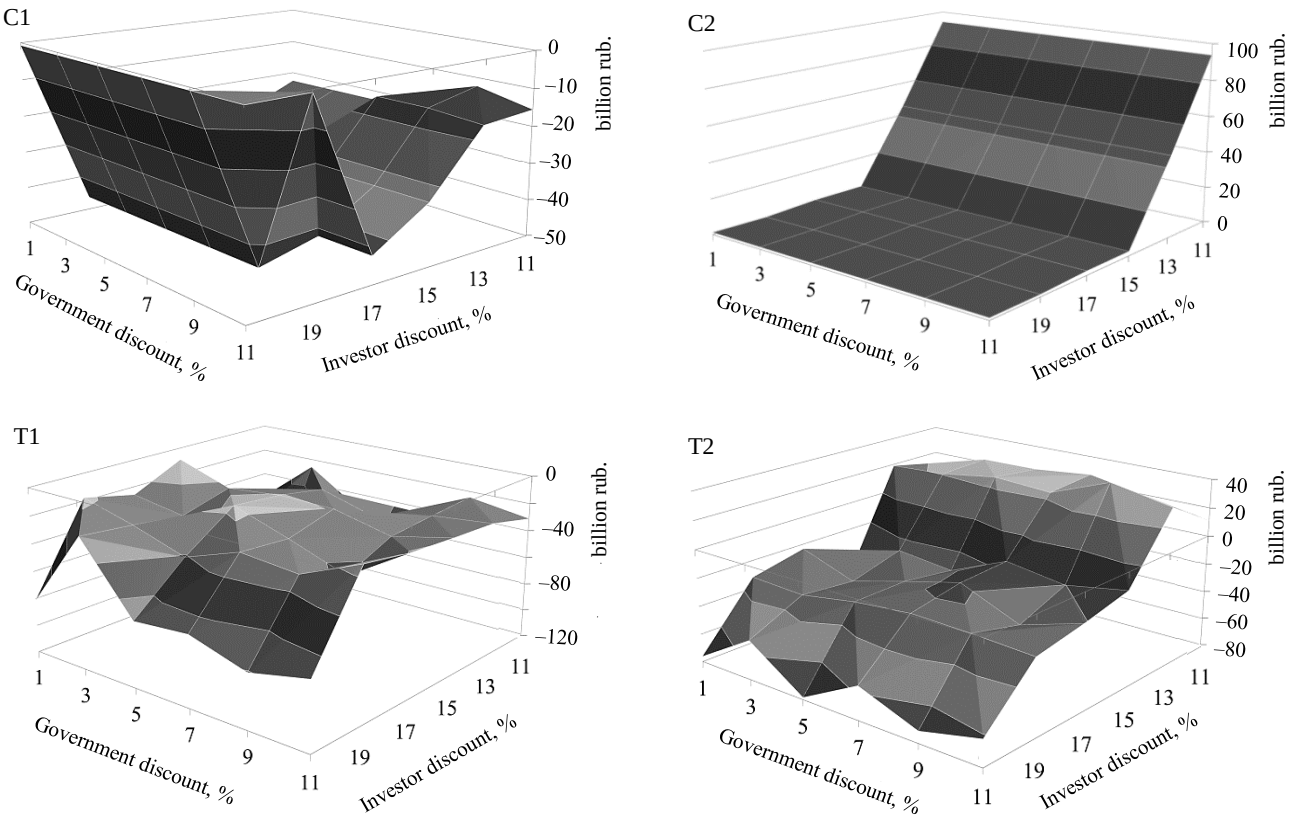

Fig.7. Balance of the infrastructure costs and compensation payments to the investor

Considering the models T1 and T2 as a transition to the classical scheme and taking into account that they assume partial participation of the government in direct infrastructure investments, we can leave only the classical models C1 and C2. We choose from this pair by analyzing the balance between the resulting infrastructure and the compensations paid to the investor, i.e., the difference between the total cost of the provided infrastructure facilities and the total amount of compensation payments to the investor (Fig.7). The C2 model turns out to be preferable since it ensures a positive balance across the entire range of *DI* values. This choice is further confirmed by the fact that the C2 model requires compensations that are an order of magnitude smaller than C1 (see Fig.2), which is the most powerful argument in the case of a budget deficit.

Thus, faced with today's severe budget deficit, the government has a clear goal to implement the classical PPP model in the C2 modification. The methodological foundation of this scheme lies with an integral assessment of the investor's *NPV* in the implemented subsoil development program. This approach requires a higher level of trust in the partnership and the presence of institutions for monitoring the investor's effects.

One of the possible institutions of this kind could be a consortium headed by a public-owned management company, aimed to organize, coordinate, and establish an effective territorial development program based on horizontal interactions of private investors. In the case of a budget deficit, this partnership scheme can generate effects from the consolidation of investors' resources, open up the possibility of harmonizing their goals, and, in the long term, adapt the classical scheme to the Russian realities. A similar model, in which the classical partnership is supplemented by a consortium, was examined in [53]. It was shown that under certain conditions, i.e., the possibility of clustering the territory or the presence and proximity of highly profitable deposits, setting up a consortium is economically feasible. The participation of Russian Railways in the implementation of such projects expands the possibilities of this approach and increases the stability of this institution.

Conclusions

Our analysis of the PPP models allows us to give an economic assessment of consequences following a gradual transformation of the partnership institution in industrial infrastructure construction from investor support (model R) to government support in the classical model. The results of numerical experiments based on actual information for a typical resource-rich region, in our case, Transbaikalia, lead us to the following conclusions:

• Under a severe budget deficit, the partnership scheme in which the government itself builds the necessary infrastructure (model R) has no economic prospects.

• The intermediate partnership models, T1 and T2, serve as a transitional institution, allowing one to reduce the budget burden and increase the level of trust of the private investor to the government. These schemes can be useful for the introduction and development of the PPP institution in Russia and, after a thorough model analysis, can be recommended for practical use in some regions. In most cases, the T2 model is preferable for the government.

• Under budget deficit, the classical PPP model in the C2 modification best meets the interests of the government. This model ensures the minimum possible amount of compensation payments to the investor and a positive balance between the cost of the provided infrastructure and the amount of compensations.

• A necessary condition for the feasibility of the C2 model is the presence of an institution for a coordinated assessment of the investor's *NPV* in a given subsoil development program, i.e., an assessment that takes into account the investor's incidental infrastructure costs, the compensation payments it receives, and the share of the rent it has obtained.

• One of the possible forms of this institution is a collaboration based on clustering the deposits and setting up a consortium to implement the construction of the necessary industrial infrastructure. This approach allows one not only to construct the necessary industrial infrastructure but also to establish a practical foundation for the transformation of the Russian PPP institution towards the classical forms.

REFERENCES

1. Addink H. Good Governance: Concept and Context. Oxford: Oxford University Press, 2019, p. 352. DOI: 10.1093/oso/9780198841159.001.0001

2. Ivanov O., Inshakova A.O. Public-Private Partnerships in Russia. Institutional Frameworks and Best Practices. Springer, 2020, p. 312.

3. Yescombe E.R., Farquharson E. Public-Private Partnerships for Infrastructure. Principles of Policy and Finance. Butterworth-Heinemann, 2018, p. 548.

4. Reznichenko N.V. Public-Private Partnership Models. *Vestnik of Saint Petersburg University. Management.* 2010. Iss. 4, p. 58-83 (in Russian).

5. Quiggin J. Risk, PPPs and the Public Sector Comparator. *Australian Accounting Review*. 2004. Vol. 14. Iss. 33, p. 51-61. DOI: 10.1111/j.1835-2561.2004.tb00229.x

6. Grimsey D., Levis M.K. Public Private Partnerships: The Worldwide Revolution in Infrastructure Provision and Project Finance. Edward Elgar, 2004, p. 288.

7. Mayston D.J. The Private Finance Initiative in the National Health Service: An Unhealthy Development in New Public Management? *Financial Accountability & Management*. 1999. Vol. 15. Iss. 3-4, p. 249-274. DOI: 10.1111/1468-0408.00084

8. Grout P.A. The economics of the private finance initiative. *Oxford review of economic policy*. 1997. Vol. 13. Iss. 4, p. 53-66. DOI: 10.1093/oxrep/13.4.53

9. Adamou M., Kyriakidou N., Connolly J. Evolution of public-private partnership: the UK perspective through a case study approach. *International Journal of Organizational Analysis*. 2021. Vol. 29. Iss. 6, p. 1455-1466. DOI: 10.1108/IJOA-08-2020-2397

10. Zhe Cheng, Yongjian Ke, Zhenshan Yang et al. Diversification or convergence: An international comparison of PPP policy and management between the UK, India, and China. *Engineering, Construction and Architectural Management*. 2020. Vol. 27. Iss. 6, p. 1315-1335. DOI: 10.1108/ECAM-06-2019-0290

11. Gleeson T.P., Grimsey D., Lewis M.K. How Successful Has the PPP Model Been in Australia? *Public Private Partnerships. Cham: Springer*, 2019, p. 167-192. DOI: 10.1007/978-3-030-24600-6_9

12. Dao N.H., Marisetty V.B., Jing Shi, Tan M. Institutional quality, investment efficiency, and the choice of public–private partnerships. *Accounting & Finance*. 2020. Vol. 60. Iss. 2, p. 1801-1834. DOI: 10.1111/acfi.12514

13. Grimsey D., Lewis M.K. Are Public Private Partnerships value for money? Evaluating alternative approaches and comparing academic and practitioner views. *Accounting Forum*. 2005. Vol. 29. Iss. 4, p. 345-378. DOI: 10.1016/j.accfor.2005.01.001

14. Karnes Y. Are There Optimal Forms of Public-Private Partnerships? *Journal of Behavioral and Applied Management*. 2020. Vol. 20. Iss. 2, p. 51-68. DOI: 10.21818/001c.14178

15. Nannan Wang, Minxun Ma. Public–private partnership as a tool for sustainable development – What literatures say? *Sustainable Development*. 2021. Vol. 29. Iss. 1. P. 243-258. DOI: 10.1002/sd.2127

16. Petersen O.H. Evaluating the costs, quality, and value for money of infrastructure public-private partnerships: A systematic literature review. *Annals of Public and Cooperative Economics*. 2019. Vol. 90. Iss. 2, p. 227-244. DOI: 10.1111/apce.12243

17. Rybnicek R., Plakolm J., Baumgartner L. Risks in Public–Private Partnerships: A Systematic Literature Review of Risk Factors, Their Impact and Risk Mitigation Strategies. *Public Performance & Management Review*. 2020. Vol. 43. Iss. 5, p. 1174-1208. DOI: 10.1080/15309576.2020.1741406

18. Hongyu Jin, Shijing Liu, Chunlu Liu, Udawatta N. Optimizing the concession period of PPP projects for fair allocation of financial risk. *Engineering, Construction and Architectural Management*. 2019. Vol. 26. Iss. 10, p. 2347-2363. DOI: 10.1108/ECAM-05-2018-0201

19. Carbonara N., Pellegrino R. Revenue guarantee in public–private partnerships: a win–win model. *Construction Management and Economics*. 2018. Vol. 36. Iss. 10, p. 584-598. DOI: 10.1080/01446193.2018.1467028

20. Cheng Chen, Caixia Man. Are good governance principles institutionalised with policy transfer? An examination of public–private partnerships policy promotion in China. *Australian Journal of Social Issues*. 2020. Vol. 55. Iss. 2, p. 162-181. DOI: 10.1002/ajs4.99

21. Hueskes M., Verhoest K., Block T. Governing public–private partnerships for sustainability: An analysis of procurement and governance practices of PPP infrastructure projects. *International Journal of Project Management*. 2017. Vol. 35. Iss. 6, p. 1184-1195. DOI: 10.1016/j.ijproman.2017.02.020

22. Jie Tan, Jerry Zhirong Zhao. The Rise of Public–Private Partnerships in China: An Effective Financing Approach for Infrastructure Investment? *Public Administration Review*. 2019. Vol. 79. Iss. 4, p. 514-518. DOI: 10.1111/puar.13046

23. Litvinenko V.S., Petrov E.I., Vasilevskaya D.V. et al. Assessment of the role of the state in the management of mineral resources. *Journal of Mining Institute.* 2023. Vol. 259, p. 95-111. DOI: 10.31897/PMI.2022.100

24. Zaernyuk V.M., Anisimov P.F., Zabaikin Yu.V. Assessment of the status and development prospects of public-private partnerships in mineral extraction industry. *Economics: Yesterday, Today and Tomorrow.* 2019. Vol. 9. N 6A, p. 85-94 (in Russian).

25. Vasilchikov A.V. Ways to realize the potential of the region through the public-private partnerships mechanism. *Izvestiâ Sankt-Peterburgskogo gosudarstvennogo èkonomičeskogo universiteta.* 2019. N 6, p. 68-73 (in Russian).

26. Chung D., Hensher D.A. Public private partnerships in the provision of tolled roads: Shared value creation, trust and control. *Transportation Research Part A: Policy and Practice*. 2018. Vol. 118, p. 341-359. DOI: 10.1016/j.tra.2018.08.038

27. Yudin S.S., Cherepovitsyn A.E. Partnership between government and business to ensure the economic sustainability of complex industrial oil and gas systems in the Arctic. *The North and the Market: Forming the Economic Order*. 2022. N 2, p. 7-18 (in Russian). DOI: 10.37614/2220-802X.2.2022.76.001

28. Filatova I., Nikolaichuk L., Zakaev D., Ilin I. Public-Private Partnership as a Tool of Sustainable Development in the Oil-Refining Sector: Russian Case. *Sustainability*. 2021. Vol. 13. Iss. 9. N 5153. DOI: 10.3390/su13095153

29. Agarchand N., Laishram B. Sustainable infrastructure development challenges through PPP procurement process: Indian perspective. *International Journal of Managing Projects in Business*. 2017. Vol. 10. Iss. 3, p. 642-662. DOI: 10.1108/IJMPB-10-2016-0078

30. Vaslavskiy Ya. Public-Private Partnership: Prospects for the Development of Socially Significant Infrastructure. *Federalism.* 2019. N 4, p. 75-94 (in Russian). DOI: 10.21686/2073-1051-2019-4-75-94

31. Bednyakov A.S. Public-Private Partnership as a Model of Public Infrastructure Development. *MGIMO Review of International Relations.* 2022. Vol. 15. N 1, p. 143-176 (in Russian). DOI: 10.24833/2071-8160-2022-1-82-143-173

32. Malov V.Yu., Tarasova O.V., Ionova V.D. Lower Angara Region as a Link between the North and South of Siberia. *ECO.* 2018. Vol. 48. N 6, p. 50-74 (in Russian). DOI: 10.30680/ECO0131-7652-2018-6-50-74.

33. Popodko G.I., Nagaeva O.S., Bukharova E.B. Application of the project approach in the territorial development of the eastern regions of Russia. *Journal of Siberian Federal University. Humanities & Social Sciences.* 2021. Vol. 14. Iss. 12, p. 1851-1862 (in Russian). DOI: 10.17516/1997-1370-0864

34. Glazyrina I.P., Faleychik L.M., Faleychik A.A. Investments and the Growth Potential of the Quality of Life in the Russian Far East. *Journal of Siberian Federal University. Humanities & Social Sciences.* 2022. Vol. 15. Iss. 7, p. 921-929. DOI: 10.17516/1997-1370-0897

35. Glazyrina I.P., Faleychik L.M., Faleychik A.A. "Far Eastern" Investment Policy and Income of Citizens by Major Industries: An Empirical Analysis. 2022. *ECO.* Vol. 52. N 7, p. 80-98 (in Russian). DOI: 10.30680/ECO0131-7652-2022-7-80-98

36. Mestnikov N.A., Nikolaeva I.V., Pavlova S.N. Investment project "South Yakutia complex development": perspectives, problems, solutions. *National Interests: Priorities and Security.* 2012. Vol. 8. N 20 (161), p. 24-33 (in Russian).

37. Samarukha V.I., Krasnova T.G., Trusova S.V. The model of creation and implementation of the interregional project "Yenisei Siberia". *Bulletin of Baikal State University.* 2019. Vol. 29. N 2, p. 324-331 (in Russian). DOI: 10.17150/2500-2759.2019.29(2).324-331

38. Bryukhanova E.A., Efimov V.S., Shishatsky N.G. Research on the Issues of Economic Growth Centres' Establishment in the South of the Angara-Yenisei Macroregion. *Journal of Siberian Federal University. Humanities & Social Sciences.* 2020. Vol. 13. Iss. 11, p. 1736-1745. DOI: 10.17516/1997-1370-0679

39. Bryukhanova E.A., Shishatsky N.G., Efimov V.S. Strategic Analysis of the Prospects for the Sayano-Yenisei Mesoregion Using the Balance Model. *Journal of Siberian Federal University. Humanities & Social Sciences.* 2021. Vol. 14. Iss. 12, p. 1760-1769 (in Russian). DOI: 10.17516/1997-1370-0856

40. Hong Zhang, Lu Yu, Wenyu Zhang. Dynamic performance incentive model with supervision mechanism for PPP projects. *Engineering, Construction and Architectural Management*. 2020. Vol. 27. Iss. 9, p. 2643-2659. DOI: 10.1108/ECAM-09-2019-0472

41. Xiangtian Nie, Kai Feng, Guoxiang Zhao et al. The Evolutionary Game of Trust in Public-Private Partnership Project Networks. *Mathematical Problems in Engineering*. 2021. Vol. Iss. 1. N 5514708. DOI: 10.1155/2021/5514708

42. *Lavlinskii S.M., Panin A.A., Plyasunov A.V.* A Bilevel Planning Model for Public–Private Partnership. *Automation and Remote Control*. 2015. Vol. 76. N 11, p. 1976-1987. DOI: 10.1134/S0005117915110077

43. Lei Shi, Lu Zhang, Onishi M. et al. Contractual Efficiency of PPP Infrastructure Projects: An Incomplete Contract Model. *Mathematical Problems in Engineering*. 2018. Vol. 2018. Iss. 1. N 3631270. DOI: 10.1155/2018/3631270

44. Kalgina I.S. Models for Assessment of Public-Private Partnership Projects in Sub-surface Management. *Journal of Mining Institute.* 2017. Vol. 224, p. 247-254. DOI: 10.18454/PMI.2017.2.247

45. Lavlinskii S.M., Panin A.A., Plyasunov A.V. Comparison of Models of Planning Public-Private Partnership. *Journal of Applied and Industrial Mathematics.* 2016. Vol. 10. N 3, p. 356-369. DOI: 10.1134/S1990478916030066

46. Lavlinskii S.M., Panin A.A., Plyasunov A.V. The Stackelberg Model in Territorial Planning. *Automation and Remote Control.* 2019. Vol. 80. N 2, p. 286-296. DOI: 10.1134/S0005117919020073

47. Luming Shang, Aziz A.M.A. Stackelberg Game Theory-Based Optimization Model for Design of Payment Mechanism in Performance-Based PPPs. *Journal of Construction Engineering and Management*. 2020. Vol. 146. Iss. 4. N 04020029. DOI: 10.1061/(ASCE)CO.1943-7862.0001806

48. Alekseeva E., Kochetov Y., Talbi E.-G. A matheuristic for the discrete bilevel problem with multiple objectives at the lower level. *International Transactions in Operational Research*. 2017. Vol. 24. Iss. 5, p. 959-981. DOI: 10.1111/itor.12268

49. Dempe S., Khamisov O., Kochetov Yu. A special three-level optimization problem. *Journal of Global Optimization*. 2020. Vol. 76. Iss. 3, p. 519-531. DOI: 10.1007/s10898-019-00822-w

50. Davydov I., Kochetov Y., Dempe S. Local Search Approach for the Competitive Facility Location Problem in Mobile Networks. *International Journal of Artificial Intelligence*. 2018. Vol. 16. Iss. 1, p. 130-143.

51. Lavlinskii S.M. Indicative Planning Models for Socioeconomic Development of a Resource-Rich Region Novosibirsk: Izd-vo SO RAN, 2008, p. 247 (in Russian).

52. Lapinskas A.A. Influence of mining rent on the efficiency of using natural potential: the paradox of plenty and its Russian specifics. *Journal of Mining Institute.* 2023. Vol. 259, p. 79-94. DOI: 10.31897/PMI.2023.13

53. Lavlinskii S., Zyryanov A. Model for Long-Term Partnerships Between the Government and Subsoil Users in Production and Infrastructure Construction. 19th International Asian School-Seminar on Optimization Problems of Complex Systems (OPCS), 14-22 August 2023, Novosibirsk, Moscow, Russia. IEEE, 2023, p. 53-58. DOI: 10.1109/OPCS59592.2023.10275768

***Authors*: Sergei M. Lavlinskii,** *Doctor of Engineering Sciences, Leading Researcher, lavlin@math.nsc.ru, https://orcid.org/0000-0002-4607-0632* (*Sobolev Institute of Mathematics, Siberian Branch of the RAS, Novosibirsk, Russia*), **Artem A. Panin,** *Candidate of Physics and Mathematics, Senior Researcher, https://orcid.org/0000-0002-1844-6276* (*Sobolev Institute of Mathematics, Siberian Branch of the RAS, Novosibirsk, Russia*), **Aleksandr V. Plyasunov,** *Doctor of Physics and Mathematics, Leading Researcher, https://orcid.org/0000-0002-7199-3092* (*Sobolev Institute of Mathematics, Siberian Branch of the RAS, Novosibirsk, Russia*).

The authors declare no conflict of interests.

ISSN 2411-3336; e-ISSN 2541-9404

JOURNAL OF MINING INSTITUTE
Zapiski Gornogo instituta
Journal homepage: pmi.spmi.ru

Research article *Energy*

Thyristor booster device for voltage fluctuation reduction in power supply systems of ore mining enterprises

Elena N. Sosnina✉, Anatolii A. Asabin, Rustam Sh. Bedretdinov, Evgenii V. Kryukov, Daniil A. Gusev
Nizhny Novgorod State Technical University named after R.E.Alekseev, Nizhny Novgorod, Russia

***How to cite this article*:** Sosnina E.N., Asabin A.A., Bedretdinov R.Sh., Kryukov E.V., Gusev D.A. Thyristor booster device for voltage fluctuation reduction in power supply systems of ore mining enterprises. Journal of Mining Institute. 2025. Vol. 272. N 16450, p. 159-170.

Abstract
The article is devoted to solving the problem of voltage fluctuations in the power supply systems of ore mining enterprises. The connection of high-power consumers with abruptly variable operating mode (for example, high-voltage mining excavators) causes voltage fluctuations and sags, disabling electrical equipment, communication, and automation devices in the 6-10 kV distribution network, which disrupts technological processes, etc. The use of existing solutions and methods to reduce voltage variations caused by dynamic loads is not effective. To solve the problem, booster transformers with high-speed thyristor switches can be used to work out switching the control steps towards increasing or decreasing the voltage. The authors offer a new circuitry solution for a thyristor booster device (TBD) with a pulse-phase control method. The purpose of the research is to determine the control laws of TBD, which enable to effectively reduce voltage fluctuations from dynamic load in the power supply systems of mining enterprises. The article provides a schematic diagram of the TBD and describes the principle of operation of the device. Some modes of increasing and decreasing the output voltage of the TBD, as well as the basic mode (without voltage addition) are provided. Mathematical modeling of TBD control processes was carried out and adjustment characteristics were set taking into account the load power factor. On a simulation computer model of a 6 kV electric network with a dynamic load, the verification of the adjustment characteristics of TBD obtained during mathematical modeling was carried out. Based on the research results, the laws for regulating the output voltage of TBD were established. The TBD effective control range with normal permissible limits of odd harmonics have been determined. The conducted research will make it possible to implement the device control system.

Keywords
ore mining enterprises; power supply systems; dynamic load; voltage fluctuations; thyristor booster device; laws of regulation

Funding
The research was conducted with the support of a Russian Science Foundation grant N 24-29-00872, https://rscf.ru/en/project/24-29-00872/.

Received: 11.04.2024 ***Accepted: 07.11.2024*** ***Online: 17.01.2025*** ***Published: 25.04.2025***

Introduction

The mining industry plays an important role in the Russian economy [1]. The strategy of the Russian Federation mineral resource base development until 2035* includes the development of advanced technologies for mining, transporting and processing minerals, and building new infrastructure elements. The solution to these problems is associated with a continuous increase in the capacity of power plants and the consumption of electrical energy.

The power supply of ore mining enterprises is characterized by the consumers' territorial dispersion [2], the continuous advancement of the mining front and the displacement of electric energy consumers [3, 4]. The connection of high-power consumers with abruptly variable operating mode

* Decree of the Russian Federation Government, dated 22 December 2018, N 2914-r "The strategy of the Russian Federation mineral resource base development until 2035".

(for example, megawatt mining excavators) causes voltage fluctuations which exceed permissible values in the electrical network that negatively affects other loads [5]. Thus, a malfunction in the operation of powerful elevator machines, autogenous tumbling mills and other mining loads sensitive to voltage fluctuations leads to a shutdown of the production process, accidents, etc. Therefore, the issues of developing technical solutions for high-speed devices that provide voltage variations reduction in the electrical grid of ore mining enterprises are essential.

The facilities to reduce voltage fluctuations include soft-start devices, static reactive power sources, longitudinal compensation units, twin reactors, etc. [6, 7]. It is known that the inrush current of an electric motor can exceed the rated current eight times, causing mechanical and electromagnetic shock loads on both the electric drive and the actuators [8, 9]. Soft-start devices can ensure a smooth load increase [10]. However, it is possible that the soft starters and electric motor overheating is critical with drive frequent starts and shutdowns.

Siemens Industry Inc. produces active input frequency converters (AFE – Active front end) based on IGBT transistors for dragline operation (a monobucket excavator widely used in the mining industry) [11]. Despite the fact that AFE are more resistant to grid insurges (voltage sags, fluctuations) even when operating in inverting modes, this reliability depends on the dynamic response of the rectifier control circuit [12, 13].

A distribution static compensator (D-STATCOM) [14-16] based on a voltage inverter with controlled IGBT transistors can be used to eliminate voltage fluctuations and sags. The D-STATCOM compares the shape of the linear and reference signals that provides the correct measure of compensation for a reactive power delay or advance [17]. However, IGBT transistors have a lower overload capacity compared to thyristors, so it is more appropriate to use high-speed thyristor devices in a 6-10 kV electrical grid.

A new type of mine flameproof stabilizing transformer has been developed [18] to reduce voltage fluctuations in mine power supply systems. The compensating voltage is applied to the electrical grid voltage through a compensating transformer connected in series with the power supply line. Thus, the deviation of the electrical grid voltage amplitude is restored in real time.

The Energy Equipment Company has proposed a dynamic voltage compensator (DVC), a device with double voltage conversion [19-21] and individual phase control. The DVC is built based on controlled rectifiers, through which voltage is transmitted to capacitors [22, 23]. DVC output terminals are connected to the load via an inverter unit with IGBT modules and a booster transformer with secondary winding that induces EMF to compensate voltage sags [24, 25].

An uninterruptible power system using renewable energy sources [26] and a multi-stage device for automatic switching over to a reserve source [27] is known. However, even if the power source of a mining enterprise is a sufficiently powerful power plant, additional generators are needed to maintain the required short circuit level, which increases operating costs.

A two-transformer substation with a common dual-band controlled voltage regulator [28] can be distinguished among the approaches and devices for reducing voltage fluctuations.

The devices under consideration allow to reduce voltage fluctuations. However, their significant disadvantages are the high cost and control schemes complexity. As fluctuations relate to voltage changes lasting from half a period to several seconds, it is necessary for the device to respond quickly to voltage changes for subsequent regulation. In existing electrical grids, operational voltage regulation is performed using an electromechanical on-load tap changing device (OLTC) [29, 30]. The OLTC taps switching time is about 10 s, and the device does not have time to respond to voltage fluctuations.

The authors have developed a high-speed thyristor booster device (TBD) [31], which implements the function of longitudinal regulation that allows using a voltage boost to compensate for voltage variations on the consumer's buses. The relevance of the work is due to the need to find effective and low-cost measures to improve the power supply quality of ore mining industry facilities.

The research purpose is to determine the TBD regulation laws, which allow to effectively reduce voltage fluctuations due to dynamic load in the power supply systems of ore mining enterprises.

Methods

To conduct the research, it is necessary to develop simulation math and computer models of the electrical grid with TBD and dynamic load, that allow to obtain TBD adjustment characteristics for various modes of operation of the device and load parameters. Schematic circuit diagram and equivalent circuit of the developed TBD are shown in Fig.1.

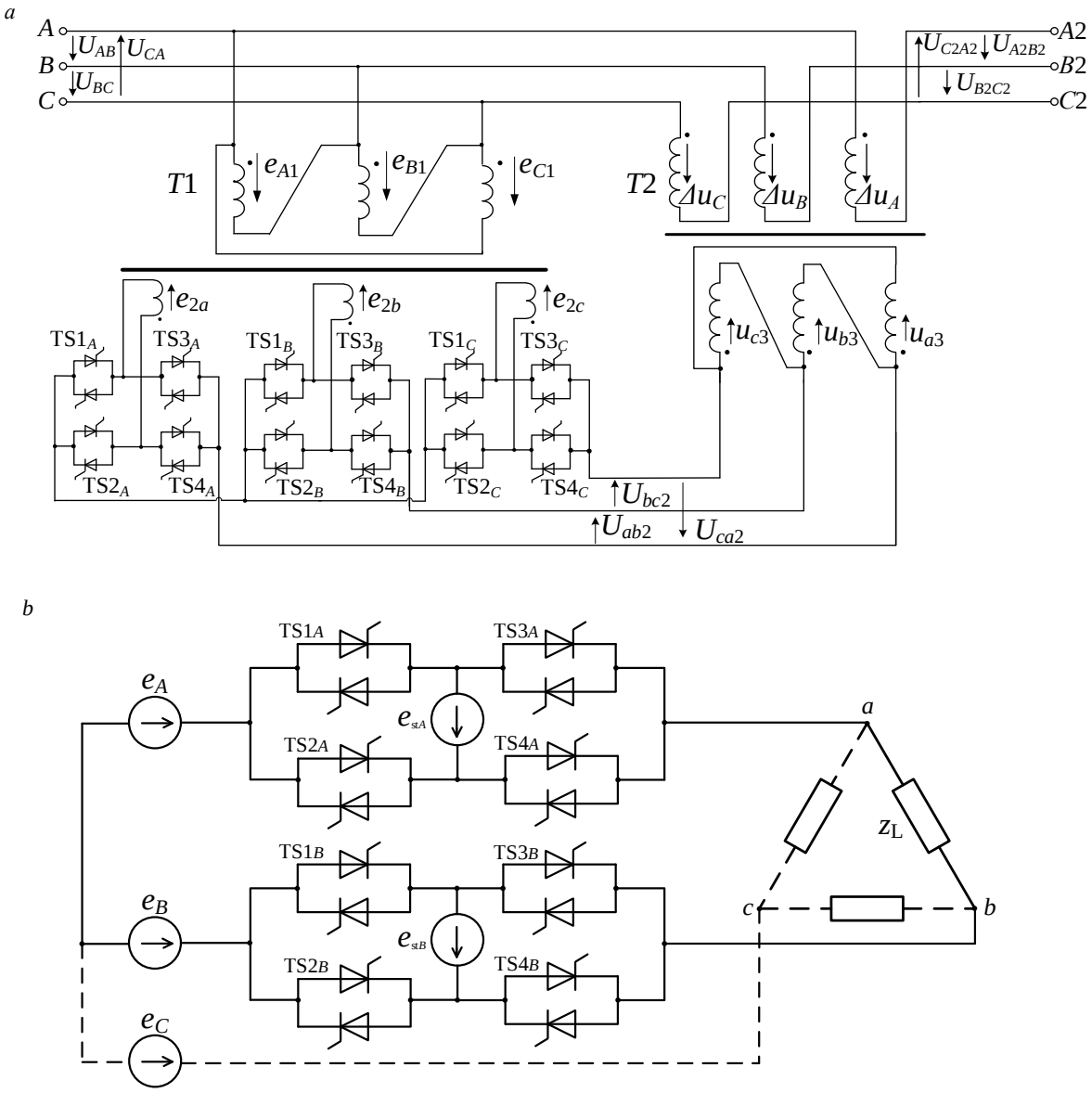

Fig.1. Thyristor booster device:
a – schematic circuit diagram; *b* – equivalent circuit

*T*1, *T*2 – shunt and series transformers;
TS1-TS4 – phase *A*, *B* and *C* thyristor switch modules

The TBD includes a three-phase thyristor switch, three-phase shunt *T*1 and series *T*2 transformers. Each phase of the thyristor switch is a bridge converter with two-direction switches TS1-TS4 in each branch (Fig.1, *a*). The TBD operation principle is based on the introduction of a boost voltage when the device output voltage amplitude changes relative to the input voltage.

32 control stages are provided for the three main TBD operation modes (1 – output voltage increase; 2 – basic mode (without voltage boost); 3 – output voltage reduction): 16 steps correspond to mode 1 (0-15 steps); 16 steps correspond to mode 3 (17-32 steps); control stage 16 corresponds to basic mode 2. Each stage corresponds to definite values of thyristor control angles α_1 and α_2. The required block of counter-parallel thyristors is opened in each phase depending on the set mode – TS1 and TS4 for mode 1, TS2 and TS3 for mode 3. The forward conductance mode (basic) corresponds to the opening of counter-parallel thyristors blocks TS2 and TS4. The time of one TBD switching is about 20 ms, the maximum switching time of all 32 control stages is 1 s.

EMF of control stage e_{st} is added in mode 1, when it is necessary to increase the voltage level on the load buses:

$$U_L = U_g + e_{st},$$

where U_L and U_g are the load and electrical grid RMS voltage.

EMF of control stage e_{st} excluded from the current circuit in mode 2 (basic).

In mode 3, if the voltage level on the load needs to be reduced, the following equation is true:

$$U_L = U_g - e_{st}.$$

Two-zone control is provided: the conversion from mode 1 to mode 2 is carried out by increasing the thyristors control angle α_1 from 0 to 180° with a constant value of the control angle α_2 = 180°, and then decreasing α_2 from 180 to 0° with a constant α_1 = 180°. The same alternating two-zone control is used for a smooth conversion from mode 3 to mode 2.

The TBD control system includes active adaptive algorithms that allow the device to operate in automatic mode. TBD thyristors are controlled in a phase-pulse method, ensuring the accuracy and efficiency of voltage regulation [32]. The current sensors application is not required, that preserve the TBD control properties while responding promptly to load currents changes.

The line voltage (there is no neutral wire) is regulated in 6-10 kV electrical grid, using the TBD. The TBD operation principle is considered using the example of line voltage regulation U_{AB}: $TS1_A$, $TS4_A$, $TS1_B$, $TS4_B$ are activate in mode 1; $TS2_A$, $TS4_A$, $TS2_B$, $TS4_B$ – in mode 2; $TS2_A$, $TS3_A$, $TS2_B$, $TS3_B$ – in mode 3.

The advantages of TBD over thyristor regulators [33, 34] are a reduced number of thyristor switch modules and reduced transformer power (that increases the device reliability and safety), as well as less distortion of the output voltage curve.

Math and computer simulation of TBD increasing and decreasing voltage modes, taking into account the load parameters, enable to determine regulation laws which will form the basis of the device control system in the electrical grid.

Math simulation of TBD operation modes. The laws of load voltage change (phase and linear) when TBD switching from mode 1 or 3 to basic mode 2 by alternating changing the thyristor control angles α_1 (in the intervals of the positive power direction) and α_2 (in the intervals of the negative power direction) are described in detail in [35]. An example of diagrams of voltage changes is shown in Fig.2 when the TBD is switched from mode 1 to mode 2 by alternating changing the angles α_1 (Fig.2, *a*) and α_2 (Fig.2, *b*).

Due to TBD operation analysis based on the diagrams, it is possible to describe mathematically the processes of TBD output voltage regulation and determine the main parameters, that affect the behavior of the device adjustment characteristics, i.e., it is possible to identify the dependence of RMS output voltage on the control voltage U_{cont} at different load angles.

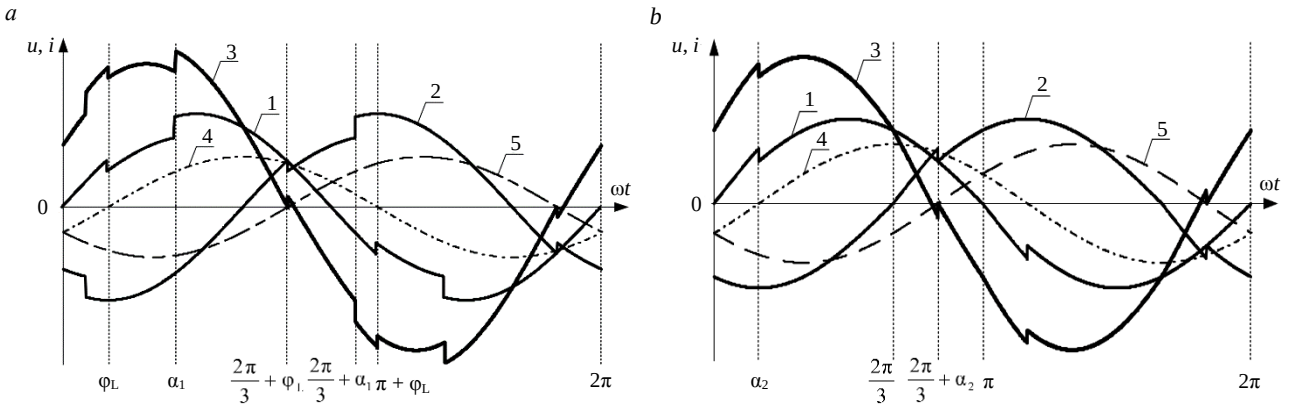

1 – u_A; 2 – u_B; 3 – u_{AB}; 4 – i_A; 5 – i_B

Fig.2. Load instantaneous phase and line voltage in TBD mode 1 on change α_1 (*a*) and α_2 (*b*)

Math equations describing the adjustment characteristics were obtained using the method of alignment boundary values [36, 37]. The method allows to describe processes in piecewise-linear systems. The integration constants are determined by conjugating equations at the boundaries of adjacent intervals in each time interval, using the first and second switching laws (conditions for continuity of current in inductive elements and voltage across capacitors) at the switching moments. The Accepted assumptions are: the resistance of the magnetic circuit and winding *T*2 is not taken into account (Fig.1, *a*); the load is active-inductive, linear. The amplitude of the electrical grid phase voltage is taken as the basic value.

Instantaneous values of phase voltages on the load side are obtained based on the analysis of TBD modes 1 and 3, according to the diagrams. The instantaneous values of the line voltage of the load, which connected between *A* and *B* phases, are determined by the formula

$$u_l^* = u_{AL}^* - u_{BL}^*, \tag{1}$$

where u_{AL}^*, u_{BL}^* are the load instantaneous voltages on phase *A* and *B*, a.u.

The RMS load voltage are calculated using the formula

$$U_{\text{RMS}}^* = \sqrt{\frac{1}{\pi}\int_0^{\pi}\left(U_l^*\right)^2 d\theta}, \tag{2}$$

where U_l^* is a load line voltage, a.u.

The conversion of TBD from modes 1 and 3 to mode 2 in the effective variation intervals α_1 and α_2 is considered. Effective intervals are intervals that provide a significant change in the shape and amplitude of the voltage.

TBD mode 1 in the range of increasing α_1 from 0 to 180 ° while α_2 = 180 ° = const. It can be seen from the diagram (Fig.2, *a*) that the change in the line load voltage during the half-cycle can be divided into four ranges: $\varphi_L - \alpha_1$; $\alpha_1 - \frac{2\pi}{3} + \varphi_L$; $\frac{2\pi}{3} + \varphi_L - \frac{2\pi}{3} + \alpha_1$; $\frac{2\pi}{3} + \alpha_1 - \pi + \varphi_L$. Instantaneous values of phase and line voltages on the load side are obtained for all ranges (1).

Instantaneous value of the line voltage:

• for the first range

$$U_{l1}^* = U_{AL}^* - U_{BL}^* = \sin\theta - \left(1 + k_{\text{st}}\right)\sin\left(\theta - \frac{2\pi}{3}\right);$$

• for the second range

$$U_{l2}^{*}=U_{AL}^{*}-U_{BL}^{*}=\left(1+k_{st}\right)\sin\theta-\left(1+k_{st}\right)\sin\left(\theta-\frac{2\pi}{3}\right);$$

• for the third range

$$U_{l3}^{*}=U_{AL}^{*}-U_{BL}^{*}=\left(1+k_{st}\right)\sin\theta-\sin\left(\theta-\frac{2\pi}{3}\right);$$

• for the fourth range

$$U_{l4}^{*}=U_{AL}^{*}-U_{BL}^{*}=\left(1+k_{st}\right)\sin\theta-\left(1+k_{st}\right)\sin\left(\theta-\frac{2\pi}{3}\right).$$

The law of regulation of RMS output voltage according to the equation (2):

$$U_{RMS}^{*}=\sqrt{\frac{\left(\sin\left(2\alpha_1\right)-\sin\left(2\varphi_L\right)+2\left(\varphi_L-\alpha_1\right)\right)\left(3k_{st}+2k_{st}^{2}\right)+3\pi\left(1+k_{st}^{2}\right)}{2\pi}}. \quad (3)$$

Similarly, equations are obtained for TBD mode 1 in the range of effective variation α_2; for mode 3 in the ranges of effective variation α_1 and α_2.

TBD mode 1 in the range of reduction α_2 from 180 to 0 ° while α_1 = 180 ° = const. Changes of the load line voltage (Fig.2, *b*) during the half-cycle are divided into four ranges: $0-\alpha_2$; $\alpha_2-\frac{2\pi}{3}$; $\frac{2\pi}{3}-\frac{2\pi}{3}+\alpha_2$; $\frac{2\pi}{3}+\alpha_2-\pi$.

Instantaneous value of the line voltage:

• for the first range

$$U_{l1}^{*}=U_{AL}^{*}-U_{BL}^{*}=\left(1+k_{st}\right)\sin\theta-\sin\left(\theta-\frac{2\pi}{3}\right);$$

• for the second range

$$U_{l2}^{*}=U_{AL}^{*}-U_{BL}^{*}=\sin\theta-\sin\left(\theta-\frac{2\pi}{3}\right);$$

• for the third range

$$U_{l3}^{*}=U_{AL}^{*}-U_{BL}^{*}=\sin\theta-\left(1+k_{st}\right)\sin\left(\theta-\frac{2\pi}{3}\right);$$

• for the fourth range

$$U_{l4}^{*}=U_{AL}^{*}-U_{BL}^{*}=\sin\theta-\sin\left(\theta-\frac{2\pi}{3}\right).$$

RMS load voltage

$$U_{RMS}^{*}=\sqrt{\frac{\left(2\alpha_1-\sin\left(2\alpha_2\right)\right)\left(3k_{st}+k_{st}^{2}\right)+3\pi}{2\pi}}. \quad (4)$$

TBD mode 3 in the range of reduction α_1 from 180 to 0 ° while α_2 = 180 ° = const. Changes of the load line voltage are divided into four ranges during the half-cycle, according to [35]: from 0 to α_1; from α_1 to $\frac{2\pi}{3}$; from $\frac{2\pi}{3}$ to $\frac{2\pi}{3}+\alpha_1$; from $\frac{2\pi}{3}+\alpha_1$ to π.

Instantaneous value of the line voltage:

• for the first range

$$U_{l1}^{*} = U_{AL}^{*} - U_{BL}^{*} = \sin\theta - (1-k_{st})\sin\theta\left(\theta - \frac{2\pi}{3}\right);$$

• for the second range

$$U_{l2}^{*} = U_{AL}^{*} - U_{BL}^{*} = (1-k_{st})\sin\theta - (1-k_{st})\sin\left(\theta - \frac{2\pi}{3}\right);$$

• for the third range

$$U_{l3}^{*} = U_{AL}^{*} - U_{BL}^{*} = (1-k_{st})\sin\theta - \sin\left(\theta - \frac{2\pi}{3}\right);$$

• for the fourth range

$$U_{l4}^{*} = U_{AL}^{*} - U_{BL}^{*} = (1-k_{st})\sin\theta - (1-k_{st})\sin\left(\theta - \frac{2\pi}{3}\right).$$

RMS load voltage

$$U_{RMS}^{*} = \sqrt{\frac{\left(2\alpha_1 - \sin(2\alpha_2)\right)\left(3k_{st} - 2k_{st}^2\right) + 3\pi(1-k_{st})^2}{2\pi}}. \quad (5)$$

TBD mode 3 in the range of reduction α_2 from 180 to 0 ° while α_1 = 180 ° = const. Changes of the load line voltage are divided into ranges during the half-cycle, according to [35]: from φ_L to α_2; from α_2 to $\frac{2\pi}{3} + \varphi_L$; from $\frac{2\pi}{3} + \varphi_L$ to $\frac{2\pi}{3} + \alpha_2$; from $\frac{2\pi}{3} + \alpha_2$ to $\pi + \varphi_L$.

Instantaneous value of the line voltage:

• for the first range

$$U_{l1}^{*} = U_{AL}^{*} - U_{BL}^{*} = (1-k_{st})\sin\theta - \sin\theta\left(\theta - \frac{2\pi}{3}\right);$$

• for the second range

$$U_{l2}^{*} = U_{AL}^{*} - U_{BL}^{*} = \sin\theta - \sin\left(\theta - \frac{2\pi}{3}\right);$$

• for the third range

$$U_{l3}^{*} = U_{AL}^{*} - U_{BL}^{*} = \sin\theta - (1-k_{st})\sin\left(\theta - \frac{2\pi}{3}\right);$$

• for the fourth range

$$U_{l4}^{*} = U_{AL}^{*} - U_{BL}^{*} = \sin\theta - \sin\left(\theta - \frac{2\pi}{3}\right).$$

RMS load voltage

$$U_{RMS}^{*} = \sqrt{\frac{\left(\sin(2\varphi_L) - \sin(2\alpha_2) + 2(\alpha_2 - \varphi_L)\right)\left(k_{st}^2 - 3k_{st}\right) + 3\pi}{2\pi}}. \quad (6)$$

The analysis of the control laws (3)-(6) indicates the influence of the load phase angle φ_L, the control angles α_1 and α_2 and the depth of the control stage k_{st} on the TBD RMS output voltage.

The control angles α_1 and α_2 depend on the control voltage U_{cont} with range from 0 to 2. Thus, the TBD RMS output voltage also depends on the U_{cont}. The amplitude of the reference sawtooth voltage of the phase-pulse control circuit is taken as the base value. At the same time, thyristor switching pulses are formed at the moments when the control voltage and the reference voltage are equal.

The TBD adjustment characteristics in modes 1 and 3 at φ_L = 0°, 30° and 60° are determined according to equations (3)-(6). The graphs are constructed at the depth of the control stage k_{st} = 0.1 and electrical grid voltage U = 6,000 V.

Computer simulation. A computer simulation model of a 6-10 kV electrical grid section was developed in the Matlab (Simulink) simulation environment, and it enables to verify and refine the TBD adjustment characteristics obtained during the math simulation. Both existing elements of the SimPowerSystems library and masked blocks missing from the standard library are used in the model. The high calculation accuracy and high performance of the TBD model are due to a two-step approach to solving differential equations (the ode23tb method was used for the solution). The Runge – Kutta method is used at the first stage, and the method based on the second – order inverse differentiation formulas is used at the second stage.

Rated load power S_L = 630 kV·A. The power regulated in the developed TBD model when changing the angle of shift of the main harmonic of the output voltage relative to the input voltage in the range of ± 5° and regulation the output voltage in the range of ±14 % is ~20 % of the load power. The passport values of device power elements (transformers, thyristors, etc.) are entered in the block of parameters of the TBD model elements to simulate the operation of the device in real conditions.

Fig.3 shows a block diagram of the electrical grid section computer simulation model with the TBD.

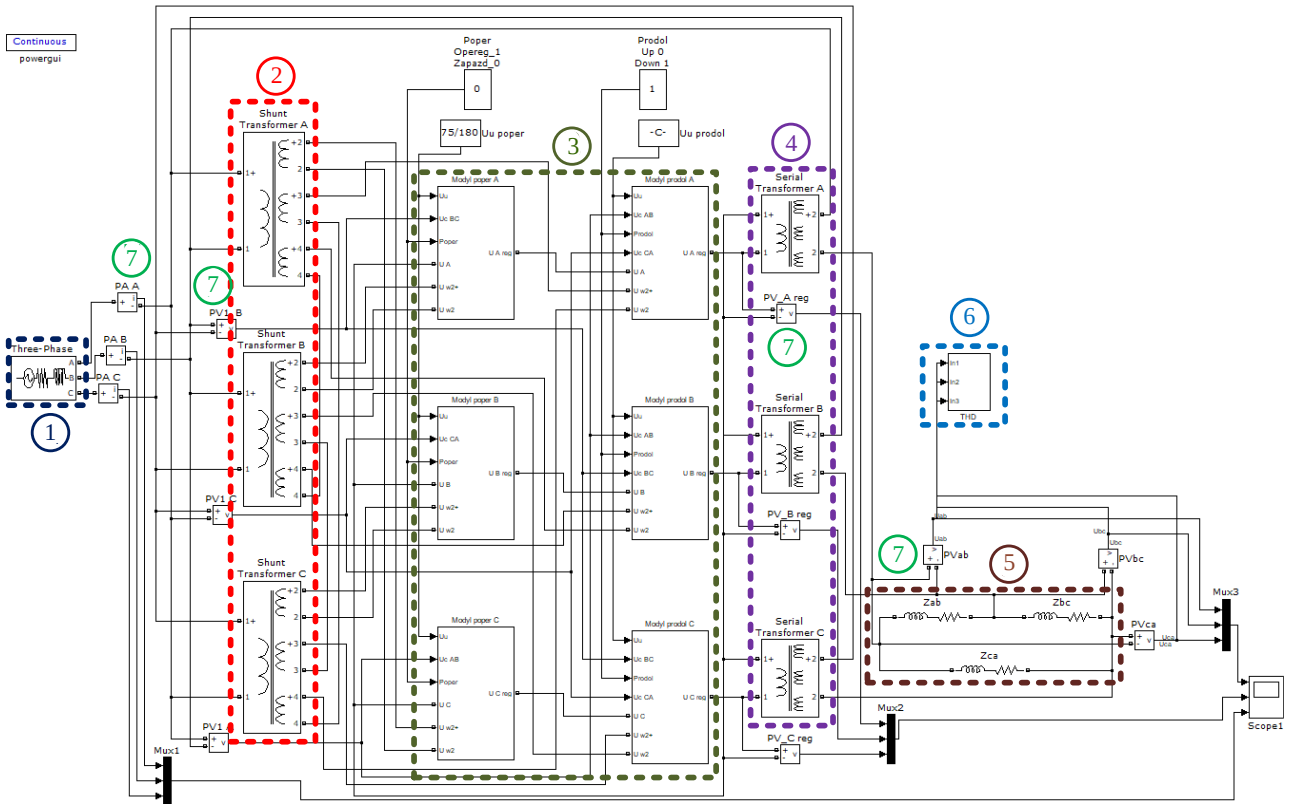

Fig.3. Simulation model of electrical grid section with TBD

1 – three-phase power supply block (U = 6 kV; f = 50 Hz; R = 0.231 Ohm; L = 0.00368 H);
2 – shunt transformer block (S = 106 kV·A); 3 – thyristor switches module;
4 – series transformers block (S = 3×28 kV·A); 5 – electrical load block (U = 6 kV; S = 630 kV·A);
6 – higher harmonics measuring block (Fourier transform); 7 – measuring instruments

The computer simulation model includes seven main blocks: a power source (three-phase voltage source); three single-phase shunt transformers; three TBD single-phase longitudinal regulation modules; three single-phase series transformers; three-phase electric load; measuring instruments (oscilloscope, ammeters and voltmeters); a three-phase measuring block of the TBD output line voltage parameters.

Voltages that are either in phase with or out of phase with the corresponding phase voltages, are generated at the output terminal of TBD. Mode 1 is implemented when the specified voltages are in phase, and mode 3 is implemented, if the specified voltages are out of phase. A three-channel oscilloscope is used for visual control of input currents, output voltages and EMF introduced by TBD into the electrical grid. The TBD adjustment characteristics (RMS voltages) in modes 1 and 3 for different load angles are constructed using the computer simulation model.

Discussion of results

The research of the TBD adjustment characteristics obtained on the basis of the math and computer simulation under different device operating modes and load parameters allowed to determine TBD regulation laws for the control system when it is integrated into the electrical grid. Examples of TBD adjustment characteristics in mode 1 as part of the electrical grid obtained by math and computer simulation are shown in Fig.4.

An analysis of the computer simulation graphs showed that the boost voltage is 551 V (9.4 %) in the voltage increasing mode. The amplitude of the RMS output voltage is reduced by 590 V (i.e. by 10 %) in the output voltage reduction mode. The load angle influences the behavior of the TBD adjustment characteristics in both modes.

Effective change of the thyristor control angles α_1 and α_2 to change (Fig.4) the load voltage is in following ranges:

$$\varphi_L \le \alpha_1 < 180°;$$

$$0° < \alpha_2 \le \varphi_L.$$

A comparison of the math and computer simulation TBD adjustment characteristics showed a coincidence of their character and shape (Fig.5). The computer simulation dependencies are lower than math simulation dependencies. It is explained by taking into account the voltage drops in the power supply line and on the TBD power elements, as well as taking into account the switching ranges where boost voltage value is zero. The largest deviation of the characteristics δ is observed for mode 1 at φ = 60° and is 3.5 %.

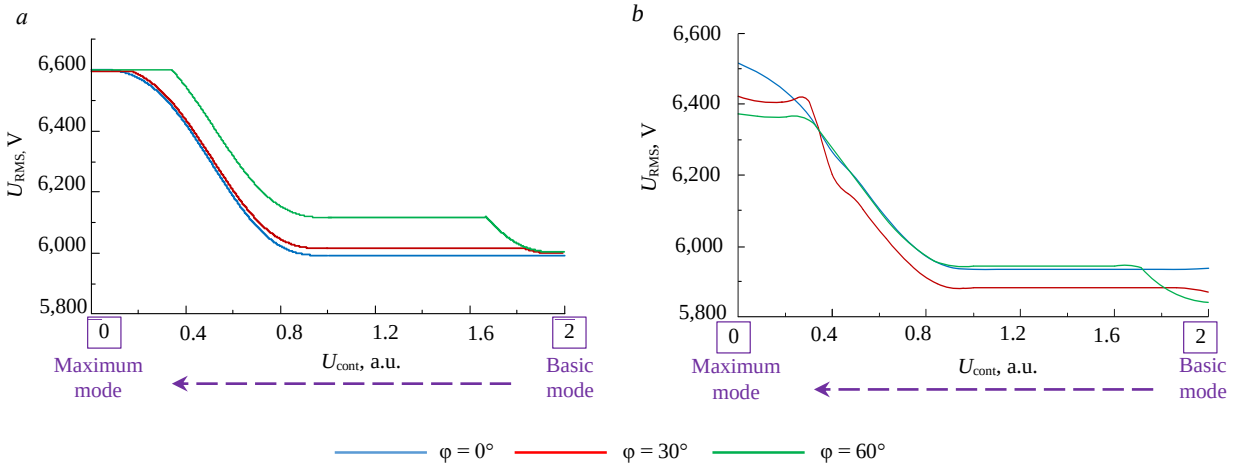

Fig.4. Adjustment characteristics of TBD in mode 1 as electrical grid part, obtained by math (*a*) and computer simulation (*b*)

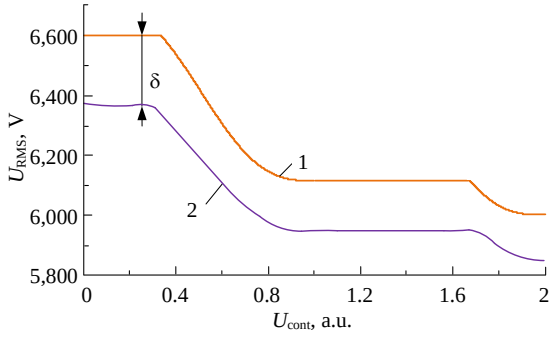

Fig.5. Adjustment characteristics for the voltage boost mode at φ = 60°:
1 – math simulation;
2 – computer simulation

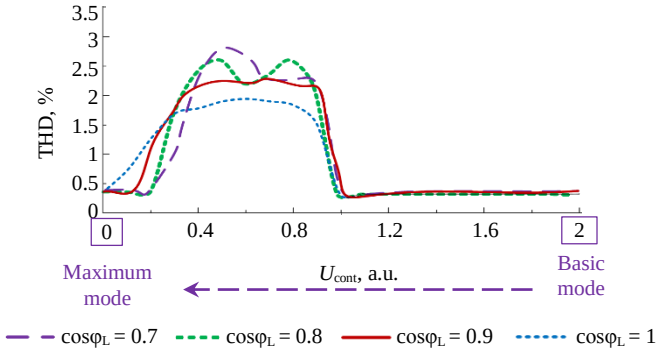

Fig.6. Graph of the total harmonic distortion of the TBD output voltage dependence in the voltage boost mode

Odd harmonics are generated in the electrical grid with the phase-pulse control method for TBD thyristors. The values of these harmonics do not exceed the allowable limits. Computer simulation allowed to obtain graphs of the change in the total harmonic distortion THD of the TBD output voltage in modes 1 and 3. An example of the TBD output voltage THD graph in mode 1 at different load power factors ($\cos\varphi_L$) is shown in Fig.6.

It can be seen from Fig.6 that TBD output voltage THD is inversely proportional to the load power factor, i.e. THD increases with a $\cos\varphi_L$ reduction. THD takes the lowest value at active load ($\cos\varphi_L = 1$).

Conclusion

As a result of the conducted research, the TBD regulation laws that allow to reduce voltage fluctuations by adding a voltage boost to the electrical grid have been obtained. The regulation laws represent the dependences of the TBD RMS output voltage on the load phase angle φ_L, the depth of the voltage step regulation k_{st}, control angles α_1 and α_2. The required stage of regulation U_{cont} is automatically selected depending on the magnitude of the voltage variation.

The Equations of the TBD regulation laws allowed us to obtain the TBD adjustment characteristics. Depending on the control voltage, the limits of RMS output voltage regulation were ±10 %. The TBD thyristors phase-pulse control method ensures a smooth change in the output voltage. At the same time sine voltage total harmonic distortion coefficient over the entire range of effective control zones is within the range of acceptable values set by State standard 32144-2013.

The introduction of the TBD into the electrical grid of the ore mining enterprises will improve the reliability of power supply and increase the capacity of power transmission lines.

REFERENCES

1. Andreev D.V. Role of the mining industry in the economy of the country. *Moscow Economic Journal*. 2020. N 12, p. 175-185 (in Russian). DOI: 10.24411/2413-046X-2020-10870
2. Nazarychev A.N., Ustinov D.A., Pelenev D.N., Babyr K.V. Studying the Single-Phase Earth Fault Protection Based on Measuring the Negative-Sequence Current. *Elektrichestvo*. 2024. N 2, p. 31-41 (in Russian). DOI: 10.24160/0013-5380-2024-2-31-41
3. Skamyin A.N., Dobush V.S., Jopri M.H. Determination of the grid impedance in power consumption modes with harmonics. *Journal of Mining Institute*. 2023. Vol. 261. p. 443-454. DOI: 10.31897/PMI.2023.25
4. Abdallah W.J., Hashmi K., Faiz M.T. et al. A Novel Control Method for Active Power Sharing in Renewable-Energy-Based Micro Distribution Networks. *Sustainability*. 2023. Vol. 15. Iss. 2. N 1579. DOI: 10.3390/su15021579
5. Yaghoobi J., Abdullah A., Kumar D. et al. Power Quality Issues of Distorted and Weak Distribution Networks in Mining Industry: A Review. *IEEE Access*. 2019. Vol. 7, p. 162500-162518. DOI: 10.1109/ACCESS.2019.2950911
6. Chun-Hsi Su, Yian-Ting Chen. A Remote-Controllable Variable Frequency Drive. Sixth International Symposium on Computer, Consumer and Control (IS3C), 30 June – 3 July 2023, Taichung, Taiwan. IEEE, 2023, p. 292-294. DOI: 10.1109/IS3C57901.2023.00084

7. *Tokarev I.S.* Development of parameters for an industry-specific methodology for calculating the electric energy storage system for gas industry facilities. *Journal of Mining Institute*. 2025. Vol. 272, p. 171-180.

8. Sinvula R., Abo-Al-Ez K.M., Kahn M.T. Harmonic Source Detection for an Industrial Mining Network with Hybrid Wind and Solar Energy Systems. Control and Operation of Grid-Connected Wind Energy Systems. Cham: Springer, 2021, p. 153-192. DOI: 10.1007/978-3-030-64336-2_7

9. Le Van Tung. The structure and control algorithms for conveyors electric drive to increasing the energy efficiency of their operation in mining enterprises: Avtoref. dis. … kand. tekhn. nauk. SPb: Sankt-Peterburgskii gornyi universitet, 2021, p. 20.

10. Volotkovskaya N.S., Semenov A.S., Fedorov O.V. Energy efficiency and energy saving in the power supply systems of mining enterprises. *Vestnik Gomelskogo gosudarstvennogo tekhnicheskogo universiteta imeni P.O.Sukhogo*. 2019. N 3, p. 52-62.

11. Morán L., Espinoza J., Burgos R. Voltage regulation in mine power distribution systems: Problems and solutions. IEEE Industry Application Society Annual Meeting, 5-9 October 2014, Vancouver, BC, Canada. IEEE, 2014, p. 7. DOI: 10.1109/IAS.2014.6978453

12. Sukanth T., Jayanthu S., Jayalaxmi A. Mitigation of power quality problem in underground mine using different control strategies. IEEE Region 10 Humanitarian Technology Conference (R10-HTC), 21-23 December 2016, Agra, India. IEEE, 2016, p. 4. DOI: 10.1109/R10-HTC.2016.7906798

13. Serebryannikov S.V., Serebryannikov S.S., Kovalchuk V.G. et al. Electromagnetic Parameters of the Ferrite Materials for Electromagnetic Compatibility. Radiation and Scattering of Electromagnetic Waves (RSEMW), 26-30 June 2023, Divnomorskoe, Russia. IEEE, 2023, p. 316-319. DOI: 10.1109/RSEMW58451.2023.10201985

14. Negi P., Pal Y., Leena G. A Review of Various Topologies and Control Schemes of DSTATCOM Implemented on Distribution Systems. *Majlesi Journal of Electrical Engineering*. 2017. Vol. 11. N 1, p. 25-35.

15. Salkuti S.R. An efficient allocation of D-STATCOM and DG with network reconfiguration in distribution networks. *International Journal of Advanced Technology and Engineering Exploration*. 2022. Vol. 9. Iss. 88, p. 299-309. DOI: 10.19101/IJATEE.2021.874812

16. Xuefeng Wang, Li Peng. Dynamic Voltage Equalization Control of D-STATCOM Under Unbalanced Grid Faults in a Low-Voltage Network. *IEEE Transactions on Power Electronics*. 2023. Vol. 38. Iss. 2, p. 2384-2397. DOI: 10.1109/TPEL.2022.3213405

17. Dash S.K., Mishra S., Abdelaziz A.Y. A Critical Analysis of Modeling Aspects of D-STATCOMs for Optimal Reactive Power Compensation in Power Distribution Networks. *Energies*. 2022. Vol. 15. Iss. 19. N 6908. DOI: 10.3390/en15196908

18. Malafeev S.I., Serebrennikov N.A. Increasing energy efficiency of mining excavators through upgrade of electrical equipment and control systems. *Ugol*. 2018. N 10, p. 30-35 (in Russian). DOI: 10.18796/0041-5790-2018-10-30-34

19. Mohite S., Jape V.S., Bankar D.S. Power Quality Problems Mitigation by DVR Using SC Structured Cascaded MPAC. Proceedings of the 1st International Conference on Data Science, Machine Learning and Applications. Springer, 2019. Vol. 601, p. 796-804. DOI: 10.1007/978-981-15-1420-3_86

20. Seershak M., Muhammed Ramees M.K.P. Power Quality Improvement Using ZSI-DVR. International Conference on Futuristic Technologies in Control Systems & Renewable Energy (ICFCR), 21-22 July 2022, Malappuram, India. IEEE, 2022, p. 6. DOI: 10.1109/ICFCR54831.2022.9893660

21. Jape V.S., Kulkarni H.H., Lokhande N.M., Ubale D. Observations and Analysis of Power Quality Indices Using Custom Power Devices in Power Distribution Network. Information and Communication Technology for Competitive Strategies (ICTCS 2021), 17-18 December 2021, Rajasthan, India. Springer, 2021. Vol. 401, p. 121-130. DOI: 10.1007/978-981-19-0098-3_13

22. Amarendra A., Srinivas L.R., Rao R.S. Contingency Analysis in Power System- Using UPFC and DVR Devices with RDOA. *Technology and Economics of Smart Grids and Sustainable Energy*. 2022. Vol. 7. Iss. 1. N 17. DOI: 10.1007/s40866-022-00129-y

23. Kandil T., Ahmed M.A. Control and Operation of Dynamic Voltage Restorer With Online Regulated DC-Link Capacitor in Microgrid System. *Canadian Journal of Electrical and Computer Engineering*. 2020. Vol. 43. Iss. 4, p. 331-341. DOI: 10.1109/CJECE.2020.3002855

24. Bakhteev K.R. Improving the efficiency of centralized and autonomous power supply systems through the integrated use of electrochemical energy storage devices, low-power generation, and forced excitation of synchronous machines: Avtoref. dis. … kand. tekhn. nauk. Kazan: Kazanskii gosudarstvennyi energeticheskii universitet, 2019, p. 24.

25. Yerbayev Y., Artyukhov I., Zemtsov A. et al. Negative Impact Mitigation on the Power Supply System of a Fans Group with Frequency-Variable Drive. *Energies*. 2022. Vol. 15. Iss. 23. N 8858. DOI: 10.3390/en15238858

26. Jahromi M.G., Mirzaeva G., Mitchell S.D., Gay D. Powering Mobile Mining Machines: DC Versus AC Power. *IEEE Industry Applications Magazine*. 2016. Vol. 22. Iss. 5, p. 63-72. DOI: 10.1109/MIAS.2015.2459082

27. Abramovich B.N. Uninterruptible power supply system for mining industry enterprises. *Journal of Mining Institute.* 2018. Vol. 229, p. 31-40. DOI: 10.25515/PMI.2018.1.31

28. Tabarov B.D., Solovyev V.A., Ivanov V.I. A Two-Transformer Substation with a Common Dual-Band Controlled Voltage Regulator. *Elektrichestvo.* 2024. N 4, p. 74-84 (in Russian). DOI: 10.24160/0013-5380-2024-4-74-84

29. Hem P., Heang S., Eam D. et al. Service Restoration in Distribution Systems with a Load Tap Changer. International Electrical Engineering Congress (iEECON), 9-11 March 2022, Khon Kaen, Thailand. IEEE, 2022, p. 4. DOI: 10.1109/iEECON53204.2022.9741590

30. Dyussembekova N., Schütt R., Leiße I., Ralfs B. Decision Process for Identifying Appropriate Devices for Power Transfer between Voltage Levels in Distribution Grids. *Energies*. 2024. Vol. 17. Iss. 9. N 2158. DOI: 10.3390/en17092158

31. Asabin A.A., Sosnina E.N., Kralin A.A., Kriukov E.V., Bedretdinov R.Sh., Gusev D.A. Patent N 2813363 RF. Thyristor voltage booster device of longitudinal voltage control. Publ. 12.02.2024. Bul. N 5 (in Russian).

32. Zhmurov V.P., Stelmakov V.N., Tarasov A.N., Timoshenko A.L., Kazennova I.I. Patent N 2450420 RF. Semiconductor phase shifter. Publ. 10.05.2012. Bul. N 13 (in Russian).

33. Bedretdinov R.Sh., Verkhovskii S.Ya., Sosnina E.N., Kisel D.A., Asabin A.A., Gardin A.I. Patent N 157116 RF. Solid-state phase shifter device. Publ. 20.11.2015. Bul. N 32 (in Russian).

34. Asabin A., Sosnina E., Belyanin I. et al. Control System of the Thyristor Voltage Regulator. 7th International Conference on Control, Decision and Information Technologies (CoDIT), 29 June – 2 July 2020, Prague, Czech Republic. IEEE, 2020, p. 802-806. DOI: 10.1109/CoDIT49905.2020.9263984

35. Kryukov E.V. The use of thyristor booster devices to improve the quality of electric energy in power supply systems: Avtoref. dis. … kand. tekhn. nauk. Nizhnii Novgorod: Nizhegorodskii gosudarstvennyi tekhnicheskii universitet im. R.E.Alekseeva, 2018, p. 18.

36. Belov G.A., Malinin G.V. Vector-matrix method for transients calculating in dc resonant converter of the LCL-T type. *Practical power electronics*. 2020. N 1 (77), p. 28-37 (in Russian).

37. Umarov Sh. Comparative analysis of two methods for modeling valve converter devices. *Universum: engineering science*. 2023. N 11 (116), Part 6, p. 13-18 (in Russian). DOI: 10.32743/UniTech.2023.116.11.16253

Authors: **Elena N. Sosnina,** *Doctor of Engineering Sciences, Professor, sosnyna@yandex.ru, https://orcid.org/0000-0001-6207-9103* (*Nizhny Novgorod State Technical University named after R.E.Alekseev, Nizhny Novgorod, Russia*), **Anatolii A. Asabin,** *Candidate of Engineering Sciences, Associate Professor, https://orcid.org/0009-0000-1505-5918* (*Nizhny Novgorod State Technical University named after R.E.Alekseev, Nizhny Novgorod, Russia*), **Rustam Sh. Bedretdinov,** *Candidate of Engineering Sciences, Associate Professor, https://orcid.org/0000-0003-0767-1096* (*Nizhny Novgorod State Technical University named after R.E.Alekseev, Nizhny Novgorod, Russia*), **Evgenii V. Kryukov,** *Candidate of Engineering Science, Associate Professor, https://orcid.org/0000-0002-9145-2453* (*Nizhny Novgorod State Technical University named after R.E.Alekseev, Nizhny Novgorod, Russia*), **Daniil A. Gusev,** *Junior Researcher, https://orcid.org/0000-0002-2183-6582* (*Nizhny Novgorod State Technical University named after R.E.Alekseev, Nizhny Novgorod, Russia*).

The authors declare no conflict of interests.

ISSN 2411-3336; e-ISSN 2541-9404

JOURNAL OF MINING INSTITUTE

Zapiski Gornogo instituta

Journal homepage: pmi.spmi.ru

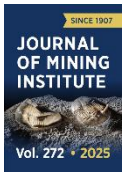

Research article *Energy*

Development of parameters for an industry-specific methodology for calculating the electric energy storage system for gas industry facilities

Ivan S. Tokarev

Empress Catherine II Saint Petersburg Mining University, Saint Petersburg, Russia

***How to cite this article*:** Tokarev I.S. Development of parameters for an industry-specific methodology for calculating the electric energy storage system for gas industry facilities. Journal of Mining Institute. 2025. Vol. 272. N 16516, p. 171-180.

Abstract

The issue of determining the main parameters of electric energy storage systems – power and energy intensity – is being considered, the determination of which is a fundamentally important task when introducing such devices into the power supply systems of enterprises for both technical (technological) and economic reasons. The work analyzes problems that can be solved by installing electricity storage systems at gas industry facilities. An industry-wide methodology has been developed for calculating the parameters of an electricity storage system based on traditional methods and methods aimed at minimizing the standardized cost of electricity with adaptation to the conditions of the gas industry. A distinctive feature of the presented methodology is the ability to determine the power and energy intensity of electricity storage systems when performing several functions. The methodology was tested at a typical gas industry facility – the Yarynskaya compressor station of OOO Gazprom Transgaz Ukhta, a characteristic feature of which is an autonomous power supply system. An example is given of calculating the electricity storage normalized cost using an improved LCOS indicator, which takes into account the effect of changing the fill factor of the electrical load schedule on the amount of gas consumption by a power plant for its own needs. To confirm the economic efficiency of introducing electricity storage systems calculated using the above methodology, calculations of the integral effect, net present value and efficiency index are presented.

Keywords

electricity storage system; autonomous power supply system; electrical load control; hot reserve replacement; standardized cost of electricity; gas industry

Received: 12.06.2024 ***Accepted: 18.07.2024*** ***Online: 26.07.2024*** ***Published: 25.04.2025***

Introduction

One of the main problems of energy supply to autonomous facilities and technological complexes in the gas industry is the autonomous power supply systems technical and economic efficiency insufficient level [1], associated with the need to simultaneously ensure reliability and uninterrupted power supply, stability and electrical energy sources operation efficiency, especially in cases of creating systems for power supply to consumers widely separated from each other or consumers with sharply variable schedule of electrical loads (in accordance with the Concept for the development of energy supply to production facilities of PAO Gazprom for the period up to 2030).

The solution to this problem may be the use of an electrical energy storage system (ESS). The development of electricity storage technologies makes it possible to seriously consider these devices as the main element of power supply systems [2-4]. A distinctive feature of electricity storage systems, which stimulates their widespread implementation, is the ability to perform several functions with one device [5]. Even without taking into account the functional features of the ESS when integrating renewable energy sources (RES) [6-8] the use of these devices in centralized and autonomous systems allows the following:

• reduce the payment for installed capacity by covering load peaks with ESS means;

• reduce capital investments in the creation and operating costs of power plants for own needs by reducing the number of operating units and covering peak loads with ESS;

• improve the regularity of power supply and power quality;

• reduce the costs of ensuring the required level of categorization by eliminating the loaded (rotating) reserve for electrical units and replacing it with ESS means;

• reduce the rapidly changing load on motor drive of power plants negative impact by covering the variable part of the load with ESS means.

When considering the ESS as the main element of the power supply system, it is necessary to calculate its physical parameters: rated energy intensity, rated power, maximum number of complete charge/discharge cycles, dependence characteristics of the maximum number of charge/discharge cycles on their depth, efficiency, self-discharge constant, specific energy intensity, etc. At the same time, given the wide functionality of electricity storage systems, determining its parameters becomes labor-intensive, since it comes down to multi-criteria optimization, when it is necessary to simultaneously consider a set of several incommensurable, contradictory objective functions [9-11].

Despite active work to determine the criteria that have the greatest impact on the ESS parameters choice, currently there is no single established methodology for calculating the ESS main parameters of power and energy intensity. In the works [12-14] the methods were developed based on the power supply systems with renewable energy sources functioning characteristics; in the article [15] the methodology is aimed at calculating the parameters of ESS for use in microgrids. In paper [16] the methodology is based on empirical expressions aimed at determining the energy intensity of an electrical energy storage device for energy recovery of traction rolling stock. In the article [17] the methodology for calculating the optimal parameters of the ESS based on the available power of the technological connection is described, and is supplemented with the maintaining a certain voltage in the busiest network node criteria. In the source [18] it is proposed to calculate the parameters of electricity storage systems using linear filtering, which consists of analyzing the harmonic composition of the load diagrams of generating units and determining those harmonics that are subject to suppression. In the article [19] an alternative method for selecting ESS parameters according to the conditions for limiting the depth of voltage dips is presented.

The use of these methods to solve problems in the gas industry is very difficult, since they either are focused on another industry and are practically not adaptable, or are aimed at solving only one problem, which, in turn, affects the final effect of the implementation of the ESS. Therefore, the purpose of this study is to generalize and formulate a universal methodology for determining the main parameters of the energy saving system for gas industry facilities with an autonomous power supply system [20-22].

Methods

To formulate a methodology for determining the parameters of the ESS, promising tasks for autonomous power supply systems in the gas industry have been formulated – replacing the rotating reserve of a power plant for its own needs and ensuring stable operation or changing the installed capacity of generating units by aligning electrical load schedules.

The ESS implementation will reduce the cost of maintaining the unit in operating condition, which in turn will reduce fuel consumption and increase the service interval. It is also expected to ensure a more uniform loading of electrical units with energy accumulation during the hours of least consumption and energy release during the hours of highest consumption. If necessary, it is possible to reduce the power of the technological connection to the external power system by reducing consumption from it during peak hours [23, 24].

Taking into account the identified tasks and the analysis of already developed methods for calculating the parameters of the ESS, the most suitable are the traditional (classical) method [25] and a methodology aimed at minimizing the standardized cost of electricity [26]. However, they require additional adaptation to the peculiarities of the gas industry.

The traditional calculation method is simple, but does not take into account the economic component of the implementation of such systems; only technical and technological aspects appear in the calculations. According to the adapted traditional methodology, the power of the EES is determined from several components:

• The power required to cover the generation capacity in the event of an emergency shutdown of one of the generators, which is calculated by determining the power of the rotating reserve unit being replaced, equal to the product of the generating unit installed capacity and the load factor (without taking into account derating):

$$P_{\text{ESS}} = P_{\text{unit}} k_{\text{load}}, \quad (1)$$

where P_{unit} – estimated power of the unit being replaced, kW; k_{load} – unit load factor, p.u.

The unit load factor depends on the number of operating units and is determined by internal regulatory documents, for example STO Gazprom 2-6.2-208-2008, STO Gazprom 2-6.2-1028-2015.

• Power required for uniform loading of electrical units. The need to limit the power consumed by the load has technical and organizational conditions related to the number of operating electrical units.

Figure 1, *a* shows the load graph as an example. Let us say, it is the required that the power to supply the load received from electrical units does not exceed the limit value P_{lim}, determined by the number of operating units. The area in which the load exceeds the maximum power marked with red. The ESS is designed to ensure the elimination of this imbalance.

Figure 1, *b* shows the same load graph with the installed ESS. When the load power exceeds the maximum power, the energy storage system switches to the electricity supply (discharge) mode and eliminates the imbalance. In this case, the calculated power of the ESS should correspond to the following inequality:

$$P_{\text{ESS}} \geq P_{\text{max load}} - P_{\text{lim}},$$

where $P_{\text{max load}}$ – maximum load power, kW.

Electricity consumption of the ESS (charging) occurs during periods when the load power does not exceed the maximum – such areas are shown with green in Fig.1, *b*. In this case, the total area of the charge zones must be greater than the area of the discharge zones by η^2 times to ensure energy balance for a given period of time (η is the equivalent efficiency of the ESS elements – matching transformer, filter and inverter, according to GOST R 58092.2.1-2020, GOST R 58092.3.1-2020).

In addition, in order to more accurately determine the estimated power of the ESS, it is necessary to take into account the safety factor established by the requirements of the facility:

$$P_{\text{ESS}} \geq \left| P_{\text{max load}} - P_{\text{lim}} \right| k_{\text{saf}}, \quad (2)$$

where k_{saf} – safety factor, p.u. (determined by regulatory documents); if there are no requirements for stock availability, then $k_{\text{saf}} = 1$.

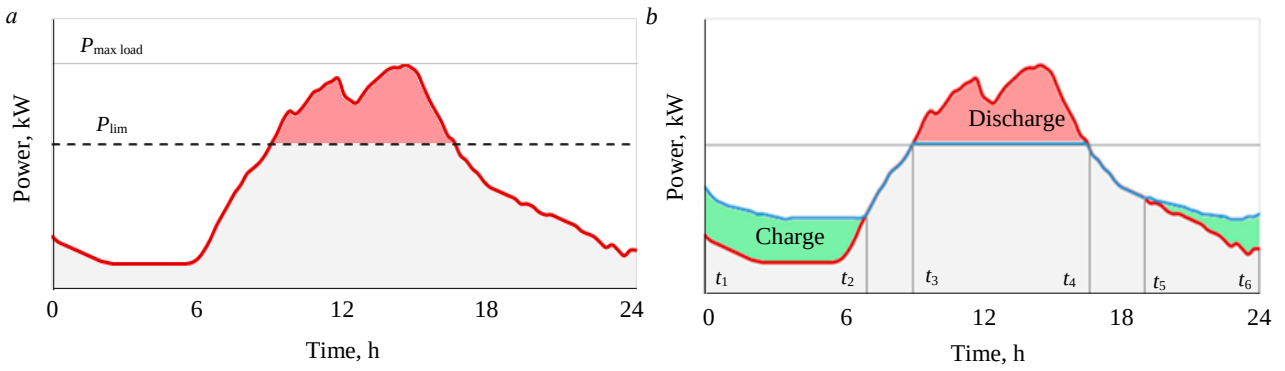

Fig.1. Electrical load (*a*) and load with operating ESS (*b*) daily graph

The ESS energy intensity calculation using an adapted traditional methodology, consisting of several stages, must begin with the calculation of the energy intensity required to start up the backup unit (the time before start-up is 15 min – the maximum possible time):

$$E_{\text{ESS}} = \frac{1}{k_{\text{saf}}} \frac{1}{\eta} \int_0^{15} P_{\text{unit}}(t)dt. \quad (3)$$

Determining the energy intensity required to limit the electrical units load, it should be divided into the following subtasks, solved sequentially:

• exchange energy intensity determination – the amount of energy that the ESS exchanges with the power system in the process of power control when performing the stated functions;

• storage subsystem minimum energy intensity determination.

The exchange energy calculation using the example of the graph (Fig.1, *b*) should begin with the energy produced by the storage subsystem calculation, which is numerically equal to the red zone area divided by the ESS efficiency:

$$E_{\text{ESS prod}} = \int_{t_4}^{t_3} \left(P_{\text{current}}(t) - P_{\text{dem}}(t)\right) dt\, \eta^{-1},$$

where $P_{\text{current}}(t)$ – current power, kW; $P_{\text{dem}}(t)$ – demanded power, kW.

The energy accumulated by the storage subsystem is equal to the area of the green zone multiplied by the efficiency of the energy storage system:

$$E_{\text{ESS acc}} = \int_{t_1}^{t_2} \left(P_{\text{dem}}(t) - P_{\text{current}}(t)\right) dt\, \eta + \int_{t_6}^{t_5} \left(P_{\text{dem}}(t) - P_{\text{current}}(t)\right) dt\, \eta.$$

In the considered daily time interval, the ESS produces the same amount of energy as it accumulates ($E_{\text{ESS prod}} = E_{\text{ESS acc}}$). However, various options for the configuration of the load schedule and, accordingly, the ESS charge/discharge schedule are possible, when the power output modes or consumption in the period under consideration alternate – one mode is replaced by another for a short time [27, 28]. In this case, it is necessary to take an individual approach to analyzing the load schedule and calculating energy intensity, based on the above approach.

Rules for determining exchangeable energy intensity:

• If in order to achieve the demanded $P(t)$ dependence it is necessary to output some E_{dem} (determined by integration), the accumulation subsystem should be able to output the value E_{dem}/η (a larger value).

• If to achieve the demanded $P(t)$ dependence it is necessary to consume some E_{dem}, the storage subsystem must be able to consume a value of $E_{\text{dem}}\eta$ (smaller value).

To determine the minimum energy intensity of the storage subsystem, the following data is required: the required exchange energy intensity of the storage subsystem, taking into account losses on the E_{ex} elements; required service life (years) of the battery or required service life number of charge/discharge cycles [29]; parameters of the batteries used (number of available cycles on the depth of discharge dependence) [30].

Based on the specified data, the of the service life in cycles on the energy storage device depth of discharge dependence is constructed. Using interpolation and extrapolation methods and having knowledge of the approximate number of charge/discharge cycles, it is possible to determine the ESS depth of discharge limiting value (DoD, p.u.). After determining the estimated discharge depth, the final energy capacity of the ESS is calculated. Next, the obtained energy intensity value is used to select the layout of the storage subsystem according to the formula

$$E_{\text{ESS final}} = \frac{E_{\text{ex}}}{\text{DoD}}. \quad (4)$$

However, in the traditional method, when calculating ESS parameters, attention is focused only on the technical aspects of solving the problem; the economic component of the project does not appear in the calculations, which is fundamentally important when implementing such systems [31, 32].

Taking into account the economic component will allow the use of a methodology based on minimizing the specific cost of energy storage Levelized Cost of Storage – LCOS [33-35]. This indicator is an alternative to the levelized cost of electricity indicator Levelized Cost of Electricity – LCOE [36] and allows comparing different energy storage systems and alternative solutions, for example, as is done when planning the power plants construction. A detailed state analysis of LCOS indicator calculation, as well as adaptation of this indicator for the tasks solved during the implementation of the ESS in the electrical complexes of the gas industry, is presented in the article [37].

A distinctive feature of the proposed method for calculating LCOS [37] is the ability to take into account the versatility of the ESS, which also corresponds to the purpose of the study:

$$\mathrm{LCOS} = \frac{\mathrm{Capital} + \sum_{t=1}^{T} \frac{OM_t \left(1+i\right)^t + \left(Aux_t\right)\left(1+e\right)^t + Am_t}{\left(1+r\right)^t} - \Delta ST}{\sum_{t=1}^{T} \frac{k_2 Phn\left(1+e\right)^t + MWh_t \left(1+e\right)^t}{\left(1+r\right)^t}}, \quad (5)$$

where Capital – capital costs, thousand rub.; t – operation year number; T – lifetime; OM_t – operating and maintenance costs for the year, thousand rub.; i – inflation rate, p.u.; Aux_t – electricity cost for ESS own needs per year, thousand rub.; e – annual change rate in the cost of electricity, p.u.; Am_t – annual depreciation costs, thousand rub.; r – discount rate, p.u.; P – estimated power of the unit being replaced, kW; k_2 – unit load factor; h – backup unit start-up time, s; n – number of emergency launches per year; MWh_t – amount of energy supplied by the ESS to level the load curve, MW·h; ΔS – reduction in fuel costs, thousand rub.

For the first time, an indicator that allows us to correlate the state of electrical load schedule leveling and changes in fuel consumption by generating equipment has been introduced:

$$\Delta S = 0.537\, \mathrm{C}_0 MWh_t \left(\gamma^{-1} - \gamma_{\mathrm{level}}^{-1}\right), \quad (6)$$

where γ – load curve fill factor (load curve density); γ_{level} – load graph fill factor after leveling (load graph density); C_0 – total fuel costs per year, thousand rub.

The formula (6) allows us to take into account the effect of replacing the rotating reserve and leveling the electrical load schedule, which, in turn, allows us to more accurately calculate the LCOS value.

The generalized methodology for calculating ESS parameters based on adapted traditional methods and methods based on minimizing the specific cost of electricity storage is the following sequence of actions:

1. Calculation of the ESS parameters for replacing the rotating reserve using formulas (1), (3).
2. Calculation of ESS parameters for leveling the electrical load graph at $\gamma_{\mathrm{level}} = 1$ using formulas (2), (4).
3. Calculation of the LCOS indicator using an improved method (5).
4. If the LCOS indicator exceeds the value allowing a positive effect (according to the concept of the development of the market for electricity storage systems in the Russian Federation – 36 rub. / kW·h), it is necessary to recalculate the ESS parameters to align the graph of electrical loads at $\gamma_{\mathrm{level}} < 1$. However, the value of the load graph fill factor after leveling should ensure that the condition for the minimum LCOS value (min {LCOS}) is met.
5. If the LCOS indicator provides a potential positive economic effect, then the ESS parameters used in the calculation can be taken into account for further detailed feasibility study of the use of the selected system.
6. If it is not possible to achieve the minimum LCOS value, it is necessary to abandon a number of functions performed by the ESS and recalculate this indicator. If even in this case the LCOS value exceeds the minimum permissible value that ensures a positive economic effect, then the use of these devices should be abandoned.

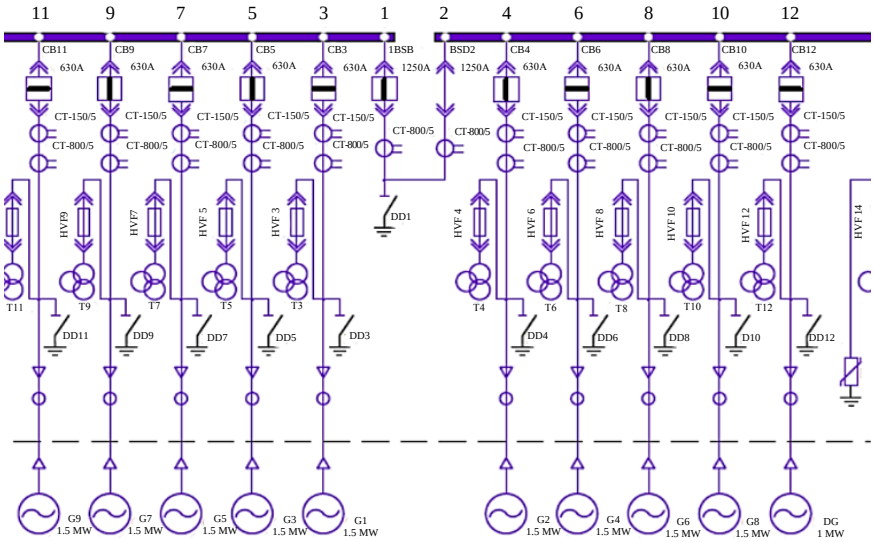

Fig.2. The power plant self-needs operation design scheme
CB – circiut braker; BSB – bus-section breaker; BSD – busbar section disconnector;
CT – current transformer; HVF – high-voltage fuse; DD – disconnecting device;
DG – diesel-generator stand-by set; T – voltage transformer; G – generator

To test the presented methodology, the ESS parameters are calculated using the example a real facility in the gas industry – a standard compressor station "Yarynskaya" of OOO Gazprom Transgaz Ukhta, an element of the design diagram of which is presented in Fig.2. The compressor station (CS) is a modern high-tech gas transportation facility that ensures gas transportation along the northwestern corridor of the PAO Gazprom gas trunkline system. The main electricity consumers at the Yarynskaya CS are gas air cooling units and gas pumping units with gas turbine drives. The power system of this compressor station is completely autonomous, and electricity is supplied from an auxiliary power plant based on nine gas-piston electric units with a capacity of 1.5 MW with an average load of 3-4 MW. Such a load requires the constant use of at least four power units to provide a rotating reserve, and in the event of a shutdown of one of the power units, the distribution of the load among the remaining units without stopping the technological process.

Results discussion

To confirm the ESS implementation economic efficiency, calculated using the given methodology, the integral effect is used – net present value (NPV) and efficiency index. Due to the introduction of an electricity storage system, it is planned to change the number of constantly operating units from four, with load of 70 %, to three, with load 90 %, and also achieve an additional effect from leveling the electrical load schedule by reducing gas consumption.

As a result of the scientific sources [2, 3, 5] analysis it can be concluded that the electrochemical type storage subsystem based on lithium-ion batteries is most promising for use as part of an energy storage system to solve the problems posed in the study, since it allows you to control both the operating modes of electrical grid equipment and network parameters. In this case, the ESS is not just a local buffer of electrical energy, but an active element that directly affects the energy efficiency of power supply.

The following functions can be implemented when using ESS based on lithium-ion batteries – ensuring power quality, managing power consumption, shifting consumption peaks, leveling the load curve, cold reserve – which are fully consistent with the objectives of this study.

Despite the fact that the limiting factor for the drives of this type use was their high cost, it is expected that by 2030 the drives of this type cost will be reduced by four times compared to 2018.

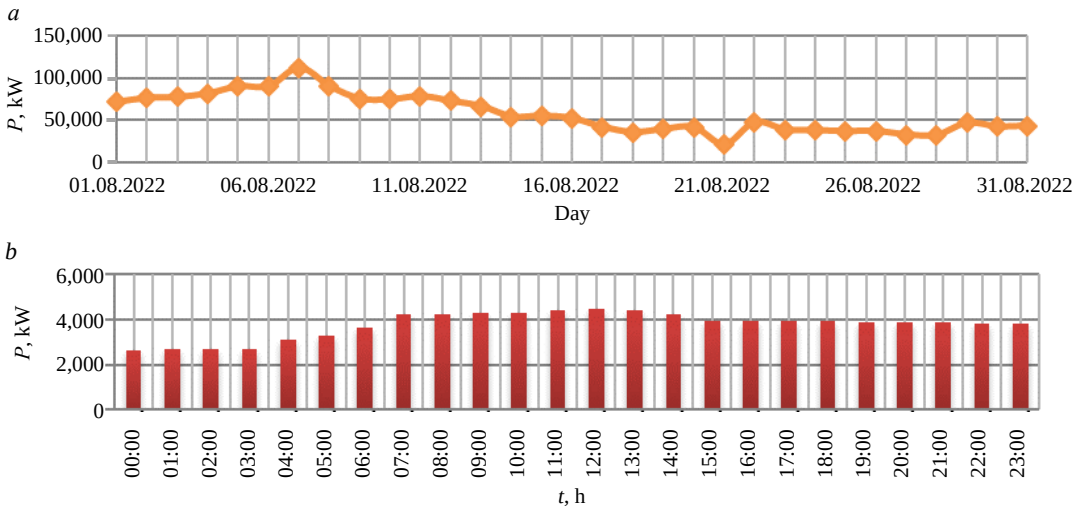

Fig.3. Electrical load schedule of the Yarynskaya CS:
a – the busiest month (August); *b* – busiest day (August 7)

The main parameters of the ESS are calculated according to points 1 and 2 of the proposed methodology. If calculating the ESS power and energy intensity to replace the spinning reserve does not cause difficulties (unit power 1.5 MW; load factor 0.8; start-up time 15 min), then to calculate the parameters for regulating the load schedule, a detailed analysis of the electrical loads of the selected facility is required.

When analyzing the electrical loads of the Yarynskaya CS, it was found that the busiest month is August (Fig.3, *a*), and the busiest day is August 7 (Fig.3, *b*). The averaging period for the electrical load schedule is determined based on the conditions and method of solving the problem. In the case under consideration and for the unification of calculations, the averaging period is taken to be equal to six heating time constants for cable lines with voltages up to 6 kV and higher, supplying workshop transformer substations and distribution devices, which correspond to one hour. At the same time, the specified averaging interval does not contradict the conditions for using the ESS to solve the problem of leveling the electrical load graph – the averaging interval of the load graph should be longer than the battery response time and the discharge time of the minimum battery charge level, but should not exceed the discharge time of the current battery charge level. These conditions ensure that the energy stored in the battery is available to complete the task at hand.

The load graph (Fig.3, *b*) shows that during peak hours of the day, electricity consumption exceeds 4,000 kW/h, which leads to the launch of an additional generator and, accordingly, additional consumption of resources. This can be avoided by redistributing excess energy to the morning minimum hours. Then the ESS produces the same amount of energy as it accumulates ($E_{\text{ESS prod}} = E_{\text{ESS acc}}$), while, according to the electrical load schedule, the power should not exceed 4,000 kW. Power and minimum permissible energy intensity are calculated using formulas (2) and (4), and a load graph is plotted after regulation (Fig.4).

The use of ESS to regulate the electrical load schedule makes it possible to achieve a change in the schedule density from 0.83 to 0.86 with a storage energy intensity of 800 kW·h. However, even

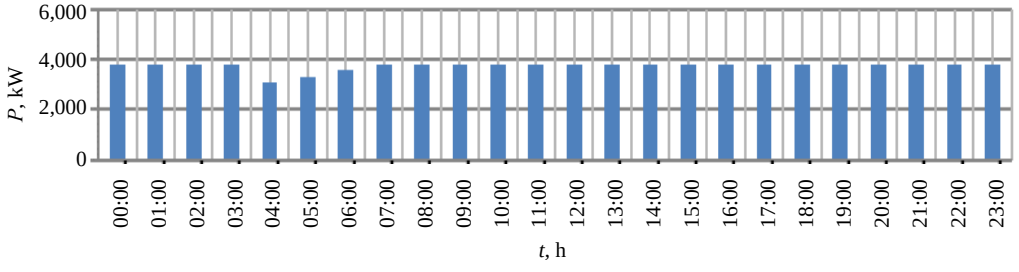

Fig.4. Daily load schedule of the Yarynskaya CS after regulation using the ESS

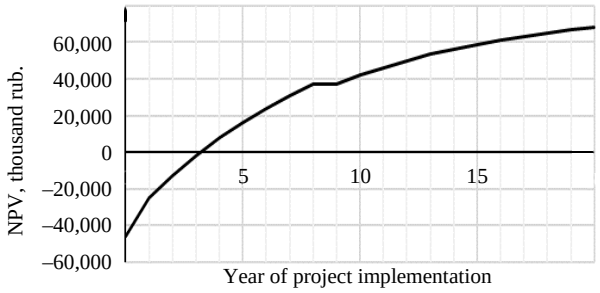

Fig.5. Change in NPV depending on the year project implementation

such a small difference in density will allow gas savings of up to 2,000,000 rub. per year, according to calculation using formula (6).

Next, it is necessary to calculate an improved indicator of the levelized cost of energy storage. Initial data for calculating LCOS: total capital costs (Capital), cost of energy saving energy (including the cost of transportation to the facility), installation, commissioning and testing – 119,541.65 thousand rub.; costs of operation and maintenance (O&M), maintenance and repair – 796 thousand rub.; the cost of electricity for the auxiliary subsystem is 6364.872 thousand rub.; the amount of electricity that the ESS produced over the estimated service life is 6,714 kW·h; design power of the ESS – 1,600 kW; calculated energy intensity of the ESS – 2,745 kW·h; ESS efficiency – 94 %; calculated lifetime – 20 years; discount rate – 0.08 p.u.; annual correction factor for the cost of electricity – 0.06 p.u.; annual inflation – 0.077 p.u.; reduction in fuel costs per year – 23,000 thousand rub. The initial data for calculating capital costs, installation costs and the cost of the ESS are determined based on the operating experience of similar systems by the ESS manufacturer.

Using formula (5), the LCOS indicator was calculated as 20.68 rub./kW·h, which confirms the effectiveness of combining several functions for one ESS and allows us to predict a positive economic effect from the project.

As a result of calculating the indicators of the integral effect without taking into account the reduction in capital repair costs and indicators of depreciation deductions and property taxes, the following values were obtained: NPV – 68.207 million rub.; NPV payback period is three years; internal rate of return – 23 %. The graph of changes in NPV depending on the year of project implementation is presented in Fig.5.

The implementation of the ESS that is calculated using the presented methodology will be cost-effective, since the amount of the integral effect is positive, the payback period according to the NPV will be three years.

Conclusion

The conducted research confirms the possibility of power supply system parameters calculation – power and energy intensity – using the proposed industry methodology, during the development of which previous experience in studying the issue of calculating the parameters of electricity storage systems was generalized and adapted to the peculiarities of gas industry facilities autonomous power supply system functioning.

A distinctive feature of the presented methodology is an attempt to take into account the ESS multifunctionality from a technical and economic point of view when implementing such systems.

Selecting the improved LCOS minimization as the objective function provides stakeholders with the following options:

• selection of the most effective combinations of ESS functions when determining system parameters, especially power and energy intensity;

• comprehensive analysis of technical, economic and financial changes impacts on the energy saving energy systems introduction into the enterprise's power supply system;

• domestic and foreign technologies comparison, determination of various electricity storage technologies competitive advantages.

The LCOS indicator does not limit the calculation to any framework and can become infinitely more complicated by introducing additional coefficients and variables that allow you to take into account a larger number of factors and thereby increase the accuracy of the calculation. Also, in favor of the presented methodology is that the number of tasks associated with the implementation of the ESS will increase every year, so it is advisable to use the LCOS calculation model as a key criterion for determining the ESS composition and the functions performed.

The LCOS indicator should be of an industry nature, since in two identical storage systems operating at different facilities, with different technological processes, the electrical loads nature, and the

power supply system type, it will take different values. The calculation of components that influence the LCOS value, such as the initial capital investment and, especially, the exchange energy intensity of the electricity storage system, should always be adapted to the considered power supply system characteristics.

REFERENCES

1. Baburin S., Turysheva A.V., Kovalchuk M.S. Algorithm for the choice of power supply system rational structure of gas pumping stations. *Journal of Physics: Conference Series*. 2021. Vol. 1753. N 012009. DOI: 10.1088/1742-6596/1753/1/012009

2. Ping-Chang Tsai, Jia-Zhang Jhan, Samuel Sin-Shuan Tang, Cheng-Chien Kuo. Estimation of Energy Storage Requirements in an Independent Power System from an Energy Perspective. *Applied Sciences*. 2024. Vol. 14. Iss. 2. N 814. DOI: 10.3390/app14020814

3. Zyryanov V., Kiryanova N., Korotkov I. et. al. Energy storage systems: russian and international experience. *Energy Policy*. 2020. N 6 (148), p. 76-87 (in Russian). DOI: 10.46920/2409-5516_2020_6148_76

4. Tokarev I.S., Yugay V.F., Tolmachev V.N. et al. Use of electric power storage systems as part of power generating equipment of PJSC Gazprom production facilities power supply systems. *Gas Industry*. 2023. N S3 (853), p. 34-40.

5. Das C.K., Bass O., Kothapalli G. et al. Overview of energy storage systems in distribution networks: Placement, sizing, operation, and power quality. *Renewable and Sustainable Energy Reviews*. 2018. Vol. 91, p. 1205-1230. DOI: 10.1016/j.rser.2018.03.068

6. Fotopoulou M., Pediaditis P., Skopetou N. et al. A Review of the Energy Storage Systems of Non-Interconnected European Islands. *Sustainability*. 2024. Vol. 16. Iss. 4. N 1572. DOI: 10.3390/su16041572

7. Alsalman A.S., Alharbi T., Mahfouz A.A. Enhancing the Stability of an Isolated Electric Grid by the Utilization of Energy Storage Systems: A Case Study on the Rafha Grid. *Sustainability*. 2023. Vol. 15. Iss. 17. N 13269. DOI: 10.3390/su151713269

8. Mercier P., Cherkaoui R., Oudalov A. Optimizing a Battery Energy Storage System for Frequency Control Application in an Isolated Power System. *IEEE Transactions on Power Systems*. 2009. Vol. 24. Iss. 3, p. 1469-1477. DOI: 10.1109/TPWRS.2009.2022997

9. Nesterenko G., Zyryanov V., Neshta A. et al. Methodology for designing electrical energy storage system parameters to reduce enterprise energy costs. Elektroenergetika glazami molodezhi: Materialy XI Mezhdunarodnoi nauchno-tekhnicheskoi konferentsii, 15-17 September 2020, Stavropol, Russia. V 2 t. T. 2. Stavropol: North-Caucasus Federal University, 2020, p. 175-178 (in Russian).

10. Senchilo N.D., Ustinov D.A. Method for Determining the Optimal Capacity of Energy Storage Systems with a Long-Term Forecast of Power Consumption. *Energies*. 2021. Vol. 14. Iss. 21. N 7098. DOI: 10.3390/en14217098

11. Dobush V.S., Belsky A.A., Skamyin A.N. Electrical Complex for Autonomous Power Supply of Oil Leakage Detection Systems in Pipelines. *Journal of Physics: Conference Series*. 2020. Vol. 1441. N 012021. DOI: 10.1088/1742-6596/1441/1/012021

12. Nian Shi, Yi Luo. Energy Storage System Sizing Based on a Reliability Assessment of Power Systems Integrated with Wind Power. *Sustainability*. 2017. Vol. 9. Iss. 3. N 395. DOI: 10.3390/su9030395

13. Sioshansi R., Madaeni S.H., Denholm P. A Dynamic Programming Approach to Estimate the Capacity Value of Energy Storage. *IEEE Transactions on Power Systems*. 2014. Vol. 29. Iss. 1, p. 395-403. DOI: 10.1109/TPWRS.2013.2279839

14. Sokolnikova T.V., Suslov K.V., Lombardi P. Determining optimal energy storage parameters for renewable energy sources integration in isolated energy systems with active consumers. *Proceedings of Irkutsk State Technical University*. 2015. N 10 (105), p. 206-211 (in Russian).

15. Fossati J.P., Galarza A., Martín-Villate A., Fontan L. A method for optimal sizing energy storage systems for microgrids. *Renewable Energy*. Vol. 77, p. 539-549. DOI: 10.1016/j.renene.2014.12.039

16. Stepanenko V.P. Design of energy storage units for compound propulsion systems. *Mining Informational and Analytical Bulletin*. 2016. N 8, p. 166-174 (in Russian).

17. Gusev Y.P., Subbotin P.V. Novel method for sizing and placement of energy storage systems in distribution grids. *Bulletin of South Ural State University. Series "Power Engineering"*. 2019. Vol. 19. N 2, p. 48-61 (in Russian). DOI: 10.14529/power190206

18. Baluev D.Yu., Zyryanov V.M., Kiryanova N.G., Prankevich G.A. Experimental load diagram-based methods of calculating main parameters of energy storage devices. *Proceedings of Irkutsk State Technical University*. 2018. Vol. 22.N 5 (136), p. 105-114. DOI: 10.21285/1814-3520-2018-5-105-114

19. Bakhteev K., Fedotov A., Chernova N., Misbakhov R. Methodological approaches to the choice of energy storage and optimization of their parameters to improve the electric power quality in various types of electric power systems. 10th International Scientific Symposium on Electrical Power Engineering (Elektroenergetika 2019), 16-18 September 2019, Stara Lesna, Slovakia. Stara Lesna: Technical University of Kosice – Department of Electric Power Engineering, 2019, p. 488-493.

20. Shpenst V.A., Belsky A.A., Orel E.A. Improving the efficiency of autonomous electrical complex with renewable energy sources by means of adaptive regulation of its operating modes. *Journal of Mining Institute*. 2023. Vol. 261, p. 479-492.

21. Abramovich B.N., Bogdanov I.A. Improving the efficiency of autonomous electrical complexes of oil and gas enterprises. *Journal of Mining Institute*. 2021. Vol. 249, p. 408-416. DOI: 10.31897/PMI.2021.3.10

22. Belsky A.A., Glukhanich D.Y. Standalone power system with photovoltaic and thermoelectric installations for power supply of remote monitoring and control stations for oil pipelines. *Renewable Energy Focus*. 2023. Vol. 47. N 100493. DOI: 10.1016/j.ref.2023.100493

23. Zhukovskiy Y.L., Kovalchuk M.S., Batueva D.E., Senchilo N.D. Development of an Algorithm for Regulating the Load Schedule of Educational Institutions Based on the Forecast of Electric Consumption within the Framework of Application of the Demand Response. *Sustainability*. 2021. Vol. 13. Iss. 24. N 13801. DOI: 10.3390/su132413801

24. Lavrik A., Zhukovskiy Y., Tcvetkov P. Optimizing the Size of Autonomous Hybrid Microgrids with Regard to Load Shifting. *Energies*. 2021. Vol. 14. Iss. 16. N 5059. DOI: 10.3390/en14165059

25. Bachurin P.A., Gladkov D.S., Zyryanov V.M. et al. Testing of the energy storage system industrial prototype SNE-10-1200-400 working together with the GPU as part of an experimental power system. *Elektroenergiya. Peredacha i raspredelenie*. 2020. N 2 (59), p. 18-24.

26. Dulout J., Jammes B., Alonso C. et al. Optimal sizing of a lithium battery energy storage system for grid-connected photovoltaic systems. 2017 IEEE Second International Conference on DC Microgrids, 27-29 June 2017, Nuremberg, Germany. IEEE, 2017, p. 582-587. DOI: 10.1109/ICDCM.2017.8001106

27. Bardanov A.I., Vasilkov O.S., Pudkova T.V. Modeling the process of redistributing power consumption using energy storage system with various configurations to align the electrical loads schedule. *Journal of Physics: Conference Series*. 2021. Vol. 1753. N 012013. DOI: 10.1088/1742-6596/1753/1/012013

28. Ustinov D.A., Khomiakov K.A. Determination of Dynamic Characteristics for Predicting Electrical Load Curves of Mining Enterprises. *Electricity*. 2022. Vol. 3. Iss. 2. N 162-181. DOI: 10.3390/electricity3020010

29. Belskii A.A., Dobush V.S. Russian lithium-ion batteries characteristics analysis. *Promyshlennaya energetika*. 2019. N 9, p. 25-32.

30. Kuchak S.V., Brovanov S.V. Investigation of Impulse and Continuous Discharge Characteristics of Large-Capacity Lithium-Ion Batteries. *Processes*. 2022. Vol. 10. Iss. 12. N 2473. DOI: 10.3390/pr10122473

31. Fedotov A.I., Fedotov E.A., Abdullazyanov A.F. Use of electrochemical energy storage systems in autonomous power supply systems to reduce fuel consumption of power installations. *Power engineering: research, equipment, technology.* 2021. Vol. 23. N 1, p. 3-17 (in Russian). DOI: 10.30724/1998-9903-2021-23-1-3-17

32. Castro M., Alcanzare., Esparcia Jr.E., Ocon J. A Comparative Techno-Economic Analysis of Different Desalination Technologies in Off-Grid Islands. *Energies*. 2020. Vol. 13. Iss. 9. N 2261. DOI: 10.3390/en13092261

33. Moradi-Shahrbabak Z., Jadidoleslam M. A new index for techno-economical comparison of storage technologies considering effect of self-discharge. *IET Renewable Power Generation*. 2023. Vol. 17. Iss. 7, p. 1699-1712. DOI: 10.1049/rpg2.12704

34. Castro M.T., Esparcia Jr. E.A., Ocon J.D. A Comparative Future Levelized Cost of Storage of Static Electrochemical and Mechanical Energy Storage Technologies in 1-MW Energy and Power Applications. *Chemical Engineering Transactions*. 2022. Vol. 94, p. 355-360. DOI: 10.3303/CET2294059

35. Melnikov V.D., Nesterenko G.B., Lebedev D.E. et al. Problems, aspectsofapplicationandthemethodofcalculatingthe levelized cost of storage. *Vestnik Kazanskogo gosudarstvennogo energeticheskogo universiteta*. 2019. Vol. 11. N 4 (44), p. 30-36 (in Russian).

36. Prokhorov D.A., Semenov E.V. Comparison of the LCOE index of nuclear power plants and thermal power plants on the example of VVER-TOI & PGU-410 power units. *Vestnik nauki.* 2023. Vol. 4. N 6 (63), p. 964-970 (in Russian).

37. Tokarev I.S., Vasilkov O.S., Shklyarskiy Ya.E. et al. Selection of parameters of an electricity storage system based on the criterion of an improved indicator of levelized cost for high-power facilities of Gazprom PJSC. *Scientific Works of the Kuban State Technological University.* 2024. N 2, p. 170-184 (in Russian). DOI: 10.26297/2312-9409.2024.2.15

***Author* Ivan S. Tokarev,** *Candidate of Engineering Sciences, Senior Lecturer, i.s.tokarev@gmail.co, https://orcid.org/0009-0003-2172-3830* (*Empress Catherine II Saint Petersburg Mining University, Saint Petersburg, Russia*).

The author declares no conflict of interests.

ISSN 2411-3336; e-ISSN 2541-9404

JOURNAL OF MINING INSTITUTE

Zapiski Gornogo instituta

Journal homepage: pmi.spmi.ru

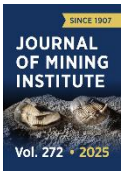

Research article *Energy*

Methodology for managing energy development of production facilities in the gas industry

Anatolii A. Shapovalo
PAO Gazprom, Saint Petersburg, Russia

***How to cite this article*:** Shapovalo A.A. Methodology for managing energy development of production facilities in the gas industry. Journal of Mining Institute. 2025. Vol. 272. N 16378, p 181-190.

Abstract
The current stage of Russia's development is characterized by dynamic changes in the operating conditions of gas industry enterprises, which leads, among other things, to significant adjustments in approaches to the development of energy production facilities. The article examines on the system level the ways to improve energy supply, taking into account the goals and objectives of the development of production facilities from the conditions of solving a single technological problem of the gas industry – high-quality gas supply to consumers. The optimal functioning of energy supply systems, taking into account the peculiarities of technological processes at production facilities, presupposes the development models coordination of production facilities energy complexes with the gas industry enterprises parameters based on an integrated unified information space at all stages of their life cycle. The structure of production facility energy complex and the connections of its elements with related systems are justified taking into account the purposes of their creation and the requirements for production facilities. Problem solving for each system element as well as the exchange of information between equivalent systems is done on the basis of a developed hierarchy of optimization problems adjusted depending on the type of tasks of energy supply improvement of a production facility. Determining the values of parameters and indicators of energy complexes, as well as optimizing the lists and content of work to improve the energy supply of production facilities, is planned to be carried out in accordance with the methodology under consideration using a set of mathematical models.

Keywords
energy supply systems; gas industry; risks; risk-oriented approach; systems approach; energy complex; optimization problems

Received: 01.02.2024 ***Accepted: 02.05.2024*** ***Online: 18.06.2024*** ***Published: 25.04.2025***

Introduction

Energy supply systems are an integral and important infrastructure component that ensures the functioning of gas industry production facilities for various purposes, located throughout the Russian Federation, including remote areas of the Arctic zone.

The gas industry has accumulated a wealth of experience in improving the energy supply of production facilities based on the developed general conceptual approach to their development[1]. The following components are carried out on a permanent basis: analysis of the functioning and implementation of energy-saving measures in energy supply systems; search for innovative solutions, participation in testing and installation of prototype samples of modern power equipment for trial operation at production facilities; research and development work in terms of updating and developing industry standards and standard solutions to improve the efficiency of facilities energy supply.

The transformation of the global economy and energy, the introduction of various types of sanctions, significant changes in the nature of the supply of products, diversification of production lead to dynamic changes in the operating conditions of gas industry enterprises in our country, changes in the nature of development, reconstruction and technical re-equipment (R&TR) of production facilities [1], make a number of issues relevant, including:

[1] Annual report of PJSC Gazprom for 2022. URL: https://www.gazprom.ru/f/posts/56/691615/gazprom-annual-report-2022-ru.pdf (accessed 31.01.2024).

• assessment, using the apparatus of a risk-based approach (RBA), of the impact on the target indicators of enterprises in the production, transportation, underground storage and processing of natural gas and liquid hydrocarbons in the gas industry of the pace and quality of maintenance and repair (M&R), as well as R&TR of energy supply facilities;

• use of this assessment data to develop measures to minimize the consequences of the application of RBA to management in the gas industry;

• development of measures to minimize resource costs at various stages of improving the energy supply of production facilities group and the gas industry as a whole.

The greatest efficiency in solving the problems of developing production facilities energy supply is achieved by creating energy complexes that are optimally functioning, taking into account the peculiarities of technological processes at production facilities, integrated into a single infrastructure and information space of gas industry enterprises. At the same time, the production facility energy complex (PFEC) is understood as a set of technical and software means of general facility energy supply systems and industrial air conditioning systems of structures with installations of electricity external networks, heat-, water supply and sanitation systems, which, through the implementation of an integrated technical solution and optimal control algorithms, including the use of elements of artificial intelligence in management, allows you to obtain the maximum value of the TCI of the PFEC under conditions of applying RBA to management in the gas industry (an integrated indicator of the technical condition ("Technical Condition Index" combines the values of other technical indicators into a value that is used for comparison and evaluation). To determine the indicator of the technical condition of electric power facilities, the physical wear rate is used, manifested in the forms of mechanical wear, corrosion and fatigue of metals, deformation and destruction, changes in the physical and chemical properties of the substance[2].

The optimal solution to the problems of improving the production facilities energy supply is associated with the joint consideration of a significant number of issues with significant uncertainty in the initial information and the inability, in some cases, of using formalized methods for determining individual indicators of energy complexes. In problems of this class, the methodology of system analysis [1-3] using RBA is usually used. As part of the transition to RBA in development management in the gas industry, the Risk Management Policy and the PAO Gazprom Internal Control Policy were developed and approved by the Board of Directors on December 25, 2018. This policy serves as the basis for the formation of the methodology for managing the development of the gas industry energy sector.

To obtain the maximum technical and economic effect in the process of improving energy supply to production facilities in the gas industry, it seems necessary to solve a number of scientific and practical problems in order to develop a methodology for managing energy development:

• Justify the concept for the development of energy supply systems for production facilities of enterprises on the scale of the gas industry, taking into account the provision of target indicators when applying RBA to industry management.

• Develop, as part of a decision support system development, a comprehensive (adaptive) model for determining and forecasting the energy complexes technical indicators for various organizational and financial scenarios for carrying out work to improve the production facilities energy supply.

• Develop standard lists of measures to improve energy supply, allowing obtaining a synergistic effect from optimizing technical solutions and operating modes of energy supply systems of jointly operating production facilities.

• Develop methods that allow you to effectively solve the problems of improving energy supply on the scale of a production facility, enterprise and industry as a whole in the context of applying RBA to management in the gas industry.

[2] Resolution of the Government of the Russian Federation dated May 30, 2023 N 878 "On introducing changes to the methodology for comprehensive determination of technical and economic condition indicators of electric power facilities, including indicators of physical wear and tear and energy efficiency of electric grid facilities". URL: http://publication.pravo.gov.ru/document/0001202306020055 (accessed 31.01.2024).

Overview of the problem

Currently, in world practice, the use of various methods of analysis and the theory of a systems approach for making economic and technical decisions in the oil and gas sector has significantly intensified. In particular, works numbered [4-6] highlight issues related to risk management in energy markets. Articles [7, 8] discuss the advantages and disadvantages of various approaches to risk modeling and management for practical use, as well as tools and strategies for manufacturers, wholesale consumers, investors and specialized participants in risk management in commodity markets.

The ways and political consequences for ensuring sustainable energy development are outlined in some works [9, 10], and in the given investigation [11] a comprehensive methodology of a systematic approach to energy saving processes at an industrial enterprise is considered. The results of the discussion of particular problems of energy saving are presented in works [12-14], and the effectiveness of the implementation of measures to improve energy efficiency is touched upon in works [15, 16].

In scientific work number [17], a fuzzy multi-criteria decision-making structure for assessing the risks of an integrated energy system is considered, sixteen risk factors from economics, technology, politics, society and management are identified, the proposed method is compared with other risk assessment methods, and its advantages are shown. Features of the application of risk management at the stage of digital transformation of industrial enterprises are analyzed in the research work number [18]. The main aspects of decision-making for assessing the risks of energy companies are given in works number [19-21].

An assessment of the consequences of the energy transition for the activities and business models of the oil and gas industry is considered in article number [22], risks during gas production and transportation are given in the following investigations [23-25]. Article [24] substantiates the relevance of risk management in oil and gas companies in modern conditions. Based on the systematization of types of risks, the main risks in the oil and gas business are identified: political, socio-economic, environmental, scientific, and technical ones.

Research works [26-28] contain information on the experience of applying a systematic approach to optimizing the production infrastructure of enterprises. Work [28] outlines the case for proactively managing energy procurement costs and discusses five key levers that support energy optimization and risk management.

The results of modern research on the use of artificial intelligence in the oil and gas industry and its contribution to the development of recommendations for increasing the sustainability of oil and gas projects are presented in the work of [29]. The paper provides information about the most promising applications and methodologies of artificial intelligence that can help solve problems for the sustainable development of the oil and gas industry.

In article [30], the relevance of conducting research in the field of energy efficiency of mineral resource complex facilities due to their specific nature and high-energy intensity is shown, including the use of the function of determining the effectiveness of energy-saving measures based on certain energy efficiency indicators.

The results of research on the development of predictive models based on retrospective data on planned electricity consumption in a region with a significant share of enterprises in the mineral resource complex are presented in the investigation of [31]. Models were obtained based on ensemble machine learning methods (random forest algorithms, gradient boosting XGBoost and CatBoost), as well as a recurrent neural network of long short-term memory (LSTM), which make it possible to create short-term forecasts of power consumption (for a period from one day to a week) with sufficiently high accuracy.

Article [32] is devoted to the development of a SCADA component for the compressor shop of a main gas pipeline. The developed component allows monitoring the characteristics of the gas pumping process selected by the operator. The development is based on the Windows operating system and the integrated environment TRACE MODE (SCADA/HMI).

Work [33] presents the theoretical basis for identifying the features of the use of neural networks at electric power enterprises in the context of digital transformation, as well as an analysis of methods for formalizing artificial intelligence systems for their use as part of automated systems.

In [34], the results of an analysis of the functioning features of autonomous electrotechnical complexes (ETC) are presented, based on the results of which a mathematical model of the ETC of a drilling rig with combined backup power sources was developed.

The main directions of energy development and modernization of power supply systems for technological facilities of the fuel and energy complex are considered in works [35-37]. Issues of improving the operation of the energy sector and ways to improve the quality of energy supply to production facilities in the gas industry are presented in works [38, 39].

It is necessary to develop a methodology for managing the development of the energy sector of production facilities to increase the efficiency of improving the energy sector of the gas industry in the conditions of applying RBA to industry management.

Methodology for managing the production facilities energy development in the gas industry

Optimization of the improving energy supply process is carried out on the basis of an analysis of the goals and objectives of the development of a set of production facilities (enterprises) in the gas industry, solving a single technological problem – high-quality gas supply to consumers – in the following sequence:

• The identification of industrial facilities which the development of energy supply is planned for is carried out on the basis of an analysis of the composition and functional purpose of production facilities (gas field facilities, main gas pipeline facilities, underground gas storage facilities, gas processing plant, gas industry facilities within a business process, etc.), affecting the solution of a single technological problem.

• Boundaries delimitation of the developed (reconstructed) PFEC is carried out on the basis of ensuring the requirements for energy supply from process equipment in all modes of operation of a group of production facilities while ensuring the required level of quality of external communications. Energy supply requirements mean the quantity and quality of energy resources, the level of reliability, safety and economic efficiency of operation, ease of use of PFEC equipment. External connections of PFEC are understood as connections with external systems of power supply, heat supply, water supply and sanitation, with existing and designed components of the facility automation system. The quality of external relations is determined by the composition of the technical and software tools responsible for the functioning of these tools. Depending on the developed requirements and features of the technological problems being solved and the composition of the objects, the set of functions implemented by the PFEC and their boundaries may change.

• The assessment of prospects for the development of PFEC is determined based on the results of a feasibility study, during which the condition and technical level of existing energy supply systems, the effects of the development (reconstruction) of energy complexes for a specific group of production facilities, the costs of their creation, etc. are assessed.

• Formulation of optimization problems for PFEC parameters and development of corresponding optimality criteria. Optimization is carried out according to a complex technical and economic indicator in order to minimize the costs of achieving a given value of the index of the technical condition of energy supply systems during the development of energy supply. The optimization process should involve taking into account the inverse influence of the technical level during the creation and operation of PFEC on the performance of a group of production facilities in the conditions of application of risk-based management principles in the gas industry by determining the individual components of the resulting effect at the pace of technological processes and (or) decision-making processes in order to prepare information for making a comprehensively informed decision on managing the improvement of energy supply.

Determination of the structure of the production facility energy complex and the connection of its elements with adjacent systems based on the formulated goals of creation and requirements for PFEC.

As components of the structure of energy complexes of production facilities, general facility power supply systems (PSS), heat supply (HSS), water supply (WSS), water disposal (WDS), ventilation and air conditioning systems of industrial and household buildings (VAC), including automated

sources, network structure, installations for ensuring the quality of energy resources, purification of source water and wastewater, as well as means of interface with automated systems of a production facility and gas industry enterprise.

It is advisable to divide the PFEC into structural components taking into account the groups of functions they perform for a specific purpose. The composition of structural components and their technical implementation, depending on the requirements for PFEC, the technical level of the existing control system, etc., may vary. An example of the structure and connections of the energy complex of a production facility with the full composition of energy supply systems is shown in Fig.1.

Reducing the dimension of the optimization problem associated with the development of energy supply to a group of production facilities.

Taking into account the variety of technical solutions of existing and energy supply facilities under formation, as well as the fact that changes in individual technical parameters have different effects on the efficiency indicators of energy complexes, the task of optimizing the process of managing their development becomes multidimensional and multicriteria. Reducing the dimension of the optimization problem is possible by replacing the set of real elements of energy complexes and their connections with equivalent systems, models of aggregated PFEC, which retain only those properties of the real system that need to be determined when solving problems of its functioning and optimization.

The number of levels of the equivalent systems hierarchy and their number at each level of the hierarchy for different scenarios for improving groups of production facilities energy supply depends on the complexity of the real group of energy complexes under study, as well as on the scenario conditions for financing the process of improving energy supply.

Units (as opposed to the structural components of individual subsystems) can be implemented both within a separate PFEC, and within a group of energy complexes of jointly functioning production facilities of a gas industry enterprise or on the scale of the gas industry as a whole. The latter depends on the requirements for the goals, structure and operation,

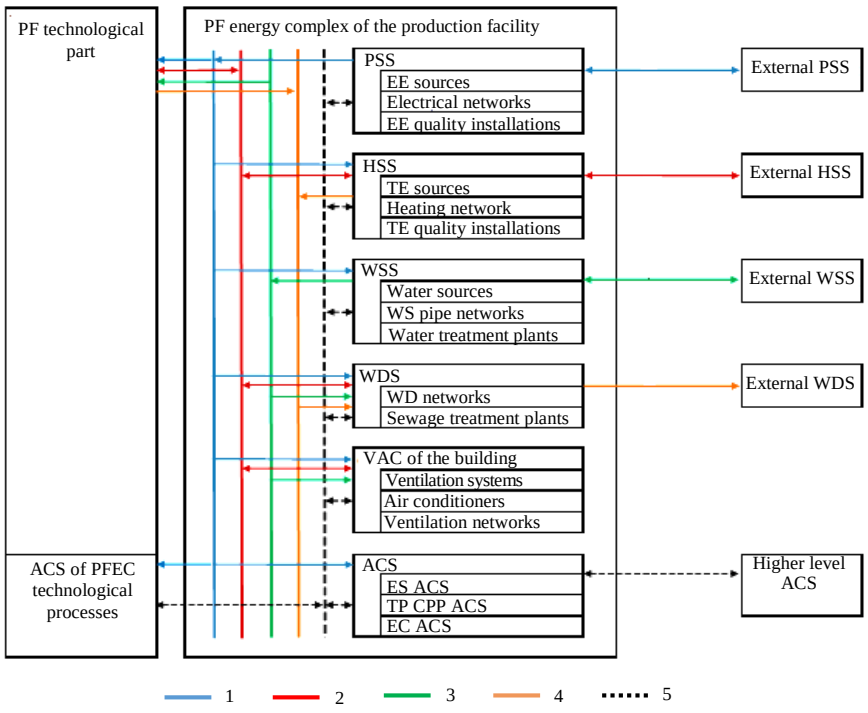

Fig.1. Structure of the production facility energy complex with a complete set of energy supply systems

1 – electrical energy (EE); 2 – thermal energy (TE);
3 – source water (W); 4 – sewer drains (WD); 5 – information flows;
ES ACS – energy supply automated control system;
ACS TP CPP – ACS for technological processes of a captive power plant

reliability, safety, maintenance and repair of components of the PFEC, etc. The aggregation of the PFEC is carried out due to the order of measures implementation for the energy supply development.

Determination of the composition of tasks for equivalent systems.

The hierarchy of optimization problems is built on the basis of a hierarchy of equivalent systems. It is created with the aim of streamlining optimization problems at each stage of improving the production facilities energy supply. At the same time, optimization problems for each stage differ in depth and detail of development. From the point of view of the hierarchy of tasks to be solved, the process of using PFEC is divided into stages: research, creation, operation (due to possible combinations of operating modes of a group of production facilities and external power supply systems).

The optimal distribution of functions between structural components and the possibility of their redistribution depending on the stage of reconstruction (creation) and the operating mode of the PFEC within the framework of improving energy supply makes it possible to create redundant groups of energy complexes.

This is necessary in cases of improving energy supply in several stages, significant changes in energy supply requirements, changes in the composition of operating sources, networks of a production facility, and external energy supply systems, and among others can be implemented by means of intelligent automation systems.

Determination of the composition of indicators and methods of exchange of energy resources and information between equivalent systems.

The structural components of the PFEC exchange with each other and external systems (power supply, higher-level automation, etc.), energy resources and information, which under certain condition can be divided into initial, intermediate, sought and reverse; into external and internal [3].

At the stages of the PFEC life cycle, three groups of optimization problems are solved:

• the task of optimizing the requirements for power supply of the PF, depending on the current TCI and achievable by means of reconstructing the TCI with the allocated amount of funding. The solution to the problem is provided by information on level 1 feedback (FB-1) for each level of the hierarchy of optimization problems of PFEC from hierarchy level 1 (gas industry FB-1.1) to hierarchy level 5 (production facility FB-1.5);

• the task of optimizing the list and scope of work for measures to develop the energy supply of PFEC in the conditions of given restrictions on financing the program to achieve the required level of TCI (general and/or for individual components) at the stage of creating the PFEC. The solution to the problem is provided by information on level 2 feedback (FB-2.1 – FB-2.5);

• the task of optimizing the list and scope of work for measures to develop the energy supply of PFEC under the given restrictions on financing the program to achieve the required level of TCI (general and (or) individual components) at the stage of operation of the PFEC. The solution to the problem is provided by information on level 3 feedback (FB-3.1 – FB-3.5).

In conditions of significant uncertainty in the initial information and the lack of strict formalization in determining a number of indicators, optimization problems in the process of managing the development of energy supply to production facilities in the gas industry are solved using combined methods – methods of narrowing Pareto-optimal outcomes and expert methods. The hierarchy of optimization problems at the stages of development of energy complexes of production facilities in the gas industry is shown in Fig.2.

Analysis of balances of production and consumption of energy resources and information that individual units must exchange between each other and external systems at various stages of the life cycle of PFEC will allow in the future to more reasonably solve the optimization problem of determining priorities in the implementation of measures to improve energy supply and the distribution of functions between units and individual structural components of energy complexes.

The search for the optimal list and scope of work for development activities of PFEC is associated with determining the current value of TCI PFEC for various levels of the hierarchy with combinations of the composition and content of activities that can be implemented using the allocated funds for the program to achieve the required level of TCI energy supply.

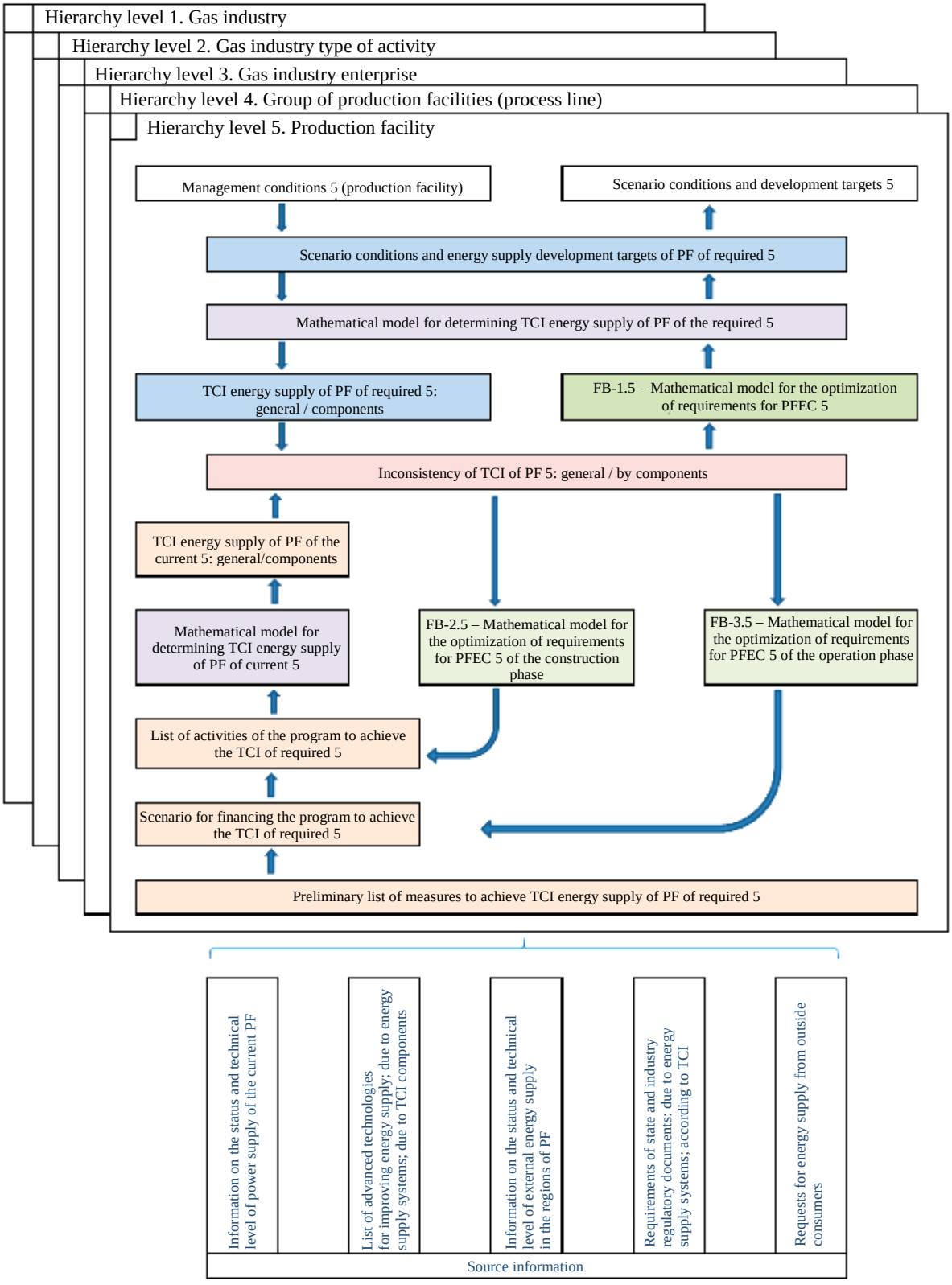

Fig.2. Hierarchy of optimization problems at the stages of development of PFEC of the gas industry

Extreme values of individual indicators of PFEC and energy supply as a whole, in most cases, are not the sum of extreme values of indicators of individual elements and subsystems [3]. If there are several irreducible criterion indicators, it is necessary to rank the criteria, highlighting one of them as the main one, and using the rest as restrictions.

The composition of mathematical models for determining the values of parameters and indicators of energy complexes, as well as optimizing the lists and content of work on the development of energy supply to production facilities.

The set of mathematical models must correspond to the list of problems solved as part of the development of energy supply to the PF. The general model should make it possible to transform the values of the specified production facilities target indicators (PFTI) into the required target indicators of energy supply PF (TIES) and then into the value of the required index of the technical condition of the energy supply of a group of production facilities (ITCESgr.pr.f), the functioning of which directly affects achieving the specified PFTI.

With the help of the model it is possible to assess the value of an integral indicator of energy supply for a given level of the ITCESgr.pr.f hierarchy and the value of its component indicators: the availability of energy resources; energy quality; reliability of energy supply; safety of energy supply; energy efficiency of energy supply; ease of operation (economical operation) of energy complexes.

The basis for the energy supply development process should be the following mathematical models:

• a model for determining the current TCI power supply of a given group of PF, as a function of the totality of initial information presented in Fig.2;

• a model for optimizing the list and scope of work to achieve the required level of TCI energy supply in the conditions of application of RBA to management in the gas industry (stage of creating an PFEC). This model should make it possible to build families of trends in the integral indicator and components of the energy supply TCI for the analyzed group of PF for various combinations of lists and scope of work, as well as capital investments in the program to achieve a given level of TCI PF for all levels of the hierarchy, taking into account the design and actually received in the creation process indicators of energy supply facilities;

• a model for optimizing the list and scope of work to achieve the required level of TCI energy supply in the conditions of application of RBA to management in the gas industry (operation stage of the created PFEC). In contrast to the models of the creation stage, models of the operation stage of PFEC evaluate various options for achieving the required level of TCI energy supply, including taking into account the optimization of the joint functioning of the created PFEC at a certain level of their operation.

The complex should include adaptive mathematical models that require the minimum required amount of initial information and allow:

• justify the level of requirements for the distribution of the balance of production and ensuring the quality of energy resources between sources and installations of PFEC and external energy supply systems, as well as to the information properties of individual structural components of PFEC;

• determine the necessary communication capabilities of the structural components of PFEC to ensure distributed generation and ensure the quality of energy resources at the required level;

• predict the implementation of given scenario conditions, loads on individual energy supply systems, etc. in order to make informed decisions on optimizing the list and scope of work to improve energy supply.

The results of modeling energy supply development processes are the basis for developing a structured proposal from a decision support system in order to optimize the process of improving the energy supply of industrial facilities in the industry.

Discussion

Using the principles of the methodology described above, the Development Concept and the Comprehensive Target Program for the reconstruction and technical re-equipment of the energy sector of production facilities in the gas industry were developed.

The methodology was a tool for the logical organization of research and a means of calculating indicators, which made it possible, based on solving a multi-criteria optimization problem, to formulate a general vision of the vector of energy supply development in the context of dynamic changes in business conditions and restrictions on financing development programs, as well as to formulate an optimal list and

sequence of implementation of reconstruction measures energy of production facilities in order to achieve the maximum value of the index of technical condition of energy facilities on an industry scale.

Previously, the main tool for developing comprehensive programs was only methods for determining indicators of the economic efficiency of reconstruction measures, which did not take into account important technical aspects of the functioning of energy complexes.

To date, the problems of developing mathematical models for finding correspondence between target production indicators of various levels and the minimum required technical level of energy supply for groups of production facilities of industry enterprises have not been solved, which is the subject of further scientific research**.**

Conclusion

Dynamic changes in business conditions and the use of RBA in the gas industry have led to the need to develop a methodological approach to improve the efficiency of managing the energy development of production facilities, based on a comprehensive analysis of the parameters of jointly functioning technological installations and energy complexes of production facilities in order to solve business problems.

The methodology developed by the author for managing the development of the energy sector of production facilities is based on the provisions of system analysis and allows optimizing, at the pace of changing operating conditions, the process of improving energy supply by solving a multicriteria optimization problem when determining the technical condition index of PFEC under conditions of restrictions.

The use of the provisions of the developed methodology made it possible to substantiate at the system level the optimal list and priority of implementation of measures to improve the energy sector of production enterprises in the gas industry as part of the development of a program for the reconstruction and technical re-equipment of the industry's energy supply.

Further scientific research is associated with the development, based on the provisions of the proposed methodology, of a decision support system, which allows, by structuring heterogeneous information about the current state and possible options for improving the energy sector of the gas industry, to optimize the process of solving business problems of production facilities within the framework of the implementation of various scenario conditions for the development of the industry.

REFERENCES

1. Nikiforov S.I., Medvedev K.A., Gitarskiy M.L. Russian oil and gas industry under fourth energy transition and climate change. *Fundamental and Applied Climatology*. 2022. Vol. 8. N 3, p. 74-87 (in Russian). DOI: 10.21513/2410-8758-2022-3-74-87

2. Markelov V.A., Bronnikov A.N., Shapovalo A.A. et al. Concept of developing the power system of production facilities under dynamically changing conditions applied to business activities of gas industry companies. *Gas Industry Journal*. 2023. N S3 (853), p. 8-11 (in Russian).

3. Voropai N.I., Podkovalnikov S.V., Trufonov V.V. et al. Justification for the development of power systems: methodology, models, methods, their use. Novosibirsk: Nauka, 2015, p. 448 (in Russian).

4. Ishutina T.A. Risk management in energy companies of the Russian Federation. Developing the energy agenda for the future: Sbornik dokladov Mezhdunarodnoi nauchno-prakticheskoi konferentsii dlya predstavitelei soobshchestva molodykh inzhenerov TEK, 10-11 dekabrya 2021, Sankt-Peterburg, Rossiya. St. Petersburg: Sankt-Peterburgskii gosudarstvennyi elektrotekhnicheskii universitet "LETI" im. V.I.Ulyanova (Lenina), 2021, p. 339-343 (in Russian).

5. Handbook of Risk Management in Energy Production and Trading. Ed. by R.M.Kovacevic, G.Ch.Pflug, M.T.Vespucci. New York: Springer, 2013, p. 505. DOI: 10.1007/978-1-4614-9035-7

6. Swindle G. Valuation and Risk Management in Energy Markets. Cambridge: Cambridge University Press, 2014, p. 487. DOI: 10.1017/CBO9781139568302

7. Burger M., Graeber B., Schindlmayr G. Managing Energy Risk. A Practical Guide for Risk Management in Power, Gas and Other Energy Markets. Wiley, 2014, p. 448. DOI: 10.1002/9781118618509

8. Kamchatova E. Risk management of generating energy companies. *Vestnik Universiteta*. 2018. N 2, p. 50-56 (in Russian). DOI: 10.26425/1816-4277-2018-2-50-56

9. Bakhteeva N.Z., Shatskikh Z.V. Some aspects of risk management in the electric power industry. *Bulletin of the Kazan State Energy University*. 2015. N 1 (25), p. 111-124 (in Russian).

10. Xianlei Chen, Manqi Wang, Bin Wang et al. Energy Consumption Reduction and Sustainable Development for Oil & Gas Transport and Storage Engineering. *Energies*. 2023. Vol. 16. Iss. 4. N 1775. DOI: 10.3390/en16041775

11. Sucic B., Peckaj M., Tomsic Z., Uranic J. Systematic approach for improving energy efficiency in industrial facilities, from energy audit to practical implementation – case study production of autoclaved aerated concrete. *E3S Web of Conferences*. 2019. Vol. 116. N 00083. DOI: 10.1051/e3sconf/201911600083

12. Kelchevskaya N.R., Shirinkina E.V., Atlasov I.V. Assessing energy efficiency factors in industrial companies. *IOP Conference Series: Materials Science and Engineering*. 2020. Vol. 862. N 042001. DOI: 10.1088/1757-899X/862/4/042001

13. Tarasenko V.N., Denisova Yu.V. The problem of energy conservation in Russia. *Bulletin of Belgorod State Technological University named after V.G.Shukhov.* 2016. Vol. 1. N 11, p. 63-68 (in Russian). DOI: 10.12737/22375

14. Ulyasheva V.M., Ponomarev N.S., Martyanova A.Yu., Sukhanova I.I. Energy saving at oil and gas production and transportation facilities. St. Petersburg: Sankt-Peterburgskii gosudarstvennyi arkhitekturno-stroitelnyi universitet, 2022, p. 216.

15. Hashim K.M., Hassim Mimi H., Ng D.K.S., Ten J.Y. Leading Energy Performance Indicator: Tracking of Energy Management Systems in Oil and Gas Companies. *ASM Science Journal*. 2019. Vol. 12, p. 16. DOI: 10.32802/asmscj.2019.312

16. Arriola-Medellín A.M., López-Cisneros L.F., Aragón-Aguilar A. et al. Energy efficiency to increase production and quality of products in industrial processes: case study oil and gas processing center. *Energy Efficiency*. 2019. Vol. 12. Iss. 6, p. 1619-1634. DOI: 10.1007/s12053-019-09803-0

17. Gasumov E., Gasumov R., Suleymanov G., Gurbanov K. Risk management in the production and transportation of natural gas under the conditions of the economic crisis in the energy market. Reliability: Theory & Applications. The Fourth Eurasian Risk Conference and Symposium, 11-13 October 2022, Baku, Azerbaijan. 2022. Vol. 17. Special Issue 4 (70), p. 502-508.

18. Pashchenko D.S., Komarov N.M. Risk Management as a Key Element in the Digital Transformation of an Industrial Enterprise. *The World of New Economy.* 2021. Vol. 15. N 1, p. 14-27. DOI: 10.26794/2220-6469-2021-15-1-14-27

19. Sterev N., Biolcheva P. Market Mechanisms for Risk Management in Energy. *Economic Alternatives.* 2022. Iss. 1, p. 132-141. DOI: 10.37075/EA.2022.1.08

20. Nazarova F., Voropayeva T., Horobets N., Sokolova O. Energy risk management in urban projects management. *International Journal of Human Capital in Urban Management*. 2023. Vol. 8. Iss. 2, p. 143-160. DOI: 10.22034/IJHCUM.2023.02.01

21. Rahmani J. The main approaches to evaluating the effectiveness of applying the risk analysis and management methodology at energy company. *T-Comm.* 2022. Vol. 16. N 9, p. 46-55. DOI: 10.36724/2072-8735-2022-16-9-46-55

22. Mastepanov A.M. Energy transition: what should the oil and gas world get ready for. *Problems of economics and management of oil and gas complex.* 2019. N 10 (178), p. 5-14 (in Russian). DOI: 10.33285/1999-6942-2019-10(178)-5-14

23. Londoño A.A., Velásquez J.D. Risk Management in Electricity Markets: Dominant Topics and Research Trends. *Risks*. 2023. Vol. 11. Iss. 7. N 116. DOI: 10.3390/risks11070116

24. Lenkova O.V. Risk management of oil and gas company in terms of strategic transformations. *Espacios.* 2018. Vol. 39. N 6, p. 30.

25. Babakov A.V., Saulin A.D. Identification and classification of risks gas transmission companies. *Voprosy ekonomiki i prava*. 2018. N 10 (124), p. 75-83 (in Russian).

26. Groten M., Gallego-García S. A Systematic Improvement Model to Optimize Production Systems within Industry 4.0 Environments: A Simulation Case Study. *Applied Sciences*. 2021. Vol. 11. Iss. 23. N 11112. DOI: 10.3390/app112311112

27. Anthony Paul, Lawrence Kelvin, Kelvin Brown. Optimizing IT Growth: Strategies for Building and Scaling Robust Infrastructure Systems. *Ladoke Akintola University of Technology*. URL: https://www.researchgate.net/publication/377447014 17.01.2024 (accessed 16.02.2024).

28. Bryan G., Carlson Ch., Gaponenko S., Mitra Sh. The Benefits of Modeling and Optimizing Production Systems: An Application on Civil Infrastructure Projects. URL: https://www.curt.org/2023/10/30/the-benefits-of-modeling-and-optimizing-production-systems-an-application-on-civil-infrastructure-projects/ (accessed 16.02.2024).

29. Waqar A., Othman I., Shafiq N., Mansoor M.S. Applications of AI in oil and gas projects towards sustainable development: a systematic literature review. *Artificial Intelligence Review*. 2023. Vol. 56. Iss. 11, p. 12771-12798. DOI: 10.1007/s10462-023-10467-7

30. Shklyarsky J.E., Zamyatina E.N., Zamyatin E.O. Evaluation of the energy efficiency of the electrotechnical complex. *News of the Tula state university. Technical sciences.* 2020. Iss. 3, p. 339-347 (in Russian).

31. Klyuev R.V., Morgoeva A.D., Gavrina O.A. et al. Forecasting planned electricity consumption for the united power system using machine learning. *Journal of Mining Institute.* 2023. Vol. 261, p. 392-402.

32. Ilyushin Yu.V., Afanaseva O.V. Development of Scada-model for trunk gas pipeline's compressor station. *Journal of Mining Institute.* 2019. Vol. 240, p. 686-693. DOI: 10.31897/PMI.2019.6.686

33. Unizhaev N.V. Particularities of the introduction of neural networks and artificial intelligence systems at power companies. *Russian Journal of Innovation Economics.* 2023. Vol. 13. № 1, p. 215-232 (in Russian). DOI: 10.18334/vinec.13.1.116945

34. Chervonchenko S.S., Frolov V.Ya. Research of the operation of an autonomous electrical complex with a combined composition of backup power sources. *Power engineering: research, equipment, technology.* 2022. Vol. 24. N 4, p. 90-104 (in Russian). DOI: 10.30724/1998-9903-2022-24-4-90-104

35. Bogachkov I.M., Khamitov R.N., Valiev M.K. The Choice of the Optimal Voltage Class of Gas Field Electricity Supply System. *Electrotechnical Systems and Complexes.* 2020. N 4 (49), p. 35-41 (In Russian). DOI: 10.18503/2311-8318-2020-4(49)-35-41

36. Saushev A.I., Erazumov M.I., Romanov L.R. et al. Intelligent control electric power system oil fields. *Avtomatizatsiya i IT v neftegazovoi oblasti*. 2023. N 4 (54), p. 30-40 (in Russian).

37. Tokarev I.S., Yugay V.F., Tolmachev V.N. et al. Use of electric power storage systems as part of power generating equipment of PJSC Gazprom production facilities power supply systems. *Gas Industry Journal.* 2023. N S3 (853), p. 34-40 (in Russian).

38. Chekanskiy A.V., Shirshov D.N., Markova V.N. et al. Prospects for the use of nuclear power generation sources at PJSC Gazprom facilities. *Gas Industry Journal.* 2024. N 3 (862), p. 74-83 (in Russian).

39. Shapovalo A.A., Konoplev T.F., Averyanov V.K. et al. Ways to improve the quality of energy supply for production facilities of PAO Gazprom in modern conditions. *Nauka i tekhnika v gazovoi promyshlennosti*. 2022. N 2 (90), p. 93-101.

***Author* Anatolii A. Shapovalo,** *Candidate of Engineering Sciences, Head of Department, An19660106@yandex.ru (PAO Gazprom, Saint Petersburg, Russia).*

The author declares no conflict of interests.